



**HAL**  
open science

# Lithium/Sulfur batteries : development and understanding of the working mechanisms

Sylwia Walus

► **To cite this version:**

Sylwia Walus. Lithium/Sulfur batteries: development and understanding of the working mechanisms. Other. Université Grenoble Alpes, 2015. English. NNT : 2015GREAI020 . tel-01212711

**HAL Id: tel-01212711**

**<https://theses.hal.science/tel-01212711>**

Submitted on 7 Oct 2015

**HAL** is a multi-disciplinary open access archive for the deposit and dissemination of scientific research documents, whether they are published or not. The documents may come from teaching and research institutions in France or abroad, or from public or private research centers.

L'archive ouverte pluridisciplinaire **HAL**, est destinée au dépôt et à la diffusion de documents scientifiques de niveau recherche, publiés ou non, émanant des établissements d'enseignement et de recherche français ou étrangers, des laboratoires publics ou privés.

## THÈSE

Pour obtenir le grade de

## DOCTEUR DE L'UNIVERSITÉ DE GRENOBLE

Spécialité : **Matériaux, Mécanique, Génie civil, Electrochimie**

Arrêté ministériel : 7 août 2006

Présentée par

**Sylwia WALUŚ**

Thèse dirigée par **Fannie ALLOIN** et  
co-dirigée par **Céline BARCHASZ** et **Jean-Frédéric MARTIN**

Préparée au sein du Laboratoire d'Electrochimie et de  
Physicochimie des Matériaux et Interfaces (LEPMI) et du  
Laboratoire des Générateurs Innovants (CEA-LITEN),  
dans l'École Doctorale I-MEP<sup>2</sup>

## Accumulateur Lithium/Soufre: développement et compréhension des mécanismes électrochimiques

Thèse soutenue publiquement le **15 janvier 2015**, devant le jury  
composé de :

**Monsieur Jean-Marie TARASCON**

Professeur, Collège de France • Paris, Président du jury

**Monsieur Robert DOMINKO**

Assistant Prof., National Institute of Chemistry • Ljubljana, Rapporteur

**Monsieur Lorenzo STIEVANO**

Professeur, ICGM • Montpellier, Rapporteur

**Madame Fannie ALLOIN**

Directeur de recherche, LEPMI • Grenoble, Directeur de thèse

**Madame Céline BARCHASZ**

Ingénieur-chercheur, CEA-LITEN • Grenoble, Co-encadrant de thèse

**Monsieur Jean-Frédéric MARTIN**

Ingénieur-chercheur, CEA-LITEN • Grenoble, Co-encadrant de thèse

**Monsieur Eric LAFONTAINE**

Responsable scientifique adjoint, DGA • Bagneux, Invité

**Monsieur Thierry LE MERCIER**

Directeur de recherche, SOLVAY • Aubervilliers, Invité





“Forget about all the reasons why something may not work.  
You only need to find one good reason why it will.”

...To my Mother



# Acknowledgements

Finally! The work has been accomplished ☺ When I actually think about all the people I am grateful to have met during this ‘PhD journey’ and who helped me (in different ways) to be where I am now, I am afraid I will need another chapter to add, to express myself well!

In a first place I would like to express my gratefulness (which cannot be measured in any scale!) to the persons who had taken my hand and went with me through this long adventure called ‘Lithium/Sulfur discovery’. Apart from their scientific knowledge, which they have transferred to me, and without which this thesis manuscript will not be in this (excellent quality☺) shape, they gave me something much more valuable! They always have been next to and for me, always believing in me and my work. And when necessary (yes, there obviously were some few bad moments of doubts and ‘thesis crisis’), they were there to bring me, my faith and motivation back on the correct track. So I would like just to say: Fannie Alloin (my thesis director), Céline Barchasz and Jean-Frédéric Martin (my co-supervisors) – Thank you! Fannie, thank you for your guidance, patience with my ‘lack of knowledge’, your humor, your brilliant advices, millions of hours spent in the evenings on never ending discussions and corrections, for your ‘mais non, on vas arriver!’, which every time made me feel so reassured. Céline, thank you for having always time for me, no matter what! For the discussion about science and not only, ideas you had shared with me. Your evenings you had to sacrifice for working on my writings. But most of all, thank you for this friendship that we built step by step, and for all the moments we had shared together. Jean-Fred, my ‘translation’ helper. Thank you for your help with everything, whenever I asked.

Although not on the ‘official’ list of my supervisors, but treating me as if I was their student, and spending their time to resolve the mysterious mechanisms hidden in my results☺ Jean-Claude Lêpretre and Renaud Bouchet, thank you for your time, the discussions and your brilliant ideas that I implemented in this work. Renaud, you actually made me understand and pretty like impedance☺ Jean-François Colin, I hope I didn’t bother you too much with always the same questions I had! Thank you so much for your help with these ‘Synchrotrons’ stories☺

I would also like to thank to DGA (Direction Générale de l’Armement) and INSTN (Institut National des Sciences et Techniques Nucléaires) for the financial founding of my PhD thesis.

I am also very grateful to the jury members who agreed to come and evaluate my work, despite their busy agenda. Thank you all for turning the part of usually ‘stressful questions’ into a fruitful discussion. To Prof. Jean-Marie Tarascon (Collège de France) – the president of the jury, to Dr. Robert Dominko (NIC, Ljubljana) and Prof. Lorenzo Stievano (ICGM, Montpellier) – the reporters, to Dr. Eric Lafontaine (DGA) and Dr. Thierry Le Mercier (Solvay) – the invited guests.

As long as the thesis by itself was not always the easiest experience, coming to work was a great pleasure every day! That is because of the great people who are making it all! I am so grateful that I had the chance to be a part of the ‘LCPB’ team for these last years. In particular,

the (top) chef Sébastien Patoux – despite his super busy schedule (yes yes, almost running on the corridors!), always having time to talk and listen to the problems. The best poulette ever KiKi Kim (officially – our secretary), whose optimism, energy and motivation was spread everywhere. My particular thoughts to my ‘office mate’ DanDanDanielll ooooo ☺, who only looks like you better don’t mess with him, but inside is the kindest person ever. A huge thank to all members of the laboratory for making these 3 years in CEA (and obviously after the working hours☺) so special, but most particularly to: Greg (and his ammonite; the master of making loud ambiance in salle café), Carol B. (possibly a McGyver in her previous life), Djamel (your ‘funny girl’), Jess and Aurore (little gossips at the tea time), JiBéééé (yes, we do have electricity in Poland!)), Justin (not Biber!), Nikita (kiwi), Aurélian, Sébastien L, Sébastien M, Claude, Eric, Benoît, Sylvie (my EC-Lab master), Barbara L., Fred, Elise & Tibo, Jérémie, Pierre Etienne, Irina & Vasily, David.

Although I did not manage to spend too much time in my other ‘équipe’ of LEPMI, I really enjoyed being there and could only regret that not enough. Thank you Val, Cristina, Thibaut, Laure, Alice (good luck☺), Marie - for always warm welcoming me there.

Apart from developing the ‘science’ I think I did much better job in developing the ‘girl power friendships’. My special thoughts to Mélody (my personal thesis’ printer), Ewelina (my polish soulmate), Ola (my polish soulmate nb. 2), Céline (yes yes, a supervisor can be a friend at the same time☺). To the girls with who vacation in Marseillan was simply a joyfull blast: Hanaa (ma petite! merci pour tout!), Adriana (ma chérie; thanks for sharing your kiné with me☺), Ségolene (who speaks the most proper French in the world). Girls: je vous aime comme un camion et ce n’est pas péjoratif ☺! Léa (ma belle), we can do it and we did it!!! And remember, what happened in Florida stays there. And at the end, like the two cherries on the cake: mes drôles de dames: LBa & BBi! Laura – my beloved ‘latarnia morska’ forever, and Barbara – my little mature girl! You all are always in my heart, no matter where I am.

And my further thoughts to the people with whom I probably spent the most time while having apéro, soirée, going on the weekend trips, repas Noël... simply enjoying my ‘after work’ time: Dodo & Célouch, Radyi & Eugenie, Florie, Ćwiekliński, Benji, Christoph, Toma Pietri & Cécile, Fannix & Itscant, Dana & Fabien, Tony & Julia, Cyril & Aurore, Cédric & Aurélie & Maxance.

I wouldn’t be actually here where I am now without my parents, but mostly – without support of my Mum – my best friend, my soulmate, the only person in this world who knows how to cheer me up immediately and whose optimism was spreading to me when I felt lost. Mamusiu, kocham Cię! I also send my thoughts to my ‘french’ family, who always believed in me and they are all always impressed with my French speaking skills☺ Thank you Anne and André for being with me during this stressful but so joyful D-Day of the ‘soutenance’.

And finally, my thanks to the one who knows me like no one else (even better than my Mum☺), and even though, despites my ‘bad humors’ sometimes, he is still there next to me and he doesn’t actually give up☺ My Charlie (Moje Koko, Mój Gayotek), thank you for your support, your help, for the fact that you are simply here....

# Table of context

<b>General introduction .....</b>	<b>9</b>
<b>Chapter 1: Literature review .....</b>	<b>13</b>
1.1. Introduction to Li-ion batteries .....	13
1.2. Introduction to Lithium/Sulfur Batteries .....	15
1.2.1. Principles and working mechanism .....	16
1.2.2. Li/S system limitations .....	19
1.2.2.a) Positive electrode issues .....	20
1.2.2.b) Electrolyte related limitations.....	21
1.2.2.c) Negative electrode issues.....	22
1.3. State of the art and the strategies undertaken for Li/S system improvements .....	22
1.3.1. Positive electrode .....	23
1.3.1.a) Sulfur/carbon composite architecture .....	23
1.3.1.b) The effect of a binder.....	25
1.3.1.c) The effect of sulfur loading vs. sulfur fraction .....	27
1.3.1.d) Carbon based current collectors .....	29
1.3.1.e) Alternative positive electrode: lithium sulfide (Li <sub>2</sub> S).....	31
1.3.2. Electrolyte .....	34
1.3.3. Negative electrode .....	37
1.4. Advanced characterization methods applied to Li/S system .....	38
1.5. Conclusions.....	42
<b>Chapter 2: Sulfur positive electrode on Al collector – studies and important parameters determination .....</b>	<b>43</b>
2.1. Motivation of the work .....	43
2.2. Experimental part.....	44
2.2.1. Preparation of the electrodes and the electrolyte .....	44
2.2.2. Battery assembly.....	46
2.2.3. Characterization methods and tests conditions .....	47
2.2.4. Discussion concerning the results' margin of error .....	48
2.3. The influence of different parameters of the electrodes .....	49
2.3.1. The effect of the conductive carbon additive.....	49



2.3.1.a) SuperP <sup>®</sup> vs. Ketjenblack <sup>®</sup> .....	49
2.3.1.b) SuperP <sup>®</sup> vs. VGCF <sup>®</sup> .....	51
2.3.2. The effect of a binder and active material loading .....	54
2.3.3. EIS investigation .....	58
2.3.3.a) The effect of the electrode thickness .....	60
2.3.3.b) The influence of the insulating nature of active material .....	60
2.3.3.c) The influence of the conducting carbon .....	62
2.3.3.d) The effect of the binder nature .....	63
2.3.3.e) The effect of the electrode elaboration process .....	63
2.3.3.f) Interpretation of ‘HF to MF’ and ‘MF’ regions response - summary .....	65
2.3.4. Correlation of the EIS results with cycling performances .....	66
2.3.4.a) Cycling results .....	66
2.3.4.b) <i>Post-mortem</i> studies .....	68
2.3.5. Conclusions .....	70
<b>Chapter 3: Porous 3D carbon current collector - a potential way for the electrode improvements .....</b>	<b>71</b>
3.1. Non-woven carbon felt (NwC) - physical and structural properties .....	71
3.2. Preparation of the electrodes .....	73
3.2.1. The effect of imprecise NwC collector mass estimation and related capacity error .....	74
3.3. Morphology of the electrode: before and after cycling .....	76
3.4. Electrochemical performances of ‘S-on-NwC’ electrode .....	78
3.4.1. Typical galvanostatic cycling response (C/20) .....	78
3.4.2. Voltage profile and capacity retention at various currents .....	80
3.4.3. Lower voltage limit and its correlation with different S/C ratios .....	83
3.4.4. Towards heavily loaded electrodes .....	85
3.4.5. Capacity based on a complete weight of the electrode .....	86
3.4.6. Aluminum vs. NwC-based electrodes: comparative studies .....	87
3.4.7. The importance of the electrolyte amount .....	94
3.4.8. Surface area vs. porosity – a dominant factor? .....	96
3.4.8.a) The effect of the surface area .....	96
3.4.8.b) The effect of pressing .....	99
3.4.9. Binder-free ‘melted sulfur-NwC’ electrodes performances .....	101
3.4.10. ‘Insulated sulfur electrode’ coin cell concept .....	103

3.5. Problems encountered when using highly loaded sulfur electrodes – Lithium as limiting factor?.....	105
3.6. Conclusions.....	108
<b>Chapter 4: Into safer cells: metallic lithium-free Li-ion/S system .....</b>	<b>109</b>
4.1. The goal of the work .....	109
4.2. Lithium sulfide (Li <sub>2</sub> S) electrode: development and studies.....	110
4.2.1. Experimental section.....	110
4.2.1.a) Electrodes preparation .....	110
4.2.1.b) Characterization techniques.....	112
4.2.2. Morphology of the electrodes and structural characterization.....	113
4.2.3. Typical electrochemical response .....	115
4.2.3.a) Galvanostatic cycling (GCPL) results .....	115
4.2.3.b) Discussion on the coulombic efficiency calculation .....	118
4.2.3.c) Cycling voltammetry profile.....	120
4.2.4. The importance of the initial charge .....	121
4.2.4.a) Disparities in the charge profiles .....	121
4.2.4.b) GITT technique.....	123
4.2.4.c) Addition of the polysulfides to the electrolyte.....	126
4.2.5. Determination of the cycling potential window.....	128
4.2.5.a) Initial charge .....	129
4.2.5.b) Initial discharge .....	134
4.2.6. C-rate influence.....	135
4.2.7. Strategies for the improvement.....	137
4.2.7.a) The effect of a ball-milling .....	137
4.2.7.b) Carbon-based current collector (NwC).....	141
4.2.8. <i>In situ</i> and <i>operando</i> XRD – Li <sub>2</sub> S structural changes upon cycling.....	144
4.2.8.a) Experimental details .....	144
4.2.8.b) <i>In situ</i> XRD – results .....	145
4.2.8.c) <i>Ex situ</i> XRD – supporting study .....	146
4.2.9. Conclusions.....	148
4.3. Complete metallic Li-free cells.....	148
4.3.1. Ether-based electrolyte with VC addition.....	149
4.3.2. Si/Li <sub>2</sub> S cell: proof-of-concept.....	151
4.4. Conclusions.....	155

<b>Chapter 5: <i>In situ</i> and <i>operando</i> XRD studies: insight into the structural changes of the active material.....</b>	<b>157</b>
5.1. Motivation of the work .....	157
5.2. Experimental section.....	158
5.2.1. Measurements description and synchrotron beam line characteristics .....	158
5.2.2. Cells design.....	159
5.3. The initial cycle evolution at C/20.....	161
5.3.1. XRD and electrochemistry – results .....	161
5.3.2. End of charge: $\beta$ -Sulfur formation.....	163
5.3.2.a) $\beta$ -Sulfur: physical characteristics.....	164
5.3.2.b) Unusual formation of metastable $\beta$ -S <sub>8</sub> : supporting experiments .....	165
5.3.3. ‘Reference’ holes evaluation.....	167
5.4. Quantitative analysis – insight into evolution of solid active material phases .....	168
5.4.1. Sulfur reduction and re-oxidation .....	169
5.4.2. Lithium sulfide (Li <sub>2</sub> S) formation and disappearance.....	171
5.4.3. <i>Ex situ</i> XRD – supporting data for analysis.....	173
5.4.4. Conclusions.....	181
5.5. Further cycles evolution at C/20.....	181
5.5.1. The second cycle.....	181
5.5.2. The twenty sixth cycle .....	184
5.6. Influence of C-rate: C/8 studies .....	185
5.6.1. XRD and electrochemistry – results .....	186
5.6.2. Quantitative interpretation .....	188
5.7. Conclusions.....	190
<b>Chapter 6: Application of Electrochemical Impedance Spectroscopy and low temperature tests.....</b>	<b>191</b>
6.1. Motivation of the work .....	191
6.2. Experimental part.....	191
6.2.1. Coin cell design.....	191
6.2.2. EIS measurements.....	192
6.3. Impedance response – Nyquist plot features .....	193
6.3.1. Symmetric coin cells approach .....	194
6.4. Li/S cells upon storage – evidence of self-discharge.....	197
6.5. Li/S battery upon cycling – initial cycle .....	200

6.5.1. Nyquist plot evolution.....	200
6.5.2. Symmetric coin cells at different DOD .....	203
6.5.3. Equivalent circuit .....	207
6.5.4. Results discussion .....	208
6.5.4.a) High frequency region (> 100 kHz).....	209
6.5.4.b) High to medium frequency region (50 kHz - 1 Hz) .....	212
6.6. Further cycles evolution.....	218
6.7. The influence of the low temperature .....	222
6.7.1. Changes of the cycling voltage profile .....	222
6.7.2. Variation of the EIS parameters.....	223
6.8. Conclusions.....	227
<b>Conclusions &amp; Perspectives .....</b>	<b>229</b>
<b>References .....</b>	<b>235</b>



## General Introduction

Primary energy sources exist in many forms, including fossil energy (*i.e.* oil, coal and natural gas), nuclear energy and finally renewable energy sources like solar, wind and hydropower. In 2013, energy consumption and production increased for all types of fuels, reaching the record levels, with the exception for nuclear power<sup>1</sup>. Moreover, for every energy types, the consumption rate increases faster than the production one. The general trend of primary energy world consumption is shown on Figure A, where it is clearly demonstrated that until today, oil is the world's energy source leader, with 32.9 % of global energy consumption<sup>1</sup>.

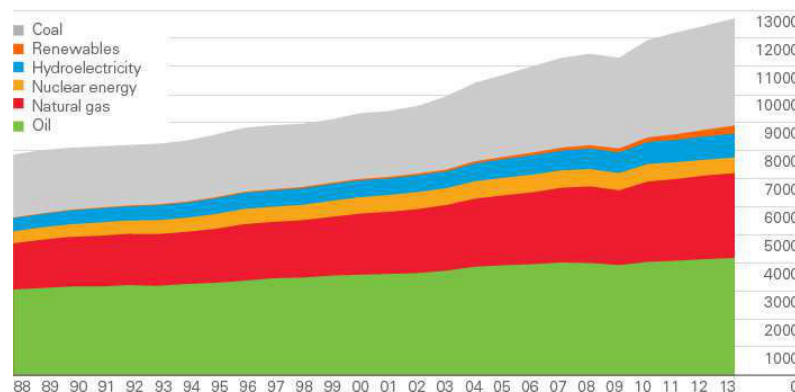


Figure A. Primary energy world's consumption statistics from 1988 until today, in million tones oil equivalent<sup>1</sup>.

As a consequence, the global growth of CO<sub>2</sub> emissions is also accelerated, having an enormous impact on global warming effect. The worldwide awareness towards low carbon emission encourages to decrease the consumption of fossil fuels and to replace them by renewable energy sources<sup>2</sup>. It is still a long process to go, but the statistics demonstrate already that the renewable energy sources, both in power generation as well as in transportation, continue increasing, reaching a record of 2.7 % of global energy consumption in 2013, as compared to 0.8 % a decade ago<sup>1</sup>.

The need of reducing CO<sub>2</sub> emissions is also strongly debated in terms of transportation aspect. As a matter of fact, an increasing attention is paid on the hybrid electric vehicles (HEV) and/or pure electric vehicles (EV) development. Moreover, the ever increase demand for renewable energy sources utilization also strongly highlights the importance of reliable energy storage systems, in order to match the intermittency with both production and demand. In this energy landscape, electrochemical energy storage systems, and most particularly batteries, play a crucial role for current and next generation applications<sup>3</sup>.

The battery type is adaptable directly to a desired application, *i.e.* large scale (like redox-flow or Na/S systems) or more portable ones. Currently, the most popular rechargeable batteries are lithium-ion (Li-ion), nickel-metal hydride (NiMH), lead acid (Pb) and nickel cadmium (Ni-

Cd). However, it is Li-ion technology that has undoubtedly attracted the most of attention since 1990, when first commercialized by Sony. Based on Li-intercalation compounds, Li-ion cells offer the best performances in terms of energy densities, and outperform other portable battery systems by a factor of 2.5 (250 - 300 Wh kg<sup>-1</sup> as compared to ~100 Wh kg<sup>-1</sup> at most in the case of Ni-MH), while also providing a higher specific power (up to 300 W kg<sup>-1</sup>)<sup>4</sup>.

It is unquestionable thus, that Li-ion cells have revolutionized the market of portable devices, and are the battery of choice for many kinds of applications such as laptops, cameras, telephones, etc. However, development of new electronic devices, as well as of (hybrid) electric vehicles, requires also an improved battery system, in terms of energy density, durability, flexibility, safety and costs. Li-ion technology, even if considered as a mature one, is known to slowly reach its performances limits<sup>5</sup>. Moreover, its high cost is still an issue, especially when it comes to a larger applications, such as HEV or EV, the fields which are predominantly driving the current developments of high energy batteries. In other words, advances in (H)EV market are strongly dependent on the battery features, both in terms of energy density (which tunes the car driving distance) and price (*e.g.* the cost of a battery in a Tesla EV car stands for around ~ 50 k\$<sup>6</sup>).

Therefore, a formidable challenge lies in reaching the horizon beyond the classical Li-ion technology. It requires, however, going into direction of other chemistries, electrochemistry and new materials<sup>5</sup>. Two promising technologies which are widely discussed today are lithium-oxygen (Li-O<sub>2</sub>) and lithium/sulfur (Li/S) systems<sup>5</sup>. While Li-O<sub>2</sub> cells are still relatively far from being commercialized, the Li/S batteries are strongly considered as one of the next generation energy storage system. They have a great potential to offer 2-3 fold increase in terms of stored gravimetric energy density as compared with classical Li-ion's, for a much lower price expected for the full cell. This is because of sulfur, known as naturally abundant and very cheap material (~100 US\$ per ton of sulfur<sup>7</sup>). Many research teams are focused nowadays on development of Li/S technology<sup>8</sup>, and two start-up companies are present on the market at this moment (Sion Power<sup>9</sup> in USA and OXIS Energy<sup>10</sup> in UK). However, despite of a significant progress which has been made during last decades, there are still many unresolved challenges for this technology.

This PhD work has been devoted for development and study of both Li/S and Li-ion/S systems, and was performed in collaboration with two laboratories: LGI (Laboratoire des Générateurs Innovants) at CEA-LITEN (Grenoble) and LEPMI (Laboratoire d'Electrochimie et Physicochimie des Matériaux et Interfaces; UMR5279, CNRS, Grenoble).

During this work, two main axes have been systematically followed. The first one was mainly devoted for better understanding of the phenomena occurring inside the Li/S batteries, the complexity of the working mechanisms and of the limiting parameters. Although the literature is very rich of many explanations, a controversial and confusing opinion can still be found up to now, while a deep understanding of the system is absolutely required for improvements and further developments. Another axis was targeted rather on improvements of already existing

solutions, understanding the way they perform, along with development and tests of new and innovative solutions.

The manuscript is composed of six chapters, where extensive description of obtained results is presented. In the first chapter, a general introduction to Li/S technology along with its working principles and limiting parameters is provided. A brief summary of today's state of art is given, with attention paid at most on the aspects which we were working on during this thesis.

Second chapter is devoted to sulfur positive electrode, prepared in a simple manner, always keeping in mind facility of fabrication. In this part, we mostly focused on the parameters related with a positive electrode solely, *i.e.* nature of carbon additives and binder, preparation methods and active material loading. More particularly, a study aimed at finding a correlation between the electrodes' morphology, its electric properties (studied by Electrochemical Impedance Spectroscopy) and electrochemical performances is also included in this chapter.

As a continuation of the work focused on further development and improvements of the positive electrode performances, a third chapter propose a solution based on the use of a porous conductive carbon felt as a current collector. Different aspects were taken into consideration when trying to correlate improved electrochemical performances with the properties offered by such carbon collector, *i.e.* surface area, electrolyte amount, porosity, etc. An extensive comparison of similar electrodes but coated on two different collectors, classical aluminum (Al) foil and non-woven carbon (NwC), is also included.

The fourth chapter is devoted to development of an alternative positive electrode, where instead of sulfur, a lithium sulfide ( $\text{Li}_2\text{S}$ ) was used as an active material and which aimed to be a transition step towards the safer cells, *i.e.* metallic-lithium-free batteries. During this work, parallel to the practical aspect of the electrodes fabrications and electrochemical performance tests, a large part was devoted to deeper understanding of the particularity of these electrodes and the redox reactions occurring during Li/Li<sub>2</sub>S cells operation. Last but not least, a Li-ion/S cell proof-of-concept was demonstrated, where metallic Li was successfully replaced by a silicon (Si) negative electrode.

Two last chapters are fully dedicated to a deeper understanding of the working mechanisms occurring in the Li/S cells upon cycling. For that purposes, *in situ* and *operando* XRD analyses were performed to study the evolution of the active material upon cycling. The obtained results together with qualitative and quantitative interpretation are presented in chapter 5.

In parallel to XRD studies, Electrochemical Impedance Spectroscopy (EIS) was applied to the same Li/S system as a supplementary technique, in order to have more complete vision on the complex reactions occurring in the cells, especially at the interfaces. The obtained results confirmed to some extent the XRD-based findings, as well as brought new facts. The influence of applying low temperature on cycling performances is also included in this chapter.

A final conclusions and perspectives are proposed at the end of this manuscript, as a summary of a complete work.





# Chapter 1: Literature review

## 1.1. Introduction to Li-ion batteries

Development of new portable devices and electronics has been regularly increasing during the last few years. With the competitive market of smartphones, tablets, PCs and electrical vehicles (EV), this trend is even more accelerated currently. The market of EV is actually a strong motivation to work on the development of ‘better’ batteries with enhanced cycle life, increased energy density and power, and of lower cost.

This new era of communication and mobility would not be possible without efficient solutions for energy storage. Among a wide range of energy storage systems, rechargeable secondary batteries, especially lithium-ion (Li-ion) cells, are currently the dominant technology for powering portable devices, mostly due to their capability of delivering electrical energy with high power and energy densities (Figure 1-1).

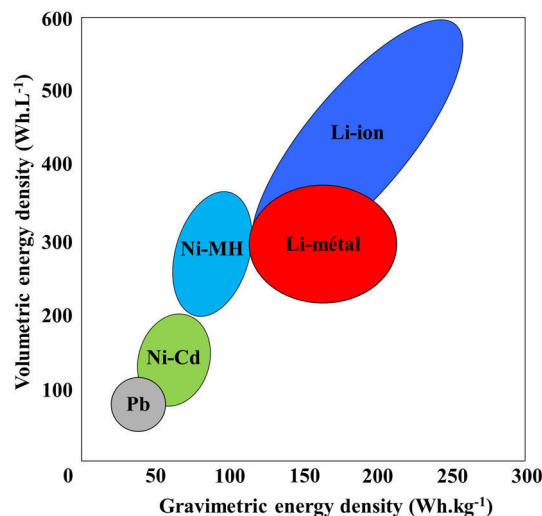


Figure 1-1. Comparison of different rechargeable battery technologies, in terms of gravimetric and volumetric energy densities.

A classical Li-ion cell system<sup>4,11</sup> consists of both positive and negative electrodes, which are separated by an ionically conducting electrolyte. Transition metal oxides, or more generally the oxide compounds, are often employed as active materials for the positive electrode, and graphite for the negative one, where intercalation reactions of Li<sup>+</sup> ions occur during discharge and charge respectively. The electrolyte is usually imbibed in a porous separator, which acts as a physical barrier avoiding the contact between the electrodes, while allowing for Li<sup>+</sup> ions

transportation. During discharge,  $\text{Li}^+$  ions spontaneously flow through the electrolyte from the negative electrode and intercalate into the positive one. During charge, the ions move in the opposite direction, flowing from the positive electrode and intercalating to the negative electrode, as demonstrated on Figure 1-2.

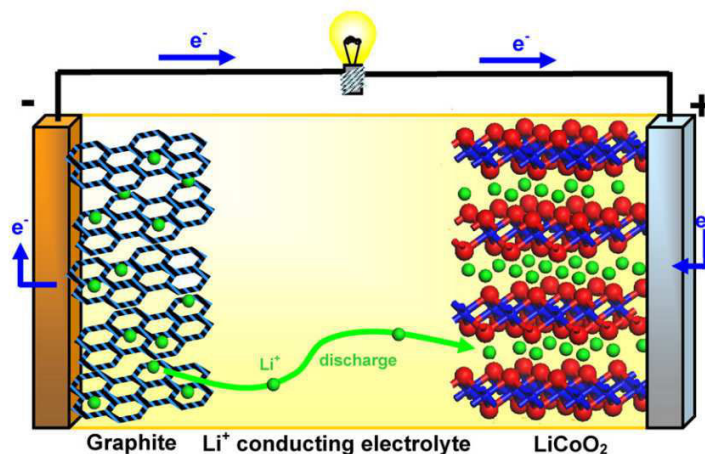


Figure 1-2. Li-ion battery representative scheme<sup>12</sup>.

Despite the evolution of energy storage systems achieved over the past decades, the capabilities of lithium battery technologies are constantly being challenged by the modern multifunctional portable devices, which are increasingly requiring more and more performances in terms of energy and power density. Energy storage systems were not able to improve with the same rate as the electronic industry progress. Therefore, alternative cathode and anode materials with higher capacities need to be developed. To overcome the charge storage limitations of insertion-compound electrodes, conversion materials, which undergo electrochemical reactions involving more ions and electrons, are becoming a promising option. However, achieving the full performances of these materials is still a challenge. With this perspective, two systems, lithium-oxygen ( $\text{Li-O}_2$ ) and lithium/sulfur ( $\text{Li/S}$ ), are under extensive investigations.  $\text{Li-O}_2$  cells suffer from many unresolved and thorny issues, and its commercialization is rather envisaged for the later years to come. On the other hand,  $\text{Li/S}$  system is far way closer to being released as a real product, and some start-ups or small companies are already aiming at developing  $\text{Li/S}$  prototypes for different applications<sup>9,10,13</sup>.

$\text{Li/S}$  technology is expected to offer 2-3 times the energy density of the best performing Li-ion batteries, and reduced costs. However, many limitations are known for this system, which hinder the complete technological transfer to the commercial market. Next paragraph presents the basics of the  $\text{Li/S}$  batteries, along with its main limitations. The state-of-art of existing achievements is also briefly presented.

## 1.2. Introduction to Lithium/Sulfur Batteries

Sulfur was introduced as a positive electrode material for the first time in 1960s by Herbert and Ullmann<sup>14</sup>. Since that time, quite many attempts have been undertaken to develop the metal-sulfur batteries, some of them mainly focusing on primary Li/S cells<sup>15</sup>. After 2008, very rapid increase in the development of emerging applications (such as EV, military power supplies and stationary storage systems for renewable energy) provoked even higher demand for high performing batteries<sup>3,12,16</sup>. In particular, the increasing market of electric vehicles (EV) seems to be the strongest motivation for making Li/S batteries as the system of choice for the future. Indeed, the ever increasing attention of the Li/S cells can be also seen in terms of published papers number, with practically exponential growth since 2010, as shown on Figure 1-3.

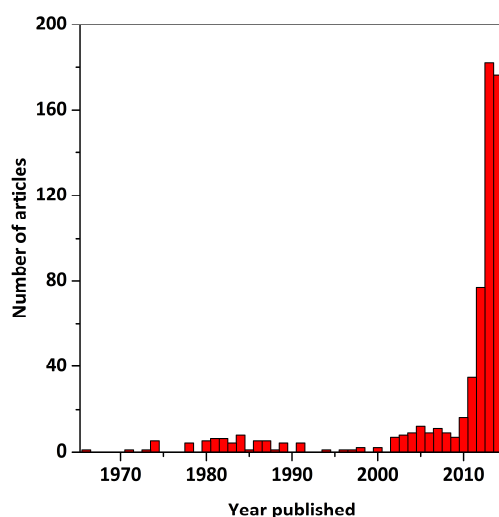


Figure 1-3. Number of articles concerning Li/S system per year. Results obtained from Scopus.com. Statistics for 2014 are not complete (up to 10/2014).

Sulfur offers one of the highest theoretical specific capacity ( $1675 \text{ mAh g}^{-1}$ ) among all existing positive electrode materials, which is an order of magnitude higher than what is currently proposed by the transition-metal oxide cathodes<sup>17</sup>. The system could theoretically deliver energy density of  $\sim 2600 \text{ Wh kg}^{-1}$ . Moreover, sulfur is an abundant element, non-toxic and extremely cheap, which may drastically decrease the final cost of the battery. A realistic target of practical energy density is in the range of  $400 - 600 \text{ Wh kg}^{-1}$ , which is higher as compared with the classical Li-ion cells<sup>18</sup>, and which would allow to extend the range of EVs automotive industry to 500 km (Figure 1-4)<sup>5</sup>.

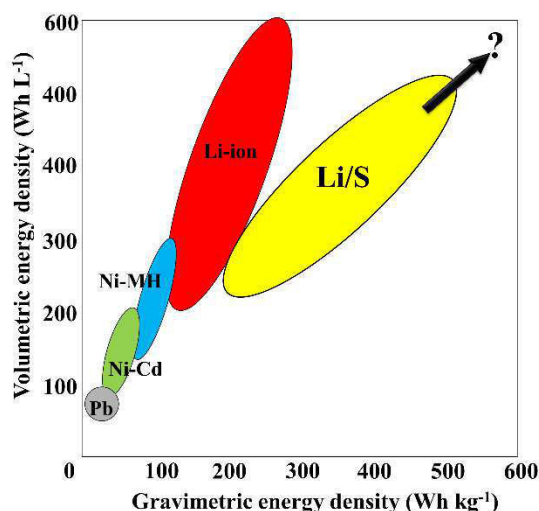


Figure 1-4. Position of Li/S batteries among the other rechargeable battery technologies, in terms of volumetric and gravimetric energy density.

There is absolutely no doubt that Li/S batteries are considered as a very realistic candidate for the next-generation energy storage systems. Significant progresses were made during past few years, which are shortly presented in further section. However, there is still a long way to go and many challenges to overcome, since the system suffers from several unresolved drawbacks, which simply induce a large gap between reality and expectations. In later part of the discussion, we also point out the main disadvantages and limitations of the Li/S technology. But before that, it is necessary to describe the way the Li/S batteries operates, as its complex working mechanism is very different from the classical Li-ion cells.

### 1.2.1. Principles and working mechanism

A typical Li/S cell is composed of a sulfur-based positive electrode, a metallic lithium negative electrode, both separated with a porous polymeric separator(s) soaked with an organic electrolyte (often based on ether solvents), as illustrated on Figure 1-5.

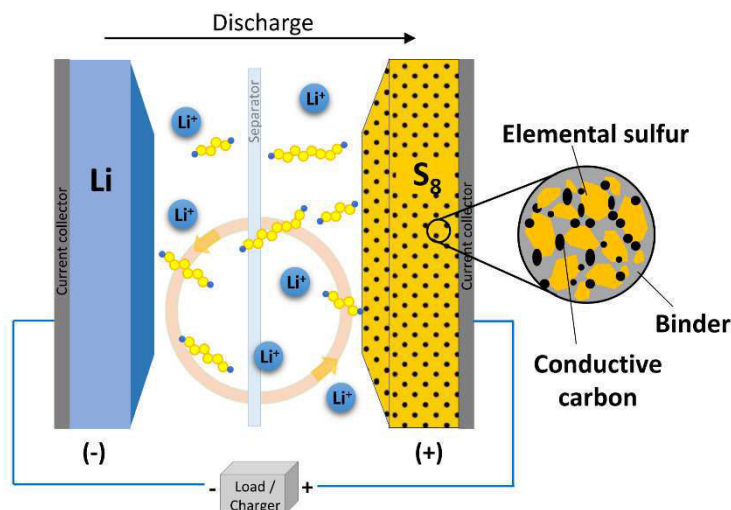


Figure 1-5. Schematic diagram of a Li/S cell.

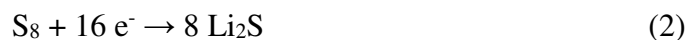
Elemental sulfur as an active material can be used as-received for the electrode preparation. A conductive carbon additive is always added to the electrode, in order to provide an electronic percolation of the whole electrode. Polymeric binder is used for bonding all the electrode components together, and provides sufficient adhesion to the current collector.

Sulfur is a yellow non-metallic solid, a cyclic molecule composed of eight atoms, so-called  $S_8$ . Sulfur forms more than 30 different allotropes<sup>19</sup>, but the most thermodynamically stable one at room temperature (RT) is orthorhombic alpha-sulfur ( $\alpha$ - $S_8$ ), with molecular mass of 32.066 g mol<sup>-1</sup> and a density of 2.07 g cm<sup>-3</sup>. Sulfur has relatively low melting temperature of 115 °C, and it can get easily sublimed. Orthorhombic  $\alpha$ -sulfur form is the one used for the sulfur electrodes preparation. Another allotropic form, monoclinic beta-sulfur ( $\beta$ - $S_8$ ) is rather known from being stable at the temperatures higher than 95.5 °C, and it is likely formed when slowly cooling down the melted sulfur solution<sup>20-22</sup>. Latest reports demonstrated on the unusual formation of this allotropic sulfur form in the Li/S system at the end of charge<sup>23-25</sup>, or as a starting material in the positive electrode (obtained through infiltration of elemental sulfur into CNT structure<sup>26</sup>).

Li/S system is based on the electrochemical reaction of sulfur with lithium to form lithium sulfide ( $Li_2S$ , final reaction product). Since sulfur is in the charged state (no  $Li^+$ ), the cell operation starts from discharge, while metallic lithium is getting oxidized at the negative electrode and produces lithium ions and electrons.  $Li^+$  ions diffuse to the positive electrode through the separator/electrolyte, while electrons go through external electrical circuit. The oxidation reaction occurring at the negative electrode is as follow:



On the positive electrode, sulfur is getting reduced by accepting  $Li^+$  ions and electrons, according to the equation (2):



The overall reaction occurring inside the Li/S cell, at the voltage of  $\sim 2.15$  V, is as described by equation (3):



Based on the molecular weight of sulfur (which is a relatively light element as compared with transition metal oxides used for insertion positive electrode materials), and the fact that 2 electrons can be accepted per one atom of sulfur, very high theoretical specific capacity of  $1675 \text{ mAh g}_{\text{sulfur}}^{-1}$  can be expected.

A particularity of this system mostly lies in its working mechanism, which is very complex. The overall reaction between element sulfur and lithium to form lithium sulfide is not an intercalation reaction. It is neither a direct one, as the reduction of solid sulfur is accompanied by the formation of a family of species, so called lithium polysulfides ( $\text{Li}_2\text{S}_x$ ,  $3 < x \leq 8$ ), which are easily soluble in the organic electrolyte. The properties of the different polysulfides (*i.e.* their solubility, color, etc.) are strongly related with their chain length<sup>27</sup>. We can distinguish thus the following polysulfides groups:

- (i) ‘high-order’ or ‘long chain’ polysulfides: these are the species with the longest chain, *i.e.*  $\text{Li}_2\text{S}_8$ ,  $\text{Li}_2\text{S}_6$ ;
- (ii) ‘medium-order’ is mainly  $\text{Li}_2\text{S}_4$ , still relatively easily solubilized;
- (iii) ‘low-order’ or ‘short chain’ polysulfides are the species:  $\text{Li}_2\text{S}_3$ ,  $\text{Li}_2\text{S}_2$  and  $\text{Li}_2\text{S}$ .

The shorter is the chain, the less soluble the species are. As a matter of fact, the final  $\text{Li}_2\text{S}$  product is a solid material.

A typical cycling profile of the Li/S cell is shown on Figure 1-6.

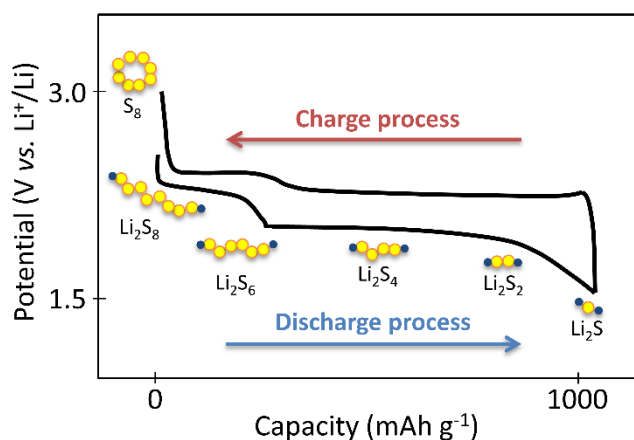


Figure 1-6. Typical voltage profile of Li/S cell<sup>5</sup>.

When the discharge starts, cyclo-octa molecules of sulfur are getting reduced and the rings open. When reacting with  $\text{Li}^+$ , soluble  $\text{Li}_2\text{S}_8$  polysulfides are formed. As the discharge proceeds, the length of the polysulfide species is getting shortened, leading to the formation of the solid final reaction product (mostly lithium sulfide,  $\text{Li}_2\text{S}$ ).

During discharge, two main quasi-plateaus are observed, at 2.4 V and 2.1 V. In a simplified description, 2.4 V plateau is usually attributed to the reduction of elemental sulfur and formation of high-order polysulfides. The step-like region between both plateaus is often attributed to the formation of medium-order polysulfides, *i.e.*  $\text{Li}_2\text{S}_4$ . During 2.1 V plateau, shorter polysulfides are formed, leading to the solid  $\text{Li}_2\text{S}_2/\text{Li}_2\text{S}$  formation. During recharging, quasi reversible process occurs, *i.e.* two quasi-plateaus are also observed, where the first one is associated with the oxidation of the short-chain polysulfides to the soluble species ( $\text{Li}_2\text{S}_3$ ,  $\text{Li}_2\text{S}_4$ ,  $\text{Li}_2\text{S}_6$ ,  $\text{Li}_2\text{S}_8$ ), and the second one to solid elemental sulfur formation at the end of charge. Aforementioned description is obviously a generalized one, since in reality the system is much more complex. Today literature is rich of deeper explanation of the reactions occurring, and further sections present some of the main explanations/propositions of these mechanisms. However, it is worth noticing that a ‘global’ model applicable to all Li/S cells does not really exist, as it is strongly dependent on several factors (solvent(s) used in the electrolyte, cathode morphology, cycling parameters, etc.).

From the practical point of view, once the Li/S cell starts to run, the active material is simply changing its form from solid to soluble phase, which also means that it is not anymore confined inside the electrode structure. Once dissolved in the electrolyte, it may also affect its properties (viscosity and conductivity, thus the resistance). However, active material further comes back into the solid form ( $\text{Li}_2\text{S}$ ) at the end of discharge. These features clearly show the difference between the classical Li-ion batteries, where  $\text{Li}^+$  are intercalated/de-intercalated between the hosting electrodes, while active material stays in the complete electrode structure and the electrolyte composition is not affected. Therefore, it is indispensable and of high interest to have deeper insight into the working mechanism of the Li/S cells, since is very different from the typical Li-ion’s one. On the other hand, these differences give the rise to the detrimental phenomena appearing in the Li/S cells, which result in lower performances as the ones expected, based on theoretical calculations. Since the Li/S cells operation is actually accompanied by the dissolution/precipitation repeated cycles, it may cause several problems and give rise to numerous limitations, which are presented with more details in the next section.

### 1.2.2. Li/S system limitations

The system limitations arise from different cell components: positive electrode, electrolyte and negative electrode. Due to the fact that the active material can easily diffuse to the electrolyte, it can be considered as all the battery components are somehow interconnected, thus the



limitations are as well. Therefore, the following description of the main problems with attribution to the positive electrode, electrolyte and the negative one, is more ‘virtual’.

### 1.2.2.a) Positive electrode issues

One of the main limitations associated with the positive electrode is the electronic property of sulfur, which is commonly known as a *poor electronic conductor* ( $\sigma = 5 \cdot 10^{-30} \text{ S cm}^{-1}$ )<sup>28</sup>, and which requires addition of conductive carbon additive, very often in high weight fractions (even up to 50 wt%)<sup>29,30</sup>. However, such high carbon content may reduce the final volumetric and gravimetric energy densities due to the presence of inactive mass, and the practical density values may not be better than the Li-ion cells<sup>31</sup>.

Sulfur is *easily soluble* in most of the organic solvents used in the electrolyte, thus self-discharge<sup>32-34</sup> can occur, visible in the OCV potential decrease and lowered discharge capacity obtained after storage.

*Significant morphology change* of the positive electrode upon cycling is another detrimental factor. Once the battery starts to operate, the active material leaves the carbon/binder matrix, and dissolves in the electrolyte in the form of soluble polysulfides. This affects the global porosity of the electrode and may give the rise to strong electrode pulverization or even collapse. It can also be imagined that some parts of the carbon/binder agglomerates may get disconnected from the current collector, resulting in the active surface area losses. As a matter of fact, a characteristic feature of Li/S cells capacity retention shows drastic capacity fading right after the initial cycle<sup>35</sup>. The aforementioned morphology changes are strongly responsible for that behavior (but are not the only reason for that).

During discharge, the final solid *Li<sub>2</sub>S product is also of insulating nature*, and gets formed on any available electronic conductive area of the positive electrode. Therefore, strong polarization increases upon discharge due to the passivation layer formed on the electrode surface. There is also a risk that such insulating layer may not be completely consumed (oxidized) in the following charge, giving a rise to an inactive material losses since unable to participate in the further reactions. This may result in progressive capacity fading, and such insulating leftovers decrease the effective active surface to perform the redox reactions<sup>36,37</sup>.

Furthermore, the difference in the densities of two solid products, 2.07 g cm<sup>-3</sup> for  $\alpha$ -S<sub>8</sub> and 1.66 g cm<sup>-3</sup> for Li<sub>2</sub>S<sup>38,39</sup>, results in a *large volumetric changes* of the global electrode upon cycling (expansion up to ~ 79 %) <sup>40</sup>.

### 1.2.2.b) Electrolyte related limitations

As previously mentioned, sulfur ( $S_8$ ) upon reduction creates lithium polysulfides ( $Li_2S_x$ ,  $3 < x \leq 8$ ), which are very *soluble in the electrolyte*, leading to the active material losses. Moreover, polysulfide species dissolved in the electrolyte significantly affect its viscosity<sup>41</sup>, thus ionic conductivity and the resistance, together with a rise of a mass transport limitations. This may in turn strongly affect the power performances of the cell.

Dissolved polysulfide species may easily diffuse back and forward between the two electrodes, giving rise to a characteristic mechanism of Li/S system, so-called “*shuttle phenomenon*”, explained in the pioneer work of Mikhaylik *et al.*<sup>32</sup>, then followed by extensive studies of other groups<sup>31,42-44</sup>. The origin of this phenomenon lies in the concentration gradient of polysulfide species inside the cell. When high-order polysulfides are formed at the positive electrode, their concentration is much higher as at the negative side. Thus they diffuse through the electrolyte to the Li metal interface, where they can react (get reduced) to form low-order polysulfides. These short chain polysulfides can then diffuse back to the positive electrode (again due to the concentration gradient that got formed), where they can be oxidized back to high-order species. The process can be further repeated, resulting in prolonged charge process, sometimes even infinitely. Figure 1-7 shows the schematic illustration of the shuttle mechanism principles.

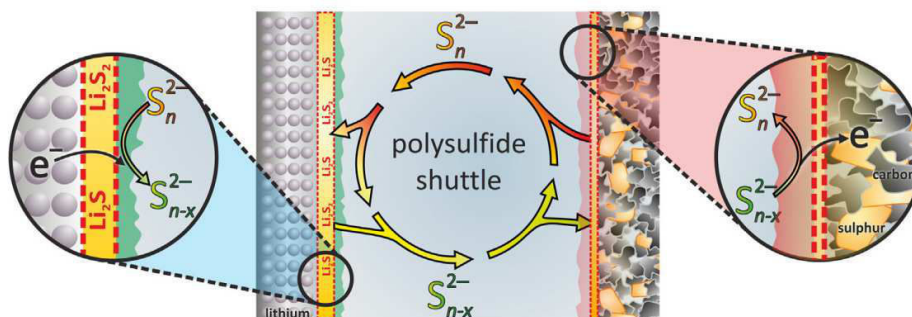


Figure 1-7. A schematic illustration of the shuttle mechanism occurring in the Li/S cell<sup>31</sup>.

As a consequence, the cell cannot complete the charging process, which on one hand protects against overcharging, while on the other hand it also significantly lowers the coulombic efficiency<sup>\*32,38</sup>. Shuttle mechanism is evidenced by a characteristic charging plateau at the constant potential of about 2.45 V vs.  $Li^+/Li$ . It is also dependent on the C-rate applied to the cell. It is thus more pronounced at slower rates<sup>31</sup>, since the soluble polysulfide species have more time to diffuse through the electrolyte to the other electrode. Also elevated temperatures increase the risk of shuttle occurrence, since the electrolyte viscosity is decreased, thus

\* Coulombic efficiency, if calculated as (n) charge / (n) discharge ratio, and if being lower than 100 %, indicates the presence of the shuttle mechanism.

diffusion of species increases<sup>31</sup>. In the same manner, more viscous electrolytes (based on more viscous solvents) also result in reduced shuttle mechanism<sup>45</sup>.

Once the ‘infinite charge’ appears, the cell may have difficulties to come back to the normal electrochemical operation, and thus the battery life is shortened. Presence of ‘shuttle’ may also result in the deposition of solid species ( $\text{Li}_2\text{S}$ ) on the metallic lithium surface, leading to a capacity fade because of the irreversible active material losses.

### **1.2.2.c) Negative electrode issues**

Metallic lithium is commonly used as a negative electrode in Li/S system, and is also impeded by its own problematics. The *dendrites growth* (due to an uneven deposition of Li during plating) may cause several micro short-circuits during battery charging<sup>46</sup>, which may in turn provoke complete cell death and safety issues. Some studies reported that, in the presence of polysulfides, the growth of dendrites may be suppressed or slowed down, due to the strong reactivity of polysulfides with lithium<sup>47,48</sup>. Nevertheless, it still stays as an unresolved problem of metallic Li negative electrode, even if some solutions are proposed currently, as presented further.

Another issue related to the use of metallic Li as negative electrode is its *high reactivity* towards air, water and organic species. In particular, a passivation layer (solid electrolyte interphase, SEI) can easily be formed on its surface during lithium lamination, cell assembly, when electrolyte is introduced in the cell, during aging etc. This SEI evolution in the cell may cause a remarkable irreversible capacity loss and lithium consumption, while also resulting in an increased internal cell resistance, if the passivation layer is too thick and/or resistive.

Aforementioned system limitations lead to the situation that, despite of intensive research which has been conducted during last two decades, Li/S batteries still offer practical energy density values rather below the expectations, together with relatively short cycle life as compared with the mature Li-ion technology. The next paragraph presents briefly state of the art of today’s Li/S batteries, with some examples of the strategies addressing these particular issues.

## **1.3. State of the art and the strategies undertaken for Li/S system improvements**

Several different strategies were undertaken in order to mitigate abovementioned limiting problems, *i.e.*:

- Low utilization of sulfur during initial discharge, due to low electronic conductivity

- Diffusion of soluble polysulfide species to the electrolyte → shuttle mechanism occurrence
- Electrode morphology changes resulting from repeated dissolution/precipitation cycles of the active material
- Reactivity of metallic Li, dendritic growth and safety issues

The strategy of improving only one single component at the same time may not bring the perfect solution, since all the issues of Li/S cells are strongly interlinked together and affecting each other. In regard to the large number of publications which have been released lately, only general examples are included in this paragraph, with a focus on the parameters closely related to the work presented in this manuscript.

### 1.3.1. Positive electrode

This would not be an exaggeration if saying that sulfur-based positive electrode has attracted most of the attention among all the other Li/S battery related topics, *i.e.* other cell components (like negative electrode, electrolyte), or investigation of the system working mechanisms. More precisely, among all the work dedicated to this part, an enormous attention was actually paid on sulfur/carbon composites, while leaving studies of binder or other electrode-related parameters relatively apart. In the next part, a brief summary is given.

#### 1.3.1.a) Sulfur/carbon composite architecture

Following the first sulfur-microporous carbon composite proposed by Wang *et al.*<sup>49</sup>, and further work of Nazar's group on sulfur-mesoporous carbon CMK-3 composites<sup>50</sup>, the approach was adopted by various groups, and new research avenues were opened, based on the concept of ***sulfur confinement inside a porous carbon structure***. This strategy was the most studied one during last four years, since it was believed to solve both issues simultaneously, *i.e.* (i) drastically improved high rate cyclability due to enhanced electronic percolation, with intimate contact between active species and carbon, and (ii) inhibited polysulfides migration due to confinement of sulfur and adsorption properties of carbon. Different carbons, depending on their porosity and synthesis routes, were utilized, *i.e.* microporous carbon (pores size < 2 nm)<sup>51,52</sup>, mesoporous carbon materials (2 nm < pores size < 50 nm)<sup>53,54,55,56,57,58</sup>, and macroporous carbon (pores size > 50 nm), which were actually the least utilized materials, due to their open architecture not providing polysulfides confinement. However, combination of two or three types of porosity in one structure brought another type of designed architectures. A family of hierarchically ordered porous carbons (HOPC) were created and intensively studied, as the "functional micro/meso/macroporous carbons" with different physical/chemical properties<sup>59-65</sup>. Inspired by work of prof. Archer's group<sup>66</sup>, another family of hollow carbon

*structures* was under intensive investigation<sup>67</sup>, with different shapes, like nanofibers<sup>68,69</sup> and nanospheres<sup>70-72</sup>. Engineering seems to have no limits, as even more complicated architectures were synthesized, like 3D hyper-branched hollow nanoroads<sup>73</sup>, hollow carbon nano-tubes (CNT) on hollow carbon-nano-fibers (CNF)<sup>74</sup>, tube in tube structure<sup>75</sup> or double shell hollow spheres<sup>76</sup>. A *yolk-shell structure* with internal void space was designed in order to encapsulate sulfur while providing enough space for volumetric changes, good reversibility even at high C-rates<sup>77,78</sup>. It was also demonstrated that not only carbonaceous materials can serve as a host for sulfur, and other structures were also proposed: metal-organic framework (MOF)<sup>79,80</sup>, covalent-organic frameworks (COF)<sup>81</sup>, mesoporous TiO<sub>2</sub><sup>82,83</sup>.

Other solutions for polysulfides trapping (aiming at improving the coulombic efficiency) were also proposed, still at the level of the positive electrode architecture: (i) *absorbing additives*, mainly composed of various metal oxides like SiO<sub>2</sub><sup>84</sup>, Mg<sub>0.6</sub>Ni<sub>0.4</sub>O<sup>85</sup>, Mg<sub>0.8</sub>Cu<sub>0.2</sub>O<sup>86</sup>, Al<sub>2</sub>O<sub>3</sub>, La<sub>2</sub>O<sub>3</sub><sup>87</sup>, and TiO<sub>2</sub><sup>88</sup>; (ii) *nitrogen-doping* of CNT<sup>89</sup>; (iii) *polymeric coating* of single particles or of complete electrodes, to provide physical (and/or chemical) barrier for the polysulfides.

By remaining in the ‘enhanced electronic conductivity’ concept, other solutions should be mentioned, starting from classical addition of carbon nanotubes (CNT or multi-walled CNT)<sup>90-94</sup> or CNF<sup>95</sup>. Since last three years, incorporation of graphene<sup>96-98</sup> (known from its excellent electronic conductivity) and graphene oxide (GO)<sup>99-101</sup> into sulfur positive electrodes was more and more popular as well. GO has the additional advantage, according to the authors, to be able to trap polysulfides thanks to its adsorption properties<sup>102</sup>.

Very impressive results were obtained with aforementioned solutions, *i.e.* long cycling life, very high C-rates applied (even 2 - 5 C) and still retaining the capacity in the range of 600-1000 mAh g<sup>-1</sup> after hundreds of cycles, etc. However, the main problems of such architectures lie in the fact that, in most of the cases, fabrication procedure is too complicated, often with the use of quite expensive precursors, and impossible to scale up. Another point concerns the practical loading of the active material (mg<sub>Sulfur</sub> cm<sup>-2</sup>) and the sulfur fraction in such obtained electrodes<sup>103,104</sup>, which in most of the proposed solutions was much below 2 mg<sub>Sulfur</sub> cm<sup>-2</sup>.

Therefore, the Li/S community is progressively coming back to simpler solutions, always keeping in mind relevancy of preparation methods with the obtained performances, for eventual potential commercialization. As a matter of fact, other parameters like electrode loading and sulfur/electrolyte ratio are today the important starting points of the discussions<sup>105,106</sup>, while few years ago not even included in the reports. They are indeed indispensable if aiming to perform a comparison between the different results obtained. It was demonstrated that simply prepared electrodes, based on commercially available and cheap products (elemental sulfur, carbon SuperP<sup>®</sup>), but with well-optimized parameters (electrolyte amount, loading, binder, etc.) are able to give the results in line with the sophisticated architectures’ ones or even better<sup>105,107-110</sup>.

### 1.3.1.b) The effect of a binder

The role of binder is very important and probably even more crucial than in Li-ion classical cells, due to the significant morphological changes appearing in the positive electrode, since repeating dissolution/deposition processes appear upon cycling. Binder is indeed responsible for maintaining the electrode integrity after the active material is dissolved, together with allowing a good adhesion to the collector. The important role of the binder is also to ensure a homogenous dispersion of sulfur and carbon particles. It should not undergo swelling when in contact with organic solvents<sup>111</sup>, and preferably being dissolved in non-toxic solvents.

The most popular polymeric binders used in Li/S cell fabrication are poly(ethylene oxide) (PEO)<sup>107,109</sup> and poly(vinylidene difluoride) (PVdF). Nevertheless, both of them are reported to possess some problems: *PEO* exhibits rather poor adhesion to the current collector and low ionic conductivity at room temperature<sup>112</sup>. Moreover, PEO can swell in some ether based electrolytes (TEGDME for example), which may induce a loss of contact<sup>113</sup>. On the contrary, according to Lacey *et al.*<sup>107,114</sup>, their PEO-based electrodes display the best performances in terms of capacity (~ 700 mAh g<sup>-1</sup> was preserved at 1C over 200 cycles) over three studied binders: PEO, CMC/SBR (carboxymethylcellulose combined with styrene-butadiene rubber) and PVP (poly(vinylpyrrolidone)). However, the studies were performed on positive electrodes with only 0.5 – 0.8 mg<sub>Sulfur</sub> cm<sup>-2</sup>.

*PVdF* is known from being chemically stable in organic electrolytes for Li-ion batteries<sup>115</sup>. However, as a poorly-conductive polymer, even if some swelling can occur when in contact with the electrolyte, it may limit both electronic and ionic conductivities, and thus limit the performances of the cell. Another negative point is that PVdF needs to be dissolved in N-methyl-1-pyrrolidone (NMP), which is a toxic organic solvent, difficult to evaporate from the prepared electrodes. Risk of sulfur sublimation (when vacuum and higher temperature are used to evaporate NMP), eventual electrode contamination by residual solvent or finally not-environmentally friendliness (due to its toxicity), leads the researchers to look deeper into more friendly and cost-effective solutions. It was also reported by Lacey *et al.*<sup>116</sup> that PVdF binder is blocking the electrode pores of the electrode (simply prepared carbon/sulfur composite using ball-milling, with eventual heat treatment applied further for sulfur infiltration inside the pores), which in turn results in decreased surface area accessible to the electrolyte.

As 'ecological' alternative to PVdF, several binders which are water-soluble or water-dispersed in the form of latex, were also investigated in the literature, like carboxymethylcellulose combined with styrene-butadiene rubber (CMC+SBR)<sup>111</sup>, gelatin<sup>112,117,118</sup>, polyacrylic acid (PAA)<sup>119</sup>, Teflon<sup>108</sup>, Nafion<sup>®108</sup>.

Schneider *et al.*<sup>108</sup> demonstrated that binder may effectively influence the cycling behavior and the stability of the positive electrode. Their comparison studies were performed on three aqueous-based electrodes, using Nafion<sup>®</sup>, Teflon and PAN-CMC (polyacrylonitrile/carboxymethylcellulose). Teflon-based electrode gave the best performances in terms of

cyclability and stable capacity retention. After 100 cycles, a capacity of  $\sim 600 \text{ mAh g}^{-1}$  was preserved, when applying C/5 rate.

He *et al.*<sup>111</sup> reported on improved cyclability and cycle life when **CMC/SBR** binder was used, as compared with PVdF-based electrodes. According to their results, final S/carbon/binder electrodes displayed better dispersion, higher homogeneity, together with better electrochemical performances, when using CMC/SBR binder.

Apart from galvanostatic cycling evaluation of the binder effect on prolonged cycling and capacity value, electrochemical impedance spectroscopy (EIS) was also applied for evaluation of the binder effect. Lacey *et al.*<sup>120</sup> performed systematic investigation of the electrode compositions with different binders, by comparing the voltage profiles obtained at higher rates (1C; equivalent to  $i = 0.84 \text{ mA cm}^{-2}$ ) and resulting hysteresis. They further correlated GCPL results to EIS findings, with the main focus on the evaluation of the electron transfer kinetics of the polysulfides reaction. For that purposes, EIS was measured on standard two-electrode cells at the end of charge/discharge at different cycles, and the major semicircles were compared in terms of resistance value, together with relaxation time constant. This semicircle was attributed to the reactions of polysulfides at the positive electrode side (Figure 1-8).

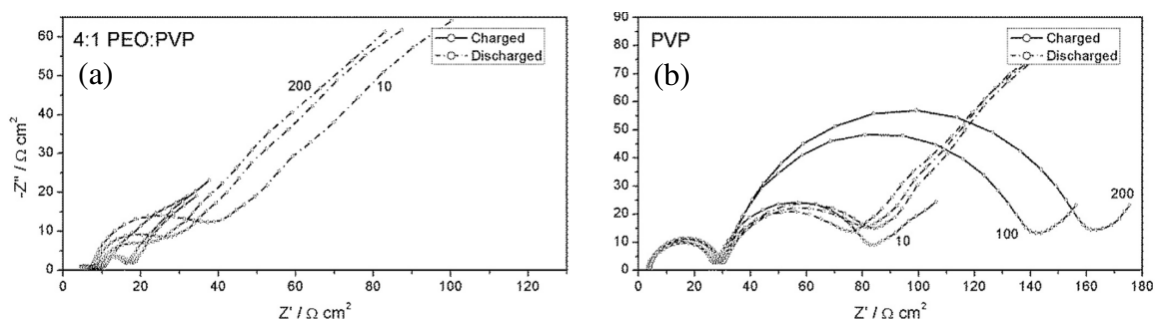


Figure 1-8. Nyquist plots of Li/S two-electrode cells recorded at the end of charge and discharge of 10<sup>th</sup>, 100<sup>th</sup> and 200<sup>th</sup> cycles. Positive electrode is composed of different binder compositions: PEO:PVP 4:1 (a) and PVP solely (b)<sup>120</sup>.

The EIS studies were in correlation with the overpotential observation, *i.e.* PVP-based electrode showed the slowest kinetics among all compositions (the lower relaxation time constant and the highest resistance of the semicircle) through EIS tests, together with the highest overpotential recorded on the voltage profile curves.

Urbonaite *et al.*<sup>109</sup> reported that the influence of binder can actually be visible, resulting in better cycling performances between the electrodes based on different polymers. However, they also pointed out that sometimes such differences are relatively small and in the global view, electrodes with different binders behave similarly in terms of capacity value and retention. In the same manner, effects of the initial sulfur particle size and of the type of carbon used do not lead to drastically improved performances. On the contrary, this work highlights the influence of electrolyte parameters, (*i.e.* amount, solvent, additives, etc.), which are the key

factors that should be taken into consideration when further developing and designing the Li/S cells.

### 1.3.1.c) The effect of sulfur loading vs. sulfur fraction

If considering utilization of Li/S batteries for high energy applications, the target for positive electrode loading should be of at least  $2.4 \text{ mg}_{\text{sulfur}} \text{ cm}^{-2}$ , thus leading to an area capacity of  $4 \text{ mAh cm}^{-2}$  with 100 % sulfur utilization<sup>31,121</sup>.

Therefore, it is clear that most of the sophisticated architectures proposed in the literature (see section 1.3.1.a), very often costly and complicated, will not allow for high energy density Li/S batteries, if the maximum loading is of about  $\sim 1 - 2 \text{ mg}_{\text{sulfur}} \text{ cm}^{-2}$ , and even if displaying impressive specific capacity values. The main issues of these “sulfur confined in micro/mesoporous carbons” structures relate to the small pore volume of the host material and resulting low sulfur fraction. Today’s tendency seems to come back slowly to the simplest solutions, keeping always in mind the simplicity of the preparation methods and low cost of raw materials, together with acceptable sulfur loading and fractions<sup>122-124</sup>. When targeting high energy applications, there are two important parameters to be taken into account: sulfur fraction (wt%) and sulfur loading ( $\text{mg}_{\text{sulfur}} \text{ cm}^{-2}$ ).

**Sulfur fraction (wt%)** in the electrode is simply the mass of sulfur in relation to the other components. It can vary in the literature between 20 wt% (very low ratio) to up to 80 wt%, as summarized by Hagen *et al*<sup>104</sup> on Figure 1-9.

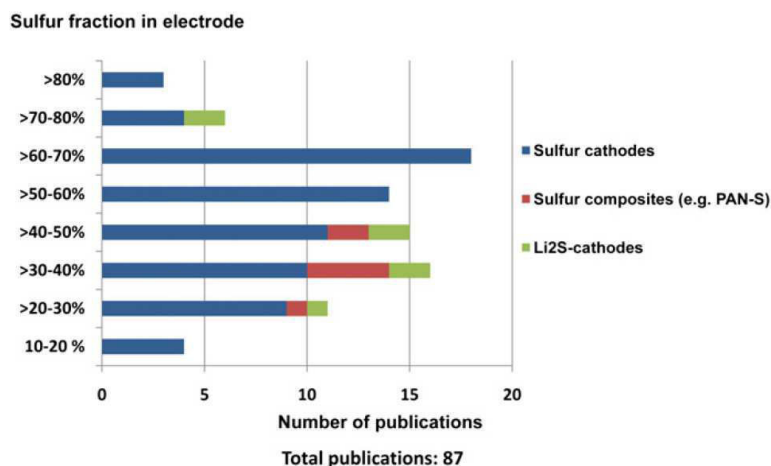


Figure 1-9. Overview of some of the existing sulfur positive electrodes with respect to the sulfur fraction in the electrode composition<sup>104</sup>.



Sulfur fraction may also be represented as a sulfur to carbon (S/C) ratio. Figure 1-10 demonstrates the voltage profile behavior together with the capacity retention when different S/C ratios are studied.

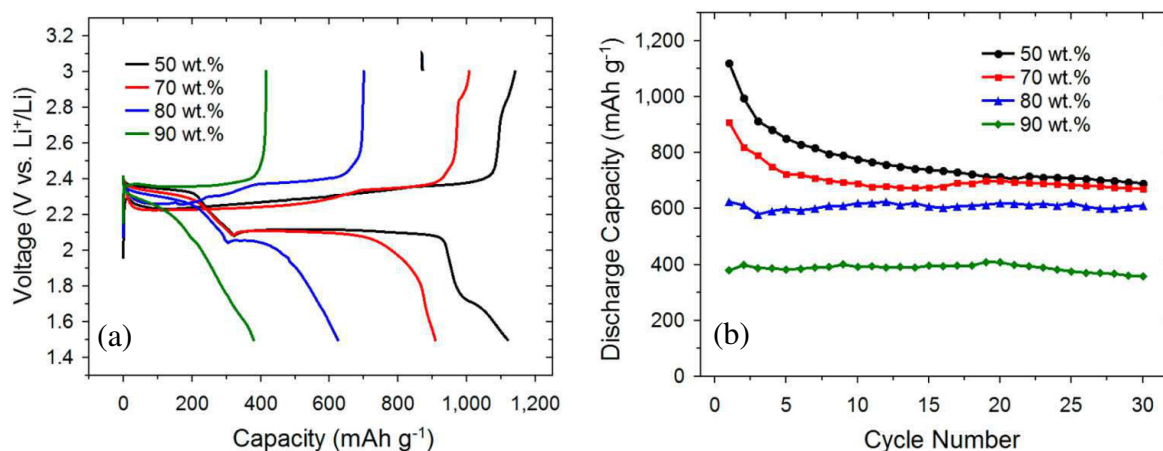


Figure 1-10. Examples of voltage profiles (a) and capacity retention (b) of the electrodes with different wt% of sulfur (thus varying S/C ratios), cycled at a current density of 100 mA g<sup>-1</sup>.<sup>122</sup>

It is relatively obvious that lower S/C ratio (lower wt% of sulfur in the electrode) results in better performances, since more carbon is available for less amount of sulfur. However, as suggested by Barchasz *et al.*<sup>35,45</sup>, the relation is not fully linear, since other system limitations interfere and prevent reaching the full capacity (at least in simply prepared electrodes).

Another parameter that is of very high importance is the **sulfur loading (mg<sub>sulfur</sub> cm<sup>-2</sup>)**. Figure 1-11 illustrates that there is a maximum limit in the sulfur loading until which the benefits are visible, *i.e.* increased areal capacity is obtained. The initial voltage profile for each electrode loading is also shown for illustration.

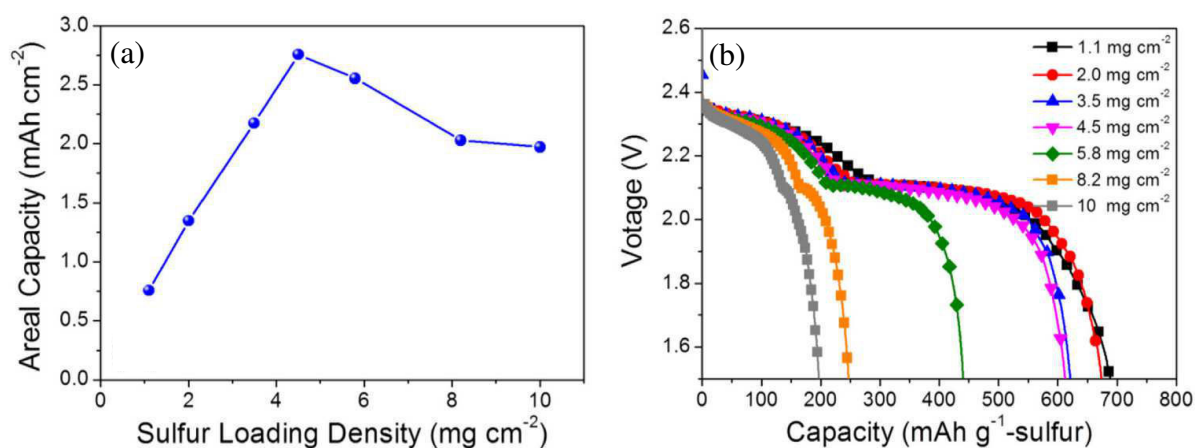


Figure 1-11. Examples of the influence of the sulfur loading on the obtained discharge capacity (a) and corresponding voltage profiles (b)<sup>125</sup>.

It is worth noticing that different sulfur loadings also imply different sulfur/electrolyte ratio (for the same electrolyte amount, which is quite often the case when aiming for comparing solely different sulfur electrodes). This is another parameter that should be carefully considered and reported in every experimental section, which, unfortunately, is not often the case.

### 1.3.1.d) Carbon based current collectors

Among other proposed solutions in terms of application as a porous current collectors (*i.e.* metal foams<sup>126,127</sup>), carbon-based current collectors are definitely attracting the highest attention<sup>128,104,129-133</sup>, as an alternative solution to the classical 2D aluminum foil. The macroporous structure of such collector allows for high loads of sulfur per geometric cathode area, reaching dramatically improved loadings (even  $\sim 7 \text{ mg}_{\text{Sulfur}} \text{ cm}^{-2}$ ), as compared with classical aluminum based electrodes. As reported in the literature, utilization of such collectors improves significantly the electronic conductivity of the electrode, by providing better connection of sulfur particles to the 3D conductive network. Electrode resistance is decreased thanks to facilitated electrons propagation along the 3D continuous conductive network<sup>8,124</sup>. The porous structure also offers much easier electrolyte penetration throughout the whole cathode structure<sup>124</sup>.

Carbon porous collectors can be applied in a different manners into the Li/S cell. Depending on the way how it is incorporated, we can distinguish between following architectures, as illustrated on Figure 1-12:

- **‘catholyte’ all liquid cells** (Figure 1-12a), where active material is dissolved directly in the electrolyte in the form of soluble lithium polysulfide species<sup>126,134</sup>, and pure carbon collector is used as a positive electrode. Different ways of ‘catholyte’ preparation are presented in the literature (*i.e.* reaction of solid  $\text{S}_8$  with Li in ether solvents, reaction of  $\text{Li}_2\text{S}$  and  $\text{S}_8$  powders). Nevertheless, what matters is the equivalent amount of sulfur introduced into the system, which reflects the active material loading.
- **‘binder-free cells’** (Figure 1-12d) with sulfur impregnated directly into the pores of carbon collector<sup>124,133</sup>, or simply elemental sulfur melted on the surface of carbon-based current collector<sup>104,131,132,135</sup>.
- **‘composite electrodes’ supported by a carbon collectors** (Figure 1-12c), where a standard electrode ink is coated on the porous carbon sheet, instead of Al foil<sup>128,136</sup>.
- **‘inter-layer’ structure** (Figure 1-12b), where porous carbon electrode is placed between the positive electrode and the separator<sup>129,137,138</sup>. Carbon collector used in such configuration is aimed for increasing the obtained capacity and mitigating polysulfides diffusion to the negative side

In most of the cases, carbon collectors are available commercial products of different suppliers, initially providing this kind of materials for fuel cells industry (gas diffusion layers, GDL). Several different types of substrates, varying in thickness and mass were used. Some literature

also reports on the specific collector substrate, developed for the purpose of 3D electrode architecture, like vertically aligned carbon nanotubes (VA-CNT)<sup>135</sup> or CNT grown on a commercial products such as GDL<sup>104</sup>.

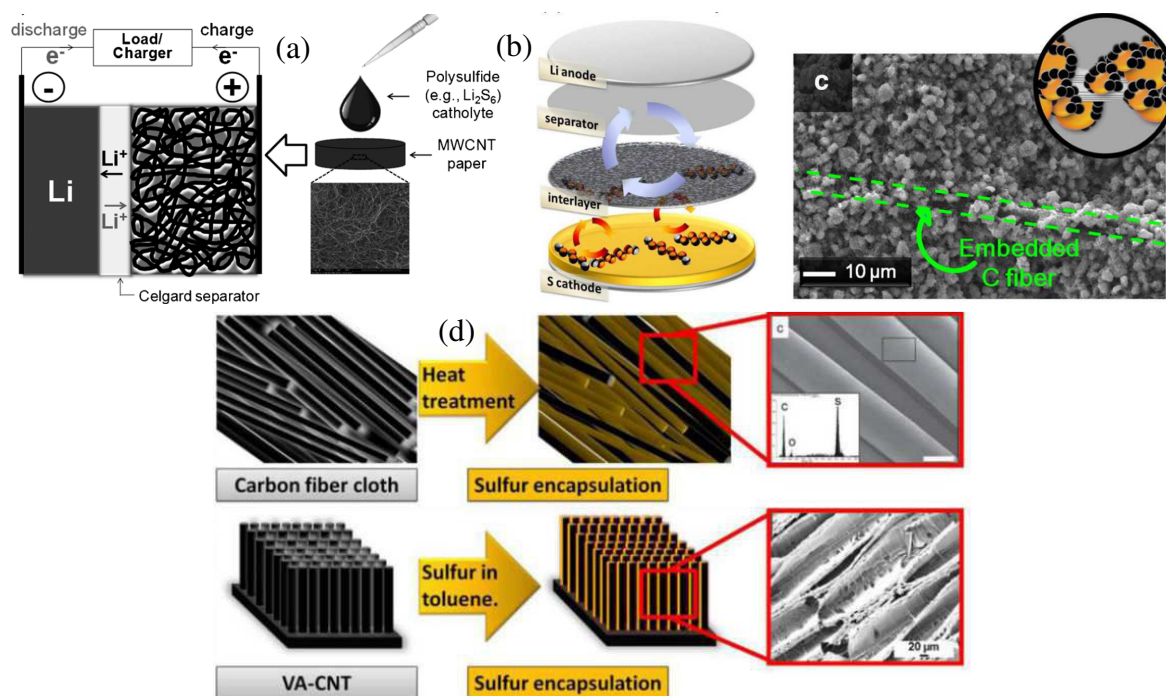


Figure 1-12. Some examples of different incorporation of a porous carbon collector: 'catholyte' cell (a)<sup>134</sup>; as an interlayer (b)<sup>137</sup>; 'composite' electrode (c)<sup>136</sup>; binder-free sulfur melted electrode (d)<sup>135</sup>.

Generally speaking, all these selected examples show superior performances as compared with Al-based collectors, at constant active mass loadings. As an example, pioneer work in this field was presented by Elazari *et al.*<sup>124</sup>, where sulfur got impregnated into the fibers cloth, reaching the sulfur loading of  $6.5 \text{ mg cm}^{-2}$ , and stable capacity of  $\sim 1000 \text{ mAh g}^{-1}$  for 80 cycles at  $0.98 \text{ mA cm}^{-2}$  current density.

However, it is also important noticing that the risk of using such porous collectors, even if displaying excellent performances when taking into account sulfur mass only ( $\text{mAh g}_{\text{sulfur}}^{-1}$ ), may lead to drastic decrease of the cell practical energy density (both gravimetric and volumetric, since they are usually heavier, and sometimes even 10 times thicker than the classical Al foil). Therefore, the complete mass of the electrode should be kept in mind, as demonstrated by Hagen *et al.*<sup>104</sup>.

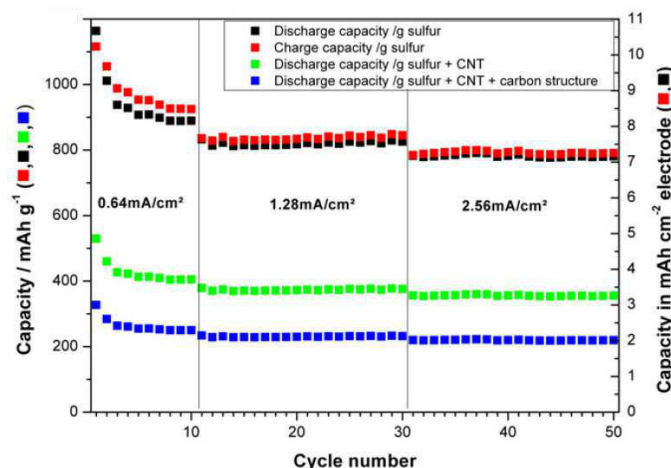


Figure 1-13. An example where capacity is presented with respect to: only sulfur mass (in black), sulfur + CNT mass (in green) and total electrode weight with GDL collector included (in blue)<sup>104</sup>.

### 1.3.1.e) Alternative positive electrode: lithium sulfide (Li<sub>2</sub>S)

Lithium sulfide (Li<sub>2</sub>S) is a lithiated counterpart of sulfur. Recently this positive electrode material has received increasing attention<sup>139-144</sup>, because it gives the possibility of being paired with metallic lithium-free anodes (like silicon, tin, etc.). Thus, the problems encountered when using metallic Li as negative electrode (*i.e.* dendrites formation affecting safety and cell life, reactivity, stability against water) could be eliminated. Moreover, the battery would be built directly in the discharged state, thus also eliminating the risk of self-discharge during initial storage, which is a well-known issue of sulfur positive electrodes<sup>33</sup>. Li<sub>2</sub>S offers a capacity of 1166 mAh g<sup>-1</sup>. Even if lower than the one of sulfur (1675 mAh g<sup>-1</sup>), it is still exceeding several times the capacity of the transition-metal oxides (positive electrode materials in Li-ion batteries)<sup>11</sup>.

However, the main hindrance from using Li<sub>2</sub>S as an active material lies in its insulating nature, both electronic and ionic ( $\sigma = 10^{-13} \text{ S cm}^{-1}$ )<sup>145</sup>. Therefore, in order to improve its utilization, it requires an intimate contact with a carbon additive. Moreover, it is poorly soluble in most of the organic solvents, which also hinders its oxidation as compared with easily reduced sulfur (very soluble). Last but not least, Li<sub>2</sub>S is very sensitive to air moisture, and its reaction with water leads to the formation of LiOH and release of H<sub>2</sub>S gas<sup>146,147</sup>, with characteristic odor of rotten eggs<sup>148</sup>. Thus, the electrode preparation must be performed under protective atmosphere (glove box).

Typical Li<sub>2</sub>S-based electrodes are composed of Li<sub>2</sub>S active material (often used as received with an average particles size of 10 – 20  $\mu\text{m}$ ), conductive additive and binder. The loadings presented in the literature vary in the range of 0.8 – 3.0 mg<sub>Li<sub>2</sub>S</sub> cm<sup>-2</sup><sup>141,149</sup>. As commonly known, initial charge of Li<sub>2</sub>S is a particular process, during which activation of Li<sub>2</sub>S particles occurs. A characteristic potential barrier at the beginning is present (even > 1 V), related with its

insulating nature and large average particles size, leading to a difficult first oxidation step<sup>141,143</sup>. Once the initial charge is finished, the cell behaves in a similar way as a typical Li/S battery (Figure 1-14).

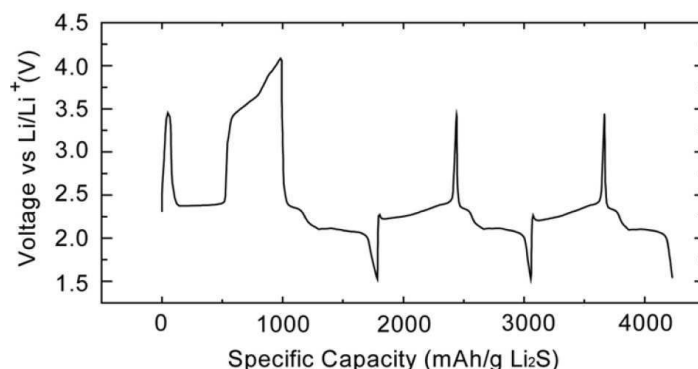


Figure 1-14. Galvanostatic cycling performances of Li<sub>2</sub>S electrode cycled vs. Li.<sup>141</sup>

It is now recognized that the particle size together with the good contact between Li<sub>2</sub>S/carbon allow for better utilization of active material, and that it provides easier oxidation process (decrease of the initial activation barrier). Strategies undertaken to obtain smaller Li<sub>2</sub>S particle size, as proposed in the literature, are: (i) mechanical grinding of commercially available Li<sub>2</sub>S powder through the ball-milling process<sup>141,149-152</sup>, (ii) dissolution in anhydrous EtOH and impregnation in a carbon structure, as proposed by Yushin's group<sup>142</sup>, (iii) using a synthesis process to form directly the nano-sized powder, like for example: sulfur dissolution in toluene and further reduction with lithium triethylborohydride (LiEt<sub>3</sub>BH) in tetrahydrofuran<sup>145,149</sup>.

Apart from standard mixing of Li<sub>2</sub>S with a classical carbon black (either by ball milling, or in mortar), other strategies were proposed for improving Li<sub>2</sub>S/carbon contact: (i) carbon coating through reduction of polyacrylonitrile (PAN) or sucrose during carbonization<sup>148</sup>, (ii) spark-plasma sintering process<sup>147</sup>, or (iii) Li<sub>2</sub>S powder sandwiched between CNT disks<sup>153</sup>.

When combining both strategies, *i.e.* reduced particles with intimate carbon coating, impressive results could be obtained, where a stable capacity of ~ 980 mAh g<sub>Li<sub>2</sub>S</sub><sup>-1</sup> (or 1400 mAh g<sub>sulfur</sub><sup>-1</sup>) over 100 cycles at C/5 could be preserved, as demonstrated by Yushin *et al.*<sup>142</sup> Up to date, these capacity values seem to be the best performing ones. However, the final electrode loading was relatively low (1.4 mg cm<sup>-2</sup>), while the Li<sub>2</sub>S fraction was not given. For comparison, the electrodes prepared from commercial Li<sub>2</sub>S and simply mixed with carbon, displayed capacity in the range of ~ 480 mAh g<sub>Li<sub>2</sub>S</sub><sup>-1</sup> (or 680 mAh g<sub>sulfur</sub><sup>-1</sup>), as shown on Figure 1-15.

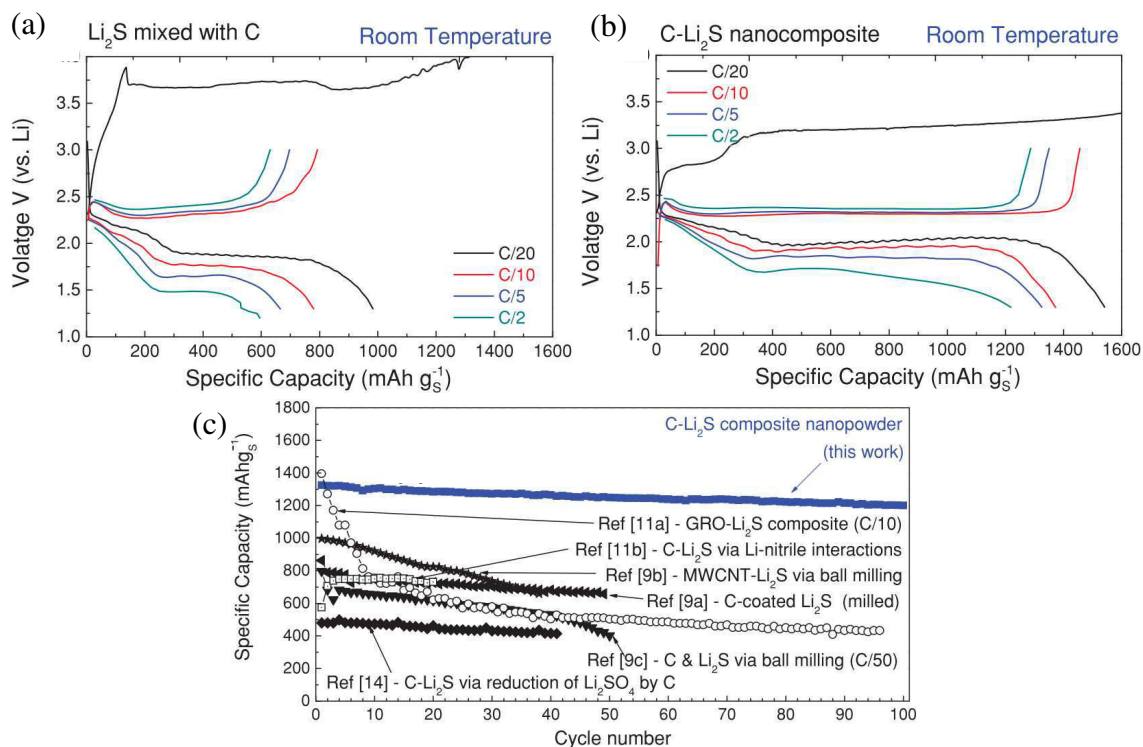


Figure 1-15. Comparison of electrochemical properties of simply mixed commercial  $\text{Li}_2\text{S}$  and C powders (a), with C- $\text{Li}_2\text{S}$  nano-composite prepared through dissolution procedure in anhydrous EtOH with PVP binder (b). Capacity retention of improved  $\text{Li}_2\text{S}$  electrodes, as compared with other existing literature reports (c).<sup>142</sup>

It is also interesting to see how the literature refers to a simple  $\text{Li}_2\text{S}$ /carbon mixing in comparison with the “optimized composite electrodes”. Yang *et al.*<sup>154</sup> claim that simple mixing of commercial as-received powder with carbon black results in almost no capacity ( $25 \text{ mAh g}^{-1}$ ), while nano- $\text{Li}_2\text{S}@\text{CMK-3}$  confined structure (with relatively complicated fabrication procedure) displays initial discharge capacity of  $580 \text{ mAh g}^{-1}$ , as presented on Figure 1-16.

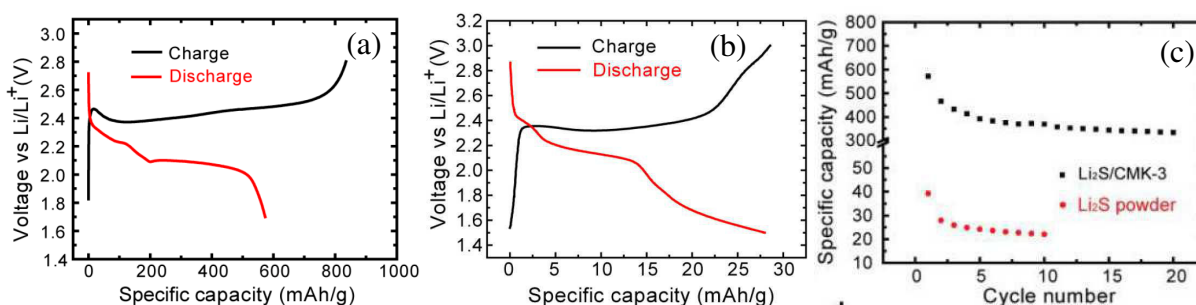


Figure 1-16. Initial cycle voltage profile of nano- $\text{Li}_2\text{S}@\text{CMK-3}$  confined structure (a) as compared with simply mixed commercial  $\text{Li}_2\text{S}$  and C powders (b), and corresponding capacity retention of both electrodes (c).<sup>154</sup>

Since  $\text{Li}_2\text{S}$  first charge significantly differs from the following cycles, Yang *et al.*<sup>141</sup> proposed a mechanism for this initial oxidation (Figure 1-17). As  $\text{Li}_2\text{S}$  is relatively difficult to oxidize,

the initial charge can be performed with higher cut-off voltage potentials (up to 4.0 V or even 4.1 V). However, according to Aurbach *et al.*<sup>143</sup> such high potentials may result in strong electrolyte degradation. Instead, utilization of redox-mediators was proposed by this group for easier  $\text{Li}_2\text{S}$  activation. Addition of soluble polysulfides to the electrolyte was also proved to eliminate the initial energy activation barrier and to facilitate the oxidation of  $\text{Li}_2\text{S}$ <sup>139,141</sup>, possibly through the chemical activation of  $\text{Li}_2\text{S}$  in the presence of polysulfides, as explained by Belharouak *et al.*<sup>139</sup>

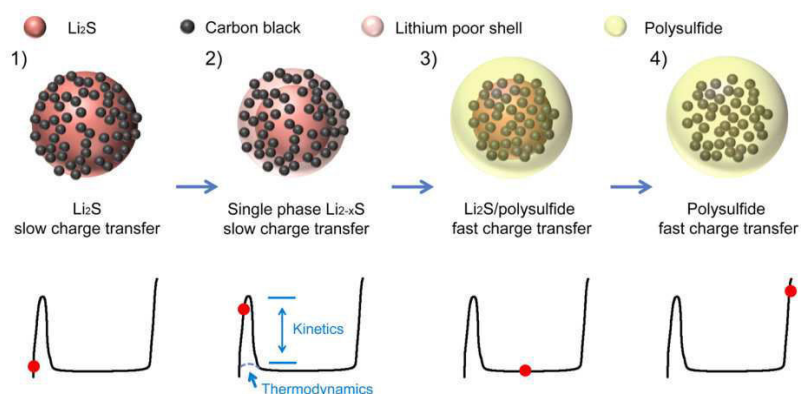


Figure 1-17. Mechanism of  $\text{Li}_2\text{S}$  initial activation proposed by Yang *et al.*<sup>141</sup>.

Development of  $\text{Li}_2\text{S}$ -based electrodes targets to integrate them in a complete metallic Li-free sulfur cell. Some examples in the literature were demonstrated and are discussed in the further section.

### 1.3.2. Electrolyte

From the practical point of view, Li/S system is basically a semi-liquid one, since most of the redox reactions involve somehow soluble species that turn to be unavoidable products for correct battery operation. The choice of electrolyte is thus a parameter of high importance and should be strongly taken into consideration. In particular, solvents need to be carefully selected in order to be chemically compatible with soluble, but also very reactive polysulfide species, especially  $\text{S}_3^-$ . For example,  $\text{Li}_2\text{S}_x$  soluble species (especially radical ones) are strongly reactive with carbonate-based electrolytes, these latter being therefore not usable in the Li/S system<sup>45,155</sup>. However, there are some reports demonstrating a successful application of carbonate-based electrolytes into Li/S system<sup>156,157</sup>.

The nature of the solvent(s) and their properties (viscosity, donor number, dielectric constant) are of high importance, since these properties dictate the electrolyte behavior in regards to the polysulfide species (solubility, dissociation, mobility) and lithium metal passivation. Majority of today's electrolytes are based on binary mixtures of different ethers, mostly 1,3-dioxolane

(DIOX) and 1,2-dimethoxyethane (DME), usually in equal volumetric proportions. A whole family of high molecular weight ethers, such as diethylene glycol dimethylether (diglyme, DEGDME), tetraethylene glycol dimethylether (tetraglyme, TEGDME), polyethylene glycol dimethylether (PEGDME), has also been extensively studied. Several systematic investigations were conducted on single or binary electrolyte systems, in order to find the most optimal composition<sup>158,159,160</sup>. Other solvents were also considered, such as sulfolanes<sup>161,162,163,164</sup>, tetrahydrofuran (THF)<sup>165</sup>, toluene<sup>166</sup>. Apart from liquid electrolytes, other alternative solvents were proposed, *i.e.* gel polymer electrolytes<sup>167</sup>, solid polymer electrolytes<sup>168</sup>, ionic liquids<sup>169,170</sup> or liquid electrolytes with high salt concentration<sup>171</sup>, mostly targeting for polysulfide shuttle mitigation.

Due to the different properties of electrolyte solvents, not only the solubility of sulfur may vary, but also behavior of polysulfide species may differ. Indeed, UV-Vis spectroscopy tests<sup>27,172</sup> and rotating-ring disk electrode (RRDE) studies<sup>173</sup> performed on two systems with both sulfolane and ether-based electrolytes, showed different polysulfides behaviors.

Concerning the choice of Li salt, it seems that its effect was not studied a lot for Li/S system<sup>174</sup>, even if well-known to impact electrolyte conductivity, passivation film on lithium, etc. The most popular salt is LiTFSI (lithium bis(trifluoromethanesulfonyl)imide), used in the concentration of 1M. Indeed, this salt presents high conduction properties, high thermal, chemical and electrochemical stabilities, and substantially lower sensitivity towards moisture (no hydrolysis) as compared with LiPF<sub>6</sub> (most common salt used in Li-ion batteries)<sup>175</sup>. In the case of Li/S system, the high cut-off potential value is 3.0 V *vs.* Li<sup>+</sup>/Li (maximum 4.0 V in case of the initial cycle of Li<sub>2</sub>S), thus no corrosion of the aluminum current collector is expected. On the contrary, the presence of LiTFSI in carbonate based electrolyte is responsible for parasitic current at potential above 4.0 V *vs.* Li<sup>+</sup>/Li, which is attributed to aluminum corrosion<sup>176</sup>.

The most popular approaches conducted in terms of electrolyte improvement are related with the use of **additives**. The commonly known one is *lithium nitrate (LiNO<sub>3</sub>)*, used to stabilize the metallic lithium surface as initially studied by Aurbach *et al.*<sup>47</sup>, and followed by extensive reports of Zhang<sup>177,178</sup>. LiNO<sub>3</sub> proves to be highly efficient to suppress the shuttle mechanism due to efficient passivation of the lithium surface, and drastic improvements of coulombic efficiency are reported. However, beneficial lithium passivation is also accompanied with irreversible reduction of LiNO<sub>3</sub> at the carbon surface in the positive electrode, when discharging to the potentials below 1.6 V<sup>177</sup>. Its beneficial effects may also be decreased during prolonged cycling due to the additive consumption.

Introduction of soluble *lithium polysulfides* into the electrolyte is also reported. Lee *et al.*<sup>179</sup> and Xu *et al.*<sup>180</sup> added polysulfides as an electrolyte buffer to prevent dissolution of positive electrode actives material. However, it is really likely that these already dissolved polysulfides participate to the electrochemical process, *i.e.* resulting in an extra-capacity (not related to the positive electrode). Moreover, if added in a sufficient concentration, polysulfides may also be



used in so-called ‘all-liquid cell’, *i.e.* ‘catholyte’, where sulfur active material is directly dissolved in the electrolyte, in the form of  $\text{Li}_2\text{S}_x$  ( $x = 6$  or  $8$ )<sup>126</sup> or  $\text{Li}_2\text{S}_5$ <sup>164</sup>.

*Phosphorus pentasulfide* ( $\text{P}_2\text{S}_5$ ) was reported as an additive by Liang *et al.*<sup>181</sup>.  $\text{P}_2\text{S}_5$  prevents the formation of solid  $\text{Li}_2\text{S}$  on both positive and negative electrodes. Thus, during discharge, no solid phase is formed on the positive electrode, eliminating the risk of passivation. It can also get reduced on the metallic lithium surface by forming  $\text{Li}_3\text{PS}_4$ , which may suppress polysulfide shuttle phenomenon and irreversible losses of active mass (because of  $\text{Li}_2\text{S}$  precipitation on lithium). This additive, however, is much less studied and utilized as compared with the most popular  $\text{LiNO}_3$ , probably to its sensitive manipulation.

As previously discussed (section 1.3.1.c), an important parameter that should be taken into consideration is the **electrolyte/sulfur ratio**, since it was proved to influence both cyclability and capacity<sup>105,106,109,125</sup>. Electrolyte added in a large excess may provide better solubility of sulfur and polysulfides species. However, it can also strongly decrease the practical energy density of the cell<sup>123</sup>, and may also be responsible for fast capacity fading during initial few cycles (Figure 1-18). In the work of Ding *et al.*<sup>125</sup>, this capacity fading was attributed to the large amount of electrolyte, which acts as a polysulfides reservoir, preventing further utilization of this lost active mass. Lower amount of electrolyte was demonstrated to provide more stable cycling, however, at much lower sulfur utilization. Thus, the literature rather refers to an ‘optimized S/E’ ratio, which may be different for each system studied. Therefore, different values can be found in the literature ( $50 \text{ g}_{\text{sulfur}} \text{ L}_{\text{electrolyte}}^{-1}$ , or  $\sim 100 \text{ g}_{\text{sulfur}} \text{ L}_{\text{electrolyte}}^{-1}$  for example<sup>105,106</sup>).

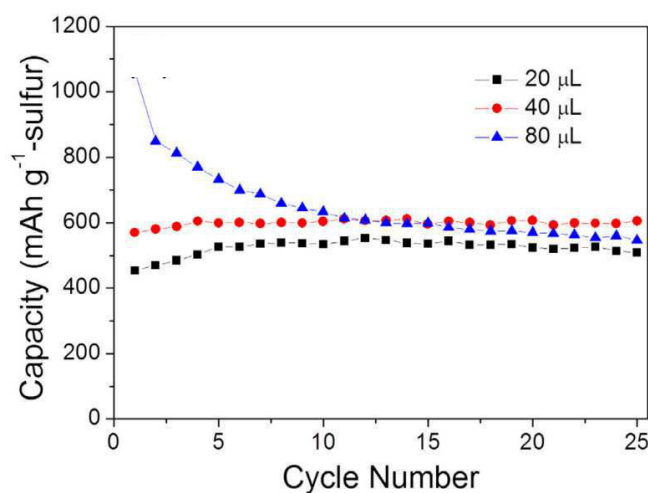


Figure 1-18. Capacity retention of a S/C composite electrode (S/C = 2/1) with a sulfur loading of  $2.4 \text{ mg cm}^{-2}$ , cycled with different electrolyte volumes at a current density of  $57 \mu\text{A cm}^{-2}$ <sup>125</sup>.

### 1.3.3. Negative electrode

As previously mentioned, one of the most important issues related with the use of metallic lithium negative electrode is dendrites formation leading to a safety concerns, together with its high reactivity towards air, electrolyte components and polysulfides.

One of already discussed solution consists in the use of  $\text{LiNO}_3$  electrolyte additive, known from its beneficial impact on lithium electrode passivation<sup>47,177,182</sup>. Lithium bis-(oxalate) borate (LiBOB) was also tested as an additive<sup>183</sup>, in order to protect lithium surface.

The problems of lithium metal electrodes are known for many years, and are common to all lithium metal technologies such as Li-O<sub>2</sub> system for instance. For this purpose, Visco *et al.*<sup>184</sup> presented the concept of protected lithium electrode, using water-stable NASICON-type Li-ion conducting ceramic electrolyte. Yushin *et al.*<sup>185</sup> proposed the deposition of a very thin lithium-aluminum alloy layer on the lithium surface, which was reported to mitigate the polysulfides shuttle. Other solutions like silan-based coating<sup>186</sup>, UV cured polymerization for Li surface protection<sup>187</sup> and dual phase electrolyte<sup>188</sup>, were also reported in the last few years.

While this kind of solutions are devoted to sufficiently protect the surface of metallic lithium, parallel to that, another concept consists of using metallic-lithium free negative electrodes. The literature presents examples of alternative anode materials (pre-lithiated or not) that were combined with sulfur-based positive electrodes, *i.e.* silicon (Si)<sup>189,190</sup>, tin (Sn)<sup>151</sup>. However, pairing such alternative anode with a sulfur positive electrode requires one of the electrode to be pre-lithiated. To this purpose,  $\text{Li}_2\text{S}$  electrode allows for direct utilization of metallic lithium-free negative electrodes.

Silicon (Si) or tin (Sn) are usually combined with  $\text{Li}_2\text{S}$  (or eventually  $\text{S}_8$ ), as being ideal choices due to their high theoretical specific capacity. In particular, Si/ $\text{Li}_2\text{S}$  couple has a theoretical energy density of  $1550 \text{ Wh kg}^{-1}$ <sup>154</sup>. Hagen *et al.*<sup>189</sup> reported on the use of pre-lithiated Si nanowires with sulfur positive electrode. Capacities as high as  $800 \text{ mAh g}_{\text{Sulfur}}^{-1}$  were obtained during 200 cycles. Scrosati *et al.*<sup>191</sup> demonstrated similar concept, based on lithiated Si-C negative electrode coupled with a sulfur positive electrode. Prof. Kaskel's group presented impressive cycling performances of Li-free cells based on pre-lithiated hard carbon (HC) negative electrode combined with a sulfur positive electrode<sup>192</sup>. More than 600 cycles with specific capacity retained at  $\sim 400 \text{ mAh g}_{\text{Sulfur}}^{-1}$  were obtained.

Other examples of pairing Si or Sn negative electrodes with  $\text{Li}_2\text{S}$  can also be mentioned (Figure 1-19). Pioneer work in this field was presented by prof. Scrosati's group<sup>151,193</sup>, where Sn was combined with  $\text{Li}_2\text{S}$ , while prof. Cui's group demonstrated first complete cell of Si/ $\text{Li}_2\text{S}$ <sup>154</sup>.

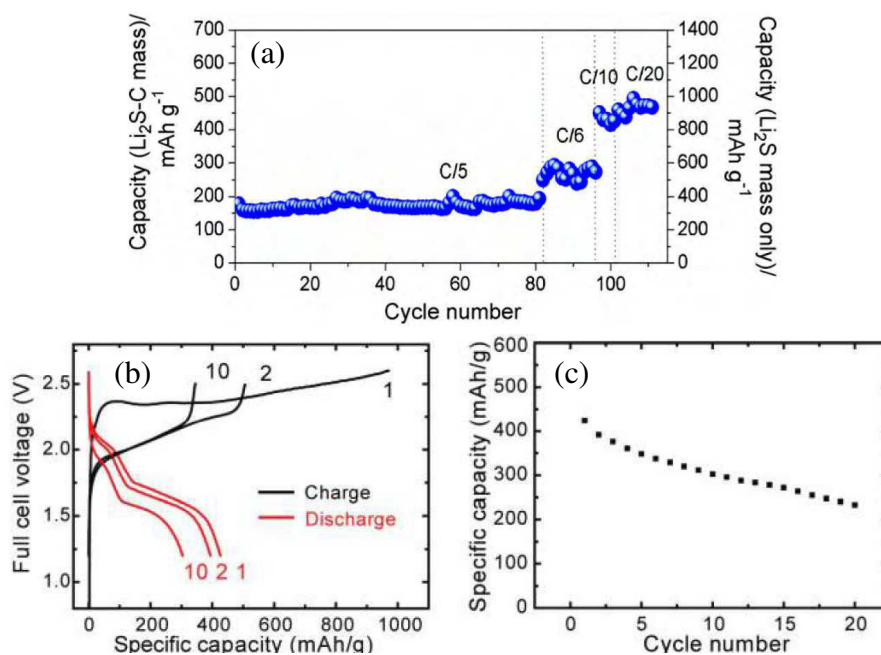


Figure 1-19. Examples of a complete metallic Li-free cells, involving Li<sub>2</sub>S positive electrode, cycled vs. Sn (a)<sup>151</sup> and vs. Si (b,c)<sup>154</sup>.

## 1.4. Advanced characterization methods applied to Li/S system

Understanding of the working mechanism is an extremely important aspect, because any improvement could not be done without prior broader insight into the limiting parameters and involved reactions. In order to better utilize the complete potential of the Li/S cells (and its high energy density), a comprehensive understanding of the redox reactions is necessary. Thus it is highly desired to provide deeper fundamental understanding of the Li/S system, which is very complex.

In the first section (1.2.1), a simplified and very general description of working mechanism was given. However, it is important to note that in reality, different redox reactions together with chemical disproportionation and dissociation reactions occur.

Barchasz *et al.*<sup>194</sup> proposed a complete description of the reactions occurring during discharge, by coupling three techniques: UV-Vis spectroscopy, HPLC (High Performance Liquid Chromatography) and ESR (Electron Spin Resonance). A mechanism of sulfur reduction in TEGDME-based electrolyte was proposed, as shown on the illustrative graph (Figure 1-20).

It is also important to underline that a “reference” model of a working mechanism, which could be applicable to all Li/S systems, does not exist. The reason for that lies in the fact that so many parameters (cycling conditions, electrolyte nature, sulfur/carbon composite, S/E ratio, active

material loading, etc.) may change the equilibria and the involved redox reactions. Working mechanism of Li/S batteries is, therefore, composed of many pieces of puzzle, which could not be directly compared. However, all together, they bring very fruitful information to the Li/S community and deeper understanding of the mechanisms and redox reactions hidden behind.

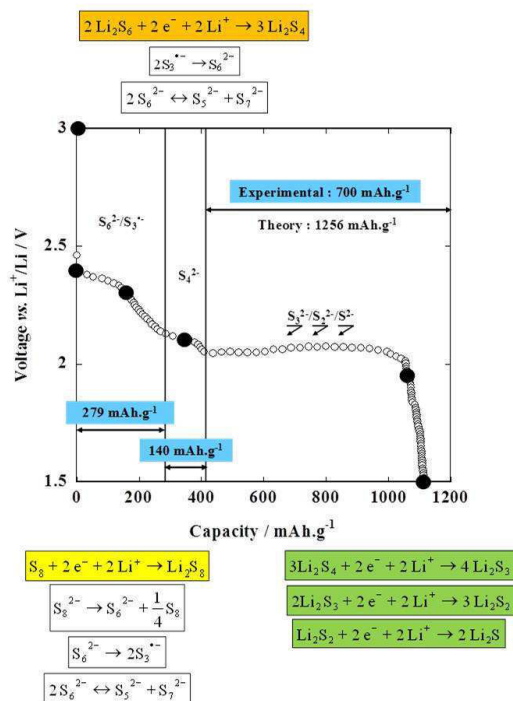


Figure 1-20. Proposed detailed redox reactions together with disproportionation and dissociation reactions, during initial discharge studied by coupling three techniques: UV-Vis, HPLC and RPE<sup>194</sup>.

The kinetics of the reactions, where longer chain polysulfides are involved (more soluble species), starting from  $S_8$  through  $Li_2S_4$  formation (thus, along upper discharge plateau and the sloping step) are believed to be fast<sup>195,196</sup>. On the other hand, the reactions of shorter chain polysulfides (along the lower discharge plateau), together with solid product(s) formation, are known to present much slower kinetics (large overpotential)<sup>197</sup>.

The specificity of the Li/S system, as previously mentioned, comes from the fact that the physical state of active material (solid, soluble, both) is strongly dependent from the state of discharge/charge of the battery. Therefore, depending on their particularity, some of the techniques can be applied with more success to analyze solid reaction products, like X-ray diffraction (XRD)<sup>23-25,198-200</sup>, transmission X-ray spectroscopy (TXM)<sup>199,201</sup>, K-edge X-ray absorption near edge structure (XANES), scanning electron microscopy (SEM). On the contrary, other techniques are more appropriate for soluble polysulfides investigation/identification, *i.e.* UV-Vis spectroscopy<sup>27,172,194</sup>, Raman spectroscopy<sup>196</sup>, X-Ray Absorption spectroscopy (XAS)<sup>29,202-204</sup>, HPLC<sup>194</sup>, or Rotating Ring Disk Electrode technique (RRDE)<sup>173</sup>.

Monitoring of the system with few techniques coupled together also brings deeper understanding. Patel *et al.*<sup>203</sup> have applied *operando* XANES with *ex situ* and *post mortem* Li magic-angle spinning nuclear magnetic resonance (<sup>6,7</sup>Li MAS NMR). An approach where *in situ* and *operando* XRD technique was coupled with another *operando* technique, like XAS by Lowe *et al.*<sup>200</sup>, or TXM by Nelson *et al.*<sup>199</sup>, was also reported. A clear benefit of applying techniques *via in situ* and *operando* mode lies in the direct response of the system in the real time battery operation. Moreover, preparation of *ex situ post mortem* samples is not required anymore, which may also be an issue, as possibly changing the equilibriums (an example: dilution of polysulfides solution for UV-Vis observation) or leading to undesirable electrode/material degradations/evolutions (an example: risk of washing out the sulfur formed at the end of charge when cleaning electrodes for *post mortem* analyses).

As regard to the solid phase(s) evolution, the first XRD results were obtained from *ex situ* XRD studies<sup>28,117,205-207</sup>. However, the opinion was divided when concerning the most important questions related with sulfur and Li<sub>2</sub>S formation, *i.e.* (i) does the crystalline phases appear/disappear reversibly; (ii) if Li<sub>2</sub>S<sub>2</sub> can be detected; (iii) if sulfur is completely reduced during initial discharge and then formed back in the following charge, etc. Moreover, *ex situ* studies eliminate the possibility to determine the exact moment of these solid/soluble phases evolutions, thus another questions related with that appeared. Further *in situ* and *operando* tests performed by Nelson *et al.*<sup>199</sup> and Cañas *et al.*<sup>198</sup> did not completely give a clear answer to the debates. Nelson's results reported on complete disappearance of elemental sulfur during initial discharge and reformation at the end of charge, in agreement to Cañas' statements. However, the main discrepancies lied in Li<sub>2</sub>S product. Nelson did not find any traces of crystalline Li<sub>2</sub>S (however, the presence of amorphous phase was not verified), while Cañas reported that it starts to form at ~ 60% DOD, and disappears completely during following charge. Latest *in situ* XRD reports were in agreement in terms of sulfur reduction and recrystallization<sup>24,25,200</sup>. Li<sub>2</sub>S formation was also confirmed, however, the precise moment of nucleation was sometimes difficult to define<sup>24</sup>.

Solid phases evolution, together with other soluble polysulfide species (high to medium-order polysulfides) were investigated by Cuisinier *et al.* using *in operando* XANES<sup>202</sup>. They reported on rather delayed formation of Li<sub>2</sub>S during discharge process (somehow in the middle of the lower discharge plateau), and on its complete oxidation to soluble species upon following charge. However, in the contrary to most of the XRD and TXM findings concerning sulfur reduction/nucleation<sup>201</sup>, they reported on about 25 % unutilized sulfur along the complete cycle.

Electrochemical Impedance Spectroscopy (EIS) is also a very useful method for investigating the Li/S system, as a powerful and non-destructive technique for describing the electrochemical response of the cell, kinetics of the reactions, limiting processes, eventual presence of passivation layers, etc. EIS is often used as a characterization technique applied for the evaluation of different electrode composite materials, where some improvements (addition of carbon fibers, change of the current collector etc.) have been made<sup>107,128,129,136,208</sup>. EIS applied

in such mode is recorded at only one point on the cycling curve, often at the end of charge or discharge. There are also some reports where EIS was applied upon battery cycling, in order to evaluate the mechanisms hidden behind<sup>35,132,207,209-213</sup>. The main difficulty in using this technique, however, lies in correct interpretation of the obtained results. Therefore, the main discrepancies come from the correlation of the semicircles (visible in the Nyquist plot representation) with their physical meanings. As a matter of fact, if from the beginning the correlation is done incorrectly, further interpretations may be (partially or completely) wrong. It also seems that this technique is sometimes used without providing the minimum of the necessary information for the reader (like for example characteristic frequency values) to evaluate the pertinence of the given interpretation.

In regard to the soluble polysulfide species, their detection and evolution upon battery operation may strongly depend on the electrolyte system. Indeed, Patel *et al.*<sup>172</sup> have clearly demonstrated that polysulfides evolution in sulfolane-based electrolyte is different from the one observed in ether-based electrolyte. More particularly, in case of sulfolane solvent, the polysulfides composition during discharge and charge seems to be similar, with only differences in their concentration. On the contrary, in TEGDME/DIOX system, differences in polysulfide compositions as well as in concentration for the same state of charge/discharge were noticed. This simply indicates that the redox reactions involved during discharge and charge processes are not similar and do not follow the same pathways. An example of the soluble species evolution is shown on Figure 1-21a. Cuisinier *et al.*<sup>202</sup> also reported on the presence of so-called hysteresis between charge and discharge processes, which was explained by different steps involved in redox processes during both discharge and charge. The evolution of different sulfur species is shown on Figure 1-21b. EIS reports presenting the evolution of electrolyte resistance<sup>214</sup>, also show such hysteresis *i.e.* different electrolyte resistance values along the complete cycle (charge and discharge).

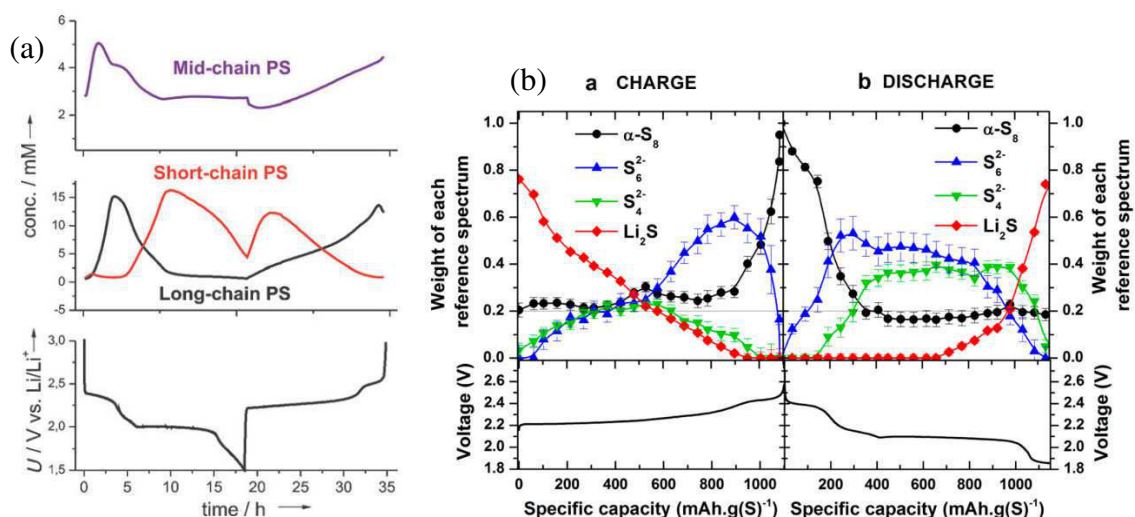


Figure 1-21. UV-Vis studies in TEGDME/DIOX-based electrolyte (a) where evolution of different polysulfides (long, short and mid-chain) is presented along with the voltage profile<sup>172</sup>. Parallel to that, evolution of sulfur species ( $\text{Li}_2\text{S}$ ,  $\text{S}_8$ ,  $\text{S}_4^{2-}$  and  $\text{S}_6^{2-}$ ) observed by XANES in DME/DIOX-based electrolyte is shown<sup>202</sup> (b). Both techniques were applied *via in situ* and *operando* methodology.

## 1.5. Conclusions

Already by looking at the ‘exponentially’ increasing number of publications, it is clear that Li/S batteries have attracted enormous attention. Despite decades of research, the system limitations do not seem to be fully resolved, even if impressive progresses have been made during last 4-5 years, in majority related to the sulfur positive electrode development. Hundreds of examples, where high capacities, almost reaching the theoretical values, and of good capacity retention, have been demonstrated. Nevertheless, most of the proposed architectures are very sophisticated, relatively difficult to scale up, and mostly implying active material loadings not really compatible for designing a high energy Li/S cells. Therefore, it is likely that nowadays the researchers turned back into simpler and cheaper solutions, keeping in mind possible commercialization of the product. Thus, strong attention is paid on the parameters which would seem to be trivial at first, but which are expected to affect deeply the performances of the system. It also seems that unrealistic electrode loadings (less than  $1 \text{ mg}_{\text{sulfur}} \text{ cm}^{-2}$ ) are less and less studied, and a lot of work is proposed for increasing the active material loading. The problems of metallic lithium also promoted the development of metallic lithium-free systems, with lithium sulfide ( $\text{Li}_2\text{S}$ ) as the most envisaged candidate.

Last but not least, an impressive progress was made in terms of deeper understanding of the working mechanism. Advanced techniques were applied, sometimes *via in situ* and *operando* methodology, which gave fruitful information on the real time response of the battery upon operation. However, despite these last progresses, some questions are still to be solved in terms of exact mechanisms and limitations.

Therefore in this work, we focused mostly on simple solutions, *i.e.* easily prepared sulfur electrodes. In parallel to the optimization of the Li/S cells, we were deeply interested in the understanding of the key parameters and their role to tune the battery performances. In particular, the next two chapters are devoted to the sulfur positive electrode, including both understanding and improvement aspects.

# Chapter 2: Sulfur positive electrode on Al collector – studies and important parameters determination

## 2.1. Motivation of the work

The literature data review concerning the positive electrode development (see paragraph 1.3.1) shows that complicated methods are very often applied for the fabrication of carbon/sulfur composites, leading to sophisticated electrode architectures. However, it is often the case that gain in the performances is not relevant to the work implied during the fabrication process. In addition, many of these electrodes are characterized by low active mass loadings. Therefore, our work was based on very simple positive electrode, *i.e.* prepared in a simple way with the use of cheap and commercially available products, and bearing in mind the following aspects:

- Practical electrode loading:  $\geq 2.0 \text{ mg cm}^{-2}$  or  $\geq 3.35 \text{ mAh cm}^{-2}$
- Relevance of the preparation methods toward practical improvements of performances and procedure scalability<sup>35</sup>

In the first part of this chapter, experiments concerning the electrodes preparation, cell assembly and testing are described. In the second part, we purely focus on development of positive electrodes on aluminum current collector. Comparative studies were done the electrodes coated on aluminum substrate, in order to better understand the system and determine the crucial parameters. In particular, we aimed at finding a correlation between the electrodes' morphology, their electric properties (studied by Electrochemical Impedance Spectroscopy) and electrochemical performances. We also demonstrate how the conductive carbon and binder natures, as well as the electrode loading affect those properties. While carbon particles play an important role in providing an electronic percolation for the insulating sulfur particles, binder material is responsible for the electrode's components cohesion, and its choice may be crucial for the final electrode morphology. Therefore, the importance of a binder was investigated, related to the connection of carbon and sulfur particles, their interaction with the current collector, and the mechanical properties of electrodes.



## 2.2. Experimental part

### 2.2.1. Preparation of the electrodes and the electrolyte

The procedure for the *electrode preparation* was referred to the work of Céline Barchasz - a former PhD student in our research groups<sup>35,45,126</sup>. Based on general conclusions obtained previously, as well as on our preliminary studies, it turned that the source of sulfur and active material pretreatment did not affect significantly the practical discharge capacity and cyclability, and we established a simple way of electrode fabrication.

As received sulfur (-325 mesh, Alfa Aesar) was used as an active material without any pretreatments. SuperP<sup>®</sup> (Timcal) was used as a conductive carbon additive and poly(vinylidene difluoride) (PVdF 5130, Solvay; dissolved in *N*-methyl-2-pyrrolidinone as 12 wt% solution) was selected as a “reference” polymeric binder. “Standard” electrode composition was set up to be 80/10/10 wt% (S/C/binder), unless mentioned differently. This ratio was arbitrarily chosen<sup>45</sup>, to maintain a high sulfur loading and a high sulfur percentage, keeping in mind the practical application of the electrodes. Other electrodes were also prepared, depending on the aim of the study. Therefore the composition varied in terms of: (i) sulfur/carbon (S/C) ratio; (i) type of carbon: SuperP<sup>®</sup>, Ketjenblack<sup>®</sup> (EC-300J, AkzoNobel), Vapor Growth Carbon Fibers (VGCF<sup>®</sup>, Showa Denko) and (ii) type of binder: PVdF, mixture of carboxymethyl cellulose sodium salt/nitrile-butadiene rubber (under common abbreviation of CMC/NBR).

In order to prepare sulfur/carbon mixtures, precise amounts of sulfur and carbon powders (SuperP<sup>®</sup>, Ketjenblack<sup>®</sup>, VGCF<sup>®</sup>, or mixture of both SuperP<sup>®</sup>/VGCF<sup>®</sup>) were simply grinded together in an agate mortar during ~ 15 min, with addition of few drops of cyclohexane (Aldrich, anhydrous, 99.5 %). After a thorough grinding and the solvent evaporation, S/C powder mixture was recuperated into a beaker, and no additional heat treatment was applied. To finish the ink preparation, a polymeric binder was added into the S/C mixture:

- a) *PVdF based electrodes (10 wt% fraction of a binder)*: an appropriate amount of PVdF 5130 solution (12 wt% in NMP) was added. An additional volume of NMP was also incorporated in order to obtain an optimal viscosity of the ink to facilitate the electrode coating. The volume of NMP added was different, depending on the carbon nature and its specific surface area. All components were stirred together manually with a spatula until homogenous slurry was obtained.
- b) *CMC/NBR based electrodes (10 (6+4) wt% fraction of a binder)*: an appropriate amount of CMC solution (3 wt%; Sigma Aldrich; 250,000 g mol<sup>-1</sup>) dissolved in deionized water was incorporated, with additional amount of solvent (deionized water) to obtain a desired viscosity. All components were mixed intensively with Dispermat<sup>®</sup> dissolver (VMA-Getzman; model LC55) during 15 min at ~ 4000 rpm. Indeed, pure carbon particles are hydrophobic, and the interfacial energy between SuperP<sup>®</sup> and water is high, which prevents

from good wetting of the carbon spheres. Therefore, CMC polymer is used as a dispersive and thickening agent, and a high rotation speed of mixing is applied. In the next step, a precise amount of NBR was added, and dispersion was subjected to additional mixing with Dispermat<sup>®</sup> (5 min). This time, however, the stirring was performed at lower rotation speed (500 rpm) in order not to break NBR polymeric chains. In further discussion, these electrodes, even if composed of mixtures of two polymers, are named as CMC-based electrodes, for simplicity.

Such prepared homogenous ink was then coated using doctor-blade technique onto 20  $\mu\text{m}$  thick Al foil. Freshly coated electrode was dried in an oven at 55 °C during 24 h. Once dried,  $\varnothing$  14 mm electrode disks (surface area of 1.539  $\text{cm}^2$ ) were punched out, precisely weighed and exposed to additional drying at RT under vacuum (in BÜCHI<sup>®</sup>) during few hours in order to remove the eventual residuals of water and NMP. Dried electrodes were then entered inside the argon-filled glove box for further coin cells fabrication. A schematic graph (Figure 2-1) illustrates all the steps of electrode preparation.

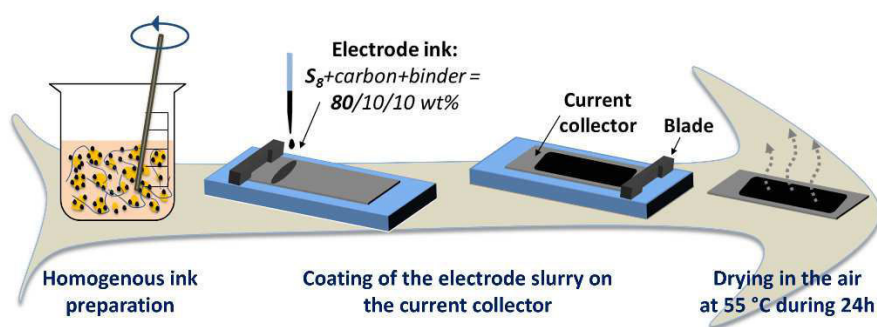


Figure 2-1. Schematic illustration of the electrode preparation procedure.

The resulting electrode loading and thickness were mainly ruled by the ink viscosity and the thickness of the blade. The “thin” electrodes were aimed to be  $\sim 2.5 \text{ mg cm}^{-2}$  (which is  $\sim 2 \text{ mg}_{\text{Sulfur}} \text{ cm}^{-2} \leftrightarrow$  theoretically  $\sim 3.35 \text{ mAh cm}^{-2}$ ). Thicker electrodes were also prepared, with loadings up to  $7 \text{ mg}_{\text{Sulfur}} \text{ cm}^{-2}$ .

A “standard” *liquid electrolyte* composition was chosen, based on former results obtained by Céline Barchasz<sup>45</sup>. The electrolyte was prepared in an argon-filled glove box by dissolving lithium bis(trifluoromethane sulfone)imide salt (LiTFSI, 99.95 %, Rhodia Asia Pacific), in a mixture of ether-based solvents: tetraethylene glycol dimethyl ether (TEGDME, 99 %, Aldrich) and 1,3-dioxolane (DIOX, anhydrous, 99.8 %, Aldrich) in 1/1 volume ratio. Lithium nitrate ( $\text{LiNO}_3$ , Aldrich) was used as an additive commonly known from its beneficial effect against polysulfide shuttle<sup>177,182,215</sup>. The salt concentrations in the solvents were as follow: 1M LiTFSI and 0.1M  $\text{LiNO}_3$ . The solvents were stored on molecular sieves for at least 72 h prior being used, while LiTFSI and  $\text{LiNO}_3$  salts were dried under vacuum during 48h at 120 °C and 80 °C, respectively.

## 2.2.2. Battery assembly

### Two-electrode cells:

The CR2032 coin cells (Figure 2-2) were fabricated in a glove box under inert atmosphere to avoid any reactions of lithium and electrolyte with air.

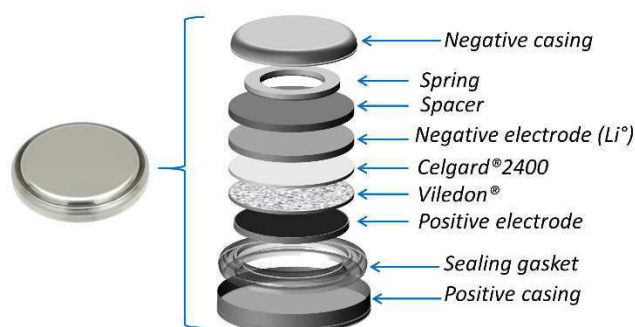


Figure 2-2. Schematic representation of a two-electrode coin cell (CR2032).

External stainless steel casings served both as a current collectors and a container of the battery. They were separated with a plastic gasket, to avoid any electronic contact between them and provide perfect sealing of the cell. Positive electrode disk ( $\varnothing$  14 mm) was placed inside one of the cap and covered with two layers of separator (both  $\varnothing$  16.5 mm): Viledon<sup>®</sup> (Freudenberg) - a 240  $\mu$ m thick polyolefin non-woven tissue, and Celgard<sup>®</sup>2400 - a 25  $\mu$ m thick polypropylene microporous layer. Liquid electrolyte was then poured onto the separators, filling all their pores, as well as the pores of the positive electrode. The amount of liquid electrolyte (150  $\mu$ L) was fixed for simplicity to already existing procedures of coin cell preparation, and was much in excess. Nevertheless, the influence of lower electrolyte amount was also investigated, and the results are presented in further discussion. Metallic lithium (Li, 135  $\mu$ m, Rockwood Lithium) was used as a counter electrode. Disk of Li ( $\varnothing$  16 mm) was punched, placed on the soaked separators and covered with a 0.5 mm thick stainless steel spacer ( $\varnothing$  16 mm). Before closing the complete coin cell with the top casing, a stainless steel spring was placed on the spacer, in order to provide sufficient pressure and contact between all the components.

### Symmetric coin cells:

Symmetric coin cells composed of two identical sulfur electrodes were prepared for the electrochemical impedance (EIS) tests. The coin cell preparation was identical to the two-electrode configuration described above, with the difference lying in a Li disk replaced by a positive electrode. If both electrodes were rather thin ( $> 100 \mu$ m), a thicker spacer (1 mm thick instead of 0.5 mm typically used) was used, in order to reduce to the minimum any issues related to the contact resistances.

**'Catholyte' all-liquid cells:**

The catholyte cell was prepared as a typical two-electrode coin cell described above, where positive electrode was replaced by Ø 14 mm NwC collector (GDL felt, H2315<sup>216</sup>) and the electrolyte contained already dissolved lithium polysulfides<sup>15</sup>. An example of a catholyte solution composition is as follow: 1M LiTFSI + 0.1M LiNO<sub>3</sub> + 0.5M Li<sub>2</sub>S<sub>6</sub> in TEGDME/DIOX 1/1 volume ratio. The procedure of a catholyte preparation was directly adopted from the work of C. Barchasz<sup>45,126</sup>. Li<sub>2</sub>S<sub>6</sub> was prepared by mixing together equivalent amounts of elemental sulfur and lithium in TEGDME solvent. Once Li and S<sub>8</sub> compounds were fully dissolved and Li<sub>2</sub>S<sub>6</sub> formation was completed (red dark color), other components (DIOX, the salts) were added. During coin cell preparation, unless marked differently, 40 µL of a catholyte solution was introduced to the cell, fulfilled with additional amount of standard electrolyte (60 µL) without Li<sub>2</sub>S<sub>6</sub>. Theoretical capacity of such coin cell was calculated with respect to the amount of sulfur introduced to the system in the form of Li<sub>2</sub>S<sub>6</sub> (no other source of sulfur in the positive electrode).

**2.2.3. Characterization methods and tests conditions**

Two-electrode Li/S coin cells were galvanostatically cycled (GCPL – galvanostatic cycling with potential limitations) in the voltage range between 1.5 V and 3.0 V vs. Li<sup>+</sup>/Li on Arbin<sup>®</sup> battery cycler, at the temperature of 25 °C (± 2 °C). Different currents were applied to test the cell performances at various C-rates, which are specified for each experiment in this manuscript. Cell capacities and thus the current values were calculated, based on the theoretical specific capacity of sulfur active material (1675 mAh g<sup>-1</sup>) and the amount of sulfur in each electrode.

Coulombic efficiency ( $\Phi$ , %) was determined as a capacity ratio of (n) discharge/(n) charge, and not like in classical Li-ion cells, *i.e.* (n+1) discharge/(n) charge. Thanks to that, we can have information concerning the presence of a shuttle mechanism and drastic capacity fade in the initial cycle. Calculated that way, efficiency higher than 100 % may indicate that a capacity fade occurs. This capacity fade may be related to the different reasons: loss of active material, no complete active mass utilization during charge, etc. If lower than 100 %, a shuttle mechanism is present. However, such calculation does not allow to evaluate the efficiency of the (n) charge towards the next (n+1) discharge (parasitic reactions, uncompleted sulfur utilization). Anyway, with the presence of the shuttle phenomenon, it may always be difficult to differentiate other parasitic processes appearing.

Electrochemical Impedance Spectroscopy (EIS) was recorded on symmetric coin cells on a VMP3 (Bio-Logic<sup>®</sup>) adapted for EIS measurements. Each spectrum was recorded over the

frequency range of 1 MHz – 10 mHz, with voltage amplitude of 10 mV. The experimental data were analyzed with ZView software.

Morphology of the samples (mainly electrodes) was investigated with the use of a Scanning Electron Microscope (SEM; LEO 1530, Gemini). 5 kV accelerating voltage was used. A sample was placed on SEM stubs onto adhesive conductive carbon tape. Air-sensitive samples (*i.e.* discharged electrodes with  $Li_2S$  deposit) were transferred to the SEM with a special transfer box as shown on Figure 2-3a.



Figure 2-3. SEM transfer box permitting to keep the analyzed samples under argon protective atmosphere without air exposure at any step of the measurement (a,b); XRD sample protected by thin Kapton<sup>®</sup> film (c).

The structural characterization was performed by X-Ray Diffraction (XRD) technique *via* BRÜKER powder diffraction system (model D8 Advance), using  $CuK_{\alpha}$  as the radiation source. In case of air-sensitive samples (mostly *post mortem* analysis), electrode was recuperated from a coin cell inside the glove box, washed gently with DIOX and left for solvent evaporation for 10-15 minutes. Once dried, the electrode was stuck on a glass plate with the use of double side tape and covered with a thin (13  $\mu m$ ) Kapton<sup>®</sup> foil to protect from air (Figure 2-3b).

#### 2.2.4. Discussion concerning the results' margin of error

All results presented here were carefully selected to keep the best reproducibility and reliability, *i.e.* (i) sulfur electrodes prepared not far from each other in terms of date, (ii) same batch of electrolyte used, (iii) same conditions for battery assembly and testing (room temperature for Arbin<sup>®</sup> cyclers), etc. In most of the cases, the data were obtained from few cells in parallel. Nevertheless, despite of all precautions taken, different natures of error were still present, which could influence the experimental capacity.

The error related with the electrode weight was rather low, and estimated according to the equation (4):

$$\frac{\Delta\text{Capacity}}{\text{Capacity}} = \frac{\Delta M(\text{electrode}) + \Delta M(\text{Al})}{M(\text{electrode}) - M(\text{Al})} + \frac{\Delta\%S}{\%S} \quad (4)$$

where:

$\Delta M_{(\text{electrode})} = 0.001$  mg (imprecision of the micro scale where electrode mass was checked)

$\Delta M_{(\text{Al})} = 0.01$  mg (imprecision of Ø14 mm Al current collector mass)

$\Delta\%S = 0.5$  % (error of the final sulfur ratio in the composite electrode, aimed to be  $\%S = 80$  %)

Thus, for the sulfur electrode with theoretical capacity of 5 mAh ( $M_{(\text{electrode})} = 12.131$  mg;  $M_{(\text{Al})} = 8.400$  mg),  $\Delta\text{Capacity}$  would be only  $\sim 1.0$  %, which is almost negligible.

Another error may come from the non-homogenous morphology of the electrodes, which could also be associated in some extent to the manual preparation of the electrodes, which may give some uncertainty and lack of reproducibility. This point is discussed in further discussion.

## 2.3. The influence of different parameters of the electrodes

In this paragraph, we investigate the parameters strictly related with the positive electrode, *i.e.* conductive carbon nature, binder and electrode loading, and in which extent they influence the performances of a complete Li/S cell. We were also interested in finding a correlation (if any?) between the electrode morphology obtained with different carbons and/or binders, the impedance response and the cycling properties of the electrodes, especially at faster C-rates.

It is important to underline here again, that our positive electrodes were prepared from cheap and commercially available products, in a very simple way, where no thermal treatment neither complex fabrication procedures were used. It is also worth noting that even if obtained capacity values were sometimes much lower as compared with the impressive numbers existing in the literature<sup>79,137,217</sup> (reaching almost theoretical capacity), these studies were devoted more to the understanding aspect rather than optimization in terms of specific capacity (in mAh g<sub>Sulfur</sub><sup>-1</sup>).

### 2.3.1. The effect of the conductive carbon additive

#### 2.3.1.a) SuperP<sup>®</sup> vs. Ketjenblack<sup>®</sup>

In the first step, two nano-carbon black additives, SuperP<sup>®</sup> and Ketjenblack<sup>®</sup>, with similar spherical particle size (40 vs. 30 nm) but essentially different specific surface areas (60 vs. 800 m<sup>2</sup> g<sup>-1</sup>), were taken into consideration. Both electrodes were of identical composition (80/10/10 wt% = S/C/PVdF) and of sulfur loading  $\sim 2.1$  mg cm<sup>-2</sup> ( $\sim 3.5$  mAh cm<sup>-2</sup>). SEM pictures of the

corresponding electrodes (SuperP<sup>®</sup> or Ketjenblack<sup>®</sup> based compositions) are presented on Figure 2-4. From a macroscopic point of view, the morphologies of both electrodes are rather the same.

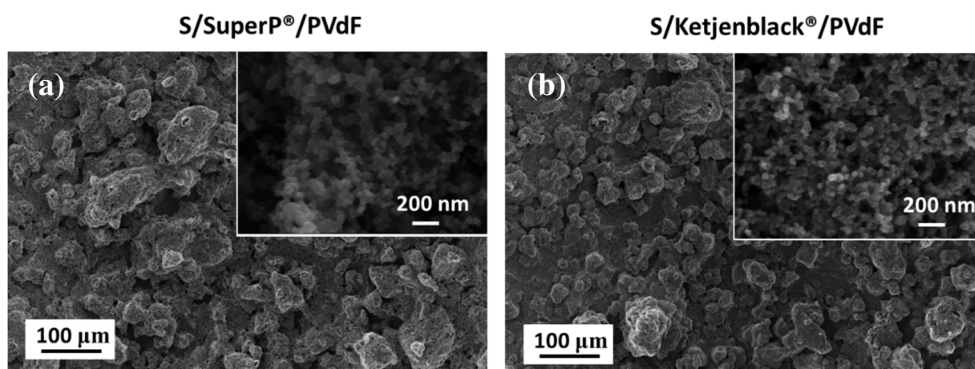


Figure 2-4. SEM pictures of sulfur positive electrodes (S/C/PVdF = 80/10/10 wt%) prepared with different carbon materials: (a) SuperP<sup>®</sup> and (b) Ketjenblack<sup>®</sup>, but with the same preparation method.

Galvanostatic cycling (C/10) of both electrodes shows practically identical capacity retention over 50 cycles (Figure 2-5). Even if some electrodes display slightly higher/lower capacity, the values were still in the error margin previously discussed (see section 2.2.4). Initial capacity of  $\sim 650 \text{ mAh g}^{-1}$  is followed by a drastic fading and stabilization at around  $300 - 400 \text{ mAh g}^{-1}$ . Such capacity retention, with drastic fade just at the beginning, is very common to observe in Li/S cells<sup>35</sup>.

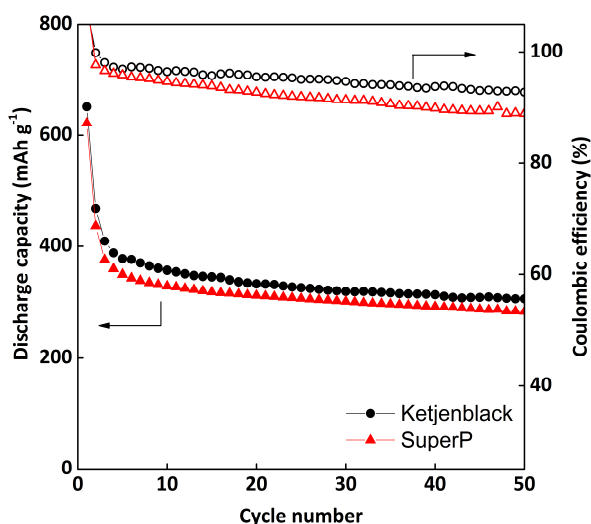


Figure 2-5. Galvanostatic cycling results (C/10) of sulfur electrodes (S/C/PVdF = 80/10/10 wt%) prepared with two different carbons, SuperP<sup>®</sup> (in red) and Ketjenblack<sup>®</sup> (in black).

When replacing SuperP<sup>®</sup> by Ketjenblack<sup>®</sup>, which has specific surface area 13 times higher, no difference is found. Indeed, these results prove that, even if highly developed surface area is present, but not necessarily accessible for lithium polysulfides, no beneficial effect is obtained

in terms of discharge capacity. These findings are in accordance with previous reports<sup>45</sup>. Since both carbons gave similar performances, SuperP<sup>®</sup> was kept for further studies as a reference conductive additive, as requiring less solvent during the ink slurry preparation.

### 2.3.1.b) SuperP<sup>®</sup> vs. VGCF<sup>®</sup>

In the next step, the effect of different shapes of carbon material was taken into consideration. For this purpose, Vapor Growth Carbon Fibers (VGCF<sup>®</sup>, Showa Denko) were used, which are 10 – 20  $\mu\text{m}$  long fibers with average diameter of  $\varnothing$  150 nm and surface area of  $13 \text{ m}^2 \text{ g}^{-1}$ <sup>218</sup>. The literature is rich of examples where addition of carbon (nano)fibers improves electronic conductivity/properties of the electrode<sup>91,94,219</sup>. According to Barchasz *et al.*<sup>45</sup>, its beneficial effect is more visible in thicker electrodes, since it facilitates the electronic pathway from the current collector through the whole electrode thickness.

Electrodes with different carbon compositions (10 wt% of SuperP<sup>®</sup>, 10 wt% of VGCF<sup>®</sup> or 5+5 wt% of SuperP<sup>®</sup> + VGCF<sup>®</sup>) were prepared, while ratios of sulfur (80 wt%) and PVdF binder (10 wt%) were constant. For simplicity, the names of the electrodes refer to the carbon used, *i.e.* “SuperP<sup>®</sup>”, “VGCF<sup>®</sup>” and “SuperP<sup>®</sup>/VGCF<sup>®</sup>”. The electrodes’ morphology at the macroscopic level is rather similar: sulfur particles enrobed by a carbon particles/fibers (Figure 2-6a,d,g). The differences due to the carbon shape are significantly visible at the microscopic level, as shown on Figure 2-6c,f,i.

It can be seen that sulfur particles are covered better if only SuperP<sup>®</sup> is used. On the other hand, pure VGCF<sup>®</sup> fibers do not provide complete coating, due to their lower specific surface ( $13 \text{ m}^2 \text{ g}^{-1}$  vs.  $60 \text{ m}^2 \text{ g}^{-1}$  of SuperP<sup>®</sup>). Indeed, VGCF<sup>®</sup> additive is rather efficient when added in low amount in combination with carbon nano-spheres. Moreover, the real length of a VGCF<sup>®</sup> fibers seems to be much shorter than claimed by the supplier (10 – 20  $\mu\text{m}$ ), and is more like 3 – 10  $\mu\text{m}^\ddagger$ , with still many broken and shorter fibers of  $\sim 2 \mu\text{m}$ . Besides, they look rather like rigid sticks without entanglement.

---

<sup>‡</sup> Calculated visually based on the SEM photos.



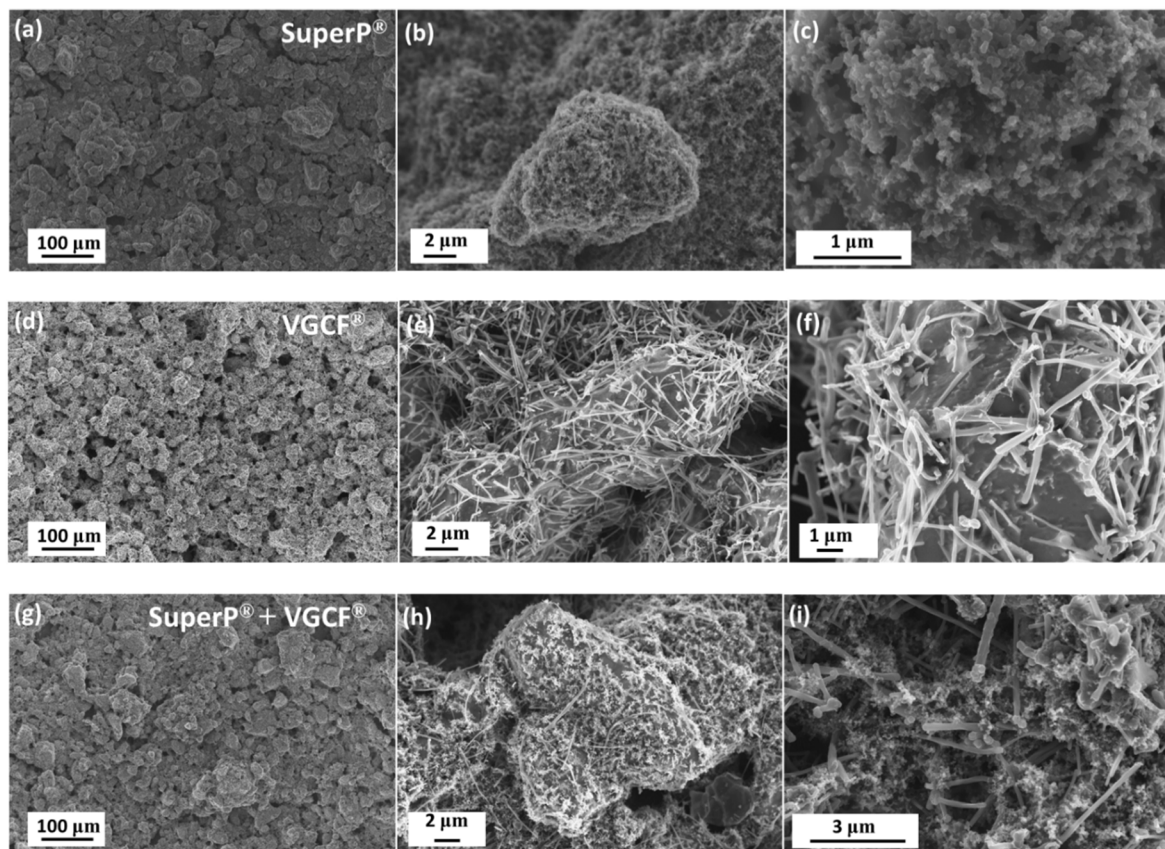


Figure 2-6. SEM photos of S/C/PVdF (80/10/10 wt%) electrodes prepared with different carbons: SuperP® (a-c), VGCF® (d-f) and mixture of SuperP®+VGCF® (g-i).

The eventual effect of different carbons was tested by galvanostatic cycling in capacity retention tests, and the results are presented on Figure 2-7. The tests were performed on the electrodes with sulfur loading of  $\sim 2.5 \text{ mg}_{\text{Sulfur}} \text{ cm}^{-2}$  ( $\sim 4.2 \text{ mAh cm}^{-2}$ ).

In general, the three different compositions display rather similar trend of capacity retention at different C-rates (C/20, C/10, C/5, 1C and 2C). Right after the initial cycle, a drastic capacity fade is observed. This is the moment when the most significant changes in the electrode occur. Active material (80 wt% of the electrode) is leaving the carbon/binder matrix, and diffuses into the electrolyte in the form of lithium polysulfides. Therefore, significant active material loss, together with electrode pulverization, may be responsible for such initial drastic capacity fade.

The differences between the three compositions are rather small, even if “SuperP®” composition displays the lowest initial capacity ( $680 \text{ mAh g}^{-1}$ ). At faster C-rates, the differences in the capacity values start to be more detectable, and we can notice that the electrodes with the “SuperP®/VGCF®” mixture perform slightly better. At 1C, obtained capacities (for 25<sup>th</sup> cycle) are 104, 80 and 60  $\text{mAh g}^{-1}$  for the composition “SuperP®/VGCF®”, “SuperP®” and “VGCF®” respectively. Beneficial effect of VGCF® addition may be explained by the highest stability of the electrode morphology during cycling in the presence of fibers, even though they are too short to induce fiber entanglement, and improved electronic conductive pathway retention, which is the most important for high currents. However, pure

VGCF<sup>®</sup> fibers surprisingly provide the lowest capacity at faster rates, which may be related to the lack of carbon nano-particles to allow for good conductive network.

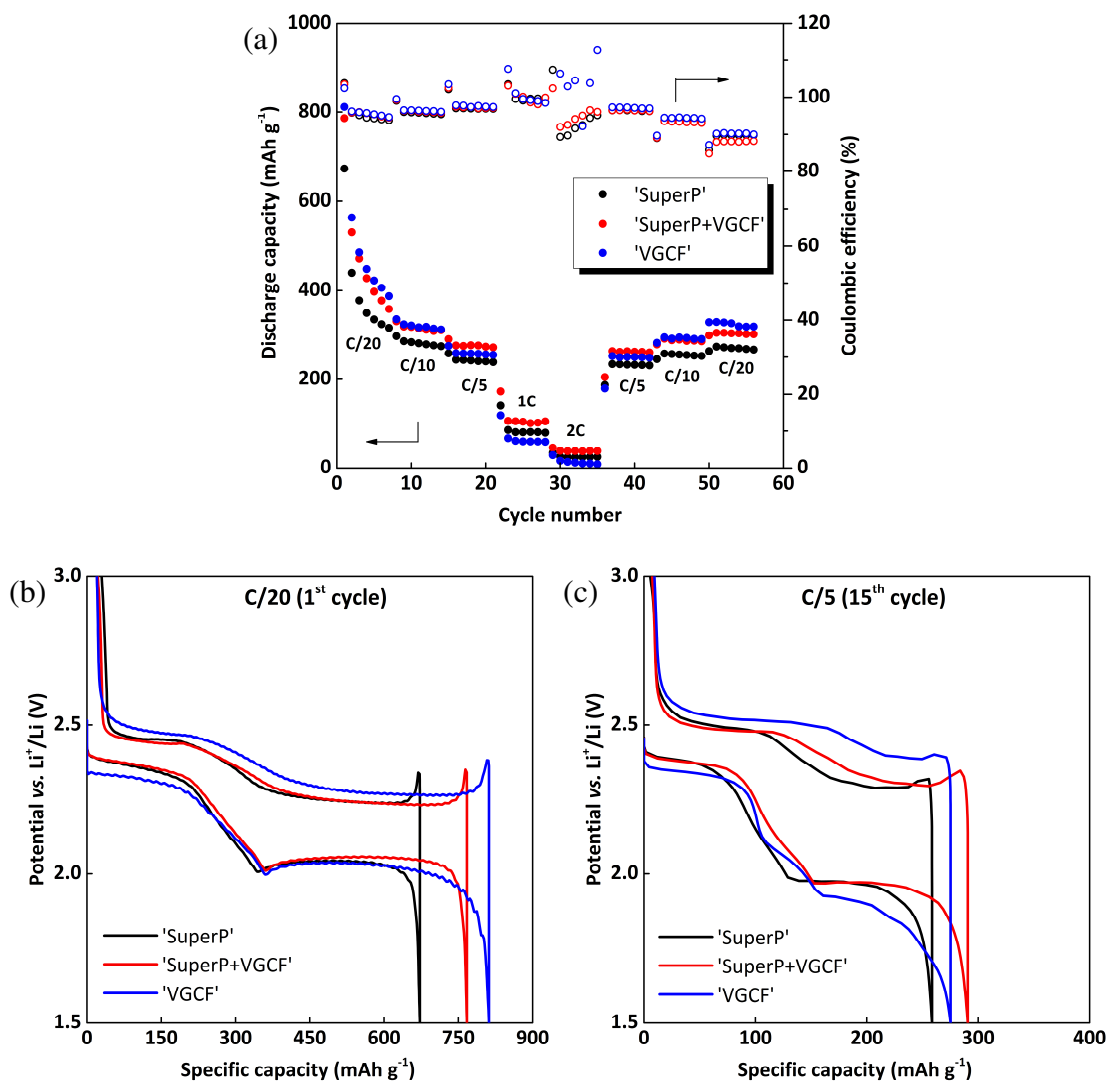


Figure 2-7. Rate capability tests of three sulfur electrodes prepared with different carbons: SuperP<sup>®</sup> (in black), VGCF<sup>®</sup> (in blue), SuperP<sup>®</sup>+VGCF<sup>®</sup> (in red), and with similar sulfur loadings of  $\sim 2.5$  mg cm<sup>-2</sup>. Capacity retention at different C-rates over 55 cycles (a), corresponding voltage profiles obtained during 1<sup>st</sup> cycle at C/20 (b) and 15<sup>th</sup> cycle at C/5 (b).

The efficiency of the binder adsorption on the two different types of carbon materials (especially with different shapes: nano-spheres *vs.* fibers) may also have a large impact, and it can influence the accessible specific surface of carbon and the cohesion of the electrode. That may probably explain the differences observed in terms of polarization, where “VGCF<sup>®</sup>” electrode displays slightly higher overpotential during initial sulfur reduction, as compared to other electrodes, and all along charge process (Figure 2-7b), and more noticeably at faster rates (Figure 2-7c). The initial polarization may be probably related with not completely connected sulfur particles with VGCF<sup>®</sup>, as can be seen from the SEM photos (Figure 2-6d-f).

Nevertheless, the beginning of the low discharge plateau (initial cycle at C/20; Figure 2-7b) starts at exactly the same point, indicating that sulfur reduction occurs quantitatively in the same manner anyway.

More remarkable difference is visible in the lower discharge plateau length, where soluble actives species are reduced into shorter insoluble polysulfides. These results seem to be in contradiction to some reports, saying that the higher the conductive surface area is, the higher the capacity would be<sup>220</sup>. Indeed, VGCF<sup>®</sup> fibers have only 13 m<sup>2</sup> g<sup>-1</sup> and display the best capacity at slower rate (C/20), while SuperP<sup>®</sup> has a surface of 60 m<sup>2</sup> g<sup>-1</sup>, and the discharge capacity is lower. Yet, what is important to take in mind, is that after active material got dissolved into the electrolyte, the cohesion of the electrode is a very important property required for a good electrochemical performances. The way the different types of binder adhere to the different types/shapes of carbon has not been studied here, but it should be strongly taken into consideration in the future. In particular, the remaining electrode's structure may be slightly improved by using a fiber-type carbon additive as compared to the spherical shape, and carbon-binder matrix may suffer less from the pulverization during sulfur dissolution process.

To conclude, even if beneficial effect when using carbon fibers in the electrodes is very well described in the literature, our results did not show any significant improvement. This may come from the fact that the electrodes were prepared in a simple manner, without sulfur confinement or mixing methods were not fully optimized. Our electrodes are also of relatively high loadings. In the next step, we focused on the effect of a binder, which seems to be a parameter not often taken into consideration during electrode fabrication.

### 2.3.2. The effect of a binder and active material loading

As previously explained in the literature review (see section 1.3.1.b), the most popular binder used for sulfur electrode is poly(vinylidene fluoride) (PVdF). It is known from its electrochemical stability even up to elevated potentials, as well as from good adhesion properties<sup>221</sup>. Moreover, the large elongation at break, reported to be at least 50 %<sup>222</sup>, allows the film to resist to expansion/retraction. *N*-methyl-2-pyrrolidone (NMP) is mostly used as a solvent, however, its toxicity and necessity of temperature higher than 80°C for complete evaporation, makes it as not the most preferable choice. In our work, PVdF was selected from the beginning as the “reference” binder. Another binder, CMC/NBR<sup>‡</sup> (carboxyl methyl cellulose/nitrile butadiene rubber) was also tested. The literature mostly reports on CMC/SBR mixture (SBR – styrene butadiene rubber), as a very popular binder for Li-ion systems. Indeed, CMC/SBR is known from its high flexibility, strong binding force and high heat resistance<sup>111</sup>. Additionally, it can be easily dispersed (for SBR) and dissolved (for CMC) in deionized water which makes it a good choice for green electrodes' preparation method and for easier

---

‡ The choice of NBR instead of SBR latex was purely dictated by the procedures adopted in the laboratory.

processability. Although the reported elongation at break for CMC is very low (being around 2 – 6 %), it seems to be compensated by much larger elongation at break for SBR (~ 30 to 160 %) <sup>223</sup>, and thus gives better mechanical resistance for the electrode during successive cycles, *i.e.* SBR acting more as a binder joining the different particles, while CMC as a dispersive additive for better homogeneity.

The literature reports are rather in agreement in pointing out better CMC binder's properties between the two aforementioned ones (PVdF *vs.* CMC), their choice being justified by higher capacity, better cycling stability, lower charge transfer resistance, more homogenous dispersion of carbon and less blocked carbon pores <sup>110,111</sup>. However, there are also some reports claiming the complete opposite conclusions, proving that PVdF-based electrodes offer much better cyclability and electronic properties over the CMC-based one <sup>146</sup>.

In our work, we were interested to see how the cycling performances together with electrochemical properties (studied by EIS) of the sulfur electrodes differ, depending on the binder composition. Both electrodes had the same standard composition 80/10/10 wt% of sulfur/SuperP<sup>®</sup>/binder (in case of CMC/NBR binder, the fraction distribution was 6/4 wt%). Preparation of sulfur/SuperP<sup>®</sup> mixture was the same for both electrodes, and it was done by manual mixing in a mortar with cyclohexane. The main difference lied in the binder nature, as well as in the way of its incorporation: CMC/NBR was dispersed with Dispermat<sup>®</sup>, while PVdF was manually mixed with the spatula (detailed information in section 2.2.1).

The SEM photos show the morphology of both electrodes. It can be seen that they look rather similar, with sulfur particles well-enrobed by SuperP<sup>®</sup> carbon nano-particles. However, based on the SEM photos only, it is hard to distinguish precisely the difference (if any?) in the way how carbon particles are connected together with the binder.

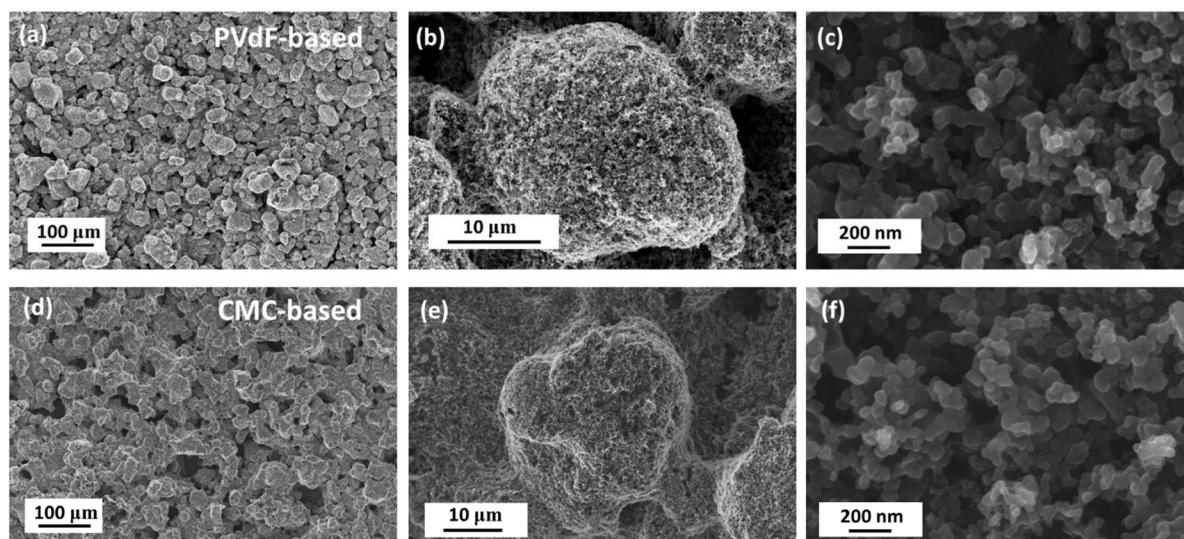


Figure 2-8. SEM photos of S/SuperP<sup>®</sup>/binder (80/10/10 wt%) electrodes prepared with different binders: PVdF 5130 (a-c) and CMC/NBR (d-f).

As a supporting information, BET measurements were done on three samples (Table 2-1).

Sample	S/SuperP <sup>®</sup> (90/10 wt%)	S/SuperP <sup>®</sup> /PVdF (80/10/10 wt%) <sup>(*)</sup>	S/SuperP <sup>®</sup> /CMC/NBR (80/10/6/4 wt%) <sup>(*)</sup>
<b>BET surface area (m<sup>2</sup> g<sup>-1</sup>)</b>	5.7	5.5	3.0

Table 2-1. BET data measured on S/SuperP<sup>®</sup> mixture and after binder (CMC/NBR or PVdF) incorporation, on TRISTAR II 3020 equipment. BET tests were performed at RT (to avoid sulfur sublimation at elevated temperatures) and under N<sub>2</sub> gas. (\*) BET tests of complete electrodes were done on the powders scratched from the Al collector, to avoid having the contribution of Al foil mass during the measurement.

As the sulfur particles are in the micro scale (-325 mesh, *i.e.* an average particle size of ~ 44 μm, which corresponds – by assuming a spherical particles – a surface area of 0.00659 m<sup>2</sup> g<sup>-1</sup>), the surface area is mainly associated to SuperP<sup>®</sup> carbon's one (60 m<sup>2</sup> g<sup>-1</sup>). The surface area of S/SuperP<sup>®</sup> was found to be 5.7 m<sup>2</sup> g<sup>-1</sup>, which is rather an expected value, since the fraction of SuperP<sup>®</sup> in the mixture was 10 wt% (10 % x 60 m<sup>2</sup> g<sup>-1</sup> = 6.0 m<sup>2</sup> g<sup>-1</sup>). Further addition of PVdF resulted in only slight decrease of the surface area (5.5 m<sup>2</sup> g<sup>-1</sup>) as compared with the CMC-based electrode, where the surface got decreased almost twice (3.0 m<sup>2</sup> g<sup>-1</sup>). Such behavior may indicate that CMC/NBR disperses and covers better the clusters of carbon particles, which results in lower BET value. On the contrary, PVdF may not provide an efficient coverage of carbon, while manual mixing of the ink may not allow for good dispersion of the different electrode's components, *i.e.* PVdF and carbon particles. Indeed, this hypothesis is coherent with previous work of He *et al.*<sup>111</sup>, who reported on better dispersion of S/C particles in the electrode slurry while using CMC/SBR binder.

Cycling performances of PVdF-based electrodes were demonstrated previously on Figure 2-7, where quite drastic capacity fade was observed, followed by a stable discharge capacity of around 300-400 mAh g<sup>-1</sup>. Cyclability of CMC-based electrodes was also verified (Figure 2-9). The effect of different active mass loadings was also taken into consideration. For that purpose, a larger quantity of the electrode ink was prepared and coated on Al foil sheets with different blade thicknesses. Such obtained electrodes had increasing coating thicknesses (74 → 86 → 91 → 107 → 117 μm), linearly proportional to the sulfur loadings (2.77 → 3.35 → 4.03 → 4.71 → 5.69 mg<sub>Sulfur</sub> cm<sup>-2</sup>).

Figure 2-9 shows the initial voltage profiles obtained at C/20 and C/5 for the electrodes with different loadings (indicated on the graphs), together with capacity retention over prolonged cycling.

It can be seen that at slow rate (C/20), the voltage profile is only slightly affected (slight increase in overpotential with increased loading). At faster rate (C/5), the lower discharge plateau is more affected, with high polarization, that could be expected due to the slow reaction kinetics of solid phase formation and a large increase of the electrolyte viscosity (higher polysulfide concentration in the electrolyte). Very surprisingly, upon prolonged cycling, highly loaded electrodes (~ 5.69 mg<sub>Sulfur</sub> cm<sup>-2</sup>) give much higher capacities as the lower loaded ones

( $\sim 2.77 \text{ mg}_{\text{Sulfur}} \text{ cm}^{-2}$ ). One explanation could relate to the lower diffusion of the polysulfides coming from the electrode into the electrolyte, due to their lower solubility in the presence of already dissolved polysulfides. The literature also proposes that higher sulfur/electrolyte ratios (*i.e.* more loaded electrodes) display lower shuttle mechanism and better coulombic efficiency. Due to the fact that less electrolyte is in the cell, polysulfides diffusion to the negative electrode may be decreased (because of higher electrolyte viscosity), and the capacity retention is improved<sup>105,125</sup>. This particular behavior is still under investigation at the moment. PVdF-based electrodes display very similar trend, *i.e.* more loaded electrodes give better capacity values upon cycling.

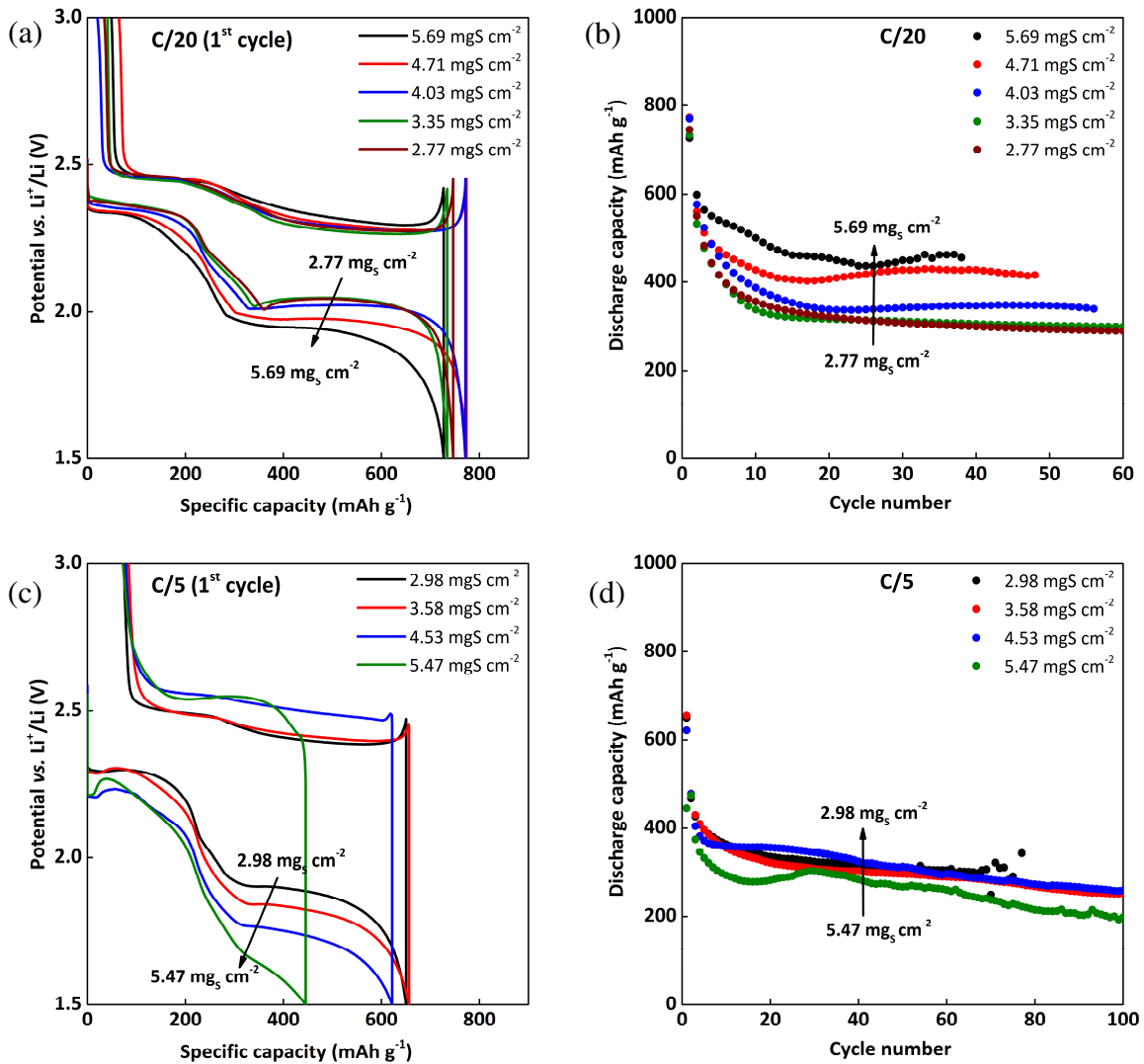


Figure 2-9. Cycling performances of S/SuperP®/CMC electrodes having different sulfur loadings: initial cycle voltage profiles at C/20 (a) and at C/5 (c). Corresponding capacity retention upon prolonged cycling at C/20 (b) and at C/5 (d).

It can be seen from Figure 2-10, that when the initial discharge capacity is plotted vs. sulfur loading, an optimum point can be found (as previously discussed in the literature review part).

For both electrodes, CMC and PVdF-based ones, similar trend is observed, *i.e.* the maximum point is shifted to higher sulfur loading ( $\sim 6 \text{ mg}_{\text{sulfur}} \text{ cm}^{-2}$ ) when the C-rate is slower (C/20). Globally CMC-based electrodes give better capacity as compared with PVdF-based one.

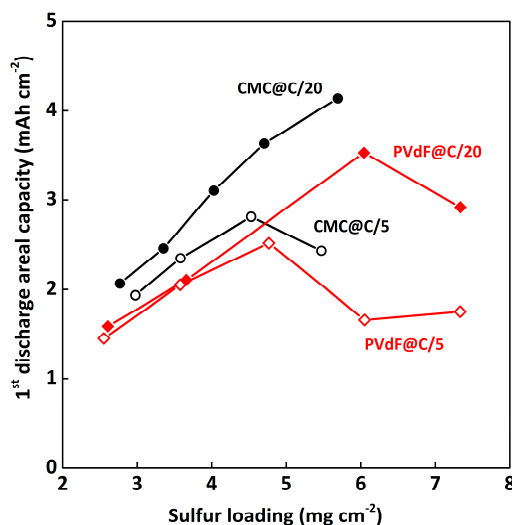


Figure 2-10. Initial discharge capacity as a function of sulfur loading ( $\text{mg}_{\text{sulfur}} \text{ cm}^{-2}$ ), for both electrodes: CMC (in black) and PVdF-based (in red) compositions. Two current rates were applied: C/20 and C/5.

To summarize, no significant difference was found when using different binders. Quite similar overall capacity retention (with slightly better performances of CMC composition) was obtained for both types of electrodes. More significant differences in terms of capacity retention were found for different electrodes' loadings. In the next section, we see how the electronic properties differ, depending on different parameters, among which the nature of the binder is studied.

### 2.3.3. EIS investigation

In order to study the electric properties of the electrodes, EIS technique was used. The concept of using symmetric cell impedance has already been applied to study the insertion electrodes for Li-ion batteries<sup>224-226</sup>. However, to our best knowledge, it was never applied to the sulfur positive electrodes. All the impedance studies of Li/S system are usually conducted in a classical two-electrode coin cell configuration<sup>111,128,129,132,209,227</sup>. Such conventional EIS measurements are not the most suitable for expressing the accurate response of the positive electrode only, because of the counter electrode's presence – a metallic lithium – which is commonly known from its large contribution to the impedance of a complete cell<sup>224</sup>. Thus, aiming at observing solely the contribution of sulfur positive electrode, it was necessary to

eliminate metallic Li. Therefore, symmetric coin cells composed of two identical<sup>§</sup> sulfur electrodes were used, and an example of a Nyquist plot is shown on Figure 2-11.

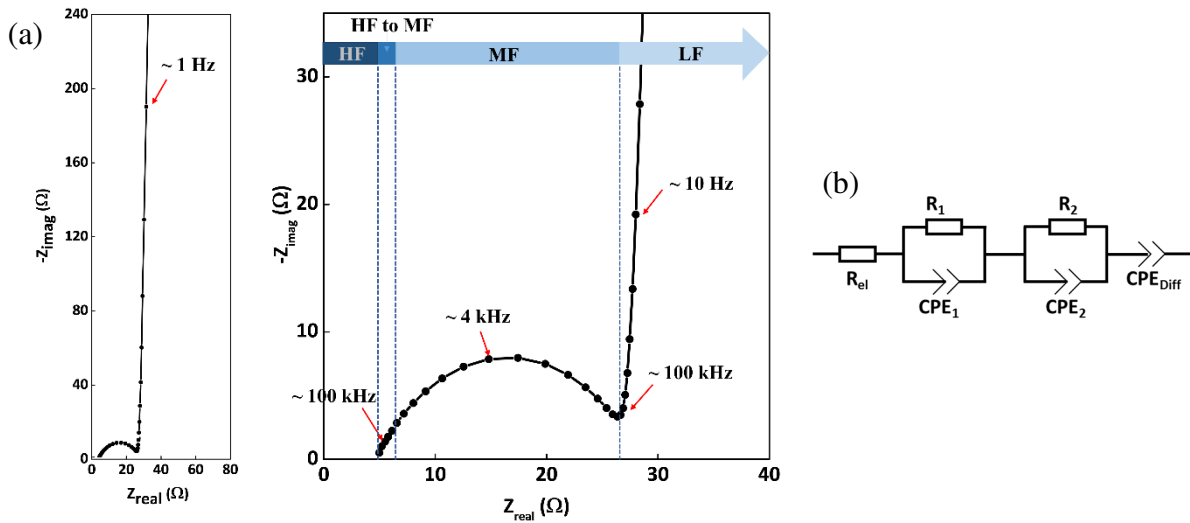


Figure 2-11. Nyquist plot of the symmetric coin cell composed of two identical sulfur positive electrodes (S/SuperP<sup>®</sup>/PVdF), with loadings of  $\sim 7.0 \text{ mg}_{\text{sulfur}} \text{ cm}^{-2}$  and electrode coating thickness of  $\sim 130 \mu\text{m}$  (a). Corresponding equivalent circuit (b).

Three main regions, with different time constants, can clearly be distinguished (and are separated by vertical blue lines for easier visualization): high, medium and low frequency regions. A very narrow fourth region (named as ‘high to medium’ frequency region) is also marked, since a small semicircle can be visible with a characteristic frequency in the range of 150-300 kHz. High frequency (HF) region refers to the electrolyte resistance, coin cell casing, sample holder, and cable connections responses<sup>225,226</sup>, and can be modeled as a pure resistor (R).

The response at the low frequency region (LF) of a porous electrode corresponds to a restricted Warburg Impedance, associated with semi-infinite diffusion, due to the blocking character of the electrode, *i.e.* impossible intercalation of lithium. Such phenomenon has been previously shown by Levi and Aurbach, and can be directly correlated with the electrode thickness<sup>228</sup>. However, CPE is also proposed for modelling this part of the spectra<sup>212</sup>, when the diffusion part and the blocking one are not well-separated in frequency.

The interpretation of the middle frequency (MF) region and semicircle(s) present is more controversial, and in the literature generally associated to the charge transfer reaction<sup>207,212</sup>. However, since the electrode presents a blocking character (visible as a vertical line in the low frequency region, due to the insulating character of sulfur active material), such interpretation can be questionable. Further experiments were performed in order to remove this ambiguity, and are present in the following sections.

<sup>§</sup> Electrodes were carefully selected based on the weight and the thickness of each  $\varnothing 14 \text{ mm}$  disk, to be as similar as possible.



### 2.3.3.a) The effect of the electrode thickness

An additional experiment was performed, where symmetric coin cells were built with the electrodes having different thicknesses (68 – 85 – 110 μm), and corresponding EIS spectra are shown on Figure 2-12a. For simplicity, in further discussion we will refer only to the MF semicircle, however, it is important to note that a small semicircle in the ‘HF to MF’ is present. The semicircle can be modeled as a resistance (R) in parallel with a constant phase element (CPE). The choice of CPE instead of an ideal capacitor (C) is governed by the non-ideal behavior of the system and electrodes<sup>207,209,226</sup>. Middle frequency semicircle was fitted with ZView software, and obtained parameters are shown on Figure 2-12b.

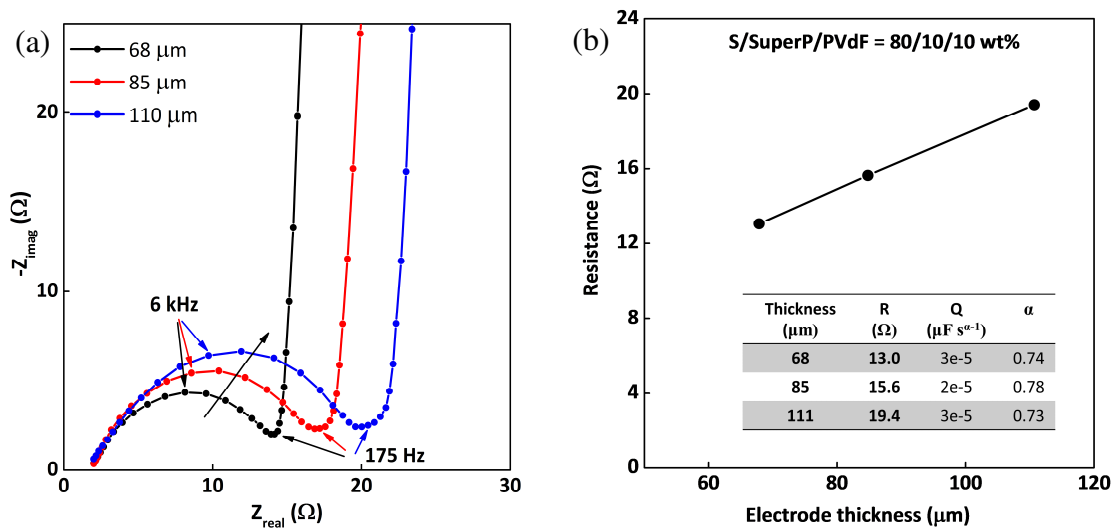


Figure 2-12. Evolution of the Nyquist plot for three symmetric coin cells built with sulfur electrodes (S/SuperP®/PVdF) having linearly increasing thicknesses (a). Summary of the fitting parameters of the MF semicircle as well as the resistance value plotted as a function of the electrode thickness (b).

The size of MF semicircle is increasing with the increased thickness of the electrodes (Figure 2-12a, grey arrow), pointing out that the corresponding resistance value is linearly proportional to the electrode thickness, as shown on Figure 2-12b. However, the characteristic frequency of the semi-circle stays unchanged with the thickness increase. This evolution clearly indicates that the MF response is associated with the bulk properties of the electrode and not to the electrode/current collector interface.

### 2.3.3.b) The influence of the insulating nature of active material

To evaluate if the electrode response obtained by EIS at the MF region is associated (or not) with the active material particles (*i.e.* charge transfer reaction), sulfur was replaced by insulating particles of Al<sub>2</sub>O<sub>3</sub> (Sigma Aldrich, average particle size of ~20 μm, *i.e.* quite similar in size to sulfur particles), and electrodes with composition 80/10/10 wt% =

$Al_2O_3$ /SuperP<sup>®</sup>/PVdF and varying thicknesses (42 – 64 – 81  $\mu m$ ) were prepared. Figure 2-13 shows SEM photos of the electrode morphology. It can be seen that  $Al_2O_3$  particles are not completely enrobed by SuperP<sup>®</sup> particles, as it is in the case of sulfur material, probably because of different hardness of both materials. Sulfur is very soft, which permits to obtain good S/SuperP<sup>®</sup> contact, while it is more difficult in the case of harder crystalline particles of  $Al_2O_3$ .

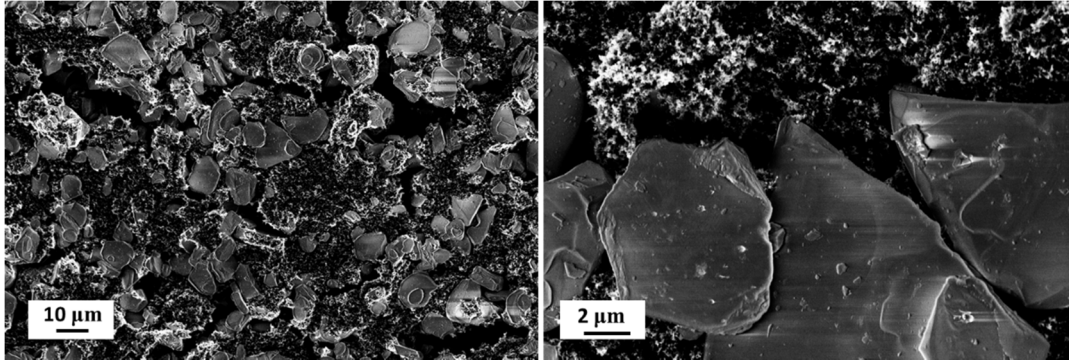


Figure 2-13. SEM photos of  $Al_2O_3$ /SuperP<sup>®</sup>/PVdF (80/10/10 wt%) electrodes.

Symmetric coin cells were built with three electrode thicknesses, and the obtained results were found very similar to the ones of sulfur-based electrodes, previously presented. Figure 2-14 shows the Nyquist plot evolution together with the fitting parameters of the MF semicircle.

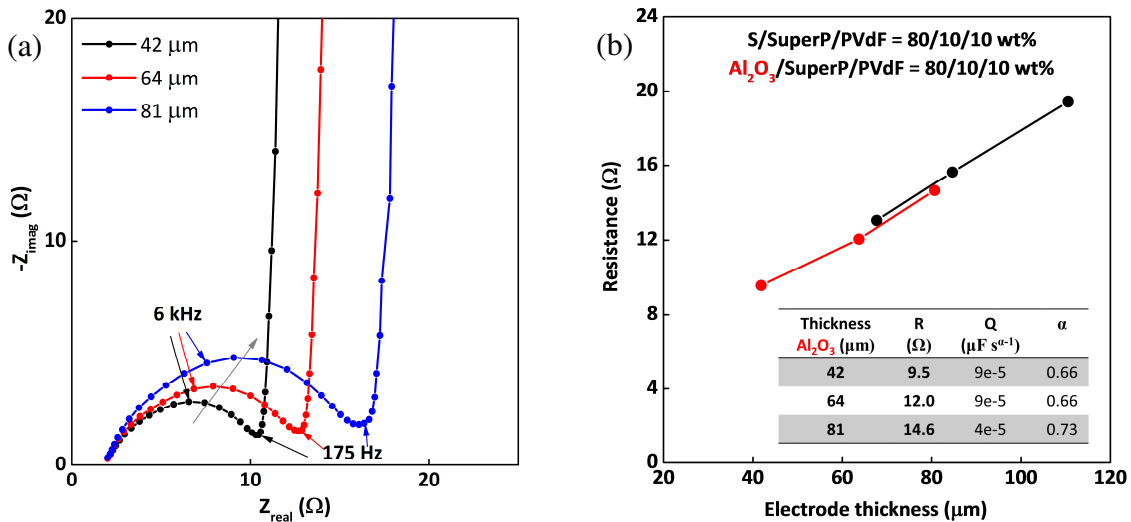


Figure 2-14. Nyquist plot evolution of three symmetric coin cells built with  $Al_2O_3$ /SuperP<sup>®</sup>/PVdF electrodes having linearly increasing thicknesses (a). Summary of the fitting parameters of the MF semicircle as well as the resistance value plotted as a function of the electrode thickness (in red); in comparison with  $S_8$ -based electrode (in black) (b).

The resistances and characteristic frequencies (around  $\sim 4 - 6$  kHz) are very close to those obtained with the electrodes made with sulfur, and a linear increase of the resistance values was also found (Figure 2-14b).

These results prove that no matter the material used, *i.e.* active species ( $S_8$ ) *vs.* insulating inactive compound ( $Al_2O_3$ ), with rather the same shape and size of the particles, the impedance response is practically the same. Then, it is unquestionable that the origin of the MF loop is not associated with the charge transfer reaction. The response seems to be governed by the morphology and electric network of the electrode, which is fixed by the carbon/binder ratio, elaboration process and/or conductive particles and binder used.

### 2.3.3.c) The influence of the conducting carbon

The EIS responses of the electrodes with VGCF<sup>®</sup> carbon ( $S/VGCF^{\text{®}}/PVdF = 80/10/10$  wt%) and three different thicknesses were also fitted, and the results are shown on Figure 2-15, in comparison to equivalent electrode but with SuperP<sup>®</sup> used instead.

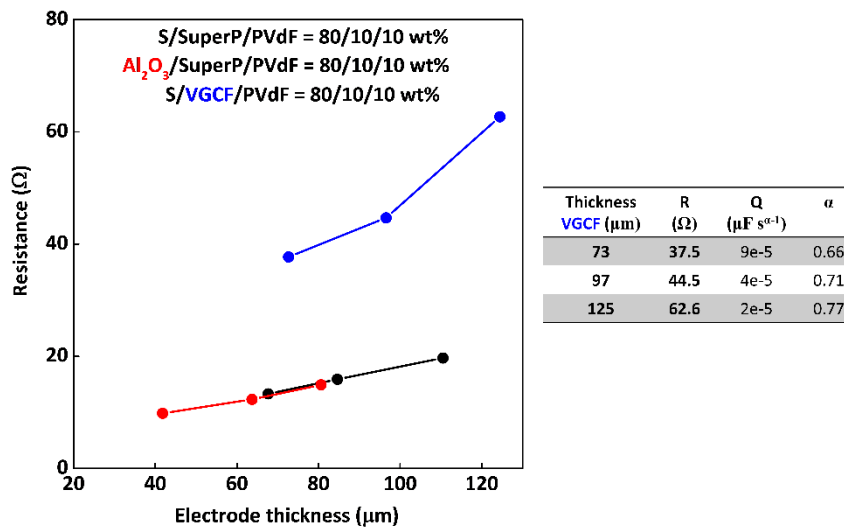


Figure 2-15. Resistance values of the middle frequency (MF) semicircle obtained from EIS measurements on the symmetric coin cells, as a function of the electrode effective thickness. Comparison between two types of the electrodes, with composition  $S/X/PVdF = 80/10/10$  wt%, where 'X' stands for SuperP<sup>®</sup> (in black) or VGCF<sup>®</sup> (in blue). For comparison, electrode with  $Al_2O_3/SuperP^{\text{®}}/PVdF$  composition is also shown (in red).

The electrodes with VGCF<sup>®</sup> exhibit quite similar behavior as the SuperP<sup>®</sup>-based electrodes, *i.e.* the resistance is linearly increasing with increased thickness. The characteristic frequencies are slightly shifted to lower frequencies ( $\sim 1 - 3$  kHz), as compared to SuperP<sup>®</sup>-based electrodes ( $\sim 4 - 6$  kHz). However, the resistance values are much higher for VGCF<sup>®</sup> than SuperP<sup>®</sup> compositions. One can note that when changing the conducting particles nature, the physical meaning of the MF semicircle seems not to be impacted (quite the same characteristic

frequencies). However, the particle shape/morphology may have significant effect on the resistance value.

### 2.3.3.d) The effect of the binder nature

Figure 2-16 shows typical Nyquist plot of a symmetric coin cell built with CMC-based electrodes (in black). A remarkable difference in the EIS response can be observed, as compared with previously described PVdF-based electrodes (in red).

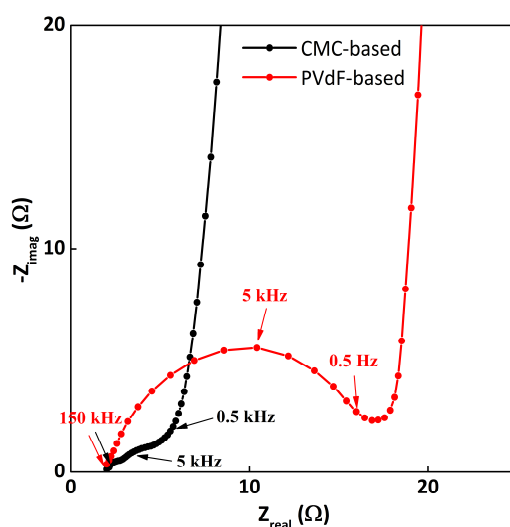


Figure 2-16. Nyquist plot of the symmetric coin cells built with the electrodes having different binders: PVdF (in red) and CMC/NBR (in black), with composition S/SuperP<sup>®</sup>/binder = 80/10/10 wt%. Both types of electrodes having very similar thickness of ~ 80–85  $\mu\text{m}$  and sulfur loading of ~ 3.5–4.0  $\text{mg}_{\text{sulfur}} \text{cm}^{-2}$ .

CMC-based electrode clearly displays two well-separated semicircles, but very small in size. A drastic decrease of the MF semicircle (previously associated with the bulk response of the electrode) is observed for the CMC-based electrode as compared with the PVdF-based one, whereas the first semicircle, observed at higher frequency, seems not to be impacted. Moreover, the characteristic frequencies of both semicircles are very close to those obtained with PVdF binder. Furthermore, the CMC-based electrodes display very similar EIS spectra, no matter the electrode thickness (which was not the case for the PVdF-based samples).

### 2.3.3.e) The effect of the electrode elaboration process

Previously demonstrated results made us questioned the way how the binder got incorporated into the ink, and if the manual ink preparation of the PVdF-based electrodes could explain alone the large resistance response, or if the EIS response is dependent from the binder nature. To verify that, a PVdF-based electrode was prepared the same way as the CMC-based one, *i.e.*

with the use of Dispermat<sup>®</sup>. From the same ink, five different electrodes, with linearly increased coating thicknesses, were obtained (77 – 95 – 109 – 130 – 147  $\mu\text{m}$ ). Symmetric coin cells were built with these electrodes and the results are presented on Figure 2-17.

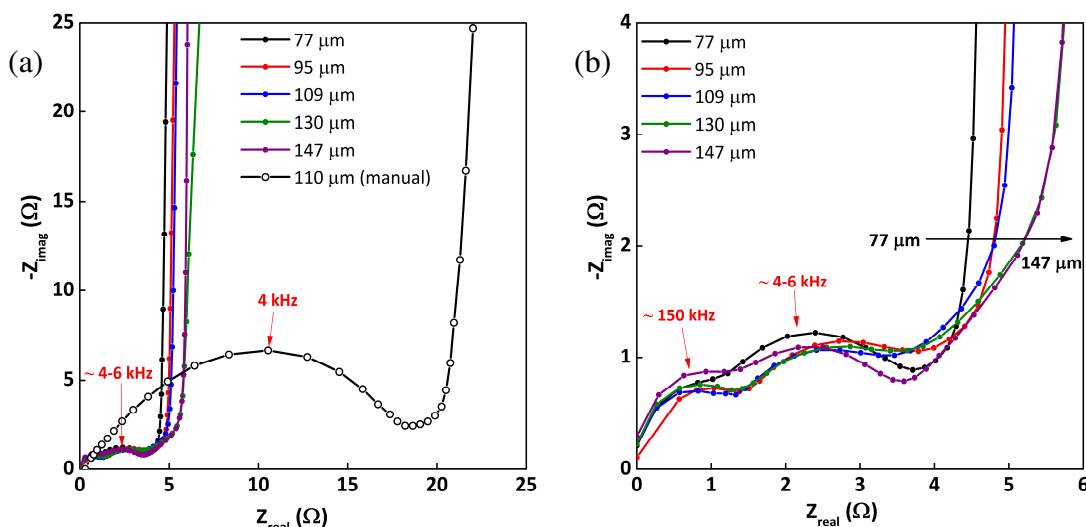


Figure 2-17. Nyquist plots of the symmetric coin cells built with the PVdF-based electrodes ( $S/\text{SuperP}^{\text{®}}/\text{PVdF} = 80/10/10$  wt%), where binder was incorporated to the electrode ink through intensive stirring with Dispermat<sup>®</sup>. Different thicknesses of the electrodes are indicated on the graph. For comparison, Nyquist plot of a ‘typical’ PVdF-based electrode (obtained by manual ink mixing) is presented (a). A zoomed view (b).

For the electrodes obtained through mixing with Dispermat<sup>®</sup>, very similar behavior to the CMC-based electrodes can be observed: two small semicircles are present, very stable regardless the electrode thickness. Moreover, the characteristic frequency values for both visible loops are almost the same, as the one observed for the CMC-based electrodes (Figure 2-16, in black). However, an increase of the thickness is visible in the MF→LF transition region, which has previously been associated with restricted diffusion impedance, and is coherent with restricted diffusion behavior explained by Aurbach and Levi<sup>228</sup>.

This results clearly indicate that the preparation method, and mostly the way of a binder incorporation, influences the electrode EIS response. More precisely, the binders’ response in terms of the resistance could be expressed as follow:  $\text{CMC}_{\text{dispermat}} \sim \text{PVdF}_{\text{dispermat}} \ll \text{PVdF}_{\text{manual}}$ . In addition, we also evaluated the BET surface of the PVdF-based electrode obtained with Dispermat<sup>®</sup>. The modification of the process results in a slightly decreased surface area ( $5.1 \text{ m}^2 \text{ g}^{-1}$ ), as compared with  $5.5 \text{ m}^2 \text{ g}^{-1}$  for the classical electrode preparation (*i.e.* manual stirring). Thus, even if the specific surface is not largely modified, the evolution of the BET value is coherent with better dispersion of PVdF, which permits to cover better carbon particles. However, the impedance response is impacted more significantly than the BET values.

### **2.3.3.f) Interpretation of ‘HF to MF’ and ‘MF’ regions response - summary**

The following points summarize clearly the conclusions coming from the different measurements described previously:

- The MF semicircle response is not attributed to the charge transfer reaction;
- The MF semicircle is notably decreasing when binder incorporation and mixing of the electrode ink is done *via* well-dispersing procedure (*i.e.* use of Dispermat<sup>®</sup>);
- For not well-dispersed electrodes (*i.e.* manually stirred), the MF semicircle characteristics (R, CPE) depend on both electrode thickness and electronic conductive additive;
- The HF→MF little semicircle response is observed for all the studied samples (is more or less visible), and its clear visibility depends on the size of the MF semicircle.

Seid *et al.*<sup>229</sup> evaluated the multiscale electric transport mechanism on LiFePO<sub>4</sub> composite electrodes by broadband dielectric spectroscopy. The authors associate the dielectric relaxation observed between 10<sup>6</sup> – 10<sup>7</sup> Hz with the existence of the polarization at the cluster surface. The clusters are formed, in their study, by LiFePO<sub>4</sub> particles bound together by the carbon coating layer. Another relaxation at lower frequency (10<sup>3</sup> – 10<sup>4</sup> Hz) is also noticed, and associated with a dielectric relaxation due to the existence of an interfacial polarization between the composite electrode and the current collector.

Supported by their studies, we may attribute the HF→MF little semicircle to the clusters polarization. By analogy to their work, the clusters are formed by sulfur particles bound together by the carbon particles and the binder. Since it is a local phenomenon and the distances for the electrons to go through are very small (in the range of 10<sup>-6</sup> m), the characteristic time constant of this phenomenon is in high to medium frequency domain.

The physical meaning of the relaxation observed in our work at the middle frequency range (10<sup>3</sup> – 10<sup>4</sup> Hz) is more difficult to evaluate. Indeed, in the case of not well-dispersed electrodes, the EIS response at the MF region is significantly dependent from the electrode thickness, whereas for well dispersed samples, no difference is marked. A contribution of the ‘electrode/current collector interface’ resistance could be present at such frequency values, as indicated by Seid *et al.* However, it should be rather stable regardless the electrode thickness, since the coating of the three thicknesses was made from the same ink. An additional phenomenon seems to occur, which response contributes in a large extent to the MF semicircle. Therefore, we may associate the origin of the MF loop with the bulk response of the electrode. The large resistance values (even ~ 20 Ω) may be related to a weak homogeneity of the electrode morphology with not efficient ionic and/or electronic pathways, which involve some polarization due to charge accumulation inside the electrode. The thicker the electrode is, more heterogeneous the electrode is along the thickness. An illustrative scheme summarizing the contribution of different phenomena inside the electrode is shown on Figure 2-18.

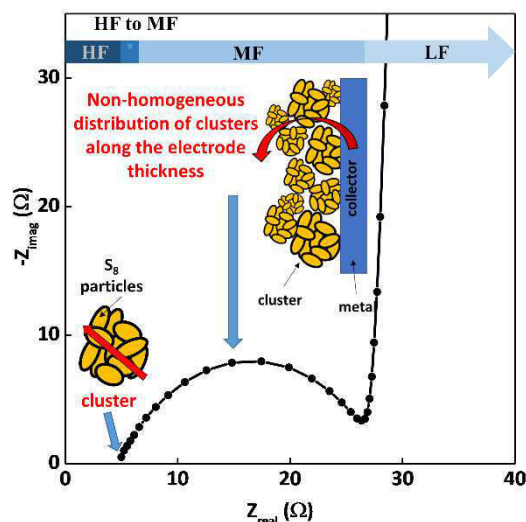


Figure 2-18. An illustrative summary of different phenomena appearing in  $S_8$  electrode, responsible for Nyquist plot shape recorded by EIS on a symmetric sulfur-based coin cell.

A significant difference in the EIS response was observed for three prepared electrodes (CMC<sub>dispermat</sub>, PVdF<sub>manual</sub>, PVdF<sub>dispermat</sub>), mostly due to the differences in the electrode elaboration process. We were interested to determine if a correlation between the EIS response and cycling performances could be established. *Post mortem* studies on cycled electrodes were done, and the results are presented in the following section.

## 2.3.4. Correlation of the EIS results with cycling performances

### 2.3.4.a) Cycling results

In order to have the most comparative and reflective results, we took into consideration highly loaded electrodes (with sulfur loading of  $\sim 3.9 - 4.7 \text{ mg cm}^{-2}$ ) cycled at faster rate (C/5).\*\* Figure 2-19 shows the shape of the initial voltage profile, together with capacity retention.

\*\* For thin electrodes cycled at a slow rate (C/20), no difference in the potential value was observed.

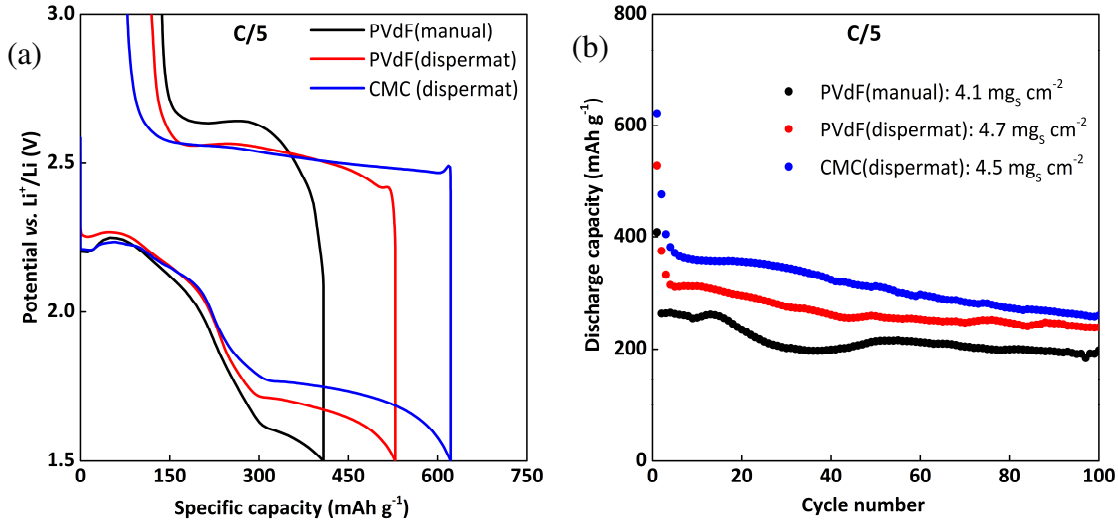


Figure 2-19. Galvanostatic cycling results of sulfur electrodes ( $S/SuperP^{\circledR}/binder = 80/10/10$  wt%) with different binders, in regard to binder type, *i.e.* CMC and PVdF, and the way it was incorporated: PVdF<sub>manual</sub> (in black), PVdF<sub>dispermat</sub> (in red) and CMC<sub>dispermat</sub> (in blue). Three cells were of relatively high and similar sulfur loading  $\sim 4.5\ mg_{sulfur}\ cm^{-2}$ . Initial cycle voltage profile recorded at  $C/5$  (a) and corresponding capacity retention upon 100 cycles (b).

We can see that the polarization of PVdF<sub>manual</sub> electrode is the highest, especially during the second plateau, while CMC one displays the lowest overpotential. Consequently, initial discharge capacities were 621, 529 and 406  $mAh\ g^{-1}$ , obtained for CMC, PVdF<sub>dispermat</sub> and PVdF<sub>manual</sub> respectively. The difference could directly be associated with the polarization effect. Indeed, the amounts of sulfur oxidized in the three cells are very close (same length of high voltage plateau upon discharge, of  $\sim 280\ mAh\ g^{-1}$ ), while the capacity decrease is mainly due to the reduction of the lower discharge plateau. This observation may relate to the fact that the low voltage plateau is definitely linked to the electrode morphology, its homogeneity and conductivity, and it could be expected to be linked to the way the electrode was fabricated. One should, however, note that the capacity retention over 100 cycles was proportional to the initial values.

Figure 2-20 presents the capacity evolution *versus* C-rate for the three formulated electrodes. The compared electrodes are of high sulfur loadings ( $\sim 5.6 - 7.5\ mg_{Sulfur}\ cm^{-2}$ ). However, due to not exactly the same loadings, direct quantitative comparison of the capacity values is difficult, and large dispersions of the data can be obtained. Nevertheless, the evolution of the capacity *vs.* C-rate could give some information about the limiting processes. Rather stable capacity value is obtained up to  $C/5$  rate, with the exception for PVdF<sub>manual</sub>, which starts to slowly lose its capacity at this rate. However, limiting processes start to be visible already at  $C/2$  or  $1C$  rates, and these are much lower C-rates values than what is generally observed in classical Li-ion cells<sup>11,230</sup>. Such behavior may be associated with the solubility of the active species, *i.e.* electrochemical reaction requires mass transport through the electrolyte and to the electrode. Furthermore, the fact of using very thick separators (Viledon<sup>®</sup> + Celgard<sup>®</sup>2400 with



a total thickness of  $\sim 275 \mu\text{m}$ ) may be detrimental for the mass transport and provides a long pathway for the active species diffusion.

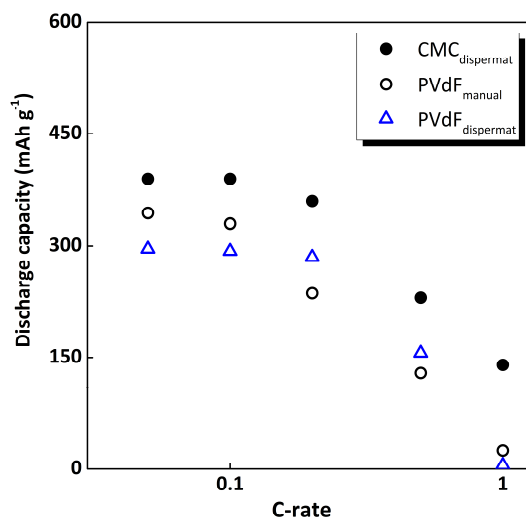


Figure 2-20. Average discharge capacity as a function of applied C-rate, for three sulfur electrodes, with different binders, *i.e.* PVdF<sub>manual</sub>, PVdF<sub>dispermat</sub> and CMC<sub>dispermat</sub>, cycled vs. Li. Electrodes of high sulfur loadings of  $5.6 - 7.5 \text{ mg}_{\text{Sulfur}} \text{ cm}^{-2}$ .

The galvanostatic cycling behavior of the PVdF<sub>manual</sub> and PVdF<sub>dispermat</sub> electrodes are very close, with a capacity close to zero at 2C. However, their EIS response measured in symmetric coin cells is very different (Figure 2-17), which clearly shows that the morphology of the electrode (conductive pathways) may not be a single limiting parameter in the Li/S system, and that an improved EIS response (*i.e.* lower resistance values for the CMC or PVdF<sub>dispermat</sub> electrodes) does not necessarily lead to better capacity retention upon cycling and high performances at high rate, contrarily to what is commonly said in the literature<sup>11</sup>.

### 2.3.4.b) Post-mortem studies

*Post mortem* analyses were done on sulfur electrodes after prolonged cycling (electrodes recuperated from the cells cycled at C/5 during  $\sim 100$  cycles, shown on Figure 2-19), and the photos are presented on Figure 2-21. CMC-based electrode presents the best state, *i.e.* the carbon/binder matrix is still completely stuck to the aluminum current collector, even after scratching the electrode. PVdF<sub>dispermat</sub> electrode looks similar, however, the carbon/binder pieces went out very easily when slightly scratching the electrode surface. The worst case was found for PVdF<sub>manual</sub> electrode, where carbon/binder mixture was completely peeled away from the collector. These observations would lead to the conclusions concerning the adhesion properties of the electrodes: CMC  $\gg$  PVdF<sub>dispermat</sub>  $>$  PVdF<sub>manual</sub>.

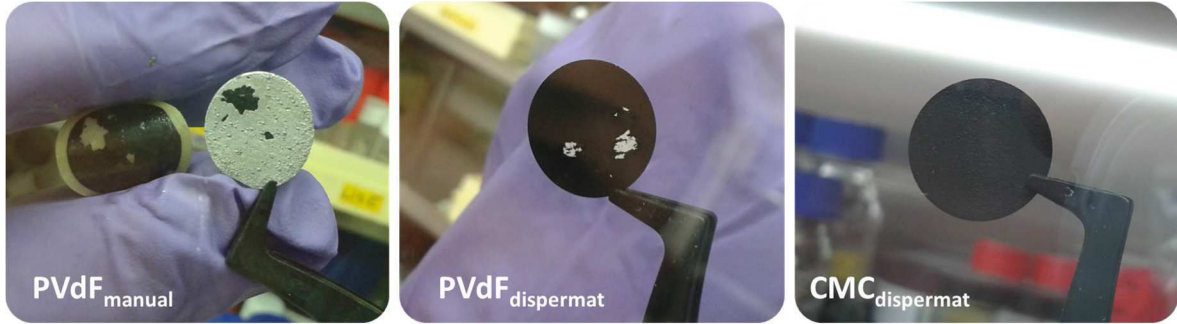


Figure 2-21. *Post mortem* photos of three sulfur electrodes (loading of about  $\sim 4.5 \text{ mg}_{\text{Sulfur}} \text{ cm}^{-2}$ ) with different binders, *i.e.* PVdF<sub>manual</sub>, PVdF<sub>dispermat</sub> and CMC<sub>dispermat</sub>, recuperated after 100 cycles at C/5.

Other tests were done with symmetric coin cells prepared with the electrodes recuperated after 10<sup>th</sup> charge. For the purpose of this experiment, four CMC-based electrodes (similar in thickness and mass) were selected. Two of them were used for making a symmetric coin cell, on which EIS was measured at the initial stage. The two others were used for fabrication of two identical Li/S complete cells, which were then galvanostatically cycled at C/20 for 10 cycles and stopped at the end of charge. Such pre-cycled electrodes were recuperated from the Li/S coin cells, gently washed with DIOX, symmetric coin cell was built and EIS was measured. Similar steps were carried out with four PVdF<sub>manual</sub> electrodes. EIS results of the coin cells built with fresh and pre-cycled electrodes are shown on Figure 2-22.

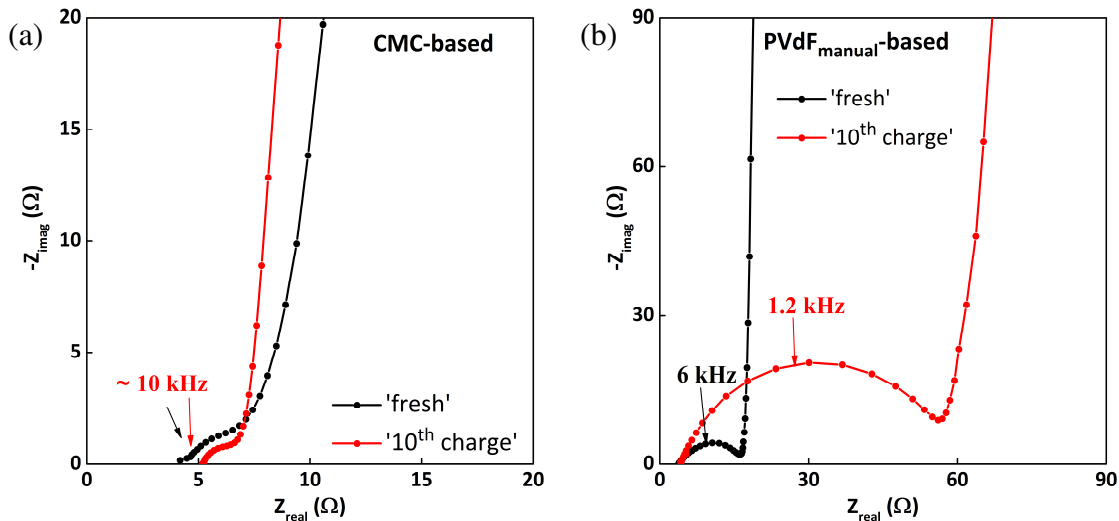


Figure 2-22. Nyquist plots of symmetric coin cells built with fresh and cycled electrodes (recuperated at the end of 10<sup>th</sup> charge), using different binders: CMC (a) and PVdF<sub>manual</sub> (b).

Already when recuperating the electrodes after 10 cycles, it was noticed that PVdF<sub>manual</sub>-based electrodes were slightly unstuck from Al collector, while CMC ones were fully adhering. EIS results show that the resistance of CMC-based electrode stays almost unchanged after cycling. A significant increase of the resistance of PVdF-based electrodes can be noticed. Moreover, the characteristic frequency is shifted to lower domain (from 6 kHz to 1 kHz). This may be

explained by more pronounced response of the electrode/collector contact resistance, as the adhesion is getting worse. The resistance increase due to a bad electrode/current collector interface may explain the low capacity obtained at 2C (after more than 20 cycles). Better performance of CMC-based electrode at 2C can be then associated with good interface contact and high efficient conductive pathways inside the electrode.

### 2.3.5. Conclusions

For simply prepared electrodes, we did not observe any significant modifications of the capacity values neither of the capacity retention, when using different carbons of different shapes (fibers vs. nano-spheres) and with different specific surface areas (13 – 60 – 800 m<sup>2</sup> g<sup>-1</sup>), while keeping the same electrode composition, *i.e.* S<sub>8</sub>/carbon/PVdF (80/10/10 wt%). Thus, we did not find any correlation between carbon surface area and practical discharge capacity, which may question the fact of accessible conductive surface area.

With EIS technique, we tested the electrical properties of sulfur electrodes (measurements in symmetric coin cells). It was found out that the main contribution in the Nyquist plot is the bulk response of sulfur electrode, which is strongly related to the electrode's homogeneity and preparation method. The attribution of different components of EIS spectra was performed, and the MF response was correlated with the response of the electrode morphology and efficiency of its electric network, and not with the nature of active material used.

Well-dispersed and homogenous inks (made with Dispermat<sup>®</sup>) resulted in significantly decreased resistance value. It seems that the binder nature (CMC or PVdF) does not matter so much in terms of capacity and fading. However, the differences between two binders are more visible in terms of adhesion properties on *post mortem* electrodes. CMC-based electrodes may provide better electrode adhesion and lower resistance at OCV potential, which is not necessarily visible in capacity retention upon cycling. In other word, prediction of cycling behavior based on improved resistance of the pristine electrode is not a clue. Nevertheless, these parameters must not be neglected, especially for high rate tests. It was also demonstrated that the preparation method and the homogeneity of the ink *priori* electrode coating has a crucial effect on the EIS response of the bulk electrode.

Last but not least, as previously mentioned, a key parameter relates to the active material loading. In particular, the rate capability as well as the initial discharge capacity is decreasing with increased loading. On the contrary, capacity retention is surprisingly improved with higher loadings, which may arise from the higher polysulfides concentration in the electrolyte upon cycling. This fact needs to be investigated deeper in the future. To go towards higher sulfur electrode loadings, the nature of the current collector was modified, and aluminum was replaced by a 3D porous carbon material. Alternative electrode morphologies were obtained and studied in details. Corresponding results are presented in the next chapter.

## Chapter 3: Porous 3D carbon current collector - a potential way for the electrode improvements

In the previous paragraph we saw the performances of a simply prepared positive electrodes, coated on aluminum foil – a current collector mostly used for cathodes fabrication. It was indeed shown that very high loadings of sulfur (even 5.7 mg cm<sup>-2</sup>) can be prepared, with relatively good discharge capacities obtained at slow (C/20) rates. However, after the active material leaves the electrode and dissolves in the electrolyte, strong pulverization could appear, thus the carbon/binder matrix and the conductive network through the whole electrode thickness may be strongly affected. When applying higher currents (C/5) for such highly loaded electrodes, high polarization occurs, resulting in much lower capacities and probably not complete sulfur utilization.

Another way to increase the electrode loading and to improve the mechanical integrity of the global electrode, without sacrificing capacity values, is to use a 3D type porous current collector. Indeed, a 3D collectors provide cohesive conductive network along with a stable surface area during cycling for the deposition of solid reaction products. A non-woven carbon tissue (NwC) has already been applied to the Li/S batteries by the former PhD student in our groups, mainly as a current collector in a ‘catholyte’ cell architecture (semi-liquid cell)<sup>45,126</sup>. The literature also presents electrodes with porous carbon collectors<sup>128,104,129-133</sup>, with successfully improved electrochemical performances, as demonstrated in the state of the art review (section 1.3.1.d). Therefore, we applied such NwC collector in our simply prepared electrodes. We mostly focused on understanding how the electrode’s performances may get improved when using such type of collector. Different aspects were taken into consideration, *i.e.* surface area, electrolyte amount, porosity, etc. Apart from aiming to obtain better cycling performances, the point of view of going deeper into understanding the Li/S system, its functioning and limitations, was always kept in mind.

### 3.1. Non-woven carbon felt (NwC) - physical and structural properties

Non-woven carbon tissue used in this work is a GDL felt (gas diffusion layer), produced by Freudenberg under its commercial name H2315. It is an electronically conductive and porous material composed of randomly dispersed carbon fibers of ~ Ø 10 µm approximately. It

exhibits a high tortuosity, as seen on the scanning electron microscopy (SEM) photos (Figure 3-1). Visually, it is a very flexible sheet,  $\sim 210 \mu\text{m}$  thick<sup>216</sup> with average through plane porosity of 80%<sup>231</sup> and area weight of  $\sim 9.5 \text{ mg cm}^{-2}$ <sup>216</sup>. This particular NwC is heavier and thicker as compared to a classical Al foil ( $20 \mu\text{m}$ ;  $5.5 \text{ mg cm}^{-2}$ ), which is not the ideal choice from the gravimetric and volumetric energy density point of view. Nevertheless, its application in sulfur electrodes as a current collector was rather a proof-of-concept. In further discussion, we show that, despite of its high mass and thickness, it already brings improvement to the sulfur electrode behavior.

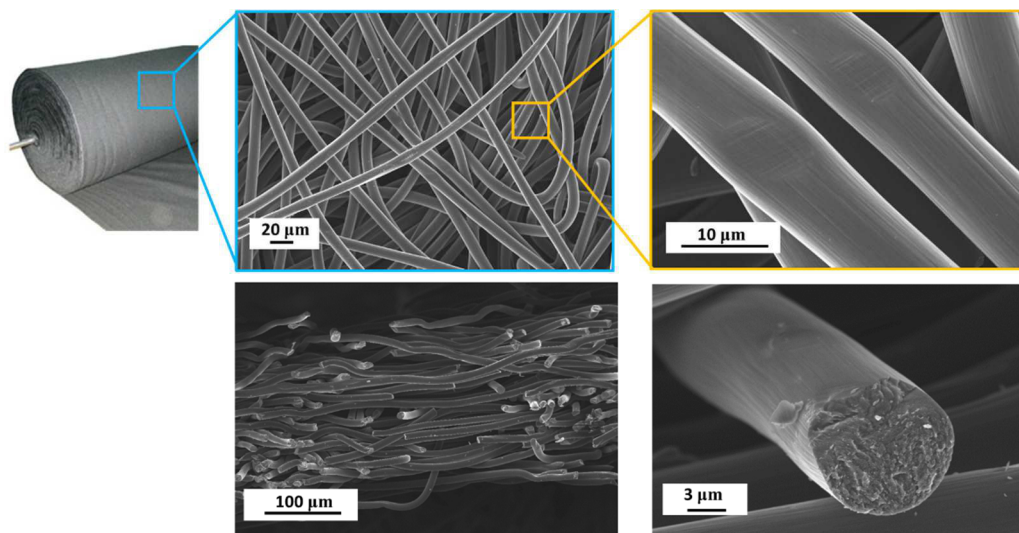


Figure 3-1. SEM photos of GDL felt (non-woven carbon tissue, NwC), a commercial product of Freudenberg (H2315).

Its surface area was found to be about  $0.05 \text{ m}^2 \text{ g}^{-1}$ , value which is really close to the detection limit by BET technique. All the physical parameters of the NwC felt are summarized in Table 3-1.

GDL commercial name	Thickness ( $\mu\text{m}$ )	Area weight ( $\text{mg cm}^{-2}$ )	BET surface area <sup>§</sup> ( $\text{m}^2 \text{ g}^{-1}$ )	Through plane porosity (%)
H 2315 (standard)	210	9.5	0.05	80

<sup>§</sup> BET measured with TRISTAR II 3020 equipment; degassing was done at  $180^\circ\text{C}$  during 6h, while BET measurement was performed under nitrogen  $N_2$ .

Table 3-1. Physical parameters of non-woven carbon (NwC) tissue.

## 3.2. Preparation of the electrodes

Two kinds of electrodes were prepared with the use of NwC as current collector:

- a) A composite electrode (named as ‘S-on-NwC’), with classical ink composition of 80/10/10 wt% (sulfur/SuperP<sup>®</sup>/PVdF 5130), coated onto NwC instead of Al foil sheet, using doctor blade technique.

Due to the fact that NwC sheet is not perfectly homogenous, the weight of  $\varnothing$  14 mm disks may oscillate in the range of  $14.7 \text{ mg} \pm 1.0 \text{ mg}$ . Such significant discrepancy may lead to an important error of the active mass determination in the final electrode. Therefore, the preparation route had to be slightly modified as compared to the preparation method of Al-based electrodes, in order to know precisely the weight of each NwC disk before the ink was coated. A schematic illustration (Figure 3-2) shows the steps of the electrode fabrication.

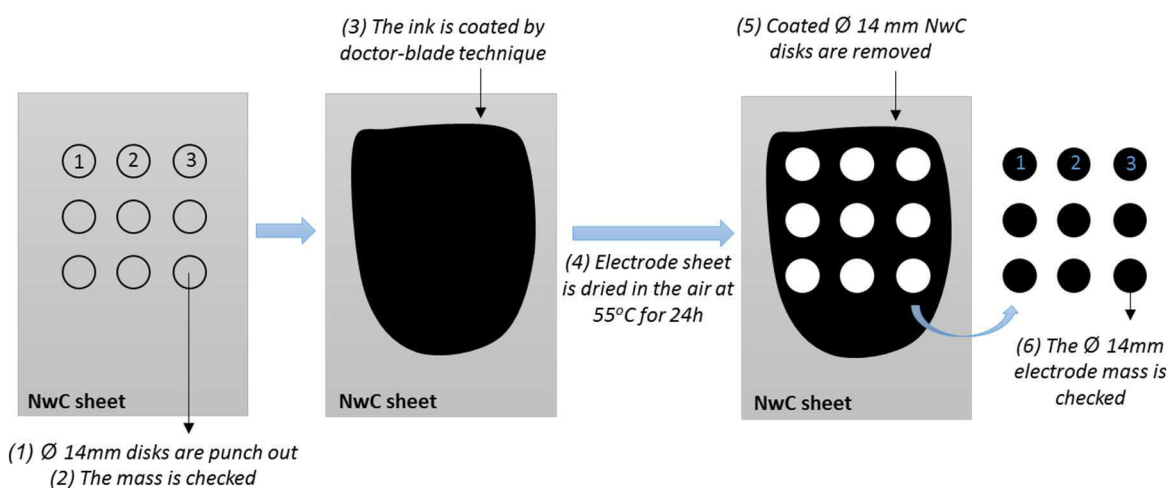


Figure 3-2. Schematic illustration of modified procedure for the electrodes fabrication, when using NwC sheet as a current collector, in order to minimize uncertainty of the current collector mass.

The ink preparation and the drying procedure were exactly the same as for the Al-based electrodes (preparation described previously in 2.2.1). In this particular case, the ink viscosity and the speed of doctor blade coating were playing relatively important role on the final electrode’s morphology. It was thus necessary to optimize those parameters to find the best combination. Too liquid ink casted too slowly may risk in the ink penetration through the whole thickness of NwC up to the other side.

The targeted loadings were between  $3.9$  to  $5.0 \text{ mg}_{\text{Sulfur}} \text{ cm}^{-2}$  (theoretical areal capacities of  $6.5$  to even  $8.4 \text{ mAh cm}^{-2}$ ). Effective thickness was about  $270 \pm 10 \mu\text{m}$  (considering  $\sim 210 \mu\text{m}$  of NwC, a  $\sim 60 \mu\text{m}$  thick electrode was deposited on the surface, while some part of the ink penetrated into the porosity of NwC). These composite electrodes were mostly the interest of

our further studies. Sulfur electrodes of even higher loadings ( $\sim 10 - 12 \text{ mg}_{\text{Sulfur}} \text{ cm}^{-2}$ ) were prepared as well, and their cycling performances were investigated.

For some of the experiments (before optimization of the preparation method, as shown on Figure 3-2), the  $\varnothing$  14 mm electrode disks were punched out after the ink was coated on complete NwC sheet. Such electrodes were burdened with an error of imprecise collector weight. In that case, theoretical capacity is based on estimated sulfur mass only, with the possible deviation indicated, and the results are rather presented in respect to the obtained areal capacities ( $\text{mAh cm}^{-2}$ ).

b) A binder-free electrode with melted sulfur (so-called ‘S-melted-NwC’).

There are several methods described in the literature concerning sulfur infiltration into carbon structures<sup>131,227</sup>. We used a simple sulfur powder melting route, as reported to be an easy and efficient way to deposit sulfur on a carbon surface<sup>131</sup>. In order to prepare the electrode, as-received S<sub>8</sub> powder was first gently grinded in the mortar, then dispersed on the NwC  $\varnothing$  14 mm disk of known mass, and placed on the hot plate surface until all sulfur got melted. The heating process took less than 1 minute, since the hot plate was preheated up to  $\sim 150^\circ\text{C}$  and sulfur rapidly diffused into the NwC layer thanks to good S/C interactions. After that, the mass of NwC+S<sub>8</sub> disk was verified again and precise amount of sulfur was calculated. Such prepared electrode was then tested in a coin cell (fabrication already described in section 2.2.2).

### 3.2.1. The effect of imprecise NwC collector mass estimation and related capacity error

Having such large imprecision of NwC  $\varnothing$  14 mm ( $\pm 1 \text{ mg}$ ) due to its inhomogeneity, it was mandatory to verify the error related to the NwC mass, which may strongly affect the final capacity values. Taking into consideration a composite electrode ‘S-on-NwC’ with total weight of 23.000 mg, where the mass of NwC current collector is not precisely known but only estimated to be  $14.7 \pm 1 \text{ mg}$ , the uncertainty of the theoretical capacity ( $\Delta\text{Capacity}$ ) can be as high as 12.7 %, according to the equation (5) in Table 3-2.

This error could indeed be detected on electrochemical profiles as well, as shown on Figure 3-3. In black, cycling curve based on precisely known active mass (AM) is shown. Red and blue dashed curves illustrate the cases when the active mass is overestimated and underestimated respectively, due to the imprecise weight of NwC.

Preparation method of Ø 14 mm electrode	Equation number	Equation for the error estimation	Error value (% of the theoretical capacity)
'S-on-NwC' cut/weighed after ink coating	(5)	$\frac{\Delta\text{Capacity}}{\text{Capacity}} = \frac{\Delta\text{M}(\text{electrode}) + \Delta\text{M}(\text{NwC})}{\text{M}(\text{electrode}) - \text{M}(\text{NwC})} + \frac{\Delta\%S}{\%S}$	12.7
Modified procedure (ink coated on NwC disks previously cut/weighed)	(6)	$\frac{\Delta\text{Capacity}}{\text{Capacity}} = \frac{2 \times \Delta\text{M}(\text{electrode})}{\text{M}(\text{electrode}) - \text{M}(\text{NwC})} + \frac{\Delta\%S}{\%S}$	0.7
Sulfur melted on previously cut/weighed NwC	(7)	$\frac{\Delta\text{Capacity}}{\text{Capacity}} = \frac{2 \times \Delta\text{M}(\text{electrode})}{\text{M}(\text{electrode}) - \text{M}(\text{NwC})}$	< 0.05

Where:

$\Delta\text{M}(\text{electrode}) = 0.001$  mg (imprecision of the micro scale where electrode mass was checked)

$\Delta\text{M}(\text{NwC}) = 1$  mg (imprecision of NwC current collector mass due to inhomogeneity)

$\Delta\%S = 0.5$  % (error of the final sulfur ratio estimation in the composite electrode, aimed to be  $\%S = 80$  %)

$2 \times \Delta\text{M}(\text{electrode})$  – it results from double checking of the mass: pure NwC Ø 14 mm disk & final electrode

Table 3-2. Estimation of the error made on the capacity estimation, depending on the weighing procedure of the Ø 14 mm disk of NwC current collector, *i.e.* punching out after ink being coated on complete NwC sheet (5), ink coating done on separated NwC disks (6), or elemental sulfur directly melted on a separated Ø 14 mm disk (7).

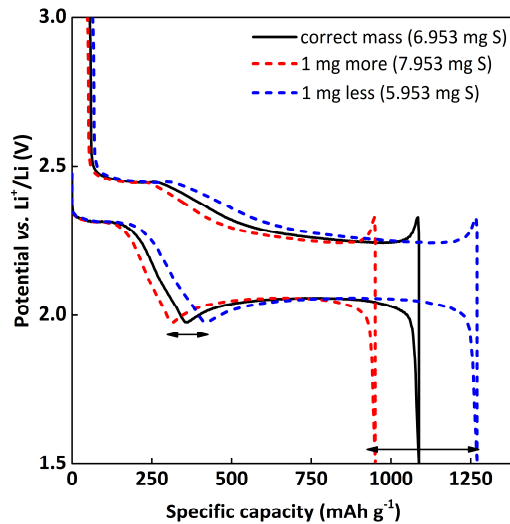


Figure 3-3. Variation of the initial cycle voltage profile of 'S-on-NwC' electrode cycled vs. Li at C/20, depending on the error due to the imprecise active mass estimation, resulting from imprecisely known mass of NwC: precisely known S<sub>8</sub> mass (in black), underestimated/overestimated of 1 mg (blue/red).

In order to help detecting this possible estimation error, the position of the little dip at the beginning of the low voltage discharge plateau ( $\leftrightarrow$ ) could be roughly verified. If observed at a discharge capacity higher than 418 mAh g<sup>-1</sup> (theoretical value, based on simplified sulfur reduction  $\text{S}_8 + 4\text{e}^- \rightarrow \text{S}_4^{2-}$ )<sup>194,195</sup>, it would mean that the active mass was incorrectly estimated. Moreover, based on our experience, we noticed that for this electrolyte system and at moderate



currents (C/20, C/10), the little “dip” should be found at about 370 – 380 mAh g<sup>-1</sup>\*. One can also see the significant impact of the error of NwC weight on the capacity of the lower discharge plateau, which can end up with a practical discharge capacity ranging from 950 mAh g<sup>-1</sup> to 1270 mAh g<sup>-1</sup> for 1 mg overestimated and underestimated sulfur masses, respectively. Therefore, the capacity variation in such situation may be as high as 320 mAh g<sup>-1</sup>.

### 3.3. Morphology of the electrode: before and after cycling

Figure 3-4 shows typical Scanning Electron Microscope (SEM) images of ‘S-on-NwC’ electrode. From the top view (Figure 3-4 a,b), very big particles of sulfur (active material was used as received, without any pretreatment) wrapped by the conductive carbon nano-particles can be seen. Carbon fibers are not visible, as they are completely covered by the coating.

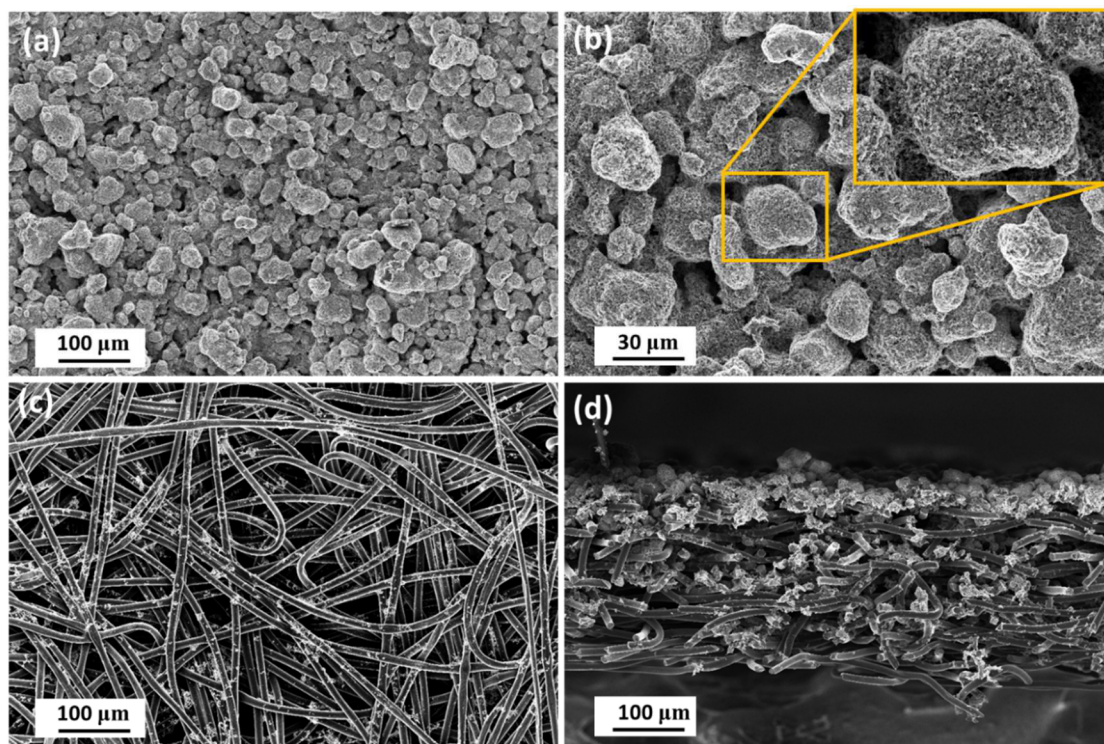


Figure 3-4. SEM photos of ‘S-on-NwC’ electrode before cycling: top view (a,b), bottom side (c), and cross-section image (d).

Electrode morphology resembles to the aluminum-based electrode. Images of the electrode from the bottom side, as well as the cross-section view (Figure 3-4 c,d), show that the ink rather remains on the NwC surface, without any deeper penetration throughout the collector

\* Based on reproducibility tests performed on a large number of ‘S-on-NwC’ electrodes, with precisely known active mass.

thickness. XRD pattern is composed of peaks solely attributed to orthorhombic  $\alpha$ -S<sub>8</sub> phase (PDF-2; no. 00-008-0247), which was used for electrodes preparation. It may be expected that carbon fibers introduced to the composite electrode in the form of current collector participate in the discharge process, by offering a conductive area for solid products deposition. SEM photos recorded on the electrode at the end of 1<sup>st</sup> discharge are shown on Figure 3-5. The electrode was carefully rinsed with TEGDME/DIOX (50/50 vol%) mixture of solvents under protective atmosphere in the glove box, in order to remove the lithium salt (LiTFSI) and eventual traces of soluble polysulfides. After solvent evaporation, the cross section was made with the scissors and the piece of electrode was placed on SEM sample holder inside the air-tight transfer box, as previously shown on Figure 2-3a,b. Such solution allowed to keep the sample without exposure to air.

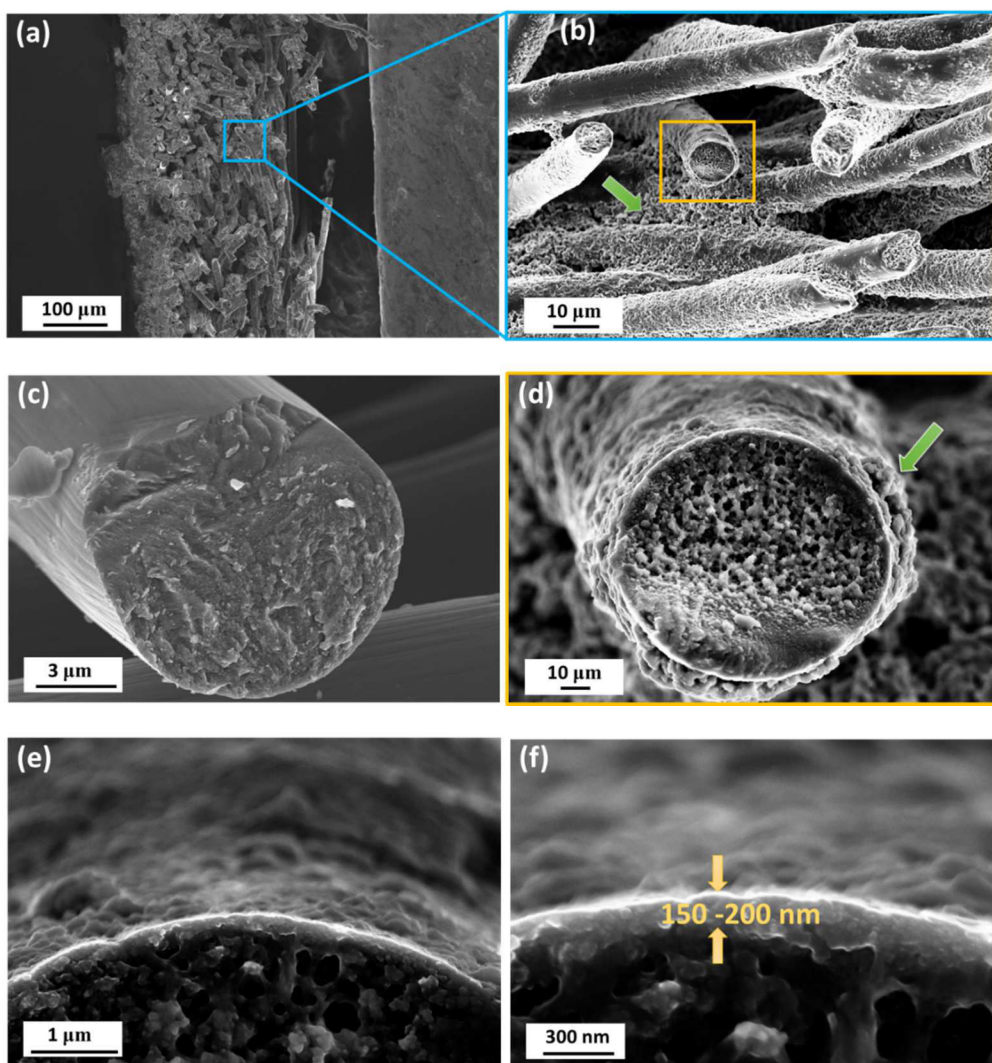


Figure 3-5. SEM photos of ‘S-on-NwC’ electrode after initial discharge: cross-section view (a,b) with zoomed image on a single carbon fiber (d), and on the dense thin layer deposited on its surface (e,f). Air-sensitive sample was totally protected from air atmosphere thanks to transferring in a special box designed for that purpose (‘transfer box’). An image of fresh carbon fiber is also shown for comparison (c).

It can be seen that all available conductive area is covered by a dense layer. The solid reduction product deposited on the conductive surface of the composite electrode (*i.e.* on the SuperP®/PVdF matrix, found on the top of NwC) as well as on the carbon fibers. It means that the polysulfides formed during progressive discharge were able to penetrate throughout the whole electrode thickness, reaching also the bottom side of the collector. However, it can be also seen that two types of deposits got formed on the fibers' surface (Figure 3-5d-f). A very dense but thin nano-layer (estimated to be around ~ 150 – 200 nm) was created in close contact with the 'fresh' carbon fibers. In addition, less dense precipitate can be seen on the surface of this thin nano-layer, as well as more in the volume of the electrode, *i.e.* between the fibers (marked with the green arrow). As the final discharge product (expected to be solid Li<sub>2</sub>S) is known from its insulating nature, it is surprising to see that it was observed in the whole volume of the electrode, and at a large distance from the conductive fibers (few μm). Therefore, this second but less dense layer may also arise from precipitated polysulfide species as Li<sub>2</sub>S<sub>2</sub>. Indeed, some literature studies proposed an insoluble behavior (or poorly soluble) of Li<sub>2</sub>S<sub>2</sub> in the electrolyte<sup>37,38,194</sup>. Further discussion concerning this observation is included later in this chapter.

### 3.4. Electrochemical performances of 'S-on-NwC' electrode

#### 3.4.1. Typical galvanostatic cycling response (C/20)

An example of charge/discharge voltage profiles of a Li/S cell with 'S-on-NwC' electrode (loading of 4.42 mg<sub>Sulfur</sub> cm<sup>-2</sup>), measured by galvanostatic cycling at C/20, is shown on Figure 3-6a. During the initial discharge, two characteristic plateaus are visible: (i) at 2.32 V, which is commonly attributable to reduction of solid elemental sulfur and formation of longer chain polysulfides, and (ii) the lower plateau at 2.02 V, related with the reduction of shorter chain polysulfides and formation of final solid products Li<sub>2</sub>S<sub>2</sub>/Li<sub>2</sub>S. A discharge capacity of 1116 mAh g<sup>-1</sup> was obtained practically, which is about 67 % of the theoretical value (1675 mAh g<sup>-1</sup>). If we thus consider the areal specific capacities, a relatively high value of 4.96 mAh cm<sup>-2</sup> was obtained, which is much higher as compared to what is usually reported in many publications, and what we already presented for the aluminum based composite electrodes (see 2.3.2). For the same loading (*i.e.* 4.5 mg<sub>sulfur</sub> cm<sup>-2</sup>), areal capacity of 2.5 mAh cm<sup>-2</sup> was obtained for Al-based electrode, a half of what was reached with NwC-based one.

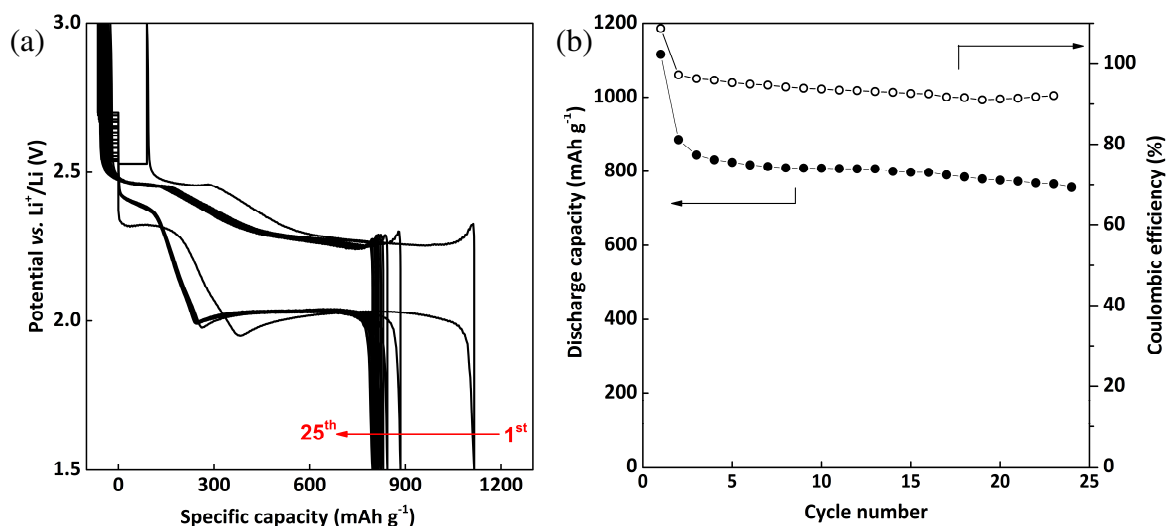


Figure 3-6. Galvanostatic cycling results of typical ‘S-on-NwC’ electrode (sulfur loading of  $4.42 \text{ mg cm}^{-2}$ ) cycled at C/20 vs. Li. Voltage profiles (a), as well as capacity retention with coulombic efficiency over 24 cycles (b).

Charging process starts with a relatively sharp peak (Figure 3-6a), corresponding to the overpotential necessary to break the passivation layer formed during previous discharge<sup>38,45</sup>. The overvoltage of this peak decreases slightly within subsequent cycles, however it does not vanish completely. Further charging results in two ‘quasi’ plateaus: at 2.26 V – corresponding to the oxidation of solid products and shorter chain polysulfides, and at 2.46 V – related with oxidation of longer chain polysulfides and formation of sulfur. Charge capacity of  $1027 \text{ mAh g}^{-1}$  was obtained, which is lower than the initial discharge (loss of  $90 \text{ mAh g}^{-1}$ ). That clearly indicates an irreversible capacity loss of  $\sim 8 \%$ , which can be associated with not complete utilization of active material, *i.e.* disconnected conductive part of the electrode, loss of active mass in the electrolyte, and possibly on the negative electrode side due to precipitation process.

In the second cycle, the upper discharge plateau is shifted to higher potential value (2.4 V). The overpotential indeed decreases as compared with the 1<sup>st</sup> discharge, due to active material reorganization. It is usually more difficult to reduce big particles of sulfur (of even  $50 \mu\text{m}$ , which initially exists in the electrode), while relatively easier when produced in smaller size by the electrochemical reaction at the end of charge (refer to chapter 5). The overpotential of first discharge may also depend on the lithium surface and its resistive passivation layer, which may be improved by the first cycle and lithium stripping/plating processes. It can be noticed that the second discharge capacity ( $885 \text{ mAh g}^{-1}$ ) is lower as compared with the first cycle (79 % of the initial value). However, the capacity fade is still lower than what is usually observed for typical Al-based electrodes (second discharge capacity is classically of  $\sim 60 - 70 \%$  of the initial value; see Figure 2-5 as an example).

Both discharge plateaus were significantly shortened. However, the ratio of upper/lower plateaus capacity seems not to change that much along cycling. Initially, the upper/lower plateaus ratio is  $34 \%$  /  $66 \%$ , and is changed to  $\sim 30 \%$  /  $70 \%$  during the second and further cycles. As

discussed previously for the first cycle, the capacity loss may be associated with some polysulfides precipitation inside the electrolyte/separator, polysulfides leftovers in the electrolyte and/or reduction of the positive electrode active surface.

A shuttle phenomenon starts to be visible at the second cycle already, despite the use of  $LiNO_3$  as an electrolyte additive. The presence of shuttle can easily be determined based on coulombic efficiency values (Figure 3-6b), which are only slightly superior to 90 %. Coulombic efficiency ( $\Phi$ ) was calculated as a ratio of (n) discharge over (n) charge capacities. Efficiency determined such way gives directly the information about the presence of shuttle mechanism, if  $\Phi < 100\%$ .

The capacity is relatively stable during those 24 cycles (Figure 3-6b), resulting in a capacity decay of 0.1 % – 0.8 % per cycle (starting from the second one, where the highest fade is observed). However, the capacity retention could only be measured during a limited number of cycles, and the cell sudden death was observed afterwards. In further discussion, we explain the reasons for such short cycle life of the cells and related problems.

The NwC-based electrodes were then galvanostatically cycled at different current densities, and the results are reported in the following section.

### 3.4.2. Voltage profile and capacity retention at various currents

Five cells were prepared with ‘S-on-NwC’ electrodes of similar weight (sulfur loading varying between 4.0 to 4.4  $mg_{sulfur} cm^{-2}$ ) and were cycled at different current densities during prolonged cycling. The results are presented on Figure 3-7. For all cells, the same typical trend is observed, *i.e.* capacity fading during few cycles, followed by rather stable cycling. Initial capacity values are strongly affected by the C-rate (Figure 3-7a), being 1121, 1116, 1035, 673 and 257 mAh  $g^{-1}$  at C/100, C/20, C/10, C/5 and 1C, respectively.

The capacity values slowly decrease while increasing the current density from C/100 to C/5, and shut down drastically for higher C-rates. Concerning the coulombic efficiency, opposite trend is observed, where the highest efficiency is obtained for the cell cycled at the fastest rate. The red line on Figure 3-7b visually marks the value where the discharge capacity is equal to charge (efficiency = 100 %), *i.e.* no irreversible capacity loss neither shuttle mechanism is present. The slower is the rate, the more pronounced the shuttle effect is (efficiency lower than 100 %; points under the red line), since the polysulfides dissolved in the electrolyte have more time to diffuse back and forward between the electrodes. At C/100, shuttle appears already during initial cycle, while for the cells cycled at C/20, C/10 and C/5, it starts to be more pronounced already after few cycles. Only 1C cell has virtually the efficiency of 100 %, however, the capacity values are extremely low ( $\sim 100$  mAh  $g^{-1}$  after 50 cycles). Enlarging the voltage window for such high rates, and setting the lower cut-off voltage down to 1 V for

example, would probably help to proceed the lower plateau much longer, and thus to obtain improved electrochemical response. However, such solution may induce additional parasitic reactions of electrolyte or faster reduction of  $LiNO_3$  additive. Furthermore, this observation also proves that such electrodes and cell configuration are not designed for power application.

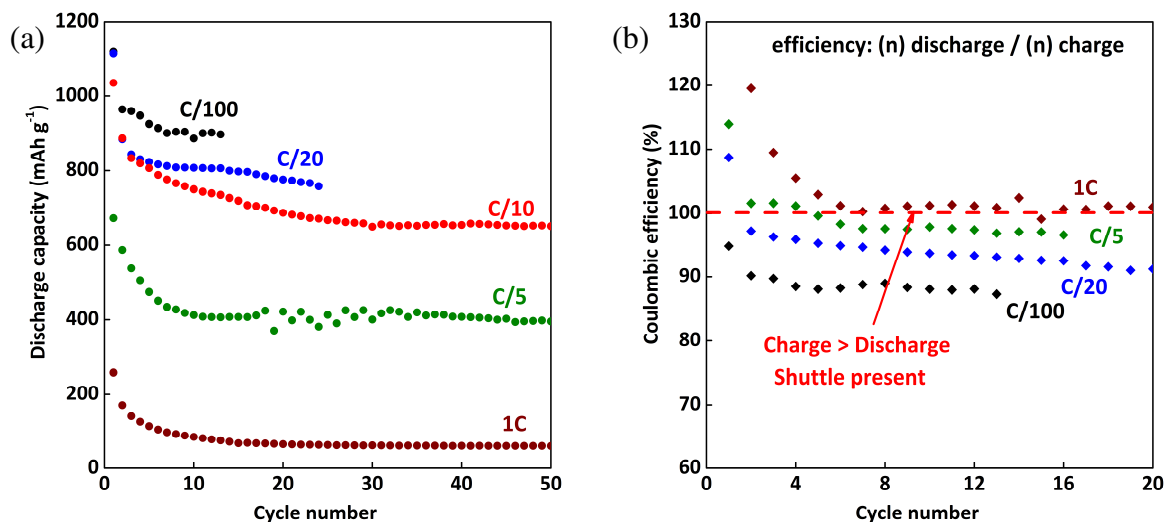


Figure 3-7. Galvanostatic cycling results of ‘S-on-NwC’ electrodes at different C-rates applied for prolonged cycling: capacity retention (a) coulombic efficiency values calculated as a ratio of (n) discharge / (n) charge (b).

Figure 3-8 shows corresponding voltage profiles together with overpotential values calculated from the derivative curves ( $dQ/dE$  vs.  $E$ ) for each C-rate and at equilibrium (after potential relaxation).

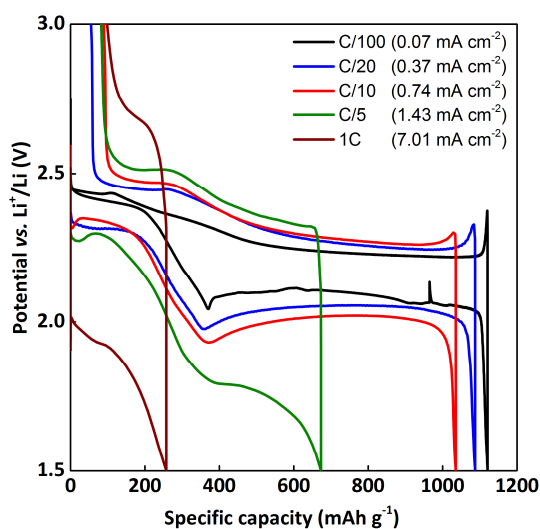


Figure 3-8. Initial voltage profile of ‘S-on-NwC’ electrodes cycled at different C-rates.

The overpotential is higher for the discharge processes than for the charge ones, moreover, lower discharge plateau is affected in higher extent than the upper plateau. This could be

expected, since the lower plateaus are assigned to the formation of insulating species which cover the electrode surface. This process is thus mostly governed by both diffusion phenomena and decrease of the surface area due to  $Li_2S$  and/or  $Li_2S_2$  precipitation.

At a very fast current density (1C), a unique sloping plateau is observed. Probably, the current is too fast to reduce all sulfur through the multi-step process, and the reaction takes place at the extreme surface of the electrode only, which is rapidly blocked and polarizes. The other explanation could be a limitation by mass transport, which induces a large polarization.

Rate capability tests were also performed. The C-rate was gradually increased every five cycles in following sequence:  $C/20 \rightarrow C/10 \rightarrow C/5 \rightarrow C/2 \rightarrow 1C \rightarrow C/5 \rightarrow C/10 \rightarrow C/20$ . As first trials, the charge and discharge currents were chosen to be the same. But since the electrodes were highly loaded ( $4.66 \text{ mg}_{\text{sulfur}} \text{ cm}^{-2} \leftrightarrow 7.18 \text{ mAh cm}^{-2}$ ), a current density as high as  $14 \text{ mA cm}^{-2}$  was used at 2C during charge, and caused a severe dendrites growth on lithium electrode and short circuit. Therefore, the cycling procedure was slightly modified (so called ‘asymmetric’ cycling), and charging rate was set up to  $C/20$  for each cycle. Thanks to such slow recharge, dendrites formation was minimized and the cells could be discharged at the different C-rates. Figure 3-9 shows comparison of discharge capacities obtained in classical power rate tests and ‘asymmetric’ one. Coulombic efficiency values are not presented, since they do not have a significant meaning (charge always performed at  $C/20$ ). Very stable capacity retention is obtained.

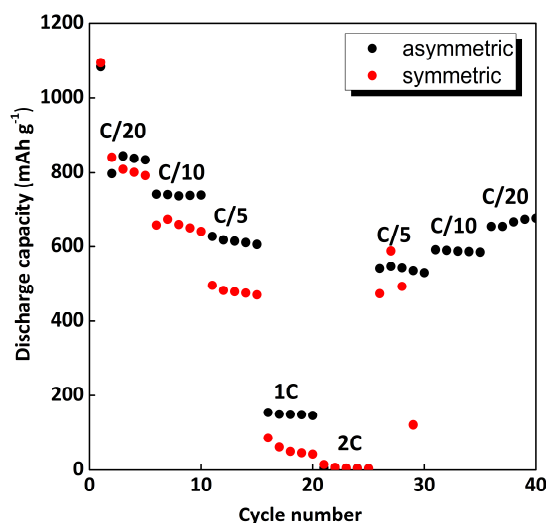


Figure 3-9. Rate capability tests done on ‘S-on-NwC’ electrodes (sulfur loading of  $\sim 4.7 \text{ mg}_{\text{sulfur}} \text{ cm}^{-2}$ ) in two cycling configurations: ‘symmetric’ *i.e.* the same current applied during both discharge and charge processes (in red), ‘asymmetric’ *i.e.* slow charge at  $C/20$  applied for each cycle, while varying only the discharge rate (in black).

Moreover, such ‘asymmetric’ cycling procedure results in better discharge capacities as compared with the standard ‘symmetric’ one, as the charge process allows for more complete re-oxidation of the active species. From these power rate tests, it can be seen again that the cell cannot really perform well at faster C-rates (1C, 2C), resulting in very low capacity ( $< 200$

$\text{mAh g}^{-1}$ ). However, when returning to moderate and slow C-rates ( $C/5$ ,  $C/10$ ,  $C/20$ ), the capacity almost comes back to its initial values. When comparing the rate capability tests performed on NwC and on Al-based electrodes, the capacities at low rate are much higher for ‘S-on-NwC’ electrode as previously discussed. However, at 2C, the capacity is practically equal to zero. The limiting process at high C-rate is clearly associated to the mass transport limitation, more important with ‘S-on-NwC’ as the complete cell is thicker.

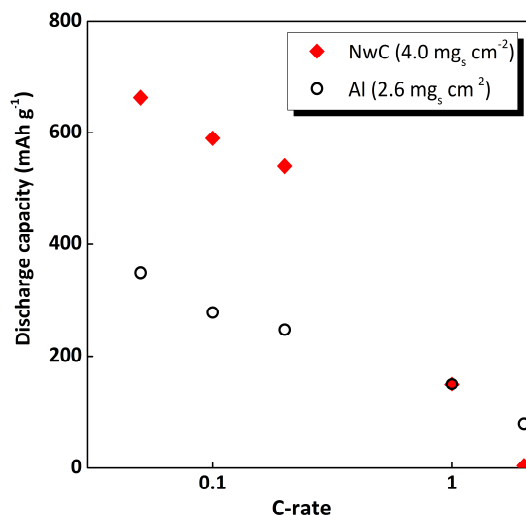


Figure 3-10. ‘Asymmetric’ rate capability tests performed on the electrodes coated on different collectors: NwC and Al foil. Electrodes of different sulfur loadings.

### 3.4.3. Lower voltage limit and its correlation with different S/C ratios

Most of our work was based on ‘reference’ electrode composition (80/10/10 wt% of sulfur/SuperP<sup>®</sup>/binder). However, when increasing the carbon content in the electrode, an additional plateau started to be visible at  $\sim 1.5$  V, getting longer when increasing fractions of carbon. This additional electrochemical process was attributed to the reduction of  $\text{LiNO}_3$  additive contained in the electrolyte. Different compositions were prepared, as shown on Table 3-3. The electrodes were galvanostatically cycled in the potential window of 3.0 V – 1.5 V at  $C/10$ . It can be seen that, when having carbon content of 45 %, the contribution of this additional reduction tail is as high as  $\sim 18$  % of the total capacity.



Average sulfur loading (mg cm <sup>-2</sup> )	Composition S/C/PVdF (wt%)	3 <sup>rd</sup> plateau contribution to the capacity (%) <sup>(*)</sup>
3.6	70/20/10	1.7
1.68	60/25/15	1.7
1.58	50/35/15	8.4
0.45	45/45/10	17.7

<sup>(\*)</sup> % calculated based on the capacity difference obtained between 1.8 V and 1.5 V

Table 3-3. Different electrode compositions (S/SuperP<sup>®</sup>/PVdF), with increasing carbon fraction from 20 wt% to 45 wt%, and the corresponding data of the cycled electrodes.

As an example, Figure 3-11 shows the initial voltage shape of two identical coin cells with electrode composition 50/35/15 wt%, with two electrolyte compositions, containing or not LiNO<sub>3</sub> additive. We can clearly see that LiNO<sub>3</sub> reduction occurs at the potential below ~ 1.7 V, and is responsible for an extra discharge plateau. Once deposited on the conductive surface of the positive electrode during discharge, the reaction by-products also affect the following charge, giving the rise for an additional overpotential. Without LiNO<sub>3</sub>, on the other hand, no extra discharge plateau at ~ 1.5 V is observed.

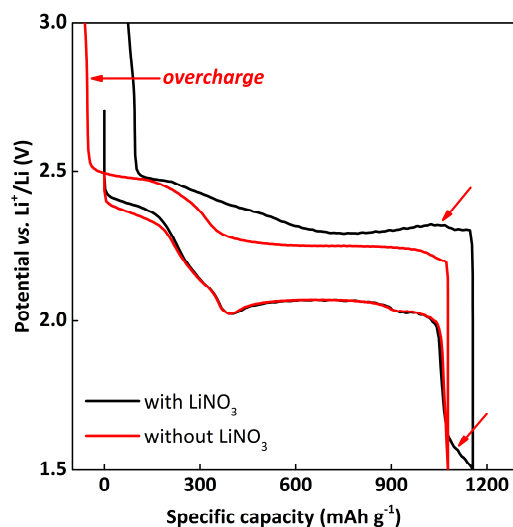


Figure 3-11. Cycling results of sulfur electrode with S/SuperP<sup>®</sup>/PVdF = 50/35/15 wt% composition, cycled with electrolyte containing LiNO<sub>3</sub> (in black) or without additive (in red).

The LiNO<sub>3</sub> reduction tail is shortened with following cycles. This may be related to a progressive consumption of LiNO<sub>3</sub> additive, or to the fact that the electrode is getting passivated upon cycling. Indeed, the reduction of LiNO<sub>3</sub> is an irreversible process which may passivate the electrode. Those results highlight the fact that the lower voltage limit should be selected carefully, especially when using LiNO<sub>3</sub>-containing electrolyte and positive electrode with high carbon fraction. Discharging to lower values than 1.7 V may risk in faster capacity

fading, irreversible consumption of  $\text{LiNO}_3$ , higher charge overpotential (red arrow) and more importantly – a “fake” contribution to the discharge capacity in the form of the additional discharge plateau, which, if not extracted from the practical value, may be misinterpreted. Our conclusions are very close to the one of Zhang<sup>178</sup>.

### 3.4.4. Towards heavily loaded electrodes

We already saw the enhanced electrochemical performances of ‘S-on-NwC’ electrodes with relatively high sulfur loading ( $\sim 4.0 - 4.5 \text{ mg}_{\text{Sulfur}} \text{ cm}^{-2}$ ), where quite stable capacities of  $700 - 800 \text{ mAh g}^{-1}$  were obtained at  $C/10$  and  $C/20$ <sup>†</sup>. NwC collector allowed us to increase the sulfur loading even more, and composite electrodes ( $\text{S/C/PVdF} = 80/10/10 \text{ wt\%}$ ) with up to  $10 - 12 \text{ mg}_{\text{Sulfur}} \text{ cm}^{-2}$  were prepared. Figure 3-12 compares the initial cycle profile of two cells cycled at  $C/100$  with different sulfur loadings:  $4.0 \text{ mg}_{\text{Sulfur}} \text{ cm}^{-2}$  (cell 2; in red) and  $11.3 \text{ mg}_{\text{Sulfur}} \text{ cm}^{-2}$  (cell 1; in black).

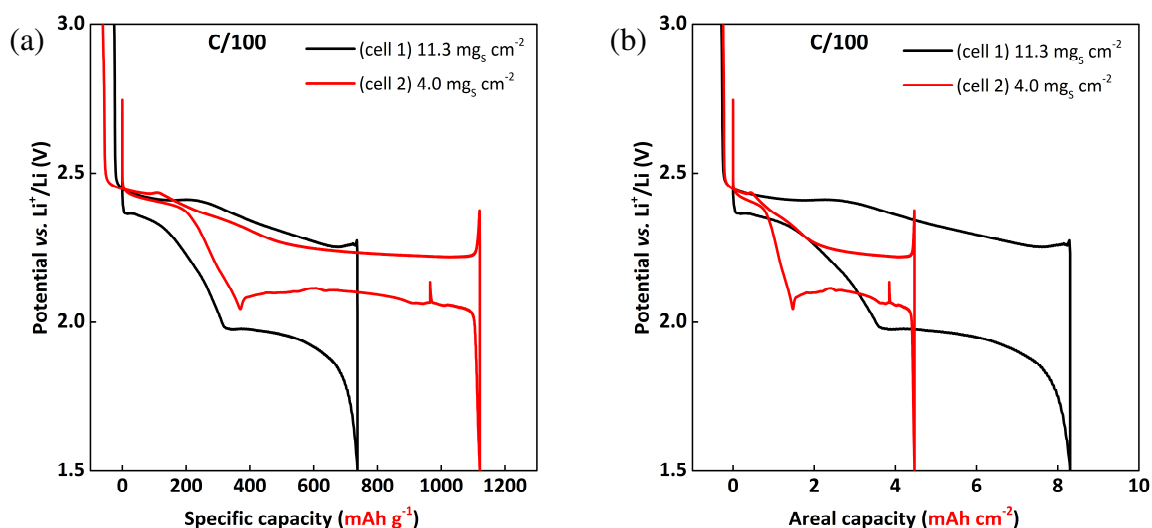


Figure 3-12. Initial cycle voltage profile of ‘S-on-NwC’ electrodes with different sulfur loadings:  $4.0 \text{ mg cm}^{-2}$  (cell 2) vs.  $11.3 \text{ mg cm}^{-2}$  (cell 1), and cycled at  $C/100$  rate. Discharge capacity in regard to:  $\text{mAh g}_{\text{sulfur}}^{-1}$  (a) and  $\text{mAh cm}^{-2}$  (b).

Cell 1 (very highly loaded electrode) gives a discharge capacity of  $734 \text{ mAh g}^{-1}$ , which is lower as compared to cell 2 –  $1120 \text{ mAh g}^{-1}$ . The difference may lie in polarization phenomena. Indeed, as the loading increases, the current applied at a constant  $C$ -rate increases proportionally. Then, even with same resistance values of the cell, the overpotential automatically increases. The capacity corresponding to the sulfur reduction and formation of high-order polysulfides (at the little dip, a transition point between both plateaus) is relatively similar:  $330$  and  $370 \text{ mAh g}^{-1}$  for cell 1 and cell 2, respectively. More significantly,

<sup>†</sup> to recap: Al-based electrodes for the same loading gave  $\sim 300 - 400 \text{ mAh g}^{-1}$

overpotential is visible for the lower discharge plateau. A large dissimilarity is visible in much earlier end of discharge, which may be associated with a quicker electrode passivation, polysulfide precipitation, and/or mass transport limitations (more active species with respect to the NwC surface and the amount of electrolyte). If we consider the complete reduction of sulfur present in the electrode (17.34  $\text{mg}_{\text{Sulfur}}$  for cell 1 and 6.14  $\text{mg}_{\text{Sulfur}}$  for cell 2), and having the same electrolyte volume in both coin cells ( $\sim 150 \mu\text{L}$ ), we could estimate the concentration in equivalent  $\text{Li}_2\text{S}_4$  at the transition point between the two main plateaus. The concentration values were found to be  $\sim 0.9 \text{ mol L}^{-1}$  and  $\sim 0.32 \text{ mol L}^{-1}$ , for cell 1 and cell 2, respectively. Such differences in polysulfides concentration may likely affect the electrolyte viscosity and polysulfides solubility. This conclusion is supported by the viscosity measurements, which shows that the viscosity increases by a factor of 10, when the polysulfides concentration raises from  $0.1 \text{ mol L}^{-1}$  to  $1.0 \text{ mol L}^{-1}$ ‡.

To conclude, the benefit of heavily loaded electrodes lies in its delivered areal capacity, and values as high as  $8.1 \text{ mAh cm}^{-2}$  were obtained. However, with such highly loaded electrodes, only three cycles were obtained, further cycling resulted in a shuttle phenomenon and severe short circuits during the charge process. Indeed, these problems are related to the lithium negative electrode and not directly to the sulfur one. This proof-of-concept allowed us to demonstrate that it could be possible to prepare high capacity electrodes, but rather targeting the low power applications.

### 3.4.5. Capacity based on a complete weight of the electrode

In most of the existing publications, capacity values usually refer to the mass of sulfur, and definitely minority refers to the full electrode mass<sup>104,132</sup>. In fact, the capacities related to the complete electrode should always be discussed, since it gives more realistic comparison of the results. Nowadays, with the rapidly increasing number of publications, it is difficult to make a thorough comparison between different reports and obtained capacity values. Indeed, the electrode parameters which strongly affect the discharge capacity and cyclability, such as electrode loading and sulfur fraction in the electrode, differ significantly between the reports, or sometimes are not even mentioned at all. In some papers, the electrode loading is even misunderstood and taken as the sulfur fraction in the S/C composite. In the same manner, a comparison based on the C-rate only is not completely informative, since the current related to an impressive rate of 1C for low loaded electrodes ( $< 1 \text{ mg}_{\text{Sulfur}} \text{ cm}^{-2}$ ), may be equivalent to a moderate current (at C/5) applied to highly loaded electrodes ( $\sim 5 \text{ mg}_{\text{Sulfur}} \text{ cm}^{-2}$ ).

In our work, we replaced the classical Al foil ( $5.45 \text{ mg cm}^{-2}$ ) with much heavier NwC current collector ( $9.55 \text{ mg cm}^{-2}$ ). Therefore, it was mandatory to compare the values in respect to the total electrode weight. Our standard ‘S-on-NwC’ electrodes ( $\sim 4.4 \text{ mg}_{\text{sulfur}} \text{ cm}^{-2}$ ) are composed

---

‡ Solutions of polysulfides ( $\text{Li}_2\text{S}_6$  in TEGDME/DIOX + 1M LiTFSI) with different concentrations were prepared and viscosity was measured.

of following sulfur fractions: 80 wt% – if referring to the ink composition only, and 30 wt% – when taking also into account the NwC collector. If we then take as an example an electrode with 60 wt% of sulfur in the final ink composition (as this fraction is often considered in the literature), loaded with  $1 \text{ mg cm}^{-2}$  of active material, and coated on Al foil, the final sulfur amount would be less than 15 %, taking into account the weight of the complete electrode (including collector)<sup>232</sup>.

Figure 3-13 illustrates the capacity retention of a ‘S-on-NwC’ electrode (with sulfur loading of  $4.44 \text{ mg}_{\text{sulfur}} \text{ cm}^{-2}$ ; cycled at C/20), calculated with respect to: sulfur, complete electrode ink (with carbon and binder additives) and electrode with current collector included. We can see that due to the high weight of NwC collector, the capacity in respect to the total electrode mass decreases to  $\sim 200 \text{ mAh g}^{-1}$  only. In the following section, we compare these values with the same composite electrode casted on Al foil and similar sulfur loading.

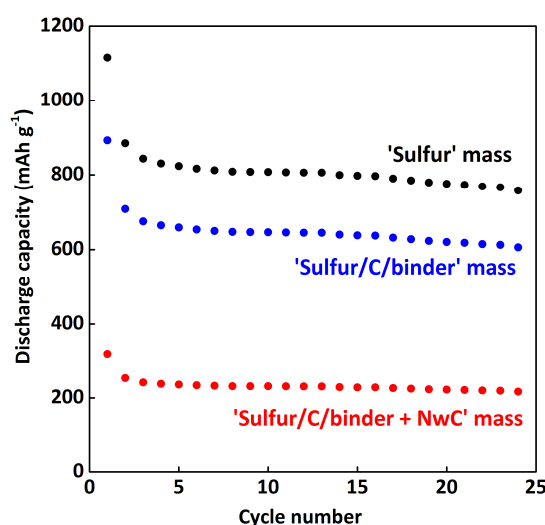


Figure 3-13. Capacity retention over 25 cycles obtained with ‘S-on-NwC’ electrode (loading of  $\sim 4.4 \text{ mg}_{\text{sulfur}} \text{ cm}^{-2}$ ), cycled at C/20. Discharge capacity values presented in respect to only sulfur mass (in black), composite electrode mass (in blue) and total electrode weight, including NwC (in red).

### 3.4.6. Aluminum vs. NwC-based electrodes: comparative studies

We have previously seen that NwC-based electrodes give much higher discharge capacity values, which is strongly related with the fact of having such porous 3D conductive current collector. Apart from offering a 3D highly conductive network, it provides available surface for  $\text{Li}_2\text{S}$  deposition. However, its high weight may be a serious obstacle when comparing with almost twice lighter Al foil. In this paragraph, we compare performances of both Al and NwC-based electrodes, of identical sulfur loadings.

An electrode ink (S/SuperP<sup>®</sup>/PVdF = 80/10/10 wt%; preparation described in section 2.2.1) was made with a classical way of preparation (*i.e.* manual incorporation of all ingredients; without Dispermat<sup>®</sup>) and tape-casted on two collector sheets: Al foil and NwC, in order to obtain electrodes with identical sulfur loadings ( $4.44 \text{ mg}_{\text{sulfur}} \text{ cm}^{-2}$ ). The reason of preparing both electrodes from exactly the same ink aimed at eliminating to the maximum the other factors' influence, like inhomogeneity of the electrodes due to the way sulfur/carbon powders were mixed or how the binder was dispersed. Thanks to that, the effect of current collector could be compared more accurately. The thicknesses of final electrodes after drying were  $\sim 260 \mu\text{m}$  for 'S-on-NwC' ( $\sim 210 \mu\text{m}$  NwC +  $\sim 50 \mu\text{m}$  the resulting electrode) and  $\sim 160 \mu\text{m}$  for 'S-on-Al' ( $20 \mu\text{m}$  Al +  $\sim 140 \mu\text{m}$  the resulting electrode). Both electrodes were assembled into identical coin cells (as described in section 2.2.2), and galvanostatically cycled at C/20 ( $i = 0.372 \text{ mA cm}^{-2}$ ). The cycling results are shown on Figure 3-14.

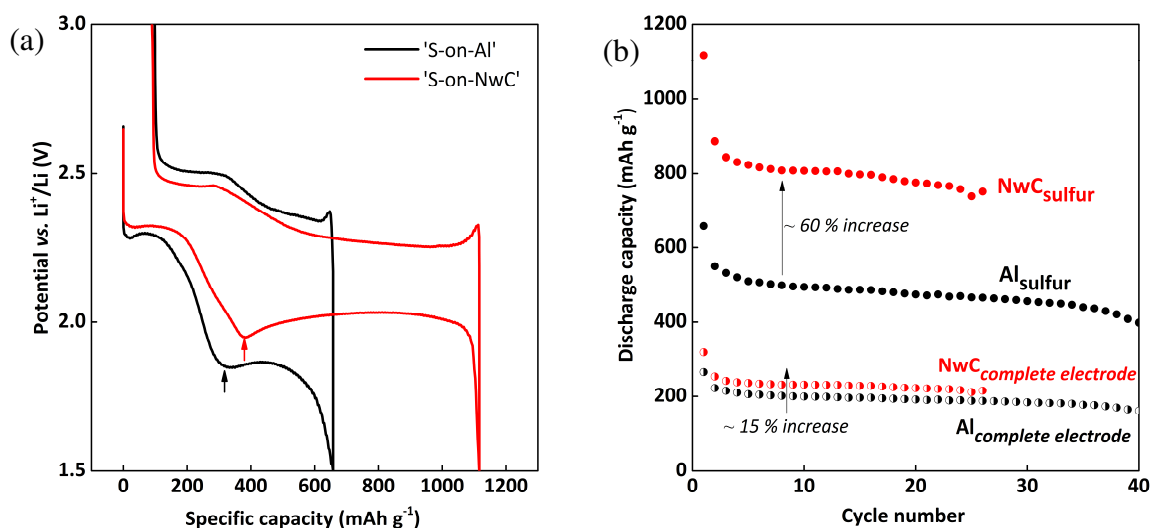


Figure 3-14. Galvanostatic cycling results obtained from sulfur electrodes of identical composition and sulfur loading ( $\sim 4.4 \text{ mg cm}^{-2}$ ), but coated on two different current collectors: Al (in black) and NwC (in red). Voltage shapes of the initial cycle obtained at C/20 (a) and capacity retention (b).

The initial discharge capacity obtained with 'S-on-NwC' ( $1116 \text{ mAh g}^{-1}$ ) is clearly much higher than the one obtained with 'S-on-Al' ( $658 \text{ mAh g}^{-1}$ ). Afterwards, similar capacity retention is observed upon cycling for both cells, with still superior capacity values of 'S-on-NwC' cell. 20<sup>th</sup> discharge capacities are  $474 \text{ mAh g}^{-1}$  and  $775 \text{ mAh g}^{-1}$ , for Al and NwC-based electrodes, respectively. Slow capacity loss per cycle is visible for both cells (Figure 3-14b). However, noisy charge problems appeared for both cells after a certain number of cycles, and the cells had to be stopped afterwards. This problem is further discussed in section 3.5, but was attributed to dendrites formation at the surface of lithium electrode and to the fact of using quite heavily loaded electrodes.

§ 'S-on-NwC' electrodes with precisely known mass of NwC, therefore the error of active mass estimation is reduced to the minimum.

Moreover, being aware of much higher weight of NwC (9.55 mg cm<sup>-2</sup>) as compared with Al (5.46 mg cm<sup>-2</sup>), we also compared the capacity values based on complete electrode mass for this particular example (23.832 mg for ‘S-on-NwC’ and 16.965 mg for ‘S-on-Al’). We can clearly see that ‘S-on-NwC’ electrode still displays slightly better capacity (320 and 222 mAh g<sub>electrode</sub><sup>-1</sup> during 1<sup>st</sup> and 20<sup>th</sup> cycles respectively) over ‘S-on-Al’ (265 and 192 mAh g<sub>electrode</sub><sup>-1</sup> during 1<sup>st</sup> and 20<sup>th</sup> cycles), which is a very positive aspect. We should also keep in mind that NwC used in this work was a commercial product, not optimized in terms of thickness and weight. Thus, on-demand NwC papers with the optimized parameters (thickness, porosity, specific surface, etc.) should be developed in the future, which would in turn allow for even better performances of NwC-based electrodes in terms of capacity per complete mass of the electrode.

When comparing the initial cycle voltage profiles (Figure 3-14a), ‘S-on-Al’ electrode displays much higher overpotential, mostly visible on both, the region between the two plateaus and the lower discharge plateau. The upper plateau is indeed weakly affected, and capacity values corresponding to the high voltage plateau were found to be 174 and 200 mAh g<sup>-1</sup>, for ‘S-on-Al’ and ‘S-on-NwC’ respectively, while expecting 209 mAh g<sup>-1</sup> in theory, according to the sulfur reduction reaction: S<sub>8</sub> + 2e<sup>-</sup> → S<sub>8</sub><sup>2-</sup>. This observation may point out slightly lower sulfur utilization in the case of Al-based electrode. Also the capacity values at the little dip (black and red arrows on Figure 3-14a) are then proportional to the amount of sulfur initially reduced, and are about ~ 315 mAh g<sup>-1</sup> and 380 mAh g<sup>-1</sup> for ‘S-on-Al’ and ‘S-on-NwC’ respectively.

We could also imagine that, even if the same amount of electrolyte was poured to both coin cells (150 μL), ‘S-on-NwC’ electrode, due to its higher thickness and porosity (80 %), could capture more electrolyte as compared with ‘S-on-Al’ (porosity estimated to ~ 40 %). The excess of electrolyte was evacuated during the coin cell closing. As a matter of fact, the electrolyte amount in the pores of both electrodes and separators is higher in case of NwC-based electrode than for Al-based one<sup>\*\*</sup>. Table 3-4 illustrates the estimated ‘empty’ volumes of each component of the coin cell, when NwC and Al-based electrodes are used.

Having the same amounts of sulfur in both electrodes (6.84 mg), concentration of the polysulfides created during sulfur reduction (S<sub>8</sub> + 4e<sup>-</sup> → 2 S<sub>4</sub><sup>2-</sup>) is higher in the ‘S-on-Al’ cell (because of lower amount of the electrolyte captured in the electrode’s pores). Indeed, NwC provides a very thick and porous architecture, with easily accessible spaces for the electrolyte and the polysulfides to penetrate inside the electrode. Thus, the electrolyte viscosity may also be higher, which likely influences the cell polarization. The most significant difference is visible on the low voltage discharge plateau, in terms of capacity obtained as well as of average operating voltage, as mentioned above for heavily loaded electrodes.

---

<sup>\*\*</sup> It is important to keep in mind that, due to the ‘dead volumes’ in the coin cell and the loss of some electrolyte volume during coin cell closing, it is difficult to precisely estimate the real amount of electrolyte remaining in each cell. Also because of that reason, and due to the fact that the coin cell configuration is not an optimized ‘packaging’, the gravimetric neither volumetric energy density values were not taken into account.

	Porous coin cell component (Ø in mm)	Surface area (cm <sup>2</sup> )	average thickness (µm)	porosity (%)	"Empty" volume (µL)	Total "empty" volume (µL)
<i>Separators</i>	Viledon (Ø 16.5 mm)	2.137	240	55	28.21	
	Celgard (Ø 16.5 mm)	2.137	25	37	1.98	
<b>S-on-NwC</b>	NwC collector (Ø 14 mm)	1.539	210	80	25.86	59.12
	Electrode (Ø 14 mm)	1.539	50	40 †	3.08	
<b>S-on-Al'</b>	Al foil (Ø 14 mm)	1.539	20	0	0	38.80
	Electrode (Ø 14 mm)	1.539	140	40 †	8.62	

† estimated value

Table 3-4. Summary of all porous components of the coin cell, which require filling with the electrolyte. 'Empty' volume is estimated in regard to the geometric volume of the component and its porosity. Both electrodes are compared: 'S-on-Al' and 'S-on-NwC'.

Moreover, the low overpotential of NwC-based electrode may point out the enhanced electronic conductivity of the complete electrode, thanks to the 3D highly conductive continuous network offered by NwC. Such current collector also physically participates in the discharge reactions, by offering an additional conductive surface area for Li<sub>2</sub>S deposition (in contrary to Al foil), *i.e.* in agreement with what has already been demonstrated on SEM photos (Figure 3-5). We then tried to correlate available surface area of NwC with the discharge capacity values.

Taking into consideration the BET results performed on NwC material (surface area barely detectable:  $\sim 0.05 \text{ m}^2 \text{ g}^{-1}$ ), the contribution of conductive surface area by NwC to the Ø 14 mm electrode is only  $\sim 7.3 \text{ cm}^2$  (taking into account  $9.55 \text{ g m}^{-2}$  of NwC). This value is about 110 times lower than the surface area of a composite electrode S/SuperP<sup>®</sup>/PVdF = 80/10/10 wt%, having a surface area of  $5.5 \text{ m}^2 \text{ g}^{-1}$  (BET values in Table 2-1). It should be reminded that BET data represents the surface accessible for gas, which may not necessarily be the same as the one accessible for polysulfides during battery operation (especially at high concentrations). Nevertheless, these BET measurements allowed us to compare the contribution of different electrode components in terms of active surface.

Following this idea and based on BET data, taking into consideration these two particular electrodes presented on Figure 3-14 (S/SuperP<sup>®</sup>/PVdF, weight of 8.56 mg), surface area of the electrode coating on a Ø 14 mm disk was found to be as high as  $471 \text{ cm}^2$ . Figure 3-15 schematically illustrates the contribution of each electrode component regarding the surface area.

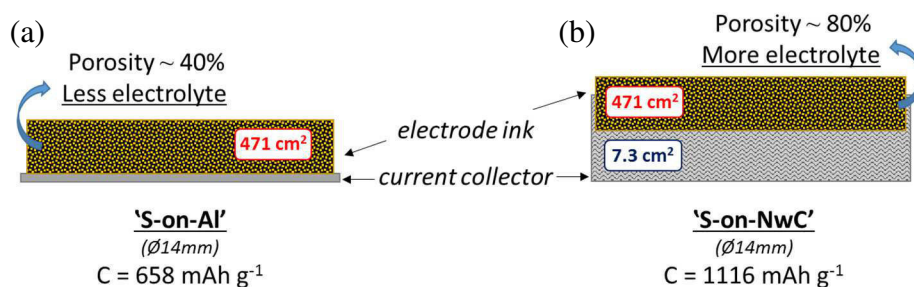


Figure 3-15. Schematic illustration of the surface area contribution coming from NwC and/or electrode ink (S/SuperP®/PVdF = 80/10/10 wt%) coated on the collector, for both electrodes: ‘S-on-Al’ (a) and ‘S-on-NwC’ (b). Surface area of the electrode ink was found to be  $\sim 471 \text{ cm}^2$ , calculated with respect to the coating weight (8.56 mg on the  $\text{\O} 14 \text{ mm}$  disk) and BET value ( $5.5 \text{ m}^2 \text{ g}^{-1}$ ). The area of solely NwC disk, with its BET of  $\sim 0.05 \text{ m}^2 \text{ g}^{-1}$ , was found to be  $\sim 7.3 \text{ cm}^2$ .

It is clear that a direct correlation between the surface area and the discharge capacity could not be evidenced. Indeed, in this particular case, differences in terms of surface area do not allow to explain the beneficial impact of NwC collector to the overall capacity and cyclability. It may be more relevant to talk about accessible surface area, when trying to correlate the electrode surface area with the practical capacity, as largely discussed in the literature<sup>104</sup>.

We already mentioned that carbon fibers offer more efficient electronic percolating network over classical Al foil, due to its 3D structure. In order to go deeper into understanding of the polarization phenomena, Electrochemical Impedance Spectroscopy (EIS) measurements were performed on symmetric coin cells (cell preparation and EIS conditions previously described in section 2.2.1), composed of two identical electrodes. The EIS results show (Figure 3-16) that the presence of NwC in the electrode structure is accompanied by a significant decrease of the resistive response of the system, as compared with the Al-based electrode, with characteristic frequencies in the range of few kHz for both electrodes.

As previously described, such large resistance value of ‘S-on-Al’ electrodes in symmetric cells, may be related to the poor homogeneity of the electrode, and attributed to its bulk resistance, resulting in poorly efficient ionic and electronic pathways, and polarization due to the charge accumulation. Since NwC is a non-woven electronic conducting tissue with a large porous structure and internal resistance of  $0.8 \text{ }\Omega^{216}$ , the electronic and even the ionic conductive pathways are more efficient than in a 1D electrode, and induce a neat decrease of the electrode response ( $\sim 2 \text{ }\Omega$  instead of  $\sim 40 \text{ }\Omega$ ). Therefore, the reason for such remarkable decrease of the MF semicircle resistance might relate to the fact that the carbon/sulfur clusters (cluster: sulfur particles bound together by the carbon particles and binder) are directly connected with the NwC carbon fibers, and the fact of having a non-homogenous ink (manual incorporation of a PVdF binder) does not necessarily give a rise of electrode bulk impedance, as electronic conductive pathway inside the electrode is very efficient. Then the response at the MF region seems to be well connected with the electronic pathway of the electrode.



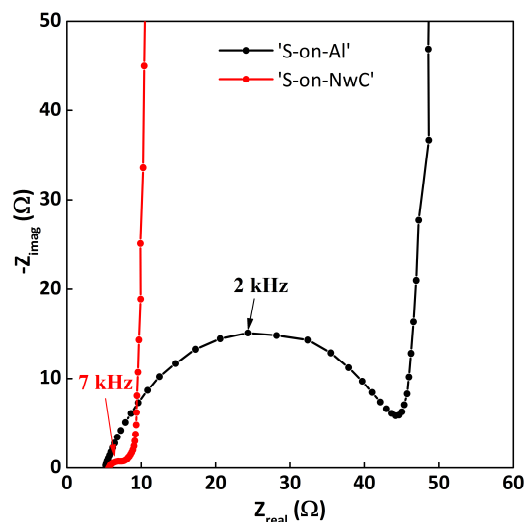


Figure 3-16. EIS measurement and resulting Nyquist plots performed on symmetric coin cells with two types of electrodes for comparison: ‘S-on-Al’ (in black) and ‘S-on-NwC’ (in red), both made from the same electrode ink and with identical sulfur loadings.

To evaluate the NwC ability to act as an electrolyte reservoir, electrolyte absorptivity test was done on pure NwC and showed to be  $20 \mu\text{L}^{\dagger\dagger}$ . This value is quite coherent with the calculated empty volume of NwC ( $0.0259 \text{ cm}^3$ ). Therefore, we removed Viledon<sup>®</sup> (commonly used in the laboratory as an electrolyte reservoir), and compared the electrochemical responses of both Al and NwC-based electrodes, cycled with Celgard<sup>®</sup>2400 layer only (Figure 3-17). During coin cell preparation, the same amount of electrolyte ( $150 \mu\text{L}$ ) was poured into two coin cells. However, after the coin cell closing, a larger electrolyte amount was expected to remain in the ‘S-on-NwC’ cell, due to higher free volume inside the NwC collector.

It can be seen that in such conditions, *i.e.* without Viledon<sup>®</sup>, the capacity of ‘S-on-Al’ cell is quite low, of only  $260 \text{ mAh g}^{-1}$ , while the voltage profile is largely modified. Indeed, with such low amount of electrolyte, we may expect to have a lack of the electrolyte inside the electrode, then not efficient ionic conductive pathway, which in turn induces weak sulfur utilization and large overpotential. In case of ‘S-on-NwC’ electrode, the voltage profile is consistent with the expected one, even if a neat decrease of capacity is observed with the removal of Viledon<sup>®</sup> ( $826 \text{ mAh g}^{-1}$ , as compared with previous value of  $1116 \text{ mAh g}^{-1}$ ). This decrease in capacity could be associated with faster precipitation of short polysulfides in the electrolyte due to higher polysulfides concentration (lower amount of electrolyte, as Viledon<sup>®</sup> was removed).

<sup>††</sup> NwC  $\emptyset$  14 mm disks of precisely known masses were immersed into a beaker with the electrolyte and left for impregnation for 1h. After this time, the NwC mass was verified again. Based on the weight gain and the electrolyte density ( $d = 1.17 \text{ g cm}^{-3}$ ), an average volume of the electrolyte adsorbed was calculated to be  $13 \mu\text{L cm}^{-2}$ , which is  $20 \mu\text{L}$  for a NwC disk ( $1.539 \text{ cm}^2$ ).

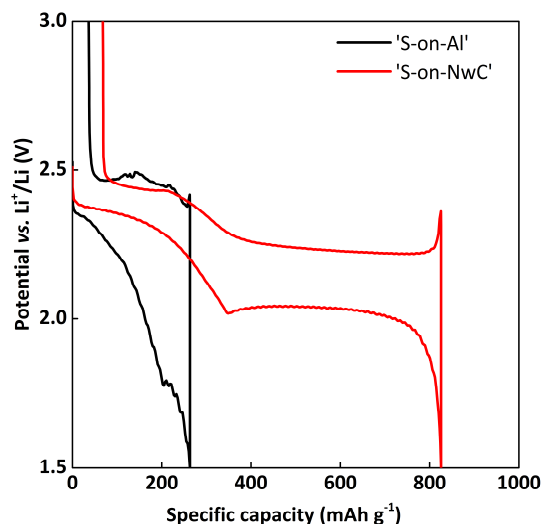


Figure 3-17. Initial cycle voltage profile of both electrodes, 'S-on-Al' and 'S-on-NwC' cycled at C/20 with only Celgard®2400 separator in the coin cell (without the Viledon®, as normally used).

These results prove again that the porous structure of NwC permits an increase of the electrolyte amount near the active species, and probably facilitates the electrolyte penetration inside the whole electrode, which delays the species precipitation and provides good contact between sulfur particles and the electrolyte. Incorporation of NwC as a positive electrode current collector may thus allow to prevent the use of a thick non-woven like separators (such as Viledon®), by substituting the insulating 3D polymer network with a conducting one at the positive electrode for electrolyte absorptivity. This would in turn allow to gain even more in terms of energy density, as compared to Al-based cells. The role of NwC would may be then triple: (i) current collector, (ii) 3D network for positive electrode's porosity and surface, and (iii) electrolyte reservoir.

To conclude, the beneficial effect of NwC was already proven when looking at relatively highly loaded electrodes. The presence of this 3D porous conductive structure also permits to limit the polarization phenomena whatever the state of charge/discharge of the battery, and to improve the capacity (per g of sulfur). A schematic illustration on Figure 3-18 summarizes the benefits of NwC as current collector over classical Al foil.

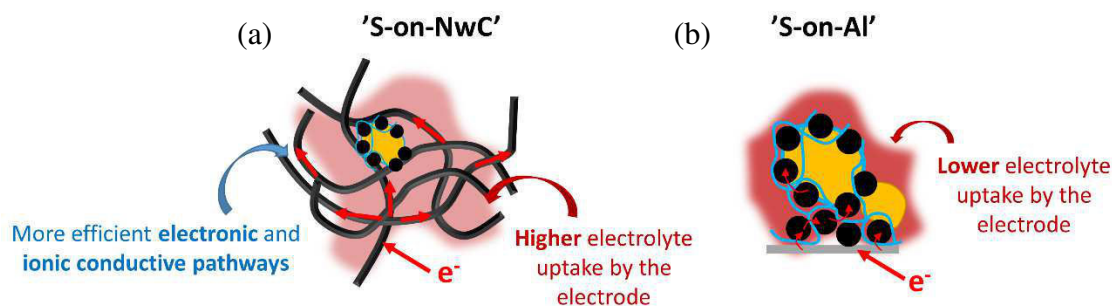


Figure 3-18. Schematic illustration of the beneficial effects when incorporating a 3D porous NwC current collector (a) over the classical 2D Al foil (b).

### 3.4.7. The importance of the electrolyte amount

It is clear, in regard to our previous study<sup>45,157</sup>, that electrolyte added in a large excess provides better cyclability to the Li/S cells, but a lower energy density as well. Low amount of electrolyte, on the other hand, may affect the cyclability, reduce the capacity and increase the polarization<sup>105</sup>. As a consequence, if the electrolyte amount is not sufficient, it may result in incomplete sulfur utilization already in the initial cycles. To study the performances of 'S-on-NwC' electrodes with reduced amounts of electrolyte, two coin cells were prepared using standard method (keeping both Viledon<sup>®</sup> and Celgard<sup>®</sup>2400 as separators), but with the lower amount of electrolyte than used as reference (150  $\mu\text{L}$ ), *i.e.* 75  $\mu\text{L}$  and 50  $\mu\text{L}$ . The electrodes had slightly different sulfur loadings:  $\sim 3.78 \text{ mg}_{\text{Sulfur}} \text{ cm}^{-2}$  for the '75  $\mu\text{L}$ ' cell and  $\sim 4.54 \text{ mg}_{\text{Sulfur}} \text{ cm}^{-2}$  for the '50  $\mu\text{L}$ ' cell. Both cells were discharged and charged at  $C/20$  only one time (the aim was to observe the voltage profiles rather than to perform prolonged cycling). The results are shown on Figure 3-19, while the '150  $\mu\text{L}$ ' reference cell is also presented on the graph for easier comparison.

When decreasing the electrolyte amount to 75  $\mu\text{L}$ , reasonably good capacity can still be obtained ( $\sim 1000 \text{ mAh g}^{-1}$ ), even if lower than for the cell with highest electrolyte amount (1110  $\text{mAh g}^{-1}$ ). However, end of discharge is slightly modified while the overpotential is slightly increased as well. This may be related with the difference in terms of polysulfides concentration (thus the electrolyte viscosity). On the other hand, 50  $\mu\text{L}$  is not enough to cycle the cell, which is actually an expected behavior, when keeping in mind the theoretical volume necessary to fulfill all the porosity (59  $\mu\text{L}$ ; see Table 3-4).

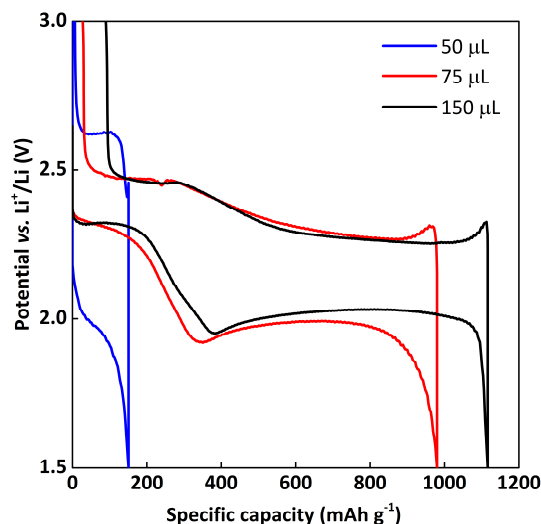


Figure 3-19. Initial voltage profile of ‘S-on-NwC’ electrodes (average sulfur loading of  $\sim 3.8 \text{ mg}_{\text{sulfur}} \text{ cm}^{-2}$ ) cycled vs. Li and with different electrolyte amounts: 150  $\mu\text{L}$ , 75  $\mu\text{L}$  and 50  $\mu\text{L}$ . In all coin cells, both separators were kept, *i.e.* Viledon<sup>®</sup> + Celgard<sup>®</sup>2400, according to the standard procedures.

The voltage profile shows only one short plateau at  $\sim 2.0 \text{ V}$  with large polarization. In order to have a deeper insight into elemental sulfur reduction process in the presence of not sufficient electrolyte amount, XRD technique was applied. Another ‘50  $\mu\text{L}$ ’ coin cell was prepared and discharged to 1.5 V. The electrode was then recuperated, carefully washed with DIOX, and XRD was recorded (XRD sample preparation was done in the glove box; as previously described in section 2.2.3). The XRD pattern clearly shows peaks of orthorhombic sulfur (PDF-2; no. 00-008-0247) used for the electrode preparation, meaning that there was still a part of inactive material. This allowed to confirm our hypothesis of incomplete sulfur utilization with insufficient amount of electrolyte.

One should remember that all these tests were done in a coin cell configuration, where the exact amount of electrolyte in the cell is practically unknown. More systematic studies should be done in the future, rather in a pouch cell design, with controlled amount of the electrolyte used.

The literature proposes different optimized values concerning sulfur/electrolyte ratio<sup>105,106</sup>. Nevertheless, a ‘standard’ value that could be applied generally to Li/S cells does not really exist, since it strongly depends on the system: electrode composition, electrolyte, etc. More particularly, the nature of a carbon additive (and its specific surface), the final porosity of the electrode, the nature of separator (thickness, absorptivity, porosity) are indispensable parameters to take into consideration when optimizing the electrolyte/sulfur ratio. For instance, when replacing Viledon<sup>®</sup> and Celgard<sup>®</sup>2400 with another separator (non-commercial grade of inorganic fibers; thickness  $< 100 \mu\text{m}$ ; porosity  $> 70 \%$ ), the ‘S-on-NwC’ electrode was able to cycle with 50  $\mu\text{L}$  of electrolyte already, which was not the case in our standard configuration of the separators.

### 3.4.8. Surface area vs. porosity – a dominant factor?

#### 3.4.8.a) The effect of the surface area

It has been demonstrated in the literature that, when increasing the surface area of typical GDL carbon collector by growing CNTs on them, higher discharge capacities were obtained<sup>104</sup>. In our study, we also aimed at investigating different NwC-type materials (commercially available products, purchased from Freudenberg) as porous current collectors, with different surface areas and/or modification of one NwC side. Physical properties of three different NwC felts used (Table 3-5), as well as their SEM photos (Figure 3-20), are presented below.

NwC type (name)	H2315	H2315-I2C8	H2315-C2	H2315-T10A
<b>Characteristics</b>	‘classic’	2 sides: hydrophobic treatment / microporous layer	2 sides: microporous layer	Similar to ‘classic’; hydrophobic treatment
<b>Weight (mg cm<sup>-2</sup>)</b>	9.7	13.2	13.6	10.6
<b>Thickness (μm)</b>	209	238	250	209
<b>BET (m<sup>2</sup> g<sup>-1</sup>)</b>	0.05	10.04	4.55	<i>not measured</i>

Table 3-5. Physical properties of different types of NwC sheets (GDL felt) – a commercial products of Freudenberg<sup>216</sup>. Some of them presenting surface treatment or additional layer of microporous carbon particles.

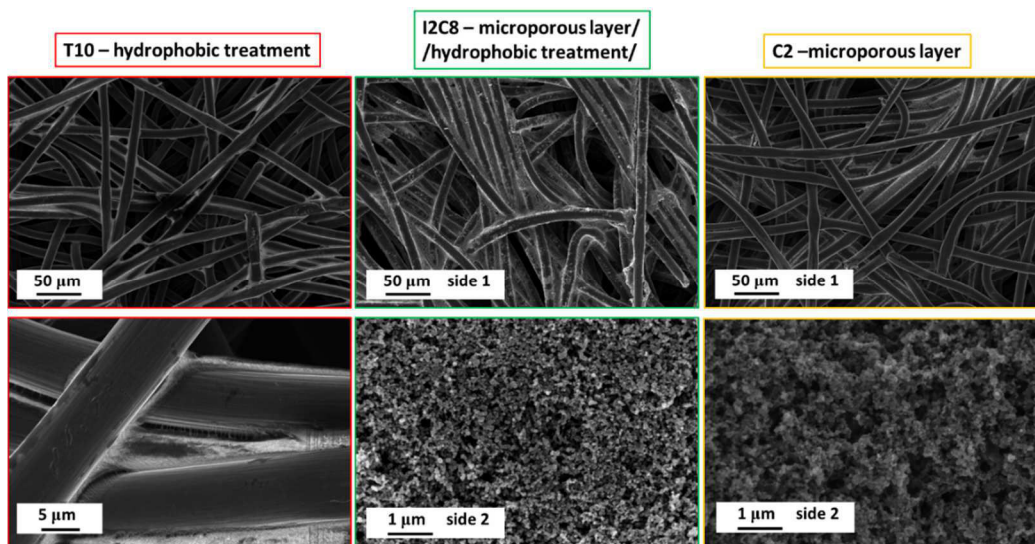


Figure 3-20. SEM photos of three different NwC felts: T10 type (in red), I2C8 (in green) and C2 type (in yellow). All purchased from Freudenberg<sup>216</sup>.

All four different non-woven felts were tested in coin cells by galvanostatic cycling. However, for simplicity, they were used as-received as current collectors in semi-liquid Li/S cells, so-called ‘catholyte’ cells. Preparation of catholyte solution (1M LiTFSI + 0.1M LiNO<sub>3</sub> + 0.5M Li<sub>2</sub>S<sub>6</sub> in TEGDME/DIOX = 1/1 vol ratio) together with a coin cell architecture were described in section 2.2.1. For these tests, coin cells with 40  $\mu$ L of catholyte solution (+ 60  $\mu$ L of standard electrolyte) were made. Theoretical capacity of such prepared semi-liquid coin cell (6.43 mAh) was calculated in respect to the amount of sulfur present in the volume of added catholyte solution. Galvanostatic cycling results obtained at C/20 are presented in Figure 3-21.

The voltage profiles do not show any upper discharge plateaus, since the active material was introduced in the form of soluble Li<sub>2</sub>S<sub>6</sub>. We can see that during initial cycle, double-side NwC’s (C2 and I2C8) have higher capacities. If we look at the voltage profile, it is clear that higher initial capacities are due to the presence of an additional discharge plateau at  $\sim 1.7$  V, which significantly contributes to the final value. This plateau is related with the irreversible reduction of LiNO<sub>3</sub> additive on the positive electrode<sup>177,178</sup>, and was previously observed for the composite electrodes with high carbon/sulfur ratios. In this case, LiNO<sub>3</sub> must reduce on the modified side of the C2 and I2C8 NwC layers, where the active surface of carbon is highly developed by the modification with additional microporous layer (BET surface area, see Table 3-5).

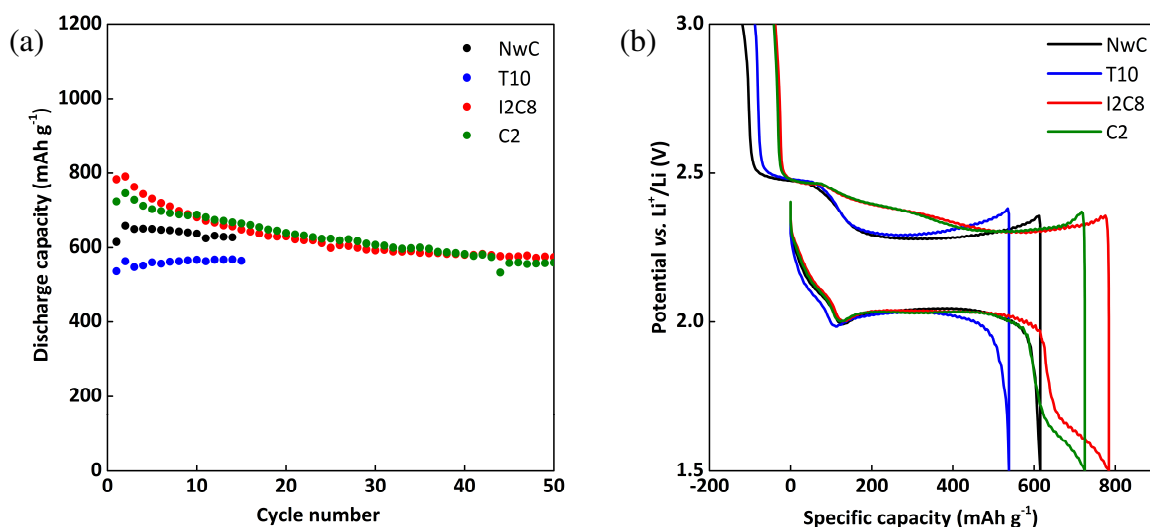


Figure 3-21. Capacity retention obtained at C/20 (a) and corresponding first discharge profiles (b) of four ‘catholyte’ cells with different NwC felts used as a positive electrode collectors: classic NwC (in black), T10 (in blue), C2 (in green), I2C8 (in red). The electrolyte solution was containing 40  $\mu$ L of 0.5M Li<sub>2</sub>S<sub>6</sub> + 1M LiTFSI + 0.1M LiNO<sub>3</sub> in TEGDME/DIOX = 1/1 vol, resulting in theoretical capacity of 6.43 mAh.

One should note that the reduction of LiNO<sub>3</sub> at the potential lower than 1.7 V allowed us to question the effective complete passivation of the electrode by Li<sub>2</sub>S at the end of discharge. Indeed, if all conductive surface area is passivated by an insulating film of Li<sub>2</sub>S, further reduction of LiNO<sub>3</sub> at  $\sim 1.5$  V would be impossible. After  $\sim 15$  cycles, the capacity values

reach approximately the same level as the ‘classic’ NwC collector. This is clearly related with the progressive disappearance of  $LiNO_3$  reduction plateau.

Very similar discharge capacity values were obtained for all four collectors, even if their BET surface area differed a lot (Table 3-5). It confirmed our conclusions: the accessibility of the conductive surface area for the active species dissolved in the electrolyte and the amount of electrolyte contained in the electrode pores, may govern the precipitation of the short polysulfides in the electrolyte and in turn the practical capacity, more significantly than the surface area by itself.

NwC current collector presents a well-defined active surface area, thus in such configuration, it could be easier to evaluate the amount of solid  $Li_2S$  passivating the overall electrode. For that purpose, a ‘catholyte’ cell (75  $\mu$ L of 0.25M  $Li_2S_6$  + 1M LiTFSI + 0.1M  $LiNO_3$  in TEGDME/DIOX 1/1 vol; *i.e.*  $\sim$  3.6 mg of sulfur introduced in the form of polysulfides) was built and discharged, and the NwC collector was recuperated for SEM observation. The cell displays discharge capacity of 345  $mAh\ g^{-1}$  (Figure 3-22a), among which  $\sim$  280  $mAh\ g^{-1}$  represent the capacity obtained along the lower discharge plateau. SEM photos recorded on the electrode at the end of 1<sup>st</sup> discharge are shown on Figure 3-22b. (More SEM photos of the fibers cross-section were already shown on Figure 3-5).

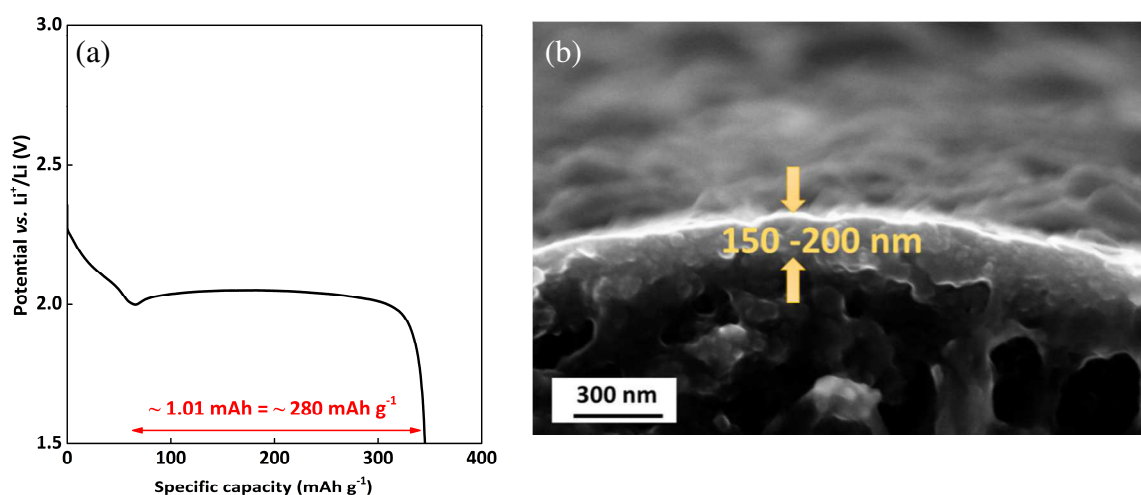


Figure 3-22. Discharge profile (a) and SEM photo with a zoomed view on the thin dense layer formed on each carbon fiber of NwC collector (b). The NwC collector was recuperated from the ‘catholyte’ cell at the end of initial discharge, when cycling with 3.6 mg of sulfur in the form of  $Li_2S_4$ .

As previously said (section 3.3), two types of deposits got created on the fibers’ surface, a very dense but thin nano-layer (estimated to be around  $\sim$  150 – 200 nm) and a less dense precipitate between the fibers. If we consider that the dense layer of  $\sim$  150 nm is composed of  $Li_2S$  deposited on the  $\varnothing$  5  $\mu$ m (average radius) carbon fiber, we can determine the amount of  $Li_2S$  practically deposited, which was found to be  $\sim$  0.7 mg. Cycling voltage profile permits also to evaluate the amount of  $Li_2S$  produced. Indeed, the length of the low voltage plateau, which is

often assigned to the  $Li_2S$  formation, is of about  $280 \text{ mAh g}^{-1}$ , which corresponds to the formation of 1.25 mg of  $Li_2S$ , and which is not so far from the amount determined based on the SEM image. Moreover, we point out the fact that  $Li_2S$  may not be the only product formed during the low voltage discharge plateau, which is further discussed in chapter 5, and a part of the current is dedicated to the  $S_2^{2-}$  formation. Furthermore, the presence of the precipitates between the fibers may indicate that the amount of solid phase inside the electrode is larger than the one calculated using only the dense layer. Further investigations must be performed to have a clear idea about the nature of precipitates presented in the volume of the whole electrode.

### 3.4.8.b) The effect of pressing

To follow this direction and to confirm that, indeed, the empty volume inside such porous carbon collector dictates the discharge capacity, we pressed the NwC T10-types disks on the pressing machine with: 1, 1.5, 2 and finally 5 tons<sup>‡‡</sup>, in order to decrease the thickness, thus the electrode porosity. ‘Catholyte’ type coin cells were prepared and cycled galvanostatically at C/10.

Figure 3-23 shows the SEM photos of the pressed NwC T10 materials, with 0, 1 and 2 tons. It can be clearly seen that not only the carbon fibers are more packed, thus influencing the effective porosity, but they are also destroyed when pressed with too high load (2 tons).

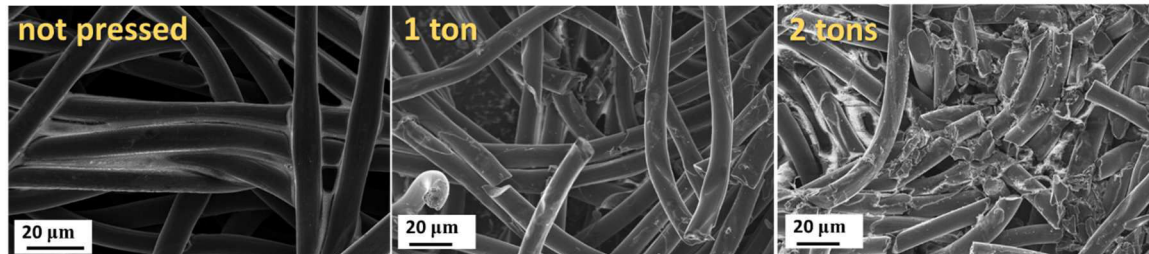


Figure 3-23. SEM photos of T10-NwC collectors: not pressed (a), pressed with 1 ton (b) and 2 tons (c).

Figure 3-24 shows the initial cycle of five ‘catholyte’ cells, and their capacity retention upon few cycles (prolonged cycling was not obtained due to the “problematic” charge). During coin cell preparation, 75  $\mu\text{L}$  of catholyte solution (0.25M  $Li_2S_6$  + 1M LiTFSI + 0.1M  $LiNO_3$  in TEGDME/DIOX) was poured onto NwC disks. Cells were cycled at C/10, while the current was calculated in respect to the mass of sulfur introduced with the catholyte solution (*i.e.*  $3.6 \text{ mg}_{\text{sulfur}} \leftrightarrow 6 \text{ mAh}$ ).

<sup>‡‡</sup> When pressing the NwC  $\varnothing$  14mm disk ( $1.539 \text{ cm}^2$ ) with 1 ton, a pressure of 63.7 MPa ( $\text{MN m}^{-2}$ ) is applied. Proportionally, when pressing with 1.5, 2 and 5 tons, the pressure of 95.5 MPa, 127.4 MPa and 318.5 MPa is applied, respectively. Nevertheless, for clarity, the unit ‘ton’ instead of ‘Pa’ (or  $\text{N m}^{-2}$ ) was kept when referring to the pressed electrodes.



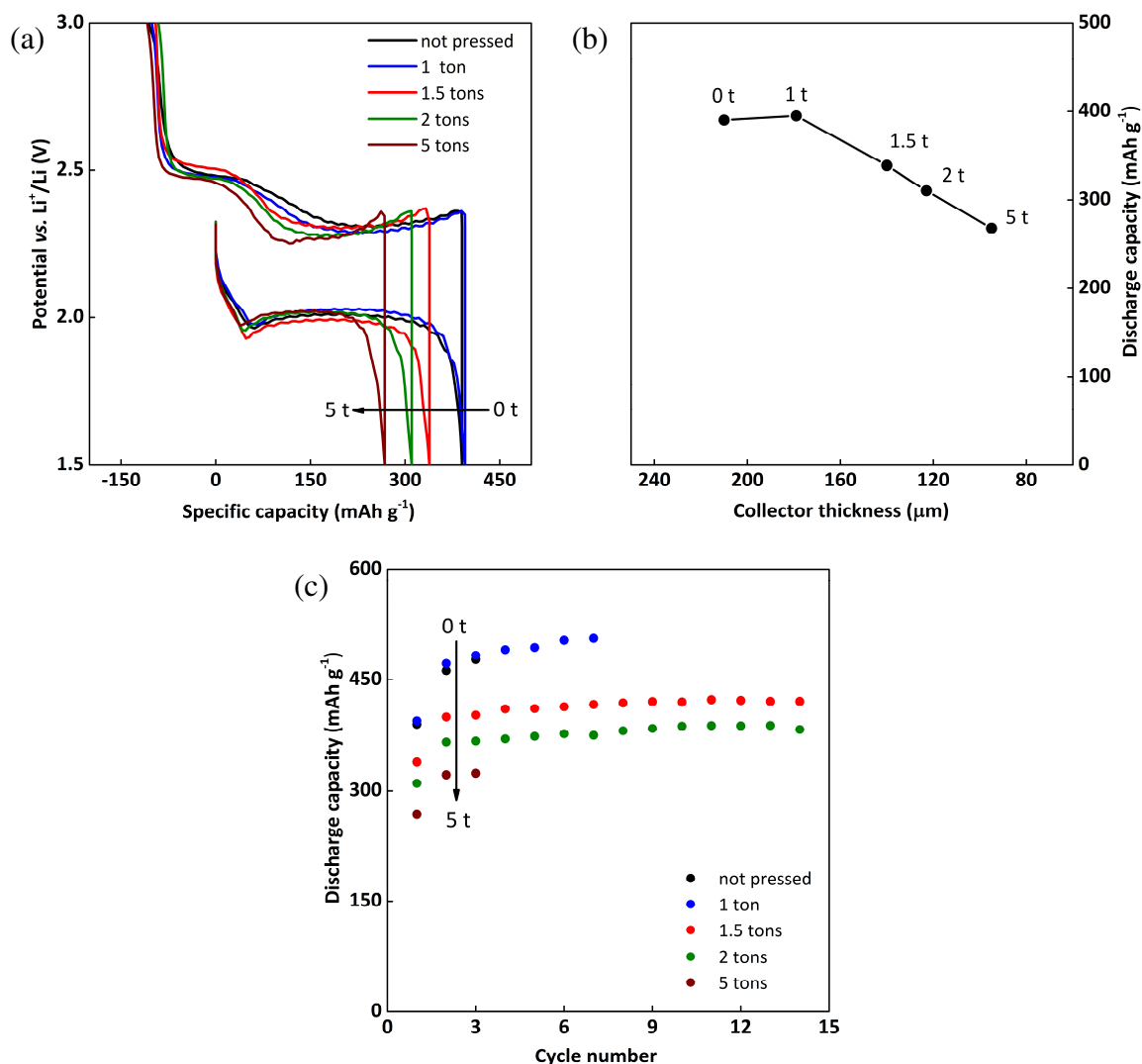


Figure 3-24. Galvanostatic cycling results of the ‘catholyte’ cells with T10-NwC collector pressed with different weight: 0, 1, 1.5, 2 and 5 tons. The electrolyte solution was containing 75  $\mu\text{L}$  of 0.25M  $\text{Li}_2\text{S}_6$  + 1M  $\text{LiTFSI}$  + 0.1M  $\text{LiNO}_3$  in  $\text{TEGDME}/\text{DIOX} = 1/1$  vol, resulting in the theoretical capacity of 6.0 mAh. Initial voltage profiles (a), discharge capacity as a function of the current collector thickness after pressing (b) and capacity retention during several cycles (c).

It can be seen that the discharge capacity is lower for more pressed electrodes (268  $\text{mAh g}_{\text{Sulfur}}^{-1}$  for the cell pressed with 5 tons). Slight pressure (pressing with 1 ton) does not affect the electrochemical performances, and the capacity is practically identical as the ‘non-pressed’ sample (390  $\text{mAh g}_{\text{Sulfur}}^{-1}$ )<sup>§§</sup>. This results somehow confirm that a strong relation exists between obtained capacity and available porosity. For highly pressed electrodes (2 tons or more), a ‘broken fiber’ structure is observed, which may affect the percolation network, thus the conductive available area. Nevertheless, even if fibers were broken, we believe that the electronic contact between the fibers in the cell was preserved thanks to applied pressure.

§§ This value is different from 538  $\text{mAh g}^{-1}$  presented on Figure 3-21, because both experiments were performed in large time interval/space, therefore not exactly the same ‘catholyte’ solutions were used. Also different cycling rates were applied ( $C/20$  and  $C/10$ ).

Similar observation was found when applying different pressures on ‘S-on-NwC’ composite electrodes. Lower discharge capacity was obtained for highly pressed electrode (pressing with 5 tons resulted in a thickness of 135  $\mu\text{m}$ ; not-pressed electrode was having a thickness of 270  $\mu\text{m}$ ).

### 3.4.9. Binder-free ‘melted sulfur-NwC’ electrodes performances

The fact of using a porous carbon collector and the low melting temperature of sulfur allowed us to simply prepared, binder-free electrodes (preparation procedure described in section 3.2), further named as ‘S-melted’ electrodes. The morphology of these electrodes are shown on the SEM photos (Figure 3-25), and is quite different from the ‘S-on-NwC’ electrodes (*i.e.* when the ink is composed of S/SuperP<sup>®</sup>/PVdF and casted on NwC).

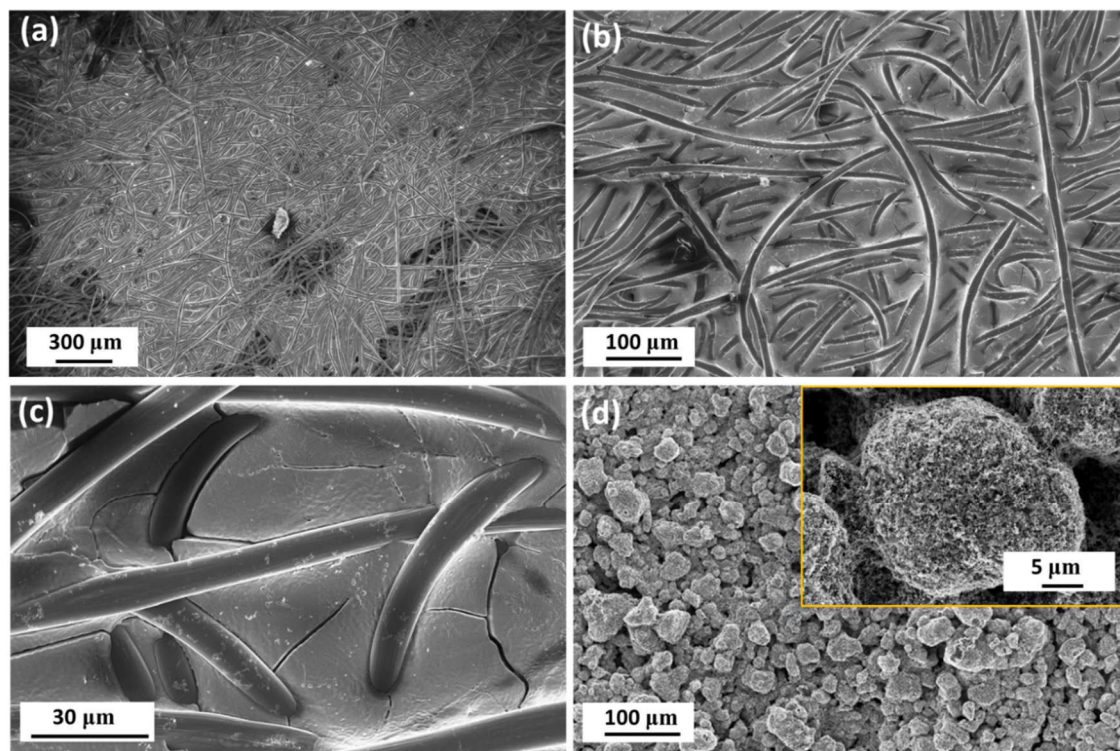


Figure 3-25. SEM photos of sulfur electrode prepared by melting elemental sulfur onto NwC disk (a, b, c), in comparison with the standard composite ‘S-on-NwC’ electrode (d).

It can be seen that sulfur after melting is not uniformly distributed on the NwC disk’s surface. It looks like melted sulfur fulfilled empty spaces between the carbon fibers (Figure 3-25b,c). The main difference seems to lie in the active material distribution and S/C contact. ‘S-on-NwC’ being composed of sulfur particles nicely coated by SuperP<sup>®</sup> particles and enrobed by PVdF binder, while sulfur in ‘S-melted’ electrode being much less in contact with carbon (only

with few NwC fibers) (Figure 3-25c). In this case, the only conductive surface area is provided by NwC fibers ( $\sim 7.1 \text{ cm}^2$ ). ‘S-melted’ and ‘S-on-NwC’ electrodes were prepared with almost identical sulfur loadings for better comparison ( $\sim 4.5 \text{ mg}_{\text{Sulfur}} \text{ cm}^{-2}$ ).

XRD pattern confirms the presence of orthorhombic sulfur. However, additional peaks were observed, which were attributed to the monoclinic  $\beta$ -Sulfur (PDF-2; no. 01-071-0137). Appearance of another allotropic form is related with the fact that sulfur quickly solidified after melting<sup>20</sup>, and it appeared in another form, next to the major orthorhombic one.

Figure 3-26 shows the cycling performances of the three cells for comparison: ‘S-on-NwC’ composite electrode, ‘S-melted’ and ‘catholyte’ cells, all cycled at C/20.

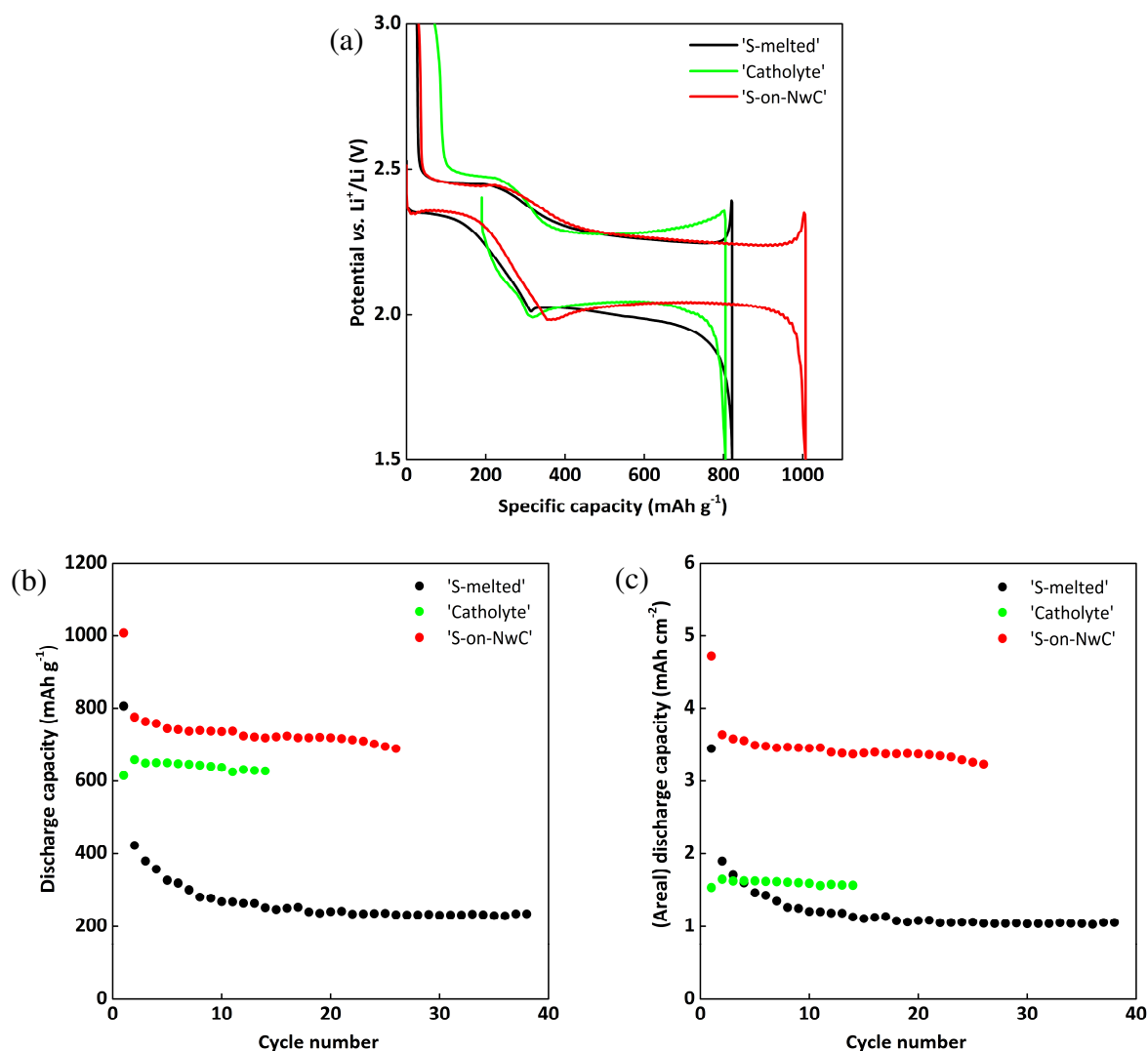


Figure 3-26. Galvanostatic cycling results obtained from three NwC-based electrodes, with different forms of active material: pure sulfur deposited on NwC fibers by melting (in black), composite S/SuperP<sup>®</sup>/PVdF coated on NwC collector (in red), and ‘catholyte’ cell (in green). Comparison of initial cycle voltage profiles (a) and capacity retention with respect to  $\text{mAh g}_{\text{sulfur}}^{-1}$  (b) and  $\text{mAh cm}^{-2}$  (c).

It is interesting to see that rather good initial discharge capacity ( $806 \text{ mAh g}^{-1}$ ) is obtained from the cell with melted sulfur. This results, as well as SEM photos of the electrode morphology

(Figure 3-25b,c), may prove that sulfur reduction in TEGDME/DIOX-based electrolyte can proceed relatively easily, without necessarily good coating of each sulfur particle with carbon, when C/20 was used. However, the low voltage discharge plateau is much shorter in case of ‘S-melted’ and ‘catholyte’ than ‘S-on-NwC’. As the capacity of the low voltage plateau is not only/directly related to the electrode surface (as discussed in section 3.4.6), the use of coated composite electrode (‘S-on-NwC’) may only slightly increase the performances, while having the surface of about 60 times higher than pure NwC  $\varnothing$  14 mm disk area (to recap: based on BET measurements, the NwC collector area is about 7.3 cm<sup>2</sup>, while the area of composite ink S/SuperP<sup>®</sup>/PVdF was found to be 471 cm<sup>2</sup>). It proves again, that higher surface area does not necessarily result in proportionally higher discharge capacity, and that we should rather talk about ‘available for polysulfides’ conductive area and porosity.

When comparing capacity retention over several cycles (Figure 3-26b,c), in both practical mAh cm<sup>-2</sup> and mAh g<sup>-1</sup>, it can be noticed that the ‘S-melted’ electrode does not behave as good as the ‘S-on-NwC’ one, this latter containing additional amount of SuperP<sup>®</sup> carbon. Indeed, even if the first discharge capacities are relatively high for the two electrodes (~ 3.5–5.0 mAh cm<sup>-2</sup> or 800 – 1000 mAh g<sup>-1</sup>), the ‘S-melted’ one shows severe capacity fading, with only 25 % of the initial capacity remaining, while the ‘S-on-NwC’ electrode retains about 75 % of the initial capacity.

To conclude, these results prove that the preparation method based on melting sulfur on NwC, even if offering simplicity and quite nice initial discharge capacity, is not an optimized solution for prolonged cycling. The most stable capacity retention was observed with ‘catholyte’ cell. Further tests must be performed to explain the large differences in cyclability behavior of ‘S-melted’ and ‘catholyte’ cell. In fact, after the reduction of sulfur, the two aforementioned configurations are the same. The only difference lies in their loading, much higher for ‘S-melted’ than the ‘catholyte’ cell. Therefore, in future studies the loading effect on the performances must be also taken into consideration.

### 3.4.10. ‘Insulated sulfur electrode’ coin cell concept

We previously demonstrated that even if sulfur is melted onto a NwC disk, and it occupies all the volume between carbon fibers, without necessarily intimate connection with conductive surface of a carbon nano-material, sulfur can still be easily reduced. To give additional clues of that, a special coin cell was built as shown on Figure 3-27.

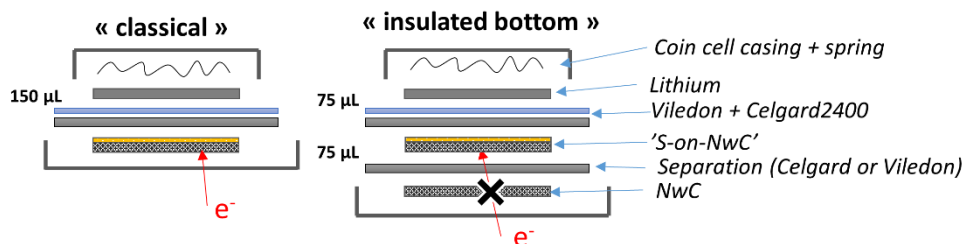


Figure 3-27. Schematic illustration of the 'insulated sulfur electrode' proof-of-concept, where sulfur electrode is insulated from the current collector (electron source) by placing a separator layer on the bottom of the coin cell, and additional NwC disk to accept the electrons from the external circuit.

The idea of 'insulated sulfur electrode' cell was, as indicated by name, to completely insulate the 'S-on-NwC' composite electrode from the bottom current collector (coin cell casing), thus insulate from direct electrons source. An additional disk of NwC ( $\varnothing$  12 mm, to prevent any electrical contacts on the edges of the coin cell casing) was placed at the bottom of the coin cell, in this case being in contact with electrons, and separated from the composite electrode by using additional layers of Celgard<sup>®</sup>2400 or Viledon<sup>®</sup>.

Coin cells with different separation methods between NwC disk and 'S-on-NwC' electrode were made (Celgard<sup>®</sup>2400 or Viledon<sup>®</sup> only, or Celgard<sup>®</sup>2400 + Viledon<sup>®</sup>). The electrode loading was estimated to be  $\sim 6.2 \text{ mAh cm}^{-2}$ . Galvanostatic cycling was performed at low (C/100) rate. The initial discharge profiles are shown on Figure 3-28.

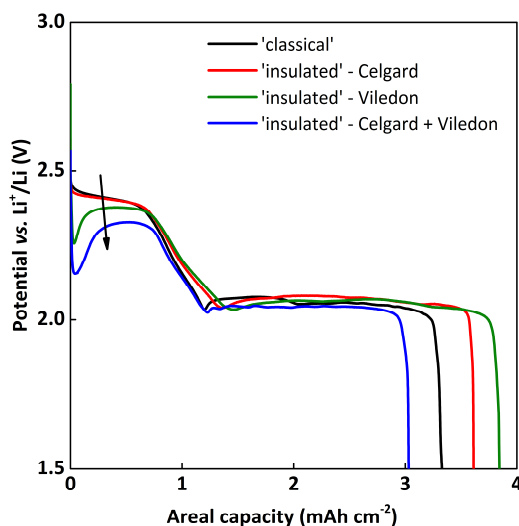


Figure 3-28. Voltage profiles of the initial discharge of 'insulated sulfur electrode' cells. Cycling done at C/100 rate; estimated sulfur loading for each electrode:  $\sim 3.7 \text{ mg}_{\text{sulfur}} \text{ cm}^{-2}$ .

As the electrode loadings were similar, the capacities only refer to  $\text{mAh cm}^{-2}$ , in order to demonstrate the proof-of-concept of this special cell design. First, an initial polarization is visible, which is associated with the thickness of the separation layer(s) between the insulated sulfur electrode and the current collector: Celgard<sup>®</sup>2400 < Viledon<sup>®</sup> < Celgard<sup>®</sup>2400 +

Viledon<sup>®</sup>. This means that the initial polarization is also related with the time needed for the species to diffuse through this separation layer. In any case, sulfur present in the ‘S-on-NwC’ electrode can be reduced even when fully insulated from the current collector. Indeed, sulfur is known to get easily dissolved in the ether-based electrolytes, thus soluble sulfur can leave the electrode and diffuse to other parts of the cell.

These results also show that dissolved sulfur may readily diffuse to the positive electrode current collector, and get electrochemically reduced to form polysulfides. Once activated, with an overpotential at the beginning of discharge depending on the separation distance (thickness of Celgard<sup>®</sup>2400 and/or Viledon<sup>®</sup>), the electrochemical reduction of sulfur proceeds normally, since the expected discharge profile is still observed, despite of using this special cell design. *Post mortem* analyses with the SEM were performed on the cells after few cycles, and the NwC disk placed at the bottom of the coin cell casing was analyzed. These analyses showed that all the solid product formation occurred on this bottom NwC disk, while the ‘S-on-NwC’ matrix was not containing any active species. All sulfur material left the insulated electrode and diffused to get electrochemically reduced on the positive current collector. This important fact allows to point out the unnecessary need of well-mixed carbon and sulfur mixture, or of sophisticated sulfur/carbon composites design, as the dissolution process will profoundly change the positive electrode morphology upon cycling. These conclusions are in agreement with our previous reports<sup>45</sup>.

### **3.5. Problems encountered when using highly loaded sulfur electrodes – Lithium as limiting factor?**

Most of our coin cells with ‘S-on-NwC’ electrodes ended up with so-called ‘problematic charge’. Until today, to our best knowledge, only Hagen *et al.*<sup>132</sup> have shown these problems. ‘Problematic charge’ starts to appear first as a little disturbances in the voltage profile, which can become more severe within the next few cycles, sometimes even leading to complete death of the cell. We attributed this problem to the dendritic growth of metallic lithium, which provokes micro-short circuits. Interestingly, such ‘problematic charge’ is not always infinite, and the cells are sometimes able to reach complete charge at one moment, and discharge normally afterwards. As a matter of fact, charge process is getting enlarged with every other cycle, gradually decreasing the coulombic efficiency. Figure 3-29 presents the occurrence of a ‘problematic charge’ and how it develops upon prolonged cycling.

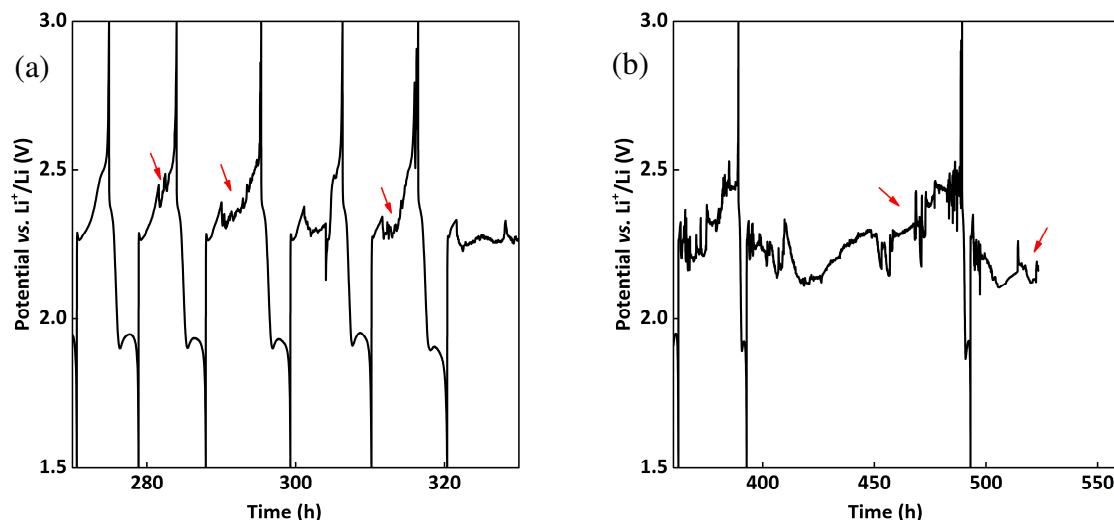


Figure 3-29. Example of voltage profile obtained from galvanostatic cycling of ‘S-on-NwC’ electrode, where pronounced ‘short circuiting’ phenomenon occurred during charge: appeared for the first time, while the cell was still able to cycle (a), leading to more severe short circuits and finally to the death of the cell (b).

Since these problematic charges phenomena were mainly observed for ‘S-on-NwC’ electrodes, the two hypothesis concerning its origin are as follow: (i) highly loaded electrodes require high density current to be applied, and/or (ii) the use of 3D electrode architecture, which may lead to non-uniform current distribution at a microscopic scale. Both of them may result in severe lithium consumption and dendrites formation. However, some tests were performed on heavily loaded ‘S-on-Alu’ electrodes, and a similar ‘problematic charge’ behavior was observed in this case as well. This led us to the conclusion that this problem may not relate only to the use of a 3D NwC current collector.

To validate our hypothesis of micro-dendrites formation and to better understand the reason of this strong overcharge, we performed *post mortem* analysis. Once a cell was unable to recharge, we opened it and recuperated the positive electrode. New coin cell was fabricated with already cycled positive electrode, while lithium was replaced into a fresh one. The separators were replaced as well, and filled with new amount of the electrolyte (150  $\mu$ L). By doing so, the cell was able to cycle again at the same current density during additional 60 cycles, as shown on Figure 3-30 (C/20 rate). The lower capacity may be explained by the fact that some of the polysulfide species were lost during cell re-assembly.

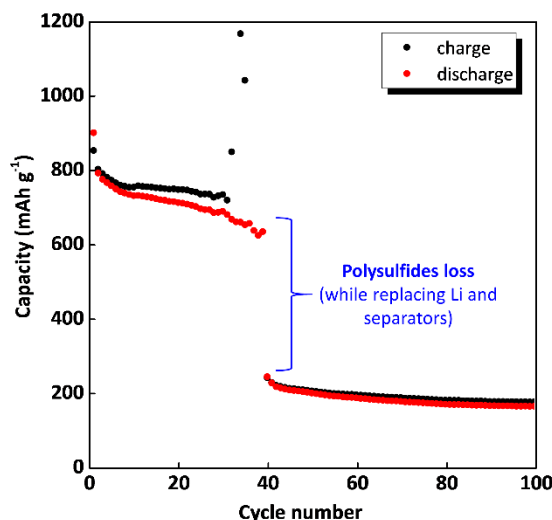


Figure 3-30. Capacity retention of a ‘S-on-NwC’ cell (sulfur loading of  $\sim 5.0 \text{ mg}_{\text{Sulfur}} \text{ cm}^{-2}$ ; C/10 rate) where severe short circuiting occurred starting from  $\sim 30^{\text{th}}$  cycle, leading to a complete death of the cell. After replacing the Li, separators and electrolyte by the fresh ones, the cell was cycled again (at C/20).

Figure 3-31 shows the photos of lithium electrode recuperated from a coin cell encountering overcharge problems, together with SEM photos.

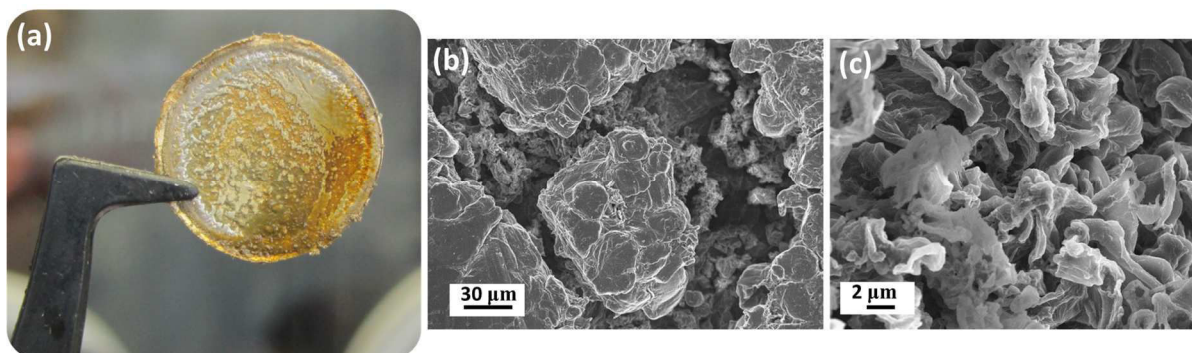


Figure 3-31. Picture (a) and SEM images (b,c) of metallic lithium electrode recuperated from a Li/S coin cell. SEM samples were air-protected during transportation in a special airtight transfer box.

It can be clearly seen (already based on a visual observations) that lithium electrodes present a rough surface, and it is really likely that dendrites were formed. This experiment confirms that the problems of noisy charge are related with lithium. However, it does not exclude separator or positive electrode failures. Deeper studies in this direction should be applied, like for example studies of negative electrode/positive electrode/separator morphology after ‘problematic’ charge (SEM, EDX). One should note, however, that in our experiments, this phenomenon was observed relatively randomly, starting at different cycles: sometimes very early – even at  $15^{\text{th}}$  cycle, or much after – such as after  $50^{\text{th}}$  cycles for example. We did not find any dependence from applied current neither. No matter the C-rate (C/100, C/20, C/10, C/5, 2C...) and the corresponding applied current densities, this phenomenon was sooner or later observed, even if slightly more pronounced at faster rates and higher loadings. More studies



need to be done in order to understand this phenomenon better, minimize it or even avoid for the future.

### 3.6. Conclusions

The use of carbon based porous current collector allowed to obtain highly loaded electrodes, without sacrificing the practical discharge capacities. Relatively high discharge capacities of  $\sim 1200 \text{ mAh g}^{-1}$  can be obtained at moderate C-rates (up to C/5). This architecture, however, is not optimized yet for power rate applications.

The benefit of NwC over Al collector is mostly visible, when comparing highly loaded electrodes. It is then obvious that much higher capacity values can be obtained with NwC-based electrodes, with lower polarization. The reason for such improved capacity values when using NwC sheet, is not directly related with the fact, that it offers an additional conductive surface area for solid products precipitation ( $\text{Li}_2\text{S}$ ) at the end of discharge, as cleared out by the calculations of surface area. Thus, a more important factor is linked to its high porosity ( $\sim 80\%$ ) and 3D conductive network, which improve both efficient ionic and electronic conductive pathways. It also provides a rigid and stable carbon matrix for the electrode, which is beneficial from the point of view of dissolution/precipitation cycles that occur in Li/S batteries and capacity retention. One should also keep in mind that NwC used in this work was a commercial product, not optimized in terms of thickness and weight. Thus, development of on-demand NwC papers with optimized parameters (in terms of thickness, porosity, specific surface, etc.) should be consider in the future as it may result in better performances.

Last but not least, one of the main obstacle systematically observed was the appearance of micro short circuits during charge, since we were working with relatively highly loaded electrodes (profound depth of lithium stripping/plating). This phenomenon, when occurring, was progressively becoming more severe, leading in the worst case to the cell death. This problem points out the requirement to investigate and focus on the lithium metal problematics. It also allows to evidence the motivation to develop alternative anode materials for Li/S cells, and the next chapter is dedicated to Li-ion/sulfur cells development and studies.

# Chapter 4: Into safer cells: metallic lithium-free Li-ion/S system

## 4.1. The goal of the work

In the previous chapter, we saw several examples where lithium dendrites formation effectively shorten (or ended) the life of the battery. These findings, supported by the general trend of lithium metal safety issues, gave us the motivation to go into the direction of safer lithium-ion/sulfur (Li-ion/S) cells, by eliminating metallic lithium electrode and replacing it by other insertion or alloying type negative electrodes.

Our first choice focused on the use of a silicon (Si) negative electrode. Indeed, Si active material offers the highest specific capacity among all negative electrode materials, and is usually foreseen to be combined with sulfur positive electrode<sup>189,190,233</sup>. Moreover, it is known that Si electrode can be cycled with ether-based electrolytes, the electrolyte of choice for sulfur-based materials<sup>189,234</sup>. Indeed, lithium polysulfides are strongly reactive with carbonyl groups<sup>29,155,157</sup>, thus classical carbonate electrolytes of Li-ion batteries would not be an optimized choice for Li-ion/S system. One should note that Si electrode is also known from its issue of cycle life and large volumetric changes<sup>233,235</sup> occurring upon cycling, but optimization of these was not the goal of this study.

In order to pair silicon with sulfur ( $\text{S}_8$ ) into a full lithium metal-free cell, one of these components requires pre-lithiation. Another solution consists in the use of an alternative cathode material, lithium sulfide ( $\text{Li}_2\text{S}$ ), known as a lithiated counterpart of sulfur. As already presented in the bibliographic study chapter (section 1.3.1.e),  $\text{Li}_2\text{S}$  is lately receiving an increasing attention, mainly due to its high specific capacity ( $1166 \text{ mAh g}^{-1}$ ) and the fact that it offers the possibility of direct combination with Li-free negative electrode: Si<sup>141,154</sup>, tin (Sn)<sup>193</sup> or even graphite<sup>140</sup>.

Another considered option for Li-ion/S cell was the use of graphite electrode, which is currently widely used in Li-ion systems, is well-known in terms of structure and electrochemical mechanisms, and which shows a stable electrode morphology and discharge capacity upon cycling. However, due to the reactivity of the polysulfide species with C=O groups, carbonate solvents are *a priori* not usable, while graphite electrode is getting exfoliated in the presence of ethers<sup>236,237</sup>. On the other hand, vinylene carbonate additive (VC) is well-known to improve the passivation layer (SEI) on the graphite electrode in carbonate-based electrolyte mixtures. Therefore, we investigated the effect of adding a low amount of VC to the ether-based

electrolyte composition. More precisely, we studied the impact of this additive on the cyclability of sulfur electrode, and of graphite one, when cycling in ether-based electrolyte.

The first part of this chapter will be devoted to the development of Li<sub>2</sub>S electrodes: beginning from the fabrication process, to the understanding of the phenomena which govern the electrochemistry of this material, until final conclusions. A comparison with sulfur cathodes will also be provided. In the following part, a proof-of-concept of full Li-ion/S system composed of Li<sub>2</sub>S and Si electrodes will be demonstrated.

## 4.2. Lithium sulfide (Li<sub>2</sub>S) electrode: development and studies

The main drawbacks of Li<sub>2</sub>S material arise from its low ionic ( $\sim 10^{-13}$  S cm<sup>-1</sup>)<sup>145</sup> and electronic conductivity, which give rise to low utilization of Li<sub>2</sub>S active material. Therefore, a sufficient mixing and intimate contact with conductive additives are required, and a specific electrode optimization for this particular material needs to be performed as compared with the case of S<sub>8</sub>. Last but not least, preparation methods are also restricted due to its high reactivity against moisture, and the next section describes the method of electrode preparation applied in this work.

### 4.2.1. Experimental section

#### 4.2.1.a) Electrodes preparation

Lithium sulfide is very sensitive to air moisture, thus all the steps of the electrodes preparation and other manipulations were carried out in an argon-filled glove box. Li<sub>2</sub>S was purchased from two different suppliers: Sigma Aldrich (99.98% trace metal basis) and Alfa Aesar (99.9% metal basis, -200 mesh powder) and used as-received. This choice is further discussed in this chapter, and eventual differences between the two grades of powders are commented. For some electrodes, ball milling pre-treatment of Li<sub>2</sub>S powder was applied, and more detailed description can be found in section 4.2.7.a). SuperP<sup>®</sup> (Timcal)<sup>\*</sup> and PVdF 6020 (Solvay) were used as a standard conductive additive and polymeric binder, respectively. The ‘reference’

---

<sup>\*</sup> Ketjenblack<sup>®</sup> carbon additive (EC-300J, AkzoNobel; particle size of 30 nm, BET of 800 m<sup>2</sup> g<sup>-1</sup>) was also tested. The cyclability tests gave practically the same results, as when using SuperP<sup>®</sup>, as it was also the case for sulfur-based electrodes. Thus, SuperP<sup>®</sup> was selected as a ‘reference’ choice for carbon additive.

composition was selected to be 70/20/10 wt% (Li<sub>2</sub>S/SuperP<sup>®</sup>/PVdF 6020), based on preliminary cycling results of other compositions.<sup>†</sup>

SuperP<sup>®</sup> and PVdF 6020 powders were dried in BUCHI<sup>®</sup> during 48h at 80°C and 60°C, respectively, and then transferred to the glove box prior the electrodes preparation. Bottles of Li<sub>2</sub>S powder were stored in the fridge (2°C – 8°C; according to the supplier recommendations), and were entered in the glove box only for the time of the electrode preparation. A 6 wt% solution of PVdF 6020 in *N*-methyl-2-pyrrolidone (NMP; stored under molecular sieves, H<sub>2</sub>O < 0.01%) was prepared inside the glove box.

In the first step, precisely weighed amounts of Li<sub>2</sub>S and SuperP<sup>®</sup> powders were grinded together in a mortar with few drops of cyclohexane (anhydrous, 99.5%). After manual grinding (~ 15 min), the wet powders were left for solvent evaporation in the oven (integrated in the glove box). Once the Li<sub>2</sub>S/SuperP<sup>®</sup> mixture got dried, the powders were recuperated into the beaker. Appropriate amount of PVdF solution was added to the beaker, together with extra volume of NMP solvent to provide optimal viscosity of the ink. All ingredients were mixed with spatula until homogenous slurry was obtained. The ink was then casted on a 20 μm thick aluminum foil (or non-woven carbon collector 'NwC'<sup>‡</sup>; product of Freudenberg under commercial name H2315) using doctor blade technique with a thickness of 100 μm. Casting was done manually with the blade, as the preparation was carried out in the glove box. Such prepared electrode sheets were left for drying inside an oven (integrated inside the glove box) for 48 h at 80 °C under vacuum. The resulting electrodes' loadings were rather low, and were varying between 0.8 – 2.3 mg<sub>Li<sub>2</sub>S</sub> cm<sup>-2</sup> for aluminum based electrodes. NwC collector allowed to obtain higher loadings, of up to ~ 3.5 mg<sub>Li<sub>2</sub>S</sub> cm<sup>-2</sup>, since large porosities of NwC paper (80%) permitted for the ink penetration. Once dried, electrode disks of Ø 14 mm were punched (or simply removed from coated NwC sheet), weighed (Ohaus, scale precision ± 0.1 mg) and transferred to another glove box for coin cells fabrication. Coin cells were prepared as described in section 2.2.2, using standard electrolyte (150 μL of 1M LiTFSI + 0.1M LiNO<sub>3</sub> in TEGDME/DIOX 1:1 vol; Viledon<sup>®</sup> and Celgard<sup>®</sup>2400 as separators) and metallic Li as counter electrode. Figure 4-1 illustrates the main steps of the electrode preparation.

---

<sup>†</sup> Being aware of rather poor conductivity of crystalline commercial Li<sub>2</sub>S, the electrodes were prepared with higher amount of carbon (20 wt%) as compared with the 'reference' composition of sulfur electrode (10 wt% of carbon). Later on, two other electrode compositions (Li<sub>2</sub>S/SuperP<sup>®</sup>/PVdF = 80/10/10 wt% and 60/30/10 wt%) were also made and tested by galvanostatic cycling. The results were not included in this manuscript, but no remarkable difference in terms of practical capacities was found. Therefore the composition 70/20/10 wt% - as a compromise between sufficient amount of carbon and high Li<sub>2</sub>S fraction - was kept for further studies.

<sup>‡</sup> The preparation procedure of NwC-based electrodes was the same as already described in section 3.2, *i.e.* Ø 14 mm NwC disks were punched, weighed and placed back into the NwC paper sheet before the electrode slurry was coated on their surface. Such preparation method allowed to know precisely the weight of current collector and to minimize the error related with over/under estimated active material weight.

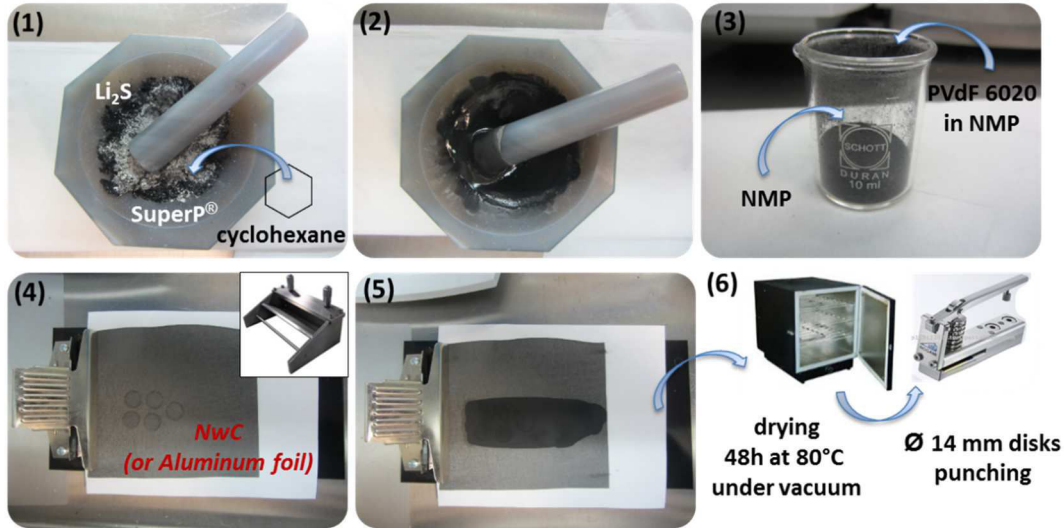


Figure 4-1. Schematic illustration of the  $\text{Li}_2\text{S}$ -based electrode preparation procedure. All the preparation steps were carried out inside the glove box.

In the previous chapter (section 2.2.4), we discussed the nature of errors in relation to sulfur electrode, which may influence calculated capacity values. In case of  $\text{Li}_2\text{S}$  electrodes, similar errors related to inhomogeneity of manually prepared electrodes should also be considered. Moreover, because of the lower scale precision ( $\Delta M_{(\text{electrode})} = 0.1 \text{ mg}$ ), average  $\Delta \text{Capacity}$  for  $\text{Li}_2\text{S}$  electrodes is slightly higher as compared to the typical ‘S-on-Al’ electrode, and is in the range of 3.8 %, according to the equation (8).

$$\frac{\Delta \text{Capacity}}{\text{Capacity}} = \frac{\Delta M(\text{electrode}) + \Delta M(\text{Al})}{M(\text{electrode}) - M(\text{Al})} + \frac{\Delta \% \text{S}}{\% \text{S}} \quad (8)$$

where:

Capacity: 2.94 mAh;  $M_{(\text{electrode})}$ : 12.0 mg;  $M_{(\text{Al})}$ : 8.4 mg;  $\Delta M_{(\text{Al})}$ : 0.01 mg;  $\Delta \% \text{S}$ : 0.5 %;  $\% \text{S}$ : 70 %.

#### 4.2.1.b) Characterization techniques

Galvanostatic cycling (GCPL; performed on Arbin<sup>®</sup> battery cycler) and cycling voltammetry (CV; recorded on VMP3 Bio-Logic<sup>®</sup>) have been applied as standard electrochemical methods for cycling performances evaluation, at room temperature (RT). Typical  $\text{Li}_2\text{S}$  electrode cycling was performed at medium C-rates (C/20 or C/10). Other C-rates (C/100 or even 1C) were also applied, depending on the aim of the measurements. Current density values were calculated with respect to the theoretical capacity of active material ( $1166 \text{ mAh g}^{-1}$ ) and its loading. CV measurements were conducted at a scanning rate of  $0.03 \text{ mV s}^{-1}$ . Selection of potential window is extensively discussed in paragraph 4.2.5, and is provided for each electrochemical test separately.

Galvanostatic intermittent titration technique (GITT, conducted on VMP3 Bio-Logic®) is a measurement where a series of constant current cycling steps are interspersed with a relaxation time, during which no current passes through the cell and the potential quickly increases/decreases to reach equilibrium potential. Thanks to this technique, information about thermodynamic behavior of the active material present in the positive electrode can be obtained. Constant current ( $i = 98 \mu\text{A cm}^{-2}$ ; C/20 rate) was applied for 20 min, followed by a relaxation step of 30 min.<sup>§</sup>

It is important to notice that sensitivity of  $\text{Li}_2\text{S}$  powder to air moisture strongly limited the number of techniques that could be applied for evaluation, or required some modifications of standard procedures.

Scanning Electron Microscopy (SEM; LEO 1530, Gemini) was used for powder/electrode morphology observation (at accelerating voltage of 5 kV. X-Ray Diffraction (XRD) measurements were performed on D8 Bruker Advanced with  $\text{CuK}_\alpha$  ( $\lambda = 1.5406 \text{ \AA}$ ). In case of both techniques, special precautions were taken into consideration while preparing air-sensitive samples. The detailed procedure was described previously (refer to 2.2.3).

#### 4.2.2. Morphology of the electrodes and structural characterization

Figure 4-2 shows the SEM photos of as-received  $\text{Li}_2\text{S}$  powder (Alfa Aesar) grinded with SuperP®. As-received  $\text{Li}_2\text{S}$  purchased from Sigma Aldrich and grinded with carbon gave very similar global view. The appearance of final  $\text{Li}_2\text{S}$  electrode resemble to the  $\text{Li}_2\text{S}/\text{SuperP}^\circledast$  SEM photo, and did not differ depending on the powder batch either. The size of  $\text{Li}_2\text{S}$  particles is ranging from 5  $\mu\text{m}$  to 20  $\mu\text{m}$ . It can clearly be noticed that the  $\text{Li}_2\text{S}$  particles are not uniformly covered by nano-carbon spheres, as it was seen previously for sulfur particles (see Figure 3-4b). Such difference may result from different hardness of both materials. Elemental sulfur is very soft (1.5 – 2 in the Mohs scale<sup>238</sup>) and basic grinding in the mortar provided complete enrobing with SuperP®. On the contrary,  $\text{Li}_2\text{S}$  particles are much harder and probably mechanical grinding is not sufficient to provide intimate contact between  $\text{Li}_2\text{S}$  and carbon. A visual indication of that difference could also be seen from the colors of the mixed powders: S/SuperP® totally turned black after grinding, while  $\text{Li}_2\text{S}/\text{SuperP}^\circledast$  was rather grayish after similar grinding.

---

<sup>§</sup> Such short relaxation time was selected in order not to provoke eventual shuttle phenomenon. However, it was sufficient to be near the stable potential.

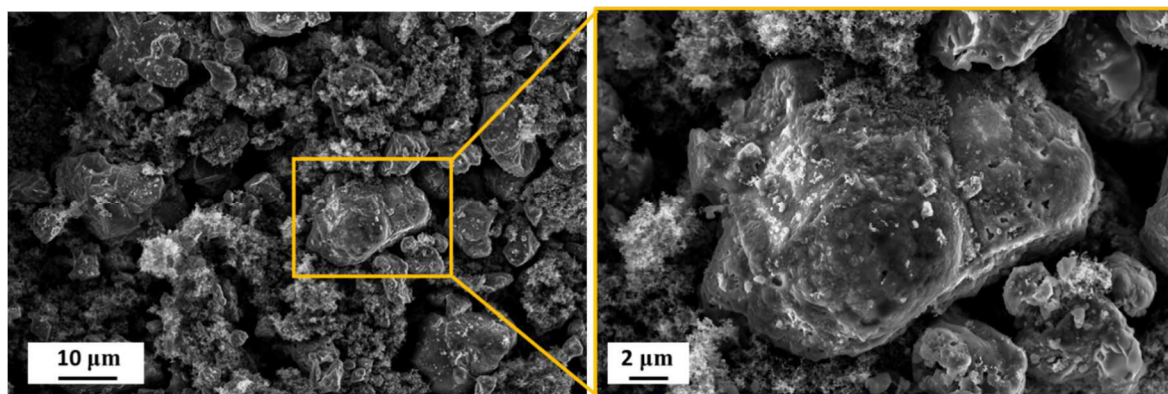


Figure 4-2. SEM photos of  $\text{Li}_2\text{S}$  powder (used as-received from Alfa Aesar supplier) manually grinded with SuperP<sup>®</sup> in an agate mortar, with few drops of cyclohexane.  $\text{Li}_2\text{S}/\text{SuperP}^{\text{®}}$  ratio of 78/22 wt%, aimed for final electrode composition of 70/20/10 wt% after binder addition.

Figure 4-3 shows XRD patterns of as-received  $\text{Li}_2\text{S}$  samples, purchased from both Sigma Aldrich and Alfa Aesar suppliers, and grinded with SuperP<sup>®</sup>. Both patterns, as well as the scan of pure  $\text{Li}_2\text{S}$ , are identical, and most of the peaks were assigned to the crystalline  $\text{Li}_2\text{S}$  (PDF 2 # 00-023-0369; cubic unit cell with lattice parameters:  $a, b, c = 5.72 \text{ \AA}$ ;  $\alpha, \beta, \gamma = 90^\circ$ ). Small peaks, assigned to lithium hydroxide ( $\text{LiOH}$ ; PDF-2; no. 00-032-0564), were also detected, possibly meaning that some impurities were present in the samples, however, their amount was rather small. Another explanation could be that Kapton<sup>®</sup> foil did not provide perfect airtightness, and  $\text{LiOH}$  got formed because of partial hydrolysis of  $\text{Li}_2\text{S}$  in contact with air moisture during measurement. Takeuchi *et al.*<sup>147</sup> and Hiesgen *et al.*<sup>146</sup> reported on similar presence of  $\text{LiOH}$  in  $\text{Li}_2\text{S}$  samples.

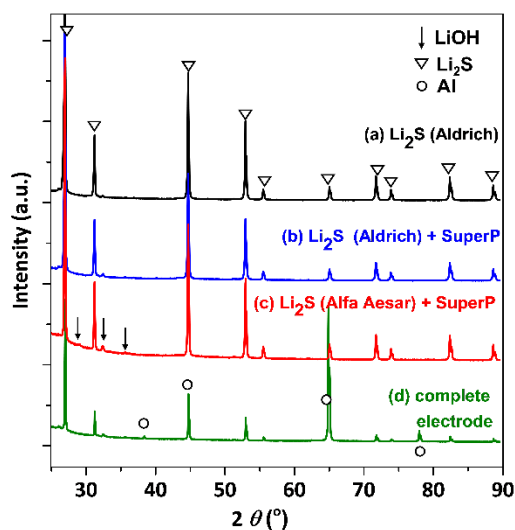


Figure 4-3. XRD patterns of  $\text{Li}_2\text{S}$  powders: pure (a), after manual grinding with SuperP<sup>®</sup> in the presence of cyclohexane (b,c) and incorporated into final electrode with composition 70/20/10 wt% =  $\text{Li}_2\text{S}/\text{SuperP}^{\text{®}}/\text{PVdF}$  (d). Powders from both suppliers, *i.e.* Sigma Aldrich and Alfa Aesar, were compared.

### 4.2.3. Typical electrochemical response

#### 4.2.3.a) Galvanostatic cycling (GCPL) results

The voltage profiles of two initial cycles (at C/20 and RT) of  $\text{Li}_2\text{S}$  positive electrode (reference composition 70/20/10 wt% =  $\text{Li}_2\text{S}$ /SuperP<sup>®</sup>/PVdF; active material loading of  $1.23 \text{ mg}_{\text{Li}_2\text{S}} \text{ cm}^{-2}$ ) cycled with lithium as counter electrode, are as shown on Figure 4-4. Since the battery was assembled in the discharged state (lithium in the  $\text{Li}_2\text{S}$  positive electrode), the cycling process started with a charge (oxidation of  $\text{Li}_2\text{S}$ ).

It can be seen that the voltage profile of the initial charge significantly differs from the following charge, and a characteristic potential barrier just at the beginning is present, encircled in blue. This behavior is typical for  $\text{Li}_2\text{S}$  positive electrode, and has been already reported in the literature<sup>139,141,143</sup>. Appearance of such ‘activation’ barrier is strongly related with the difficulties to oxidize  $\text{Li}_2\text{S}$  active material, since it is a very poor electronic and ionic conductor ( $\sigma_{\text{ion}} = 10^{-13} \text{ S cm}^{-1}$ )<sup>145</sup>, and as initially is present in the electrode in the form of micrometric particles. Furthermore, contrary to sulfur,  $\text{Li}_2\text{S}$  is practically insoluble in most of the organic solvents<sup>45</sup>, which may also hinder the initial activation step.

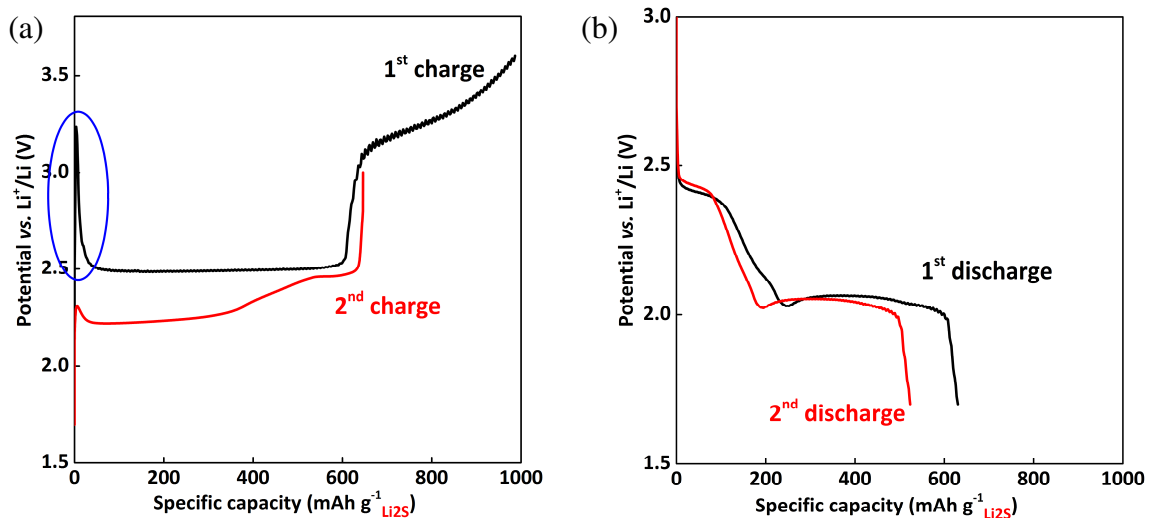


Figure 4-4. Typical cycling response of  $\text{Li}_2\text{S}$ /SuperP<sup>®</sup>/PVdF positive electrode cycled vs. Li at C/20. Voltage profiles of two initial charges (a) and two initial discharge processes (b) are shown. Electrode loading of  $1.23 \text{ mg}_{\text{Li}_2\text{S}} \text{ cm}^{-2}$ . Blue circle marks the initial activation step.

Once the cell starts to charge, the voltage increases rapidly up to  $\sim 3.25 \text{ V}$  (almost  $1 \text{ V}$  overpotential), followed by a fast drop and stable charge plateau at  $\sim 2.5 \text{ V}$ . Further discussion provides more detailed information concerning the origin of this barrier and its relation with cycling parameters and electrolyte additives. The end of charge is accompanied by a continuous increase of the potential along with an oxidation process at above  $3.0 \text{ V}$ , which is not observed



during further cycles anymore. Because of such particular behavior of initial charge, the cut-off voltage is usually set up to higher values ( $> 3.0$  V), while the following charges are reaching typical potential limits of Li/S cells, *i.e.* 3.0 V (or 2.8 V). More detailed discussion concerning the cut-off voltage potential is presented in section 4.2.5. Obtained charge capacity is as high as  $970 \text{ mAh g}^{-1}$ , which is 85% of the theoretical value ( $1166 \text{ mAh g}^{-1}$ ).

During subsequent discharge, typical behavior of sulfur electrode is seen. Two main kind-of-plateaus can be distinguished: a  $\sim 2.4$  V sloping plateau corresponding to the sulfur reduction and formation of long chain polysulfides, and a  $\sim 2.1$  V plateau related to the creation of shorter chain polysulfides and solid  $\text{Li}_2\text{S}$  product. The capacity obtained in the initial discharge is  $630 \text{ mAh g}^{-1}$ , which stands for 54 % of the theoretical value. It is also important to note here that the capacity values are presented with respect to the mass of  $\text{Li}_2\text{S}$  active material (molar mass:  $46 \text{ g mol}^{-1}$ ). If converted per mass of sulfur ( $32 \text{ g mol}^{-1}$ ), capacity value of  $906 \text{ mAh g}_{\text{Sulfur}}^{-1}$  would be obtained\*\*, which is in line with the results reported in chapter 2.3.2. Further cycle profiles exhibit exactly the same features as the cell with sulfur electrode. Very large irreversible capacity loss is observed ( $340 \text{ mAh g}^{-1}$ ), and possible explanation is discussed later.

Figure 4-5 compares the voltage profiles of  $\text{Li}_2\text{S}$  and sulfur-based electrodes during initial cycle, both cycled with metallic Li, where the capacity values are presented in respect to the sulfur mass ( $\text{mAh g}_{\text{sulfur}}^{-1}$ ) for both cells. Initial charge of Li/ $\text{Li}_2\text{S}$  cell, due to its particularity, was not taken into consideration, thus the second charge profile was used instead. The capacity values are not exactly the same and should not be compared quantitatively, since both cells were of different active material loadings, thus the performances might also differ ( $1.23 \text{ mg}_{\text{Li}_2\text{S}} \text{ cm}^{-2} \leftrightarrow 1.43 \text{ mAh cm}^{-2}$ , and  $2.46 \text{ mg}_{\text{Sulfur}} \text{ cm}^{-2} \leftrightarrow 4.12 \text{ mAh cm}^{-2}$  for these particular cells).

It can be seen that the discharge profiles are very similar (Figure 4-5a) and both plateaus appear at the same potential<sup>††</sup>. During the charge process presented on Figure 4-5b, both voltage profiles display characteristic little overpotential dip just at the beginning (related with breaking the insulating barrier formed during preceding discharge), followed by two main plateaus, typically assigned to the oxidation of shorter lithium polysulfides to longer chains (1<sup>st</sup> plateau), then further oxidized to elemental sulfur.

---

\*\* All along this chapter, the capacity values are presented with relation to  $\text{Li}_2\text{S}$  weight and not sulfur. This needs to be kept in mind, since it is not a conventional way of reporting the capacity results in the Li/S batteries.

†† Slight overpotential of upper discharge plateau of  $\text{S}_8$  electrode is due to the big particles of sulfur raw material (even up to  $50 \mu\text{m}$ ), which vanishes in the following discharges due to sulfur dissolution and changes in particles distribution and morphology.

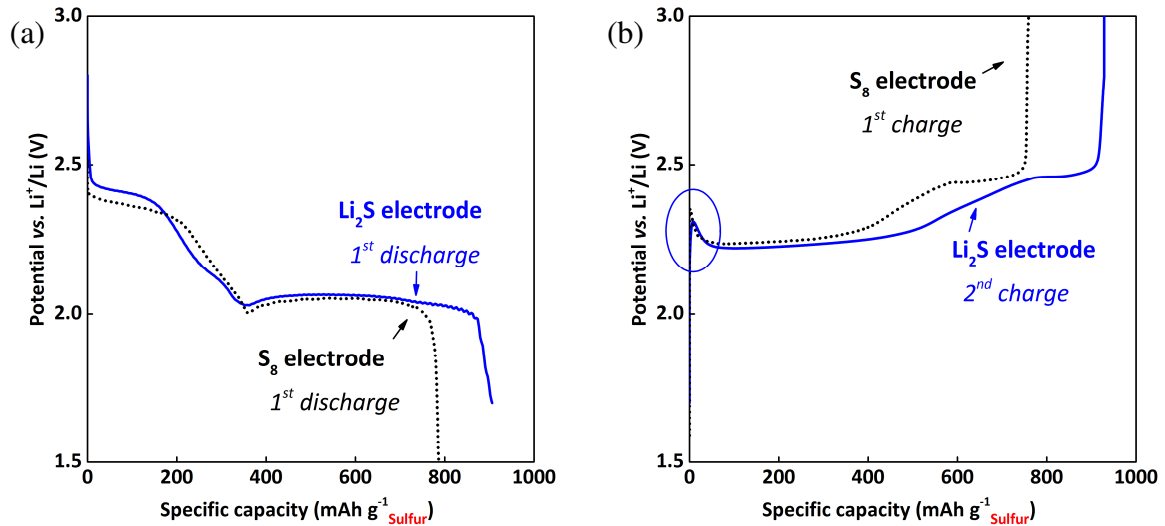


Figure 4-5. Voltage profiles of  $\text{Li}/\text{Li}_2\text{S}$  (in blue) and  $\text{Li}/\text{S}$  (in black) cells cycled at  $C/20$ . Comparison of discharge (a) and charge (b) voltage profiles. In both cases, capacities are presented with respect to the sulfur mass. The active material loadings for both electrodes ( $\text{Li}_2\text{S}$  and  $\text{S}_8$ -based) are as follow:  $1.23 \text{ mg}_{\text{Li}_2\text{S}} \text{ cm}^{-2}$  and  $2.46 \text{ mg}_{\text{sulfur}} \text{ cm}^{-2}$ .

These data confirm the fact that, once the cell starts to run, solid active material present in the electrode is changing its form into liquid state, and further cell operation is exactly the same for both  $\text{Li}_2\text{S}$  and  $\text{S}_8$ -based systems, no matter the initial active material used during the electrode fabrication.

The presence of sharp overpotential peak at the beginning of charge (blue circle on Figure 4-5b) may bring another explanation for the initial and characteristic activation barrier of  $\text{Li}_2\text{S}$  electrode (blue circle on Figure 4-4a). It has been shown that at the end of discharge, nano-sized particles of  $\text{Li}_2\text{S}$  are formed<sup>200</sup> (refer to chapter 5). On the contrary, initial particles of  $\text{Li}_2\text{S}$  used for electrode preparation are much bigger (of about  $10 - 20 \mu\text{m}$ ). As a matter of fact, less energy is needed to break a passivation layer made of nano- $\text{Li}_2\text{S}$ , while higher activation energy is required to activate a fresh electrode of  $\text{Li}_2\text{S}$  after preparation, resulting in more remarkable voltage jump.

Figure 4-6 shows an example of the capacity retention over 100 cycles obtained at  $C/20$ , with initial cycle performed with the  $3.8 \text{ V} - 1.7 \text{ V}$  potential window, followed by  $2.8 \text{ V} - 1.7 \text{ V}$  for the next cycles. Such capacity retention is very close to the one already observed when using sulfur as a starting electrode, *i.e.* drastic capacity fade during few initial cycles, followed by rather stable capacity. The reason for such behavior would be similar as for sulfur electrode: active material loss, pulverization of the electrode, continuous electrode passivation. Discharge capacity values, when calculated with respect to the sulfur mass, are very similar as compared to the cells with ‘S-on-Al’ electrodes (stable capacity at about  $350 - 400 \text{ mAh g}^{-1}$ ).

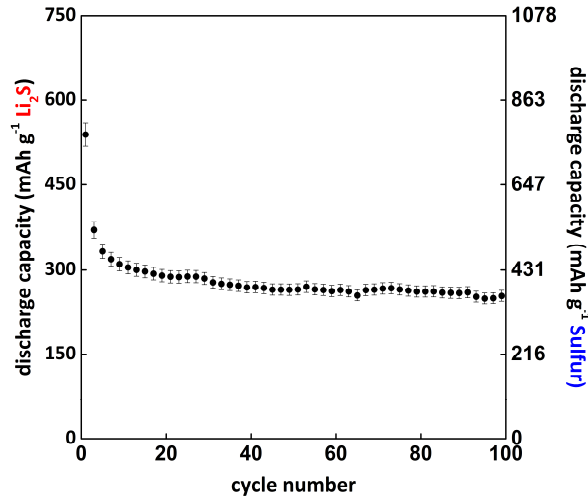


Figure 4-6. Capacity retention over 100 cycles of a Li<sub>2</sub>S/SuperP<sup>®</sup>/PVdF electrode cycled vs. Li at C/20, in the potential window 3.8 V – 1.7 V for the initial cycle, and 2.8 V – 1.7 V for the next cycles. Active material loading of 2.27 mg<sub>Li<sub>2</sub>S</sub> cm<sup>-2</sup>. Error bars in relation to the 3.8 % error due to active mass imprecision (see section 4.2.1.a).

#### 4.2.3.b) Discussion on the coulombic efficiency calculation

In parallel to the discharge profile and capacity retention, it is also important to discuss about the coulombic efficiency, and to explain how it is calculated. Two different methods can be employed for efficiency calculations, both providing different information. Calculation method for a Li<sub>2</sub>S/Li system is proposed according to equation (9):

$$\Phi = \frac{(n) \text{ discharge}}{(n + 1) \text{ charge}} \quad (9)$$

This calculation method allows to determine the efficiency of the charge as compared to the prior discharge, and to evidence the occurrence of shuttle mechanism, with an efficiency being usually below 1 after few cycles. One should note that, in the specific case of sulfur system, even if the efficiency is far below 1, this is not necessarily linked to the capacity fading, as commonly observed for Li-ion system. On the contrary, the low coulombic efficiency is mainly linked to the occurrence of shuttle mechanism, which is responsible for longer charge, while not being detrimental for the following discharge in terms of capacity. This calculation method also allows for relatively easy comparison of sulfur and Li<sub>2</sub>S-based systems, by leaving apart the first charge of Li<sub>2</sub>S, which is quite different from further cycles.

Regarding the first cycle of Li<sub>2</sub>S electrode, an irreversible capacity can be calculated, using the following formula:

$$\frac{1^{\text{st}} \text{ charge} - 1^{\text{st}} \text{ discharge}}{1^{\text{st}} \text{ charge}} \quad (10)$$

and it can be as high as 35 % (example from Figure 4-4). This irreversible capacity in Li<sub>2</sub>S-based system reflects the capacity loss between first charge and following discharge, mainly due to the structural changes of the electrode after Li<sub>2</sub>S dissolution, the electrode pulverization, the loss of carbon/active material contact, loss of active material in the electrolyte leading to the uncompleted transformation back to Li<sub>2</sub>S during following discharge.

Another calculation method of efficiency ( $\Phi$ ), inspired by Li-ion systems, can be proposed as follow:

$$\Phi = \frac{(n) \text{ discharge}}{(n) \text{ charge}} \quad (11)$$

This calculation method gives information on the efficiency of the charge process regarding to the following discharge, *i.e.* structural changes of materials, electrolyte degradation, loss of lithium ions. This method is more correlated to the capacity fading, and rather related to the structural changes of the positive electrode during the first cycle (in case of the sulfur system). For the example presented previously on Figure 4-6, two different calculation methods of coulombic efficiency were applied (equations (9) and (11)) and are shown on Figure 4-7.

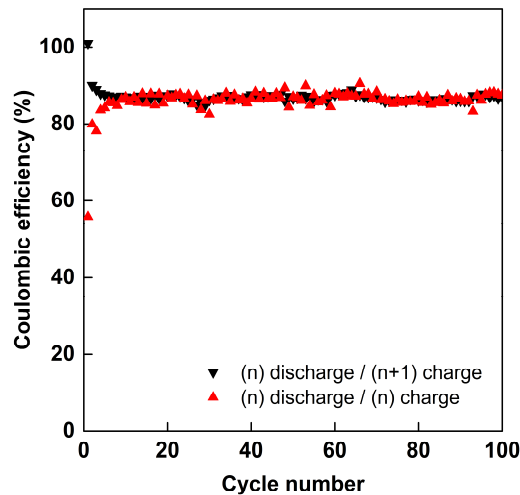


Figure 4-7. Coulombic efficiency comparison, calculated for a Li/Li<sub>2</sub>S cell, with two different ways: as a ratio ‘(n) discharge / (n+1) charge’ – which allows to evidence the shuttle phenomenon (in black); as a ratio ‘(n) discharge / (n) charge’, by analogy to classical Li-ion cells (in red).

For the black curve, the initial efficiency is above 100 %, and decreases down to ~ 90 %, while for the red curve the efficiency is far below 100 %, and increases up to ~ 90 % after few cycles. The first 5 – 10 cycles show kind of transitory efficiency, as a demonstration of initial capacity fading. Afterwards, coulombic efficiencies calculated in both ways, come to the same point, *i.e.* of about ~ 90 %, meaning that the presence of shuttle mechanism is dominant while almost no capacity fading is occurring anymore.

### 4.2.3.c) Cycling voltammetry profile

Typical CV profile (Figure 4-8), recorded at a scanning rate of 0.03 mV s<sup>-1</sup> is very coherent with GCPL curves previously shown (Figure 4-4a). While the potential was swept from the open-circuit voltage (~ 2.23 V) up to 3.2 V, a large oxidation peak related with Li<sub>2</sub>S oxidation appeared. The position of this first oxidation peak is shifted to higher potential values (~ 2.6 – 2.9 V), as compared with the other oxidation peaks recorded during next cycles. As previously discussed, oxidation of large Li<sub>2</sub>S particles induces high polarization. Once Li<sub>2</sub>S gets activated in the first charge, a characteristic response of a Li/S cell (when starting with a sulfur electrode) is observed, *i.e.* two cathodic peaks at 2.4 V and 2.0 V, corresponding to the reduction steps: (i) sulfur → high-order polysulfides and (ii) formation of low-order polysulfides<sup>153</sup>. During charging, a broad oxidation peak at ~ 2.35 V is observed, *i.e.* reflecting the oxidation of shorter polysulfides to longer chain polysulfides, together with a shoulder peak at ~ 2.5 V, interpreted by Manthiram *et al.*<sup>153</sup> as the oxidation of an active material in confined structure. On the contrary, we believe that this peak should rather be attributed to the final oxidation of high-order polysulfides into elemental sulfur, in regard to the potential of sulfur formation by galvanostatic experiment, and supported by *in situ* XRD tests (see chapter 5), and the fact that in our electrodes no confinement of the active material was performed. The area of the peaks can be directly correlated with the practical capacity, and is relatively stable during 10 recorded cycles. Most of the changes occur during the initial cycle, which is in complete accordance with the capacity fading observed by GCPL technique. Moreover, the peaks are very sharp, probably because 20 wt% of carbon provide sufficient electron's pathway for the reaction to occur at the applied scan rate.

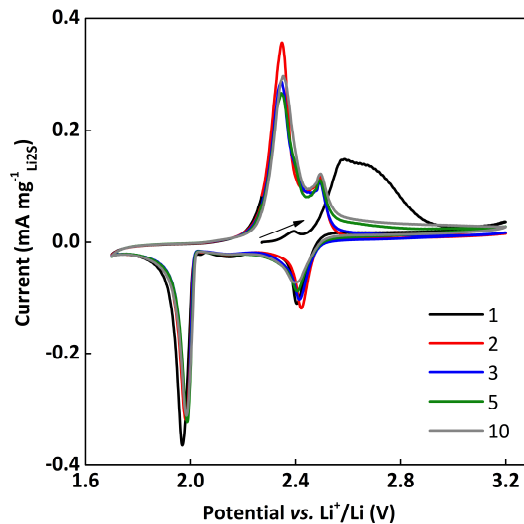


Figure 4-8. Cycling voltammetry curves of Li<sub>2</sub>S/SuperP<sup>®</sup>/PVdF electrode (with Li<sub>2</sub>S loading of 0.68 mg cm<sup>-2</sup>) at 0.03 mV s<sup>-1</sup> scan rate, starting at OCV of ~ 2.23 V.

## 4.2.4. The importance of the initial charge

### 4.2.4.a) Disparities in the charge profiles

After preparing several batches of electrodes, even if aiming at reproducibility (*i.e.* keeping the same composition and preparation method), we quickly realized that the voltage profile of the initial charge significantly varied one from the other, being sometimes very far from the ‘typical’ shape, as shown on Figure 4-4a. This ‘typical’ profile (or very close one) is the one mostly presented in the literature<sup>141,147,154,143,239</sup>. While working with Li<sub>2</sub>S electrodes, many other shapes with strong overpotential or different durations/lengths of the plateau were recorded, and selected examples are shown on Figure 4-9. The required cut-off voltage was rather high for these cells (3.8 V or even 4.0 V), and the choice of such high values is discussed later.

The obtained charge capacities are very close, and varied between 970 to 1100 mAh g<sup>-1</sup>. In the literature, only few reports present such different profiles<sup>142,153</sup>, while some do not provide any initial charge curve at all<sup>240</sup>.

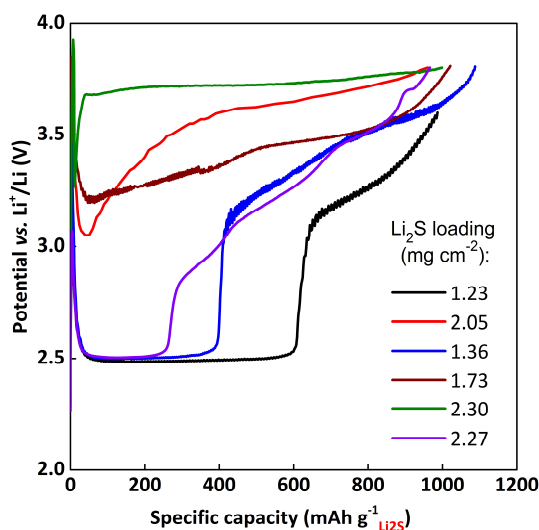


Figure 4-9. Examples of variety of the charge profiles obtained experimentally from the Li<sub>2</sub>S/SuperP®/PVdF = 70/20/10 wt% electrodes, punched from several batches of the electrode sheet. GCPL performed at C/20. The electrode loadings vary between 1.23 and 2.30 mg<sub>Li<sub>2</sub>S</sub> cm<sup>-2</sup>.

The examples presented above come from various batches of electrodes. However, we also noticed that even Ø 14 mm electrode disks punched out from the same electrode sheet, gave sometimes quite different results. This clearly point out a significant lack of reproducibility of the results.

Trying to better understand this phenomenon, the main questions to answer were:

- Which voltage profile should be considered as the ‘correct’ one (?)
- If a standard profile exists (?)
- What are the reasons for such high polarizations (?)

In the first attempt, we tried to verify if a large overpotential might come from the lithium electrode, and its highly passivated surface at the initial state (more information in chapter 6). By performing different treatments on Li surface before closing in the coin cell (*i.e.* cleaning the surface with dimethyl carbonate (DMC) solvent, scratching it with Teflon<sup>®</sup> knife), we did not see any improvements, thus Li was eliminated from the suspected parameters. Also freshly prepared electrolyte solution indicated that such a lack of reproducibility was rather coming from the positive electrode. In the next step, we also eliminated SuperP<sup>®</sup> and PVdF 6020 powders from the suspected limitations, as well as cyclohexane and NMP, by simply replacing these compounds with freshly dried powders and new solvents or solutions. After preparing the electrodes with different  $\text{Li}_2\text{S}$  powders (three bottles purchased from Sigma Aldrich and 1 from Alfa Aesar), we realized that the quality/purity of the active material was not necessary equal for all the batches, and that it significantly influenced the initial charge profile. As previously presented in section 4.2.2, XRD patterns recorded on  $\text{Li}_2\text{S}$  powders showed mainly the pure  $\text{Li}_2\text{S}$  phase, with small peaks of LiOH, which could affect the oxidation process of  $\text{Li}_2\text{S}$  particles during initial charge. However, no clear relation between the amount of LiOH impurity and the first charge behavior could be noticed, and the presence of impurities did not allow to explain the lack of reproducibility during the first charge process (furthermore, the origin of the LiOH presence in the  $\text{Li}_2\text{S}$  powder is not sure, and the observed impurity could be linked to the XRD analysis). In order to have more accurate information about the surface state of individual  $\text{Li}_2\text{S}$  particles and electrodes, surface characterization techniques (like XPS) should be applied for further studies.

Figure 4-10 shows the initial discharge profiles of the six cells, whose initial charges displayed different behaviors, as previously demonstrated on Figure 4-9. They all turn to show the typical features of a standard discharge curve, with two well-known plateaus, regardless the way the first charge has proceed, and capacities between  $580 \text{ mAh g}^{-1}$  and  $660 \text{ mAh g}^{-1}$  are obtained. It is worth noticing that the oxidation process occurring at high voltage ( $> 3.0 \text{ V}$ ) is not linked to the parasitic reactions, as the following discharge capacity is dependent on this charging activation step (more detailed discussion is provided in further parts). As a matter of fact, a deeper understanding of this first charge behavior was sought for, and Galvanostatic Intermittent Titration technique (GITT) was applied to this purpose.

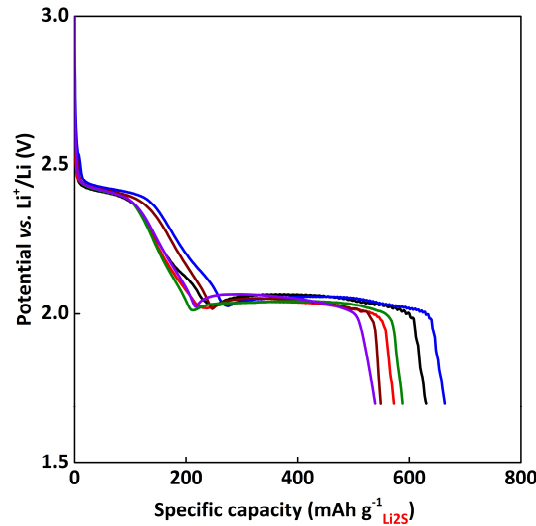


Figure 4-10. Discharge profiles recorded on the cells showing different charge behaviors, presented on Figure 4-9.

#### 4.2.4.b) GITT technique

GITT was applied in order to follow the equilibrium potential of the system at different states of charge/discharge. It also brought information on the dynamic of the cell, *i.e.* evolution of the potential *vs.* relaxation time. Figure 4-11 presents the GITT curve obtained when cycling the Li/ $\text{Li}_2\text{S}$  cell.

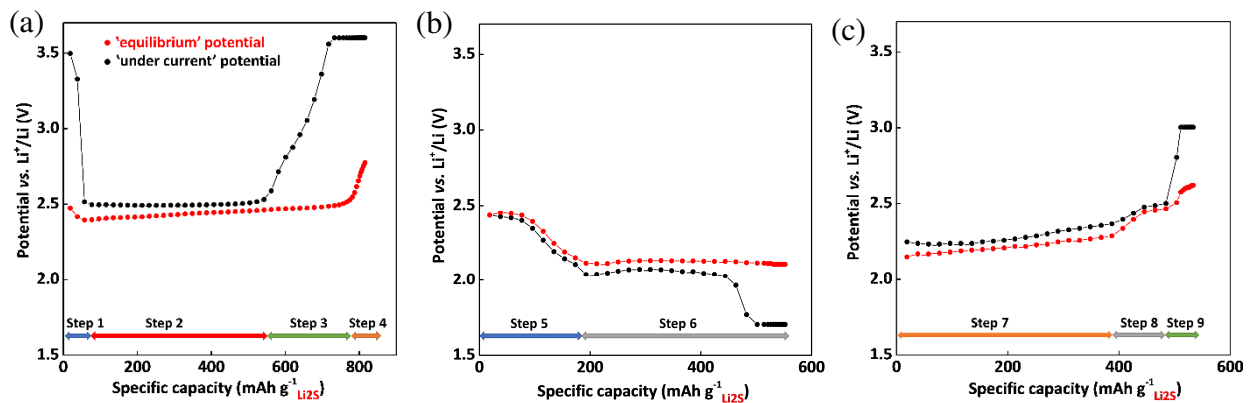


Figure 4-11. GITT results obtained from Li/ $\text{Li}_2\text{S}$  cell, with positive electrode of classical composition 70/20/10 wt% =  $\text{Li}_2\text{S}$ /SuperP<sup>®</sup>/PVdF and active material loading of  $1.68 \text{ mgLi}_2\text{S cm}^{-2}$ . GITT test was composed of short (20 min) repeating sequences of galvanostatic cycling at  $C/20$ , *i.e.* at a current of  $98 \mu\text{A cm}^{-2}$ , followed by relaxation time of 30 min: 1<sup>st</sup> charge (a), 1<sup>st</sup> discharge (b), 2<sup>nd</sup> charge (c).

At the beginning of the initial charge (marked as 'step 1'), a rapid increase of the potential is observed, related to a high polarization of more than 1.0 V, which corresponds to the initial activation of  $\text{Li}_2\text{S}$ . Regarding the relaxation potential (potential obtained at the equilibrium; in red), a decrease between  $\sim 2.5 \text{ V}$  and  $\sim 2.4 \text{ V}$  is observed. Once the activation step has proceeded, the sharp decrease of the potential 'under current' to about 2.5 V is observed. The



polarization also falls rapidly down to less than 100 mV. Afterward, the polarization slowly decreases during ‘step 2’ of the charge, reaching the minimum value of 50 mV at the end of this step. Such low polarization along the charge plateau (‘step 2’), indicates that the kinetic of the overall reaction occurring at this region is fast.

During ‘step 1’ and ‘step 2’, the relaxation potential value, *i.e.* of about 2.4 V, could be related to the electrochemical reactions involving high-order polysulfides (as this is the potential corresponding to high-order polysulfides oxidation, already reported for Li/S system.). Then, at this state of charge, high-order polysulfides coexist together with  $\text{Li}_2\text{S}$  solid phase<sup>31</sup>. Indeed, the electrode potential, where several electrochemical reactions take place, is fixed by the easiest redox equilibrium, which in our case is the oxidation of high-order polysulfides.

Therefore, one of proposed explanation for the atypical first charge profile would be that initially, during the very rapid voltage jump, only a part of  $\text{Li}_2\text{S}$  is getting oxidized, and its oxidation is very short. The capacity corresponding to the ‘step 1’ is usually about  $\sim 50 \text{ mAh g}^{-1}$ , which stands only for 5 – 6% of the theoretical value ( $874 \text{ mAh g}^{-1}$ ), when assuming complete oxidation of  $\text{Li}_2\text{S}$  according to the reaction:  $4 \text{Li}_2\text{S} \rightarrow \text{Li}_2\text{S}_4 + 6\text{Li}^+ + 6\text{e}^-$ . In this first oxidation step, the cell voltage is increasing even up to 3.6 V, meaning that the long chain polysulfides may be formed. Furthermore,  $\text{Li}_2\text{S}_2$  is known to be non-thermodynamically stable<sup>241</sup>, thus direct oxidation of  $\text{Li}_2\text{S}$  to  $\text{Li}_2\text{S}_4$  could be expected. During the pseudo plateau (‘step 2’), it is still not clear but really likely that several electrochemical reactions may occur: slow kinetic oxidation of  $\text{Li}_2\text{S}$  and oxidation of mid-to-longer polysulfides *i.e.*  $\text{S}_4^{2-}$ ,  $\text{S}_6^{2-}$  (this last process fixing the potential) to  $\text{S}_8^{2-}$ . Indeed, the equilibrium potential is nearly the same for ‘step 2’ and ‘step 1’, then the electrochemical reactions involved should be very close. As soon as the potential starts to increase again upon charging (‘step 3’), quite high polarization is observed, indicating the slow kinetics of the overall oxidation reaction occurring in that region. However, the relaxation potential is still close to the one obtained in the previous steps (2.4 – 2.45 V; equilibrium potential of ‘step 1’ and ‘step 2’), thus related, once again, to the same electrochemical reactions, *i.e.* oxidation of middle-to-high-order polysulfides in the presence of  $\text{Li}_2\text{S}$ . These data seems to show that, in the third part of the charge curve (‘step 3’), the kinetic of the overall oxidation reaction decreases notably as compared with those observed during ‘step 2’. The kinetic of the overall oxidation reaction could limit the  $\text{Li}_2\text{S}$  oxidation into medium-to-high-order polysulfides ( $\text{S}_4^{2-}$ ,  $\text{S}_6^{2-}$ , etc.), which requires a large overpotential. On the contrary, the electrochemical couples dictating the electrode potential are still the same: the oxidation of mid-to-high-order polysulfides.

At the end of charge (‘step 4’), the relaxation potential is about 2.8 V, which is consistent with the oxidation of  $\text{S}_8^{2-}$  and formation of  $\text{S}_8$ . However, the electrochemical production of sulfur is shifted to higher potential (up to 3.6 V) under the current flow, due to polarization effect. The coexistence of both  $\text{Li}_2\text{S}$  and  $\text{S}_8$  at the end of charge cannot be excluded, as  $\text{Li}_2\text{S}$  oxidation limits the overall process, and oxidation of soluble polysulfides is expected to be notably easier.

Moreover, these results clearly eliminate the possible presence of the parasitic reactions, which might have explained the potential evolution observed. Indeed, the equilibrium potential corresponds, in all charge process, to expected polysulfide oxidation.

The GITT measurements also provide qualitative information on the cell kinetics, by evaluating the different relaxation profiles between each current pulse. Selected relaxation profiles obtained for different states of charge are shown in Figure 4-12.

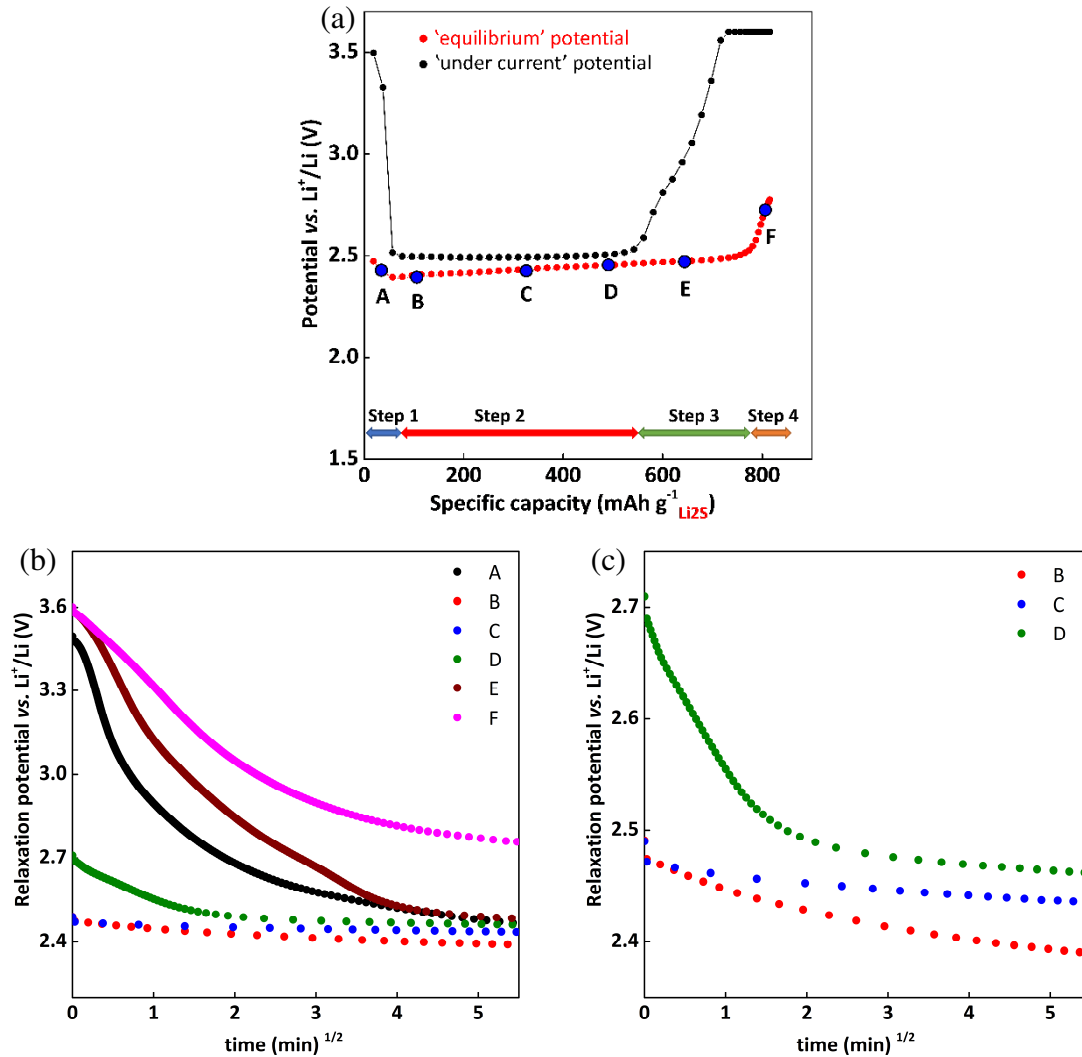


Figure 4-12. Comparison of selected relaxation curves profiles ( $t_{\text{relax}} = 30 \text{ min}$ ) obtained with GITT measurement on  $\text{Li}/\text{Li}_2\text{S}$  cell (b,c). The points at which relaxation potential evolution was selected, correspond to different steps during the charge process, as marked on the voltage curve (a).

During 'step 2', where the overpotential is very low, the potential evolution with the time during relaxation is coherent with a process limited by diffusion process, *i.e.* linear potential evolution as a function of time  $- t^{1/2}$  (point B, C and partially point D on Figure 4-12b). In the other parts of the curve (point A, E, F), the relaxation of the potential vs. time ( $t^{1/2}$ ) is more complex. This complexity could be associated with the fact that several electrochemical

reactions are involved in the process, *i.e.* reactions with both soluble and insoluble species, chemical reactions (disproportionation) coupled with electrochemical ones and thus, the potential is fixed by several redox couples, which may change with the time.

During discharge, the features of a classical Li/S cells are visible, and the GITT data are similar to the one reported in the literature<sup>31</sup>. In higher discharge plateau region, the potential is dictated by the equilibrium between soluble polysulfides and solid sulfur. In the sloping region between the two plateaus (2.4 – 2.1 V, second part of ‘step 5’ on Figure 4-11), only soluble polysulfides are present and fix the potential. Starting from the beginning of lower discharge plateau (‘step 6’), the relaxation potential is always at the same value of ~ 2.1 V. This potential is thus dictated by the presence of solid  $\text{Li}_2\text{S}$  phase and soluble polysulfides all along the plateau. The overpotential is low, in accordance with the reduction of nanometric sulfur and soluble species. A large overpotential is visible at the end of discharge, where the electrode is getting passivated by  $\text{Li}_2\text{S}$  material. These observations are fully coherent with the results of Li/S system, presented in further chapters: 5 and 6.

The second charge is significantly different from the first one, and much lower polarizations are observed. The first lower potential pseudo-plateau at about 2.1 V to 2.3 V, is the one of a classical Li/S cells, with the relaxation potential lower as the one obtained during the first charge (*i.e.* 2.4 V – 2.5 V). Such potential evolution shows clearly that the electrochemical processes in the presence of nanometric and micrometric  $\text{Li}_2\text{S}$  compound are not the same. During the second charge, the potential in the region marked as ‘step 7’ (Figure 4-11) is fixed by  $\text{S}^{2-}/\text{S}_2^{2-}/\text{S}_4^{2-}$  redox couples. At higher state of charge, two pseudo-plateaus are clearly distinguished, *i.e.* at 2.4 V (named as ‘step 8’) and 2.6 V (‘step 9’), which can be related to the oxidation of  $\text{S}_6^{2-}$  to  $\text{S}_8^{2-}$  along with some contribution from the shuttle mechanism, and the oxidation of  $\text{S}_8^{2-}$  to  $\text{S}_8$ , respectively.

#### **4.2.4.c) Addition of the polysulfides to the electrolyte**

In the previous paragraph it was proposed, that the first oxidation step of  $\text{Li}_2\text{S}$  is accompanied by the formation of medium-to-long chain polysulfides, such as  $\text{S}_4^{2-}$  and  $\text{S}_6^{2-}$ . As a matter of fact, we wanted to verify if the addition of soluble lithium polysulfides to the electrolyte when building the cell, can facilitate the activation process of  $\text{Li}_2\text{S}$ , thanks to:

- The addition of possible intermediate species available for  $\text{Li}_2\text{S}$  material
- The possible promotion of disproportionation reactions, and possible  $\text{Li}_2\text{S}$  chemical reaction with soluble polysulfides

For that reason, three coin cells, with electrodes having similar masses (~ 1.47  $\text{mg}_{\text{Li}_2\text{S}} \text{cm}^{-2}$  ↔ 1.71  $\text{mAh cm}^{-2}$ ) and coming from the same electrode sheet (70/20/10 wt% =

$\text{Li}_2\text{S}^*/\text{SuperP}^\circ/\text{PVdF}$ ) were prepared. During coin cell fabrication, 20  $\mu\text{L}$  of ‘catholyte’ solution (0.25 M  $\text{Li}_2\text{S}_6$  + 0.1 M  $\text{LiNO}_3$  + 1 M  $\text{LiTFSI}$  in  $\text{TEGDME}/\text{DIOX} = 1/1$  vol) was poured onto  $\text{Li}_2\text{S}$  electrode, which was then covered with separators. Additional 130  $\mu\text{L}$  of standard electrolyte (without polysulfides) was added and all was covered with  $\varnothing$  14 mm disk of Li. Before charging, the cells were left for 0 h, 10 h and 20 h at OCV, in order to verify eventual influence of possible reaction between  $\text{S}^{2-}$  (present in the electrode) and long polysulfides  $\text{S}_6^{2-}$ ,  $\text{S}_4^{2-}$  (existing in the ‘catholyte’) due to disproportionation reactions prior to charge. After that, the coin cells were cycled at  $C/20$ , with initial cut-off voltage of 3.8 V. The current was calculated with respect to the capacity of  $\text{Li}_2\text{S}$  electrode only ( $\sim 86 \mu\text{Ah cm}^{-2}$ ). The contribution of the ‘catholyte’ to the total capacity of the cell was calculated, taking into consideration the oxidation reaction of  $\text{Li}_2\text{S}_6$  to form  $\text{S}_8$ . Based on number of electrons exchanged in this reaction, a value of 0.27 mAh was found, which is  $\sim 10\%$  of the  $\text{Li}_2\text{S}$  electrode’s capacity. We can consider thus, that the majority of the capacity in this cell configuration ( $\text{Li}_2\text{S} + \text{Li}_2\text{S}_6$  addition) originated from  $\text{Li}_2\text{S}$  electrode. Figure 4-13 shows initial cycle voltage profile<sup>†</sup> of the cells with added polysulfides, in comparison to the polysulfides-free one.

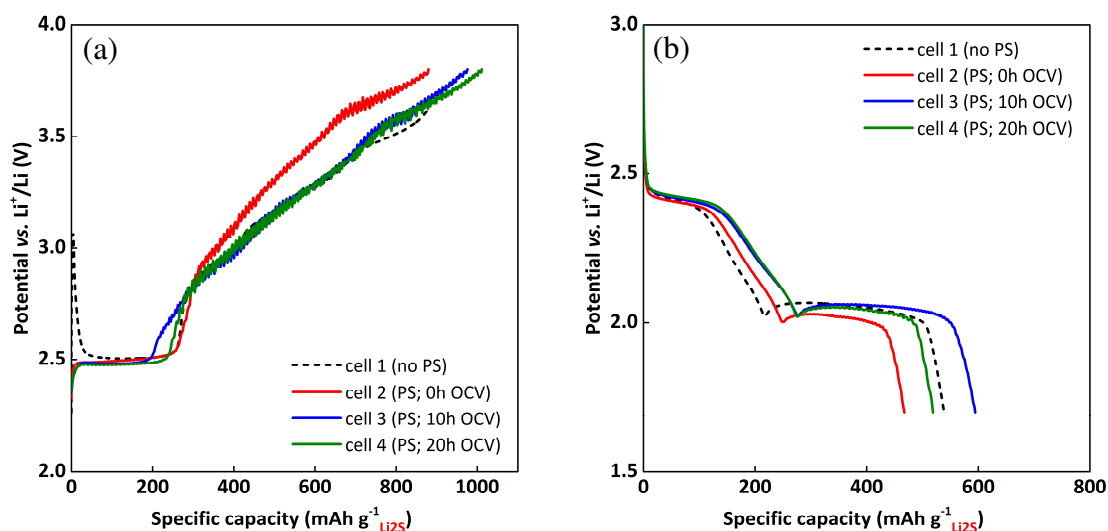


Figure 4-13. Initial charge (a) and discharge (b) voltage profiles obtained from galvanostatic cycling of  $\text{Li}_2\text{S}$ -based electrodes cycled vs. Li at  $C/20$  rate, with addition of ‘catholyte’ solution (20  $\mu\text{L}$  of 0.25 M  $\text{Li}_2\text{S}_6$  + 0.1 M  $\text{LiNO}_3$  + 1 M  $\text{LiTFSI}$  in  $\text{TEGDME}/\text{DIOX} = 1/1$  vol) to the standard electrolyte. Different times before launching the GCPL were applied (*i.e.* 0 h, 10 h, 20 h). Average  $\text{Li}_2\text{S}$  electrode loading is  $\sim 1.47 \text{ mg}_{\text{Li}_2\text{S}} \text{ cm}^{-2} \leftrightarrow 1.71 \text{ mAh cm}^{-2}$ . For comparison, standard Li/ $\text{Li}_2\text{S}$  cell without any polysulfides is shown (black dashed line).

We can clearly notice complete disappearance of the potential barrier, which would indicate that, indeed, addition of polysulfides to the electrolyte may suppress the need for ‘activation’

\* The batch of  $\text{Li}_2\text{S}$  was purchased from Alfa Aesar, giving the electrodes with less polarized initial charge.

† A noisy charge profile observed for some of the cells is the effect of the frequent temperature oscillation in the Arbin<sup>®</sup> battery cycler room.

step of  $\text{Li}_2\text{S}$ . This barrier, according to Belharouak<sup>139</sup>, is eliminated because of the synergetic presence of both: reduced ( $\text{Li}_2\text{S}$ ) and oxidized ( $\text{Li}_2\text{S}_6$ ) forms, but no clear explanation of this synergetic effect was given.

The presence of soluble polysulfides permits the initial activation/oxidation processes to occur without a large overpotential. A very stable 2.5 V plateau is observed for all cells, corresponding to the presence of long polysulfides in  $\text{Li}/\text{Li}_2\text{S}$  cell. With or without ‘catholyte’, the same potential for this charging plateau is obtained, which indicates that the same electrochemical processes may occur. It seems then, that the potential of the 2.5 V plateau is fixed by the oxidation of long polysulfides, which are initially present: (i) because of the ‘catholyte’ addition (for cells 2, 3 and 4) or (ii) which are obtained during the ‘activation’ process of  $\text{Li}_2\text{S}$  electrode in a ‘classical’ cell (cell 1). Afterwards, if the oxidation of solid  $\text{Li}_2\text{S}$  is not a limiting process, *i.e.* there is enough polysulfides species in the solution to consume electrons injected during the charge, the potential is constant and fixed by these long chain polysulfides introduced with the ‘catholyte’ or produce by  $\text{Li}_2\text{S}$  oxidation. After that, when the overall oxidation reaction starts to be limited by the oxidation of solid  $\text{Li}_2\text{S}$  (still present in the electrode), a large overpotential is observed, as previously discussed.

Concerning the different times applied before starting the charge process (*i.e.* monitoring of OCV during 10 h and 20 h), the direct reaction of  $\text{S}_6^{2-}$  with  $\text{S}^{2-}$  seems not to have any influence on the potential profile. Then, the kinetic of the direct reaction of long polysulfides and  $\text{S}^{2-}$  to form mid-order polysulfides, if it occurs, has a slow rate. Indeed, even 20 h at OCV did not permit to increase the capacity, thus did not permit to increase the concentration of soluble polysulfides due to disproportional reaction between  $\text{S}^{2-}$  and the ‘catholyte’. These observations concerning the disappearance of activation barrier in the presence of polysulfides is in agreement with the literature reports<sup>242,243</sup>, with pioneer work of Cui *et al.*<sup>141</sup>.

While the addition of polysulfides plays a beneficial role on the activation of  $\text{Li}_2\text{S}$  electrode, the cycling results upon prolonged tests at  $C/20$  did not show any improvement of coulombic efficiency, neither of the capacity retention. Indeed, capacity retention over 60 cycles was found to be very similar for the cells with or without addition of ‘catholyte’. This observation is in contradiction to some reports<sup>141,240</sup>, but is still coherent with the explanation we proposed for the first charge process of  $\text{Li}_2\text{S}$ .

#### 4.2.5. Determination of the cycling potential window

On the contrary to the sulfur positive electrode, system based on  $\text{Li}_2\text{S}$  positive electrode is far less studied, and by the time we started to work with  $\text{Li}_2\text{S}$  material, much less information about  $\text{Li}_2\text{S}$  could have been found in the literature. Therefore, a simple step, however an important one, was to determine correctly the potential limits during cycling. We have previously seen that the initial charge is a particular process which differs significantly from

the other cycles. Therefore, in this paragraph we separately discuss the cycling conditions required for the initial charge and further cycles.

#### 4.2.5.a) Initial charge

As previously discussed, the charging of  $\text{Li}_2\text{S}$  electrode starts with an ‘activation’ barrier resulting in a fast increase of the voltage value (unless polysulfides are added to the electrolyte). The maximum of this potential jump may differ from one electrode to another, and is strongly related with the electrode morphology (the size of particles, the quality of contact between  $\text{Li}_2\text{S}$ /carbon, etc.) and the fact that the  $\text{Li}_2\text{S}$  oxidation is a difficult process. For a given C-rate (C/20, see Figure 4-9), variety of maximum potential values (between 3.2 V – 4.0 V) during the activation step were recorded. As the height of this activation step could not be predicted before the cell started to run, it was therefore important not to limit the cell potential during first moments of charge (up to  $\sim 50 \text{ mAh g}^{-1}$ ), and to give enough freedom in terms of potential for the system to pass through this barrier. An example is illustrated on Figure 4-14, which presents the GCPL results of two cells, aimed to be identical ( $\text{Li}_2\text{S}$  electrodes punched out from the same electrode sheet with very low active material loading of  $0.89 \text{ mg}_{\text{Li}_2\text{S}} \text{ cm}^{-2}$ ), and both cycled at C/10 in potential window 3.0 V – 1.7 V. It can be noticed that during initial activation step, potential of cell 2 (in red) rises up to 2.97 V and quickly drops down to 2.5 V, forming a stable plateau. Cell 1 (in black), however, reached the 3.0 V cut-off voltage limit already at the beginning (black arrow on Figure 4-14). As a matter of fact, the activation of  $\text{Li}_2\text{S}$  active material could not proceed properly in this case, and the cell did not display any capacity. Indeed, some literature reports show relatively poor performances of commercial  $\text{Li}_2\text{S}$  powder.

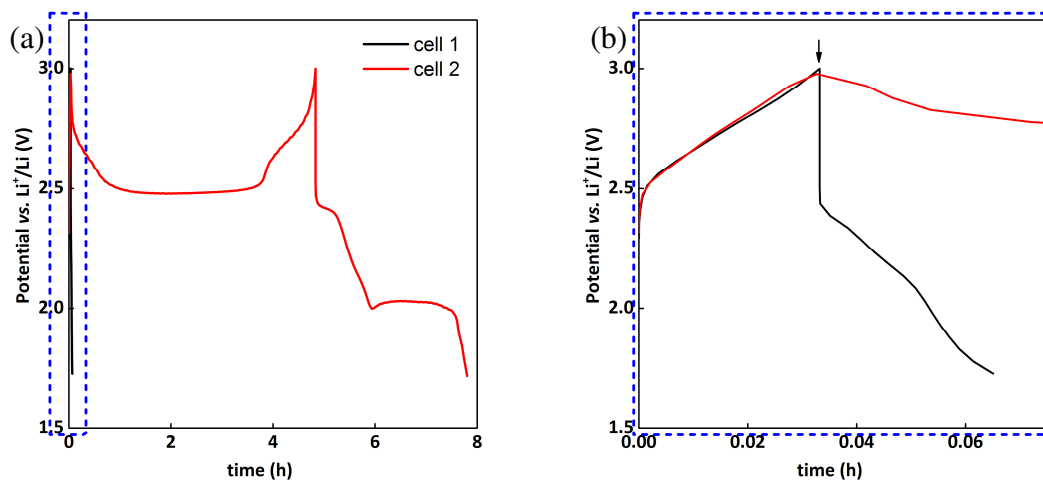


Figure 4-14. An illustrative example of the importance of the initial moments of charging (up to  $\sim 50 \text{ mAh g}^{-1}$ ) and the eventual influence of cut-off voltage limitations. Both  $\text{Li}_2\text{S}$  electrodes, with active material loading of  $0.89 \text{ mg}_{\text{Li}_2\text{S}} \text{ cm}^{-2}$ , were cycled at C/10, in the potential window 3.0 V – 1.7 V (a). Zoomed image (b) clearly shows the consequence of early end of charge due to too low cut-off limit during activation step (in black).

It is thus probably related to the fact that  $\text{Li}_2\text{S}$  did not get activated because of too low potential limitation at the initial step. To avoid such problems, a slight modification of cycling program had to be carried out, without limiting the potential of the cells at the beginning. Another practical solution could also be the systematic addition of very little amount of polysulfides during cell fabrication, to completely eliminate the activation barrier. This alternative, however, was not implemented as a standard solution in this study.

We have previously seen that the voltage shape of the initial charge (Figure 4-9) does not impact the cycling performances, and further cycle curves show the typical feature of a typical Li/S cell. GITT experiments proved that a large overpotential is not related with parasitic reactions, but is due to a difficult process of solid  $\text{Li}_2\text{S}$  oxidation. Following this direction, we compared several coin cells' results, in which different voltage profiles as well as variety of initial charge capacity values were obtained (Figure 4-15). The results presented here come from the  $\text{Li}_2\text{S}$  electrodes punched out ( $\varnothing$  14 mm disks) from two batches of electrode sheets (with reference composition 70/20/10 wt%), cycled at C/20 or C/10 rates, and using different potential limits.

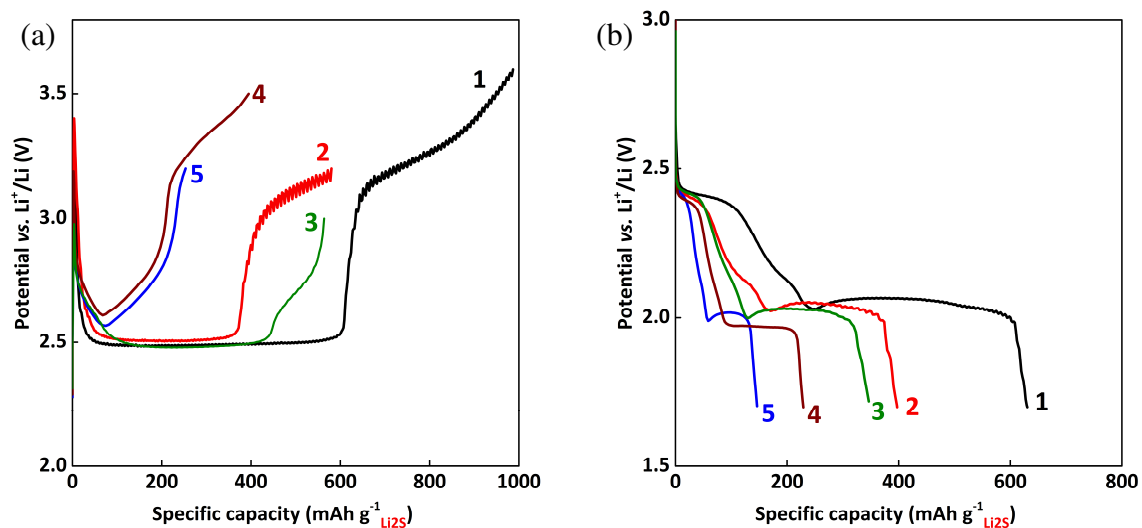


Figure 4-15. Examples of various different initial charge (a) and corresponding discharge (b) voltage profiles obtained when cycling  $\text{Li}_2\text{S}/\text{SuperP}^{\text{®}}/\text{PVdF} = 70/20/10$  wt% electrodes vs. Li at C/20 either C/10 rate, with a different initial charge voltage limits. All selected electrodes come from two batches of the electrode sheet, aimed to be identical. Active mass loading is varying between 0.77 to 1.73  $\text{mg}_{\text{Li}_2\text{S}} \text{cm}^{-2}$ .

The numbers are given for simplicity, indicating the highest (1) to the lowest (5) capacity values obtained, both for charge and discharge. A linear relation was found between the charge vs. discharge capacity, as shown on Figure 4-16a, which proves (again) that the initial charge effectively impacts the following discharge capacity.

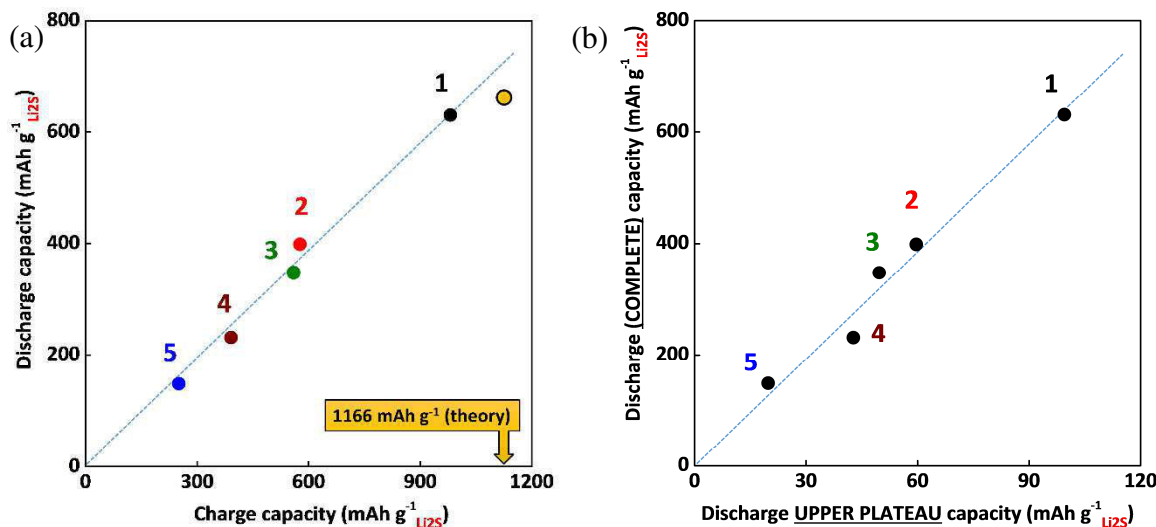


Figure 4-16. Linear relation between charge and discharge capacities, obtained for the Li/Li<sub>2</sub>S cells, presented in Figure 4-15 (a). Discharge capacity as a function of the capacity related with the upper voltage plateau, *i.e.* amount of sulfur reduced (b).

However, we can also notice that, even if reaching the full charge capacity (yellow dot added on Figure 4-16a), a discharge capacity value is not any more on the straight extrapolation line. The reason for that may be related with other limitations appear, which prevent from obtaining full discharge capacity values in return, *i.e.* higher than 650 – 700 mAh g<sub>Li<sub>2</sub>S</sub><sup>-1</sup>. This limitation seems to be very similar to the one already described in previous chapter, when working with sulfur cathode. Such linear evolution of charge-discharge relation also proportionally affects the irreversible capacity, calculated as capacity<sub>charge</sub> – capacity<sub>discharge</sub>. At that moment, a clear explanation cannot be given for this observation. Such proportionality seems to indicate that, whatever the amount of oxidized species is produced, only ~ 65 % is reduced afterward. This evolution cannot be related to some surface area problem, but perhaps more to the loss of active mass in the electrolyte, or to the large pulverization of the electrode. Other investigations must be performed in order to propose a full explanation.

When comparing the shape of the discharge curves (Figure 4-15b), and more particularly the length of higher discharge plateaus, we can notice that cell #1, which presents the highest charge capacity, shows the longest upper discharge plateau, which is usually attributed to the reduction of solid sulfur to high-order polysulfides. We estimated the capacity corresponding to the upper discharge plateau (*i.e.* reduction of solid sulfur) for each of five cells presented and plotted *vs.* complete discharge capacity obtained. A very linear relation was found (Figure 4-16b), meaning that indeed, a final discharge capacity is proportional to the amount of sulfur being reduced during the upper discharge plateau. In order to confirm the hypothesis of sulfur formation at the end of charge, an *in situ* and *operando* XRD was performed on the Li<sub>2</sub>S electrodes, and obtained results are discussed in section 4.2.8.

The necessity of applying higher voltage limit to perform Li<sub>2</sub>S activation, especially for the cells with higher initial overpotential, can also be shown by the CV experiments. Figure 4-17



shows the CV profile of a cell showing a large initial overpotential. In this case, the 1<sup>st</sup> oxidation step had to be performed up to 4.0 V. The  $\text{Li}_2\text{S}$  oxidation peak is visible at 3.65 V. Another little anodic peak at 3.9 V is observed, which may be related with a slight electrolyte degradation. Further cycles, carried out in the potential window of 1.7 V – 2.8 V, show expected peak positions (as previously demonstrated on Figure 4-8). We can consider that complete activation of  $\text{Li}_2\text{S}$  took place during the first cycle, since the charge capacity reached almost complete theoretical value (97 %).

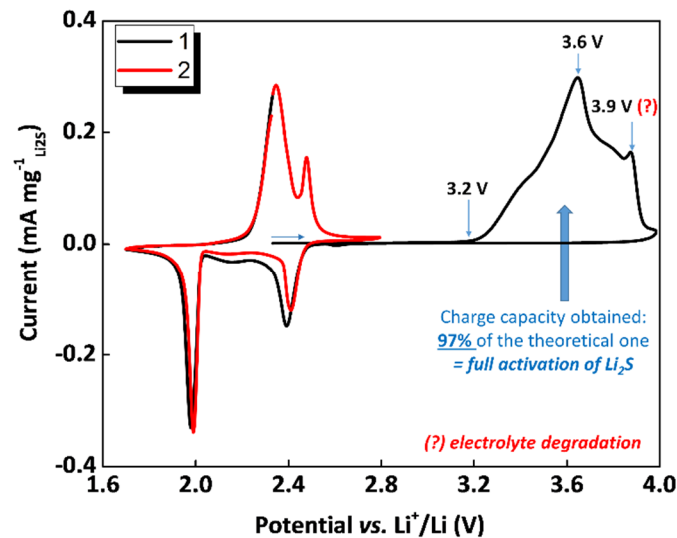


Figure 4-17. Cycling voltammetry curve of  $\text{Li}_2\text{S}/\text{SuperP}^{\text{®}}/\text{PVdF}$  electrode (with  $\text{Li}_2\text{S}$  loading of  $1.14 \text{ mg cm}^{-2}$ ) performed at  $0.03 \text{ mV s}^{-1}$  scan rate. An example where ‘highly polarized’  $\text{Li}_2\text{S}$ -based electrode requires higher than usual cut-off voltage potential for complete active material oxidation, *i.e.* in this case initial charge was performed up to 4.0 V.

On the contrary, if the initial oxidation is stopped at a lower potential, (in this example: 3.6 V; Figure 4-18), incomplete activation of  $\text{Li}_2\text{S}$  electrode is obtained, and the initial discharge capacity is lower. In the next cycle, residual  $\text{Li}_2\text{S}$  material is oxidized (the activation peak is nevertheless shifted to lower potential values), and following discharge capacity is noticeably increased.

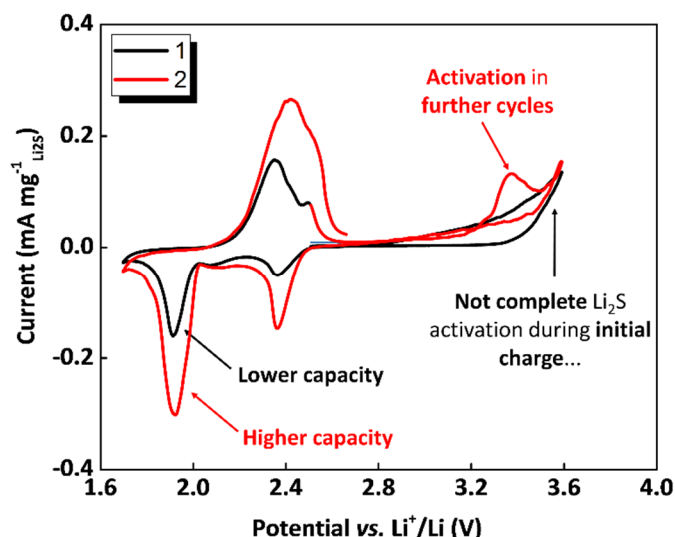


Figure 4-18. Cycling voltammetry curve of  $\text{Li}_2\text{S}/\text{SuperP}^\circledast/\text{PVdF}$  electrode (with  $\text{Li}_2\text{S}$  loading of  $1.64 \text{ mg cm}^{-2}$ ) performed at  $0.05 \text{ mV s}^{-1}$  scan rate. An example where ‘highly polarized’  $\text{Li}_2\text{S}$ -based electrode requires higher than usual cut-off voltage potential for complete active material oxidation, but where the potential limit did not allow for complete oxidation of  $\text{Li}_2\text{S}$ , *i.e.* in this case initial charge was performed to 3.6 V.

However, in typical galvanostatic cycling, if initial activation is not completely finished due to the unsuitable potential limit, the residuals of non-oxidized  $\text{Li}_2\text{S}$  will never participate to the electrochemical processes in the further cycles in the full extend (some reaction of soluble polysulfides with  $\text{Li}_2\text{S}$  may occurs, but the kinetic of this reaction seems to be very slow). Indeed, the charge potential limit is usually set to 2.8 V or 3.0 V for prolonged cycling (and not to 3.6 V – 4.0 V), in order to prevent strong electrolyte degradation and fast capacity fading. As a matter of fact, if not oxidized during the initial charge, some part of  $\text{Li}_2\text{S}$  material may remain unutilized on the electrode during prolonged cycling.

Therefore, it is considered to perform initial charge up to much higher potential limits as compare to a classical  $\text{Li}/\text{S}$  system, to provide the most complete oxidation of active material. Charging to 4.0 V seems to be lately reported in the literature<sup>152</sup>. However, an electrolyte stability should then be strongly taken into consideration, and ethers are known to be stable until  $\sim 3.9 \text{ V}$  (vs.  $\text{Li}^+/\text{Li}$ )<sup>45</sup>. Aurbach *et al.*<sup>143</sup> claimed that even initial charge up to 4.0 V results in complete electrolyte degradation. In our work, for some of the electrodes (mostly the ones with huge initial overpotential), a 4.0 V potential limit was applied. Being aware of the risk of the electrolyte degradation, we never had any evidence of detrimental effect when using such high potential (4.0 V) for the initial charge, regarding the electrolyte decomposition (and/or possible aluminum corrosion with  $\text{LiTFSI}$ ). Capacity retention for the cell activated to 4.0 V was in fact the same as when lower cut-off potential values were used, with better discharge capacity values overall.

Another solution could be to perform initial charge at very slow rate in order to facilitate  $\text{Li}_2\text{S}$  activation. In such situation, very high potential cut-off values could be avoided. Nevertheless,

a slow C-rate (like C/100) may also increase the shuttle phenomenon directly from the initial cycle, thus resulting in a poor coulombic efficiency and large irreversible capacity. When applying such procedure to some of our electrodes, *i.e.* slow initial charge at C/100 followed by faster cycling at C/10, having always the same charge potential limit of 3.0 V, very similar capacity retention, as previously presented on Figure 4-6, was obtained.

#### 4.2.5.b) Initial discharge

Based on previous discussion concerning  $\text{LiNO}_3$  reduction on the carbon surface at the potentials lower than 1.7 V (refer to section 3.4.3), and supported by literature data<sup>177,178</sup> it was then relatively easy to determine the lower potential limit for  $\text{Li}_2\text{S}$  electrodes which was set up to 1.7 V. Figure 4-19 shows the galvanostatic cycling results of two  $\text{Li}/\text{Li}_2\text{S}$  cells, both containing  $\text{LiNO}_3$  additive in the electrolyte, cycled at C/100 and discharged to different potential limits. When discharging to 1.3 V, a characteristic reduction tail of  $\text{LiNO}_3$  appears at about 1.5 V, significantly contributing to the total discharge capacity (in blue square). In parallel to the consumption of  $\text{LiNO}_3$  additive, this undesirable reduction leads to a remarkable overpotential at the beginning of the following charge, probably due to the deposition of a passivation layer on the electrode surface coming from  $\text{LiNO}_3$  reduction<sup>243</sup>.

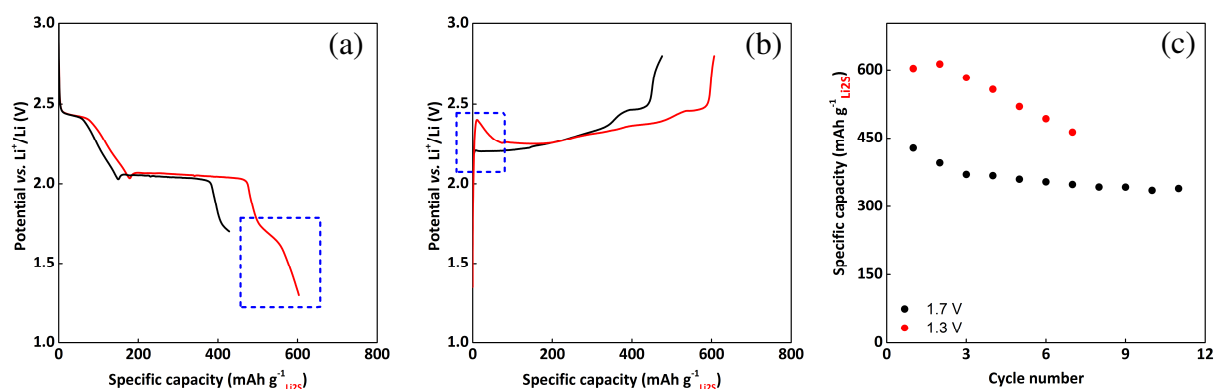


Figure 4-19. Differences in the voltage profiles when discharging to 1.3 V (in red) or 1.7 V (in black), in the presence of a  $\text{LiNO}_3$  electrolyte additive.  $\text{Li}_2\text{S}$  electrodes have an active material loading of 1.68 and 2.14  $\text{mg}_{\text{Li}_2\text{S}} \text{cm}^{-2}$ , and cycled vs. Li at C/100.

These findings were also observed by performing CV tests on similar two  $\text{Li}/\text{Li}_2\text{S}$  cells (different discharge cut-off voltage, electrolyte containing  $\text{LiNO}_3$  additive), as shown on Figure 4-20. When discharging to 1.3 V (Figure 4-20a), a third reduction peak is clearly visible at 1.56 V (blue arrow). During subsequent oxidation, the anodic peak is shifted to higher potential values (2.58 V; green arrow). Only one anodic peak is observed during 10 following cycles, with the intensity significantly decreasing upon cycling. The peak at 1.56 V associated to  $\text{LiNO}_3$  reduction vanishes after 4 – 5 cycles, but the anodic peak is nevertheless systematically shifted to higher potential values ( $\sim 2.5$  V) at each cycle, as compared with the cell discharged

to 1.7 V (oxidation peak at  $\sim 2.35$  V; Figure 4-20b). Thus, cycling tests down to 1.5 V or even lower should be avoided, because of the  $\text{LiNO}_3$  irreversible decomposition and the enhanced passivation of the  $\text{Li}_2\text{S}$  electrode at the end of discharge, as well as the lack of stability and reversibility.

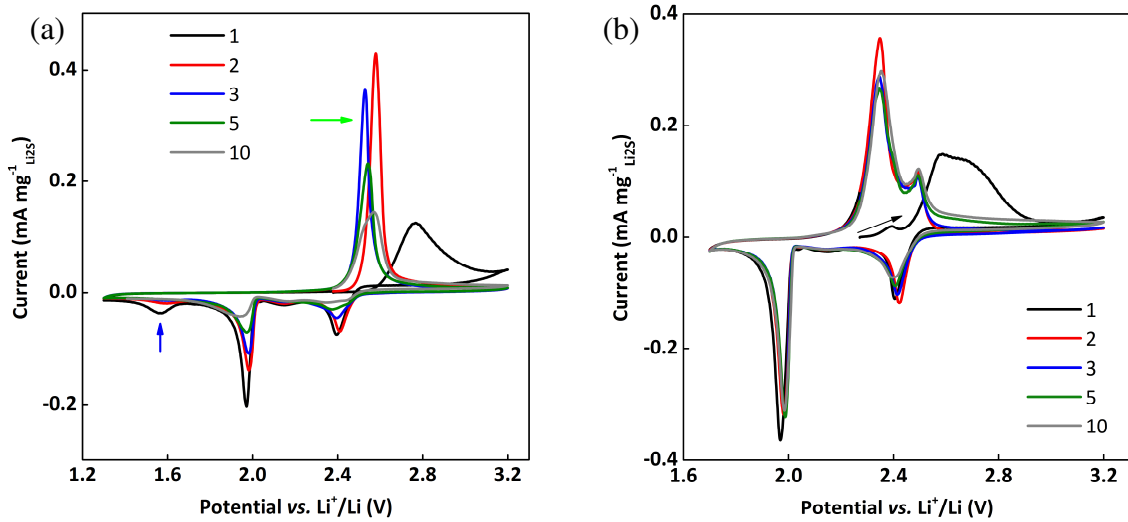


Figure 4-20. CV curves of  $\text{Li}/\text{Li}_2\text{S}$  cells containing  $\text{LiNO}_3$  as an electrolyte additive, and scanned at  $0.03 \text{ mV s}^{-1}$  with different potential windows:  $3.2 \text{ V} - 1.3 \text{ V}$  (a) and  $3.2 \text{ V} - 1.7 \text{ V}$  (b).  $\text{Li}_2\text{S}$  electrodes have the same reference composition (70/20/10 wt%) and an active material loading of  $1.35$  and  $0.86 \text{ mg}_{\text{Li}_2\text{S}} \text{ cm}^{-2}$ .

#### 4.2.6. C-rate influence

To study the evolution of cycling performances at different currents,  $\text{Li}_2\text{S}$  electrodes were carefully selected to have the most similar weights ( $\sim 1.14 - 1.27 \text{ mg}_{\text{Li}_2\text{S}} \text{ cm}^{-2}$ ). They were then cycled at following C-rates over prolonged cycling: 1C, C/5, C/10, C/20 and C/100, using the same potential window:  $3.8 \text{ V} - 1.7 \text{ V}$  and  $2.8 \text{ V} - 1.7 \text{ V}$ , for initial and following cycles, respectively. Also extreme currents (equivalent of C/200 and C/1000) were applied in order to observe the evolution of initial activation barrier with the regime. Finally, rate capability tests were also performed. Figure 4-21 shows the voltage profiles obtained during initial cycles. When increasing the current, the polarization obviously increases, since  $\text{Li}_2\text{S}$  is a very poor electronic and ionic conductor. As previously proposed, the oxidation reactions that occur along the  $\sim 2.5 \text{ V}$  plateau (clearly visible at low C-rate) is associated with the oxidation of both  $\text{Li}_2\text{S}$  and high-order polysulfides. At high current rate (*i.e.* 1C), oxidation reactions induce a large polarization and the cut-off voltage is reached easily.

Moreover, the characteristic potential barrier, visible at the beginning of charge (Figure 4-21c), is reduced with the decreased current, as expected. At extremely low current ( $\sim \text{C}/1000$ ), oxidation reaction is no more limited by the kinetics, and the thermodynamic potential is obtained. In a large C-rate range (up to C/10), a similar potential plateau is obtained, very close

to 2.5 V. This allows to point out that the electrochemical reaction fixing the potential during initial charge is all the time the same, even at very low C-rate.

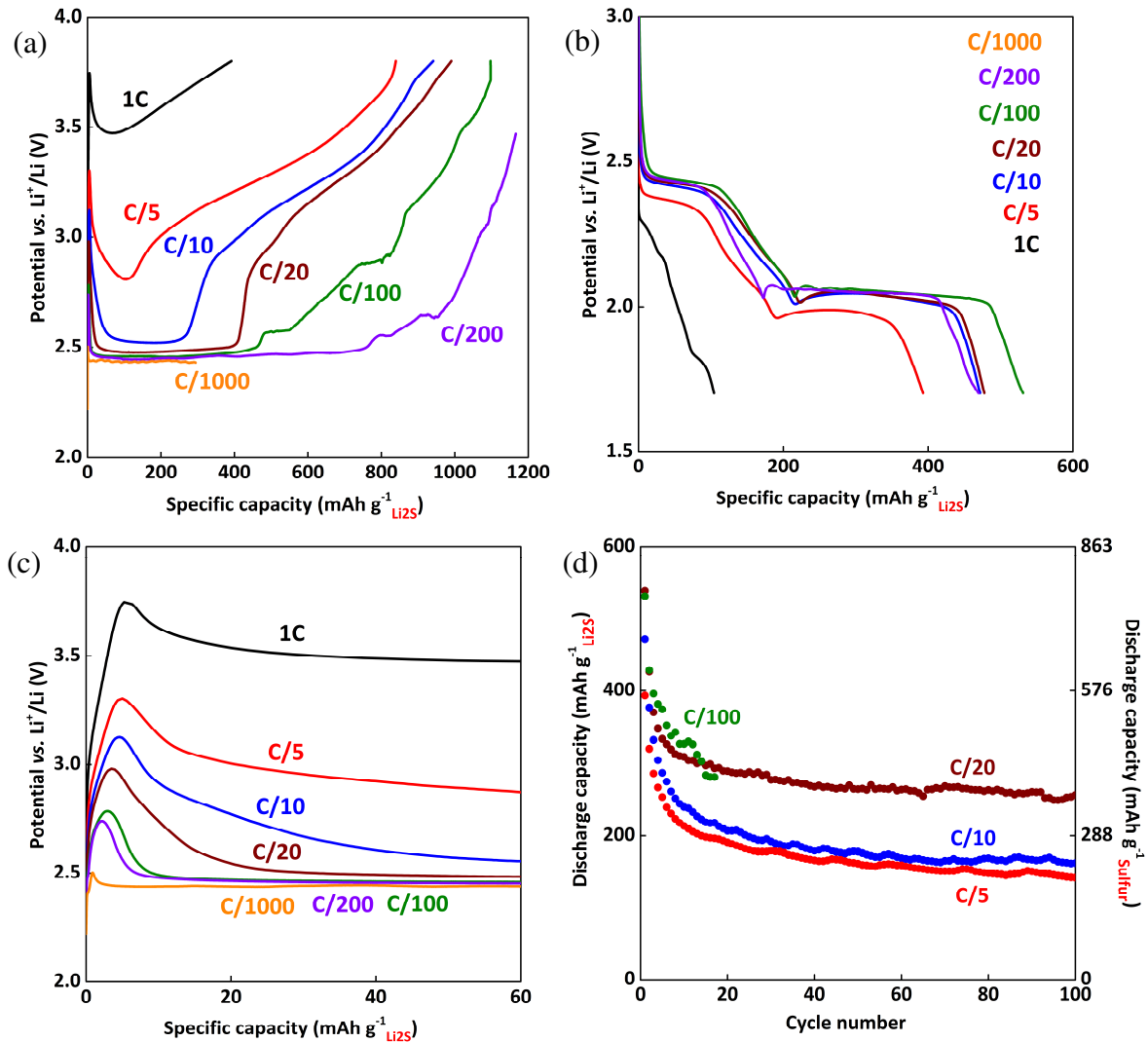


Figure 4-21. Cycling performances of  $\text{Li}_2\text{S}$  electrodes of similar loading ( $\sim 1.14 - 1.27 \text{ mg}_{\text{Li}_2\text{S}} \text{ cm}^{-2}$ ), cycled at different C-rates: 1C, C/5, C/10, C/20, C/100, C/200 and C/1000. Initial charge voltage (a) and corresponding discharge profiles (b). A zoomed image on activation potential barrier (c) and capacity retention during 100 cycles, except for lower C-rates (d).

Indeed, the potential is too high to be fixed by  $\text{Li}_2\text{S}/\text{Li}_2\text{S}_2/\text{Li}_2\text{S}_4$  redox reactions, as typically observed for Li/S cell and further cycles of Li/ $\text{Li}_2\text{S}$  cell. The initial charge capacity values are proportional to the current applied, and are: 1097, 991, 941, 840 and 392  $\text{mAh g}^{-1}$  for C/100, C/20, C/10, C/5 and 1C, respectively, except for C/1000, where strong shuttle mechanism is visible from the beginning. The full capacity ( $1166 \text{ mAh g}^{-1}$ ) is obtained for the C/200 rate. On the other hand, lower is the C-rate, more pronounced would be the shuttle phenomenon, which in turn influences the irreversible capacity ( $\text{Capacity}_{\text{charge}} - \text{Capacity}_{\text{discharge}}$ ).

Corresponding capacity retention of the cells cycled at different C-rates (C/100, C/20, C/10 and C/5) is shown on Figure 4-21d. For all four cells, typical trend of Li/S battery retention can

be seen, *i.e.* rapid capacity fading during initial cycles followed by rather stable value. Discharge capacity values recorded at 50<sup>th</sup> cycle are 264, 170 and 161 mAh g<sup>-1</sup> for the cells cycled at C/20, C/10 and C/5 respectively.

### 4.2.7. Strategies for the improvement

In the previous sections we saw that by performing the charge to higher voltage limit or using very low currents (C/100), it is possible to reach almost complete theoretical capacity of  $\text{Li}_2\text{S}$  (1166 mAh g<sup>-1</sup>). However, both of these solutions are subjected to some risks, like possible electrolyte degradation (when charging to 4.0 V) or strong shuttle phenomenon (when applying very low C-rates). Moreover, several electrodes exhibited very strong initial polarization and not-reproducible shape of charge voltage (lack of reproducibility of the electrodes). One of the alternative solutions would thus consist in performing the particle size reduction in order to provide better contact between  $\text{Li}_2\text{S}$ /carbon. For that purpose, mechanical ball-milling on  $\text{Li}_2\text{S}$  powder was performed, and the effect of such treatment was investigated.

Even if high charge capacity values could be reached, discharge capacities of  $\sim 650 \pm 50$  mAh g<sup>-1</sup> could be obtained at most. One of the reason for incomplete discharge capacity might arise from the lack of (i) sufficient conductive and accessible surface area for ‘welcoming’ all solid discharge products and/or (ii) not sufficient accessibility of created polysulfides to the whole conductive surface present in the electrode. In this manner, a proposed solution consists in utilizing a carbon-based current collector paper (NwC) for  $\text{Li}_2\text{S}$  positive electrode, which has previously proven to have very beneficial effect, when applied for sulfur positive electrode.

#### 4.2.7.a) The effect of a ball-milling

Two ball-milling equipments, different in terms of energy, were used for grinding  $\text{Li}_2\text{S}$  powder with SuperP<sup>®</sup>, aiming for particle size reduction together with providing better contact between both powders. In both cases, the final electrode composition was designed to be 70/20/10 wt% (‘reference’ composition). No additional grinding with SuperP<sup>®</sup> in a mortar was performed after the ball-milling and prior to electrode preparation. Therefore, the ball-milling containers were filled directly with appropriate amounts of powders inside the glove box, *i.e.* 0.6 g of  $\text{Li}_2\text{S}^\ddagger$  and 0.17 g of SuperP<sup>®</sup>. The containers were then tightly closed to provide hermetical sealing and avoid any contact of  $\text{Li}_2\text{S}$  powder with air during the ball milling process (performed outside the glove box). Planetary ball milling (RETSCH) was done in a 50 mL

---

<sup>‡</sup> Since two ball-milling treatments were not performed in the same interval of time, batch of active material powder was not the same.  $\text{Li}_2\text{S}$  purchased from Sigma Aldrich was used for planetary ball milling, while  $\text{Li}_2\text{S}$  from Alfa Aesar was used for high energy ball milling.

container (inner part of the jar made from agate), with 20 agate beads of  $\text{\O} 6$  mm, as shown on the Figure 4-22a,c. Metallic rings permitted to close tightly the filled container. The more energetic ball-milling (Spex 8000M Mixer) was performed using a 50 mL container and 2 beads of  $\text{\O} 10$  mm, both made of Ytria-Stabilized Zirconia (YSZ), as shown on Figure 4-22b,d. The jar was filled with powders inside the glove box, and then tightly sealed with a black insulating tape. In the further discussion, abbreviations like  $\text{Li}_2\text{S}_{\text{planetary}}$  and  $\text{Li}_2\text{S}_{\text{energetical}}$  is used for simplicity and clarity.

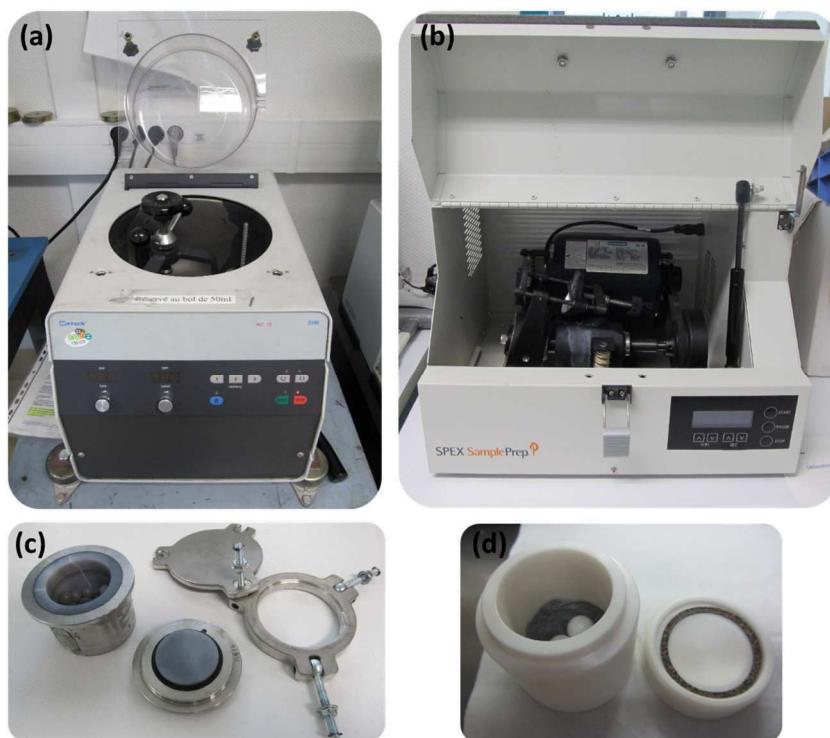


Figure 4-22. Ball-milling equipment and corresponding 50 mL containers used for ball-milling of  $\text{Li}_2\text{S}$  powder with SuperP<sup>®</sup>, in a ratio leading to final electrode composition  $\text{Li}_2\text{S}/\text{SuperP}^{\text{®}}/\text{PVdF} = 70/20/10$  wt%. Planetary ball milling performed in RETSCH (a) in the jar made from agate, filled with 20  $\text{\O} 6$  mm agate beads (c). High-energy ball milling performed in Spex 8000M Mixer (b), in a jar filled with two beads of  $\text{\O} 10$  mm, both made of YSZ (d).

The ball-milling sequence was similar for both sessions, and was as follow: three times milling for 1 h, with 30 min of break in between the cycles, to avoid overheating. ‘Planetary’ milling was performed at 300 rpm, while the speed of the ‘energetic’ one could not be really controlled. The first trial of ‘planetary’ milling was performed in dry conditions (*i.e.* with only  $\text{Li}_2\text{S}$  and SuperP<sup>®</sup>). However, it appeared that the powders stuck to the walls of the container and were difficult to retrieve. Thus, in the next step, another trial was performed with addition of cyclohexane ( $\sim 2.2$  mL added to 0.6 g of  $\text{Li}_2\text{S}$  and 0.17 g of SuperP<sup>®</sup> powders). The ‘energetic’ ball-milling was done in dry conditions, to avoid eventual solvent leakage during milling, since the hermetical protection was hand made with a tape.

After ball milling, the jars were brought back to the glove box, and ball-milled  $\text{Li}_2\text{S}/\text{SuperP}^{\text{®}}$  mixtures were recuperated. Concerning the milling with cyclohexane, the jar was left inside

the oven (integrated to the glove box) for solvent evaporation and drying of the powders, before electrode preparation. Little amounts of both samples were taken for further analysis by XRD and SEM, while the rest was used for electrode preparation, by adding PVdF binder solution and additional volume of NMP, mixing all manually with spatula and coating the inks on the Al current collectors.

SEM photos of both samples, obtained by wet ‘planetary’ ball-milling (SEM photos of ‘dry’ ball-milled powders gave similar results as the ‘wet’ one, thus not presented in this paragraph) and dry ‘energetic’ milling, are presented on Figure 4-23. It can be seen that, after less energetic milling (Figure 4-23a,b)  $\text{Li}_2\text{S}$  particles diminish to 1-5  $\mu\text{m}$  (initially  $\sim 10 - 20 \mu\text{m}$ ). However, it seems that the contact between  $\text{Li}_2\text{S}$ /carbon was not improved so much as compared with a hand milling protocol in a mortar, as the particles of active material were not completely/uniformly covered by nano-spheres of carbon.

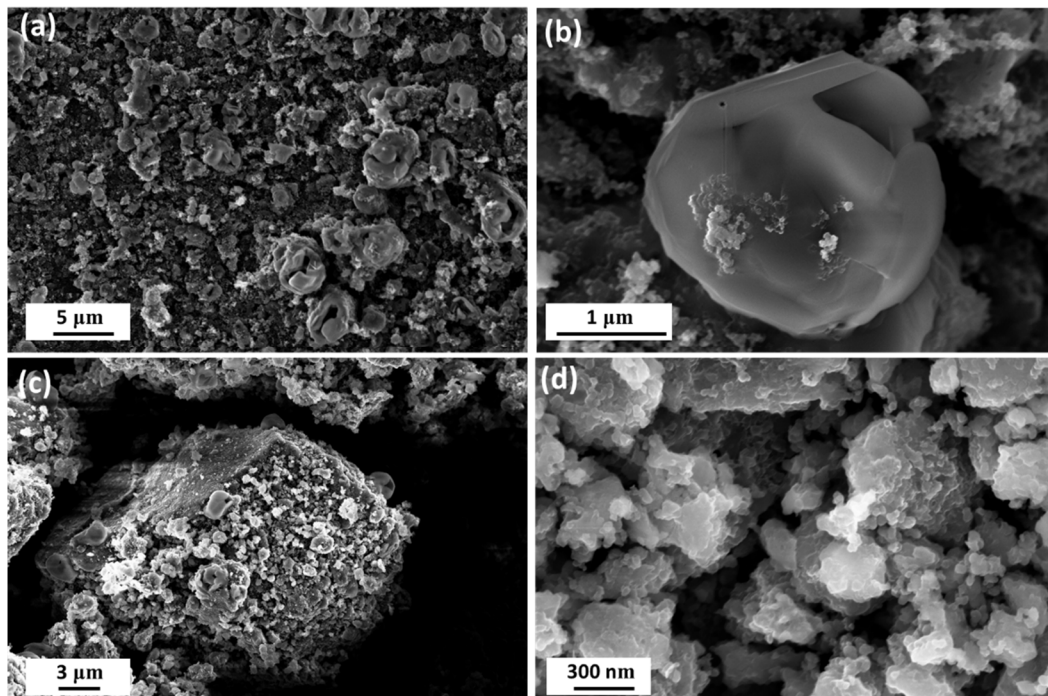


Figure 4-23. SEM photos of  $\text{Li}_2\text{S}/\text{SuperP}^{\text{®}}$  powder mixture obtained through: planetary (a, b) and high energetically (c, d) ball milling.

On the other hand, when applying highly energetic milling, it is clear that  $\text{Li}_2\text{S}$  particle size is decreased, even nano-particles are observed. However, milling protocol also provokes strong agglomeration of carbon particles, leaving  $\text{Li}_2\text{S}$  particles ‘naked’ around the agglomerates. Moreover, a visual observation of such highly ball-milled powders as compared with  $\text{Li}_2\text{S}/\text{SuperP}^{\text{®}}$  grinded manually in a mortar, shows significant differences in terms of color: a deep black color is obtained after ball milling<sub>energetical</sub>, while a greyish color is obtained for handy mixed powders. Changes in the volume of the powders were also evidenced after being



recuperated into a beaker. Indeed, the volume of ball-milled<sub>energetical</sub> powders was much lower, indicating that the carbon particles might have got compacted.

XRD patterns (Figure 4-24) of corresponding ball-milled powders and as received  $\text{Li}_2\text{S}$  show the peaks attributed to the cubic  $\text{Li}_2\text{S}$ . Slight broadening of the peaks is observed for ball-milled powders, with a more pronounced effect for energetic milling, where nano- $\text{Li}_2\text{S}$  is formed. Little traces of  $\text{LiOH}$  are also found here (probably because the sample covering with Kapton<sup>®</sup> was not sufficiently air-tight).

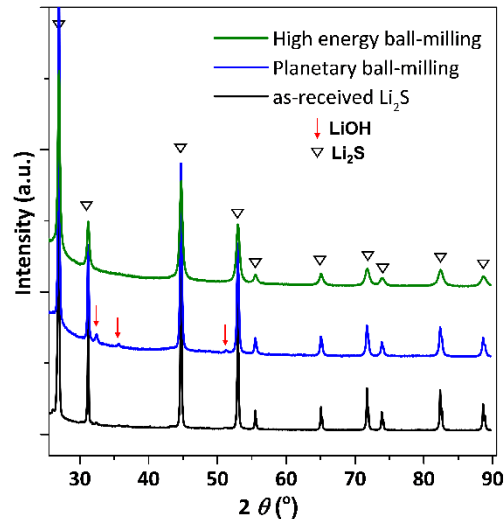


Figure 4-24. XRD patterns of  $\text{Li}_2\text{S}/\text{SuperP}^{\text{®}}$  ball-milled powders obtained through highly energetic (in green) and planetary (in blue) ball-milling. Pure as-received  $\text{Li}_2\text{S}$  is shown for comparison (in black). Traces of  $\text{LiOH}$  impurities can be also seen.

Galvanostatic cycling results of the electrode prepared with planetary ball-milled  $\text{Li}_2\text{S}/\text{SuperP}^{\text{®}}$  mixture did not show any significant improvement as compared with the manually grinded as-received  $\text{Li}_2\text{S}$  powder. Initial charge shows high polarization as well, while the capacity retention during prolonged cycling is also similar to what was previously demonstrated.

Cycling behavior of the electrode prepared from energetically ball-milled  $\text{Li}_2\text{S}/\text{SuperP}^{\text{®}}$  powders are presented on Figure 4-25, in comparison with an electrode made in parallel from as-received  $\text{Li}_2\text{S}$  powder which was manually grinded. Only initial cycle profiles are compared.

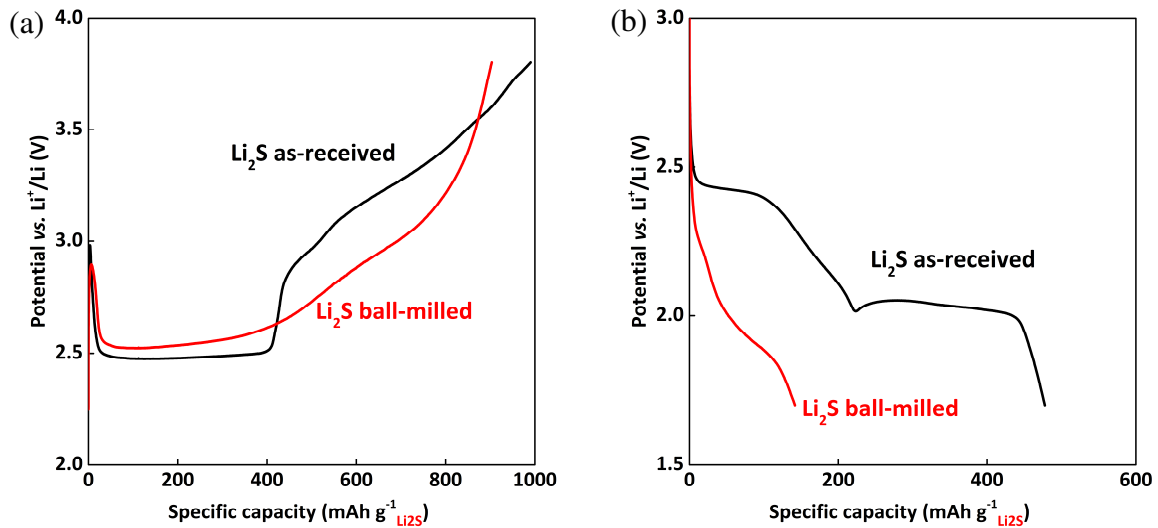


Figure 4-25. Initial charge (a) and discharge (b) voltage profiles obtained through galvanostatic cycling of  $\text{Li}_2\text{S}/\text{SuperP}^\circledast/\text{PVdF}$  electrode, made from ‘energetically’ ball-milled mixture (in red), and cycled vs. Li at C/20 rate (potential window 3.8 V – 1.7 V). For comparison, electrode made from as-received  $\text{Li}_2\text{S}$  grinded manually with SuperP<sup>®</sup> (in black). Both electrodes were prepared with the same active material loading:  $1.14 \text{ mg}_{\text{Li}_2\text{S}} \text{ cm}^{-2}$ .

It can be seen that similar charge capacities are obtained for both electrodes, even if the voltage profiles are somehow different. After the ‘activation step’, the ball-milled sample exhibits a progressive increasing in the polarization of the ‘pseudo plateau’ of charge. The drastic difference, however, and rather coherent with SEM observations, is visible in discharge values (Figure 4-25b), *i.e.* ‘ball-milled<sub>energetical</sub>’ powders exhibit very low capacity. As no additional carbon additive was incorporated to the electrodes during the ink preparation, and if carbon powder got agglomerated during the ball milling process, there may not be enough carbon nano-particles to create an efficient conductive network in the electrode, and to assure the charge process and the cohesion of the electrode, which is based on the binder adsorption on carbon particles. BET should be performed in the future for confirmation of this failure mechanism.

To conclude, ball milling of commercial powder, even if decreasing the particles size, did not provide any enhancement of the electrochemical response. On the contrary, too energetic ball-milling provokes a strong carbon agglomeration, and gives the opposite from expected effect, *i.e.* no practical discharge capacity can be recuperated.

#### 4.2.7.b) Carbon-based current collector (NwC)

In this part, we investigate the beneficial effect of NwC current collector, and how it can affect the cycling of  $\text{Li}_2\text{S}$  electrodes. For best comparison, the same slurry (70/20/10 wt% =  $\text{Li}_2\text{S}/\text{SuperP}^\circledast/\text{PVdF}$ ;  $\text{Li}_2\text{S}$  used as-received) was prepared, and two electrodes were casted

either on NwC (procedure described in section 4.2.1.a) or on Al current collectors. Figure 4-26 shows the initial cycle profiles of NwC and Al-based electrodes.

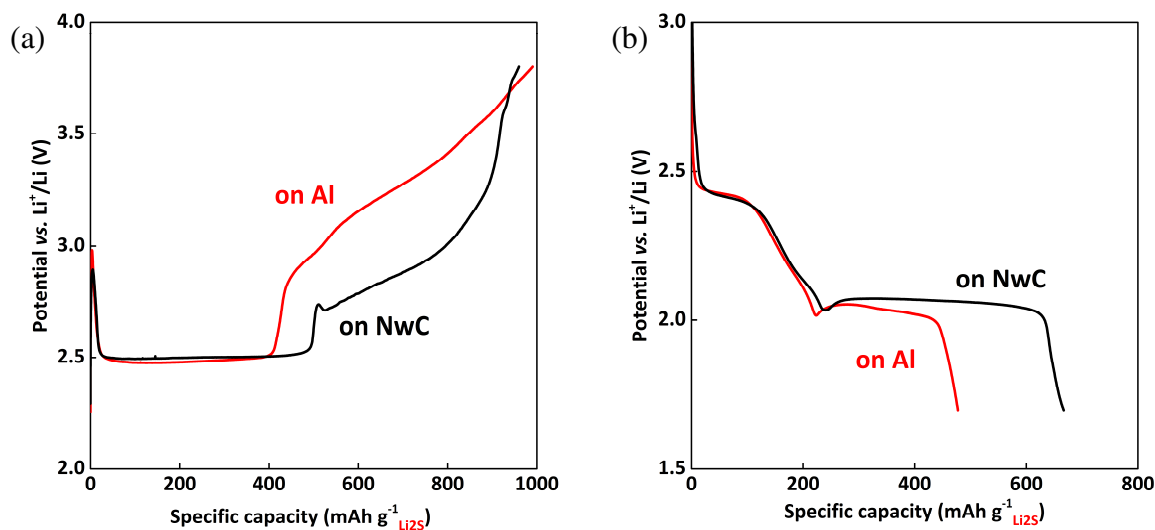


Figure 4-26. Initial charge (a) and discharge (b) voltage profiles obtained through galvanostatic cycling of  $\text{Li}_2\text{S}/\text{SuperP}^\circ/\text{PVdF}$  electrodes coated on two different collectors: classical Al foil (in red) and NwC (in black), made from as-received  $\text{Li}_2\text{S}$  powder. Both electrodes cycled vs. Li at  $C/20$  in the potential window of 3.8 V – 1.7 V for the initial cycle, followed by 2.8 V – 1.7 V. Electrodes were prepared with different active material loadings, *i.e.* 1.14 and 3.59  $\text{mg}_{\text{Li}_2\text{S}} \text{cm}^{-2}$  for Al- and NwC-based, respectively.

The resulting loadings of these two particular electrodes were not the same (1.14  $\text{mg}_{\text{Li}_2\text{S}} \text{cm}^{-2}$  and 3.59  $\text{mg}_{\text{Li}_2\text{S}} \text{cm}^{-2}$  for Al and NwC-based electrode respectively), since in general NwC permits to obtain much higher loadings due to the partial ink penetration into the collector porosity. During charge, similar charge capacities are obtained, even slightly higher for the Al-based cell. The voltage profiles are similar too, with an ‘activation’ step visible at the beginning of charge, followed by a plateau at 2.5 V vs.  $\text{Li}^+/\text{Li}$ , and then a continuous increase of the potential up to the cut-off limit (3.8 V). This observation means that NwC, with its 3D conductive network, does not provide a visible benefit regarding the kinetic of the initial charge.  $\text{Li}_2\text{S}$  is able to oxidize anyway, no matter the current collector (Al or NwC), if the charge is performed at reasonably slow rate ( $C/20$ ) and until quite high voltage value (3.8 V). Capacities relatively close to the theoretical one are obtained (990  $\text{mAh g}^{-1}$  for Al, 960  $\text{mAh g}^{-1}$  for NwC). However, more significant difference is seen for the discharge. Higher capacity is obtained with NwC collector, which may be associated with the fact that NwC fibers also offer a conductive surface area (even if extremely low, since only 7.3  $\text{cm}^2$ , but easily accessible) for  $\text{Li}_2\text{S}$  precipitation, as well as higher amount of electrolyte can be trapped inside the electrode porosity (80 %), permitting to improve the formation of  $\text{Li}_2\text{S}$  and the dimensional stability of the current collector as previously discussed for Li/S system (see chapter 3).

Figure 4-27 shows rate capability of the best performing NwC electrode, in comparison with Al-based one. The results should not strictly be taken for quantitative purposes, as the electrode loadings were not exactly the same. NwC-based electrode displays very high discharge

capacity at around  $430 \text{ mAh g}^{-1}$  after 80 cycles (or  $620 \text{ mAh}_{\text{sulfur}} \text{ g}^{-1}$ , when related to sulfur mass), and at moderate rates ( $C/20$ ,  $C/10$  and  $C/5$ ). We can also see that, at  $1C$ , the capacity is fading drastically, showing that such NwC-based electrodes are not optimal solutions for high power cycling *i.e.* long diffusion pathway, as it was already shown for ‘S-on-NwC’ composite electrodes in the previous chapter. However, once the current comes back to slower rates ( $C/10$  and  $C/20$ ), the capacity value rises up to  $430 \text{ mAh g}^{-1}$ .

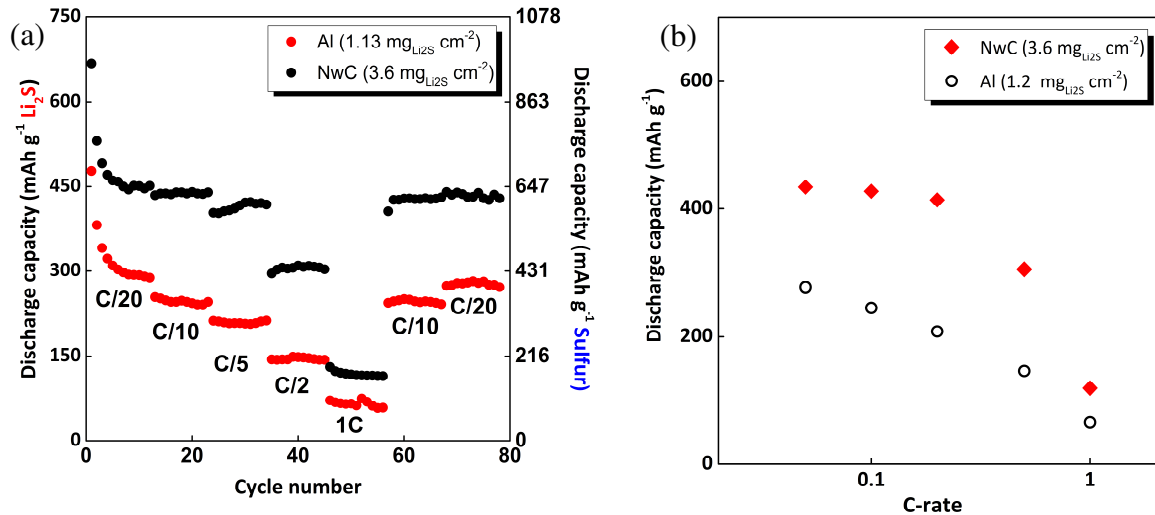


Figure 4-27. Rate capability tests performed on  $\text{Li}_2\text{S}$  electrodes coated on two different collectors: Al foil and NwC collector. Electrodes are of different active material loadings, *i.e.*  $1.14$  and  $3.59 \text{ mg}_{\text{Li}_2\text{S}} \text{ cm}^{-2}$  for Al- and NwC-based, respectively. The cycling procedure was applied *via* ‘symmetric’ methodology, *i.e.* equal C-rate during discharge and charge of the same cycle. Capacity retention (a) and average discharge capacity as a function of C-rate (b).

$\text{Li}_2\text{S}$  systems present the same behavior *vs.* C-rate (Figure 4-27b) as it was previously demonstrated for sulfur-based one, *i.e.* a slow capacity decrease up to  $C/5$ , while dramatically going down for higher C-rates. If we compare the results obtained for the two systems, on both, NwC and Al foil, in any cases the capacities at low rate are much higher for NwC based electrodes, although the capacity at higher C-rates are almost the same.

It has been demonstrated that application of carbon based current collector to the electrode structure may significantly increase the electrode loading, while still offering much better electrochemical performances as compare to the Al counterpart electrodes. Obtained capacity values if presented in respect to sulfur weight, are very promising (an example from Figure 4-27a: 80<sup>th</sup> cycle displays the capacity of  $430 \text{ mAh g}_{\text{Li}_2\text{S}}^{-1}$ , which is an equivalent of  $620 \text{ mAh g}_{\text{Sulfur}}^{-1}$ ).

### 4.2.8. *In situ* and *operando* XRD – Li<sub>2</sub>S structural changes upon cycling

In the previous section, we had an overview on the electrochemical behavior of Li<sub>2</sub>S electrodes, and how different parameters/modifications could be tuned in order to improve the electrochemical response of Li<sub>2</sub>S electrodes. The literature concerning observation of Li<sub>2</sub>S electrodes evolution during cycling by XRD technique is not as abundant as for S<sub>8</sub> electrode. Scrosati *et al.*<sup>151</sup> performed *in situ* XRD tests during initial charge, and reported on almost complete vanishing of Li<sub>2</sub>S material. No evident proof of S<sub>8</sub> formation at the end of charge was given, but they ‘reasonably assumed’ that indeed, sulfur got created. On the contrary, Cui *et al.*, in their *in situ* XRD studies<sup>141</sup>, showed complete Li<sub>2</sub>S oxidation but no S<sub>8</sub> appearance. Manthiram *et al.*<sup>153</sup> reported that some un-reacted residuals of Li<sub>2</sub>S were still present at the end of charge, however, they did not focus on observing sulfur formation.

Inspired by the literature data and trying to understand the behavior of Li<sub>2</sub>S active material upon cell operation, we focus in this part on the observation of the structural changes of Li<sub>2</sub>S material upon initial charge. The following points were questioned:

- If all Li<sub>2</sub>S active material is consumed during initial charge (?)
- If crystalline solid sulfur appears at the end of charge (?)
- If finally higher charge potential limit may influence any of these changes (?)

#### 4.2.8.a) Experimental details

The measurements were performed in synchrotron facility (ESRF-Grenoble). Li<sub>2</sub>S electrodes (3.0 x 1.8 cm) were prepared on NwC collector inside the glove box, according to the procedure described in 4.2.1.a). The mass of each NwC collector was precisely verified before electrode ink casting. The final electrodes composition was 70/20/10 wt% (Li<sub>2</sub>S /SuperP®/PVdF 6020) with average Li<sub>2</sub>S loading of ~ 2.2 mg<sub>Li<sub>2</sub>S</sub> cm<sup>-2</sup>. Preparation of pouch cells is precisely explained in chapter 5 (fully devoted to *in situ* XRD studies of Li/S cells). However, in case of Li<sub>2</sub>S-based pouch cells, all the fabrication steps were conducted in the glove box.

Two similar pouch cells were monitored in parallel during initial charge, thanks to the use of a movable sample holder. Such solution allowed displacing the cells so that the beam could penetrate through the two cells with the time interval of ~ 18 minutes. Two different charge cut-off voltage values were applied: 3.2 V and 3.6 V. Both cells were cycled at C/20 rate (i ~ 0.13 mA cm<sup>-2</sup>). XRD patterns were recorded at the wavelength of  $\lambda = 0.495936 \text{ \AA}$ .

### 4.2.8.b) *In situ* XRD – results

Figure 4-28 shows the initial charge profiles of both cells. For simplicity, only selected XRD patterns of cell 2 (charged to 3.6 V) are presented in this study, as pointed on the voltage profile (black dots). Corresponding X-Ray diffraction patterns are shown on Figure 4-29, with zoomed regions on selected Bragg peaks.

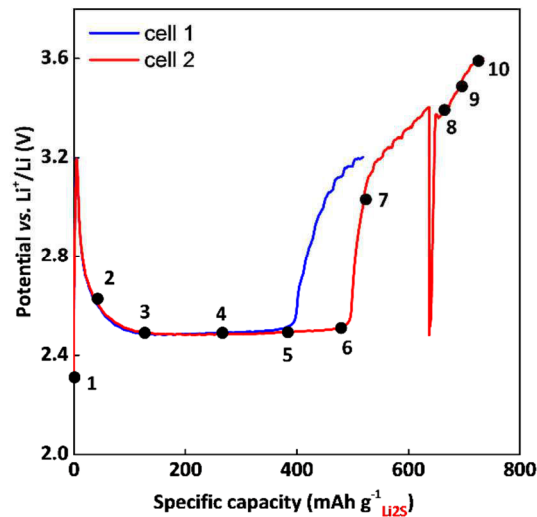


Figure 4-28. Initial charge voltage profile of two  $\text{Li}/\text{Li}_2\text{S}$  pouch cells studied during *in situ* and *operando* XRD measurements. Both  $\text{Li}_2\text{S}$  electrodes are coated on NwC collector and of similar  $\text{Li}_2\text{S}$  loading of  $2.2 \text{ mg}_{\text{Li}_2\text{S}} \text{ cm}^{-2}$ . The cells were initially charged at  $C/20$  until 3.2 V (cell 1) and 3.6 V (cell 2). Black dots correspond to selected XRD patterns presented on the Figure 4-29.

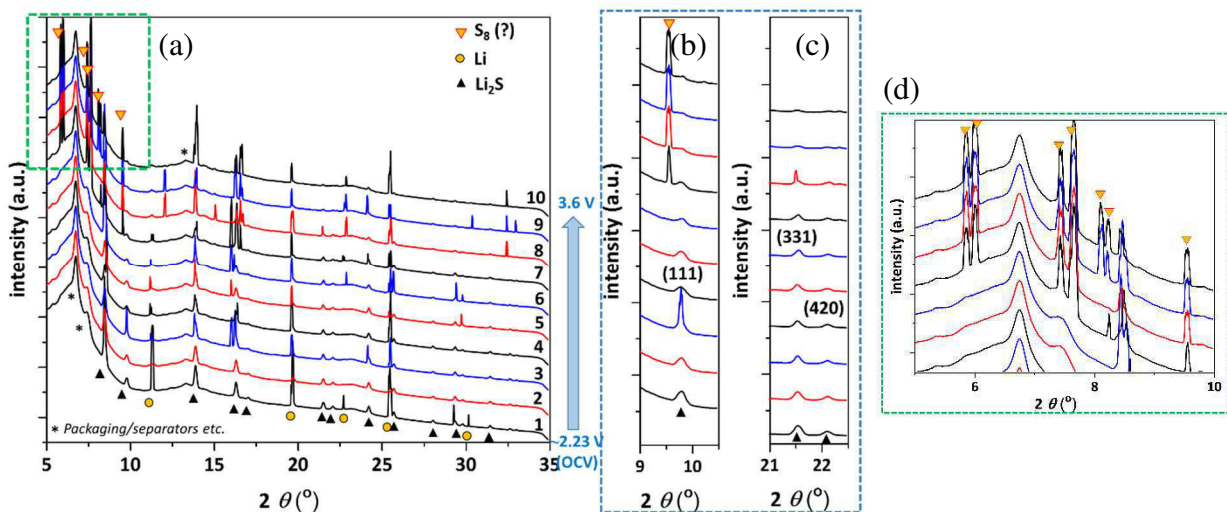


Figure 4-29. Selected XRD patterns recorded along initial charge to 3.6 V (a) and zoomed images on some  $\text{Li}_2\text{S}$  reflections (b,c), as well as on the peaks that appeared at the end of charge (d) – hypothetically elemental sulfur.

At the initial state, peaks of  $\text{Li}_2\text{S}$  (PDF-2; no. 00-023-0369) were clearly evidenced. Also some peaks of metallic lithium were detected. Upon cycling, some parasitic (or lithium) peaks were appearing randomly for some patterns, sometimes being detectable during few spectra, while sometimes only for one pattern.

We can clearly notice that, during charge, peaks of  $\text{Li}_2\text{S}$  were decreasing progressively. However, they did not disappear completely, even if the cell was charged to quite high potential of 3.6 V. Zoomed views on the peaks (111), (331) and (420) (Figure 4-29b,c) display the  $\text{Li}_2\text{S}$  evolution. Cell 1, charged to 3.2 V, showed very similar behavior and  $\text{Li}_2\text{S}$  was logically still present also at the end of charge. This may prove that, indeed, some parts of  $\text{Li}_2\text{S}$  (the quantity must be small, since the residual peaks are barely visible) was not oxidized during initial charge in our experimental conditions. On the other hand, the obtained capacity values, *i.e.* 737  $\text{mAh g}^{-1}$  and 520  $\text{mAh g}^{-1}$ , for the cells charged to 3.6 V and 3.2 V respectively, were relatively low as compared with the best performing  $\text{Li}_2\text{S}$  electrodes, presented previously in section 4.2.7.b (reaching 900 – 1000  $\text{mAh g}^{-1}$  during initial charge). The low initial charge capacity may explain the incomplete oxidation of  $\text{Li}_2\text{S}$  upon cycling. Indeed, the presence of  $\text{Li}_2\text{S}$  is coherent with our previously interpretation (section 4.2.4.b), which assumes the occurrence of  $\text{Li}_2\text{S}$  oxidation throughout the whole initial charging process, as the kinetic of  $\text{Li}_2\text{S}$  conversion may strongly limit the overall oxidation reaction.

Another point of this XRD study aimed at investigating the possible formation of elemental sulfur at the end of charge. *In situ* XRD patterns show the appearance of new peaks, starting from pattern #7 (Figure 4-29d), and marked with yellow triangles. However, no clear evidence of the formation of crystalline sulfur form could be performed through this experiment, as the position of these peaks did not match to any sulfur structure of our database. Thus, in order to complete these *in situ* XRD experiments, a supporting *ex situ* XRD study was performed.

#### 4.2.8.c) *Ex situ* XRD – supporting study

$\text{Li}_2\text{S}$  electrodes (the same as used in pouch cells for *in situ* XRD tests) were cut into  $\varnothing$  14 mm disks, and two coin cells (CR2032) were made. They were charged to 3.2 V and 3.6 V, with the same conditions as employed for *in situ* tests (C/20). Later on, these charged electrodes were recuperated from the coin cell, gently rinsed with DIOX (to minimize the dissolution of possibly formed sulfur) and XRD was recorded. The samples were not protected from the air, since the goal was to seek for sulfur. Figure 4-30 shows XRD patterns of charged electrodes. Peaks of monoclinic  $\beta$ -sulfur were detected, proving that indeed, solid sulfur is formed at the end of charge, in accordance with the potential reached by the cell, and as observed for Li/S cells (see chapter 5).

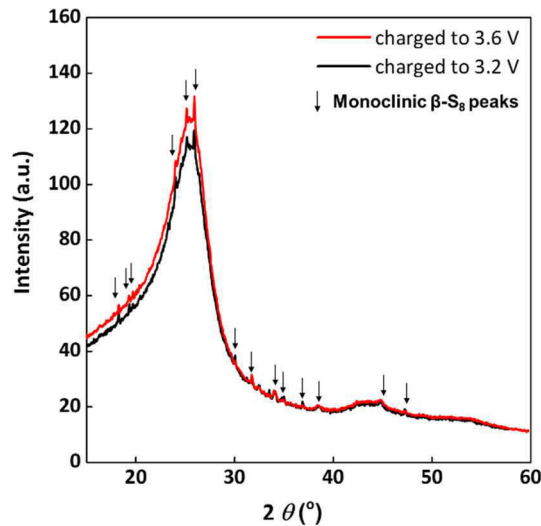


Figure 4-30. *Ex situ* XRD patterns recorded on pre-charged  $\text{Li}_2\text{S}$  electrodes (to 3.2 V and 3.6 V) in a coin cell configuration, at  $C/20$ . Electrodes were exactly the same as used for *operando* tests, thus of loading  $\sim 2.2 \text{ mg}_{\text{Li}_2\text{S}} \text{ cm}^{-2}$ . Peaks of monoclinic  $\beta$ -Sulfur can be clearly noticed (black arrows).

We do not, on the contrary to ESRF results, observe the peaks of  $\text{Li}_2\text{S}$  anymore. In the case of *ex situ* experiments, the charge capacity was much higher as the one obtained in the pouch cell configuration (Figure 4-31), thus all  $\text{Li}_2\text{S}$  material got oxidized and no traces were visible anymore.

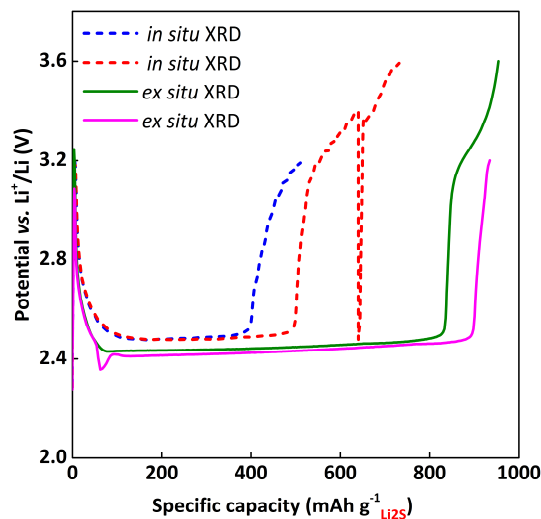


Figure 4-31. Initial charge voltage profile obtained from *ex situ* XRD (in coin cells), and compared with ESRF results obtained *in situ* in pouch cells.

This XRD study allowed to confirm the proposed mechanism for initial charge of  $\text{Li}_2\text{S}$ : if the initial charge capacity is relatively low ( $\sim 60\%$  of the theoretical value), an incomplete utilization of active material occurs. It is thus required to pay strong attention to the initial



charge, whether performing it to higher potential limits (like 3.8 V) or applying relatively low currents, in order to possibly activate all the  $\text{Li}_2\text{S}$  material present in the electrode.

### 4.2.9. Conclusions

$\text{Li}_2\text{S}/\text{Li}$  based cells exhibited the same behavior and the same limits as the  $\text{Li}/\text{S}$  cell. However, the electrochemical process of the first charge is largely different from the one obtained in  $\text{Li}/\text{S}$  cells, or during the following cycles of a  $\text{Li}/\text{Li}_2\text{S}$  cell. This large difference is attributed to the micrometric size of  $\text{Li}_2\text{S}$  starting material, in parallel of its low ionic and electric conductivities, which makes the first oxidation process very difficult. Indeed,  $\text{Li}_2\text{S}$  seems to be present during all charge period, which limits the overall oxidation reaction and induces large polarization in the main part of the charge curve. In accordance to the easy oxidation of soluble polysulfides, sulfur seems to be obtained early during charge, then  $\text{Li}_2\text{S}$  and  $\text{S}_8$  may be present together on the electrode upon charge.

## 4.3. Complete metallic Li-free cells

We have seen previously (section 3.5) that metallic lithium causes severe short circuits due to the dendrites growth. Development of  $\text{Li}_2\text{S}$  electrode allows to replace metallic Li by safer lithium metal-free negative electrodes, like Tin (Sn), graphite (C) or Silicon (Si). In this study, we aimed at combining the  $\text{Li}_2\text{S}$  cathode with both graphite and/or Si anodes.

Choosing to work with graphite - as the mostly used anode material in commercial Li-ion cells, very well-known for years and presenting a relatively stable discharge capacity upon cycling, brings additional challenges to be solved, *i.e.* electrolyte compatibility. It is commonly known that graphite material is getting exfoliated in ether-based electrolytes, the electrolytes of choice for classical  $\text{Li}/\text{S}$  batteries<sup>237</sup>. On the other hand, sulfur-based electrodes cannot be cycled with carbonate-based electrolytes, since polysulfides react with carbonyl groups.

Vinylene Carbonate (VC) is an additive commonly known for its beneficial impact on the formation of a stable SEI on the graphite electrode, and is usually added to carbonate-based electrolytes (such as in EC/PC) in the popular amount of ~ 2 vol%. We were therefore interested to test our 'reference' electrolyte composition (1M LiTFSI + 0.1M  $\text{LiNO}_3$  in TEGDME/DIOX 50/50 vol%) with this additive designed for graphite, and evaluate how it would affect the cyclability of both sulfur and graphite electrodes. Obtained results are presented further.

As previously said in the introduction of this chapter, silicon, being one of the most promising materials for negative electrode, was selected for the proof-of-concept of complete cell, *i.e.*  $\text{Li}_2\text{S}$  vs. Si.

### 4.3.1. Ether-based electrolyte with VC addition

In the first step, we investigated the effect of VC addition regarding the cycling performances of sulfur electrode. For this purpose, ‘reference’ sulfur electrodes were used, casted on aluminum foil (composition of 80/10/10 wt%; average sulfur loading of  $\sim 2.0 \text{ mg}_{\text{Sulfur}} \text{ cm}^{-2}$ ). VC was added to the reference electrolyte in two different amounts: 2 wt% and 0.24 wt%. Figure 4-32a presents the capacity retention of sulfur electrodes (vs. Li) cycled with three ether-based electrolytes: 0, 0.24 and 2 wt% of VC added to the ‘reference’ electrolyte (containing already  $\text{LiNO}_3$  additive).

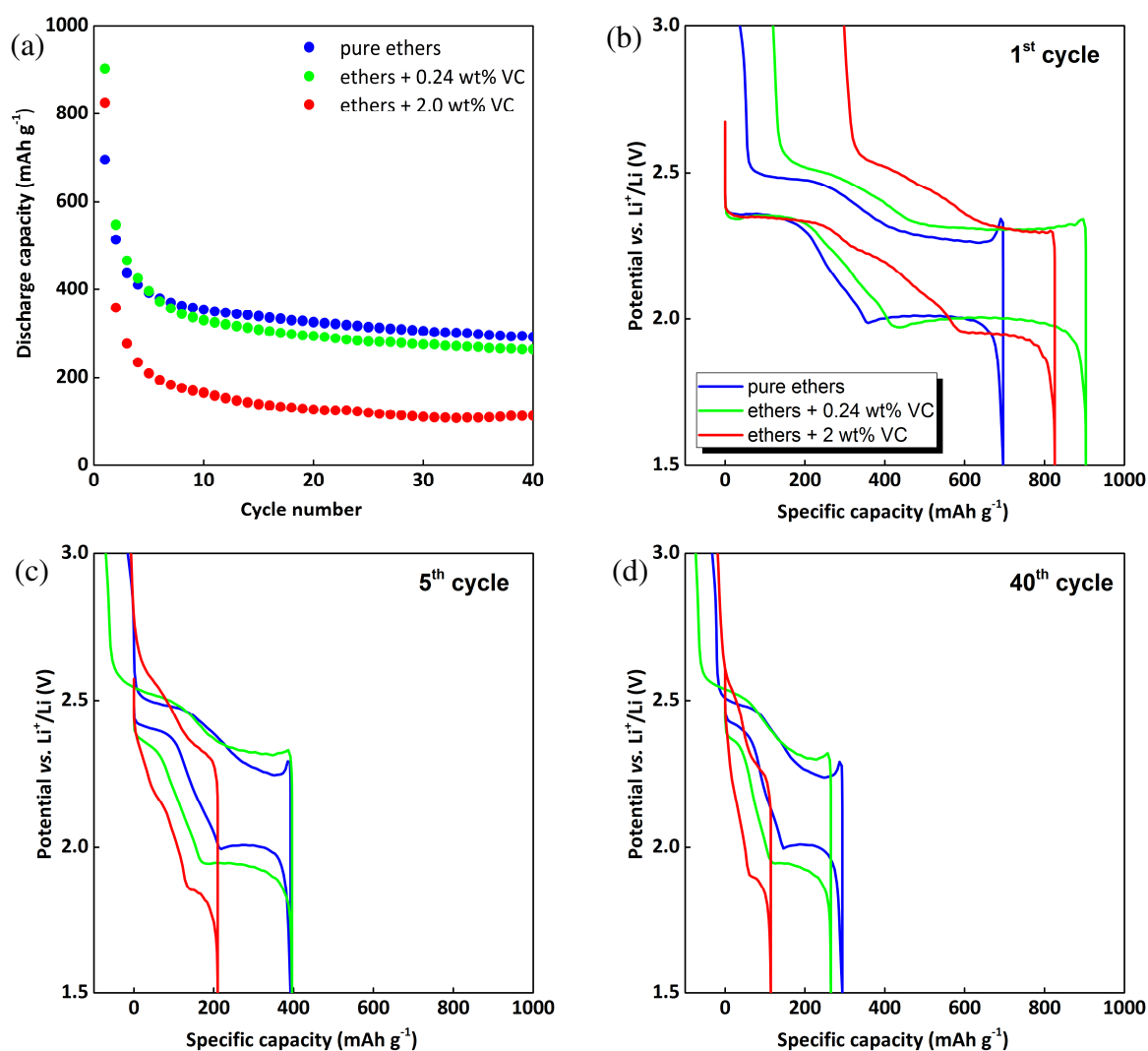


Figure 4-32. Capacity retention (a) over 45 cycles of three cells with classical sulfur electrode ( $\text{S}/\text{SuperP}^{\text{®}}/\text{PVdF} = 80/10/10 \text{ wt}\%$ ) cycled vs. Li at C/10. The cells contain ‘reference’ ether-based electrolyte (1M  $\text{LiTFSI} + 0.1\text{M LiNO}_3$  in  $\text{TEGDME}/\text{DIOX} = 1/1 \text{ vol}$ ) with different amounts of VC additive: 0 % (in blue), 0.24 wt% (in green) and 2 wt% (in red). Voltage profile of 1<sup>st</sup> (b), 5<sup>th</sup> (c) and 40<sup>th</sup> (d) cycles.

It can be observed that even 2 wt% of VC significantly affects cyclability of sulfur electrode. Very small differences between pure-ethers and enriched with 0.24 wt% VC are noticed. Further explanations can be given when comparing the cycling profiles of each cell. Figure 4-32b-d shows the feature of the voltage profiles of three cells at 1<sup>st</sup>, 5<sup>th</sup> and 40<sup>th</sup> cycles.

It can be seen that during the initial sulfur reduction process, the upper discharge plateau is practically identical for the three cells (Figure 4-32b). Sulfur may indeed be relatively stable in the presence of little amount of VC. Once the polysulfides (and resulting  $\text{S}_3^{\cdot-}$  radical, formed due to the disproportionation of  $\text{S}_6^{2-}$ ) are the dominant species in the cell (transition region between two discharge plateaus), significant changes start to appear in the system. Especially, these changes are more pronounced when 2 wt% of VC is used. The reaction between carbonyl (C=O) groups of VC with the radical  $\text{S}_3^{\cdot-}$  induces the formation of precipitated products, a large polarization and the consumption of active material. These changes are not directly correlated with the initial discharge capacity, but they strongly affected the capacity retention during the following cycles. After 40 cycles '0.24 wt% VC' and '2 wt% VC' cells display higher overpotential and lower capacity as compared with the 'reference' cell (no addition of VC).

Parallel to the cycling tests done on sulfur electrodes, graphite electrodes were cycled (vs. Li) in three different electrolytes, for comparison: (i) classical carbonates LP10 (1M  $\text{LiPF}_6$  in PC/EC/DMC (1/1/3 in vol) + 2 wt% of VC, (ii) 'reference' ether-based electrolyte, (iii) 'reference' ether-based electrolyte enriched with 2 wt% of VC. Graphite electrodes (with composition 94/2/2/2 wt% = SLP30/SuperP<sup>®</sup>/CMC/NBR) were kindly provided from SRGE laboratory (CEA-Grenoble), and they were of average active material loading  $\sim 7.34 \text{ mg}_{(\text{SLP30})} \text{ cm}^{-2}$  ( $\sim 2.64 \text{ mAh cm}^{-2}$ ), coated on Cu foil. Cycling procedure applied to the three cells was: GCPL at C/10 with a cut-off potential equal to 10 mV, completed by a constant voltage step limited by a current value of C/100 C-rate in order to complete the discharge process. Figure 4-33 shows capacity retention of the three cells.

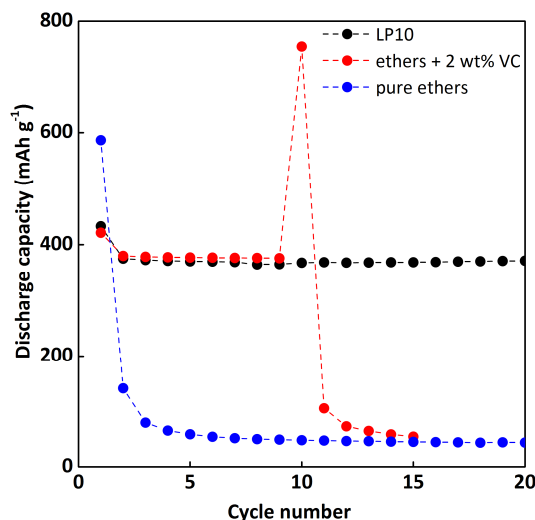


Figure 4-33. Capacity retention of graphite electrode cycled vs. Li with three different electrolytes: carbonate-based 1M  $\text{LiPF}_6$  in PC/EC/DMC (1/1/3 in vol) + 2 wt% of VC (in black), ‘reference’ ether-based electrolyte (in blue), ‘reference’ ether-based electrolyte enriched with 2 wt% of VC (in red). Cycling was performed at C/10 rate in a potential window of 0.01 V – 1.0 V, with the ‘floating’ step at C/100 at the end of each discharge.

It can be seen that addition of VC to the ‘reference’ ether-based electrolyte is sufficient to permit the graphite electrode cycling during few initial cycles. However, after some time, drastic capacity fading is observed anyway, like it is seen (but earlier) when using only ‘reference’ electrolyte.

This results proves that addition of VC to ‘reference’ ether-based electrolyte would not be a solution to apply. Anyway, these studies were only a preliminary tests, and further tests should be conducted in order to investigate new solvents, compatible with both sulfur-based and graphite electrodes. In the next part dedicated to Si electrode utilization, no change of electrolyte solvents was required.

### 4.3.2. Si/ $\text{Li}_2\text{S}$ cell: proof-of-concept

For this purpose, Si electrodes were kindly provided by the SRGE laboratory (CEA-Grenoble), where they were developed through water-based formulations. Electrode slurry made of an aqueous mixture of nano-silicon (65 wt%), carbon fibers (25 wt%), and carboxymethyl cellulose (CMC/NBR) (10 wt%,  $M_w = 250 \text{ kg mol}^{-1}$ , D.S. = 0.7) was coated on a 10  $\mu\text{m}$  copper foil current collector.  $\varnothing$  14 mm electrode disks were punched out, weighed and dried under vacuum (BUCHI®) at 80°C during 48h before entering into the glove box for coin cell preparation. Resulting active material loadings were ranging between 1.3 – 1.5  $\text{mg}_{\text{Si}} \text{ cm}^{-2}$  ( $\leftrightarrow$  4.67 – 5.40  $\text{mAh cm}^{-2}$ ).

Figure 4-34 presents the initial cycle profiles obtained with carbonates (1 M  $\text{LiPF}_6$  in ethylene carbonate (EC): diethyl carbonate (DEC) 1/1 vol)<sup>235</sup> electrolyte and with our reference electrolyte (1 M  $\text{LiTFSI}$  + 0.1 M  $\text{LiNO}_3$  in TEGDME/DIOX 1/1 vol). The cycling was done at C/20 (corresponding to a current density of  $0.23 \text{ mA cm}^{-2}$ , based on a  $3600 \text{ mA h g}_{\text{Si}}^{-1}$  capacity) in a potential window of  $1.2 \text{ V} - 0.05 \text{ V}$ .

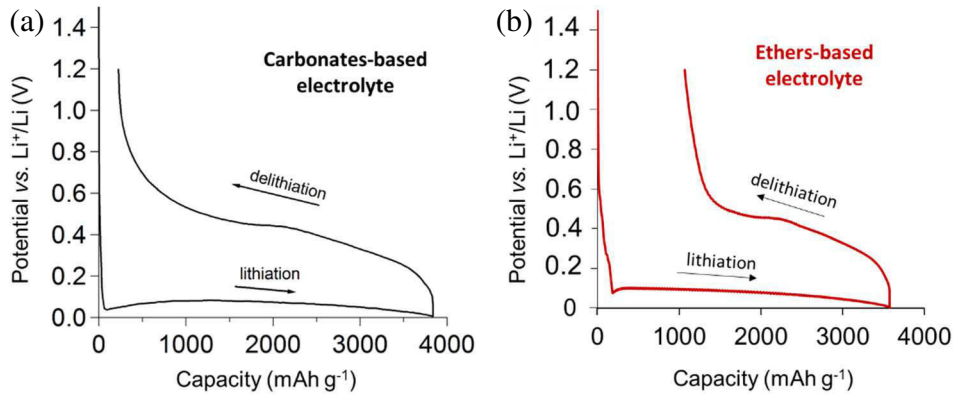


Figure 4-34. Voltage profile of Si electrode (nano-Si/carbon fibers/CMC = 65/25/10 wt%) cycled vs. Li at C/20 in carbonate-based electrolyte (1 M  $\text{LiPF}_6$  in ethylene carbonate (EC): diethyl carbonate (DEC) 1/1 vol) (a), and ether-based one (1 M  $\text{LiTFSI}$  + 0.1 M  $\text{LiNO}_3$  in TEGDME/DIOX 1/1 vol).

It can be seen that the voltage profiles are quite similar, and the initial discharge capacities are very close. However, the use of an ether-based electrolyte resulted in a larger irreversible capacity ( $1000 \text{ mAh g}^{-1}$ ). Aurbach *et al.* reported on only 3.2 % irreversible capacity<sup>234</sup> when cycling in 1 M  $\text{LiTFSI}$  + 0.1 M  $\text{LiNO}_3$  in DIOX, but at  $60^\circ\text{C}$ . These differences may arise from the use of different Si materials, which was nano-Si in our case, *i.e.* having more specific surface available for electrolyte decomposition.

Keeping in mind a large capacity excess of the Si anode ( $\sim 5.2 \text{ mAh cm}^{-2}$ ) as compared to the  $\text{Li}_2\text{S}$  electrodes ( $\sim 2 \text{ mAh cm}^{-2}$ ), coin cells were fabricated<sup>§</sup> for further cycling tests. Parallel to  $\text{Li}_2\text{S}$  vs. Si cells, half cells of  $\text{Li}_2\text{S}$  vs. Li were also built and cycled, in order to have the most comparative information.

A full Si/ $\text{Li}_2\text{S}$  cell was cycled at C/20 (current was calculated with respect to the  $\text{Li}_2\text{S}$  electrode capacity, *i.e.*  $0.125 \text{ mA cm}^{-2}$ ). The selected potential window was  $3.5 \text{ V} - 1.0 \text{ V}$  during initial cycle (in accordance with Li/ $\text{Li}_2\text{S}$  behavior), and  $2.6 \text{ V} - 1.0 \text{ V}$  during further cycles. Figure 4-35 shows the voltage profiles of 1<sup>st</sup> charge, 1<sup>st</sup> discharge and 2<sup>nd</sup> charge, as well as corresponding capacity retention.

<sup>§</sup> Coin cells were fabricated as described in section 2.2.2, with the only difference lying in the replacement of metallic Li by Si electrode.  $\text{Li}_2\text{S}$  electrodes were also carefully selected to be similar in terms of loading and electrode preparation method.

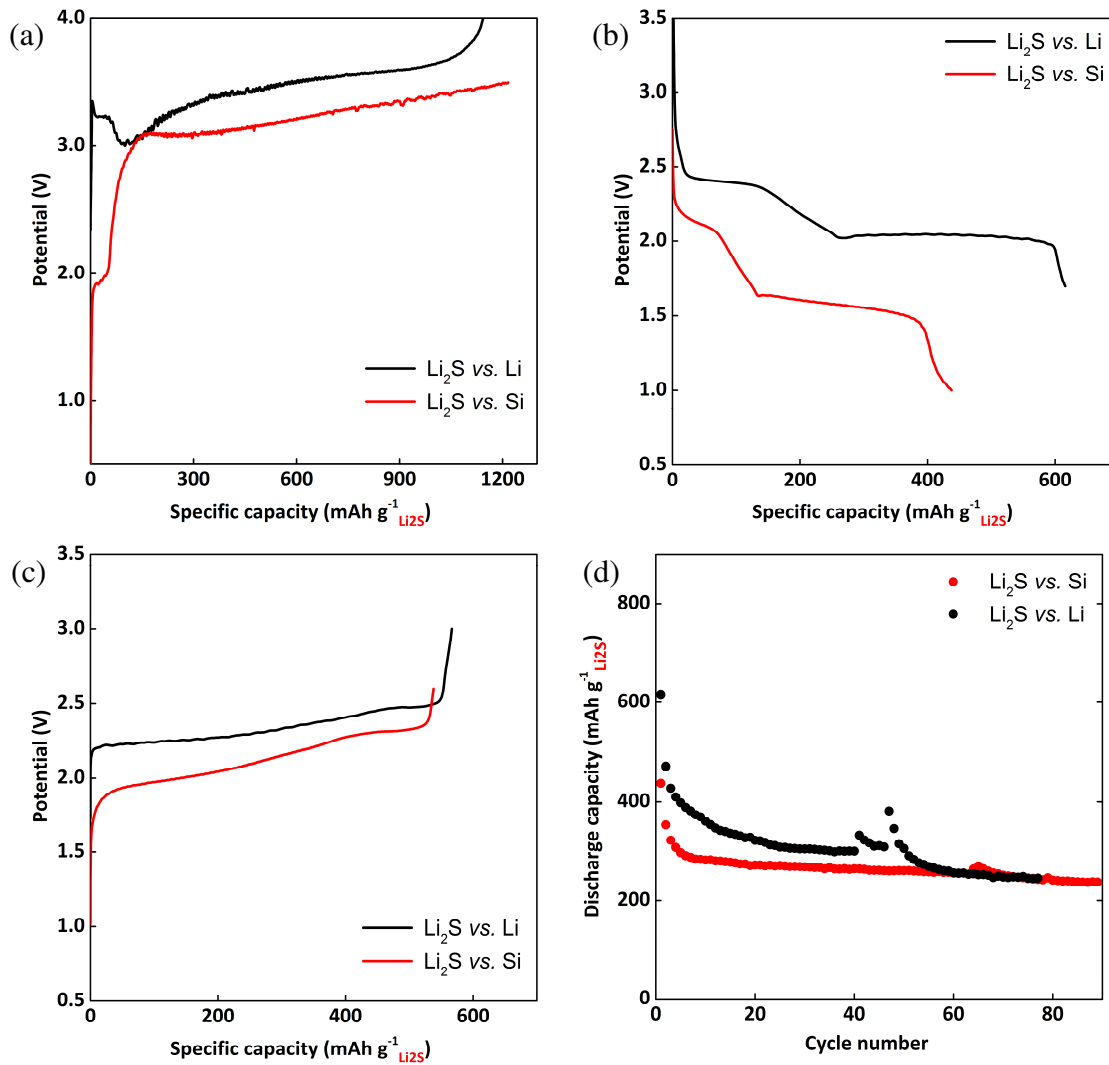


Figure 4-35. Comparison of galvanostatic cycling performances of  $\text{Li}_2\text{S}$  positive electrode (active material loading of  $2.14 \text{ mg}_{\text{Li}_2\text{S}} \text{ cm}^{-2}$ ) cycled at  $C/20$  with two different negative electrodes: Si (in red) and Li (in black). Initial charge (a), initial discharge (b), second charge (c) and capacity retention (d) for both cells is shown. Cut-off voltage limits during 1<sup>st</sup> charge – 1<sup>st</sup> discharge – 2<sup>nd</sup> charge are as follow: 4.0 V – 1.7 V – 3.0 V (for Li/ $\text{Li}_2\text{S}$  cell) and 3.5 V – 1.0 V – 2.6 V (for Si/ $\text{Li}_2\text{S}$  cell).

$\text{Li}_2\text{S}$  electrodes display very high initial polarization during charge. This overpotential is clearly visible for both cells, no matter the negative electrode used (Figure 4-35a). This non-reproducible charge profile was carefully investigated in previous section 4.2.4 a. As discussed before, this large polarization has no detrimental effect on the cell capacity. Si/ $\text{Li}_2\text{S}$  cell shows a high charge capacity, even extending the theoretical value of  $1166 \text{ mAh/g}_{\text{Li}_2\text{S}}$ . This high capacity can be associated with some shuttle mechanism, but further experiments must be performed to have a clear idea about that. During 1<sup>st</sup> discharge, Si/ $\text{Li}_2\text{S}$  cell displays lower capacity ( $438 \text{ mAh g}_{\text{Li}_2\text{S}}^{-1}$ ) as compared to the Li/ $\text{Li}_2\text{S}$  cell ( $616 \text{ mAh g}_{\text{Li}_2\text{S}}^{-1}$ ). The lower discharge capacity may be related to the irreversible consumption of lithium during the SEI formation on Si. Contrarily to the lithium negative electrode, Si indeed does not play the role of lithium reserve. Besides, the average working voltage is lower (1.7 V) than for Li/ $\text{Li}_2\text{S}$  cell

(2.1 V), since the Si anode has an average charge potential of  $\sim 0.4 - 0.5$  V vs.  $\text{Li}^+/\text{Li}$ . The lower discharge plateau also seems to be more sloped, again due to the voltage profile of Si. The second charge displays also a difference in terms of potential, even if slighter, related to the Si anode profile during charge. In general, the  $\text{Li}_2\text{S}$  positive electrodes, in both, Si/ $\text{Li}_2\text{S}$  or Li/ $\text{Li}_2\text{S}$  systems, seem to work very similarly, the difference in voltage value and profile being only related to the behaviors of the two different negative electrodes. It also seems that  $\text{Li}_2\text{S}/\text{Si}$  cell has even more stable capacity retention (Figure 4-35d). In consequence, the capacities of the two systems are very close after 70 cycles. Furthermore, the Si/ $\text{Li}_2\text{S}$  cell does not exhibit the problematic behavior of metallic lithium during charge, *i.e.* short circuit due to dendrites formation.

Similar to Li/ $\text{Li}_2\text{S}$  coin cells, the initial charge, and mainly the limiting process of  $\text{Li}_2\text{S}$  oxidation, rules the capacity obtained in the further cycles. As an example, Figure 4-36 shows the performances of the cells initially charged to 3.2 V and 3.5 V.

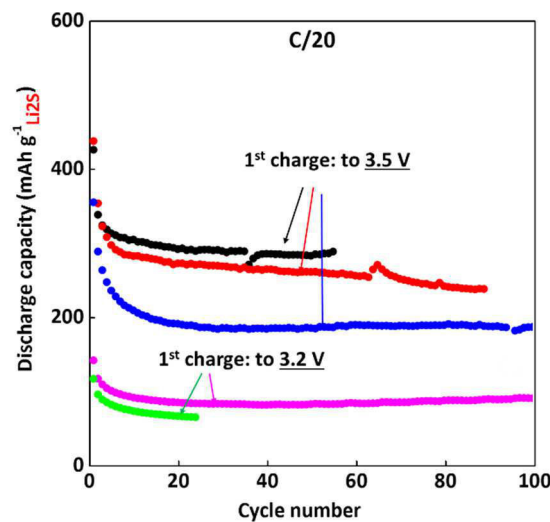


Figure 4-36. Galvanostatic performances of Si/ $\text{Li}_2\text{S}$  full cells (C/20) depending on the initial charge cut-off potential, *i.e.* 3.2 V or 3.5 V, while following cycles are in the potential window 1.0 V – 2.6 V.

These results allow to propose the following assessments:

- The irreversibility of Si in ether-based electrolyte is not detrimental towards capacity values, and may be improved in the future by electrolyte optimization, for example;
- The sulfur chemistry is not noticeably disturbed by the use of Si counter electrode;
- These preliminary results seem to confirm the interest for  $\text{Li}_2\text{S}/\text{Si}$  system as a promising alternative to the Li/S conventional system.

## 4.4. Conclusions

In this chapter, we presented the electrochemical performances of  $\text{Li}_2\text{S}$ -based electrodes, as a lithiated counterpart of sulfur positive electrode. Intensive studies were conducted in order to understand the particular behavior of  $\text{Li}_2\text{S}$  electrodes, and mechanisms of the redox reaction ruling the system.

$\text{Li}/\text{Li}_2\text{S}$  system, since initially in the discharge state, starts its operation from charging. However, this charge process is a particular one, where  $\text{Li}_2\text{S}$  oxidation is the limiting process, which dictates the cycling performances during further cycles. Nevertheless, no matter the way the initial charge performs, the discharge capacity is directly associated with the previous charge, and no detrimental influence on further cycle performances can be noticed.

In order to reach almost complete charge capacity (of  $1166 \text{ mAh g}^{-1}$ ), the cycling procedure must be adapted, *i.e.* performing the initial charge to higher potential values (max 4.0 V), applying slow currents (like C/100) or addition of a small amount of the soluble polysulfides species to the electrolyte.

It has also been shown that after the initial and particular charge process, the cell behaves in the identical manner as a classical  $\text{Li}/\text{S}$  cell. Therefore, the same limitations of the system are present, *i.e.* drastic capacity fading during few initial cycles, discharge capacity limited by insufficient surface area and/or accessibility of electrolyte and polysulfides to the whole porosity of the electrode. One of proposed improvement which shows a beneficial impact on discharge capacity value consists in using a porous carbon based current collector (NwC). Significantly improved capacity values together with capacity retentions were obtained.

By applying other characterization techniques like GITT, *in situ* and *operando* XRD (supported by *ex situ* data), and by studying the behavior of the initial charge profile when different currents were applied, or with addition of polysulfides to the electrolyte, a proposed (summarized) mechanism of the initial charge is shown on Figure 4-37.



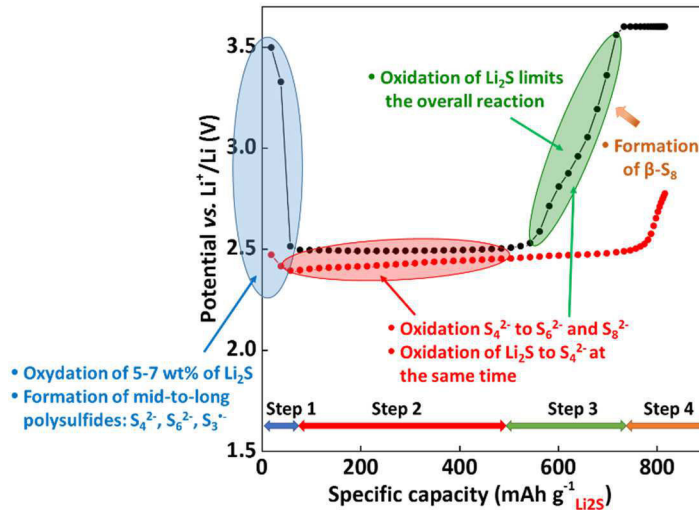


Figure 4-37. Schematic summary of the proposed mechanism for  $\text{Li}_2\text{S}$  activation during initial charge.

A complete metallic lithium-free,  $\text{Si}/\text{Li}_2\text{S}$  cell was also presented and promising results were obtained. The cycling properties were very close to the one obtained with  $\text{Li}$ , thus further improvement of  $\text{Si}/\text{Li}_2\text{S}$  cell may bring additional benefits.

Utilization of graphite with sulfur and/or  $\text{Li}_2\text{S}$ -based electrodes would be difficult to achieve, mostly due to the incompatibility of graphite with ether-based electrolytes. We have demonstrated that, indeed, even if using little amount of VC additive in ether-based electrolyte, we could not achieve stable cyclability of the graphite electrode. On the contrary, silicon electrode seems to be a promising choice for the  $\text{Li}/\text{S}$  system.

# Chapter 5: *In situ* and *operando* XRD studies: insight into the structural changes of the active material

## 5.1. Motivation of the work

As already mentioned in the bibliographic summary, before we performed this work, most of the previous XRD studies were done through *ex situ* analyses. However, the opinion was divided when concerning the most important questions related with sulfur and  $\text{Li}_2\text{S}$  formation. Predominantly, crystalline  $\text{Li}_2\text{S}$  was detected on the positive electrode just at the end of discharge<sup>28,205,206</sup> or already in the middle of lower plateau<sup>117,207</sup> and turned to disappear completely during following charge. Some other reports claimed that complete conversion of  $\text{Li}_2\text{S}$  into soluble species does not occur<sup>37</sup>. Opinion about the moment of sulfur disappearance/reappearance during cycling was divided as well<sup>117,206,207</sup>. The debate was also concerning the end of charge, whether elemental sulfur is formed<sup>117,244</sup> or soluble polysulfides never transform back to solid  $\text{S}_8$ <sup>37,207,245</sup>. Later, *in situ* and *operando* tests performed by Nelson *et al.*<sup>199</sup> and Cañas *et al.*<sup>198</sup> did not completely give a clear answer to the questions. Nelson's results reported on complete disappearance of elemental sulfur during initial discharge and reformation at the end of charge, in agreement to Cañas' statements. However, the main discrepancies lied in  $\text{Li}_2\text{S}$  product. Nelson did not find any traces of crystalline  $\text{Li}_2\text{S}$  (however, the presence of amorphous phase was not verified), while Cañas *et al.* reported that it starts to form at ~ 60% DOD, and disappears completely during following charge.

Therefore, the aim of this work was to have clearer idea on the solid/soluble phase evolution occurring in our cells and to find the answers on still unresolved or debated questions. The fact of performing two independent synchrotron sessions allowed to design variety of measurements. Obtained results gave a deeper vision of the Li/S system performances, where cycle number and C-rate were also taken into consideration. The idea of using two current densities (C-rates) aimed at verifying how the kinetic and the moment of solid products formations/disappearances would be affected.

## 5.2. Experimental section

### 5.2.1. Measurements description and synchrotron beam line characteristics

*In situ* and *operando* X-Ray Diffraction (XRD) studies were performed in two different synchrotron facilities: ESRF (Grenoble, France) and SOLEIL (Saclay, France). Table 5-1 summarizes the characteristics of both facilities.

Synchrotron facility (place)	Beam line	Energy (Wavelength)	Beam intensity	Number of patterns recorded per hour (*)	Time of: reading the image / changing the sample position
SOLEIL (Saclay, France)	CRISTAL	18.5 KeV (0.66785 Å)	Stable	6.7 (every 9 min)	1 min / ~ 2 min
ESRF (Grenoble, France)	BM 20	25 KeV (0.4959368 Å)	Injected every 6h	3.3 (every 18 min)	2 min / ~ 4 min

(\*) For the same beam position

Table 5-1. Description of two synchrotron facilities, where the experiments were performed: SOLEIL (Saclay) and ESRF (Grenoble).

We managed to monitor following sequences of cycles, at two C-rates (C/20 and C/8) and for few cells, as summarized in Table 5-2.

1 <sup>st</sup> session: SOLEIL				2 <sup>nd</sup> session: ESRF			
Cell 1		Cell 2 (back up)		Cell 3		Cell 4 (pre-cycled)	
Cycle #	C-rate	Cycle #	C-rate	Cycle #	C-rate	Cycle #	C-rate
1	C/20	1	C/20	1	C/8	1 to 25	C/20
2	C/20 *	2	C/20	2	C/8	26	C/20
		3	C/20 *				
		4	C/8 *				
		5	C/8				
		6	C/8				

Legend: C/x → in the beam  
C/x → complete cycle observed by XRD  
C/x \* → partial XRD data missing

Table 5-2. Sequences of cycling tests on which *in situ* and *operando* XRD measurements were performed, during both synchrotron sessions.

During the first session in SOLEIL ( $\lambda = 0.66785 \text{ \AA}$ ), two identical Li/S cells were cycled at the same time. Cell 1 was directly exposed to the beam, while cell 2 (so-called 'back up' cell) was cycled in parallel. After recording XRD results on cell 1 during two cycles at C/20, cell 2 was switched to the beam and XRD patterns were recorded during further cycles (3<sup>rd</sup> at C/20, 4<sup>th</sup> – 5<sup>th</sup> – 6<sup>th</sup> at C/8). Because of some technical issues, few cycles contain incomplete information

due to the missing XRD patterns (beam loss, detector disconnection, etc.), as indicated with a cross in the Table 5-2.

ESRF session allowed to monitor the evolution of two Li/S cells as well. Cell 3 was monitored during two initial cycles at C/8. Cell 4 was cycled in the laboratory for 25 cycles (at C/20) and stopped at the discharged state prior being monitored with *in situ* XRD during its following 25<sup>th</sup> charge and 26<sup>th</sup> discharge at C/20. The goal of observing later cycle was to verify if solid phase evolution could be dependent or not from the prolonged cycling.

SOLEIL-based results were used for both qualitative and quantitative interpretations, and allowed for a deeper look into the mechanisms. On the other hand, technical difficulties were encountered during the shifts at ESRF, which reduced the quality of the obtained data, for that reason ESRF-based results were mostly used for qualitative purposes.

### 5.2.2. Cells design

All the experiments were performed in a pouch cell configuration, with sulfur positive electrode (3.5 x 1.8 cm) coated on non-woven carbon-based current collector (so-called ‘S-on-NwC’; sulfur loading  $\sim 4.5 \text{ mg}_{\text{Sulfur}} \text{ cm}^{-2}$ ), lithium foil (3.6 x 2.0 cm) and separators (Viledon<sup>®</sup> with Celgard<sup>®</sup> 2400; both 3.8 x 2.2 cm) soaked with standard electrolyte (1M LiTFSI + 0.1M LiNO<sub>3</sub> in TEGDME/DIOX 1/1 vol). The pouch cells were prepared in a dry-room (dew point  $-40 \text{ }^{\circ}\text{C}$ ), while final activation step with the electrolyte (600  $\mu\text{L}$  were added, *i.e.* excess of  $\sim 250 \%$ \*\*) was done in an argon filled glove-box.

The pouch cell was designed to allow for scanning the same cell in three different positions, as shown on Figure 5-1. The idea of having such ‘3-holes’ configuration was to observe complete cell evolution (where XRD beam penetrates both electrodes at the same time, position [2]) as well as each electrode separately (so called ‘reference’ holes; a  $\varnothing$  3 mm hole in the opposite electrode permitted to scan only one of the two electrodes; position [1] for Li foil observation, position [3] for sulfur positive electrode observation). Indeed, the following questions were still unanswered: (i) if solid Li<sub>2</sub>S formation (if any?) appears on both electrodes, (ii) if having a hole in lithium in front of sulfur electrode will modify the kinetics of the observed reactions and in which extent. The pouch cell was then placed on a movable sample holder and was shifted every  $\sim 3$  min, so that the XRD beam was positioned in another part of the cell. The use of a movable sample holder did not affect neither the quality (high resolution of scan), nor the quantity of obtained patterns.

---

\*\* The volume of the electrolyte necessary to fulfill all available spaces was roughly calculated based on Viledon<sup>®</sup>, Celgard<sup>®</sup>2400 and NwC porosities, and was found to be  $\sim 220 \mu\text{L}$ . ‘Dead’ volume of a pouch cell was not taken into consideration, however, it should be low. One should also note that the effective amount of electrolyte was not known precisely, since a part of electrolyte volume was drawn off during sealing process with the vacuum machine.

The holes in the packaging (which is composed of a multi-layered film made of polymer and aluminum foil) were covered with Kapton<sup>®</sup> tape. Additional polyethylene (Low Density PE) plastic bag was used outside the pouch cell, to provide sufficient protection from air penetration. Because of its strong response in XRD (that could probably hide eventual signal of S<sub>8</sub> or/and Li<sub>2</sub>S), Viledon<sup>®</sup> had also three holes (Ø 3 mm) in the positions of beam penetration. Celgard<sup>®</sup>2400 was used without any holes in it.

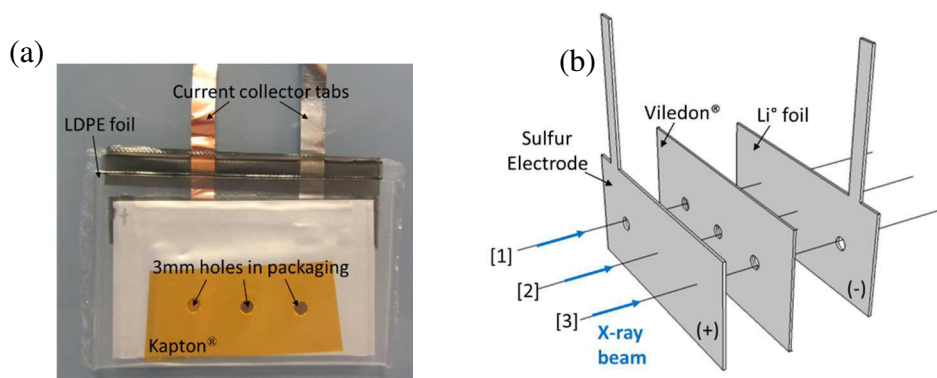


Figure 5-1. In situ XRD pouch cell picture (a) and schematic illustration (b) of the cell components, with indicated beam positions at which XRD patterns of the complete cell [2], sulfur electrode [3] and metallic Li [1] were recorded.

Sulfur electrodes (80/10/10 wt% = S/SuperP<sup>®</sup>/PVdF 5130) were prepared like previously described (section 2.2.1). However, one should note that the procedure was not optimized yet in terms of the error coming from imprecise weight of NwC collector (discussed in 3.2.1). Electrode slurry was casted on a sheet of NwC paper. Once dried (24 h at 55 °C in the air), the electrodes (3.5 x 1.8 cm) were punched while estimating the weight of underneath NwC collector. Therefore, the electrodes masses might have been slightly overestimated for *in situ* XRD experiments. In order to normalize the obtained electrochemical results (*i.e.* the capacities values), and to be able to perform quantitative analyses on the obtained data, we applied following procedure: eight other pouch cells were prepared (with the electrodes of precisely known sulfur mass; modified way of preparation as presented in 3.2) and cycled at C/20 (the same conditions as employed in SOLEIL). All eight pouch cells gave very reproducible results (in terms of capacity and voltage profile), and we normalized the SOLEIL results based on these obtained discharge capacity values (through comparing the capacity values at the ‘little dip’, at the transition point between the two plateaus). This way, we estimated the new and most probable mass of active material of SOLEIL cells. Finally, the initial weight of active mass previously reported in our paper<sup>23</sup> (4.66 mg<sub>sulfur</sub> cm<sup>-2</sup>), got modified to 4.29 mg<sub>sulfur</sub> cm<sup>-2</sup>. As a consequence, the initial discharge capacity value obtained in SOLEIL tests changed from 902 mAh g<sup>-1</sup> \* to 980 mAh g<sup>-1</sup> (8 % of change).

\* This value (902 mAh g<sup>-1</sup>) was already published in the article<sup>23</sup>. The corrected value (after normalization of discharge capacity by new estimation of correct active mass weight) was estimated to be 980 mAh g<sup>-1</sup> instead. Nevertheless, in this article, we never referred to the discharge capacity value, but rather aiming at qualitative

The cells used for ESRF session were prepared from the electrodes with precisely known sulfur mass (optimized way of the electrode preparation). Each pouch cell was scanned in one position only (complete cell response; no ‘reference’ holes in the electrodes). Since the XRD data collection frequency was of about 18 minutes\* for the same point, it would have been too long (not enough frequent) if recording on three different cell positions (like it was done for SOLEIL cells), *i.e.* risking to lose the important information of solid/soluble phase transition.

## 5.3. The initial cycle evolution at C/20

### 5.3.1. XRD and electrochemistry – results

The following results show the complete cell evolution, where the beam penetrated through both electrodes (position [2] on Figure 5-1b). The results obtained at two other beam positions are discussed in further section.

Figure 5-2 presents the XRD patterns recorded during initial galvanostatic cycle at C/20, and corresponding electrochemical data. The obtained cycling curve displays an expected voltage profile of a Li/S cell, together with high discharge and charge capacities of 980 mAh g<sup>-1</sup> and 976 mAh g<sup>-1</sup> respectively.

The first spectrum recorded at the initial state shows peaks of elemental orthorhombic  $\alpha$ -sulfur (PDF-2; no. 00-008-0247), which is fully expected from the raw material we used to prepare the electrodes. When the discharge starts to proceed, the intensities of sulfur peaks are gradually decreasing until they disappear completely with the end of the initial discharge plateau (Figure 5-2a; red line). This proves complete dissolution and reduction of sulfur already at the early stage of discharge process (*i.e.* at about 175 mAh g<sup>-1</sup>). In the ‘sloping’ region between the two discharge plateaus (2.3 V – 2.0 V), active species are present in the soluble form of high-to-mid order polysulfides, and no peaks are detected (up to about 380 mAh g<sup>-1</sup>). Right after the beginning of lower discharge plateau, the signal of crystalline Li<sub>2</sub>S (PDF-2; no. 00-023-0369) starts to appear, characterized by four peaks at  $2\theta = 11.6^\circ, 13.4^\circ, 19.0^\circ, 22.3^\circ$ , which correspond to the reflexions (111), (200), (220) and (311) respectively. The intensity of these peaks increases gradually, reaching a maximum at the end of discharge.

---

interpretations (depth of discharge (%), moment of sulfur disappearance on the voltage profile), which were independent of active mass normalization.

\* During ESRF session, three cells were observed in parallel. A real frequency of recorded pattern between the cells was ~ 6 minutes. Thus, if scanning three cells in parallel, this time was elongated to ~ 18 minutes.

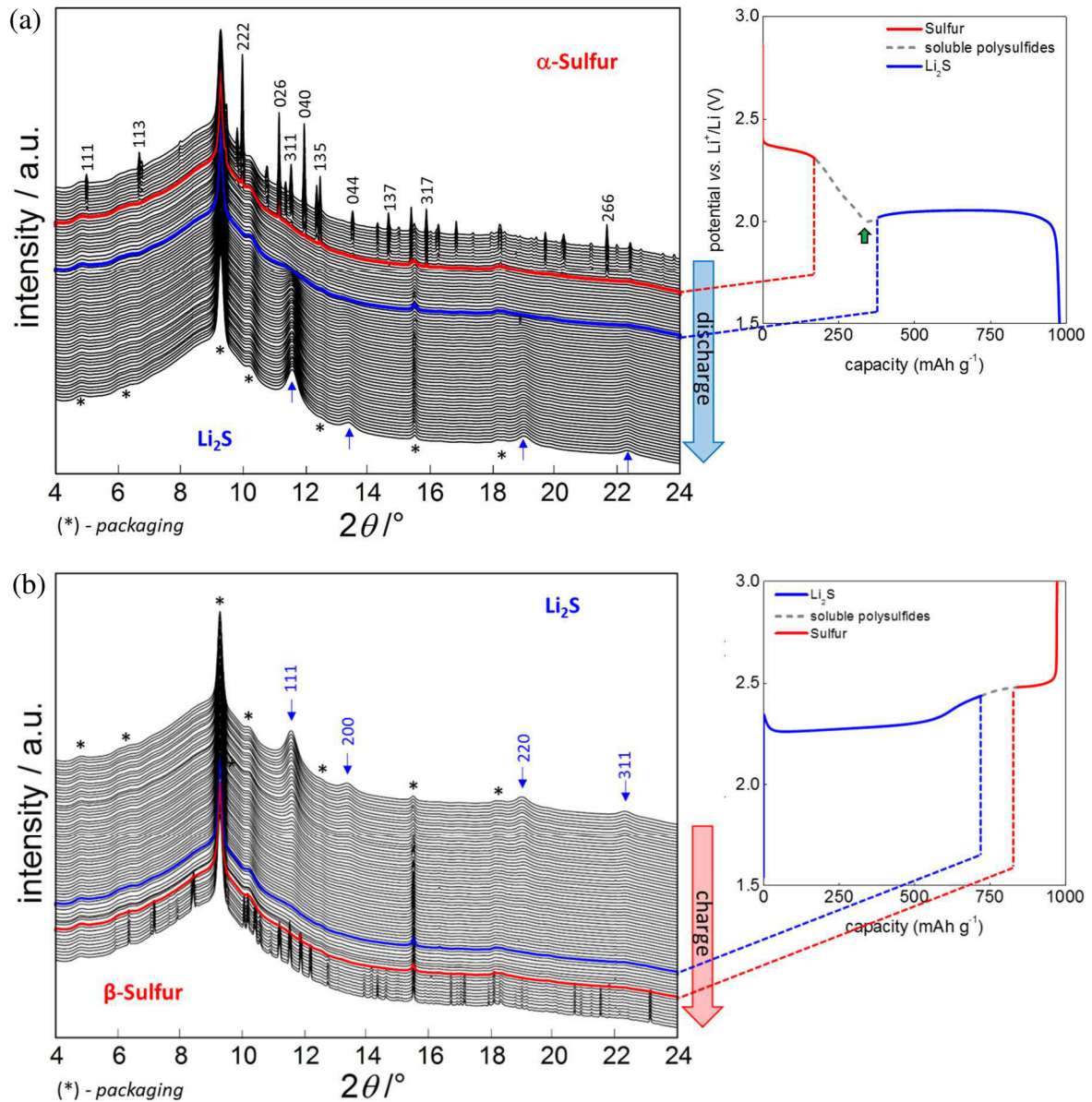


Figure 5-2. *In situ* XRD patterns of the complete cell (beam in position [2]) with corresponding experimental voltage profiles during initial discharge (a) and charge (b). Bold lines indicate precise moment of solid/soluble phase transitions.

Moreover, all along the lower discharge plateau, the four Bragg peaks are nicely centered on the positions expected for  $\text{Li}_2\text{S}$ . This indicates that solely  $\text{Li}_2\text{S}$  crystalline form was detected, and no evidence of crystalline  $\text{Li}_2\text{S}_2$  formation was found. However, quantitative analysis of the results included in further section will give deeper interpretation.

It is worth noticing that solid  $\text{Li}_2\text{S}$  was experimentally detected right after the little dip in the discharge curve (green arrow on Figure 5-2a). The formation of a solid phase (nucleation step) nicely explains the origin of this potential dip, and is in agreement with the literature statements. However, at the moment we obtained these findings, only the theoretical studies based on mathematical models were correlating the presence of such potential dip with the

beginning of solid phase nucleation. According to Mikhaylik *et al.*<sup>246</sup>, nucleation of Li<sub>2</sub>S crystals actually begins slightly before the dip, as a first step of precipitation. At exact moment of the dip appearance, electrolyte is supersaturated with the S<sup>2-</sup> species, and precipitation reaction of Li<sub>2</sub>S starts to be kinetically limited afterwards. On the contrary, other experimentally obtained *in situ* XRD results reported on later moments of Li<sub>2</sub>S formation (like 60% DOD<sup>198</sup>) or did not observe any Li<sub>2</sub>S product at all<sup>199</sup>. Our results clearly show that complete lower discharge plateau corresponds to a soluble/solid region. This is in agreement with GITT results (see section 4.2.4.b), where the equilibrium potential all along the discharge plateau is always at the same stable value (~ 2.1 V), meaning that the same redox couple is fixing the potential (*i.e.* Li<sub>2</sub>S/polysulfides). In other words, this plateau is related to the simultaneous formation of short polysulfide chains and Li<sub>2</sub>S compound. As a consequence, this also point out that the involved reactions occurring at low voltage plateau (*i.e.* reduction of S<sub>4</sub><sup>2-</sup>, S<sub>3</sub><sup>2-</sup>, S<sub>2</sub><sup>2-</sup>) are not successive but rather simultaneous.

During recharging (Figure 5-2b), the intensity of Li<sub>2</sub>S peaks decreases progressively until they completely disappear, which proves the reversible oxidation of Li<sub>2</sub>S into soluble polysulfides. However, the soluble/soluble region is much shorter upon charge (corresponding to 120 mAh g<sup>-1</sup>) as compared with discharge (205 mAh g<sup>-1</sup>). This may be explained by the fact that as Li<sub>2</sub>S is an insulating solid, the kinetic of its oxidation is slower than those of more oxidized soluble polysulfide species, formed during the charge process. Thus, Li<sub>2</sub>S product remains on the electrode until quite high SOC of ~ 75 %. Starting from ~ 2.5 V, at a ‘quasi’ charge plateau, very well-defined peaks of elemental sulfur reappear. Their intensities are gradually increasing until the end of charge is reached (3.0 V). However, sulfur does not come back to its pristine structure after recrystallization. The positions of Bragg peaks are slightly changed, and peaks identification proves the appearance of another crystalline form: monoclinic beta-sulfur (β-S<sub>8</sub>; PDF-2; n° 01-071-0137).

### 5.3.2. End of charge: β-Sulfur formation

Figure 5-3 shows the XRD patterns recorded before cycling and at the end of the 1<sup>st</sup> and 2<sup>nd</sup> charge. We can clearly notice that the positions of Bragg peaks have changed, and another crystalline structure was formed after recrystallization.



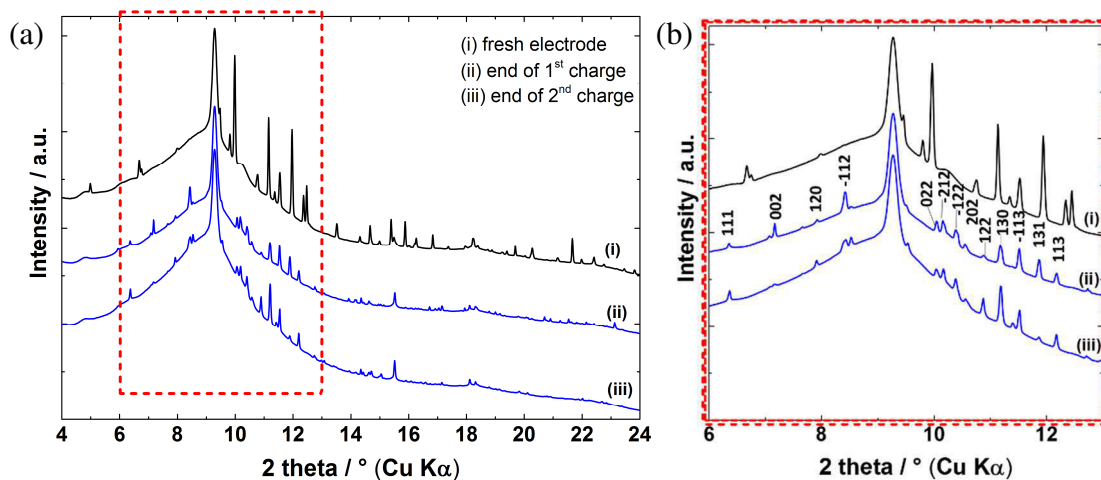


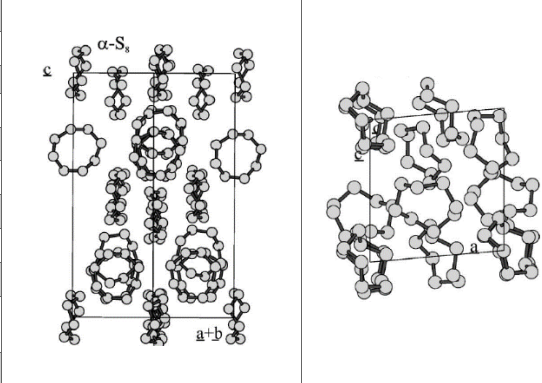
Figure 5-3. XRD patterns recorded at the initial state and at the end of 1<sup>st</sup> and 2<sup>nd</sup> charges (a). A zoomed view (b) shows slight changes in the Bragg peaks positions, clearly indicating the formation of another crystalline form, attributed to the monoclinic  $\beta$ -S<sub>8</sub>.

### 5.3.2.a) $\beta$ -Sulfur: physical characteristics

According to Templeton *et al.*<sup>20</sup>, monoclinic sulfur was determined for the first time in 1965 by Sands. In 1976, Templeton *et al.*<sup>20</sup> provided more complete report concerning  $\beta$ -S<sub>8</sub> structure and its other physical and chemical properties.

Monoclinic  $\beta$ -sulfur is known as another allotropic form of sulfur, usually stable at normal pressure, at the temperatures from 95°C to the melting point of sulfur (115°C)<sup>20,26</sup>. When molten sulfur is cooled, it may (but not always does) solidify as a monoclinic sulfur form. This is actually in agreement with our previous experiments, when preparing binder-free melted electrodes, and traces of monoclinic sulfur were detected (section 3.4.9). Below 95°C, orthorhombic  $\alpha$ -sulfur is the most thermodynamically stable form, which is classically used as elemental sulfur powder for the electrodes preparation. Table 5-3 presents the crystalline structures of both sulfur allotropes.

Alpha-sulfur ( $\alpha$ -S<sub>8</sub>) phase contains 16 molecules of S<sub>8</sub> rings in a face-centered unit cell, and is considered as orientationally ordered form. On the contrary,  $\beta$ -S<sub>8</sub> is rather known as orientationally disordered structure<sup>21,22</sup>, and is composed of six molecules of S<sub>8</sub> rings per unit cell. According to Pastorino and Gamba<sup>22</sup>,  $\beta$ -S<sub>8</sub> crystals can be grown more easily than  $\alpha$ -S<sub>8</sub> ones from the melt phase, due to its disordered structure. It has been also reported that metastable pure crystals of  $\beta$ -S<sub>8</sub> could be preserved for weeks at RT<sup>20,26</sup>.

Phase	$\alpha$ -S <sub>8</sub>	$\beta$ -S <sub>8</sub>	$\alpha$ -S <sub>8</sub>	$\beta$ -S <sub>8</sub>
PDF-2	00-008-0247	01-071-0137		
Space group	Fddd	P2 <sub>1</sub> /c		
Lattice system	orthorhombic	monoclinic		
a (Å)	10.45	10.926		
b (Å)	12.84	10.855		
c (Å)	24.46	10.790		
$\beta$	—	95.8		
Z	16	6		
d (g/cm <sup>3</sup> )	2.076	2.008		
Stability at normal pressure	< 95°C	95°C – 115°C metastable at RT		
Volume [CD]	3281.99	1272.89		

*a, b, c* – lattice parameters;  $\beta$  – monoclinic angle; Z – number of molecules in the cell

Table 5-3. Crystallographic parameters of  $\alpha$ - and  $\beta$ -sulfur crystalline phases<sup>20</sup>.

### 5.3.2.b) Unusual formation of metastable $\beta$ -S<sub>8</sub>: supporting experiments

Our *in situ* and *operando* XRD study allowed to demonstrate for the first time the formation of  $\beta$ -sulfur allotropic form in Li/S batteries upon charging<sup>23</sup>. One should note that similar observations were reported before, such as changes of peaks position of sulfur after recrystallization. However, interpretation of these changes was rather attributed to “preferential orientation after recrystallization”, which prevented the assignment of  $\beta$ -sulfur phase by the other groups<sup>198,199</sup>. Nowadays the formation of  $\beta$ -S<sub>8</sub> phase at the end of charge is admitted by the Li/S batteries community, and more recent reports, in which *in situ* XRD was applied<sup>24,25,200</sup> have confirmed our findings.

Prior to these experiments, the literature of Li/S batteries has never mentioned about formation of metastable  $\beta$ -sulfur form. Therefore, it was important to understand the reason of such formation in the battery exposed to electrochemical cycling at RT, knowing that  $\beta$ -S<sub>8</sub> formation rather appears at much elevated temperatures, when cooling down melted sulfur.

Based on aforementioned physical properties, one of proposed explanation could be as follow: monoclinic sulfur is getting created more easily from liquid solution (by analogy with melted solution). In the Li/S cell, sulfur is transformed into soluble form of lithium polysulfides, by an electrochemical reduction reaction. During oxidation reaction of soluble polysulfide species, crystallization of solid sulfur occurs at the electrode surface. However, it may be more favorable and easier to create less ordered form of sulfur ( $\beta$ -S<sub>8</sub>) than the highly ordered one,  $\alpha$ -S<sub>8</sub>. Therefore,  $\beta$ -sulfur is a metastable phase, which is formed first, during nucleation. Further phase transition from beta to alpha can appear upon relaxation, or when defects are present<sup>22</sup>.

Since  $\beta$ -sulfur was observed on the samples exposed to synchrotron radiations, and when NwC collector was used in the electrode, the first step was to verify if one of these parameters might

have induced  $\beta$ -S<sub>8</sub> phase formation. For that reasons, *ex situ* XRD measurements were performed on the electrodes at fully charged state\*, where solid sulfur is expected. The fact of performing *ex situ* measurements on the laboratory diffractometer (D8 Bruker, Cu K $\alpha$  = 1.5406 Å) could also allow to exclude the influence of synchrotron radiations. The effect of current collector nature was evaluated by studying the electrodes casted on both collectors, NwC and Al foil. The XRD results show the presence of  $\beta$ -sulfur on both electrodes, no matter the collector used (Figure 5-4).

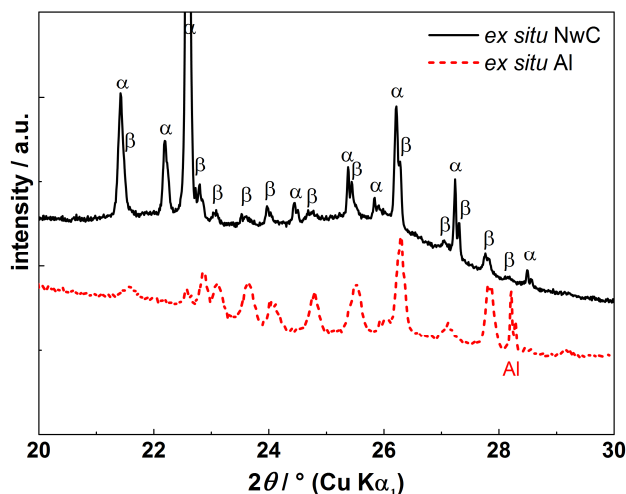


Figure 5-4. Ex situ XRD patterns of charged sulfur electrodes on different collectors: non-woven carbon tissue (NwC) and Al foil. Peaks were attributed to coexisting  $\alpha$ - and  $\beta$ -S phases.

This means that formation of beta-sulfur during *in situ* XRD tests was not influenced by synchrotron radiation neither by the collector nature. However, for *ex situ* samples, coexistence of both phases,  $\alpha$ - and  $\beta$ -S<sub>8</sub>, was observed. This could be explained by the partial transformation of beta phase into alpha one during the relaxation time (time necessary for the *ex situ* samples preparation and XRD pattern recording) at room temperature, which is in accordance with the literature<sup>20,22</sup>. Moreover, it has been found that different relaxation times led to different  $\beta/\alpha$  ratios. The longer the relaxation time was (in our case 3 hours and 4 days, respectively), the lower was the beta/alpha ratio, since more  $\beta$ -S<sub>8</sub> has been transformed back into  $\alpha$ -S<sub>8</sub>. Latest work of Kim *et al.*<sup>26</sup> has also reported on formation of monoclinic  $\beta$ -S<sub>8</sub>, which got encapsulated in between VA-CNT (Vertically Aligned CNT) while infiltrating the nanotubes with sulfur. After analyzing several spots in the cross-section image of a single carbon tube (with sulfur infiltrated inside), they observed both phases: orthorhombic  $\alpha$ -S<sub>8</sub>, that was formed more in the volume/center of the nanotube. However,  $\beta$ -S<sub>8</sub> was found in the direct contact with the carbon shell. Their conclusion is that probably  $\beta$ -S<sub>8</sub> formation is more enhanced when melted sulfur is in the contact with carbon, which is actually in close agreement

\* Sulfur electrodes were galvanostatically cycled at C/20 in the classical coin cell configuration. Once fully charged, the electrodes were recuperated from the coin cell inside the glove box, gently washed with DIOX, left for short drying at RT in the glove box, and prepared for *ex situ* XRD measurement (sample stuck to a glass plate, and covered with Kapton® to avoid any contact with air).

with our findings. Indeed, we verified both current collectors (Al, NwC) and in both cases monoclinic sulfur was detected. Electrode coated on Al foil contains anyway 10 wt% of SuperP<sup>®</sup>, thus a possible active places for  $\beta$ -S<sub>8</sub> formation.

In conclusion, during electrochemical process, it seems to be more favorable to create less disordered form of monoclinic  $\beta$ -S<sub>8</sub>, which could then transform into thermodynamically more stable one, *i.e.*  $\alpha$ -S<sub>8</sub>. However, further studies are necessary to complete understanding, in particular to determine if there could be some thermal effects dictating sulfur recrystallization.

### 5.3.3. ‘Reference’ holes evaluation

Thanks to a special pouch cell design (Figure 5-1), we were able to monitor both electrodes separately. As expected, XRD patterns evolution was observed for the solely positive electrode as for the full system, confirming the fact that positive electrode undergoes significant structural modifications upon cycling (Figure 5-5a). Since LiNO<sub>3</sub> was used as an electrolyte additive in order to provide better cyclability of the *in situ* cell with the suppression of shuttle mechanism (lower self-discharge), metallic Li side was supposed to be effectively protected by SEI layer resulting from LiNO<sub>3</sub> reduction<sup>47,177,182</sup>. Indeed, no evidence of crystalline Li<sub>2</sub>S formed on the lithium side was found, indicating the efficiency of the passivation layer (Figure 5-5b).

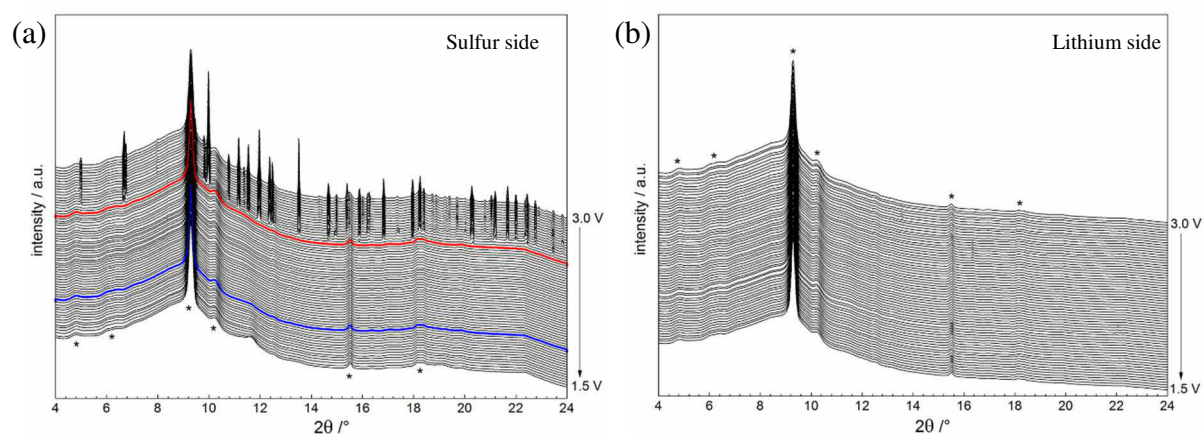


Figure 5-5. *In situ* XRD peaks evolution recorded during 1<sup>st</sup> discharge at each electrode separately, depending on the beam position: (a) sulfur cathode – beam penetrating the cell at the position [3], (b) Li anode – beam at the position [1]. For the positions [1] and [3] – refer to Figure 5-1. Peaks associated with packaging are marked by \*. Bold lines indicate appearance/disappearance moments of solid phases.

It is important to underline that having a hole in Li electrode just in front of sulfur electrode (position [3] on Figure 5-1) does not affect the structure of the crystalline products (S<sub>8</sub>, Li<sub>2</sub>S), and qualitative information could still be obtained. Nevertheless, the current lines are probably disrupted, which may affect the kinetics of the reactions. As a matter of fact, the moments of

crystalline  $S_8/Li_2S$  appearance and disappearance are significantly shifted as compared to the position [2], where the electrodes are in front of each other. Moreover, the peak intensities are smaller and less detectable (for example, presence of crystalline  $Li_2S$  is confirmed only by the most intensive peak (111) at  $2\theta = 11.6^\circ$ ). In such situation, a reliable quantitative interpretation is impossible to perform. Therefore, it also points out the importance of a cell design for *in situ* and *operando* measurements, once aiming for reliable quantitative results. As similar qualitative observations in terms of solid phases formation/disappearance were confirmed in both configurations (*i.e.* ‘complete cell’ at position [2] and ‘only sulfur’ at position [3]), only the results obtained from the ‘complete cell’ monitoring are taken into consideration for quantitative analyses.

## 5.4. Quantitative analysis – insight into evolution of solid active material phases

We previously saw that during both processes, discharge and charge respectively, three well-separated regions can be observed: ‘solid/soluble’, ‘soluble species’ and ‘soluble/solid’. In the first step, comparison of the capacity values corresponding to each region may bring important information. Theoretical capacities for each region were calculated, based on electrochemical reactions proposed by Barchasz *et al.*<sup>194</sup> and based on the amount of exchanged electrons, as illustrated on Figure 5-6.

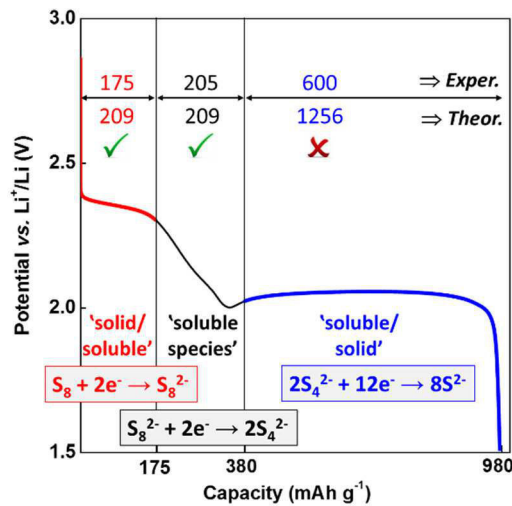


Figure 5-6. Initial discharge profile obtained experimentally during *in situ* XRD studies, with schematically illustrated regions corresponding to ‘solid/soluble’ (in red), ‘soluble species’ (in black) and ‘soluble/solid’ regions (in blue). For each region, experimental capacities are compared with the expected theoretical values, calculated in regard to simplified electrochemical reactions occurring at each step.

It can be seen that for the first two regions (sulfur reduction (in red) and long polysulfides formation (in black)), the experimental and theoretical capacity values are not so different. This allows to indicate that these two electrochemical processes are not limiting for the full cell capacity. On the contrary, the main limitation comes in the third region, where only 50 % of theoretical capacity is obtained, *i.e.* 600 mAh g<sup>-1</sup> is obtained experimentally while 1256 mAh g<sup>-1</sup> is attainable in principle (complete reduction of S<sub>4</sub><sup>2-</sup> to form Li<sub>2</sub>S). It is clear then, that one of the important limitations (however, not the only one) which prevent from obtaining full capacity (in our system), could be the formation of insulating Li<sub>2</sub>S during the low voltage plateau, which passivates the conductive surface of the electrode, and/or the formation of short polysulfides precipitates. In the following discussion, the formation/disappearance of solid phases upon cycling is investigated more into details.

### 5.4.1. Sulfur reduction and re-oxidation

Figure 5-7 shows a zoomed view on sulfur peaks disappearance, together with quantitative treatment of selected reflections' surface area. The area under the peak is directly proportional to the overall volume of the crystallites in the sample. The moment of complete sulfur disappearance was chosen when all the reflections had vanished, which corresponds to discharge capacity of 175 mAh g<sup>-1</sup>. However, it is clear that some of the peaks (mainly less intense ones, like (111), (0210) or (515)) disappear a bit before the most intense ones (for example (222), (026), (040)). This may be related with the fact that only small number of particles participate in the signal (limited by the beam size – 300 μm x 300 μm, while the initial sulfur particle is even as large as ~ 50 μm). Some particles, having the same orientation, might be reduced before the others, thus accelerating the peaks disappearance. Recent work of Lin *et al.*<sup>201</sup> by *in operando* transmission X-ray microscopy (TXM) explained that smaller particles shrink faster than the bigger ones. Nevertheless, in the global view, sulfur disappearance is found to be very linear as a function of capacity (Figure 5-7b). This linear evolution can be associated with a one-step electrochemical process. The practical capacity (175 mAh g<sup>-1</sup>) is slightly lower than the theoretical one (209 mAh g<sup>-1</sup>, based on the reduction reaction of S<sub>8</sub> to S<sub>8</sub><sup>2-</sup>).

Sciamanna *et al.*<sup>247</sup> determined sulfur solubility limit equal to 0.19 wt% in TEGDME. Taking into account the electrolyte volume, *i.e.* ~ 250 μL, and the solubility limit reported in the literature, a maximum of 0.475 mg of sulfur can be dissolved in TEGDME. As the loading of sulfur is 4.29 mg<sub>sulfur</sub> cm<sup>-2</sup> with an electrode surface of 6.3 cm<sup>2</sup> (*i.e.* 27 mg of S<sub>8</sub> initially present in the electrode), the amount of soluble sulfur could correspond to ~ 2 % of the total sulfur amount, which is in fact slightly lower than the difference between experimental and theoretical capacity values (209 – 175 = 34 mAh g<sup>-1</sup>). However, the reduction of S<sub>8</sub> at the lithium surface through self-discharge may also permit to dissolve more S<sub>8</sub> than just the amount fixed by the solubility limits.

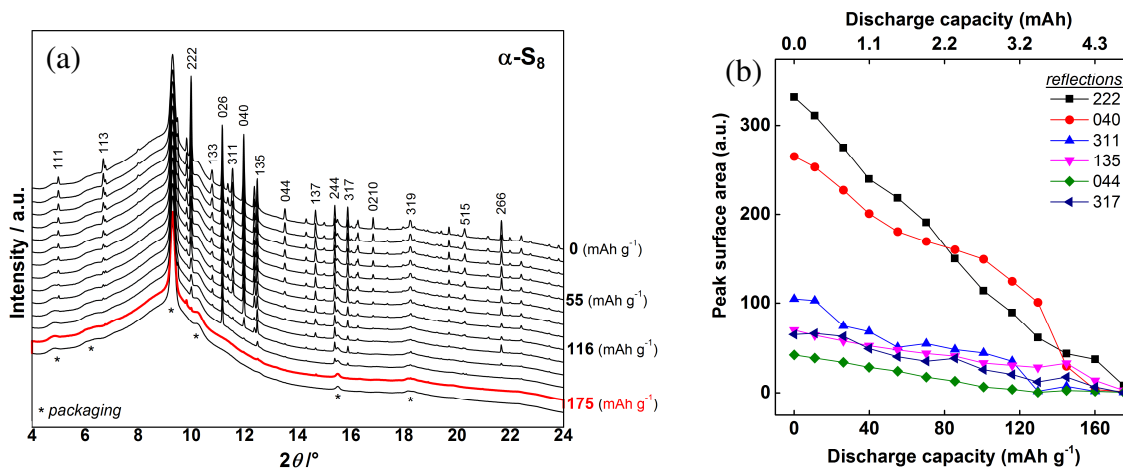


Figure 5-7. Zoomed view on  $\alpha$ -S<sub>8</sub> peaks disappearance during initial discharge (a). Integrated surface area of selected reflections as a function of discharge capacity (b).

As previously explained, monoclinic  $\beta$ -sulfur is formed at the end of charge. Since it has a different crystalline structure as compared to the initial orthorhombic  $\alpha$ -S<sub>8</sub>, the peaks appear at different positions, thus a comparison of their intensity before cycling and at the end of charge gives no pertinent data. However, surface area integration of  $\beta$ -sulfur most intense reflections (four peaks were selected: (130), (-113), (131) and (113) may give insights into the crystals growth.

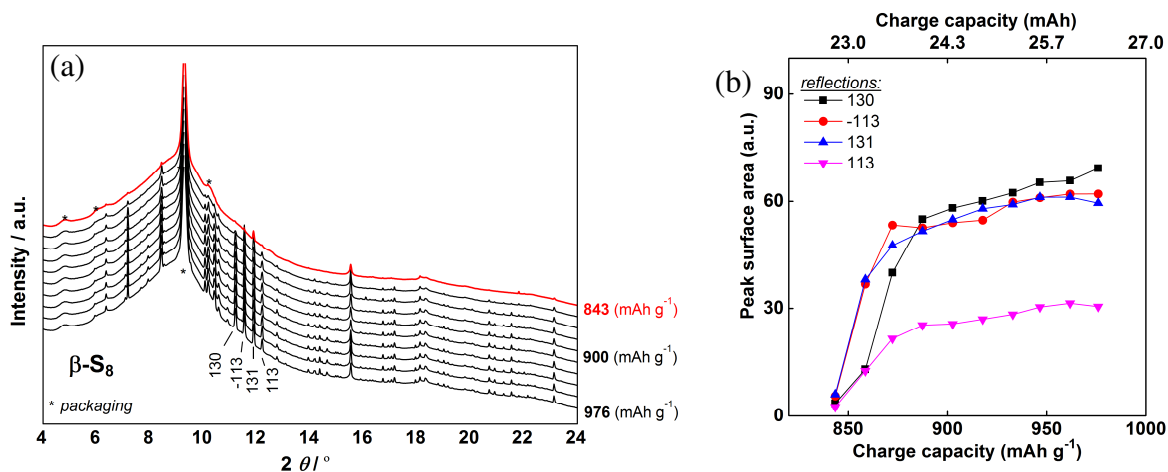


Figure 5-8. Zoomed view on  $\beta$ -sulfur peaks formation at the end of the initial charge (a). Integrated surface area of selected reflections as a function of charge capacity (b).

It can be seen that the behavior of the four selected peaks is the same, *i.e.* a rapid increase of their surface area, and then much slower evolution indicating a nonlinear formation of beta-S<sub>8</sub> vs. charge capacity. This evolution may be related to the formation of soluble sulfur which does not precipitate/crystallize, or to some part of the capacity not associated with the formation of sulfur (oxidation of S<sub>6</sub><sup>2-</sup> to S<sub>8</sub><sup>2-</sup> or shuttle mechanism). Concerning the particle size, the

sharpness of the peaks would rather indicate that the created particles are in the micrometric range. Therefore, it was impossible to determine the real particle size with Scherrer equation, which can mainly be applied to the particles between 10 and 100 nm.

### 5.4.2. Lithium sulfide (Li<sub>2</sub>S) formation and disappearance

Formation of Li<sub>2</sub>S was detected by appearance of four Bragg peaks ((111), (200), (220) and (311)), for which the surface area was integrated. Figure 5-9 shows the evolution of the most intense (111) reflection together with the voltage profile of the initial cycle.

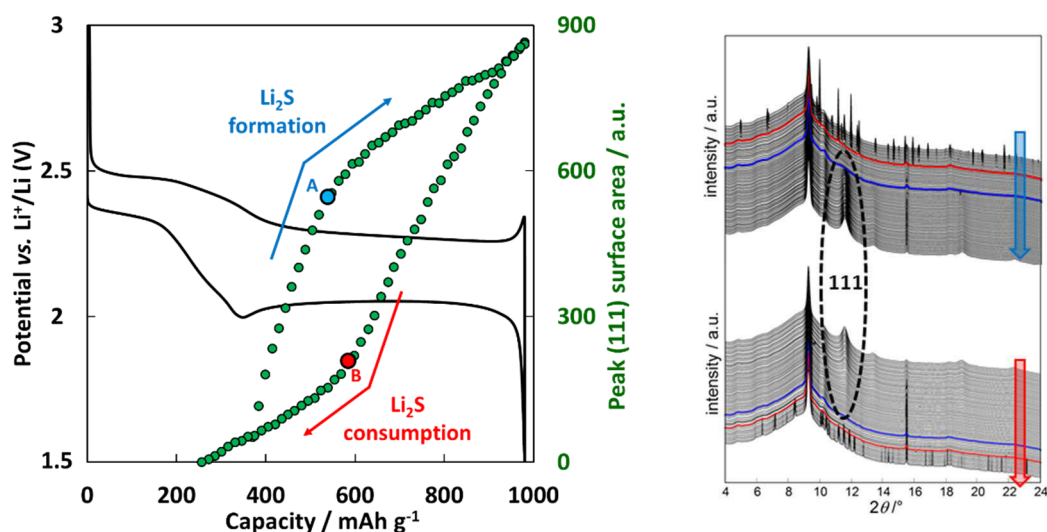


Figure 5-9. Li<sub>2</sub>S formation (blue arrow) and disappearance (red arrow) during initial cycle. Integrated surface area of (111) reflection as a function of capacity superimposed with the experimentally obtained galvanostatic profile.

The discharge profile becomes a quasi-plateau at a potential equal to 2.0 V vs. Li<sup>+</sup>/Li. In accordance with the literature, the low voltage plateau is associated to the reduction of S<sub>4</sub><sup>2-</sup> into S<sup>2-</sup> through several simultaneous electrochemical processes (refer to part 1.2.1). Starting from the capacity corresponding to 380 mAh g<sup>-1</sup> (*i.e.* detectable beginning of the crystalline Li<sub>2</sub>S appearance), the evolution of the peak intensity of Li<sub>2</sub>S vs. the state of discharge clearly shows that the efficiency of Li<sub>2</sub>S formation is higher at the beginning of this low voltage plateau (the slope is higher). Two steps of Li<sub>2</sub>S formation are clearly observed with a decrease of the efficiency at ~ 550 mAh g<sup>-1</sup> (transition point A, between the two slopes). Indeed, the decrease in the Li<sub>2</sub>S formation efficiency (the slope inclination is lower) can be associated with the incomplete reduction of S<sub>4</sub><sup>2-</sup> into S<sup>2-</sup>, which may be due to more efficient formation of intermediate species, like S<sub>2</sub><sup>2-</sup>. Next section brings additional discussion concerning this interpretation.



As concerning the disappearance of  $\text{Li}_2\text{S}$ , two steps are also noticed, however, the slopes and the capacity at the transition point (B) are different from those observed during the discharge process. It can also be noticed that complete  $\text{Li}_2\text{S}$  disappearance moment is much later than when the formation starts, probably due to the insulating nature of  $\text{Li}_2\text{S}$  and its difficulty to be oxidized (as discussed previously). This additional observation clearly indicates that there is a significant difference between discharge and charge processes, which is in agreement with the potential evolution. Recent studies of Petel *et al.*<sup>172</sup> and Cuisinier *et al.*<sup>202</sup> also reported on remarkable differences occurring between the processes involved in the discharge and charge, whether investigated by UV-Vis or XAS techniques, both applied *via in situ* and *operando* methodology.

The surface area of all four  $\text{Li}_2\text{S}$  peaks was integrated and then normalized to the same maximum value. The same formation/re-oxidation behavior was found for all reflections. It may mean that nucleation and growth of the  $\text{Li}_2\text{S}$  particles are isotropic, since the increase is similar for all directions, and there is no preferential orientation of the crystallites in the electrode.

Since  $\text{Li}_2\text{S}$  peaks are very broad, they may be considered as nano-size particles. Therefore, Scherrer equation (12) was applied to calculate the crystal size ( $d$ ), where  $k$  (instrumental factor) was assumed to be 0.9.

$$d = \frac{k \lambda}{\beta \cos\theta} \quad (12)$$

Only the most intense peak (111) was taken into consideration, and the results are presented on Figure 5-10. It seems that crystallite size increases very rapidly just at the beginning of  $\text{Li}_2\text{S}$  formation, followed by very slow increase of size, reaching the maximum value of  $\sim 8.8$  nm. The rapid increase of the crystallite size is concomitant with the large efficiency of  $\text{Li}_2\text{S}$  formation. This evolution may be related to the control of  $\text{Li}_2\text{S}$  crystallization by nucleation process. This parallel evolution may be associated with a slow growth of particles size, really likely due to the decrease of the electrode active surface by insulating  $\text{Li}_2\text{S}$  coverage. Quite similar values of  $\text{Li}_2\text{S}$  crystal sizes at the end of discharge were reported by Abruña *et al.*<sup>200</sup> (7 nm), and Cañas *et al.*<sup>198</sup> (6.5 nm). During the charge process, a two-step evolution can be also noticed regarding the crystallite size. First, in large part of  $\text{Li}_2\text{S}$  dissolution, the crystallite size decreases really slowly, which may indicate that only smaller nano-particles of  $\text{Li}_2\text{S}$  may contribute to the charge process. In the case of smaller particles consumption, calculated crystallite size may not evolve, while the total amount of  $\text{Li}_2\text{S}$  is actually decreasing. This can easily be understood, as the smaller  $\text{Li}_2\text{S}$  particles may be oxidized more easily as compared to the larger ones (as analogy to nano- $\text{Li}_2\text{S}$  and commercial micro-size  $\text{Li}_2\text{S}$ , see section 4.2). In a second part, a neat decrease of the crystallite size occurs, which may be explained by the consumption of bigger  $\text{Li}_2\text{S}$  nano-crystallites at this step.

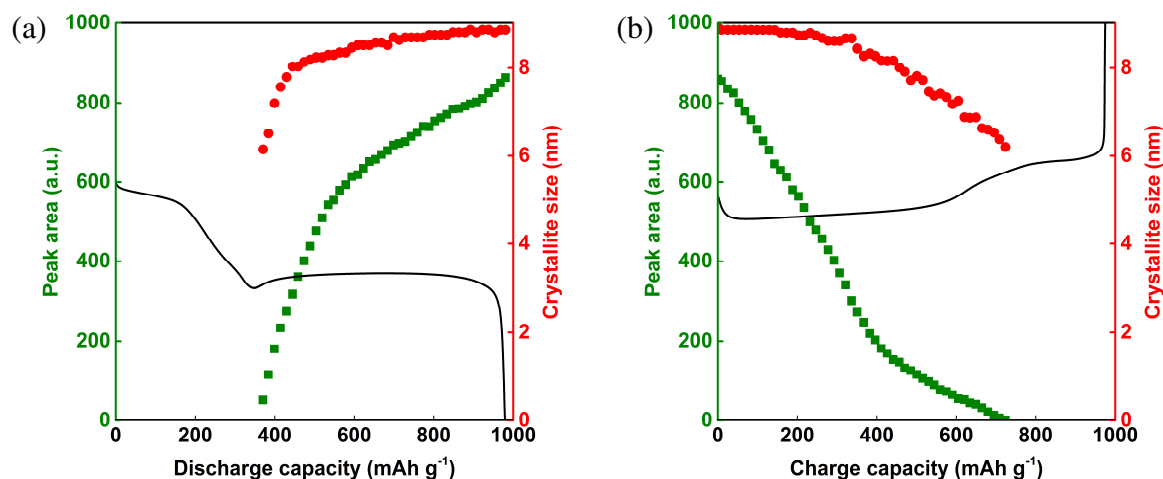


Figure 5-10. Evolution of crystallite size (calculated with Scherrer equation, applied to the most intense Li<sub>2</sub>S reflection (111)), superimposed with peak area evolution and voltage profile.

### 5.4.3. *Ex situ* XRD – supporting data for analysis

A specific methodology was applied in order to be able to quantify the real amount of Li<sub>2</sub>S being formed at the end of discharge. The main idea was as follow: since we know the amount of sulfur in the electrode at the initial state (*i.e.* 27 mg), we could theoretically estimate the amount of Li<sub>2</sub>S that would be formed at the end of discharge, assuming a complete reaction of S<sub>8</sub> to Li<sub>2</sub>S, where 16 electrons are exchanged. Knowing the amount of Li<sub>2</sub>S formed experimentally during the second plateau, thanks to the use of the Li<sub>2</sub>S peak areas at each state of discharge, we are able to compare the practical capacity of this low voltage discharge plateau with the effective amount of Li<sub>2</sub>S formed. In turn, we were able to determine the efficiency of Li<sub>2</sub>S formation *versus* the effective charges exchanged.

To perform this quantitative approach, we tried to correlate the Li<sub>2</sub>S peak area with the quantity of Li<sub>2</sub>S formed (in moles), and with the quantity/peak area of sulfur material initially present in the electrode. To this purpose, three different powder batches having different mass ratios of S<sub>8</sub>/Li<sub>2</sub>S: 2/1, 1/2 and 1/1, were prepared. In order to prepare the S<sub>8</sub>/Li<sub>2</sub>S mixtures at desired mass ratios, and to avoid direct mixing of both powders at different oxidation states, in the first step S<sub>8</sub> and Li<sub>2</sub>S powders were grinded with SuperP<sup>®</sup> (with little amount of cyclohexane), to provide kind of immediate protection of Li<sub>2</sub>S and S<sub>8</sub> from each other. Such obtained mixtures of S<sub>8</sub>/SuperP<sup>®</sup> and Li<sub>2</sub>S/SuperP<sup>®</sup>, once dried, were then mixed together in a beaker, and the same procedure was applied for three different S<sub>8</sub>/Li<sub>2</sub>S ratios. XRD was recorded on three samples obtained for quantitative purposes. All procedure, starting from powders mixing

together with XRD samples preparation, was conducted in the glove box, due to sensitivity of  $\text{Li}_2\text{S}$  powder.

The recorded XRD patterns (Figure 5-11) allowed to determine the correlation between the peak areas (*i.e.* of (222) and (111) reflections, for  $\text{S}_8$  and for  $\text{Li}_2\text{S}$ , respectively) and the  $\text{S}_8/\text{Li}_2\text{S}$  molar ratio, according to equation (13).

$$\frac{\text{Peak area (111) } \text{S}_8}{\text{Peak area (222) } \text{Li}_2\text{S}} \leftrightarrow \frac{\text{moles } \text{S}_8}{\text{moles } \text{Li}_2\text{S}} \quad (13)$$

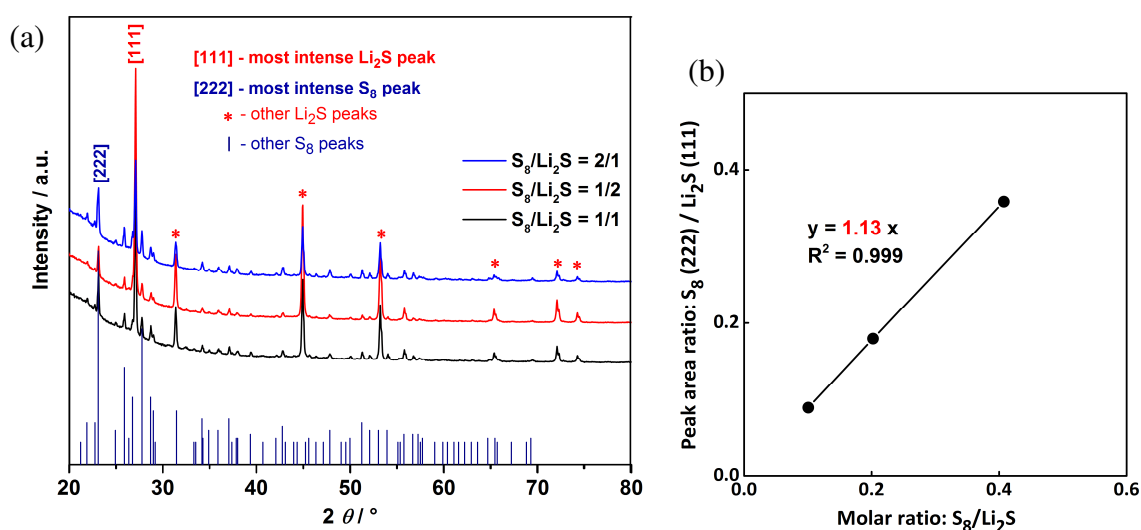


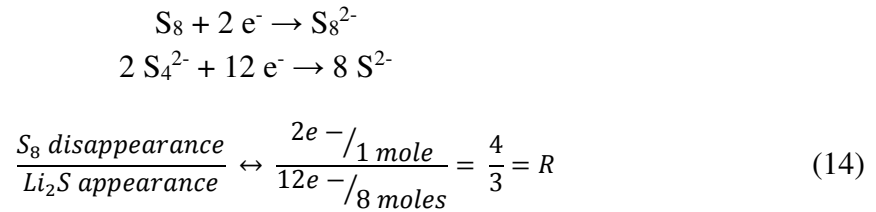
Figure 5-11. XRD patterns (a) recorded on three different mass ratios of  $\text{S}_8/\text{Li}_2\text{S}$ : 2/1 (in blue), 1/2 (in red) and 1/1 (in black). A linear relation between integrated peak surface area ratio vs. molar ratio  $\text{S}_8/\text{Li}_2\text{S}$  of prepared samples was obtained (b). Only the most intensive reflection of sulfur (222) and  $\text{Li}_2\text{S}$  (111) were taken into account.

Therefore, knowing the initial amount of sulfur in the electrode (27 mg) and the integrated peak surface areas for both  $\text{Li}_2\text{S}$  and  $\text{S}_8$ , it was possible to estimate the real quantity of  $\text{Li}_2\text{S}$  produced upon discharge and consumed upon charge. Even if micrometric  $\text{Li}_2\text{S}$  powder (commercial one) was used to prepare these  $\text{Li}_2\text{S}/\text{S}_8$  samples for quantitative purposes, while the electrochemical processes in a real Li/S cell rather involves nanometric  $\text{Li}_2\text{S}$  particles, we made the assumption that the effect of the particle size would be negligible for evaluation of molar ratios through correlation with XRD patterns.

For the three investigated  $\text{S}_8/\text{Li}_2\text{S}$  compositions, the relation between the peak area and the molar ratio gives a straight line, with a slope equal to  $A = 1.13$ . One should note that this correlation was found to be stable during the time necessary for the XRD measurement. This indicates that, even if a large reactivity between  $\text{S}_8$  and  $\text{Li}_2\text{S}$  is expected, the use of micrometric powders combined with a prior mixing with SuperP<sup>®</sup> permits to perform XRD measurements of these batches before observing any  $\text{S}_8/\text{Li}_2\text{S}$  reaction.

Coming back to the electrochemical processes occurring during discharge, we aimed at determining the quantity of  $\text{Li}_2\text{S}$  produced experimentally *versus* the theoretical quantity. All steps were investigated by looking at  $\text{S}_8$  disappearance towards  $\text{Li}_2\text{S}$  formation, *i.e.* following the global process of discharge.

According to the fact that the reduction of 1 mole of  $\text{S}_8$  consumes 2 moles of electrons, and the reduction of two moles of  $\text{S}_4^{2-}$  leads to 8 moles of  $\text{S}^{2-}$ , while consuming 12 electrons, the ratio of  $\text{S}_8$  disappearance towards  $\text{Li}_2\text{S}$  appearance, in terms of exchanged capacity, and normalized to the number of moles exchanged, is equal to  $4/3$  ( $R$ ), and calculated according to equation (14):



This ratio was further derived in order to take into account the correlation between the peaks areas of (111) and (222) reflections, and the molar ratio between  $\text{S}_8$  and  $\text{Li}_2\text{S}$ , *i.e.* the slope  $A$  ( $A = 1.13$ ), that was determined experimentally thanks to *ex situ* XRD measurements. An additional parameter, so called  $R'$ , was determined as follow:

$$\frac{\text{S}_8 \text{ disappearance}}{\text{Li}_2\text{S appearance}} \times \frac{\text{Peak area (111) S}_8}{\text{Peak area (222) Li}_2\text{S}} \leftrightarrow R \times 1.13 = 0.849 = R' \quad (15)$$

This theoretical coefficient  $R'$ , representing correlation between  $\text{S}_8$  disappearance and  $\text{Li}_2\text{S}$  appearance in terms of exchanged capacity and peaks areas of *ex situ* XRD patterns, was then compared with experimental data. Experimental coefficient  $R_{\text{exp}}$  was extracted from *in situ* XRD patterns, by correlation of the  $\text{Li}_2\text{S}$  and  $\text{S}_8$  peaks areas evolution upon discharge with the practical capacity (Figure 5-12).

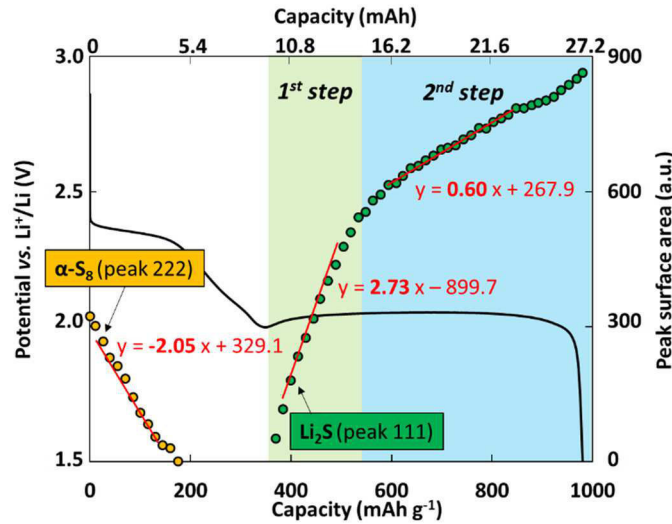


Figure 5-12. Evolution of  $S_8$  consumption and  $Li_2S$  formation upon discharge, and determination of correlation between practical discharge capacity and peaks areas of *in situ* XRD patterns.

To this purpose, Figure 5-12 allows to correlate the real and experimentally obtained evolution of  $S_8$  and  $Li_2S$  peaks areas as compared to the practical capacity (in  $\text{mAh g}^{-1}$ ). Thus, in the first part of  $Li_2S$  formation (1<sup>st</sup> step), the ratio between sulfur disappearance and  $Li_2S$  appearance experimentally obtained is 0.75, calculated as follow:

$$\frac{\text{Slope of } S_8 \text{ disappearance}}{\text{Slope of } Li_2S \text{ appearance (1}^{st} \text{ step)}} = \frac{2.05}{2.73} = 0.75 = R_{exp} (1^{st} \text{ step}) \quad (16)$$

where the two slopes refer to the correlation between peak areas of (111) and (222) reflections and the practical discharge capacity (in  $\text{mAh g}^{-1}$ ).

This experimental ratio  $R_{exp} (1^{st} \text{ step})$  should be directly comparable with the one theoretically calculated before ( $R'$ ).  $R_{exp}$  is  $\sim 10\%$  lower than the theoretical one ( $R' = 0.849$ ), indicating an efficiency of  $Li_2S$  production larger than 1, which is practically impossible. This artifact may come from the wrong estimation of sulfur amount present in the electrode at the beginning of cycling. Indeed, keeping in mind that part of the capacity of the 1<sup>st</sup> discharge may be lost due to self-discharge ( $175 \text{ mAh g}^{-1}$  experimentally obtained, instead of  $209 \text{ mAh g}^{-1}$  theoretically calculated, as discussed earlier in section 5.4). Taking into account this possible uncertainty, the experimental parameter  $R_{exp} (1^{st} \text{ step})$  is not so far from the theoretical one ( $R'$ ), indicating  $Li_2S$  formation efficiency close to 1 during the first step of the low voltage discharge plateau.

In the second part of  $Li_2S$  formation (2<sup>nd</sup> step), the experimental ratio between sulfur disappearance and  $Li_2S$  appearance is calculated according to the equation (17):

$$\frac{\text{Slope of } S_8 \text{ disappearance}}{\text{Slope of } Li_2S \text{ appearance (2}^{nd} \text{ step)}} = \frac{2.05}{0.6} = 3.4 = R_{exp} (2^{nd} \text{ step}) \quad (17)$$

In this case, the  $R_{\text{exp}}$  (2<sup>nd</sup> step) parameter is much larger than the theoretical one ( $R' = 0.849$ ), indicating an efficiency of  $\text{Li}_2\text{S}$  formation much lower than 1. As the efficiency of  $\text{Li}_2\text{S}$  formation is near 1 during the first step, we can determine the amount of  $\text{Li}_2\text{S}$  formed during the first step, and in turn we can deduce the capacity (in mAh) associated to the formation of  $\text{Li}_2\text{S}$  during the second step.

The positive electrode is composed of 27 mg of  $\text{S}_8$ , leading to a theoretical capacity of 45.2 mAh. As 16 electrons are exchanged per mole of sulfur, an exchange of one electron corresponds to 2.82 mAh. Assuming the complete reaction of  $\text{S}_4^{2-}$  to form  $\text{Li}_2\text{S}$  (through the following reaction:  $2 \text{S}_4^{2-} + 12 \text{e}^- \rightarrow 8 \text{S}^{2-}$ ), the production of  $\text{Li}_2\text{S}$  should correspond to 33.9 mAh (*i.e.*  $12 \cdot 2.82 \text{ mAh} = 33.9 \text{ mAh}$ ).

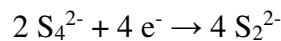
During the first step of  $\text{Li}_2\text{S}$  production, 4.6 mAh (refer to Figure 5-12) are exchanged experimentally, instead of 33.9 mAh theoretically calculated based on the amount of sulfur present in the electrode. Thus, only ~ 14 % of awaited/expected  $\text{Li}_2\text{S}$  quantity is practically formed at this moment of discharge (at  $550 \text{ mAh g}^{-1}$ ).

Using the  $\text{Li}_2\text{S}$  peak area recorded at the end of discharge, *i.e.* at  $980 \text{ mAh g}^{-1}$ , and the *ex situ* XRD data, the amount of crystalline  $\text{Li}_2\text{S}$ , which is practically deposited on the electrode and detected by *in situ* XRD, is about 24 % (equation (19)) of the  $\text{Li}_2\text{S}$  quantity expected at the end of discharge, which corresponds to 8.1 mAh in total, and only 3.5 mAh for the second step (as 4.6 mAh are exchanged during the first step of  $\text{Li}_2\text{S}$  formation):

$$\frac{\text{Peak area of Li}_2\text{S at the end of discharge}}{\text{Peak area of Li}_2\text{S (at 550 mAh g}^{-1})} * \% \text{ of Li}_2\text{S at 550 mAh g}^{-1} \quad (18)$$

$$= \frac{864}{509} * 0.14 = 0.24 = 24 \%$$

During the second step of  $\text{Li}_2\text{S}$  formation, the charge exchanged is equal to 11.6 mAh (refer to Figure 5-12), meaning that about 8.1 mAh are consumed for another reduction process, not related to crystalline  $\text{Li}_2\text{S}$  production. If we determine the amount of charge used for the  $\text{S}_4^{2-}/\text{S}_2^{2-}$  reaction:



then 11.3 mAh ( $4 \cdot 2.82 \text{ mAh} = 11.3 \text{ mAh}$ ) would be needed for this electrochemical process. Experimentally, 8.1 mAh are consumed by another reduction process, which represents 72 % of the theoretical charge associated with  $\text{S}_4^{2-}/\text{S}_2^{2-}$  reaction. The collected data show that near 24 % of  $\text{S}_4^{2-}$  is involved in the formation of  $\text{S}^{2-}$ , with only 10 % during the second step (14 % for the first step), while 72 % may be involved in the formation of  $\text{S}_2^{2-}$  afterwards. If we then add the amounts of  $\text{S}_4^{2-}$  consumed during the two proposed reactions, almost complete reduction of  $\text{S}_4^{2-}$  is obtained (72 % + 24 % = 96 %). Therefore, when using the amount of  $\text{Li}_2\text{S}$  formed and the 'extra' exchanged capacity, the composition (in mol%) of the  $\text{Li}_2\text{S}/\text{Li}_2\text{S}_2$

mixture at the end of discharge can be estimated. Taking into account the stoichiometry of the two reactions ( $S_4^{2-} + 2 e^- \rightarrow 2 S_2^{2-}$  and  $S_4^{2-} + 6 e^- \rightarrow 4 S^{2-}$ ), the molar ratio can be determined, and the mixture might then be composed of about 40% of  $Li_2S$  and 60% of  $Li_2S_2$ , without excluding the existence of other polysulfides in a small amount. A schematic illustration on Figure 5-13 summarizes the proposed mechanisms arising from XRD data treatment.

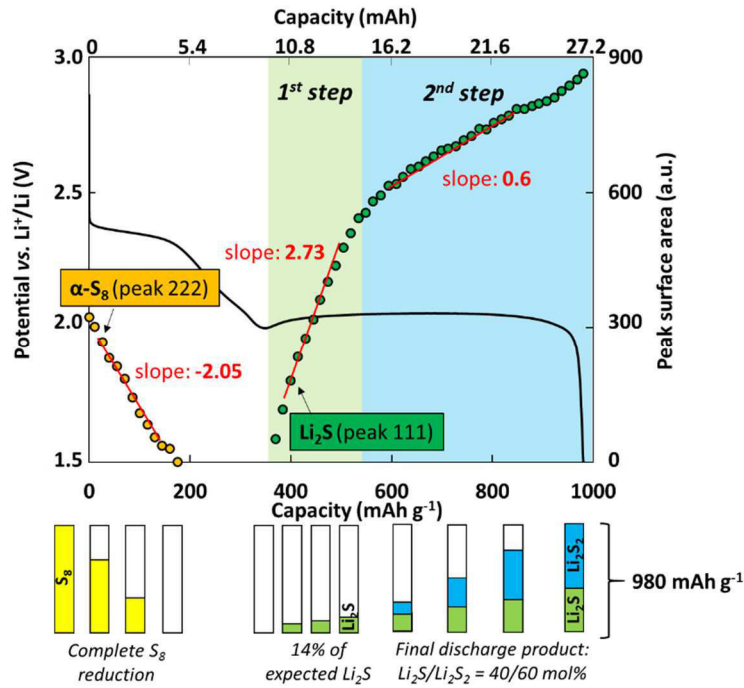


Figure 5-13. Proposed mechanism for  $Li_2S/Li_2S_2$  formation upon discharge.

The low voltage plateau can be divided into two parts, which do not follow the same mechanisms:

- during the first step,  $Li_2S$  is produced with an efficiency close to 100 %
- during the second step,  $Li_2S$  is produced with a much lower efficiency, of about 13 %, calculated with equation (19):

$$\frac{Li_2S}{Li_2S + Li_2S_2} = \frac{\frac{3.5 \text{ mAh}}{12 e^-}}{\frac{3.5 \text{ mAh}}{12 e^-} + \frac{8.1 \text{ mAh}}{4 e^-}} \quad (19)$$

while  $Li_2S_2$  is predominantly formed with an efficiency close to 87 %.

We clearly prove that  $Li_2S_4$  is directly reduced to  $Li_2S$  with 100 % of efficiency at the beginning. This behavior could be associated with the weak stability of  $Li_2S_2$  compound<sup>241</sup>. Afterward, the efficiency decreases dramatically down to 13 %.

This large modification in the reduction mechanism of  $S_4^{2-}$  ( $Li_2S$  or  $Li_2S_2$  formation) could be related to the passivation of the electrode with the formation of insulating  $Li_2S$  layer, which

may limit the kinetic of the reduction process. The decrease in  $\text{Li}_2\text{S}$  efficiency could have several explanations:

- 1) an increase of the current density associated with a decrease in the electrode surface may change the electrochemical process, with the formation of  $\text{Li}_2\text{S}_2$  as intermediate compounds, which is more soluble than  $\text{Li}_2\text{S}$ ;
- 2) a direct reaction between  $\text{Li}_2\text{S}_4$  and  $\text{Li}_2\text{S}$  produced by reduction, which forms more soluble  $\text{Li}_2\text{S}_2$  species in accordance to the disproportionation reaction:  $\text{Li}_2\text{S}_4 + 2 \text{Li}_2\text{S} \rightarrow 3 \text{Li}_2\text{S}_2$ . This reaction may constantly consume  $\text{Li}_2\text{S}$  which is produced during the reduction process, thus decreasing the apparent efficiency of  $\text{Li}_2\text{S}$  formation.

In conclusion, the final discharge product is composed of a  $\text{Li}_2\text{S}/\text{Li}_2\text{S}_2$  mixture, which conveniently explains the practical lower discharge capacity ( $980 \text{ mAh g}^{-1}$ ), which is a little bit more than half of the theoretical one. Indeed, the missing part of  $\text{Li}_2\text{S}_2$  conversion into  $\text{Li}_2\text{S}$  ( $\sim 72 \%$ ) represents a large part of the theoretical capacity ( $\sim 72 \%$  of  $838 \text{ mAh g}^{-1}$ ), *i.e.*  $\sim 600 \text{ mAh g}^{-1}$ . This part of the capacity, which seems not to be accessible based to these calculations, allows to explain the main difference between experimentally obtained capacity ( $980 \text{ mAh g}^{-1}$ ) and the theoretical one ( $1675 \text{ mAh g}^{-1}$ ). To increase the practical capacity, the conversion of  $\text{Li}_2\text{S}_2$  into  $\text{Li}_2\text{S}$  should be enhanced, which may be currently limited by the low/non solubility and the poor electronic conductivity of these two species that rapidly passivate the positive electrode during the low voltage discharge plateau.

Indeed, as previously demonstrated, *post mortem* SEM photos (Fig 3-5, chapter 3) of a discharged electrode on NwC collector clearly show that a very thin and dense layer of deposit (estimated to be  $\sim 150 - 200 \text{ nm}$ ) was formed at the surface of each fiber. However, if assuming that this layer is composed of pure  $\text{Li}_2\text{S}$ , and calculating the amount of  $\text{Li}_2\text{S}$  that is formed in this case (knowing the surface area of NwC carbon, density of  $\text{Li}_2\text{S}$  and the thickness of this thin deposit), such obtained value is much lower than if calculated based on the electrochemical data (assuming that the entire low voltage plateau corresponds to the formation of  $\text{Li}_2\text{S}$  only). Thus, it is really likely that the discharge proceeds through the formation of another intermediate compound, such as  $\text{Li}_2\text{S}_2$ . It is also clear from SEM photos that, apart from the thin and dense deposit, more ‘volumetric’ solid formation occurs in between the fibers. More investigation should be performed in this direction to conclude on the chemical composition of these different layers.

Figure 5-14 shows analogical investigation of the initial charge process.



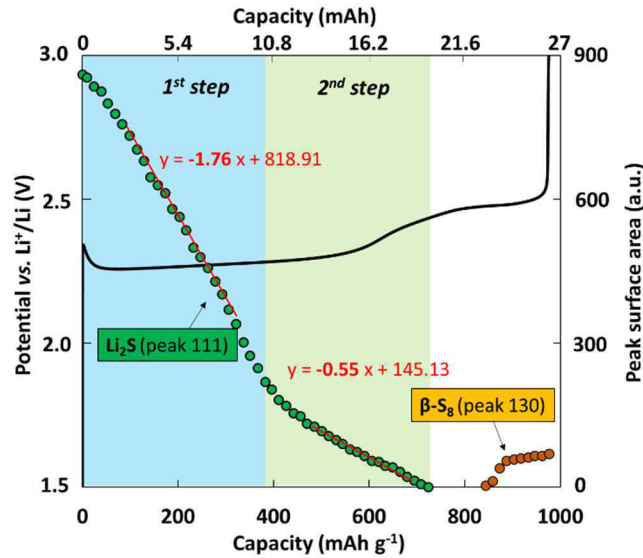


Figure 5-14. Charge process: investigation of  $\text{Li}_2\text{S}$  consumption and charging mechanism.

Upon charge, the oxidation of both  $\text{Li}_2\text{S}$  and  $\text{Li}_2\text{S}_2$  products occurs. During the first step, using the recorded evolution of  $\text{Li}_2\text{S}$  (111) peak area, 75 % of  $\text{Li}_2\text{S}$  amount that was formed at the end of discharge, is oxidized (equation (20)).

$$\frac{\text{Peak area of } \text{Li}_2\text{S} \text{ at the end of the first step of charge}}{\text{Peak area of } \text{Li}_2\text{S} \text{ at the end of discharge}} = \frac{219}{864} = 0.25 \quad (20)$$

This amount of oxidized  $\text{Li}_2\text{S}$  corresponds to:

- If we consider the reaction pathway  $8\text{S}^{2-} \rightarrow 2\text{S}_4^{2-} + 12\text{e}^-$ , 75 % of  $\text{Li}_2\text{S}$  conversion is associated with 6.1 mAh ( $0,75 \cdot 8,1 \text{ mAh}$ , *i.e.* the amount of charge related to  $\text{Li}_2\text{S}$  formation during prior discharge). As 10.5 mAh (refer to Figure 5-14) permit to oxidize both  $\text{Li}_2\text{S}$  and  $\text{Li}_2\text{S}_2$  during the first step of the charge process, the oxidation of  $\text{Li}_2\text{S}_2$  corresponds to 4.4 mAh, *i.e.* 54 % of  $\text{Li}_2\text{S}_2$  is oxidized ( $\frac{4,4 \text{ mAh}}{8,1 \text{ mAh}} \cdot 100 \%$ )
- If we consider the reaction pathway  $2\text{S}^{2-} \rightarrow \text{S}_2^{2-} + 2\text{e}^-$ , 75 % of  $\text{Li}_2\text{S}$  conversion is associated with 4.3 mAh. As 10.5 mAh (refer to Figure 5-14) permit to oxidize both  $\text{Li}_2\text{S}$  and  $\text{Li}_2\text{S}_2$  during the first step of charge process, the oxidation of  $\text{Li}_2\text{S}_2$  to  $\text{Li}_2\text{S}_4$  ( $4\text{S}_2^{2-} \rightarrow 2\text{S}_4^{2-} + 4\text{e}^-$ ) corresponds to 6.2 mAh. Since the capacity of 2.82 mAh corresponds to the exchange of one electron, 2.2 electrons would then be exchanged through this reaction pathway, which would correspond to 55 % of  $\text{Li}_2\text{S}_2$  oxidized to  $\text{Li}_2\text{S}_4$  (*i.e.* 2.2 electrons over the 4 electrons needed for the complete reappearance of  $\text{Li}_2\text{S}_4$ ).

Whatever the charging process (the direct oxidation of  $\text{Li}_2\text{S}$  to  $\text{Li}_2\text{S}_4$  or the oxidation of  $\text{Li}_2\text{S}$  to  $\text{Li}_2\text{S}_2$ ),  $\text{Li}_2\text{S}$  seems to be oxidized during the first step at higher rate than  $\text{Li}_2\text{S}_2$ . During the

second step of charge, the efficiency of  $\text{Li}_2\text{S}$  oxidation decreases notably. Indeed, as previously mentioned, oxidation of  $\text{Li}_2\text{S}_4$ , leading to the formation of long chain polysulfides, can also occur in addition to the oxidation of  $\text{Li}_2\text{S}_2$  and  $\text{Li}_2\text{S}$ , in accordance with the potential increase, as probably of faster kinetics than the solid phase reaction of  $\text{Li}_2\text{S}/\text{Li}_2\text{S}_2$ .

#### 5.4.4. Conclusions

To summarize, an original approach based on quantitative interpretation of *in situ* and *operando* XRD results, supported by *ex situ* XRD measurements (conducted on different  $\text{S}_8/\text{Li}_2\text{S}$  ratios), allowed us to propose a mechanism of solid products creation during discharge. At the beginning of lower voltage plateau, formation of  $\text{Li}_2\text{S}$  occurs with efficiency close to 1, whereas afterwards, the efficiency clearly decreases, which could indicate the formation of intermediates species such as  $\text{Li}_2\text{S}_2$ , even if not detected by XRD.

### 5.5. Further cycles evolution at C/20

It is commonly known that initial cycle of Li/S batteries is not necessarily the most representative one. Therefore, in order to have more complete vision of the active material structural changes occurring in the system, it was important to record the XRD response of sulfur electrode during further cycles.

#### 5.5.1. The second cycle

The evolutions recorded during the second cycle are very close to the initial one. Figure 5-15 shows the XRD patterns obtained during 2<sup>nd</sup> discharge and 2<sup>nd</sup> charge, together with the experimental potential curves. The electrochemical performances result in expected voltage profile together with satisfying capacity values (892 and 923 mAh g<sup>-1</sup> for discharge and charge, respectively). Higher capacity value for the charge can be associated with the shuttle mechanism. Despite of the technical issues (beam loss), leading to the loss of some XRD patterns, still valuable conclusions can be withdrawn.

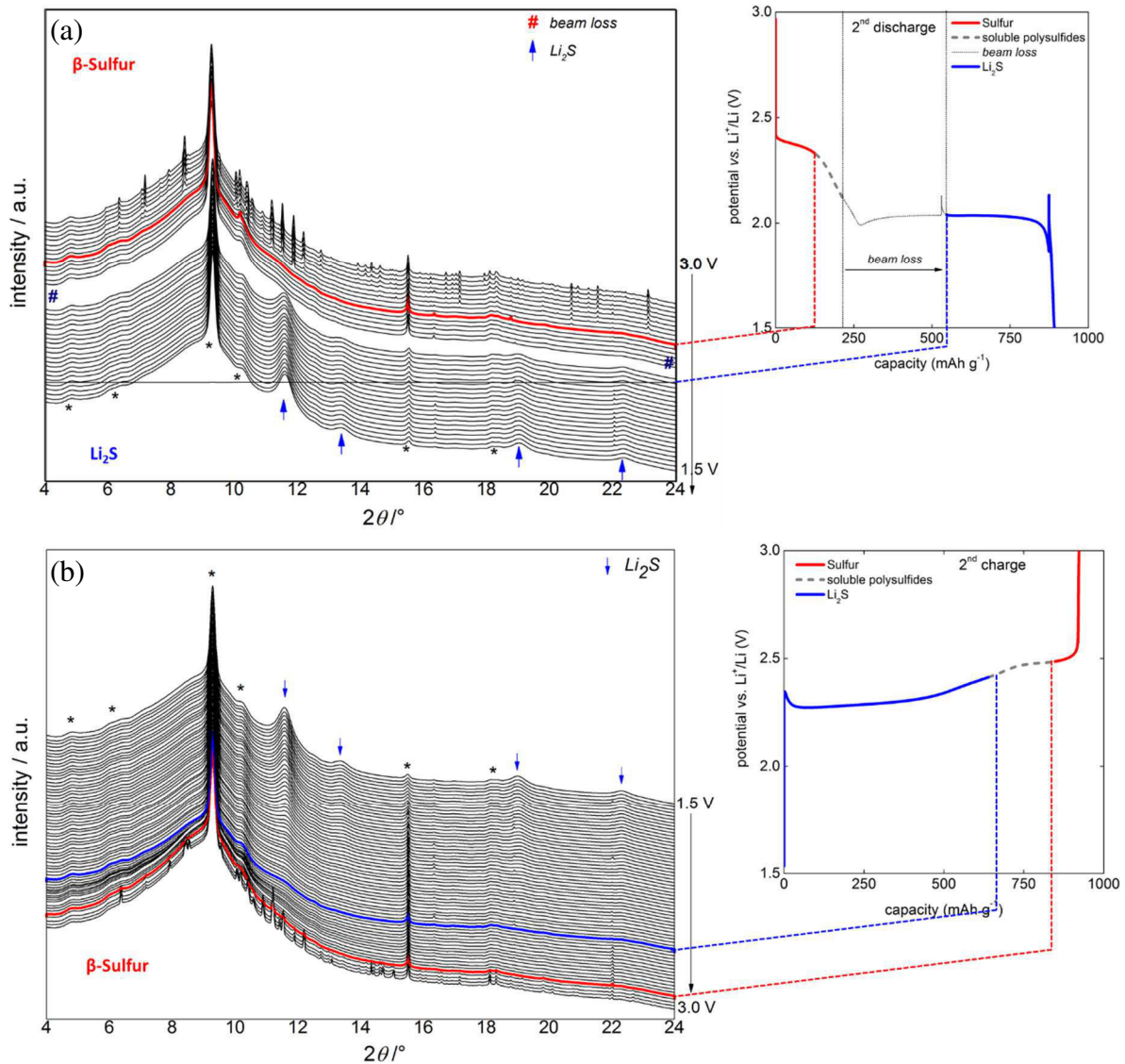


Figure 5-15. *In situ* XRD patterns evolution and corresponding electrochemical curve recorded during 2<sup>nd</sup> cycle at C/20: discharge (a) and charge (b). Peaks related with packaging are marked by \*. Loss of the beam resulted in some of the XRD patterns missing. The cell had to be stopped twice during discharge, which explains the voltage peak visible upon discharge.

Solid crystalline sulfur disappears completely with the end of higher plateau (at 126 mAh g<sup>-1</sup>) and reappeared at the end of charge (at 848 mAh g<sup>-1</sup>). In both cases, only  $\beta$ -sulfur was detected.

The general trend is very similar to the one observed at the initial cycle. Sulfur disappearance is rather linear (Figure 5-16), with no specific orientation during sulfur consumption, while sulfur recrystallizes with preferential orientations upon 2<sup>nd</sup> charge, since the intensities of the peaks evolve randomly, once higher once lower, as compared with the intensity observed at the end of previous charge. This prohibits any estimation of the amount of crystalline sulfur created at every further charge.

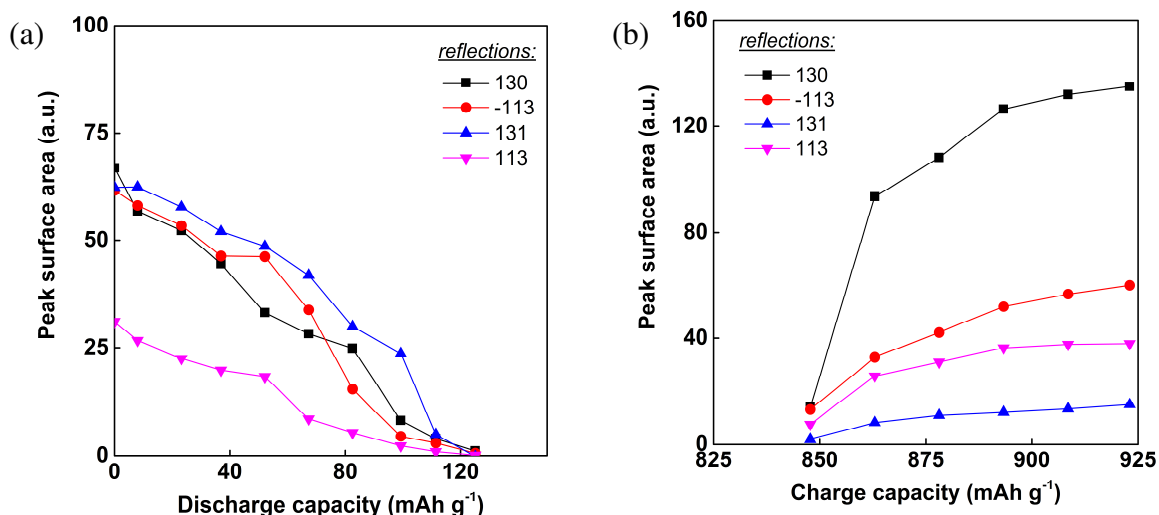


Figure 5-16. Evolutions of selected reflections' surface area as a function of capacity: reduction of  $\beta$ -sulfur at the beginning of 2<sup>nd</sup> discharge (a), recrystallization at the end of 2<sup>nd</sup> charge (b).

Evolution of crystalline  $\text{Li}_2\text{S}$  was confirmed by the presence of the same four peaks, as in the initial cycle. Unfortunately, due to the beam loss, the precise moment of  $\text{Li}_2\text{S}$  formation was missed. The first XRD pattern recorded after the beam restarted (at  $\sim 60\%$  DOD) shows already significant reflections of  $\text{Li}_2\text{S}$ . We compared then the XRD pattern recorded at  $\sim 60\%$  DOD during the first cycle, with the one obtained at the same moment during the second cycle. Both patterns were almost identical, meaning that the amounts of  $\text{Li}_2\text{S}$  formed at this point of the plateau were very close for both discharges. Based on these findings, we could conclude that the nucleation process of  $\text{Li}_2\text{S}$  should be relatively similar for both first and second cycles, starting right at the beginning of lower discharge plateau and after the potential dip visible at each cycle.

Integrated peak area of the most intense reflection (111), plotted as a function of capacity (Figure 5-17) shows very similar hysteresis, as previously described in the initial cycle. The maximum crystallite size was calculated to be  $\sim 7.9$  nm (8.8 nm in the first cycle), which allows to conclude the relatively similar behavior of these two cycles in terms of solid phase formation. Generally speaking, evolutions of active material upon cycling were found to be very similar in both cycles at the same current density ( $C/20$ ).

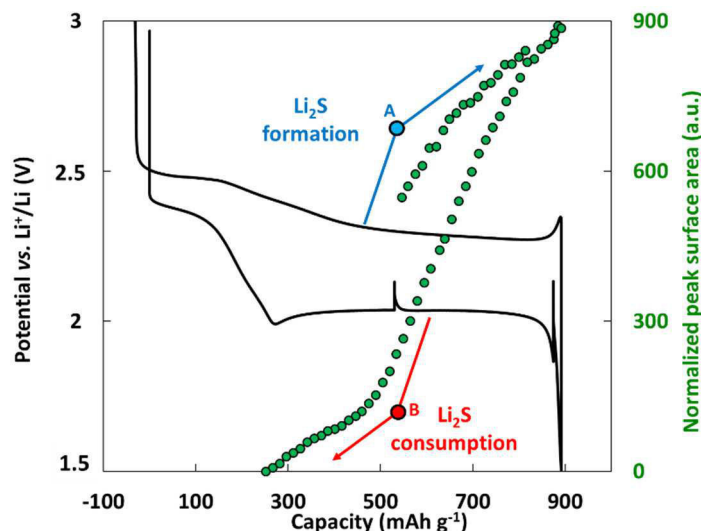


Figure 5-17.  $\text{Li}_2\text{S}$  formation and disappearance during the second cycle. Integrated surface area of (111) reflection as a function of capacity.

### 5.5.2. The twenty sixth cycle

We were also interested in monitoring the Li/S pouch cell during much later cycle, in order to see if any solid phase evolution would still be detectable. For that experiment, a pouch cell was prepared much before the planned synchrotron session, and left for cycling at  $C/20$  in the laboratory (on Arbin<sup>®</sup> cycler). The cell was then stopped at the end of 25<sup>th</sup> discharge, transferred to ESRF facilities<sup>†</sup> and cycled again during following charge and the next 26<sup>th</sup> full cycle at  $C/20$ , while exposed to the beam. Figure 5-18 presents the solid phases evolutions recorded during the 25<sup>th</sup> charge and the 26<sup>th</sup> discharge, together with the capacity retention of the pre-cycled pouch cell.

One can still observe evolution (formation and disappearance) of crystalline  $\text{Li}_2\text{S}$  upon cycling. However, only (111) peak can be detected. The others are probably not intense enough, and are covered by the strong signal of thick polypropylene bag, which was used specially to protect the cell from air during pre-cycling for 2 weeks. It was interesting to observe that the nucleation of crystalline  $\text{Li}_2\text{S}$  is starting exactly at the same moment as for the first cycle previously shown, *i.e.* at the beginning of the low voltage plateau.

<sup>†</sup> ESRF-based results were used for qualitative analysis only, and not quantitative ones. Pouch cell was monitored in one position, where the beam was penetrating through the complete cell.

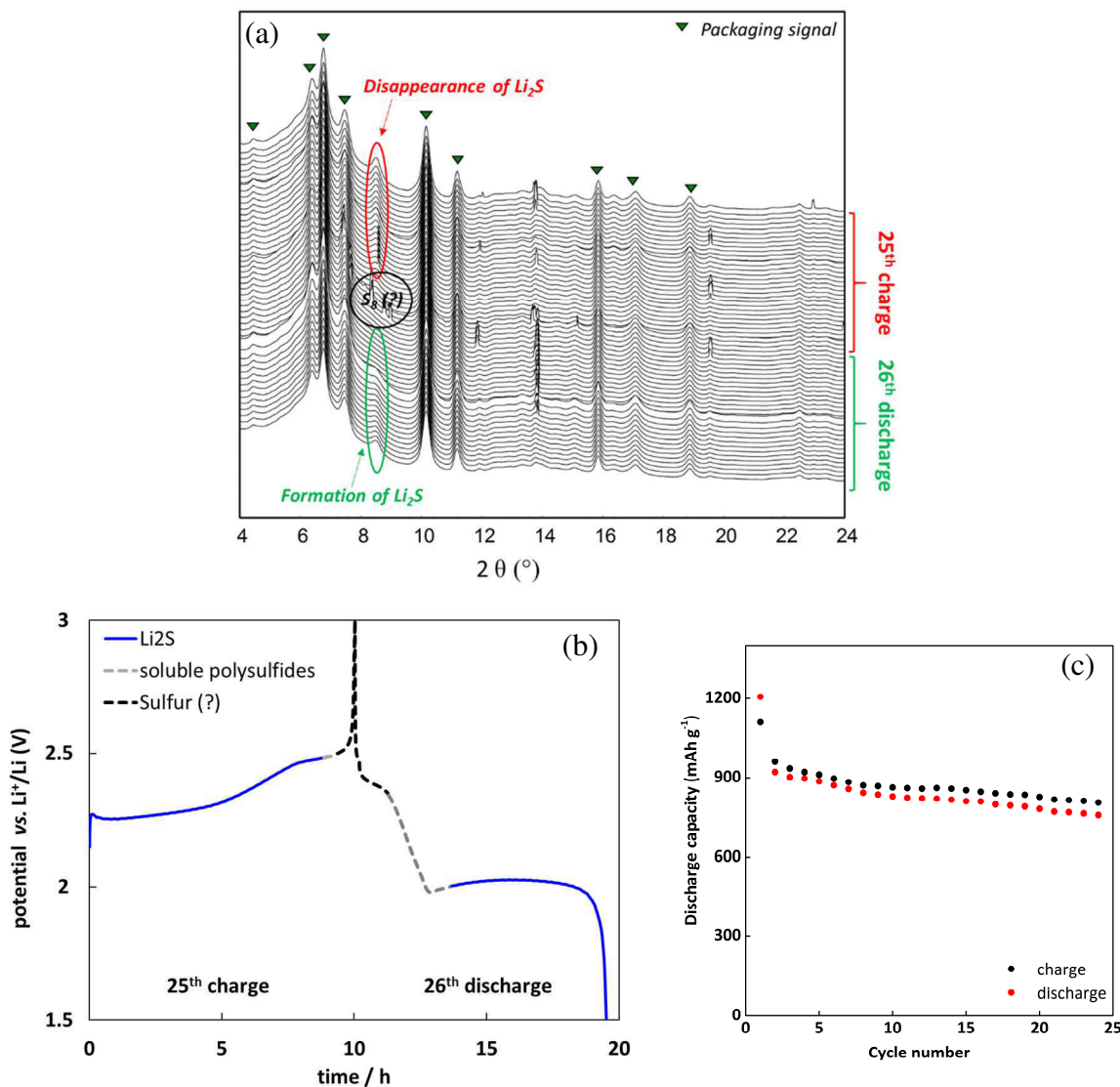


Figure 5-18. Evolution of XRD patterns of a pre-cycled cell: 25<sup>th</sup> charge and 26<sup>th</sup> discharge at  $C/20$  were observed (a), experimental voltage profile with the moments of solid phases formation/disappearance (b), capacity retention at  $C/20$  over 25 cycles prior to synchrotron measurements (c).

Formation of sulfur at the end of charge could not be entirely confirmed. Indeed, Bragg peaks appeared and disappeared at the moments expected for sulfur appearance/disappearance. However, as our statistics were quite low and as the peak profile is ill-defined due to technical problems with the beam, it was difficult to clearly assign these patterns. Therefore, it was hardly possible to conclude on the formation of beta crystalline form of sulfur.

## 5.6. Influence of the C-rate: C/8 studies

In this section, we aimed at investigating the influence of current density (almost three times higher as compared to  $C/20$ ;  $i \sim 0.9 \text{ mA cm}^{-2} \leftrightarrow C/8$ ) on the active material structural changes

and electrochemical process. In following section, the recorded results of first, second, fifth and sixth cycles are discussed.

### 5.6.1. XRD and electrochemistry – results

As already explained at the beginning of this chapter (section 5.2.1), we were able to observe 1<sup>st</sup> – 2<sup>nd</sup> cycles during ESRF session (with qualitative interpretation only), as well as 5<sup>th</sup> – 6<sup>th</sup> during SOLEIL session (where quantitative analysis are included).

Figure 5-19 shows the electrochemical curve of two initial cycles recorded in ESRF, with indicated moments of solid/soluble phase transition. Rather similar behavior, as the one at C/20, can be seen. During the initial discharge, elemental  $\alpha$ -sulfur is completely reduced by the end of higher voltage discharge plateau (~ 2.25 V). One can notice significant polarization of the voltage profile in the region corresponding to sulfur reduction, as compared to C/20 (~ 2.4 – 2.3 V). This may be related with the fact that the particles of bare sulfur are relatively large (even reaching 50  $\mu\text{m}$ ), thus more difficult to reduce. However, the cell polarization is not visible anymore during the 2<sup>nd</sup> cycle at C/8, as sulfur recrystallization may be accompanied with a reorganization of active material particles size and its contact with carbon. Total sulfur disappearance is recorded at a capacity of 165  $\text{mAh g}^{-1}$ , which is almost identical to sulfur disappearance at C/20 (175  $\text{mAh g}^{-1}$ ). This proves that sulfur can easily get reduced during initial discharge, no matter the current rate (staying in moderate current values). At the end of charge, expected peaks of sulfur material start to appear<sup>‡</sup>. Second cycle shows reduction and recrystallization of sulfur at the moments in full agreement with previous observations (C/20 cycles, refer to part 5.3).

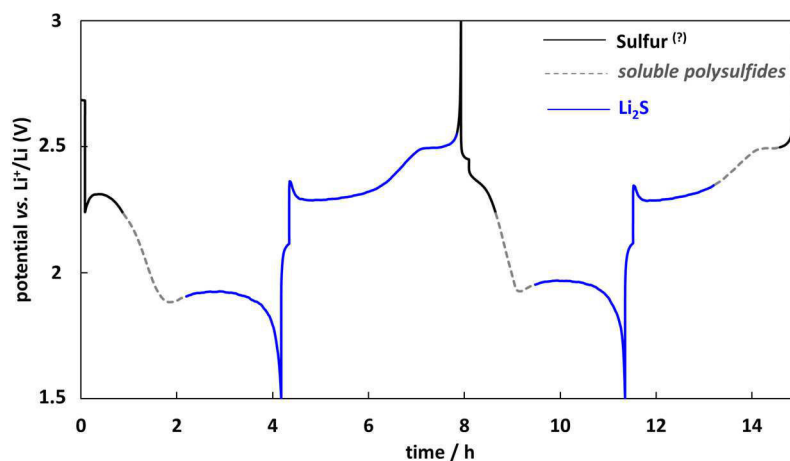


Figure 5-19. Electrochemical performances of the first and second cycle at C/8, recorded in ESRF ( $\lambda = 0.49593 \text{ \AA}$ ), with moments of solid phases  $\text{Li}_2\text{S}$  and  $\text{S}_8$  appearance/disappearance.

<sup>‡</sup> ESRF-based results. Impossible to determine clearly the sulfur phase due to the not well-defined peak profiles.

Appearance of crystalline  $\text{Li}_2\text{S}$  was confirmed by following reflections: (111), (200), (220) and (311), starting to be visible at the very beginning of lower discharge plateau, accompanied with the potential dip characteristic for  $\text{Li}_2\text{S}$  nucleation. It should be underlined here that in the case of ESRF samples, each XRD pattern was recorded every 18 min. As the complete discharge at C/8 lasts 4 h only, 13 XRD scans were recorded during initial discharge. Therefore, fidelity of detecting the exact moment of solid/soluble phase transition was less precise as in case of SOLEIL measurements at C/20 (almost 80 XRD patterns registered during initial discharge). During charge, slightly different results were observed. Upon the first charge,  $\text{Li}_2\text{S}$  remains detectable on the electrode almost until the end of charge, while it disappears already at 55 % SOC during the second charge. Such discrepancies, which were not observed at low C-rate, can indicate the heterogeneity of the oxidation process in the overall electrode. In addition, it is also likely that synchrotron-based *in situ* XRD measurements may not always represent the real response of a full electrode (6.3 cm<sup>2</sup>, while beam size being of ~ 300  $\mu\text{m}$  x 300  $\mu\text{m}$ , *i.e.* ~ 2 % of the electrode surface).

Fifth and sixth cycles at C/8 were monitored at SOLEIL, on so-called ‘back up’ cell (cell 2), which was switched to the beam after first three cycles at C/20. As the electrochemistry of two pouch cells cycled in parallel (cell 1 and cell 2, see Table 5-2) was basically identical, we assumed that the reproducibility between the two cells was good enough to quantitatively compare the results obtained at C/20 (recorded on cell 1) with the ones at C/8 (recorded on cell 2).

Figure 5-20 shows the electrochemical curves of 5<sup>th</sup> and 6<sup>th</sup> cycles and the solid/soluble phase transitions. For simplicity, only selected XRD patterns are presented.

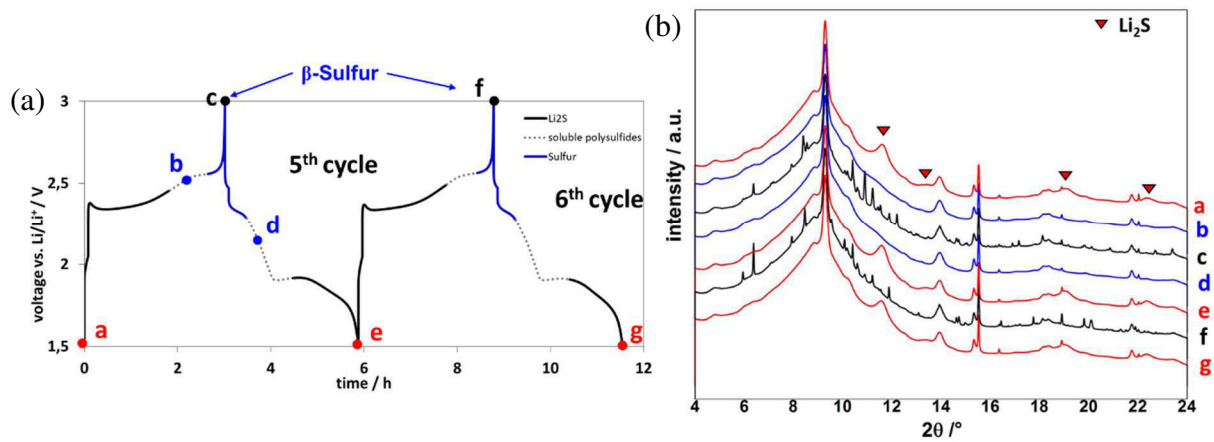


Figure 5-20. 5<sup>th</sup> and 6<sup>th</sup> cycle evolution recorded at C/8: electrochemical curve (a) and selected XRD patterns (b).

Reproducible behavior can be observed for both cycles at C/8, concerning moments of  $\text{Li}_2\text{S}$  and sulfur appearance/disappearance. Nucleation of  $\text{Li}_2\text{S}$  starts a bit after the little potential dip visible in the discharge curve. The shift of  $\text{Li}_2\text{S}$  appearance seems to be reproducible (in regard to the precision of exact appearance) between 5<sup>th</sup> and 6<sup>th</sup> cycle, confirming the delay of solid



phase formation. The explanation could be linked to a different mechanism of  $\text{Li}_2\text{S}$  formation with some delay in this low voltage plateau at high C-rate. In parallel,  $\beta\text{-S}_8$  was detected at the end of both charges. This proves that  $\alpha$ -sulfur is present in the electrode only at the initial state of the Li/S battery, *i.e.* before cycling. Once it gets reduced into soluble lithium polysulfides, all further recrystallization/reduction steps involve  $\beta$ -sulfur form, as illustrated on the schematic graph below (Figure 5-21).

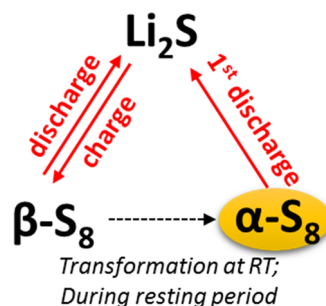


Figure 5-21. Schematic graph illustrating changes of the active material solid forms upon cycling.

### 5.6.2. Quantitative interpretation

In this part, we mostly focused on  $\text{Li}_2\text{S}$  formation/disappearance processes, and on the effect of current density on the kinetic of this reactions.

Figure 5-22 presents the evolution of (111) peak intensity as a function of capacity. We can clearly observe the slight hysteresis between formation and re-oxidation of  $\text{Li}_2\text{S}$ , even if less pronounced than at lower C-rate. We can also distinguish two steps for both  $\text{Li}_2\text{S}$  formation/consumption. However, the difference in the slope is not as remarkable as it was in the case of C/20. It can be also noticed that the presence of  $\text{Li}_2\text{S}$  on the electrode surface is much longer during its oxidation, as compared with the moment of the creation. Further detailed interpretation of the possible mechanism based on these observations was not the scope of this manuscript.

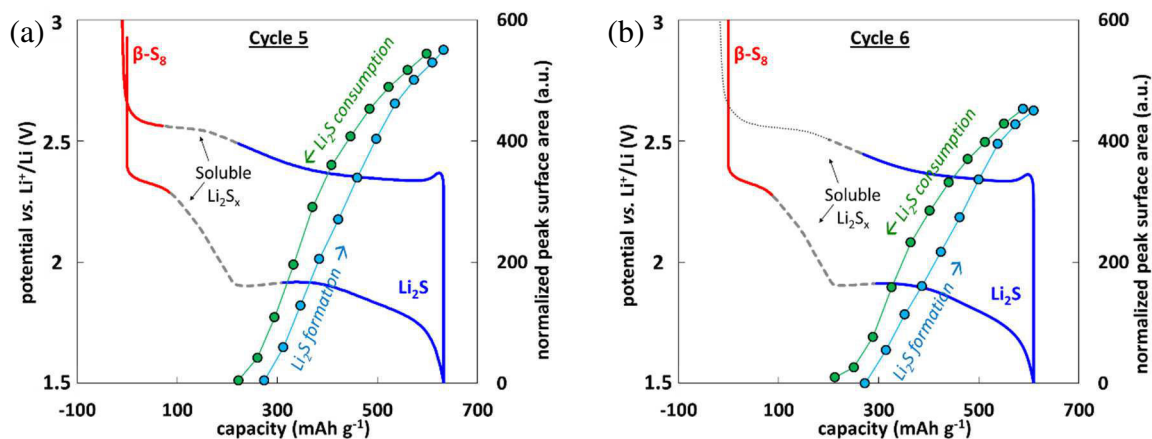
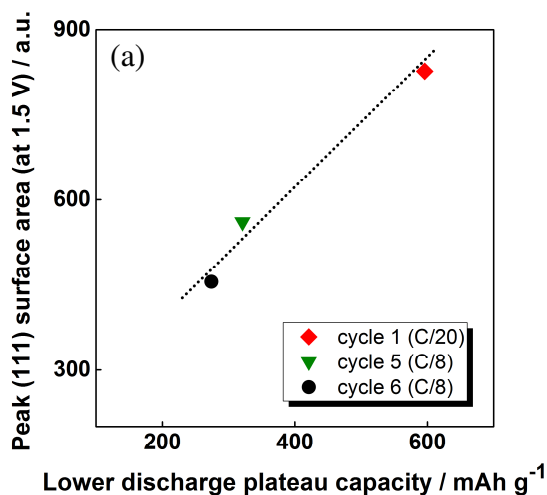


Figure 5-22. Surface area evolution of Li<sub>2</sub>S (111) peak during 5<sup>th</sup> (a) and 6<sup>th</sup> (b) cycle at C/8. β-S<sub>8</sub> appearance and disappearance is also marked (in red).

In the next step, we compared the integrated surface area of the most intense (111) reflection of Li<sub>2</sub>S recorded at the end of discharge with the capacity of lower discharge plateau for both C rates (C/20 and C/8), bearing in mind that the final amount of Li<sub>2</sub>S formed at the end of discharge is interrupted by Li<sub>2</sub>S<sub>2</sub> formation, according to the previous detailed discussion (section 5.4). Doing so, we observe rather linear behavior (Figure 5-23a), indicating that the C-rate (at least for moderate values) does not have a significant influence on the total (for both steps) efficiency of Li<sub>2</sub>S formation. We also compared the crystallite size obtained at the end of different cycle number and C-rates (Figure 5-23b). As they are relatively similar, this brings us to the conclusion that current density (C-rate) does not affect the crystallite size.



(b)

cell	cycle #	C-rate	Max. crystallite size at end of discharge (nm)
cell 1	1	C/20	8.8
	2	C/20	7.9
cell 2 ('back up')	5	C/8	8.3
	6	C/8	8.3

Figure 5-23. Capacity corresponding to the lower discharge plateau, obtained at both C-rates, *i.e.* C/20 and C/8, plotted vs. Li<sub>2</sub>S (111) peak surface area, recorded at the end of discharge (a). Summary of the crystallite size calculated for both C-rates and during several cycles (b).

## 5.7. Conclusions

This work brought new information and deeper understanding of the working mechanisms of Li/S batteries. We successfully analysed the structural changes of active materials inside a Li/S battery during few initial cycles using XRD technique. Our *in situ* synchrotron-based results clearly indicate formation of crystalline  $\text{Li}_2\text{S}$  on the positive electrode at the very beginning of lower discharge plateau. We also propose a sequential discharge mechanism related to the low voltage plateau. First, reduction of  $\text{S}_4^{2-}$  into  $\text{Li}_2\text{S}$  occurs with an efficiency close to 1, whereas for higher DOD%, a competitive reaction appears, and the obtained data seem to be coherent with the formation of  $\text{Li}_2\text{S}_2$  phase in the second step of lower discharge plateau. During charge,  $\text{Li}_2\text{S}$  complete consumption was observed. The moment of  $\text{Li}_2\text{S}$  disappearance is relatively late, probably due to the insulating nature of  $\text{Li}_2\text{S}$  and its difficulty to be oxidized. We also confirmed that soluble polysulfides are oxidized into solid  $\text{S}_8$  at the end of each charge. It was found that, after recrystallization, sulfur does not come back to its pristine structure, but it appears as another allotrope: monoclinic  $\beta$ -sulfur. The same behaviour was obtained over the next cycles, with the formation of  $\text{Li}_2\text{S}$  at the beginning of the lower discharge plateau in a two-step process, and with significant hysteresis between the charge and discharge processes. Similar evolutions were also observed at moderated C-rate (C/8).

The XRD results allow to make a step forward regarding the understanding of discharge/charge mechanisms, but electrochemical impedance spectroscopy was additionally applied to the Li/S system and correlated with the previously discussed findings. The obtained results are presented in the following chapter.

# Chapter 6: Application of Electrochemical Impedance Spectroscopy and low temperature tests

## 6.1. Motivation of the work

Existing literature contains several examples where EIS has been used to characterize Li/S cells. Indeed, it is a very powerful technique that enables the separation of electrical processes occurring in an electrochemical cell according to their specific relaxation frequencies. Therefore, important information can be elucidated from the EIS response. The literature reports on many examples where EIS technique was applied to Li/S cells, for the following purposes: characterization of the charge transport properties (conductivity measurements), investigation of insulating layer formation and dissolution<sup>207</sup>, evaluation of electrode electric response in regard to their composition<sup>128</sup> or more generally – to study the working mechanism<sup>132,209,210,213</sup> upon cycling. While EIS technique is relatively easy to apply, a proper interpretation of the obtained results is far more difficult. Therefore, several divergent interpretations and explanations of the same phenomena can exist in the literature.

Based on obtained *in situ* XRD results, which allowed for the investigation of active material modifications upon battery operation (see chapter 5), we applied EIS as a complementary technique, in order to have broader and deeper insight into the electrochemical processes. Low temperature tests (cycling and EIS) were also applied, which brought fruitful information concerning the kinetics of the reactions, since the different phenomena can be separated better at low temperature than at RT.

## 6.2. Experimental part

### 6.2.1. Coin cell design

All EIS experiments were performed on classical two-electrode Li/S CR2032 coin cells, fabricated as previously described (section 2.2.2). The positive electrode was casted on carbon-based current collector (so called ‘S-on-NwC’, with an average sulfur loading of  $\sim 4.3 \text{ mg}_{\text{Sulfur}} \text{ cm}^{-2}$  and reference composition of 80/10/10 wt% = S/SuperP<sup>®</sup>/PVdF 5130), the same as used inside the pouch cells used for *operando* XRD. Metallic lithium was used as counter electrode.

A three-electrode system, with a reliable reference electrode would be an ideal solution to observe each electrode separately. Nevertheless, this approach cannot be really applied to the Li/S cells, since until now, any stable reference electrode in the presence of soluble lithium polysulfides has been proposed. Kolosnitsyn *et al.*<sup>213</sup> have performed three-electrode cell using metallic lithium as a reference electrode, however, it was rather a supportive approach, while most of the interpretation was done on a two-electrode cell configuration.

We did not apply three-electrode configuration in our studies, in order not to question further the reliability of the obtained results. Thus, classical two-electrode coin cell configuration was chosen, with supporting information obtained from the symmetric coin cells (the concept has been already introduced in section 2.3.3), where both electrodes are either metallic Li or ‘S-on-NwC’ cathodes. For some of the symmetric cells, electrolyte was replaced by the ‘catholyte’ solution (0.25 M Li<sub>2</sub>S<sub>6</sub> dissolved in classical electrolyte).

It is also important to notice that EIS is a very sensitive technique, and a response of ‘bad’ cables/connections or sample holder may significantly modify the HF resistance value, thus more precautions should be taken in order to improve the measurement precision. Also it is necessary to provide sufficient contact between all the cell components, to minimize the contact resistances-related issues. A good example was evidenced through the careful selection of the stainless steel spacer used during coin cell fabrication (available as 0.5 mm and 1.0 mm thick), depending on the global electrodes thicknesses used in the cell.

## 6.2.2. EIS measurements

Electrochemical Impedance Spectroscopy tests were performed on Bio-Logic<sup>®</sup> VMP3 multichannel potentiostat, equipped with impedance modules. Each spectrum was recorded in the frequency range of 1 MHz to 10 mHz, with an excitation potential of 10 mV and 13 points per decade. Obtained results were then fitted using ZView software (Scribner Associates Inc.).

Before observing the Li/S cell upon cycling, the first step was to determine the impedance response of the system at the starting point (*i.e.* at OCV), and to assign the origin of the different components on EIS spectra. To this purpose, symmetric coin cell approach appeared to be a very useful tool.

*In situ* EIS was recorded on the Li/S two-electrode coin cells galvanostatically cycled at C/20 rate, in the potential window of 3.0 V – 1.5 V. The EIS spectra were registered every 1 h, after 15 min of relaxation applied prior to the measurement. This period was found as an optimal/compromise value, enough for reaching rather stable voltage (pseudo-equilibrium) and not too long to avoid polysulfide composition changes, self-discharge, disproportionation, etc.

### 6.3. Impedance response – Nyquist plot features

Nyquist plot of two-electrode Li/S response is shown on Figure 6-1. Three regions with different time constants can be clearly distinguished and are separated by vertical dot lines for easier visualization.

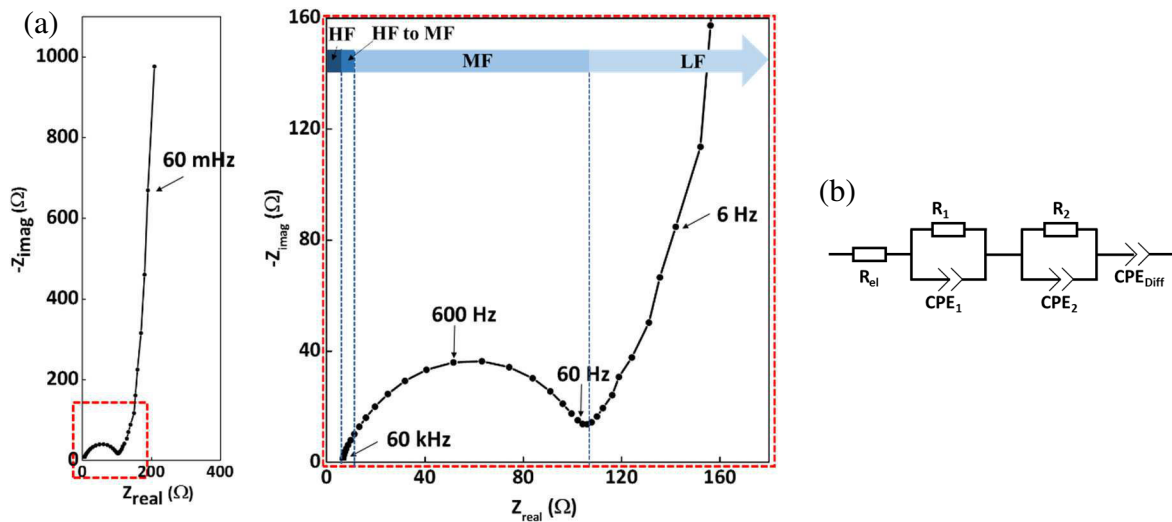


Figure 6-1. Nyquist plot of a Li/S cell at the initial state (a) and corresponding equivalent circuit (b).

As previously described in section 2.3.3, (where symmetric coin cells tests were discussed), high frequency (HF) region can be attributed to the ohmic resistance of the cell, resulting from electrolyte resistance, coin cells casing, sample holder, leads and terminals and is represented by a pure resistor ( $R$ ). A depressed semicircle in the middle frequency (MF) part is usually modeled with a resistor ( $R$ ) in parallel with a constant phase element (CPE). A straight vertical line in the very low frequency region (LF) indicates blocking character of the system *vs.* electrochemical reaction. However, the porous character of the electrode leads to a distribution of the local interfacial capacity observed at the beginning of the low frequency straight line<sup>228</sup>. A CPE can be also proposed for modeling this part of the spectra<sup>212</sup> in the situations when the inclined line (due to local interfacial capacity distribution) and the blocking part (a purely vertical straight line) are not well-separated in frequency.

While the literature data are in agreement when it comes to the HF and LF regions interpretation, the origin of the MF semicircle is still controversial. Proposed interpretations are: charge transfer resistance (often attributed to the positive electrode solely) and its relevant capacitance<sup>132</sup>, electronic contact resistance in the bulk electrode<sup>212</sup>. To our best knowledge, most of the existing reports about EIS applied to Li/S batteries were based on two-electrode cells, very often without deeper discussion concerning the separation of each electrode contribution. Therefore, the first step of our studies, before moving to *in situ* methodology, was

to ‘separate’ the contribution of both electrodes to this MF loop, and symmetric coin cells were prepared and characterized.

### 6.3.1. Symmetric coin cells approach

Figure 6-2 shows Nyquist plots of symmetric cells composed of two similar electrodes (Li||Li,  $S_8$ || $S_8$ ), which are compared with a complete Li/S cell.

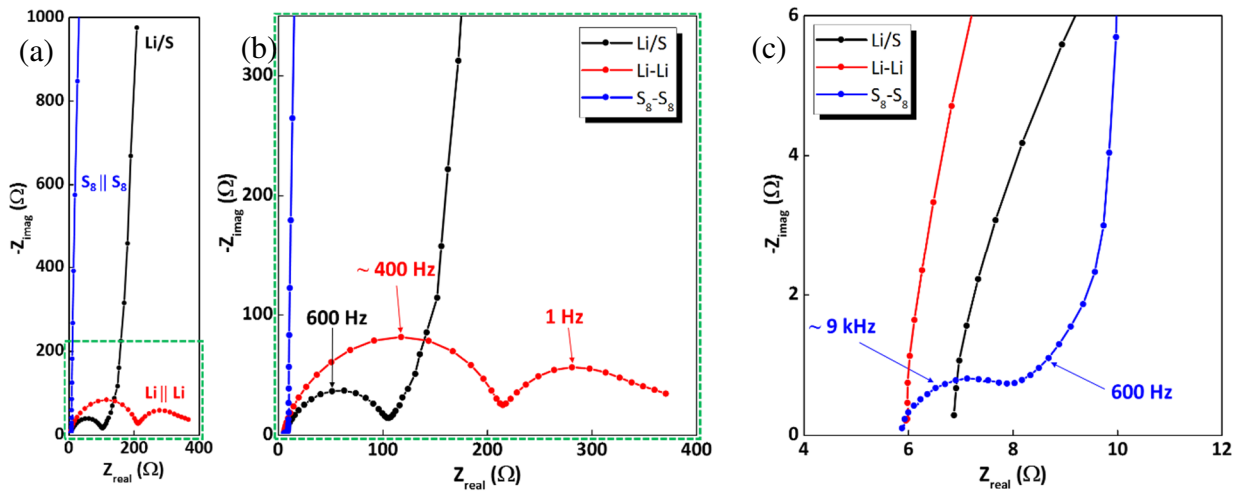


Figure 6-2. Nyquist plot obtained for Li/S complete cell (in black), symmetric Li||Li (in red) and  $S_8$ || $S_8$  (in blue) (a,b); zoomed image on the  $S_8$ || $S_8$  semicircle (c).

To confirm the validity of the symmetric cell approach, experimental data of the complete cell (Li/S) were compared with the calculated one (Figure 6-3), according to equation:  $Z_{Li-S} = \frac{1}{2} Z_{Li-Li} + \frac{1}{2} Z_{S-S}$ . Both graphs are superimposed in the whole frequency range, proving the validity of the symmetric cell approach used for separation of both electrodes to the spectrum of the complete cell.

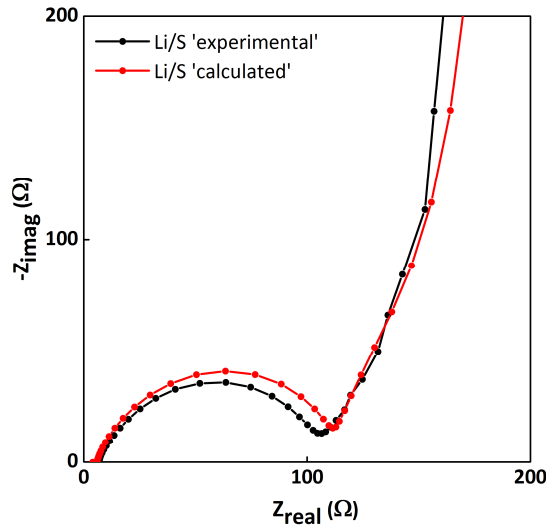


Figure 6-3. Nyquist plots of Li/S cell: comparison of experimentally measured data (in black) with the calculated one (in red).

Firstly, the  $S_8||S_8$  response is mainly dominated by a blocking behavior, which gives the low frequency contribution in the complete Li/S cell. It exhibits a very small semicircle ( $\sim 2 \Omega$ ) at quite high frequencies, *i.e.* at the characteristic frequency of  $\sim 9$  kHz, instead of 600 Hz in the complete cell. This loop was previously interpreted (chapters 2 and 3) as characteristics of the electron transport in the electronic pathway in the positive electrode. In any cases, the contribution of the positive electrode resistance to the MF loop of complete Li/S cell is very small, and cannot be distinguished in the overall response. On the contrary, we can note that the characteristic frequency of the semicircle in a complete cell (Li/S) and symmetric Li||Li cell are almost identical, and their amplitudes are very similar (in the range of  $\sim 100 \Omega$ ). Therefore, the loop in the MF range (of Li/S cell) can be attributed to the lithium negative electrode, with a main contribution coming from the passivation layer on the lithium surface<sup>225,248</sup>. One could also notice the presence of a semicircle in the LF region for the symmetric Li||Li cell (Figure 6-2b, red curve). The literature often attributes this LF semicircle to the charge transfer occurring on the negative electrode<sup>225,248</sup>. In our case however, we cannot really correlate it with the charge transfer and corresponding double layer capacitance. We roughly estimated the capacitance of this semicircle according to equation (23):

$$\begin{array}{l} \text{Resistor in parallel with pure Capacitor (C)} \\ \text{relation:} \end{array} \quad R \cdot C \cdot \omega = 1 \quad (21)$$

$$\begin{array}{l} \text{Resistor in parallel with a Constant Phase} \\ \text{Element (CPE) relation:} \end{array} \quad R \cdot Q \cdot \omega^\alpha = 1 \quad (22)$$

$$C = R^{(\frac{1}{\alpha}-1)} \cdot Q^{\frac{1}{\alpha}} \quad (23)$$

If considering  $\alpha \sim 0.575$  and  $R \sim 160 \Omega$  (obtained from LF semicircle fitting), a capacitance value of  $\sim 1 \cdot 10^{-3} \text{ F cm}^{-2}$  was found. Assuming that for a charge transfer resistance process, a



capacitance is known to be in the range of  $1 - 10 \mu\text{F cm}^{-2}$ ,<sup>249</sup> therefore our values do not match this range, and this semicircle cannot be correlated only to the charge transfer reactions on Li. More likely is that the LF semicircle could rather originate from a diffusion process through passivation layer(s) on Li surface, *i.e.* inner and outer deposited layer<sup>249</sup>. Our capacity values (range of  $\sim 10^{-3} \text{ F cm}^{-2}$ ) are in complete agreement with report of Woo *et al.*<sup>249</sup>, who studied symmetrical Li||Li cell degradation.

We have shown that the metallic lithium electrode significantly contributes to the initial impedance response of the Li/S cell, mainly through its passivation layer. Moreover, the resistance value is strongly related with the initial state of the lithium surface. Figure 6-4a shows some examples of symmetric Li||Li cells, where Li was used as-received, or when its surface was cleaned out by scratching with the Teflon<sup>®</sup>-made knife. Furthermore, this interface ages due to well-known passivation reactions, giving a rise to the significant increase of the semicircle amplitude (Figure 6-4b). It can be noticed that the resistance of the passivation layer varies between  $\sim 60 \Omega$  (for 'scratched' surface) up to even  $320 \Omega$  (when left during few hours upon storage).

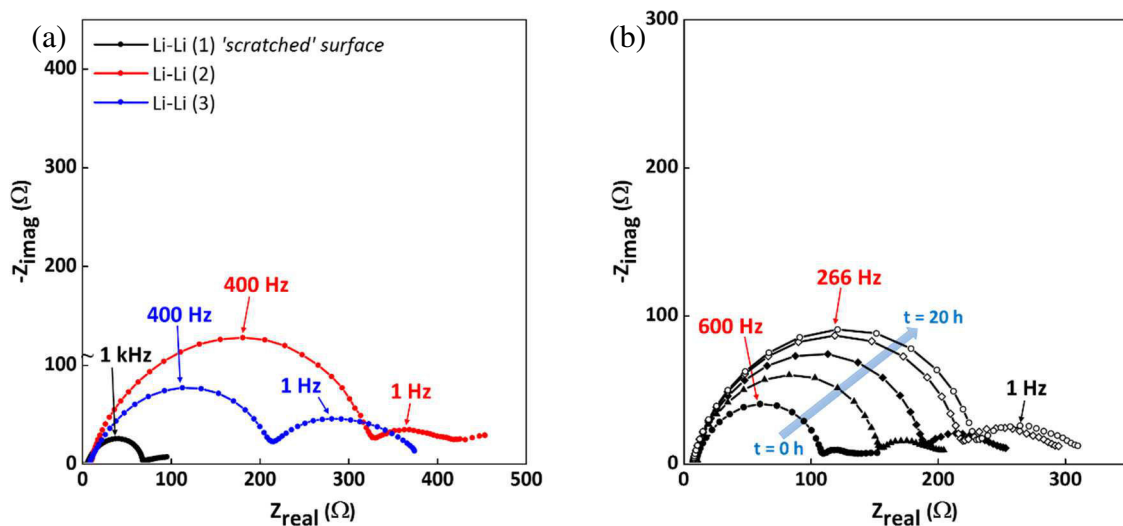


Figure 6-4. Symmetric Li||Li coin cells: three different cells showing the influence of metallic Li surface, thus resulting in large variations of the resistance value at the initial state (a); evolution of a Nyquist plot upon Li||Li cell storage (b).

It is very important to take these findings into consideration, especially during interpretation of the EIS spectra evolution upon cycling. Until now, most of the EIS-related studies of Li/S cell have completely neglected the fact of observing lithium negative electrode in such large extent, and even interpreting the MF semicircle as a charge transfer resistance of the positive electrode.

## 6.4. Li/S cells upon storage – evidence of self-discharge

Li/S coin cell was stored for 250 h at a stable temperature of 25 °C and OCV potential was monitored. EIS spectra were recorded every 30 min. Figure 6-5 shows the evolution of OCV and selected EIS spectra. It can be seen that the vertical line in the low frequency region is slowly losing its blocking character. This capacitive behavior disappearance occurs quite quickly, already during initial 10 h, where the potential decreases drastically (Figure 6-5b).

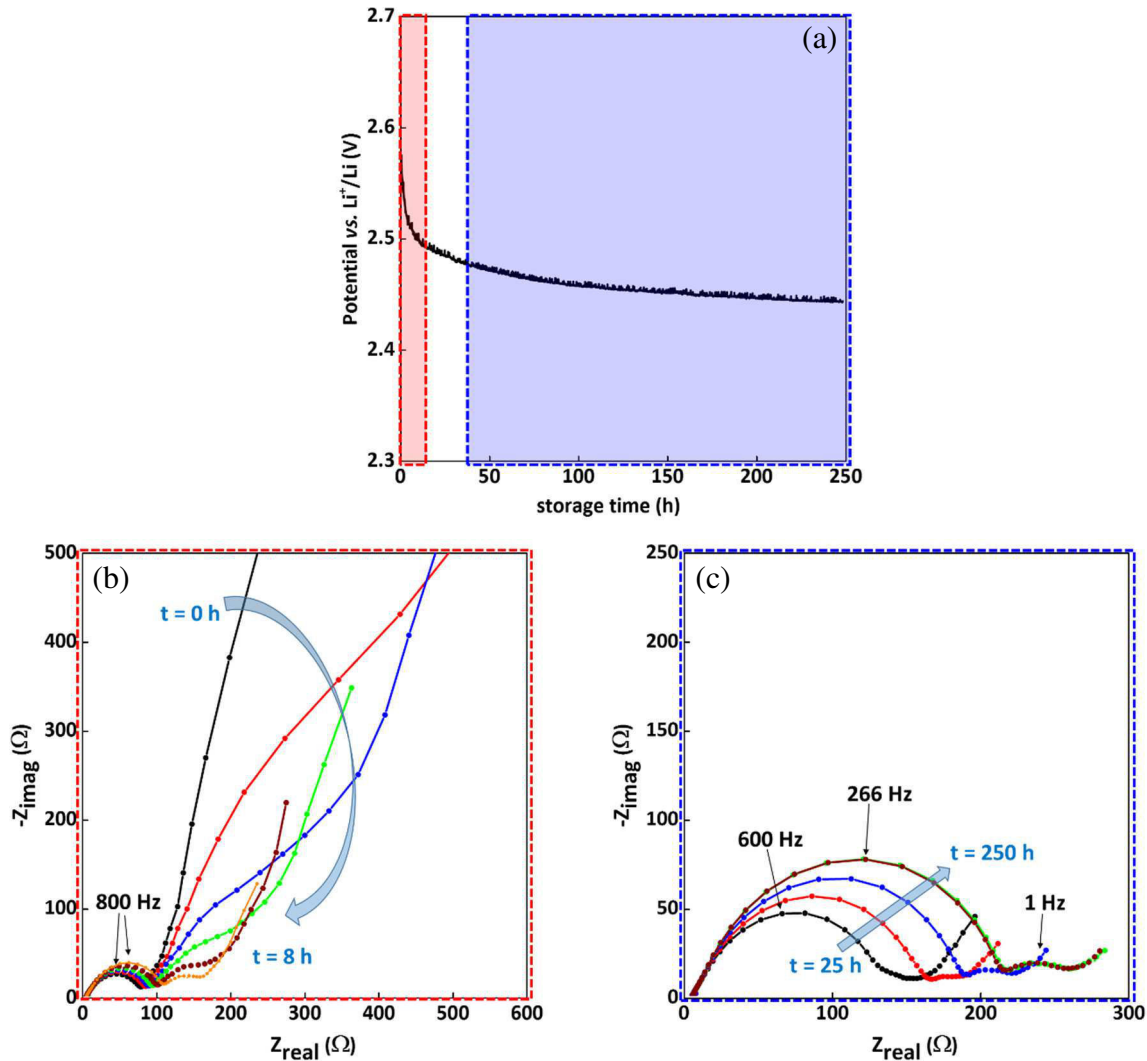


Figure 6-5. Li/S cell left for 250 h storage time, during which EIS was recorded every 30 min. OCV potential evolution (a), Nyquist plot evolution observed during initial few hours (marked in red) (b), and the spectra obtained during further hours of storage (marked in blue) (c).

The reason for that may lie in the relatively easy partial sulfur dissolution in the electrolyte. Literature data<sup>247</sup> as well as our previous experiment (section 3.4.10: the proof-of-concept of insulated sulfur electrode being able to work) proved that dissolution of solid sulfur in ether-

based electrolyte is rather an easy process. Once in liquid solubilized form, sulfur may be more reactive as the solid elemental particles, and may diffuse through the electrolyte to the negative electrode side and get reduced, giving the rise of high-order polysulfides formation. Lithium polysulfides are much more electrochemically active, which may explain the complete disappearance of blocking capacitive behavior of the system upon storage and formation of very small amount of soluble polysulfides, thus giving a rise to the self-discharge process. In order to verify if, indeed, a creation of polysulfides can be detected, three similar Li/S coin cells were prepared and left for storage for 8 h, 70 h and 250 h, during which OCV was controlled and EIS was recorded. The last coin cell, after having its OCV monitored for 250 h, was then left for additional storage of 1.5 months (this time without EIS recording). All three coin cells were opened, and the photos are shown on Figure 6-6.

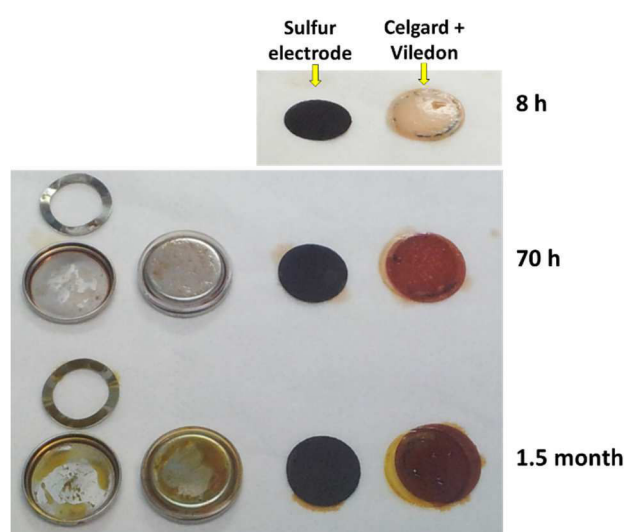


Figure 6-6. Photos of the coin cells dismantled after 8 h, 70 h and 1.5 month of storage (*i.e.* OCV monitoring with EIS recorded).

It can be noticed (even visually) that separator and electrolyte turned into yellowish-reddish color, which clearly proves creation of lithium polysulfides. Longer the storage time was (1.5 month), the more intense color was and the higher dissolved amount seemed to be formed. This also proves that self-discharge occurs relatively easily in Li/S cells, resulting in a drastic potential drop at the beginning (during initial 10 h) of storage time. However, after that time (and during further ~ 250 h of storage), the voltage decrease was relatively slow, and the potential of the cell stabilized at 2.45 V.

As concerning the MF semicircle evolution (previously attributed to the passivation layer on the lithium surface), a progressive increase of its amplitude upon storage can be noticed, together with characteristic frequency values slightly shifting into lower range (*i.e.* 864 Hz at the initial state, 266 Hz after 250 h of storage). Indeed, very similar behavior was found when symmetric Li||Li cells were left upon storage and EIS was recorded every 1 h (Figure 6-4b). Thus, it is very clear that the MF semicircle evolution observed in Li/S cell upon storage can

be directly related with the evolution of Li negative electrode, and growth/modification of its passivation layer.

The growth of the semicircle size (*i.e.* increase of the resistance) shows rather logarithmic behavior, with rapid increase during initial few hours, reaching at some point relatively stable value (in this particular example:  $\sim 220 \Omega$ ), as shown on Figure 6-7.

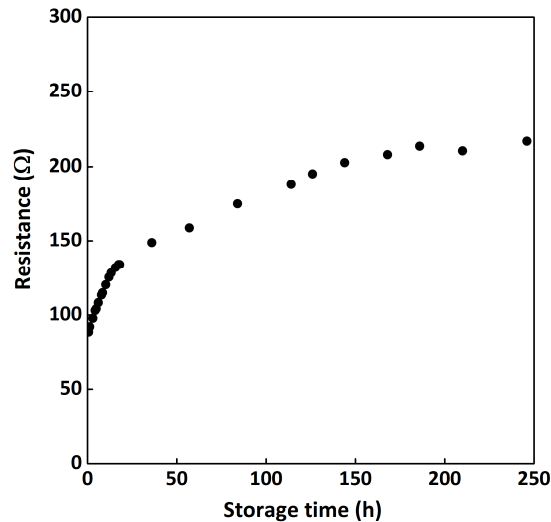


Figure 6-7. Resistance evolution of the MF semicircle during 250 h of storage of a Li/S cell. \*

As previously mentioned, it is very likely that, due to rapid sulfur dissolution and formation of polysulfides already during initial 10 h of storage, the capacitive behavior is not observed any more. The vertical straight line disappears progressively, giving rise to a small semicircle in the LF range, at the characteristic frequency very close to 1 Hz. Once the global ‘shape’ of the Nyquist plot is getting stabilized (after  $\sim 50$  h), further aging results in an increase of the MF semicircle resistance only (as demonstrated on Figure 6-7), while the LF semicircle stays practically unchanged, with characteristic frequency values always at  $\sim 1$  Hz.

It is also important to note that our positive electrode almost does not contribute to the MF semicircle, since coated on NwC collector cloth, which provides enhanced electronic conductivity. If using a classical sulfur electrode, *i.e.* coated on Al foil, and of a larger bulk internal resistance resulting from inhomogeneity of the coating for example (of even  $20 \Omega$ , as extensively discussed in section 2.3.3), the contribution of the positive electrode to the MF loop would be more pronounced, however, still a dominating response would come from the lithium electrode.

\* The error coming from the MF fitting was very small, *i.e.*  $\sim 1\%$ , therefore not included on the graph as an error bars.

After having attributed the origin of the semicircles observed at the initial state of Li/S cell, we then applied EIS technique *via in situ* methodology, upon galvanostatic cycling. Further section presents the obtained results.

## 6.5. Li/S battery upon cycling – initial cycle

Figure 6-8 shows experimental cycling voltage profile of a Li/S cell cycled at C/20. Pseudo-equilibrium potentials, at every point where the cell was stopped and relaxed for 15 min before EIS was recorded, are also indicated (red dots).

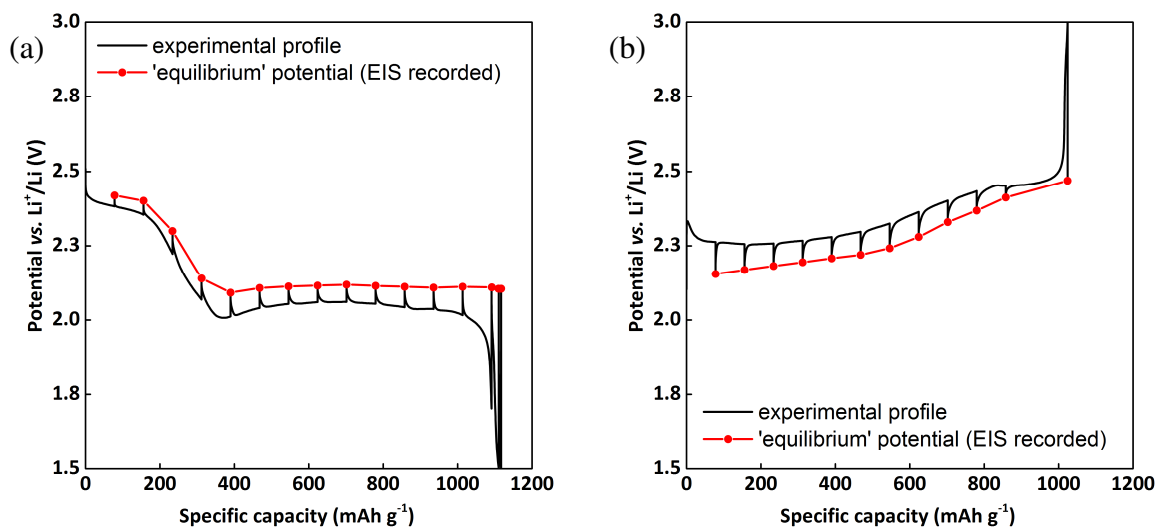


Figure 6-8. Experimental cycling curve with indicated points at which EIS spectra were recorded after 15 min of relaxation, *i.e.* equilibrium potential (red dots): discharge (a) and charge (b) profiles.

### 6.5.1. Nyquist plot evolution

Figure 6-9 shows the evolution of the Nyquist plot, obtained while recording the impedance every 1 hour during initial discharge and charge. For easier visualization, the numbers at the spectra correspond to the numbers reported on the cycling profile.

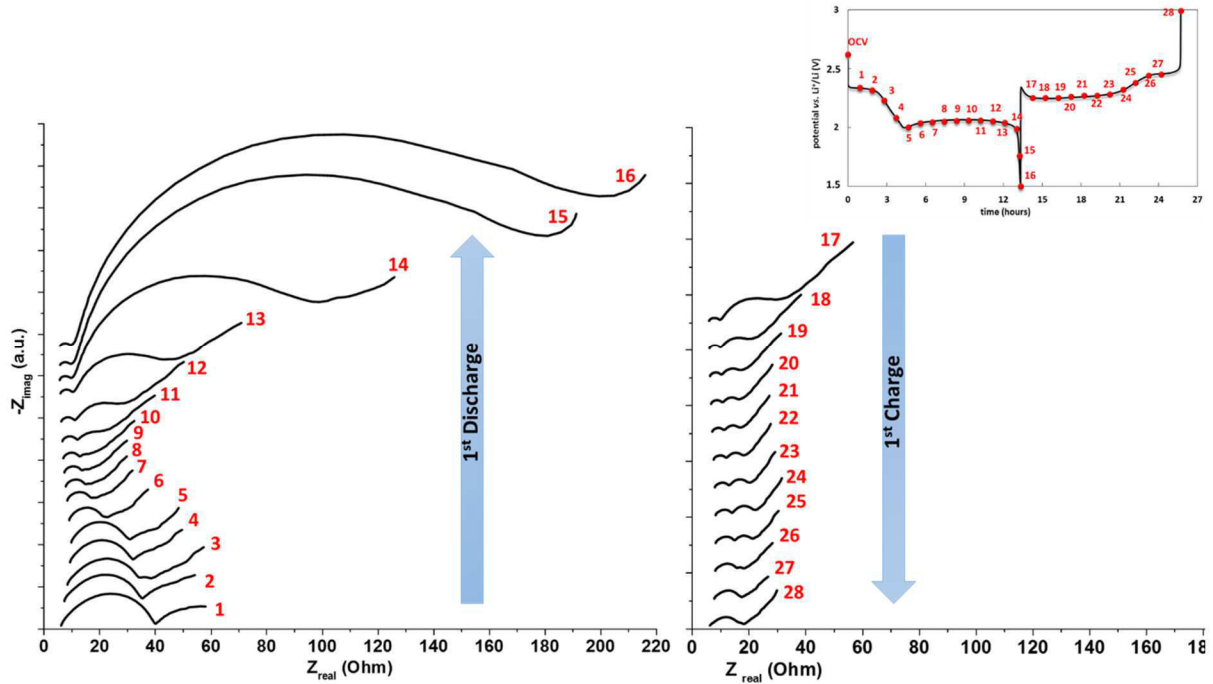


Figure 6-9. Nyquist plots evolution during initial discharge and charge. Numbers in red indicate the points (at the voltage profile) at which EIS was recorded.

Three main regions can easily be distinguished, *i.e.* high, middle and low frequency domain. It is also clearly visible that Nyquist plot ‘shape’ is strongly related with the state of discharge/charge of the Li/S cell. The spectra obtained with this particular coin cell were fitted (as a representative example) and more detailed discussion concerning each region (HF, MF, LF) is presented in further sections.

If correlating the recorded spectra with the experimental discharge voltage profile, following statements, deduced from the global observation, can be concluded:

- Zone 1: spectra 1 to 5 (corresponding to the upper discharge plateau and the region between the two plateaus) – no remarkable evolution is observed. A small decrease of the middle frequency semicircle is visible. Appearance of a little LF semicircle at spectra #3, which origin will be discussed further;
- Zone 2: spectra 6 to 10 (along the lower discharge plateau: the beginning) – strong decrease of the middle frequency semicircle is observed. A little LF semicircle starts to be visible again, however, barely detectable;
- Zone 3: spectra 10 to 16 (along the lower discharge plateau: the end) – significant increase of the low frequency semicircle, reaching the maximum at the end of discharge.

In the literature, for the reports dealing with EIS applied upon cycling, rather similar evolutions are visible. Moreover, when it comes to the fitting and proposed equivalent model, they all look quite similar, *i.e.* each visible semicircle is modeled classically as R//CPE, and CPE or

Warburg impedance is used for modeling the diffusion part. However, the main difference lies in the interpretation of the visible semicircles' origin, and thus of the phenomena correlated with them. Table 6-1 summarizes some of the proposed interpretation given in few reports, where *a priori* the same observations were detected. On purpose, original writing is preserved, taken directly from the articles.

Ref.	Region distinguished (number)	(1)	High Frequency (2)	Middle Frequency (3)	Low frequency (4)	(5)
Cañas <i>et al.</i> [209]	5	Electrolyte resistance	Anode charge transfer ( $f > 9$ kHz)	Cathode process: charge transfer of sulfur intermediates ( $9\text{kHz} < f < 18$ Hz)	Cathode process: reaction and formation of $S_8$ and $Li_2S$ ( $18$ Hz $< f < 0.3\text{Hz}$ )	Diffusion ( $f < 60$ mHz)
Hagen <i>et al.</i> [132]	3	Electrolyte resistance	Charge transfer resistance $R_{ct}$ and corresponding double layer capacity ( $CPE_{ct}$ ) (no freq. info)	Surface layer resistance $R_s$ and the double layer capacitance of the electrodes (no freq. info)		
Deng <i>et al.</i> [212]	4	Electrolyte resistance	$R_{int}/CPE_{inter}$ – interphase contact resistance and its related double layer capacity: at sulfur electrode bulk ( $100$ kHz – $1$ kHz)	$R_{ct}/CPE_{ct}$ – charge transfer resistance and its related double layer capacity: at the interface between the conductive agent and electrolyte ( $1$ kHz – $1$ Hz)	$CPE_{diff}$ – probably represents Li-ion diffusion process ( $1$ Hz – $10$ mHz)	
Yuan <i>et al.</i> [207]	4	Electrolyte resistance	Charge transfer resistance at the conductive agent interphase (no freq. info)	Charge transfer resistance and $C_{dl}$ of the $Li_2S$ ( $Li_2S_2$ ) film on the carbon matrix in the cathode (no freq. info)	Warburg impedance – probably due to the diffusion of polysulfides within the cathode (no freq. info)	
Kolosnitsyn <i>et al.</i> [213]	3	Electrolyte resistance	Overall resistance of the surface layers on both electrodes (no freq. info)	Electrochemical reactions on the sulfur electrode (no freq. info)	(not included)	

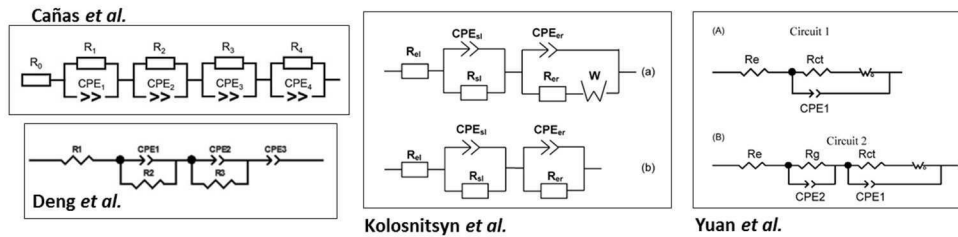


Table 6-1. Summary of five articles dealing with *in situ* EIS and their proposed explanations of different Nyquist plot parts<sup>132,207,209,212,213</sup>.

It can be seen that, apart from ideal match when it comes to the high frequency region and its assignment to the resistance of the electrolyte, further comparison cannot be done between five selected examples. A variety of different propositions are given, and discussion about their correctness is not the scope of this manuscript. Nevertheless, such significant differences between the interpretations can be simply confusing, without mentioning that a crucial information like characteristic frequency values, are not included in 80 % of the reports, thus making it difficult for a reader to conclude on its own interpretation.

In order to define the most relevant equivalent model for our *in situ* EIS results, we went a step further and a symmetric coin cell approach was applied at different states of discharge. The results are described in the following section.

### 6.5.2. Symmetric coin cells at different DOD

Similar to the approach we performed at OCV, analogical procedure of symmetric coin cells was applied in order to separate the contribution of both electrodes to the complete Li/S cell signal. This time however, it was much more delicate, since the symmetric cells were prepared from previously cycled electrodes and stopped at different moments during discharge. Two DOD% were selected (discharged to 2.1 V and to 1.5 V), based on preliminary observation of Nyquist plot evolution. The choice of ‘2.1 V’ was governed by the fact that, at this level, the Nyquist plot does not evolve that much (spectra #3 or #4 on the Figure 6-9) as compared with the initial state. Moreover, this is the moment where the presence of the soluble polysulfides species is expected. At 1.5 V, the Nyquist plot has changed dramatically at both, MF and LF levels. Therefore, we decided to perform a symmetric coin cell on completely discharged cells as well. The procedure we applied is relatively simple, and is schematically illustrated on Figure 6-10.

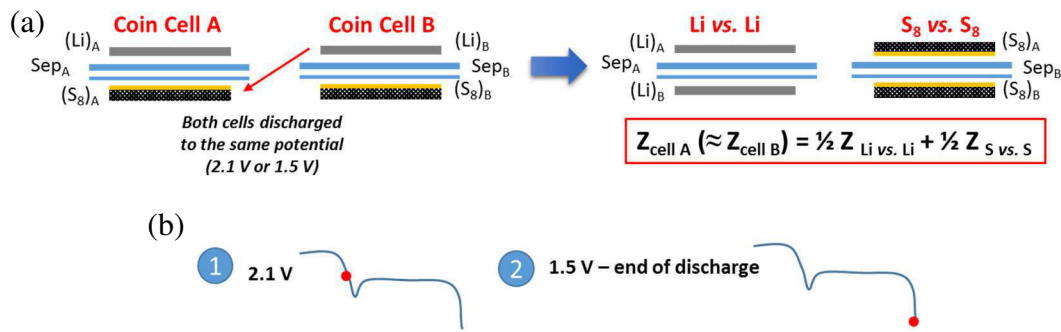


Figure 6-10. Illustrated concept of symmetric coin cells prepared from pre-cycled half cells to desired DOD (a); details of the experiments (b).

Two classical Li/S coin cells (cell A and B) with ‘S-on-NwC’ composite electrodes were discharged to the same potential of 2.1 V (identical discharge profiles were obtained) and relaxed for at least 15 min before EIS was measured. After that, coin cells were opened and sulfur electrode from coin cell A was exchanged with Li electrode from cell B (as shown on schematic illustration on Figure 6-10a). The same separators were kept. Only new coin cells components (casing, spring, spacer, etc.) were used to make these symmetric cells:  $S_8||S_8$  and  $Li||Li$ . EIS was then measured on such prepared symmetric coin cells. All these steps were repeated with another set of two Li/S cells, this time fully discharged to 1.5 V.

EIS measured at 2.1 V (refer as ‘experimental’ value, obtained from Li/S cell) was then compared with the ‘calculated’ one, based on the equation:  $Z_{Li/S} = \frac{1}{2} Z_{S/S} + \frac{1}{2} Z_{Li/Li}$ . We expected some differences between the ‘calculated’ and the ‘experimental’ values, notably in terms of the resistance amplitude, since the symmetric cells were built by recombination of the two positive and negative electrodes. Especially, such divergences in the resistance values are



mostly expected for metallic Li, and may be easily explained by its surface state. Even if cell A and cell B displayed identical discharge behavior (resulting in almost superimposed voltage profiles), the surface of the lithium (and also sulfur) electrode might have not evolved necessarily in the identical manner. Moreover, knowing the strong reactivity of the lithium surface, some changes can already appear during symmetric coin cell preparation (even if the precautions were taken).

Figure 6-11 presents the obtained EIS results of complete Li/S cell at 2.1 V, and of both  $S_8||S_8$  and  $Li||Li$  symmetric cells, together with the ‘calculated’ spectrum.

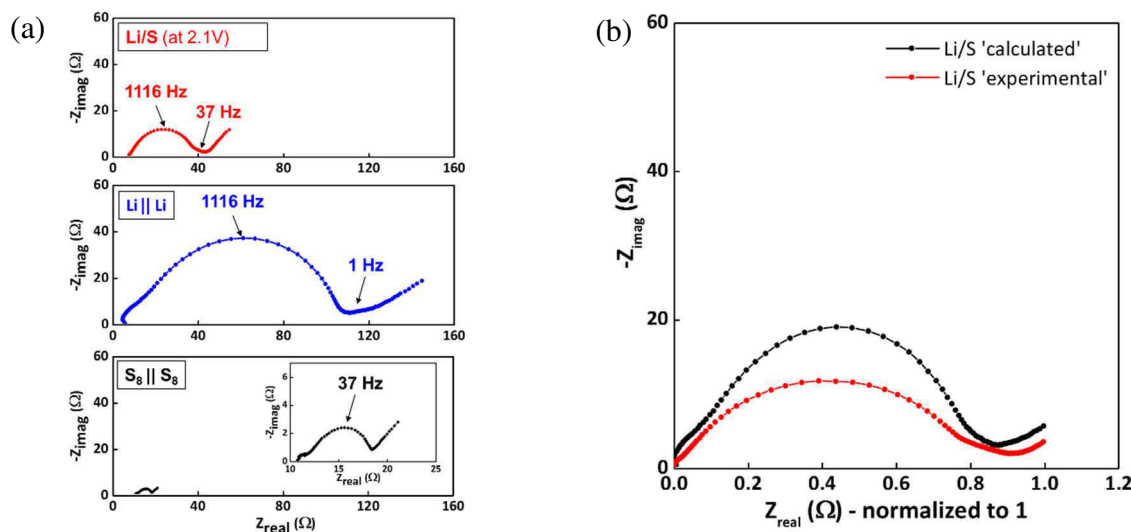


Figure 6-11. EIS spectra recorded on a Li/S cell discharged to 2.1 V (in red), and on symmetric  $S_8||S_8$  (in black) and  $Li||Li$  (in blue) cells made from pre-cycled electrodes to 2.1 V (a). Comparison of ‘experimental’ Nyquist plot of a Li/S cell with ‘calculated’ one. The ‘Z<sub>real</sub>’ axis values were normalized to 1 for easier comparison (b).

Even if slight differences in the amplitude values are noticed as previously explained, the sum of the two symmetric cells (‘calculated’) is in a good agreement with the ‘experimental’ Li/S EIS spectra recorded at 2.1 V (Figure 6-11b), and correct interpretation can be made. At 2.1 V DOD,  $S_8||S_8$  symmetric cell gives two small semicircles: the one at high frequency ( $\sim 10$  kHz,  $\sim 1$  Ω) is attributed to the intrinsic bulk response of the positive electrode (refer to chapter 3), while the larger one ( $\sim 8$  Ω) with frequency of about 37 Hz is attributed to the charge transfer reaction due to the soluble polysulfides presence. In the LF region, a straight line is visible, corresponding to the diffusion processes into the electrolyte and composite electrode.

Similar to the symmetric coin cells made from ‘fresh’ electrodes (at OCV), it appears that still at 2.1 V, lithium electrode is largely contributing to the global response of the Li/S cell, with a principal contribution due to its passivation layer at the characteristic frequency identical to the complete Li/S cell ( $\sim 1$  kHz). At last, the low frequency diffusion process is also partially due to the negative electrode, related with diffusion through the passive layer(s). Therefore, a summary of the attribution of each Nyquist plot component’s origin to the global Li/S cell is shown on Figure 6-12.

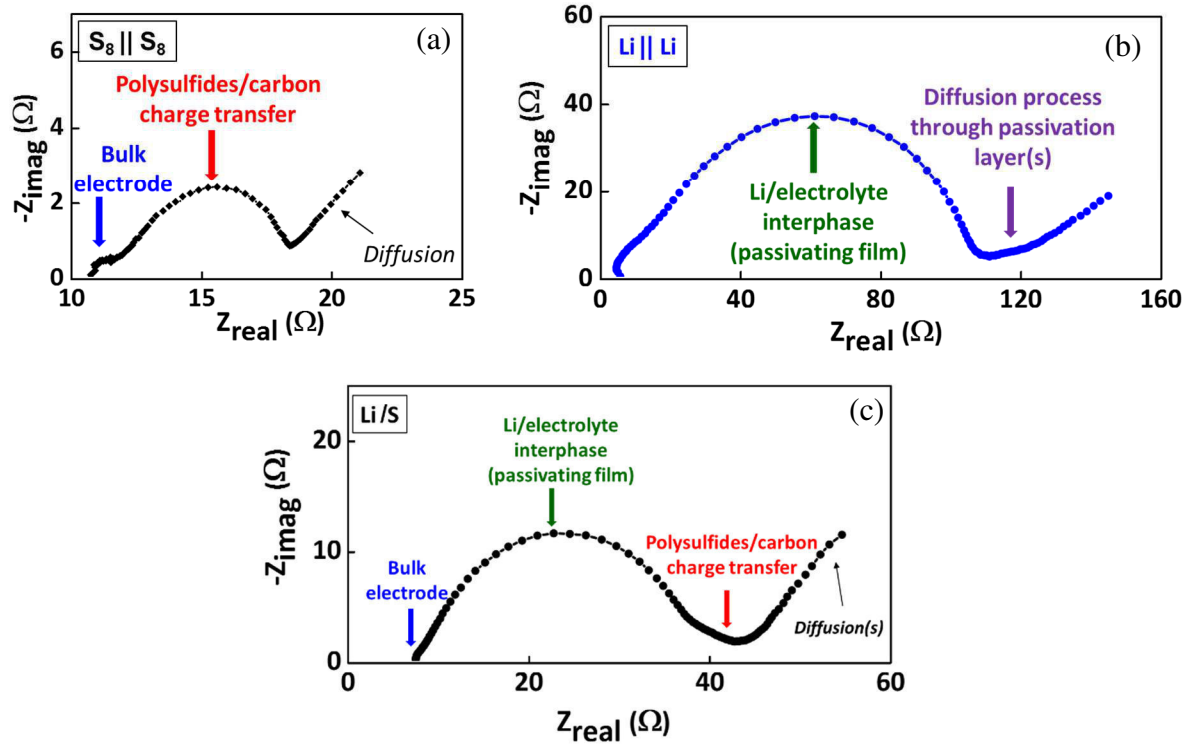


Figure 6-12. EIS response of a Li/S cell at 2.1 V (c) and of the symmetric  $S_8 || S_8$  (a) and  $Li || Li$  (b) cells – separation of semicircles' contribution and proposed interpretation of physical meaning of each Nyquist plot component.

Figure 6-13 presents the results obtained when applying similar approach to the completely discharged cells (at 1.5 V). However, it is important to note that at the end of discharge (1.5 V), once the cell is stopped, the relaxation/equilibrium potential quickly increases to  $\sim 2.1$  V (Figure 6-8).

It can be noticed that the impedance of the symmetric  $Li || Li$  cell changed, especially the MF semicircle strongly decreased with an increased to 4 kHz relaxation frequency (as compared with fresh  $Li || Li$  cell, where usually much larger semicircle is observed, at frequency  $\sim 600$  Hz). This is probably due to the impact of the polysulfides (formed already at the beginning of discharge and present in the electrolyte) on the passivation layer on the lithium surface, which may change their chemical composition and structure.

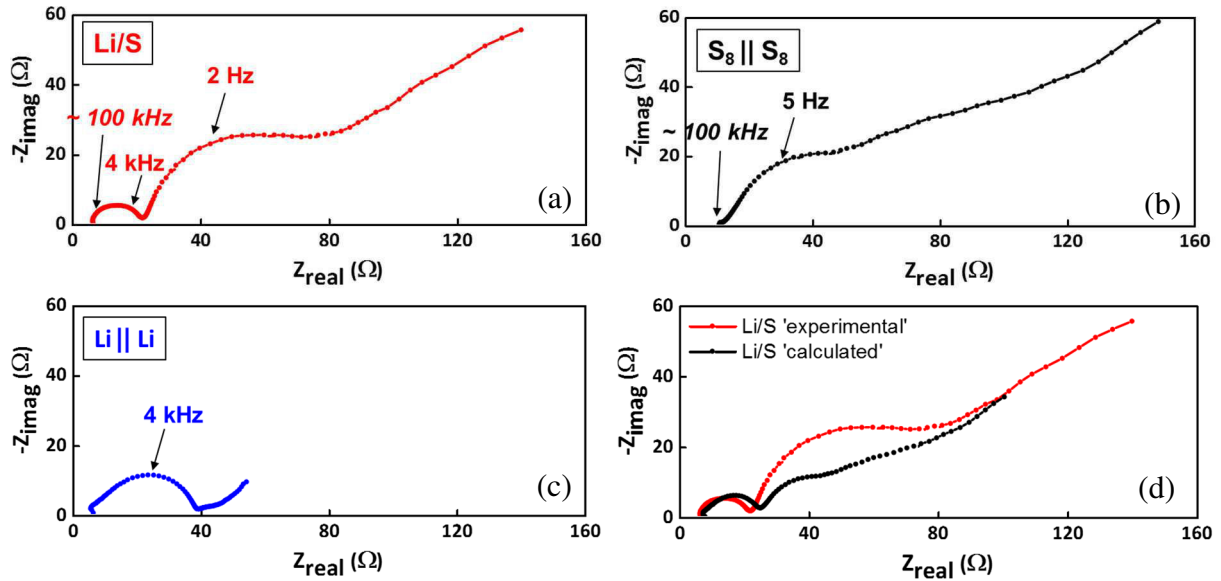


Figure 6-13. EIS spectra recorded on a fully discharged to 1.5 V Li/S cells (a) and on S<sub>8</sub>||S<sub>8</sub> (b) and Li||Li (c) symmetric cells made from pre-cycled electrodes to 1.5 V. Comparison of 'experimental' Nyquist plot of a Li/S cell with 'calculated' one (d).

As concerning the S<sub>8</sub>||S<sub>8</sub> symmetric cell (Figure 6-13b), we again observe this very small HF loop (electronic properties of the bulk of 'S-on-NwC' composite electrode), however, the middle and low frequency parts completely changed, with the appearance of a semicircle with a frequency ~ 2 Hz embedded into a Warburg type (diffusion) line at 45°. It shows thus, that at the end of the discharge, the LF part of the Li/S cell is mostly affected by the processes on the positive electrode, with a strong increase of the contribution of charge transfer and mass transport due to the formation of insulating solid Li<sub>2</sub>S on the carbon network surface.

'Experimental' and 'calculated' spectra (Figure 6-13d) are almost superimposed at the MF semicircle level. Slight differences can be seen in the size of the LF semicircle. However, again at this point, it is necessary to remind that even if two Li/S cells displayed very similar discharge profile, the passivation layer of Li<sub>2</sub>S that got formed at the end of discharge may not be totally identical, and keeping in mind sensitivity of EIS technique, such slight differences are fully understandable and acceptable.

Based on the aforementioned findings, we can now analyze Nyquist plots evolution obtained upon cycling for two-electrode coin cells, which were shown on Figure 6-9. Therefore, we parameterized the experimental results by an equivalent electric circuit that takes into account the contributions of both, positive and negative electrode. The proposed equivalent circuit is presented in the next section.

### 6.5.3. Equivalent circuit

In the literature, several propositions of equivalent circuit used for fitting the EIS data of Li/S cells were given, and some of them were presented in Table 6-1. Sometimes the model was modified (for the same cell) as a function of the discharge/charge state of the cell. Our (simple) circuit is preserved all along the cycling, even if very small contributions appear depending on the state of discharge/charge. The model is composed of following components connected in series:

- $R_{el}$  - attributed mainly to the electrolyte resistance;
- $R_{NWC} // CPE_{NWC}$  - corresponds to the positive electrode bulk contribution and more precisely, to the non-woven carbon collector;
- $R_{Li} // CPE_{Li}$  - attributed to the lithium/electrolyte interphase (SEI);
- $R_{PS} // CPE_{PS}$  - corresponds to the charge transfer of polysulfides species on positive electrode (*i.e.* polysulfides/carbon interface). When dominating species are soluble polysulfides (high-to-medium order ones), with fast kinetics of the reaction, a small semicircle is observed ( $\sim 37$  Hz). Formation of low-order ones (including solid  $Li_2S$ ) results in highly increased semicircle, and the characteristic frequency is shifted to lower values ( $\sim 5 - 2$  Hz);
- $CPE_{diff}$  - corresponds to the diffusion processes (ions and soluble polysulfides) through the electrolyte, inside the porous positive electrode and the passivation layer on lithium surface.

Figure 6-14 shows the proposed model, together with the selected fitting example (at 80% DOD). Based on this proposed equivalent model, evolution at each region, *i.e.* HF, MF and LF is discussed in further section.

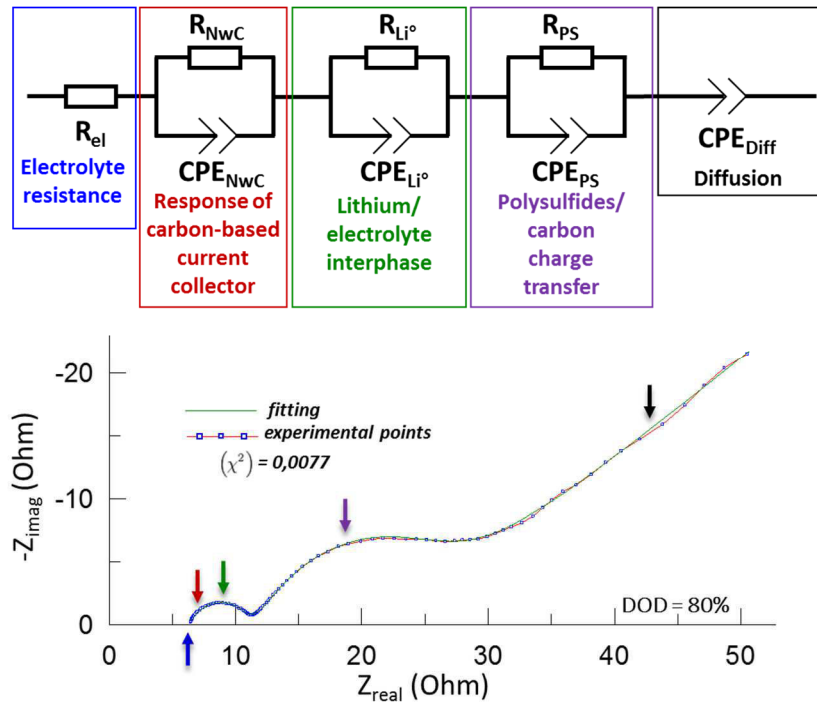


Figure 6-14. Equivalent circuit model used for fitting *in situ* EIS data together with the selected fitting example.

#### 6.5.4. Results discussion

Figure 6-15 shows the evolution of the resistance values, previously attributed to different phenomena or cell components, *i.e.* electrolyte resistance ( $R_{el}$ ), lithium/electrolyte interphase ( $R_{Li^+}$ ), polysulfides/carbon transfer resistance ( $R_{PS}$ ) and bulk response of the NwC collector ( $R_{NwC}$ ), together with corresponding voltage profile.

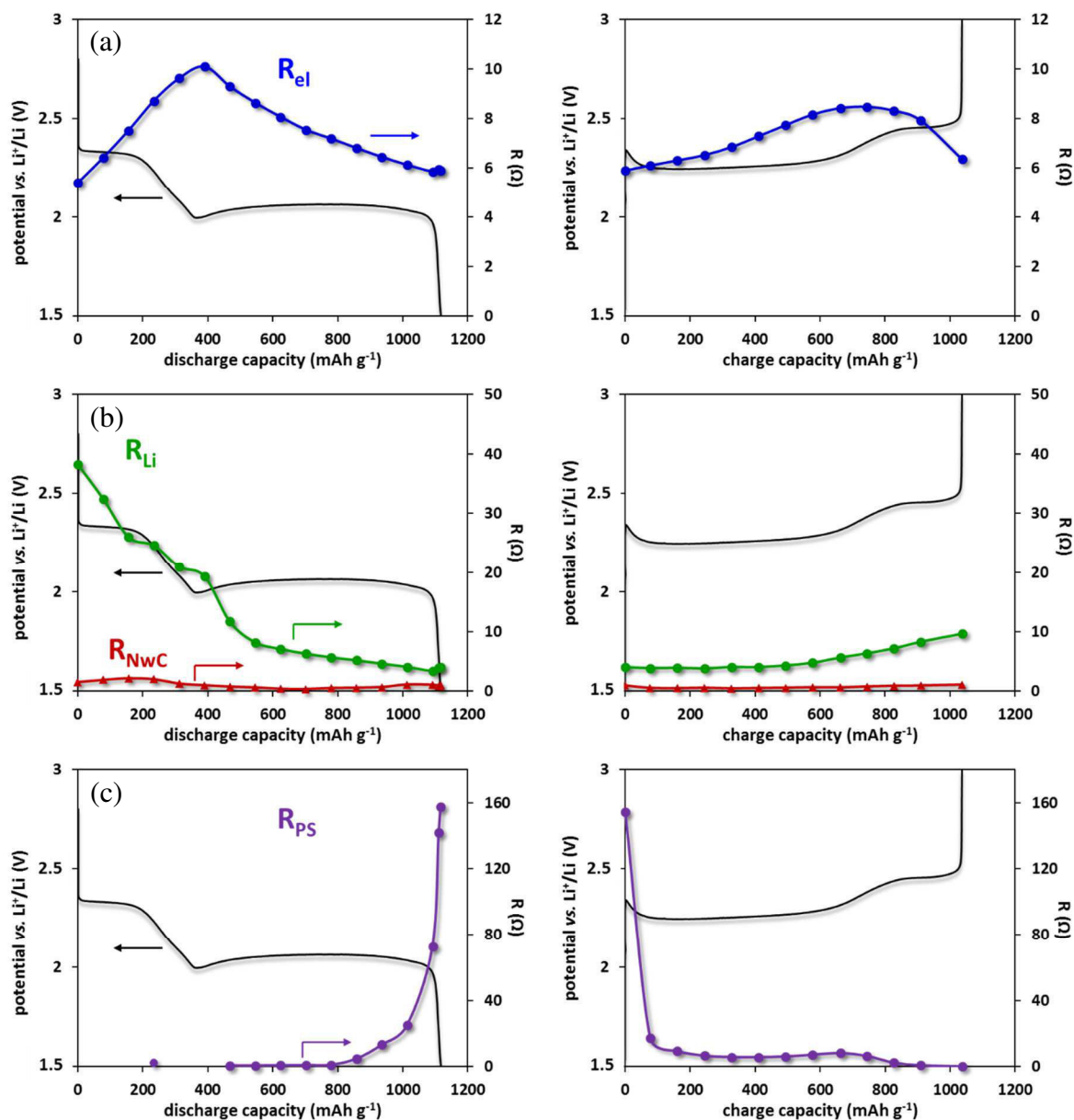


Figure 6-15. Evolution of the resistance values of: the electrolyte,  $R_{el}$  (a); Li/electrolyte interphase,  $R_{Li}$  and bulk of the positive electrode,  $R_{NWC}$  (b) and polysulfides/carbon transfer resistance,  $R_{PS}$  (c).

#### 6.5.4.a) High frequency region (> 100 kHz)

We have previously attributed the high frequency region as a contribution of connections, sample holder and electrolyte resistance. Since the same coin cell was observed upon cycling, without changing the cable, sample holder neither the channel, all observed evolutions could directly be attributed to the electrolyte resistance and its changes. Active material upon discharge is getting reduced into easily soluble polysulfide species ( $Li_2S_x$ ,  $3 < x \leq 8$ ), and dissolves in the electrolyte, modifying its viscosity and the concentration of charge carriers<sup>213</sup>. Thus, it is expected to observe evolution of the electrolyte resistance, which is not typically

observed in classical Li-ion cells, where the electrolyte resistance stays rather stable upon cycling.

The viscosity of the electrolyte containing polysulfides increases notably with the increasing polysulfides concentration, with viscosities of  $2 \cdot 10^{-2}$  Pa.s and  $8 \cdot 10^{-2}$  Pa.s at low shear rate ( $1 \text{ s}^{-1}$ ), for 0.1 M and 1.0 M solution of equivalent  $\text{Li}_2\text{S}_4$  species, respectively<sup>†</sup>. However, the electrolyte displays a thixotropic behavior, *i.e.* a decrease of viscosity under high shear rate. In other words, viscosity without outflow (which represents the behavior during the battery operation) must be then higher, as the one obtained under the shearing. This non-Newtonian behavior may indicate some organization of the ionic species during the resting period with the formation of physical cross-linking. Then, the dissolution of the polysulfides in the electrolyte largely increases the viscosity and a remarkable increase of the electrolyte resistance is expected, weakly mitigated by the increase of the charge carrier number.

An electrolyte resistance evolution recorded during initial cycle is shown on Figure 6-16. Such evolution is very similar to the one presented in some reports, where EIS was applied upon Li/S batteries operation<sup>132,213,214</sup>.

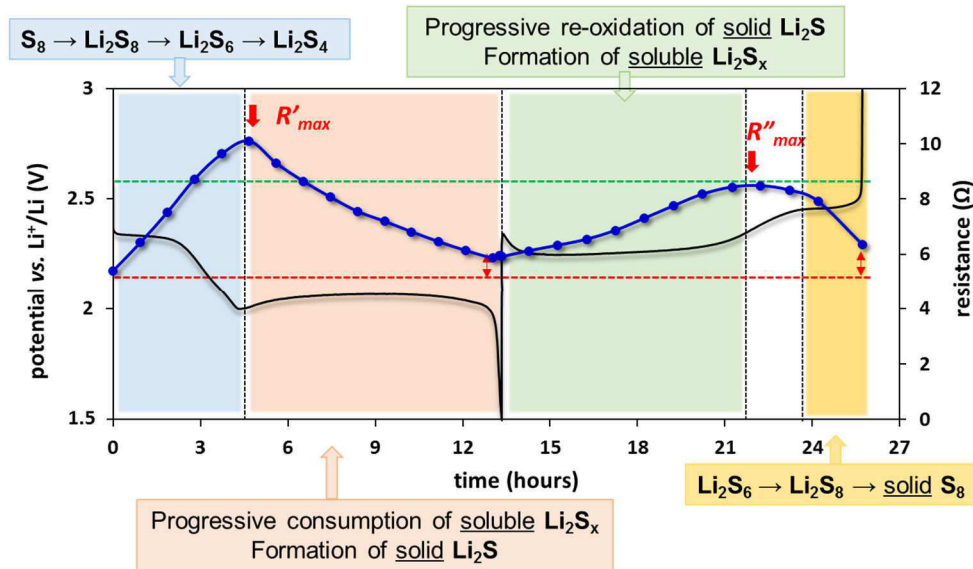


Figure 6-16. Electrolyte resistance evolution during the initial cycle, together with the voltage profile.  $R'_{\max}$  and  $R''_{\max}$  corresponds to the points where the electrolyte resistance reaches the highest value during discharge and charge, respectively. The red dashed line indicates the level of the initial electrolyte resistance, without polysulfides inside. The green dashed line indicates the level of a maximum resistance during charge.

During initial discharge, the resistance is increasing and reaches maximum at the point (marked as  $R'_{\max}$ ) where formation of solid  $\text{Li}_2\text{S}$  starts to occur. According to the literature, the little dip

<sup>†</sup> Viscosity measurements performed on ‘catholyte’ solutions, with varying  $\text{Li}_2\text{S}_4$  concentrations (0.1 M and 1.0 M) in 1M LiTFSI in TEGDME/DIOX 1/1 vol electrolyte.

on the voltage profile at the beginning of lower discharge plateau (sometimes called as ‘supersaturation’ point), is the point where the concentration of soluble polysulfides anions is the highest (middle to short soluble polysulfides)<sup>106,246,250</sup> and formation of  $\text{Li}_2\text{S}$  starts (see *in situ* XRD, section 5.4.2). very poor solubility of  $\text{Li}_2\text{S}$ <sup>210</sup> results in the nucleation of solid phase. Once the progressive formation of  $\text{Li}_2\text{S}$  occurs, soluble species are consumed, inducing the decrease of both viscosity and the resistance of the electrolyte.

During charge, in opposite manner, progressive oxidation of solid  $\text{Li}_2\text{S}$  is accompanied by the formation of mid-to-high order polysulfides, which in turn provokes the increase of viscosity. The maximum point ( $R''_{\text{max}}$ ) is in accordance with the moment of complete  $\text{Li}_2\text{S}$  disappearance, as observed by XRD (75 % SOC). Afterward, formation of solid sulfur requires further consumption of soluble species ( $\text{S}_6^{2-}$ ,  $\text{S}_8^{2-}$ ), thus the electrolyte resistance decreases. These results are indirectly coherent to the results obtained through *in situ* XRD measurements (see chapter 5), and interpretation is in agreement with the one proposed by Kolosnitsyn *et al.*<sup>213</sup> and other research teams<sup>132,209</sup>.

It is interesting to notice that the electrolyte resistance never comes back to the initial value (red dashed line), which means that even at the end of charge/discharge, some soluble polysulfides are still present in the electrolyte, which is clearly visible when opening the coin cell for *post mortem* analysis. The color of the electrolyte solution is governed by the polysulfide species present in it, and it never become transparent again, neither at the end of charge nor discharge. This points out that some part of active material may be ‘lost’ in the electrolyte, and does not participate in the further reactions. This is rather coherent with the typical capacity retention behavior, where drastic capacity fade is mainly observed after the initial cycle. According to the literature, such capacity retention is mostly characteristic for the cells with large excess of electrolyte, which is actually our case.

Another important point to mention is that the electrolyte resistance evolves in a different manner during discharge and charge. The maximum of the resistance during discharge ( $R'_{\text{max}} = 10.2 \Omega$ ) corresponds to the highest soluble polysulfides concentration and is higher than during charge (8.3  $\Omega$ ). As already discussed before for *in situ* XRD studies (chapter 5), a significant hysteresis between charge/discharge processes is observed for  $\text{Li}_2\text{S}$  formation/re-oxidation. As demonstrated previously, solid  $\text{Li}_2\text{S}$  product is detectable until 75 % SOC during charge. Since oxidation of  $\text{Li}_2\text{S}$  to the soluble species is a difficult process, it may then explain the slower increase of the electrolyte resistance measured by EIS, *i.e.* slower increase of the soluble polysulfides concentration. In the charge process, the region where only soluble species are present (according to the XRD findings) is very short, and it was previously reported by Barchasz *et al.*<sup>194</sup> that longer polysulfides ( $\text{Li}_2\text{S}_6$ ,  $\text{Li}_2\text{S}_8$ ) should be predominant in this region. It would mean that the composition of the electrolyte is not the same at the ‘maximum resistance points’ during discharge ( $R'_{\text{max}}$ ; where predominant species are  $\text{S}_4^{2-}$ ) and charge ( $R''_{\text{max}}$ ; with mostly  $\text{S}_6^{2-}$  and  $\text{S}_8^{2-}$ ). Literature also reports on differences between charge and discharge, whatever the technique used: *in situ* and *operando* UV-Vis<sup>172</sup> or *in situ* XAS<sup>202</sup>.



Viscosity measurements of different ‘catholyte’ solutions ( $\text{Li}_2\text{S}_x + 1\text{M LiTFSI}$  in TEGDME/DIOX 1/1 vol), having the same molar concentration (0.1 M) but different polysulfide composition, *i.e.*  $\text{Li}_2\text{S}_4$ ,  $\text{Li}_2\text{S}_6$  and  $\text{Li}_2\text{S}_8$ , were also performed (Figure 6-17). The results clearly show the dependence of viscosity *vs.* the polysulfides composition. The most comparable values are the one at the slower shear rate ( $1\text{ s}^{-1}$ ), since are the closest to the real battery operation (no shearing).  $\text{Li}_2\text{S}_4$  solution leads to higher viscosity ( $2 \cdot 10^{-2}\text{ Pa}\cdot\text{s}$ ) than  $\text{Li}_2\text{S}_8$  ( $8 \cdot 10^{-3}\text{ Pa}\cdot\text{s}$ ) and  $\text{Li}_2\text{S}_6$  ( $6 \cdot 10^{-3}\text{ Pa}\cdot\text{s}$ ) ones, in good agreement with the evolution of the resistance values at the ‘maximum points’ ( $R'_{\text{max}}$  and  $R''_{\text{max}}$ ) during discharge and charge. Moreover, the same resistance value as the one recorded at  $R''_{\text{max}}$  point, *i.e.*  $8.3\ \Omega$  was also recorded during discharge, just at the end of upper plateau (see the green dashed line on Figure 6-16). The end of upper discharge plateau is considered as the moment with the highest concentration of  $\text{Li}_2\text{S}_8$  and  $\text{Li}_2\text{S}_6$  species<sup>246</sup>. It clearly shows then, that the electrolyte resistance is strictly dependent on the polysulfides composition at given state of charge/discharge point.

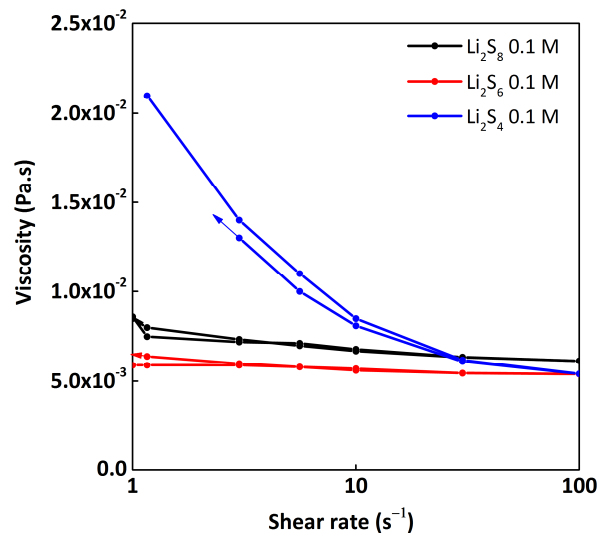


Figure 6-17. Viscosity measurement of ‘catholyte’ solution: 1 M LiTFSI in TEGDME/DIOX 1/1 vol having the same 0.1 M concentration of polysulfides species, of different compositions:  $\text{Li}_2\text{S}_4$  (in blue),  $\text{Li}_2\text{S}_6$  (in red),  $\text{Li}_2\text{S}_8$  (in black).

#### 6.5.4.b) High to medium frequency region (50 kHz - 1 Hz)

We previously showed that there is a constant contribution of the *bulk of positive electrode* ( $R_{NwC}/CPE_{NwC}$ ) (attributed to the carbon based current collector). This semicircle ( $\sim 1 - 2\ \Omega$ , at  $\sim 6 - 9\ \text{kHz}$ ) at the initial state of Li/S cell is totally covered by the significant response of Li negative electrode, while being more visible/‘uncovered’ where the lithium resistance is decreasing upon discharge (see Nyquist plot evolution at different DOD%; Figure 6-9).

Therefore, along the whole cycle, a relatively constant<sup>‡</sup> contribution of  $R_{NWC}$  is present, as shown on Figure 6-15b (in red).

All the changes of MF semicircle upon cycling thus purely originate from modification of *metallic lithium anode* ( $R_{Li}/CPE_{Li}$ ), and more precisely of the passivation layer initially present on its surface. During discharge, the resistance value decreases and the specific relaxation time increases. Figure 6-15b (in green) shows the evolution of the Li/electrolyte interphase resistance upon initial cycle. We can clearly observe significant decrease of the resistance at the beginning of discharge, followed by quasi stable value until the end of discharge. Once the battery starts to discharge, oxidation of lithium is taking place, passivation layer is rearranged, and the surface of lithium is getting modified due to lithium stripping. Such observation was already reported in the Li-ion cell studies<sup>225</sup>. Surprisingly, in the Li/S domain, such decrease of the resistance was not correlated to the lithium response in literature, and it was rather attributed to the increase of positive electrode's conductivity due to sulfur dissolution<sup>132,209</sup>.

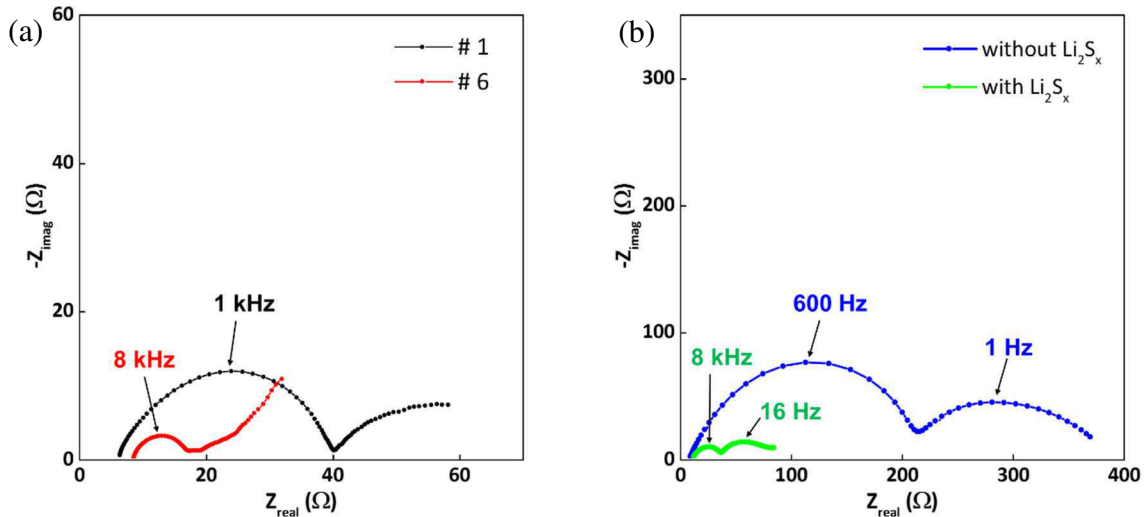


Figure 6-18. Comparison of Nyquist plot recorded at the initial state of Li/S (spectra # 1) and at the beginning of lower discharge plateau (spectra # 6) (a). Symmetric coin cells Li||Li with/without polysulfides left for storage (b).

When comparing the Nyquist plot recorded at the initial state (spectra # 1) with the one at spectra # 6, it can be noticed that, apart from significantly decreased resistance, the characteristic frequency values are also shifted into higher range (Figure 6-18a). One of the hypotheses of such changes would lie in the presence of polysulfides in the electrolyte, which may affect the passivation layer on the Li surface in regard to both, composition, its resistive nature and thickness. Thus an additional experiment was performed to verify this hypothesis, *i.e.* if this resistance changes are strongly related with lithium modifications during cyclic in the presence of polysulfides. Symmetric coin cell composed of two lithium electrodes and

<sup>‡</sup> In further discussion, more detailed information is provided.

electrolyte containing dissolved polysulfides was left for aging over several days. EIS was recorded every 1 hour. The results are presented on Figure 6-18b in comparison with the symmetric Li||Li cell without polysulfides in the electrolyte and left for storage. Almost identical behavior, as the one observed in the full Li/S cell during discharge can be noticed. The resistance of semicircle decreases, while the characteristic frequency increases of an order of magnitude. This confirms the strong impact of the polysulfides on the lithium passivation layer that probably change its composition and thickness, leading to a less resistive layer. Moreover, in regard to Li/S Nyquist plot evolution upon cycling, the most significant Li modifications occur at the moment where  $S_4^{2-}$  concentration is the highest (little dip at the discharge curve). It may thus indicate that mid-order polysulfides like  $S_4^{2-}$ ,  $S^{3-}$  (a radical species), have a stronger influence on Li surface than the higher-order polysulfides.

During following charge, the resistance of the lithium-attributed loop stays very small, and slightly increases by the end of charge. This evolution may be related to the passivation film evolution (increase of the thickness of the layer).

However, when comparing the values obtained for the bulk response of the electrode ( $R_{NWC}/CPE_{NWC}$ ) and Li/electrolyte ( $R_{Li}/CPE_{Li}$ ) interphase, further information can be extracted. Figure 6-19 presents the resistance values ( $R_{NWC}$ ) and corresponding capacities (calculated based on  $Q$  and  $\alpha$  parameters extracted from fitting the spectra). For better clarity, voltage profile and electrolyte resistance are shown as well.

It can be seen that actually the resistance of the electrode bulk contribution ( $R_{NWC}$ ) is not so stable, but is varying between 0.5 – 2.0  $\Omega$ . Slight increase is visible just at the beginning of discharge, and increasing again at the end of discharge. The corresponding capacitance is also varying, having the higher values in the region where solid  $Li_2S$  was detected by XRD (along lower discharge plateau, up to 75% SOC during charge). However, the fitting error is also very high in this region. Nevertheless, in the global view, the value of  $R_{NWC}$  seems to be stable.

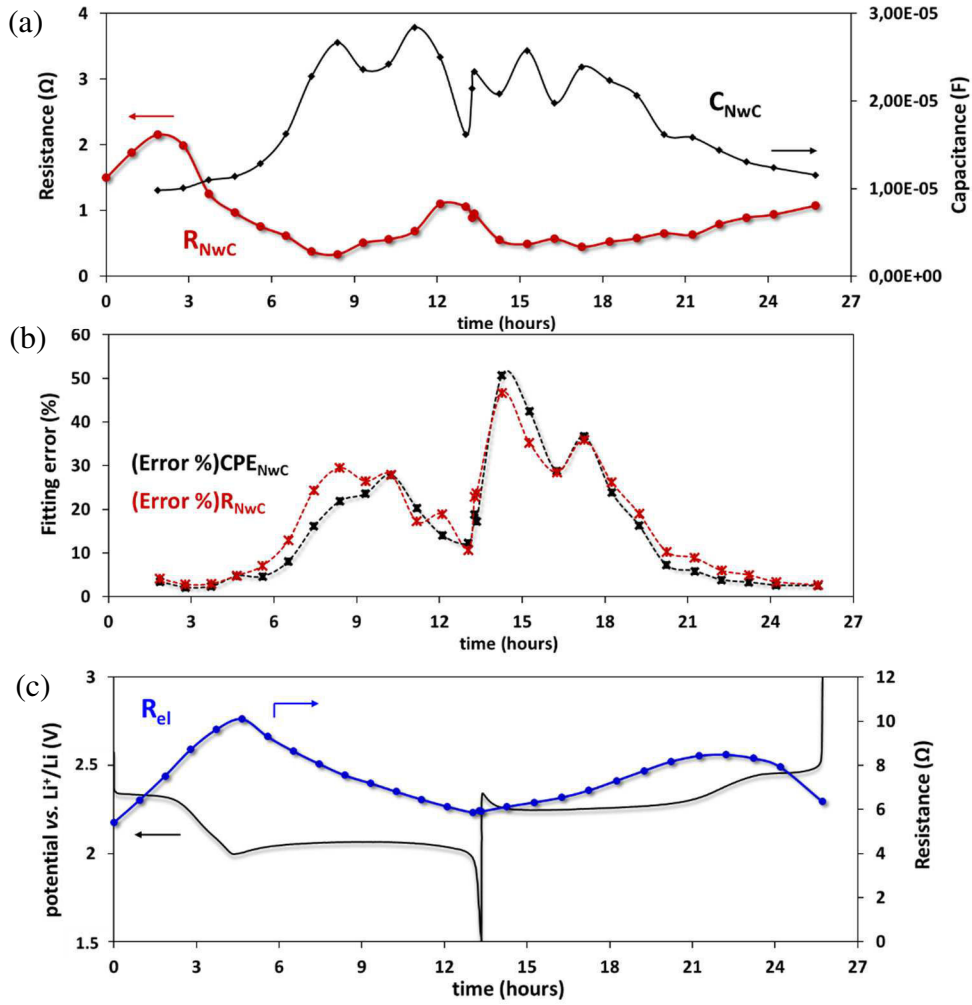


Figure 6-19. Resistance and capacitance values (a) obtained from fitting the HF semicircle (positive electrode bulk), together with the fitting errors value (b) and electrolyte resistance evolution profile (c).

Figure 6-20 presents the resistance and capacitance values, together with the fitting error, obtained for Li/electrolyte interphase.

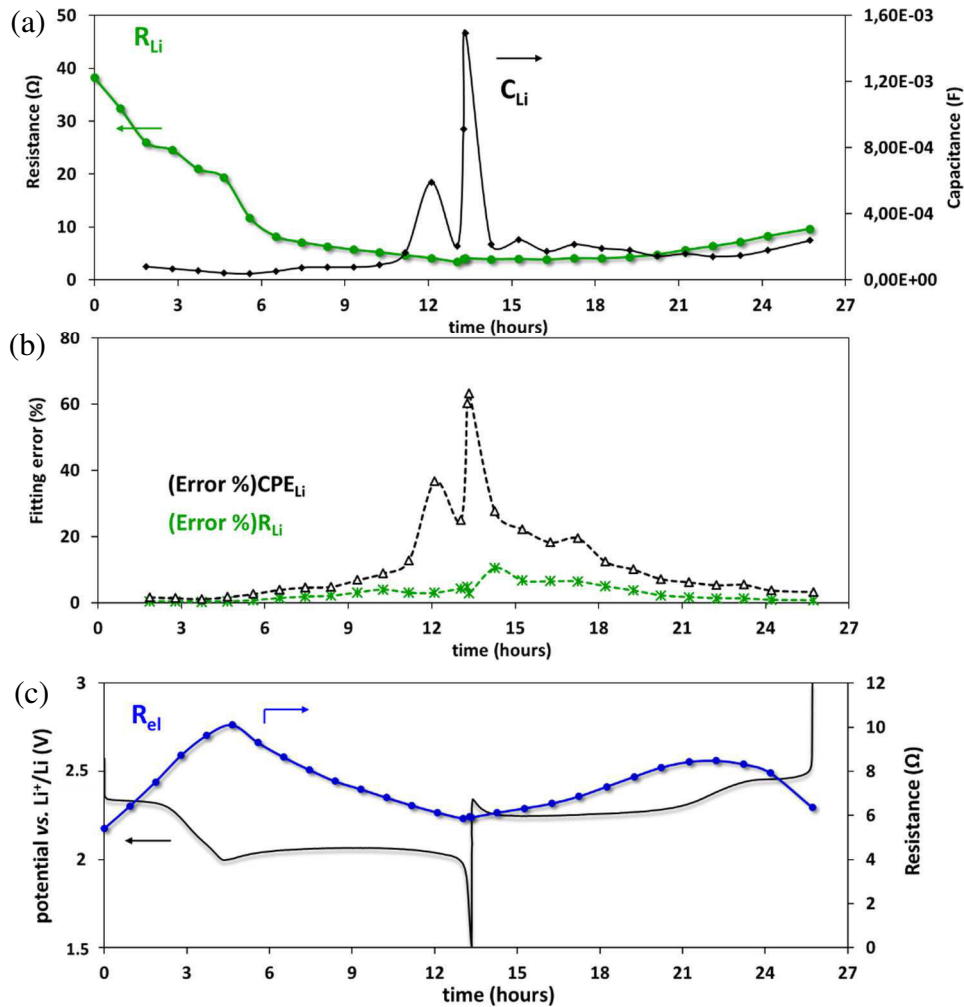


Figure 6-20. Resistance and capacitance values (a) obtained from fitting the MF semicircle (Li/electrolyte interphase), together with the fitting errors value (b) and electrolyte resistance evolution together with the voltage profile (c).

It can be seen that the capacitance values drastically increase exactly at the moment of complete discharge. On the other hand, the fitting error is also very high (even 65 %). It brings us to the conclusion that, with the simple model we designed for fitting, we can probably not extract all the information due to the presence of large errors appearing for some state of discharge/charge.

As concerning the LF semicircle evolution, previously attributed to the **charge transfer reaction of the polysulfide species ( $R_{PS}/CPE_{PS}$ )**, appearance of a small loop just after the first discharge plateau (*i.e.* spectra # 3 on Figure 6-9) can be observed. This loop has the relaxation frequency of  $\sim 37$  Hz, and its appearance corresponds to the moment where polysulfides are progressively formed in the electrolyte. During the region between two plateaus (2.3 V – 2.1 V; Nyquist plots # 4 and # 6), the concentration of polysulfides is progressively increasing (see  $R_{el}$  evolution, Figure 6-16), however, the charge transfer resistance is too small (fast kinetic) and the response is ‘hidden’ by a large response of the Li electrode. Starting from the beginning of lower discharge plateau (EIS spectra # 6), a semicircle related to charge transfer reaction contribution starts to be visible, with progressively increasing resistance by the end of

discharge, together with a change of the relaxation frequency towards lower values ( $\sim 2$  Hz). This evolution comes with a strong increase of the transport limitation, since the low frequency diffusion contribution increases as well. This phenomenon can easily be ascribed to the formation of an insulating layer on the positive electrode surface, which limits both the charge transfer and the diffusion of polysulfide active species to the carbon collector. It shows that this layer becomes highly blocking (an exponential increase of the resistance, see Figure 6-21), which is correlated to the end of discharge (a brutal increase of polarization), while full capacity was not obtained.

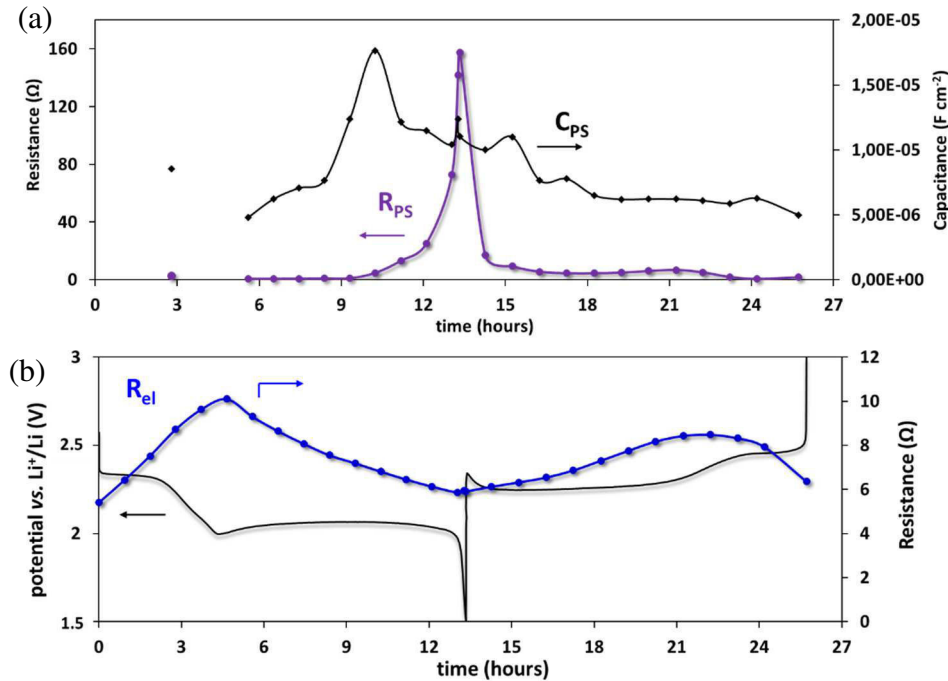


Figure 6-21. Resistance and capacitance values (a) obtained from fitting the LF semicircle (charge transfer of polysulfide species), together with the electrolyte resistance and cycling voltage profile (b).

These findings are in agreement with the XRD results (section 5.3.1), which show that the formation of  $Li_2S$  starts exactly at the beginning of lower discharge plateau. However, there are some differences, since here, the growth of the resistance is observed with a strong contribution just at the end, while XRD results showed a linear increase of the peak surface at the beginning, followed by slower formation rate. It can be explained by the fact that the large increase of the transfer resistance is only observed when the electrode is largely covered by insulating species *i.e.* the electrochemical reaction kinetic become slow (proportional to  $1/S$ , where  $S$  denotes for the surface area). SEM photos (chapter 3, Figure 3.5) show that, indeed, all available conductive surface (even on the carbon collector) is completely covered at the end of discharge by passivation film.

During following charge, the resistance drops rapidly, which is very coherent with the voltage profile. Indeed, a characteristic overpotential peak is visible just at the beginning of charge, which is attributed to the slow kinetics of the  $Li_2S$  oxidation<sup>211</sup>. Here, we can suppose that

higher polarization is required to break this resistive layer. Indeed, after the polarization barrier is overcome, the resistance values decrease very rapidly but are still present until the beginning of the upper charge plateau. Then, it seems that  $\text{Li}_2\text{S}$  stays until there, which is in agreement with XRD findings concerning the moment of complete  $\text{Li}_2\text{S}$  consumption.

In this case, also the capacitance values are shown (Figure 6-21a). However, it was noticed that for  $R_{\text{PS}}//\text{CPE}_{\text{PS}}$  semicircle fitting, very small error values were obtained (for resistance:  $\sim 1 - 2\%$ , for capacitance:  $\leq 1\%$ ). It again highlights the fact that our simplified model should be modified in order to precisely evaluate the MF responses, which are very small in the Nyquist plot, as compared with the polysulfide/carbon interface, especially at the end of discharge.

For the capacitance representation ( $\text{F cm}^{-2}$ ), we used the estimated electrode surface of  $471 \text{ cm}^2$  (based on BET measurements of composite electrode, see Figure 3-15). It can be seen that the capacitance values are increasing until the middle of the lower discharge plateau. Right after that, when the resistance starts to increase rapidly (starting from  $x \sim 9 \text{ h}$ ), the capacitance is progressively decreasing until the end of charge. Moreover, we can notice that the capacitance values are in the range of  $\sim 10^{-6} \text{ F cm}^{-2}$ , and this value is usually considered as a double layer capacitance ( $C_{\text{dl}}$ ), which in turn proves the fact that we correctly attributed this semicircle to the charge transfer resistance on the positive electrode.

The resistance value ( $R_{\text{PS}}$ ) is the lowest at the moment where the concentration of the polysulfides is the highest, in accordance with an easier charge transfer reaction on the carbon surface, in the presence of soluble polysulfides species. This evolution is correlated with electrolyte viscosity ( $\sim R_{\text{el}}$ ), *i.e.* the highest concentration of polysulfides corresponds to the highest viscosity.

The *diffusion processes* evolution is a complicated mechanism to follow, in order to understand it correctly. It is still under investigation and thus was not presented in this work.

## 6.6. Further cycles evolution

Figure 6-22 shows a visual comparison of the Nyquist plot evolution recorded during 2<sup>nd</sup> and 3<sup>rd</sup> discharges, together with a comparison to the initial discharge, as extensively discussed previously. It can be noticed that during next cycles, the contribution of the *Li/electrolyte interphase (MF semicircle)* becomes smaller than in the initial state, reaching relatively stable (and small – almost negligible as compared to a large LF semicircle appearing) resistance value in the further cycles. It proves again that the EIS response during initial discharge is strongly dictated by the Li electrode. On the contrary, other contribution evolutions, like formation of  $\text{Li}_2\text{S}$  (thus progressive increase of  $R_{\text{PS}}$ ), seem to be reversible.

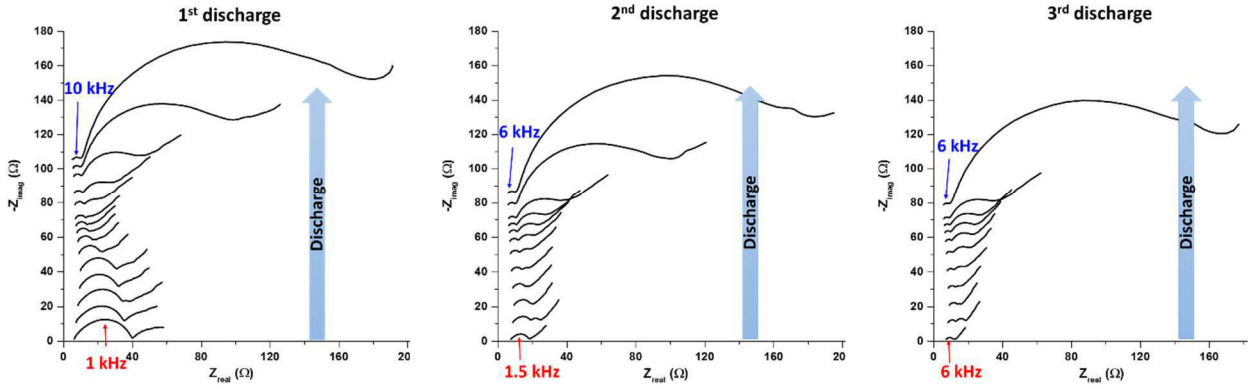


Figure 6-22. Nyquist plot evolutions during 1<sup>st</sup> – 2<sup>nd</sup> – 3<sup>rd</sup> discharge.

If now having a deeper look on the electrolyte resistance variations for corresponding 2<sup>nd</sup> and 3<sup>rd</sup> cycles presented, it can be noticed that very similar evolution as in the 1<sup>st</sup> cycle is found. The results are shown on Figure 6-23.

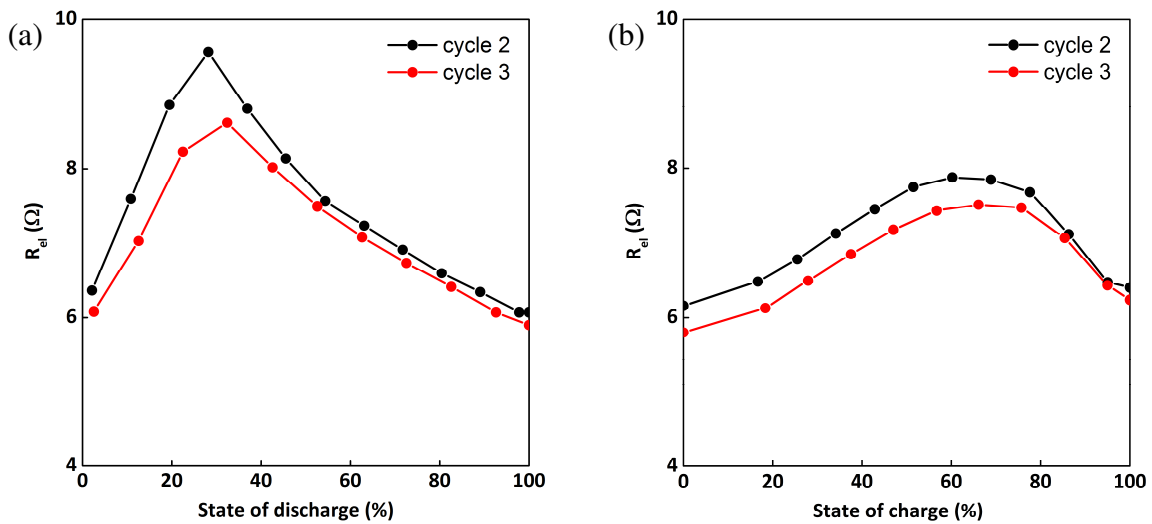


Figure 6-23. Electrolyte resistance evolution during 2<sup>nd</sup> and 3<sup>rd</sup> discharge (a) – charge (b) cycles, as a function of state of discharge/charge.

During discharge, a maximum of  $R_{el}$  always corresponds to the beginning of lower discharge plateau. During following charges, electrolyte resistance is evolving in the same manner as in the initial cycle, with significant hysteresis between charge and discharge maximum resistance values ( $R'_{max} \neq R''_{max}$ ). Such evolution was observed until the 7<sup>th</sup> cycle measured upon cycling with *in situ* EIS.

When plotting the resistance value recorded at the maximum of each discharge ( $R'_{max}$ ) with the capacity retention, a very coherent tendency can be noticed: *i.e.* decrease of electrolyte resistance along with capacity fading, except for the initial cycle (Figure 6-24).



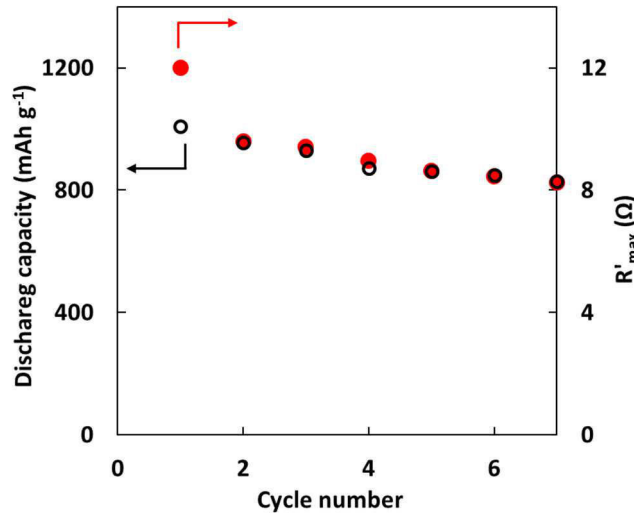


Figure 6-24. Discharge capacity retention during seven cycles (in black) together with the maximum value of the electrolyte resistance ( $R'_{\max}$ ) evolution, recorded at each discharge.

Indeed, in a typical Li/S cell behavior, a drastic capacity fade after the initial cycle is usually observed and is related with several reasons, like active material loss in the electrolyte, electrode pulverization, etc. Starting from the 2<sup>nd</sup> cycle, both curves are almost superimposed, the capacity and the resistance are progressively decreasing.

Such continuous electrolyte resistance decrease could be related with the fact that lower amount of polysulfides is present in the electrolyte upon following cycles. This loss of active material along cycling could be due to: (1) trapping of the polysulfides on the passivation layer(s) on Li, notably in the first cycle (large evolution of the lithium passivating layer properties), and (2) to the precipitation of  $\text{Li}_2\text{S}$  or  $\text{Li}_2\text{S}_2$  that cannot be re-oxidized during the next cycles due to bad connection to the electronic network, or precipitations in the separator, for example.

Fitting of MF and LF semicircles was also conducted and the results are shown below. Figure 6-25 shows the resistance and the capacitance values of bulk electrode response ( $R_{\text{NWC}}//\text{CPE}_{\text{NWC}}$ ), Li/electrolyte interphase ( $R_{\text{Li}}//\text{CPE}_{\text{Li}}$ ) and polysulfides/carbon interface ( $R_{\text{PS}}//\text{CPE}_{\text{PS}}$ ), together with voltage profile.

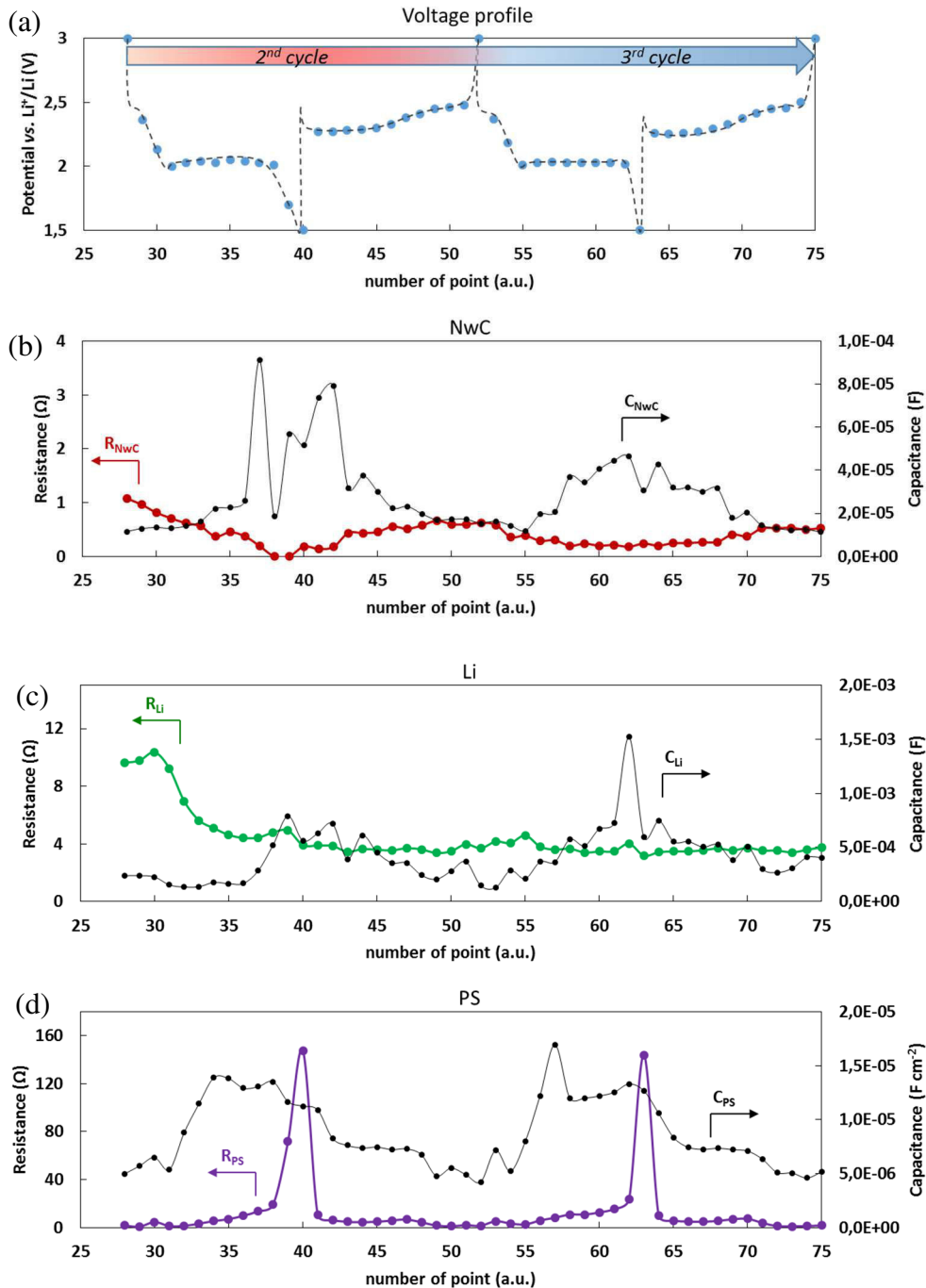


Figure 6-25. Fitting parameters of MF and LF semicircles: bulk electrode (b), Li/electrolyte interphase (c) and polysulfides/carbon interface (d) response recorded during 2<sup>nd</sup> and 3<sup>rd</sup> cycle. Evolution of resistance (colored line) and capacitance (black line) are shown, together with the voltage profile (a).

It can be seen that the resistance of the electrode bulk ( $R_{\text{NWC}}$ ) is again, in a zoomed view, slightly evolving. Similar to what have been observed in the 1<sup>st</sup> cycle, large variations of the capacitance values are visible, and mostly at the end of discharge. The error values were not included on this graph, however, they were also high (even up to 50 – 60 % for the points recorded at fully discharged state).

As concerning the Li/electrolyte interphase, it can be seen that the resistance is very small ( $\sim 4 \Omega$ ) and relatively stable. It again proves that strong variations of the MF semicircle in the 1<sup>st</sup> cycle are strictly related to the initial surface state of Li. After the 1<sup>st</sup> cycle, the surface of Li is stabilized. Very similar situation is observed for the capacitance values. A significant variation is observed rather at the end of discharge.

Figure 6-25d shows the evolution of LF semicircle fitting parameters, *i.e.* the charge transfer resistance involving polysulfides species, and corresponding  $C_{dl}$ . Very similar trend is observed as was already presented in the initial cycle, meaning reversibility of the reactions, as concerning both parameters, capacitance and resistance evolution.

To conclude, we saw that all the parameters (like  $R_{NWC}$ ,  $R_{Li}$ ,  $R_{el}$ ,  $R_{PS}$  and corresponding capacitances) in HF, MF and LF ranges are correlated together and their evolution is also depending one from the other. In order to have more precise interpretation of MF – LF semicircles, mostly when they got diminished to  $\sim 2 - 4 \Omega$  barely, probably another model should be designed, with the addition of additional contribution in a frequency range between Li interphase response and polysulfides charge transfer reaction. However, already with a simple model we proposed, fruitful information could be extracted.

## 6.7. The influence of the low temperature

### 6.7.1. Changes of the cycling voltage profile

The discharge voltage profiles of the Li/S cell cycled at different temperatures in each cycle (Figure 6-26) clearly show that upper discharge plateau is much less affected by temperature changes, since it corresponds to the fast kinetics processes. With decreasing the temperature, more pronounced plateau between the upper and the lower one is visible, since both the electrochemical reactions and the equilibriums between soluble polysulfides are slowed down. Very likely that the nature and the composition of polysulfide species are much more defined when the temperature decreases, which enables the appearance of intermediate plateaus (evolution from 0 °C to -40 °C, Figure 6-26a).

Lower discharge plateau is very dependent on the temperature, since it is related with the formation of solid products, at least of  $Li_2S$ , which precipitate on the electrode surface, thus inducing slower kinetics of the reaction. Even at the temperature of -30 °C, the lower discharge plateau displays a high polarization, but its shape is preserved, which also means that no other processes appear. At -40°C, the lower discharge plateau disappears. However, when decreasing the C-rate to C/200, the plateau was observed again. When the temperature decreases, it is also possible that the solubility limit of medium-to-low polysulfides ( $S_4^{2-}$ ,  $S_2^{2-}$ ) is significantly diminished, leading to the fast precipitation of solids onto the cell, as previously said. However,

it suggests that the same kind of reaction is occurring during the low plateau: *i.e.* formation of solids from soluble polysulfides, and no matter the temperature, it seems that  $\text{Li}_2\text{S}$  formation always starts at the beginning of lower voltage plateau.

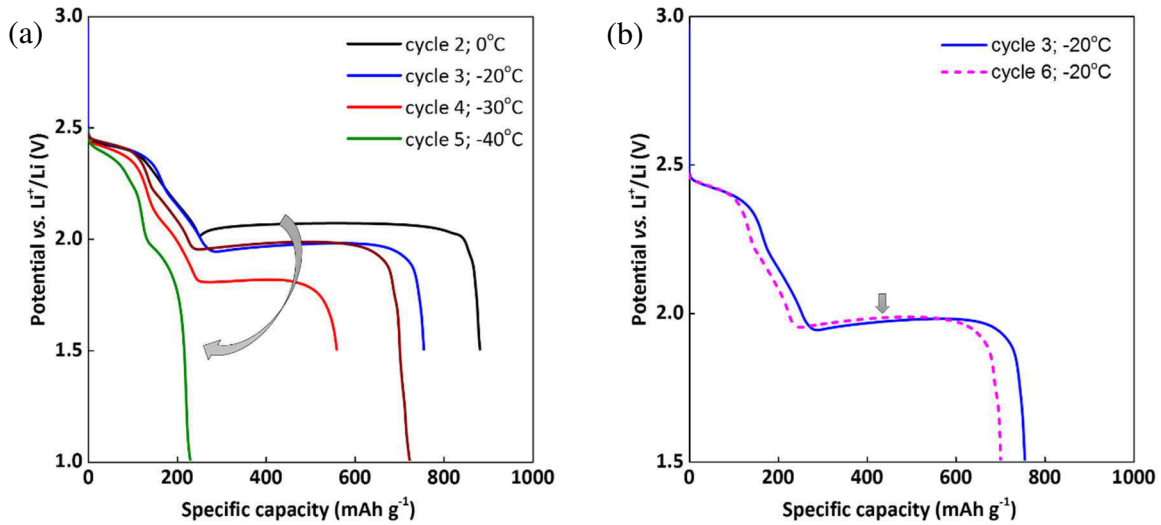


Figure 6-26. Voltage profiles of different cycles obtained when decreasing the temperature from  $0^\circ\text{C}$  to  $-40^\circ\text{C}$ , cycled at  $C/100$  (a). Comparison of discharge profiles: recorded initially at  $-20^\circ\text{C}$  (during 3<sup>rd</sup> cycle) and during 6<sup>th</sup> cycle, when the temperature came back to  $-20^\circ\text{C}$  (after being decreased to  $-30^\circ\text{C}$  and  $-40^\circ\text{C}$  during 4<sup>th</sup> and 5<sup>th</sup> cycle respectively).

When the temperature got increased back to  $-20^\circ\text{C}$  during the 6<sup>th</sup> cycle, the voltage profile displays almost identical behavior as the one obtained in 3<sup>rd</sup> cycle (also at  $-20^\circ\text{C}$ ). The lower discharge plateau comes back to exactly the same potential (1.98 V), as shown on Figure 6-26b.

### 6.7.2. Variation of the EIS parameters

*In-situ* impedance spectroscopy was also performed at low temperature, in order to be able to differentiate more easily the different electrochemical processes. In regard to the changes of the high frequency region, electrolyte resistance evolution can be followed.

As already described in the literature, lower temperature results in higher viscosity of the electrolyte<sup>251</sup>. Figure 6-27 shows how the electrolyte resistance changes between  $25^\circ\text{C}$  and  $-30^\circ\text{C}$ . The same coin cell (with the composite electrode ‘S-on-NwC’; sulfur loading  $\sim 5.4 \text{ mg}_{\text{Sulfur}} \text{ cm}^{-2}$ ) was cycled during three cycles at  $C/100$ , while the temperature was changed at each cycle ( $-30^\circ\text{C}$ ,  $-20^\circ\text{C}$  and  $0^\circ\text{C}$ ). It can be noticed that no matter the temperature applied at each cycle, the resistance evolution shows the same trend as previously discussed for  $25^\circ\text{C}$ . Maxima of the resistance during discharge ( $R'_{\text{max}}$ ) and charge ( $R''_{\text{max}}$ ) correspond to the same moments on the cycling curve, *i.e.* beginning of the lower discharge plateau for the discharge process, which may correspond to the maximum concentration of the  $\text{Li}_2\text{S}_4$  species in the

electrolyte, and the charge maximum occurring always during semi-plateau after the complete oxidation of  $\text{Li}_2\text{S}$ .

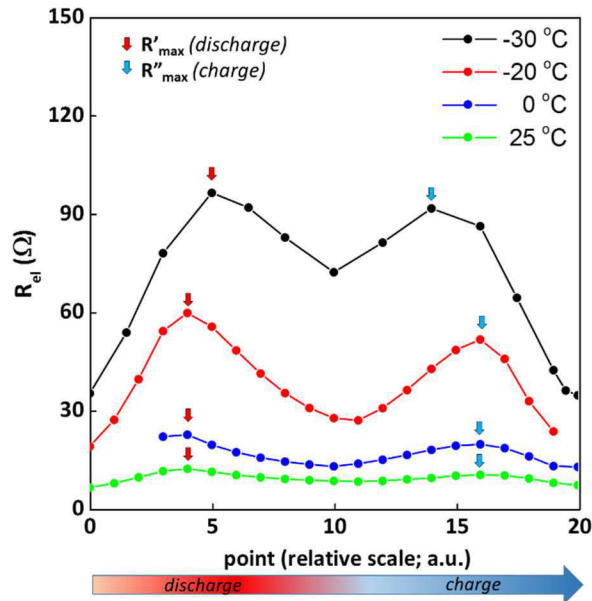


Figure 6-27. Electrolyte resistance evolution recorded during cycling at different temperatures: 25 °C, 0 °C, -20 °C and -30 °C.

As concerning the electrolyte resistance evolution, the appearance and disappearance of insoluble polysulfides seem to be independent of the temperature, in particular with the appearance of insoluble  $\text{Li}_2\text{S}$  at the beginning of the second plateau. Especially, it looks that the decrease of the electrolyte resistance during the lower discharge plateau is less and less pronounced as the temperature decreases (especially between -20 °C and -30 °C). Indeed, the resistance obtained at the end of discharge at 25 °C is closed to its initial level; more than 90% of the resistance increase is recovered. Whereas at -30 °C, the resistance at the end of discharge is much higher than its initial level, *i.e.* 70 Ω instead of 35 Ω, which means that only ~ 50% is recovered. Indeed, at low temperature, the large polarization can induce a limitation on the length of the second plateau. The formation of insoluble  $\text{Li}_2\text{S}$  should then be lower, thus more soluble polysulfides are still present in the electrolyte at the end of discharge, inducing a high  $R_{el}$  (~ 70 Ω at -30 °C). Moreover, the solubility of the short polysulfides can be lower at low temperature, inducing some earlier precipitation. The resistance at the end of charge is weakly higher than the value observed at the initial point for the all temperature investigated, indicating a good reversibility of the oxidation of soluble polysulfides to sulfur. Further studies need to be carried out to completely understand this phenomenon, in particular, conductivity measurement as function of temperature and polysulfides composition.

Vogel-Tamman-Fulcher (VTF) equation<sup>252</sup> can be used to correlate the variation of electrolyte viscosity with the temperature. In a first approximation, considering no modification of the ionic species concentration, viscosity can be proportionally correlated with the electrolyte resistance (conductivity), using Stoke-Einstein relationship. When plotting the maximum

resistance values recorded during discharge ( $R'_{\max}$ ) and charge ( $R''_{\max}$ ) as a function of temperature ( $1000/T$ ), classical activated behavior/evolution is observed (Figure 6-28).

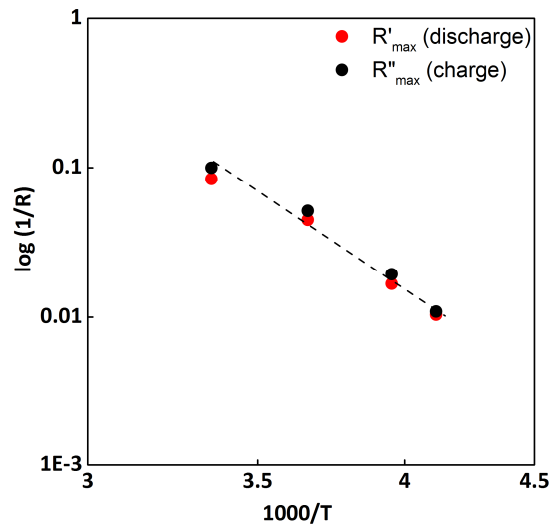


Figure 6-28. The maximum resistance recorded during discharge ( $R'_{\max}$ ) and charge ( $R''_{\max}$ ) as a function of temperature.

Figure 6-29 shows how the Nyquist plot evolves at different temperatures. Only spectra recorded at the end of discharge and charge (for each temperature) are presented. It can be seen that when decreasing the temperature, the response of lithium/electrolyte interphase is increasing as well. Indeed, the passivating layer is less conducting for  $\text{Li}^+$  at lower temperatures.

Regarding the response of  $R_{PS}/CPE_{PS}$  at the end of discharge (LF semicircle), it can be noticed that a decrease of the temperature (from 25 °C to 0 °C) induces a large increase of  $R_{PS}$ , whereas further temperature decrease (to -20 °C and -30 °C) results in the decrease of the resistance. It may be related to several antagonistic effects: (i) it can be related with the covering of the active surface, thus driven by the covering factor (geometric). Lower  $\text{Li}_2\text{S}$  formation at lower temperatures, as discussed previously, may decrease the covering factor, thus decrease the resistive character of  $\text{Li}_2\text{S}$  passivation layer; (ii) the kinetics of the polysulfide reactions may be slowed down at lower temperature, inducing resistance increase and in addition (iii) diffusion process is swept towards lower frequency when the temperature decreases, thus it is less over-imposed with the polysulfides charge transfer reaction (visual decrease of the semicircle).

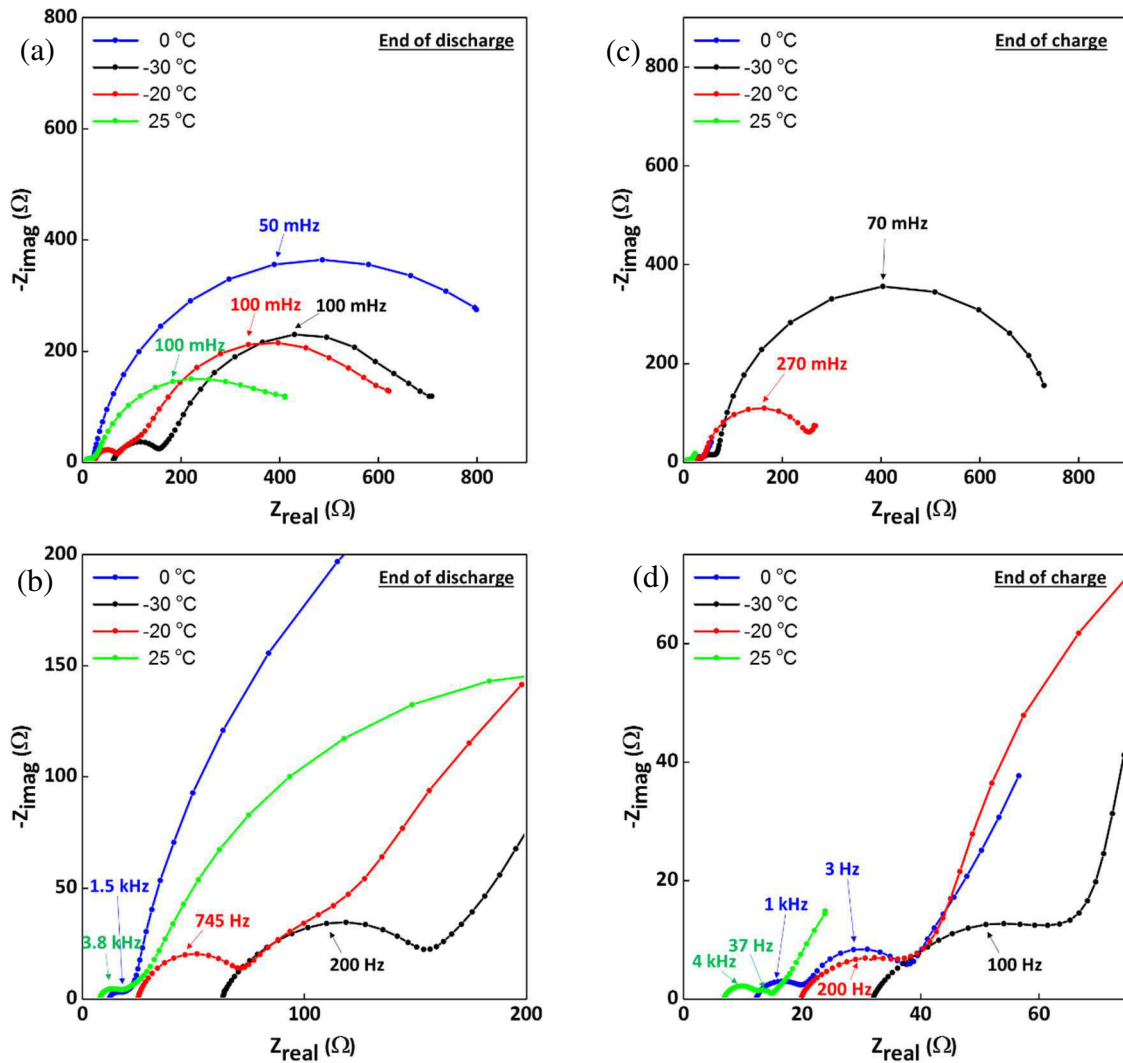


Figure 6-29. Nyquist plot recorded at the end of discharge (a,b) and charge (c,d) for all temperatures: 25 °C, 0 °C, -20 °C and -30 °C.

At the end of charge (Figure 6-29c,d) basically the same trend is observed in terms of Li/electrolyte interphase (MF semicircle), *i.e.* resistance increases with the temperature decrease. However, the semicircle at the LF ( $R_{PS}/CPE_{PS}$ ) is now more related with the soluble species (not the same response as at the end of discharge, where formation of solid form takes place), and thus with the decrease of the temperature, the resistance is increasing drastically. It is related with the fact that the electrochemical oxidation of soluble polysulfides is slowed down at lower temperatures. The activation energy of the process could be then determine (Figure 6-30), and the value of  $E_a = 0.67$  eV is found. Such high activation energy could be related to an electrochemical process coupled with chemical process involving sulfur crystallization.

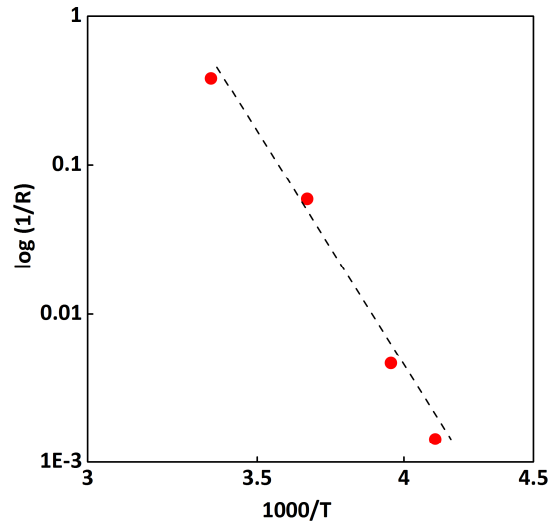


Figure 6-30. Arrhenius plot obtained with the resistance values of  $R_{PS}$  semicircle at the end of charge, at different temperatures.

## 6.8. Conclusions

EIS investigations gave a large overview on the reactions occurring upon cycling in a Li/S cell. To our best knowledge, it was the first time such completed description was performed, together with deep interpretation of obtained results at large range of characteristic frequencies. In order to correctly attribute the response of Nyquist plot obtained through EIS measurements, the use of symmetric coin cells approach was helpful and indispensable. EIS results are in a good agreement with the observations obtained through *in situ* XRD measurements.

First of all, metallic lithium electrode significantly contributes to the impedance response of a complete Li/S cell, especially visible in the initial cycle, mainly through its passivation layer, whereas this contribution is generally omitted in the literature.

Our investigation permitted to propose a simple equivalent circuit preserved all along the cycling. The circuit includes the electrolyte resistance response (at HF region), followed by three R//CPE elements connected in series between MF to LF, associated to (i) the positive electrode bulk contribution, (ii) passivating film formed at lithium/electrolyte interphase and (iii) charge transfer reaction of polysulfides at the positive electrode surface. The LF response was attributed to the diffusion processes in the overall cell, however, was not further investigated in this work. The evolution of each parameter was investigated during the first cycle and further ones as well. The main difference between different cycles, is the lower response of the lithium interphase starting with the second cycle. Moreover, we were able to correlate the capacity retention as a perfect match with the electrolyte resistance evolution, which in turn gives an indication of the limiting factors.



The decrease of temperature seems to have a weak effect on the electrochemical process, *i.e.* formation of solid  $\text{Li}_2\text{S}$  always starts at the beginning of the low voltage plateau. The significant electrolyte resistance evolutions were also observed.

## Conclusions & Perspectives

In this work, two main axes were systematically followed. The first one was mainly devoted to improvements of already existing solutions for both systems: Li/S and ‘negative electrode’/Li<sub>2</sub>S batteries, understanding the way they perform, along with carrying out developments and tests of new and innovative solutions. Another aspect was dedicated to deeper understanding of the phenomena occurring inside the Li/S batteries, the complexity of the working mechanisms and of the limiting parameters. For this purpose, two main experimental techniques were used: electrochemical impedance spectroscopy and *in situ* and *operando* X-ray diffraction.

Aiming to develop Li/S batteries, we purely focused on preparation positive electrodes on both aluminum and NwC-current collectors. Our work was based on very simple positive electrodes, *i.e.* fabricated in a facile way with the use of cheap and commercially available products along with practical electrode loadings of at least 2.0 mg<sub>sulfur</sub> cm<sup>-2</sup>, keeping in mind the future application.

Several parameters were investigated, but no significant difference in cyclability was found when using different carbon additives (SuperP<sup>®</sup>, Ketjenblack<sup>®</sup>, VGCF<sup>®</sup>) or binders (PVdF, CMC/NBR). Quite similar overall capacity retention (with slightly better performances of CMC composition) was obtained for both types of binder.

In order to find eventual correlation between the electrodes’ morphology, their electric properties and cycling performances, symmetric coin cells composed of two identical sulfur electrodes were prepared and intensively studied with EIS. It was found out that the main response in the Nyquist plot is associated with the bulk response of the electrode. The large resistance values (even ~ 20 Ω) may be related to a weak homogeneity of the electrode morphology with not efficient electronic pathways, which strongly depend on the electrode ink preparation method. Well-dispersed and homogenous inks, made with Dispermat<sup>®</sup>, resulted in significantly decreased resistance response, whatever the binder used. With well-dispersed ink, the response of bulk electrode is very small, of 1 or 2 Ω only. Moreover, no correlation was obtained between EIS response at the initial state and capacity retention, contrarily to what is claimed in literature. A main semicircle in the Nyquist plot (in the MF range) of the sulfur electrode is not associated with the charge transfer reaction, but with the electrode morphology and its structural modifications after cycling (an example: problems of adhesion were also detected by increased impedance).

An efficient way to increase the electrode loading and to improve the mechanical integrity of the electrode is to use a 3D type porous current collector. Utilization of such non-woven carbon felt (NwC) was adapted from the previous work of a former PhD student in our research groups. The use of 3D carbon-based current collector allowed to obtain highly loaded electrodes,

without sacrificing the practical discharge capacities. However, this architecture is not yet optimized for power rate applications. The benefit of NwC over Al collector is mainly visible when comparing highly loaded electrodes ( $> 4 \text{ mg}_{\text{sulfur}} \text{ cm}^{-2}$ ). It is then obvious that much higher capacity values (of even  $300 \text{ mAh g}^{-1}$ ) can be obtained with NwC-based electrodes, and with lower polarization. We also proved that the reason for such improved capacity values is not directly related with the fact that NwC collector offers an additional conductive surface area for solid products precipitation ( $\text{Li}_2\text{S}/\text{Li}_2\text{S}_2$ ). More important is its high porosity ( $\sim 80 \%$ ) and 3D conductive network, which efficiently improve both ionic and electronic conductive pathways, because of easily accessible volume for the electrolyte/polysulfides penetration and fast electron propagation through the carbon fibers. It also provides a rigid and stable carbon matrix for the electrode, which is beneficial from the point of view of dissolution/precipitation cycles.

Last but not least, one of the main obstacles we systematically observed was the appearance of micro short circuits during charge, most likely due to dendritic growth on the negative lithium electrode, since we were working with relatively highly loaded positive electrodes, thus meaning high depths of lithium stripping/plating.

The problem related to metallic lithium electrode gave us the motivation to go into the direction of safer lithium-ion/sulfur (Li-ion/S) cells, by eliminating metallic lithium and replacing it by silicon negative electrode. In the first step, investigation of the  $\text{Li}_2\text{S}$  positive electrode vs. lithium was performed and compared to the one of Li/S cell. If taking apart the first charge process of the Li/ $\text{Li}_2\text{S}$  cell, further cycles exhibit the same behavior and limitations as a classical Li/S battery. The initial charge, however, is very particular and characteristic, mostly because of the poor ionic and electronic conductivities of  $\text{Li}_2\text{S}$  particles, their micrometric size and poor solubility in the organic solvents. In particular, the electrochemical process occurring upon initial charge is different from further charge cycles. Indeed,  $\text{Li}_2\text{S}$  material seems to be present during all the 1<sup>st</sup> charge, which limits the overall oxidation reaction and induces large polarization in the main part of the charge profile. Moreover, the equilibrium potential is fixed by the equilibria existing in solutions and involving medium-to-long polysulfides ( $\text{S}_4^{2-}$ ,  $\text{S}_6^{2-}$ ,  $\text{S}_8^{2-}$ ), up to the appearance of  $\text{S}_8$  at the end of charge. After having thoroughly studied the performances of Li/ $\text{Li}_2\text{S}$  cell, in the next step a complete metallic lithium-free cell – Si/ $\text{Li}_2\text{S}$  – was also analyzed and promising results were obtained. The cycling properties were very close to the ones obtained when using metallic Li, and further improvements of Si/ $\text{Li}_2\text{S}$  cell may bring additional benefits.

The fundamental investigations of this work were carried out thanks to the application of two pertinent techniques: Electrochemical Impedance Spectroscopy (EIS) and *in situ* and *operando* X-Ray diffraction (XRD).

With the use of XRD technique, we successfully analysed the structural changes of active material inside a Li/S battery during few initial cycles. Our *in situ* synchrotron-based results clearly indicate the formation of crystalline  $\text{Li}_2\text{S}$  on the positive electrode, starting from the very beginning of lower discharge plateau. We also proposed a sequential discharge

mechanism related to the low voltage plateau. First, the reduction of  $S_4^{2-}$  into  $Li_2S$  occurs with efficiency close to 1, whereas for higher DOD%, a competitive reaction appears, which is very likely to be the formation of  $Li_2S_2$  phase. During charge, disappearance of  $Li_2S$  seems to also occur in a two-step mechanism, with higher efficiency at the beginning of the charge process, while the complete disappearance of  $Li_2S$  was obtained at 75% of DOD. A large hysteresis between discharge ( $Li_2S$  formation) and charge ( $Li_2S$  consumption) was also noticed, proving the different reactions pathways taking place. At the end of charge, soluble polysulfides are oxidized into solid  $S_8$ . It was found that sulfur after recrystallization does not come back to its pristine structure, but it appears as another allotrope: monoclinic  $\beta$ -sulfur. During oxidation of soluble polysulfides, crystallization of solid sulfur may be more favourable and easier in a less ordered form of sulfur ( $\beta$ - $S_8$ ) as compared with the thermodynamically stable and ordered  $\alpha$ - $S_8$  phase, initially present in the electrode. Very similar behaviour was observed during further cycles. These evolutions were also confirmed at higher C-rate (C/8).

In addition to XRD investigation, Electrochemical Impedance Spectroscopy was applied to the Li/S system for further understanding of discharge/charge mechanisms. EIS studies gave a large overview on the reactions occurring upon cycling in a Li/S cell. To our best knowledge, it was the first time such completed analyses were performed, together with deep interpretation of obtained results at large range of characteristic times. In order to correctly attribute the response of Nyquist plot obtained through EIS measurements on two-electrode cells, the use of symmetric coin cells approach was a helpful and indispensable. EIS results were found to be in a good agreement with the observations obtained through *in situ* XRD measurements.

We have shown that during the initial cycle, metallic lithium anode significantly contributes to the initial OCV impedance response of Li/S cell, mainly through its passivation layer. In addition, in a complete Li/S cell, only the LF response is related to the sulfur electrode, and is visible as a vertical line describing blocking character at OCV. This capacitive character is disappearing quite quickly during the cell storage, accompanied by a potential decrease, mainly lying on the easy partial sulfur dissolution in the electrolyte, and further polysulfides formations (thus inducing self-discharge process).

Several tests performed (*in situ* EIS upon cycling recorded on classical two-electrodes cells, supported by symmetric coin cells at different DOD% during discharge) permitted to propose a simple equivalent circuit preserved all along the cycling. The circuit includes the electrolyte resistance response (at HF region), followed by the three R/CPE elements connected in series between HF  $\rightarrow$  MF  $\rightarrow$  LF regions, associated to (i) the positive electrode bulk contribution, (ii) the passivating film formed at lithium/electrolyte interphase and (iii) the charge transfer reaction of polysulfides at the positive electrode surface, respectively. The LF response was related to the diffusion processes in the overall cell.

It was found that the resistance of the electrolyte is strongly dependent on the polysulfides composition present in the electrolyte. The maximum resistance values were found for the moments, where the highest concentration of soluble species is obtained, *i.e.* beginning of solid

Li<sub>2</sub>S formation during discharge and moment of complete Li<sub>2</sub>S re-oxidation, at about 75 %SOC. These findings are in complete agreement with obtained *in situ* XRD results. It was also found that the initial resistance value was never obtained anymore upon cycling, even at full charge and discharge, which proves that some amount of active material may be lost in the electrolyte.

The resistance of positive electrode bulk contribution was found to be weak and more or less stable during the cycling. However, changes of the MF semicircle upon cycling (and mostly during the initial cycle) are linked to the modification of the passivation layer on metallic lithium electrode. A strong impact of the polysulfides on the lithium passivation layer was also noticed, leading to the formation of a less resistive layer.

The charge transfer reaction of the polysulfide species starts to be visible as a small loop just after the first discharge plateau. This semicircle increases largely by the end of discharge, and this phenomenon can easily be ascribed to the formation of Li<sub>2</sub>S insulating layer on the positive electrode surface. In addition, this evolution is accompanied by a strong increase of the transport limitation. During the charge process, the oxidation of Li<sub>2</sub>S results in a global decrease of the polysulfide charge transfer resistance.

The evolution of the EIS spectra during further cycles is not so different from the evolutions obtained during initial one, except for the Li/electrolyte interphase. Indeed, initial resistance of the Li/electrolyte interphase is relatively high, since it is related with the initial state of metallic lithium surface. The contribution of lithium to the full impedance of the Li/S cell is then decreased after the first cycle. Last but not least, we were able to correlate the capacity retention as a perfect match with the electrolyte resistance evolution, which in turn gives an indication of the limiting factors.

Regarding the cycling curve at low temperatures, more pronounced plateau between the upper and lower ones is visible, very likely due to the stabilization of polysulfides equilibria in solution (slower disproportionation/dissociation kinetics). Whatever the temperature, the shape of lower discharge plateau is preserved, indicating also that the formation of solid Li<sub>2</sub>S starts just at the same moment, while no other processes can be distinguished (single plateau is observed).

At low temperature, less reversible evolution of the electrolyte resistance during discharge was observed, well-connected to the lower capacity obtained during the short plateau region. However, the resistance at the end of charge is near the initial value for all temperatures, indicating that the process of sulfur formation is much easier than Li<sub>2</sub>S one. Expected evolution of passivation layer response *vs.* temperature was found, *i.e.* increase of the resistance with a decrease of the temperature. The nonlinear evolution of the polysulfides charge transfer response, at the end of discharge and as a function of temperature, is well-correlated to antagonistic effects, *i.e.* lower kinetic at low temperature along with a lower coverage of the electrode surface by Li<sub>2</sub>S (lower capacity).

This work has open several ways for further investigations. As concerning the development of sulfur positive electrode, further studies on carbon based current collector may be a promising way to follow in order to obtain high sulphur loading with high practical capacity. Optimisation of collector's parameters, like: thickness, porosity, weight, etc. should be strongly considered for high energy density cathodes. Nevertheless, no matter the current collector used, sulphur loading should be always considered as a very important parameter, and loadings much higher than  $2\text{mg}_{\text{sulfur}}\text{ cm}^{-2}$  should be only taken into consideration, otherwise the Li/S technology will not be a 'seriously considered' candidate to beat the today's Li-ion technology. Following this aspect, also while designing the cell, fabrication process should be relatively easy and possible for future scale up. Therefore, too complicated electrodes architectures which requires too expensive techniques and processes impossible to apply in a large scale, should be simplified, otherwise will never be considered as a potential product for large scale application. Parameters like S/E ratio, sulfur loading and sulfur fraction in the electrode should be carefully controlled and always provided in any scientific report, as these are the parameters that play very important role on the cell cyclability and performances.

As regard to the  $\text{Li}_2\text{S}$  positive electrode, further optimisation and improvement of fabrication process should be considered, *i.e.* decrease of the particle size and improving the intimate contact with carbon. Further studies should be also done for deeper understanding of the mechanism occurring in the initial charge. When using  $\text{Li}_2\text{S}$  in a complete metallic lithium free cell, like Si/ $\text{Li}_2\text{S}$ , the work on balancing of the cell, improvement of the electrolyte could be carry out. Possibly more fundamental studies should be performed on the effect of the polysulfides on the negative electrode used, in that case Si. Techniques like XPS, SEM would be useful.

Nevertheless, many scientist still claim that Li/S have the potential to beat Li-ion cells only in a configuration:  $\text{S}_8$  vs. Li – the most realistic solution according to them. This however, still requires a work on the protection of the Lithium surface, to diminish polysulfides shuttle, parasitic reactions, safety issues *etc.* The work on the lithium protection has been carried out since few decades and is still not resolved. But it has great potential since other emerging technologies like Li-air are facing the same 'problems' coming from metallic lithium utilization.

Up to now, there has been an impressive progress done in the field of the understanding of the working mechanism. And this direction is definitely the one to follow, since we are still not sure about the whole reactions occurring in the Li/S cell. Moreover, the working mechanism may be very different, depending from the electrolyte or the sulfur electrode used. Therefore, an interesting and great possibilities lies there. Also, in order to have wider vision of investigated system, application of two or even three characterisation techniques in parallel should be a popular practice, and if possible, applied via *in situ* methodology to have direct response of a battery upon cycling.

Last but not least, while thinking of the improvement of the Li/S battery, we should definitely think globally about the whole system. Optimisation and/or improvement of only one component may not be sufficient, since once the battery starts to run, all the ‘issues’ are interconnected, and the limitations of the positive electrode (like for example: solubility of active material and formation of polysulfide species) strongly affects the electrolyte and the negative electrode.

# References

- (1) <http://www.bp.com/en/global/corporate/about-bp/energy-economics.html>.
- (2) Cheng, F.; Liang, J.; Tao, Z.; Chen, J. Functional materials for rechargeable batteries. *Adv Mater* **2011**, *23*, 1695-1715.
- (3) Dunn, B.; Kamath, H.; Tarascon, J. M. Electrical energy storage for the grid: a battery of choices. *Science* **2011**, *334*, 928-935.
- (4) Tarascon, J. M.; Armand, M. Issues and challenges facing rechargeable lithium batteries. *Nature* **2001**, *414*, 359-367.
- (5) Bruce, P. G.; Freunberger, S. A.; Hardwick, L. J.; Tarascon, J. M. Li-O<sub>2</sub> and Li-S batteries with high energy storage. *Nature materials* **2012**, *11*, 19-29.
- (6) <http://www.technologyreview.com/>.
- (7) <http://sulfur.nigc.ir/en/sulfurproductionprocess>.
- (8) Manthiram, A.; Fu, Y.; Chung, S. H.; Zu, C.; Su, Y. S. Rechargeable Lithium-Sulfur Batteries. *Chemical reviews* **2014**.
- (9) <http://www.sionpower.com/>.
- (10) <http://www.oxisenergy.com/>.
- (11) Ellis, B. L.; Lee, K. T.; Nazar, L. F. Positive Electrode Materials for Li-Ion and Li-Batteries<sup>†</sup>. *Chemistry of Materials* **2010**, *22*, 691-714.
- (12) Bruce, P. G. Energy storage beyond the horizon: Rechargeable lithium batteries. *Solid State Ionics* **2008**, *179*, 752-760.
- (13) <http://www.nohms.com/>.
- (14) Herbert, D.; Ulam, J.: Electric dry cells and storage batteries. U.S. Patent 3043896, 1962.
- (15) Rauh, R. D.; Abraham, K. M.; Pearson, G. F.; Surprenant, J. K.; Brummer, S. B. A Lithium/Dissolved Sulfur Battery with an Organic Electrolyte. *Journal of The Electrochemical Society* **1979**, *126*, 523-527.
- (16) Choi, N. S.; Chen, Z.; Freunberger, S. A.; Ji, X.; Sun, Y. K.; Amine, K.; Yushin, G.; Nazar, L. F.; Cho, J.; Bruce, P. G. Challenges facing lithium batteries and electrical double-layer capacitors. *Angewandte Chemie* **2012**, *51*, 9994-10024.
- (17) Manthiram, A.; Fu, Y.; Su, Y.-S. Challenges and Prospects of Lithium-Sulfur Batteries. *Accounts of Chemical Research* **2012**, *46*, 1125-1134.
- (18) Ji, X.; Nazar, L. F. Advances in Li-S batteries. *Journal of Materials Chemistry* **2010**, *20*, 9821.
- (19) Greenwood, N. N. & Earnshaw, A. (1997). *Chemistry of the Elements* (2nd ed.), Oxford: Butterworth-Heinemann.
- (20) Templeton, L. K.; Templeton, D. H.; Zalkin, A. Crystal structure of monoclinic sulfur. *Inorganic Chemistry* **1976**, *15*, 1999-2001.
- (21) Pastorino, C.; Gamba, Z. Toward an anisotropic atom-atom model for the crystalline phases of the molecular S<sub>8</sub> compound. *The Journal of Chemical Physics* **2001**, *115*, 9421-9426.
- (22) Pastorino, C.; Gamba, Z. Test of a simple and flexible molecule model for  $\alpha$ -,  $\beta$ -, and  $\gamma$ -S<sub>8</sub> crystals. *The Journal of Chemical Physics* **2000**, *112*, 282-286.
- (23) Walus, S.; Barchasz, C.; Colin, J. F.; Martin, J. F.; Elkaim, E.; Lepretre, J. C.; Alloin, F. New insight into the working mechanism of lithium-sulfur batteries: in situ and operando X-ray diffraction characterization. *Chemical communications* **2013**, *49*, 7899-7901.



- (24) Kulisch, J.; Sommer, H.; Brezesinski, T.; Janek, J. Simple cathode design for Li-S batteries: cell performance and mechanistic insights by in operando X-ray diffraction. *Physical Chemistry Chemical Physics* **2014**, *16*, 18765-18771.
- (25) Villevieille, C.; Novák, P. A metastable  $\beta$ -sulfur phase stabilized at room temperature during cycling of high efficiency carbon fibre–sulfur composites for Li–S batteries. *Journal of Materials Chemistry A* **2013**, *1*, 13089.
- (26) Moon, S.; Jung, Y. H.; Jung, W. K.; Jung, D. S.; Choi, J. W.; Kim do, K. Encapsulated monoclinic sulfur for stable cycling of li-s rechargeable batteries. *Adv Mater* **2013**, *25*, 6547-6553.
- (27) Patel, M. U.; Demir-Cakan, R.; Morcrette, M.; Tarascon, J. M.; Gaberscek, M.; Dominko, R. Li-S battery analyzed by UV/Vis in operando mode. *ChemSusChem* **2013**, *6*, 1177-1181.
- (28) Choi, Y.-J.; Chung, Y.-D.; Baek, C.-Y.; Kim, K.-W.; Ahn, H.-J.; Ahn, J.-H. Effects of carbon coating on the electrochemical properties of sulfur cathode for lithium/sulfur cell. *Journal of Power Sources* **2008**, *184*, 548-552.
- (29) Gao, J.; Lowe, M. A.; Kiya, Y.; Abruña, H. D. Effects of Liquid Electrolytes on the Charge–Discharge Performance of Rechargeable Lithium/Sulfur Batteries: Electrochemical and in-Situ X-ray Absorption Spectroscopic Studies. *The Journal of Physical Chemistry C* **2011**, *115*, 25132-25137.
- (30) Li, Z.; Yuan, L.; Yi, Z.; Sun, Y.; Liu, Y.; Jiang, Y.; Shen, Y.; Xin, Y.; Zhang, Z.; Huang, Y. Insight into the Electrode Mechanism in Lithium-Sulfur Batteries with Ordered Microporous Carbon Confined Sulfur as the Cathode. *Advanced Energy Materials* **2014**, *4*, n/a-n/a.
- (31) Busche, M. R.; Adelhelm, P.; Sommer, H.; Schneider, H.; Leitner, K.; Janek, J. Systematical electrochemical study on the parasitic shuttle-effect in lithium-sulfur-cells at different temperatures and different rates. *Journal of Power Sources* **2014**, *259*, 289-299.
- (32) Mikhaylik, Y. V.; Akridge, J. R. Polysulfide Shuttle Study in the Li/S Battery System. *Journal of The Electrochemical Society* **2004**, *151*, A1969.
- (33) Ryu, H. S.; Ahn, H. J.; Kim, K. W.; Ahn, J. H.; Cho, K. K.; Nam, T. H. Self-discharge characteristics of lithium/sulfur batteries using TEGDME liquid electrolyte. *Electrochimica Acta* **2006**, *52*, 1563-1566.
- (34) Ryu, H. S.; Ahn, H. J.; Kim, K. W.; Ahn, J. H.; Lee, J. Y.; Cairns, E. J. Self-discharge of lithium–sulfur cells using stainless-steel current-collectors. *Journal of Power Sources* **2005**, *140*, 365-369.
- (35) Barchasz, C.; Leprêtre, J.-C.; Alloin, F.; Patoux, S. New insights into the limiting parameters of the Li/S rechargeable cell. *Journal of Power Sources* **2012**, *199*, 322-330.
- (36) Cheon, S.-E.; Choi, S.-S.; Han, J.-S.; Choi, Y.-S.; Jung, B.-H.; Lim, H. S. Capacity Fading Mechanisms on Cycling a High-Capacity Secondary Sulfur Cathode. *Journal of The Electrochemical Society* **2004**, *151*, A2067.
- (37) Cheon, S.-E.; Ko, K.-S.; Cho, J.-H.; Kim, S.-W.; Chin, E.-Y.; Kim, H.-T. Rechargeable Lithium Sulfur Battery. *Journal of The Electrochemical Society* **2003**, *150*, A796.
- (38) Zhang, S. S. Liquid electrolyte lithium/sulfur battery: Fundamental chemistry, problems, and solutions. *Journal of Power Sources* **2013**, *231*, 153-162.
- (39) He, X.; Ren, J.; Wang, L.; Pu, W.; Jiang, C.; Wan, C. Expansion and shrinkage of the sulfur composite electrode in rechargeable lithium batteries. *Journal of Power Sources* **2009**, *190*, 154-156.
- (40) Yin, Y. X.; Xin, S.; Guo, Y. G.; Wan, L. J. Lithium-sulfur batteries: electrochemistry, materials, and prospects. *Angewandte Chemie* **2013**, *52*, 13186-13200.
- (41) Kolosnitsyn, V. S.; Karaseva, E. V. Lithium-sulfur batteries: Problems and solutions. *Russian Journal of Electrochemistry* **2008**, *44*, 506-509.
- (42) Diao, Y.; Xie, K.; Xiong, S.; Hong, X. Shuttle phenomenon – The irreversible oxidation mechanism of sulfur active material in Li–S battery. *Journal of Power Sources* **2013**, *235*, 181-186.
- (43) Hofmann, A. F.; Fronczek, D. N.; Bessler, W. G. Mechanistic modeling of polysulfide shuttle and capacity loss in lithium–sulfur batteries. *Journal of Power Sources* **2014**, *259*, 300-310.

- (44) Bauer, I.; Thieme, S.; Brückner, J.; Althues, H.; Kaskel, S. Reduced polysulfide shuttle in lithium–sulfur batteries using Nafion-based separators. *Journal of Power Sources* **2014**, *251*, 417-422.
- (45) Barchasz, C. Développement d'accumulateurs lithium/soufre; PhD thesis. **2011**.
- (46) Li, Z.; Huang, J.; Yann Liaw, B.; Metzler, V.; Zhang, J. A review of lithium deposition in lithium-ion and lithium metal secondary batteries. *Journal of Power Sources* **2014**, *254*, 168-182.
- (47) Aurbach, D.; Pollak, E.; Elazari, R.; Salitra, G.; Kelley, C. S.; Affinito, J. On the Surface Chemical Aspects of Very High Energy Density, Rechargeable Li–Sulfur Batteries. *Journal of The Electrochemical Society* **2009**, *156*, A694.
- (48) Mikhaylik, Y. V.; Kovalev, I.; Schock, R.; Kumaresan, K.; Xu, J.; Affinito, J. High Energy Rechargeable Li-S Cells for EV Application: Status, Remaining Problems and Solutions. *ECS Transactions* **2010**, *25*, 23-34.
- (49) Wang, J.; Liu, L.; Ling, Z.; Yang, J.; Wan, C.; Jiang, C. Polymer lithium cells with sulfur composites as cathode materials. *Electrochimica Acta* **2003**, *48*, 1861-1867.
- (50) Ji, X.; Lee, K. T.; Nazar, L. F. A highly ordered nanostructured carbon-sulphur cathode for lithium-sulphur batteries. *Nature materials* **2009**, *8*, 500-506.
- (51) Zhang, B.; Qin, X.; Li, G. R.; Gao, X. P. Enhancement of long stability of sulfur cathode by encapsulating sulfur into micropores of carbon spheres. *Energy & Environmental Science* **2010**, *3*, 1531-1537.
- (52) Xin, S.; Gu, L.; Zhao, N. H.; Yin, Y. X.; Zhou, L. J.; Guo, Y. G.; Wan, L. J. Smaller sulfur molecules promise better lithium-sulfur batteries. *Journal of the American Chemical Society* **2012**, *134*, 18510-18513.
- (53) He, G.; Ji, X.; Nazar, L. High “C” rate Li-S cathodes: sulfur imbibed bimodal porous carbons. *Energy & Environmental Science* **2011**, *4*, 2878.
- (54) Li, D.; Han, F.; Wang, S.; Cheng, F.; Sun, Q.; Li, W. C. High sulfur loading cathodes fabricated using peapodlike, large pore volume mesoporous carbon for lithium-sulfur battery. *ACS applied materials & interfaces* **2013**, *5*, 2208-2213.
- (55) Chen, S.-R.; Zhai, Y.-P.; Xu, G.-L.; Jiang, Y.-X.; Zhao, D.-Y.; Li, J.-T.; Huang, L.; Sun, S.-G. Ordered mesoporous carbon/sulfur nanocomposite of high performances as cathode for lithium–sulfur battery. *Electrochimica Acta* **2011**, *56*, 9549-9555.
- (56) Park, M.-S.; Jeong, B. O.; Kim, T. J.; Kim, S.; Kim, K. J.; Yu, J.-S.; Jung, Y.; Kim, Y.-J. Disordered mesoporous carbon as polysulfide reservoir for improved cyclic performance of lithium–sulfur batteries. *Carbon* **2014**, *68*, 265-272.
- (57) Tao, X.; Chen, X.; Xia, Y.; Huang, H.; Gan, Y.; Wu, R.; Chen, F.; Zhang, W. Highly mesoporous carbon foams synthesized by a facile, cost-effective and template-free Pechini method for advanced lithium–sulfur batteries. *Journal of Materials Chemistry A* **2013**, *1*, 3295.
- (58) Li, X.; Cao, Y.; Qi, W.; Saraf, L. V.; Xiao, J.; Nie, Z.; Mietek, J.; Zhang, J.-G.; Schweser, B.; Liu, J. Optimization of mesoporous carbon structures for lithium-sulfur battery applications. *Journal of Materials Chemistry* **2011**, *21*, 16603-16610.
- (59) Liang, C.; Dudney, N. J.; Howe, J. Y. Hierarchically Structured Sulfur/Carbon Nanocomposite Material for High-Energy Lithium Battery. *Chemistry of Materials* **2009**, *21*, 4724-4730.
- (60) Oschatz, M.; Borchardt, L.; Pinkert, K.; Thieme, S.; Lohe, M. R.; Hoffmann, C.; Benusch, M.; Wissler, F. M.; Ziegler, C.; Giebeler, L.; Rummeli, M. H.; Eckert, J.; Eychmüller, A.; Kaskel, S. Hierarchical Carbide-Derived Carbon Foams with Advanced Mesostructure as a Versatile Electrochemical Energy-Storage Material. *Advanced Energy Materials* **2014**, *4*, n/a-n/a.
- (61) Thieme, S.; Brückner, J.; Bauer, I.; Oschatz, M.; Borchardt, L.; Althues, H.; Kaskel, S. High capacity micro-mesoporous carbon–sulfur nanocomposite cathodes with enhanced cycling stability prepared by a solvent-free procedure. *Journal of Materials Chemistry A* **2013**, *1*, 9225.
- (62) Ding, B.; Yuan, C.; Shen, L.; Xu, G.; Nie, P.; Zhang, X. Encapsulating sulfur into hierarchically ordered porous carbon as a high-performance cathode for lithium-sulfur batteries. *Chemistry* **2013**, *19*, 1013-1019.

- (63) Xi, K.; Cao, S.; Peng, X.; Ducati, C.; Kumar, R. V.; Cheetham, A. K. Carbon with hierarchical pores from carbonized metal-organic frameworks for lithium sulphur batteries. *Chemical communications* **2013**, *49*, 2192-2194.
- (64) Qu, Y.; Zhang, Z.; Zhang, X.; Ren, G.; Wang, X.; Lai, Y.; Liu, Y.; Li, J. Synthesis of hierarchical porous honeycomb carbon for lithium-sulfur battery cathode with high rate capability and long cycling stability. *Electrochimica Acta* **2014**, *137*, 439-446.
- (65) Xu, G.; Ding, B.; Nie, P.; Shen, L.; Dou, H.; Zhang, X. Hierarchically porous carbon encapsulating sulfur as a superior cathode material for high performance lithium-sulfur batteries. *ACS applied materials & interfaces* **2014**, *6*, 194-199.
- (66) Jayaprakash, N.; Shen, J.; Moganty, S. S.; Corona, A.; Archer, L. A. Porous hollow carbon@sulfur composites for high-power lithium-sulfur batteries. *Angewandte Chemie* **2011**, *50*, 5904-5908.
- (67) Brun, N.; Sakaushi, K.; Yu, L.; Giebeler, L.; Eckert, J.; Titirici, M. M. Hydrothermal carbon-based nanostructured hollow spheres as electrode materials for high-power lithium-sulfur batteries. *Physical chemistry chemical physics : PCCP* **2013**, *15*, 6080-6087.
- (68) Zheng, G.; Yang, Y.; Cha, J. J.; Hong, S. S.; Cui, Y. Hollow carbon nanofiber-encapsulated sulfur cathodes for high specific capacity rechargeable lithium batteries. *Nano letters* **2011**, *11*, 4462-4467.
- (69) Li, Q.; Zhang, Z.; Zhang, K.; Fang, J.; Lai, Y.; Li, J. A simple synthesis of hollow carbon nanofiber-sulfur composite via mixed-solvent process for lithium-sulfur batteries. *Journal of Power Sources* **2014**, *256*, 137-144.
- (70) Qu, Y.; Zhang, Z.; Wang, X.; Lai, Y.; Liu, Y.; Li, J. A simple SDS-assisted self-assembly method for the synthesis of hollow carbon nanospheres to encapsulate sulfur for advanced lithium-sulfur batteries. *Journal of Materials Chemistry A* **2013**, *1*, 14306.
- (71) Tang, J.; Yang, J.; Zhou, X. Acetylene black derived hollow carbon nanostructure and its application in lithium-sulfur batteries. *RSC Advances* **2013**, *3*, 16936.
- (72) Böttger-Hiller, F.; Kempe, P.; Cox, G.; Panchenko, A.; Janssen, N.; Petzold, A.; Thurn-Albrecht, T.; Borchardt, L.; Rose, M.; Kaskel, S.; Georgi, C.; Lang, H.; Spange, S. Twin Polymerization at Spherical Hard Templates: An Approach to Size-Adjustable Carbon Hollow Spheres with Micro- or Mesoporous Shells. *Angewandte Chemie International Edition* **2013**, *52*, 6088-6091.
- (73) Chen, S.; Huang, X.; Liu, H.; Sun, B.; Yeoh, W.; Li, K.; Zhang, J.; Wang, G. 3D Hyperbranched Hollow Carbon Nanorod Architectures for High-Performance Lithium-Sulfur Batteries. *Advanced Energy Materials* **2014**, *4*, n/a-n/a.
- (74) Chen, Y.; Li, X.; Park, K.-S.; Hong, J.; Song, J.; Zhou, L.; Mai, Y.-W.; Huang, H.; Goodenough, J. B. Sulfur encapsulated in porous hollow CNTs@CNFs for high-performance lithium-sulfur batteries. *Journal of Materials Chemistry A* **2014**, *2*, 10126-10130.
- (75) Zhao, Y.; Wu, W.; Li, J.; Xu, Z.; Guan, L. Encapsulating MWNTs into Hollow Porous Carbon Nanotubes: A Tube-in-Tube Carbon Nanostructure for High-Performance Lithium-Sulfur Batteries. *Advanced Materials* **2014**, *26*, 5113-5118.
- (76) Zhang, C.; Wu, H. B.; Yuan, C.; Guo, Z.; Lou, X. W. Confining Sulfur in Double-Shelled Hollow Carbon Spheres for Lithium-Sulfur Batteries. *Angewandte Chemie International Edition* **2012**, *51*, 9592-9595.
- (77) Liu, X.; Zhu, K.; Tian, J.; Tang, Q.; Shan, Z. Preparation of yolk-shell sulfur/carbon nanocomposite via an organic solvent route for lithium-sulfur batteries. *Journal of Solid State Electrochemistry* **2014**, *18*, 2077-2085.
- (78) Zhou, W.; Yu, Y.; Chen, H.; DiSalvo, F. J.; Abruna, H. D. Yolk-shell structure of polyaniline-coated sulfur for lithium-sulfur batteries. *Journal of the American Chemical Society* **2013**, *135*, 16736-16743.
- (79) Demir-Cakan, R.; Morcrette, M.; Nouar, F.; Davoisne, C.; Devic, T.; Gonbeau, D.; Dominko, R.; Serre, C.; Férey, G.; Tarascon, J.-M. Cathode Composites for Li-S Batteries via the Use of Oxygenated Porous Architectures. *Journal of the American Chemical Society* **2011**, *133*, 16154-16160.

- (80) Wang, Z.; Dou, Z.; Cui, Y.; Yang, Y.; Wang, Z.; Qian, G. Sulfur encapsulated ZIF-8 as cathode material for lithium–sulfur battery with improved cyclability. *Microporous and Mesoporous Materials* **2014**, *185*, 92-96.
- (81) Liao, H.; Ding, H.; Li, B.; Ai, X.; Wang, C. Covalent-organic frameworks: potential host materials for sulfur impregnation in lithium–sulfur batteries. *Journal of Materials Chemistry A* **2014**, *2*, 8854.
- (82) Ding, B.; Shen, L.; Xu, G.; Nie, P.; Zhang, X. Encapsulating sulfur into mesoporous TiO<sub>2</sub> host as a high performance cathode for lithium–sulfur battery. *Electrochimica Acta* **2013**, *107*, 78-84.
- (83) Li, Q.; Zhang, Z.; Zhang, K.; Xu, L.; Fang, J.; Lai, Y.; Li, J. Synthesis and electrochemical performance of TiO<sub>2</sub>–sulfur composite cathode materials for lithium–sulfur batteries. *Journal of Solid State Electrochemistry* **2013**, *17*, 2959-2965.
- (84) Ji, X.; Evers, S.; Black, R.; Nazar, L. F. Stabilizing lithium-sulphur cathodes using polysulphide reservoirs. *Nature communications* **2011**, *2*, 325.
- (85) Zhang, Y.; Bakenov, Z.; Zhao, Y.; Konarov, A.; Doan, T. N. L.; Sun, K. E. K.; Yermukhambetova, A.; Chen, P. Effect of nanosized Mg<sub>0.6</sub>Ni<sub>0.4</sub>O prepared by self-propagating high temperature synthesis on sulfur cathode performance in Li/S batteries. *Powder Technology* **2013**, *235*, 248-255.
- (86) Zhang, Y.; Wu, X.; Feng, H.; Wang, L.; Zhang, A.; Xia, T.; Dong, H. Effect of nanosized Mg<sub>0.8</sub>Cu<sub>0.2</sub>O on electrochemical properties of Li/S rechargeable batteries. *International Journal of Hydrogen Energy* **2009**, *34*, 1556-1559.
- (87) Sun, F.; Wang, J.; Long, D.; Qiao, W.; Ling, L.; Lv, C.; Cai, R. A high-rate lithium–sulfur battery assisted by nitrogen-enriched mesoporous carbons decorated with ultrafine La<sub>2</sub>O<sub>3</sub> nanoparticles. *Journal of Materials Chemistry A* **2013**, *1*, 13283.
- (88) Evers, S.; Yim, T.; Nazar, L. F. Understanding the Nature of Absorption/Adsorption in Nanoporous Polysulfide Sorbents for the Li–S Battery. *The Journal of Physical Chemistry C* **2012**, *116*, 19653-19658.
- (89) Xu, G.; Ding, B.; Nie, P.; Shen, L.; Wang, J.; Zhang, X. Porous nitrogen-doped carbon nanotubes derived from tubular polypyrrole for energy-storage applications. *Chemistry* **2013**, *19*, 12306-12312.
- (90) Ahn, W.; Kim, K.-B.; Jung, K.-N.; Shin, K.-H.; Jin, C.-S. Synthesis and electrochemical properties of a sulfur-multi walled carbon nanotubes composite as a cathode material for lithium sulfur batteries. *Journal of Power Sources* **2012**, *202*, 394-399.
- (91) Wei, W.; Wang, J.; Zhou, L.; Yang, J.; Schumann, B.; NuLi, Y. CNT enhanced sulfur composite cathode material for high rate lithium battery. *Electrochemistry Communications* **2011**, *13*, 399-402.
- (92) Zhu, L.; Zhu, W.; Cheng, X.-B.; Huang, J.-Q.; Peng, H.-J.; Yang, S.-H.; Zhang, Q. Cathode materials based on carbon nanotubes for high-energy-density lithium–sulfur batteries. *Carbon* **2014**, *75*, 161-168.
- (93) Geng, X.; Rao, M.; Li, X.; Li, W. Highly dispersed sulfur in multi-walled carbon nanotubes for lithium/sulfur battery. *Journal of Solid State Electrochemistry* **2012**, *17*, 987-992.
- (94) Deng, Z.-f.; Zhang, Z.-a.; Lu, H.; Lai, Y.-q.; Liu, J.; Li, J.; Liu, Y.-x. Vapor-grown carbon fibers enhanced sulfur-multi walled carbon nanotubes composite cathode for lithium/sulfur batteries. *Transactions of Nonferrous Metals Society of China* **2014**, *24*, 158-163.
- (95) Rao, M.; Song, X.; Cairns, E. J. Nano-carbon/sulfur composite cathode materials with carbon nanofiber as electrical conductor for advanced secondary lithium/sulfur cells. *Journal of Power Sources* **2012**, *205*, 474-478.
- (96) Wang, J.-Z.; Lu, L.; Choucair, M.; Stride, J. A.; Xu, X.; Liu, H.-K. Sulfur-graphene composite for rechargeable lithium batteries. *Journal of Power Sources* **2011**, *196*, 7030-7034.
- (97) Cao, Y.; Li, X.; Aksay, I. A.; Lemmon, J.; Nie, Z.; Yang, Z.; Liu, J. Sandwich-type functionalized graphene sheet-sulfur nanocomposite for rechargeable lithium batteries. *Physical chemistry chemical physics : PCCP* **2011**, *13*, 7660-7665.

- (98) Wang, B.; Wen, Y.; Ye, D.; Yu, H.; Sun, B.; Wang, G.; Hulicova-Jurcakova, D.; Wang, L. Dual protection of sulfur by carbon nanospheres and graphene sheets for lithium-sulfur batteries. *Chemistry* **2014**, *20*, 5224-5230.
- (99) Wang, Y.-X.; Chou, S.-L.; Liu, H.-K.; Dou, S.-X. The electrochemical properties of high-capacity sulfur/reduced graphene oxide with different electrolyte systems. *Journal of Power Sources* **2013**, *244*, 240-245.
- (100) Ji, L.; Rao, M.; Zheng, H.; Zhang, L.; Li, Y.; Duan, W.; Guo, J.; Cairns, E. J.; Zhang, Y. Graphene oxide as a sulfur immobilizer in high performance lithium/sulfur cells. *Journal of the American Chemical Society* **2011**, *133*, 18522-18525.
- (101) Wang, X.; Wang, Z.; Chen, L. Reduced graphene oxide film as a shuttle-inhibiting interlayer in a lithium-sulfur battery. *Journal of Power Sources* **2013**, *242*, 65-69.
- (102) Evers, S.; Nazar, L. F. New Approaches for High Energy Density Lithium-Sulfur Battery Cathodes. *Accounts of Chemical Research* **2012**, *46*, 1135-1143.
- (103) Zhang, S. S.; Tran, D. T. A proof-of-concept lithium/sulfur liquid battery with exceptionally high capacity density. *Journal of Power Sources* **2012**, *211*, 169-172.
- (104) Hagen, M.; Dörfler, S.; Fanz, P.; Berger, T.; Speck, R.; Tübke, J.; Althues, H.; Hoffmann, M. J.; Scherr, C.; Kaskel, S. Development and costs calculation of lithium-sulfur cells with high sulfur load and binder free electrodes. *Journal of Power Sources* **2013**, *224*, 260-268.
- (105) Zheng, J.; Lv, D.; Gu, M.; Wang, C.; Zhang, J. G.; Liu, J.; Xiao, J. How to Obtain Reproducible Results for Lithium Sulfur Batteries? *Journal of the Electrochemical Society* **2013**, *160*, A2288-A2292.
- (106) Zhang, S. Improved Cyclability of Liquid Electrolyte Lithium/Sulfur Batteries by Optimizing Electrolyte/Sulfur Ratio. *Energies* **2012**, *5*, 5190-5197.
- (107) Lacey, M. J.; Jeschull, F.; Edström, K.; Brandell, D. Functional, water-soluble binders for improved capacity and stability of lithium-sulfur batteries. *Journal of Power Sources* **2014**, *264*, 8-14.
- (108) Schneider, H.; Garsuch, A.; Panchenko, A.; Gronwald, O.; Janssen, N.; Novák, P. Influence of different electrode compositions and binder materials on the performance of lithium-sulfur batteries. *Journal of Power Sources* **2012**, *205*, 420-425.
- (109) Urbonaitė, S.; Novák, P. Importance of 'unimportant' experimental parameters in Li-S battery development. *Journal of Power Sources* **2014**, *249*, 497-502.
- (110) Lacey, M. J.; Jeschull, F.; Edström, K.; Brandell, D. Porosity Blocking in Highly Porous Carbon Black by PVDF Binder and Its Implications for the Li-S System. *The Journal of Physical Chemistry C* **2014**.
- (111) He, M.; Yuan, L.-X.; Zhang, W.-X.; Hu, X.-L.; Huang, Y.-H. Enhanced Cyclability for Sulfur Cathode Achieved by a Water-Soluble Binder. *The Journal of Physical Chemistry C* **2011**, *115*, 15703-15709.
- (112) Sun, J.; Huang, Y.; Wang, W.; Yu, Z.; Wang, A.; Yuan, K. Application of gelatin as a binder for the sulfur cathode in lithium-sulfur batteries. *Electrochimica Acta* **2008**, *53*, 7084-7088.
- (113) Wang, H.; Matsui, M.; Takeda, Y.; Yamamoto, O.; Im, D.; Lee, D.; Imanishi, N. Interface Properties between Lithium Metal and a Composite Polymer Electrolyte of PEO18Li(CF3SO2)2N-Tetraethylene Glycol Dimethyl Ether. *Membranes* **2013**, *3*, 298-310.
- (114) Lacey, M. J.; Jeschull, F.; Edstrom, K.; Brandell, D. Why PEO as a binder or polymer coating increases capacity in the Li-S system. *Chemical communications* **2013**, *49*, 8531-8533.
- (115) Xu, G.; Ding, B.; Pan, J.; Nie, P.; Shen, L.; Zhang, X. High performance lithium-sulfur batteries: advances and challenges. *Journal of Materials Chemistry A* **2014**, *2*, 12662.
- (116) Lacey, M. J.; Jeschull, F.; Edström, K.; Brandell, D. Porosity Blocking in Highly Porous Carbon Black by PVDF Binder and Its Implications for the Li-S System. *The Journal of Physical Chemistry C* **2014**, *118*, 25890-25898.
- (117) Wang, Y.; Huang, Y.; Wang, W.; Huang, C.; Yu, Z.; Zhang, H.; Sun, J.; Wang, A.; Yuan, K. Structural change of the porous sulfur cathode using gelatin as a binder during discharge and charge. *Electrochimica Acta* **2009**, *54*, 4062-4066.

- (118) Sun, J.; Huang, Y.; Wang, W.; Yu, Z.; Wang, A.; Yuan, K. Preparation and electrochemical characterization of the porous sulfur cathode using a gelatin binder. *Electrochemistry Communications* **2008**, *10*, 930-933.
- (119) Zhang, Z.; Bao, W.; Lu, H.; Jia, M.; Xie, K.; Lai, Y.; Li, J. Water-Soluble Polyacrylic Acid as a Binder for Sulfur Cathode in Lithium-Sulfur Battery. *ECS Electrochemistry Letters* **2012**, *1*, A34-A37.
- (120) Lacey, M. J.; Jeschull, F.; Edström, K.; Brandell, D. Functional, water-soluble binders for improved capacity and stability of lithium-sulfur batteries. *Journal of Power Sources* **2014**, *264*, 8-14.
- (121) Song, J.; Xu, T.; Gordin, M. L.; Zhu, P.; Lv, D.; Jiang, Y.-B.; Chen, Y.; Duan, Y.; Wang, D. Nitrogen-Doped Mesoporous Carbon Promoted Chemical Adsorption of Sulfur and Fabrication of High-Areal-Capacity Sulfur Cathode with Exceptional Cycling Stability for Lithium-Sulfur Batteries. *Advanced Functional Materials* **2014**, *24*, 1243-1250.
- (122) Gao, J.; Abruña, H. D. Key Parameters Governing the Energy Density of Rechargeable Li/S Batteries. *The Journal of Physical Chemistry Letters* **2014**, *5*, 882-885.
- (123) Hagen, M.; Fanz, P.; Tübke, J. Cell energy density and electrolyte/sulfur ratio in Li-S cells. *Journal of Power Sources* **2014**, *264*, 30-34.
- (124) Elazari, R.; Salitra, G.; Garsuch, A.; Panchenko, A.; Aurbach, D. Sulfur-impregnated activated carbon fiber cloth as a binder-free cathode for rechargeable Li-S batteries. *Adv Mater* **2011**, *23*, 5641-5644.
- (125) Ding, N.; Chien, S. W.; Hor, T. S. A.; Liu, Z.; Zong, Y. Key parameters in design of lithium sulfur batteries. *Journal of Power Sources* **2014**, *269*, 111-116.
- (126) Barchasz, C.; Mesguich, F.; Dijon, J.; Leprêtre, J.-C.; Patoux, S.; Alloin, F. Novel positive electrode architecture for rechargeable lithium/sulfur batteries. *Journal of Power Sources* **2012**, *211*, 19-26.
- (127) Chung, S.-H.; Manthiram, A. Lithium-sulfur batteries with superior cycle stability by employing porous current collectors. *Electrochimica Acta* **2013**, *107*, 569-576.
- (128) Chung, S.-H.; Manthiram, A. Nano-cellular carbon current collectors with stable cyclability for Li-S batteries. *Journal of Materials Chemistry A* **2013**, *1*, 9590.
- (129) Chung, S. H.; Manthiram, A. A hierarchical carbonized paper with controllable thickness as a modulable interlayer system for high performance Li-S batteries. *Chemical communications* **2014**, *50*, 4184-4187.
- (130) Zhou, G.; Wang, D.-W.; Li, F.; Hou, P.-X.; Yin, L.; Liu, C.; Lu, G. Q.; Gentle, I. R.; Cheng, H.-M. A flexible nanostructured sulphur-carbon nanotube cathode with high rate performance for Li-S batteries. *Energy & Environmental Science* **2012**, *5*, 8901.
- (131) Hagen, M.; Dörfler, S.; Althues, H.; Tübke, J.; Hoffmann, M. J.; Kaskel, S.; Pinkwart, K. Lithium-sulphur batteries – binder free carbon nanotubes electrode examined with various electrolytes. *Journal of Power Sources* **2012**, *213*, 239-248.
- (132) Hagen, M.; Feisthammel, G.; Fanz, P.; Grossmann, H. T.; Dorfler, S.; Tubke, J.; Hoffmann, M. J.; Borner, D.; Joos, M.; Althues, H.; Kaskel, S. Sulfur Cathodes with Carbon Current Collector for Li-S cells. *Journal of the Electrochemical Society* **2013**, *160*, A996-A1002.
- (133) Lu, S.; Chen, Y.; Wu, X.; Wang, Z.; Lv, L.; Qin, W.; Jiang, L. Binder-free cathodes based on sulfur-carbon nanofibers composites for lithium-sulfur batteries. *RSC Advances* **2014**, *4*, 18052.
- (134) Fu, Y.; Su, Y. S.; Manthiram, A. Highly reversible lithium/dissolved polysulfide batteries with carbon nanotube electrodes. *Angewandte Chemie* **2013**, *52*, 6930-6935.
- (135) Dorfler, S.; Hagen, M.; Althues, H.; Tubke, J.; Kaskel, S.; Hoffmann, M. J. High capacity vertical aligned carbon nanotube/sulfur composite cathodes for lithium-sulfur batteries. *Chemical communications* **2012**, *48*, 4097-4099.
- (136) Chung, S.-H.; Manthiram, A. Low-cost, porous carbon current collector with high sulfur loading for lithium-sulfur batteries. *Electrochemistry Communications* **2014**, *38*, 91-95.
- (137) Su, Y. S.; Manthiram, A. A new approach to improve cycle performance of rechargeable lithium-sulfur batteries by inserting a free-standing MWCNT interlayer. *Chemical communications* **2012**, *48*, 8817-8819.

- (138) Su, Y. S.; Manthiram, A. Lithium-sulphur batteries with a microporous carbon paper as a bifunctional interlayer. *Nature communications* **2012**, *3*, 1166.
- (139) Xu, R.; Zhang, X.; Yu, C.; Ren, Y.; Li, J. C.; Belharouak, I. Paving the way for using Li(2)S batteries. *ChemSusChem* **2014**, *7*, 2457-2460.
- (140) Fu, Y.; Zu, C.; Manthiram, A. In situ-formed Li<sub>2</sub>S in lithiated graphite electrodes for lithium-sulfur batteries. *Journal of the American Chemical Society* **2013**, *135*, 18044-18047.
- (141) Yang, Y.; Zheng, G.; Misra, S.; Nelson, J.; Toney, M. F.; Cui, Y. High-capacity micrometer-sized Li<sub>2</sub>S particles as cathode materials for advanced rechargeable lithium-ion batteries. *Journal of the American Chemical Society* **2012**, *134*, 15387-15394.
- (142) Wu, F.; Kim, H.; Magasinski, A.; Lee, J. T.; Lin, H.-T.; Yushin, G. Harnessing Steric Separation of Freshly Nucleated Li<sub>2</sub>S Nanoparticles for Bottom-Up Assembly of High-Performance Cathodes for Lithium-Sulfur and Lithium-Ion Batteries. *Advanced Energy Materials* **2014**, *4*, n/a-n/a.
- (143) Meini, S.; Elazari, R.; Rosenman, A.; Garsuch, A.; Aurbach, D. The Use of Redox Mediators for Enhancing Utilization of Li<sub>2</sub>S Cathodes for Advanced Li-S Battery Systems. *The Journal of Physical Chemistry Letters* **2014**, *5*, 915-918.
- (144) Hayashi, A.; Ohtsubo, R.; Ohtomo, T.; Mizuno, F.; Tatsumisago, M. All-solid-state rechargeable lithium batteries with Li<sub>2</sub>S as a positive electrode material. *Journal of Power Sources* **2008**, *183*, 422-426.
- (145) Lin, Z.; Liu, Z.; Dudney, N. J.; Liang, C. Lithium Superionic Sulfide Cathode for All-Solid Lithium-Sulfur Batteries. *ACS Nano* **2013**, *7*, 2829-2833.
- (146) Hiesgen, R.; Sorgel, S.; Costa, R.; Carle, L.; Galm, I.; Canas, N.; Pascucci, B.; Friedrich, K. A. AFM as an analysis tool for high-capacity sulfur cathodes for Li-S batteries. *Beilstein journal of nanotechnology* **2013**, *4*, 611-624.
- (147) Takeuchi, T.; Sakaebe, H.; Kageyama, H.; Senoh, H.; Sakai, T.; Tatsumi, K. Preparation of electrochemically active lithium sulfide-carbon composites using spark-plasma-sintering process. *Journal of Power Sources* **2010**, *195*, 2928-2934.
- (148) Jeong, S.; Bresser, D.; Buchholz, D.; Winter, M.; Passerini, S. Carbon coated lithium sulfide particles for lithium battery cathodes. *Journal of Power Sources* **2013**, *235*, 220-225.
- (149) Nan, C.; Lin, Z.; Liao, H.; Song, M. K.; Li, Y.; Cairns, E. J. Durable carbon-coated Li<sub>2</sub>(S) core-shell spheres for high performance lithium/sulfur cells. *Journal of the American Chemical Society* **2014**, *136*, 4659-4663.
- (150) Nagao, M.; Hayashi, A.; Tatsumisago, M. High-capacity Li<sub>2</sub>S-nanocarbon composite electrode for all-solid-state rechargeable lithium batteries. *Journal of Materials Chemistry* **2012**, *22*, 10015.
- (151) Hassoun, J.; Sun, Y.-K.; Scrosati, B. Rechargeable lithium sulfide electrode for a polymer tin/sulfur lithium-ion battery. *Journal of Power Sources* **2011**, *196*, 343-348.
- (152) Cai, K.; Song, M.-K.; Cairns, E. J.; Zhang, Y. Nanostructured Li<sub>2</sub>S-C Composites as Cathode Material for High-Energy Lithium/Sulfur Batteries. *Nano letters* **2012**, *12*, 6474-6479.
- (153) Fu, Y.; Su, Y.-S.; Manthiram, A. Li<sub>2</sub>S-Carbon Sandwiched Electrodes with Superior Performance for Lithium-Sulfur Batteries. *Advanced Energy Materials* **2014**, *4*, n/a-n/a.
- (154) Yang, Y.; McDowell, M. T.; Jackson, A.; Cha, J. J.; Hong, S. S.; Cui, Y. New nanostructured Li<sub>2</sub>S/silicon rechargeable battery with high specific energy. *Nano letters* **2010**, *10*, 1486-1491.
- (155) Yim, T.; Park, M.-S.; Yu, J.-S.; Kim, K. J.; Im, K. Y.; Kim, J.-H.; Jeong, G.; Jo, Y. N.; Woo, S.-G.; Kang, K. S.; Lee, I.; Kim, Y.-J. Effect of chemical reactivity of polysulfide toward carbonate-based electrolyte on the electrochemical performance of Li-S batteries. *Electrochimica Acta* **2013**, *107*, 454-460.
- (156) Zheng, S.; Han, P.; Han, Z.; Zhang, H.; Tang, Z.; Yang, J. High performance C/S composite cathodes with conventional carbonate-based electrolytes in Li-S battery. *Scientific reports* **2014**, *4*, 4842.

- (157) Barchasz, C.; Leprêtre, J.-C.; Patoux, S.; Alloin, F. Electrochemical properties of ether-based electrolytes for lithium/sulfur rechargeable batteries. *Electrochimica Acta* **2013**, *89*, 737-743.
- (158) Choi, J.-W.; Kim, J.-K.; Cheruvally, G.; Ahn, J.-H.; Ahn, H.-J.; Kim, K.-W. Rechargeable lithium/sulfur battery with suitable mixed liquid electrolytes. *Electrochimica Acta* **2007**, *52*, 2075-2082.
- (159) Barchasz, C.; Lepretre, J. C.; Patoux, S.; Alloin, F. Revisiting TEGDME/DIOX Binary Electrolytes for Lithium/Sulfur Batteries: Importance of Solvation Ability and Additives. *Journal of the Electrochemical Society* **2013**, *160*, A430-A436.
- (160) Kim, H.-S.; Jeong, C.-S. Electrochemical Properties of Binary Electrolytes for Lithium-sulfur Batteries. *Bulletin of the Korean Chemical Society* **2011**, *32*, 3682-3686.
- (161) Kolosnitsyn, V. S.; Karaseva, E. V.; Shakirova, N. V.; Seung, D. Y.; Cho, M. D. Cycling a Sulfur Electrode in Electrolytes Based on Sulfolane and Linear Ethers (Glymes) in a LiCF<sub>3</sub>SO<sub>3</sub> Solution. *Russian Journal of Electrochemistry* **2002**, *38*, 1360-1363.
- (162) Kolosnitsyn, V.; Kuzmina, E.; Karaseva, E. Influence of Lithium Salts on Physicochemical Properties of Lithium Polysulphide Solutions in Sulfolane. *ECS Transactions* **2009**, *19*, 25-30.
- (163) Dominko, R.; Demir-Cakan, R.; Morcrette, M.; Tarascon, J.-M. Analytical detection of soluble polysulphides in a modified Swagelok cell. *Electrochemistry Communications* **2011**, *13*, 117-120.
- (164) Demir-Cakan, R.; Morcrette, M.; Gangulibabu; Guéguen, A.; Dedryvère, R.; Tarascon, J.-M. Li-S batteries: simple approaches for superior performance. *Energy & Environmental Science* **2013**, *6*, 176.
- (165) Yamin, H.; Gorenshstein, A.; Penciner, J.; Sternberg, Y.; Peled, E. Lithium Sulfur Battery: Oxidation/Reduction Mechanisms of Polysulfides in THF Solutions. *Journal of The Electrochemical Society* **1988**, *135*, 1045-1048.
- (166) Choi, J.-W.; Cheruvally, G.; Kim, D.-S.; Ahn, J.-H.; Kim, K.-W.; Ahn, H.-J. Rechargeable lithium/sulfur battery with liquid electrolytes containing toluene as additive. *Journal of Power Sources* **2008**, *183*, 441-445.
- (167) Zhang, S. S.; Tran, D. T. A simple approach for superior performance of lithium/sulphur batteries modified with a gel polymer electrolyte. *Journal of Materials Chemistry A* **2014**, *2*, 7383.
- (168) Zhao, Y.; Zhang, Y.; Gosselink, D.; Doan, T. N.; Sadhu, M.; Cheang, H. J.; Chen, P. Polymer electrolytes for lithium/sulfur batteries. *Membranes* **2012**, *2*, 553-564.
- (169) Sun, X. G.; Wang, X.; Mayes, R. T.; Dai, S. Lithium-sulfur batteries based on nitrogen-doped carbon and an ionic-liquid electrolyte. *ChemSusChem* **2012**, *5*, 2079-2085.
- (170) Wang, J.; Chew, S. Y.; Zhao, Z. W.; Ashraf, S.; Wexler, D.; Chen, J.; Ng, S. H.; Chou, S. L.; Liu, H. K. Sulfur-mesoporous carbon composites in conjunction with a novel ionic liquid electrolyte for lithium rechargeable batteries. *Carbon* **2008**, *46*, 229-235.
- (171) Suo, L.; Hu, Y. S.; Li, H.; Armand, M.; Chen, L. A new class of Solvent-in-Salt electrolyte for high-energy rechargeable metallic lithium batteries. *Nature communications* **2013**, *4*, 1481.
- (172) Patel, M. U.; Dominko, R. Application of in operando UV/Vis spectroscopy in lithium-sulfur batteries. *ChemSusChem* **2014**, *7*, 2167-2175.
- (173) Lu, Y.-C.; He, Q.; Gasteiger, H. A. Probing the Lithium-Sulfur Redox Reactions: A Rotating-Ring Disk Electrode Study. *The Journal of Physical Chemistry C* **2014**, *118*, 5733-5741.
- (174) Kim, H. S.; Jeong, C.-S.; Kim, Y.-T. Shuttle inhibitor effect of lithium perchlorate as an electrolyte salt for lithium-sulfur batteries. *Journal of Applied Electrochemistry* **2011**, *42*, 75-79.
- (175) Dahbi, M.; Ghamouss, F.; Tran-Van, F.; Lemordant, D.; Anouti, M. Comparative study of EC/DMC LiTFSI and LiPF<sub>6</sub> electrolytes for electrochemical storage. *Journal of Power Sources* **2011**, *196*, 9743-9750.
- (176) Myung, S.-T.; Hitoshi, Y.; Sun, Y.-K. Electrochemical behavior and passivation of current collectors in lithium-ion batteries. *Journal of Materials Chemistry* **2011**, *21*, 9891-9911.
- (177) Zhang, S. S. Role of LiNO<sub>3</sub> in rechargeable lithium/sulfur battery. *Electrochimica Acta* **2012**, *70*, 344-348.



- (178) Zhang, S. S. Effect of Discharge Cutoff Voltage on Reversibility of Lithium/Sulfur Batteries with LiNO<sub>3</sub>-Contained Electrolyte. *Journal of the Electrochemical Society* **2012**, *159*, A920-A923.
- (179) Lee, D.-J.; Agostini, M.; Park, J.-W.; Sun, Y.-K.; Hassoun, J.; Scrosati, B. Progress in Lithium–Sulfur Batteries: The Effective Role of a Polysulfide-Added Electrolyte as Buffer to Prevent Cathode Dissolution. *ChemSusChem* **2013**, *6*, 2245-2248.
- (180) Xu, R.; Belharouak, I.; Li, J. C. M.; Zhang, X.; Bloom, I.; Bareño, J. Role of Polysulfides in Self-Healing Lithium-Sulfur Batteries. *Advanced Energy Materials* **2013**, *3*, 833-838.
- (181) Lin, Z.; Liu, Z.; Fu, W.; Dudney, N. J.; Liang, C. Phosphorous Pentasulfide as a Novel Additive for High-Performance Lithium-Sulfur Batteries. *Advanced Functional Materials* **2013**, *23*, 1064-1069.
- (182) Liang, X.; Wen, Z.; Liu, Y.; Wu, M.; Jin, J.; Zhang, H.; Wu, X. Improved cycling performances of lithium sulfur batteries with LiNO<sub>3</sub>-modified electrolyte. *Journal of Power Sources* **2011**, *196*, 9839-9843.
- (183) Xiong, S.; Kai, X.; Hong, X.; Diao, Y. Effect of LiBOB as additive on electrochemical properties of lithium–sulfur batteries. *Ionics* **2012**, *18*, 249-254.
- (184) S. Visco et al., U. p., US 20050175894.
- (185) Kim, H.; Lee, J. T.; Lee, D.-C.; Oschatz, M.; Cho, W. I.; Kaskel, S.; Yushin, G. Enhancing performance of Li–S cells using a Li–Al alloy anode coating. *Electrochemistry Communications* **2013**, *36*, 38-41.
- (186) Thompson, R. S.; Schroeder, D. J.; López, C. M.; Neuhold, S.; Vaughey, J. T. Stabilization of lithium metal anodes using silane-based coatings. *Electrochemistry Communications* **2011**, *13*, 1369-1372.
- (187) Lee, Y. M.; Choi, N.-S.; Park, J. H.; Park, J.-K. Electrochemical performance of lithium/sulfur batteries with protected Li anodes. *Journal of Power Sources* **2003**, *119-121*, 964-972.
- (188) Mikhaylik, Y. *Protection of lithium anodes using dual phase electrolytes* 2011.
- (189) Hagen, M.; Quiroga-González, E.; Dörfler, S.; Fahrner, G.; Tübke, J.; Hoffmann, M. J.; Althues, H.; Speck, R.; Krampfert, M.; Kaskel, S.; Föll, H. Studies on preventing Li dendrite formation in Li–S batteries by using pre-lithiated Si microwire anodes. *Journal of Power Sources* **2014**, *248*, 1058-1066.
- (190) Elazari, R.; Salitra, G.; Gershinshy, G.; Garsuch, A.; Panchenko, A.; Aurbach, D. Rechargeable lithiated silicon–sulfur (SLS) battery prototypes. *Electrochemistry Communications* **2012**, *14*, 21-24.
- (191) Hassoun, J.; Kim, J.; Lee, D.-J.; Jung, H.-G.; Lee, S.-M.; Sun, Y.-K.; Scrosati, B. A contribution to the progress of high energy batteries: A metal-free, lithium-ion, silicon–sulfur battery. *Journal of Power Sources* **2012**, *202*, 308-313.
- (192) Brückner, J.; Thieme, S.; Böttger-Hiller, F.; Bauer, I.; Grossmann, H. T.; Strubel, P.; Althues, H.; Spange, S.; Kaskel, S. Carbon-Based Anodes for Lithium Sulfur Full Cells with High Cycle Stability. *Advanced Functional Materials* **2014**, *24*, 1284-1289.
- (193) Hassoun, J.; Scrosati, B. A high-performance polymer tin sulfur lithium ion battery. *Angewandte Chemie* **2010**, *49*, 2371-2374.
- (194) Barchasz, C.; Molton, F.; Duboc, C.; Lepretre, J. C.; Patoux, S.; Alloin, F. Lithium/sulfur cell discharge mechanism: an original approach for intermediate species identification. *Analytical chemistry* **2012**, *84*, 3973-3980.
- (195) Su, Y. S.; Fu, Y.; Guo, B.; Dai, S.; Manthiram, A. Fast, reversible lithium storage with a sulfur/long-chain-polysulfide redox couple. *Chemistry* **2013**, *19*, 8621-8626.
- (196) Hagen, M.; Schiffels, P.; Hammer, M.; Dorfler, S.; Tubke, J.; Hoffmann, M. J.; Althues, H.; Kaskel, S. In-Situ Raman Investigation of Polysulfide Formation in Li-S Cells. *Journal of the Electrochemical Society* **2013**, *160*, A1205-A1214.
- (197) Su, Y.-S.; Fu, Y.; Cochell, T.; Manthiram, A. A strategic approach to recharging lithium-sulphur batteries for long cycle life. *Nature communications* **2013**, *4*.

- (198) Cañas, N. A.; Wolf, S.; Wagner, N.; Friedrich, K. A. In-situ X-ray diffraction studies of lithium–sulfur batteries. *Journal of Power Sources* **2013**, *226*, 313-319.
- (199) Nelson, J.; Misra, S.; Yang, Y.; Jackson, A.; Liu, Y.; Wang, H.; Dai, H.; Andrews, J. C.; Cui, Y.; Toney, M. F. In Operando X-ray diffraction and transmission X-ray microscopy of lithium sulfur batteries. *Journal of the American Chemical Society* **2012**, *134*, 6337-6343.
- (200) Lowe, M. A.; Gao, J.; Abruña, H. D. Mechanistic insights into operational lithium–sulfur batteries by in situ X-ray diffraction and absorption spectroscopy. *RSC Advances* **2014**, *4*, 18347.
- (201) Lin, C.-N.; Chen, W.-C.; Song, Y.-F.; Wang, C.-C.; Tsai, L.-D.; Wu, N.-L. Understanding dynamics of polysulfide dissolution and re-deposition in working lithium–sulfur battery by in-operando transmission X-ray microscopy. *Journal of Power Sources* **2014**, *263*, 98-103.
- (202) Cuisinier, M.; Cabelguen, P.-E.; Evers, S.; He, G.; Kolbeck, M.; Garsuch, A.; Bolin, T.; Balasubramanian, M.; Nazar, L. F. Sulfur Speciation in Li–S Batteries Determined by Operando X-ray Absorption Spectroscopy. *The Journal of Physical Chemistry Letters* **2013**, *4*, 3227-3232.
- (203) Patel, M. U.; Arcon, I.; Aquilanti, G.; Stievano, L.; Mali, G.; Dominko, R. X-ray absorption near-edge structure and nuclear magnetic resonance study of the lithium-sulfur battery and its components. *Chemphyschem : a European journal of chemical physics and physical chemistry* **2014**, *15*, 894-904.
- (204) Pascal, T. A.; Wujcik, K. H.; Velasco-Velez, J.; Wu, C.; Teran, A. A.; Kapilashrami, M.; Cabana, J.; Guo, J.; Salmeron, M.; Balsara, N.; Prendergast, D. X-ray Absorption Spectra of Dissolved Polysulfides in Lithium–Sulfur Batteries from First-Principles. *The Journal of Physical Chemistry Letters* **2014**, *5*, 1547-1551.
- (205) Ryu, H. S.; Guo, Z.; Ahn, H. J.; Cho, G. B.; Liu, H. Investigation of discharge reaction mechanism of lithium|liquid electrolyte|sulfur battery. *Journal of Power Sources* **2009**, *189*, 1179-1183.
- (206) Ryu, H.-S.; Ahn, H.-J.; Kim, K.-W.; Ahn, J.-H.; Lee, J.-Y. Discharge process of Li/PVdF/S cells at room temperature. *Journal of Power Sources* **2006**, *153*, 360-364.
- (207) Yuan, L.; Qiu, X.; Chen, L.; Zhu, W. New insight into the discharge process of sulfur cathode by electrochemical impedance spectroscopy. *Journal of Power Sources* **2009**, *189*, 127-132.
- (208) Kim, N.-I.; Lee, C.-B.; Seo, J.-M.; Lee, W.-J.; Roh, Y.-B. Correlation between positive-electrode morphology and sulfur utilization in lithium–sulfur battery. *Journal of Power Sources* **2004**, *132*, 209-212.
- (209) Cañas, N. A.; Hirose, K.; Pascucci, B.; Wagner, N.; Friedrich, K. A.; Hiesgen, R. Investigations of lithium–sulfur batteries using electrochemical impedance spectroscopy. *Electrochimica Acta* **2013**, *97*, 42-51.
- (210) Fronczek, D. N.; Bessler, W. G. Insight into lithium–sulfur batteries: Elementary kinetic modeling and impedance simulation. *Journal of Power Sources* **2013**, *244*, 183-188.
- (211) Kim, C. S.; Guerfi, A.; Hovington, P.; Trottier, J.; Gagnon, C.; Barray, F.; Vijn, A.; Armand, M.; Zaghbi, K. Importance of open pore structures with mechanical integrity in designing the cathode electrode for lithium–sulfur batteries. *Journal of Power Sources* **2013**, *241*, 554-559.
- (212) Deng, Z.; Zhang, Z.; Lai, Y.; Liu, J.; Li, J.; Liu, Y. Electrochemical Impedance Spectroscopy Study of a Lithium/Sulfur Battery: Modeling and Analysis of Capacity Fading. *Journal of the Electrochemical Society* **2013**, *160*, A553-A558.
- (213) Kolosnitsyn, V. S.; Kuzmina, E. V.; Karaseva, E. V.; Mochalov, S. E. A study of the electrochemical processes in lithium–sulphur cells by impedance spectroscopy. *Journal of Power Sources* **2011**, *196*, 1478-1482.
- (214) Kolosnitsyn, V. S.; Kuzmina, E. V.; Mochalov, S. E. Determination of lithium sulphur batteries internal resistance by the pulsed method during galvanostatic cycling. *Journal of Power Sources* **2014**, *252*, 28-34.
- (215) Barchasz, C.; Leprêtre, J.-C.; Patoux, S.; Alloin, F. Revisiting TEGDME/DIOX Binary Electrolytes for Lithium/Sulfur Batteries: Importance of Solvation Ability and Additives. *Journal of The Electrochemical Society* **2013**, *160*, A430-A436.

- (216) <http://www.freudenberg.com>.
- (217) Wang, L.; Zhao, Y.; Thomas, M. L.; Byon, H. R. In Situ Synthesis of Bipyramidal Sulfur with 3D Carbon Nanotube Framework for Lithium-Sulfur Batteries. *Advanced Functional Materials* **2014**, *24*, 2248-2252.
- (218) <http://www.showa-denko.com/>.
- (219) Xu, T.; Song, J.; Gordin, M. L.; Sohn, H.; Yu, Z.; Chen, S.; Wang, D. Mesoporous carbon-carbon nanotube-sulfur composite microspheres for high-area-capacity lithium-sulfur battery cathodes. *ACS applied materials & interfaces* **2013**, *5*, 11355-11362.
- (220) Dornbusch, D. A.; Hilton, R.; Gordon, M. J.; Suppes, G. J. Effects of carbon surface area on performance of lithium sulfur battery cathodes. *Journal of Industrial and Engineering Chemistry* **2013**, *19*, 1968-1972.
- (221) Bresser, D.; Passerini, S.; Scrosati, B. Recent progress and remaining challenges in sulfur-based lithium secondary batteries--a review. *Chemical communications* **2013**, *49*, 10545-10562.
- (222) Liu, Z. H.; Maréchal, P.; Jérôme, R. Blends of poly(vinylidene fluoride) with polyamide 6: interfacial adhesion, morphology and mechanical properties. *Polymer* **1998**, *39*, 1779-1785.
- (223) Sadhu, S.; Bhowmick, A. K. Preparation and properties of styrene-butadiene rubber based nanocomposites: The influence of the structural and processing parameters. *Journal of Applied Polymer Science* **2004**, *92*, 698-709.
- (224) Ogihara, N.; Kawauchi, S.; Okuda, C.; Itou, Y.; Takeuchi, Y.; Ukyo, Y. Theoretical and Experimental Analysis of Porous Electrodes for Lithium-Ion Batteries by Electrochemical Impedance Spectroscopy Using a Symmetric Cell. *Journal of the Electrochemical Society* **2012**, *159*, A1034-A1039.
- (225) Song, J. Y.; Lee, H. H.; Wang, Y. Y.; Wan, C. C. Two- and three-electrode impedance spectroscopy of lithium-ion batteries. *Journal of Power Sources* **2002**, *111*, 255-267.
- (226) Schweikert, N.; Hahn, H.; Indris, S. Cycling behaviour of Li/Li<sub>4</sub>Ti<sub>5</sub>O<sub>12</sub> cells studied by electrochemical impedance spectroscopy. *Physical Chemistry Chemical Physics* **2011**, *13*, 6234-6240.
- (227) Peng, L.-l.; Liu, G.-b.; Wang, Y.; Xu, Z.-l.; Liu, H. A comparison of sulfur loading method on the electrochemical performance of porous carbon/sulfur cathode material for lithium-sulfur battery. *Journal of Solid State Electrochemistry* **2013**, *18*, 935-940.
- (228) Levi, M. D.; Aurbach, D. Impedance of a Single Intercalation Particle and of Non-Homogeneous, Multilayered Porous Composite Electrodes for Li-ion Batteries. *The Journal of Physical Chemistry B* **2004**, *108*, 11693-11703.
- (229) Seid, K. A.; Badot, J. C.; Dubrunfaut, O.; Levasseur, S.; Guyomard, D.; Lestriez, B. Multiscale electronic transport mechanism and true conductivities in amorphous carbon-LiFePO<sub>4</sub> nanocomposites. *Journal of Materials Chemistry* **2012**, *22*, 2641-2649.
- (230) Patoux, S.; Daniel, L.; Bourbon, C.; Lignier, H.; Pagano, C.; Le Cras, F.; Jouanneau, S.; Martinet, S. High voltage spinel oxides for Li-ion batteries: From the material research to the application. *Journal of Power Sources* **2009**, *189*, 344-352.
- (231) Fishman, Z.; Hinebaugh, J.; Bazylak, A. Microscale Tomography Investigations of Heterogeneous Porosity Distributions of PEMFC GDLs. *Journal of The Electrochemical Society* **2010**, *157*, B1643-B1650.
- (232) Wei Seh, Z.; Li, W.; Cha, J. J.; Zheng, G.; Yang, Y.; McDowell, M. T.; Hsu, P.-C.; Cui, Y. Sulphur-TiO<sub>2</sub> yolk-shell nanoarchitecture with internal void space for long-cycle lithium-sulphur batteries. *Nature communications* **2013**, *4*, 1331.
- (233) Liu, N.; Hu, L.; McDowell, M. T.; Jackson, A.; Cui, Y. Prelithiated Silicon Nanowires as an Anode for Lithium Ion Batteries. *ACS Nano* **2011**, *5*, 6487-6493.
- (234) Etacheri, V.; Geiger, U.; Gofer, Y.; Roberts, G. A.; Stefan, I. C.; Fasching, R.; Aurbach, D. Exceptional electrochemical performance of Si-nanowires in 1,3-dioxolane solutions: a surface chemical investigation. *Langmuir : the ACS journal of surfaces and colloids* **2012**, *28*, 6175-6184.
- (235) Radvanyi, E.; Porcher, W.; De Vito, E.; Montani, A.; Franger, S.; Jouanneau Si Larbi, S. Failure mechanisms of nano-silicon anodes upon cycling: an electrode porosity evolution model. *Physical chemistry chemical physics : PCCP* **2014**, *16*, 17142-17153.

- (236) Aurbach, D.; Markovsky, B.; Weissman, I.; Levi, E.; Ein-Eli, Y. On the correlation between surface chemistry and performance of graphite negative electrodes for Li ion batteries. *Electrochimica Acta* **1999**, *45*, 67-86.
- (237) Vetter, J.; Novák, P.; Wagner, M. R.; Veit, C.; Möller, K. C.; Besenhard, J. O.; Winter, M.; Wohlfahrt-Mehrens, M.; Vogler, C.; Hammouche, A. Ageing mechanisms in lithium-ion batteries. *Journal of Power Sources* **2005**, *147*, 269-281.
- (238) <http://geology.com/minerals/mohs-hardness-scale.shtml>
- (239) Hassoun, J.; Scrosati, B. Moving to a solid-state configuration: a valid approach to making lithium-sulfur batteries viable for practical applications. *Adv Mater* **2010**, *22*, 5198-5201.
- (240) Yang, Z.; Guo, J.; Das, S. K.; Yu, Y.; Zhou, Z.; Abruna, H. D.; Archer, L. A. In situ synthesis of lithium sulfide-carbon composites as cathode materials for rechargeable lithium batteries. *Journal of Materials Chemistry A* **2013**, *1*, 1433-1440.
- (241) Feng, Z.; Kim, C.; Vijh, A.; Armand, M.; Bevan, K. H.; Zaghbi, K. Unravelling the role of Li<sub>2</sub>S<sub>2</sub> in lithium-sulfur batteries: A first principles study of its energetic and electronic properties. *Journal of Power Sources* **2014**, *272*, 518-521.
- (242) Han, K.; Shen, J.; Hayner, C. M.; Ye, H.; Kung, M. C.; Kung, H. H. Li<sub>2</sub>S-reduced graphene oxide nanocomposites as cathode material for lithium sulfur batteries. *Journal of Power Sources* **2014**, *251*, 331-337.
- (243) Zhang, K.; Wang, L.; Hu, Z.; Cheng, F.; Chen, J. Ultrasmall Li<sub>2</sub>S Nanoparticles Anchored in Graphene Nanosheets for High-Energy Lithium-Ion Batteries. *Scientific reports* **2014**, *4*, 6467.
- (244) Xiong, S.; Xie, K.; Diao, Y.; Hong, X. Oxidation process of polysulfides in charge process for lithium-sulfur batteries. *Ionics* **2012**, *18*, 867-872.
- (245) Akridge, J. Li/S fundamental chemistry and application to high-performance rechargeable batteries. *Solid State Ionics* **2004**, *175*, 243-245.
- (246) Kumaresan, K.; Mikhaylik, Y.; White, R. E. A Mathematical Model for a Lithium-Sulfur Cell. *Journal of The Electrochemical Society* **2008**, *155*, A576.
- (247) Sciamanna, S. F.; Lynn, S. Sulfur solubility in pure and mixed organic solvents. *Industrial & Engineering Chemistry Research* **1988**, *27*, 485-491.
- (248) Schweikert, N.; Hahn, H.; Indris, S. Cycling behaviour of Li/Li<sub>4</sub>Ti<sub>5</sub>O<sub>12</sub> cells studied by electrochemical impedance spectroscopy. *Physical chemistry chemical physics : PCCP* **2011**, *13*, 6234-6240.
- (249) Woo, J. J.; Maroni, V. A.; Liu, G.; Vaughey, J. T.; Gosztola, D. J.; Amine, K.; Zhang, Z. Symmetrical Impedance Study on Inactivation Induced Degradation of Lithium Electrodes for Batteries Beyond Lithium-Ion. *Journal of the Electrochemical Society* **2014**, *161*, A827-A830.
- (250) Ghaznavi, M.; Chen, P. Analysis of a Mathematical Model of Lithium-Sulfur Cells Part III: Electrochemical Reaction Kinetics, Transport Properties and Charging. *Electrochimica Acta* **2014**, *137*, 575-585.
- (251) Mikhaylik, Y. V.; Akridge, J. R. Low Temperature Performance of Li/S Batteries. *Journal of The Electrochemical Society* **2003**, *150*, A306.
- (252) Sadeghi, R.; Taghi Zafarani-Moattar, M. Thermodynamics of aqueous solutions of polyvinylpyrrolidone. *The Journal of Chemical Thermodynamics* **2004**, *36*, 665-670.

# Résumé

## Introduction:

Les batteries lithium-ion (Li-ion) ont révolutionné les domaines de l'électronique portable, caméras, téléphones et ordinateurs portables. Cependant, l'apparition de nouveaux besoins, comme les véhicules électriques ou hybrides, nécessite le développement de système de stockage plus performants, à la fois en termes de densité d'énergie, de durabilité, de flexibilité, mais également en termes de sécurité et de coûts. Les batteries Li-ion, arrivées quasiment à maturité, atteignent progressivement un palier de performances, tandis que leurs coûts de production restent importants. Ainsi, leur intégration à grande échelle, notamment pour des applications véhicules électriques, se heurte à des inconvénients de coûts et de performances.

Ainsi, l'un des enjeux majeurs actuels dans le domaine du stockage de l'énergie consiste à développer des systèmes de stockage plus performants que les batteries Li-ion. Dans ce contexte, de nouvelles chimies à base de lithium sont à l'étude, notamment la chimie lithium/soufre (Li/S). En effet, l'accumulateur est considéré comme une des technologies de batteries post-lithium-ion très prometteuse, qui devrait permettre de multiplier par deux ou trois les densités d'énergie massiques embarquées dans les batteries au lithium, par rapport aux systèmes Li-ion conventionnels, le tout pour un prix bien moindre. Le soufre a en effet l'avantage d'être bas coût (~ 100 US\$ par tonne de soufre), tout en étant également abondant naturellement. En revanche, malgré des progrès importants, et de nombreuses années de recherche, de nombreux challenges concernent toujours cette technologie de batterie, et des verrous sont toujours à lever.

L'objectif de cette thèse a été dédié au développement et à l'étude des technologies d'accumulateur lithium/soufre (Li/S) et lithium-ion/soufre (Li-ion/S), dans le cadre d'une collaboration entre le : LGI (Laboratoire des Générateurs Innovants) du CEA-LITEN (Grenoble) et le LEPMI (Laboratoire d'Electrochimie et Physicochimie des Matériaux et Interfaces; UMR5279, CNRS, Grenoble). Au cours de cette thèse, deux axes majeurs ont été étudiés. Une partie des travaux s'est intéressée à la compréhension du système, et des phénomènes en présence au sein d'un accumulateur Li/S, bien connu pour la complexité de son mécanisme de décharge et les nombreuses limitations qui en découlent. Un autre axe de la thèse a été consacré au développement et à l'optimisation de solutions techniques, afin d'améliorer les performances des systèmes. Ainsi,

le manuscrit est divisé en six chapitres, et un résumé des différents résultats obtenus au cours de cette thèse est présenté.

## Chapitre 1: Etat de l'art

Une batterie Li/S est composée d'une électrode positive de soufre, d'une électrode négative de lithium métal, séparées par un séparateur polymère poreux lui-même imprégné d'électrolyte liquide organique (classiquement des éthers). Un schéma de principe est présenté sur la Figure 1a.

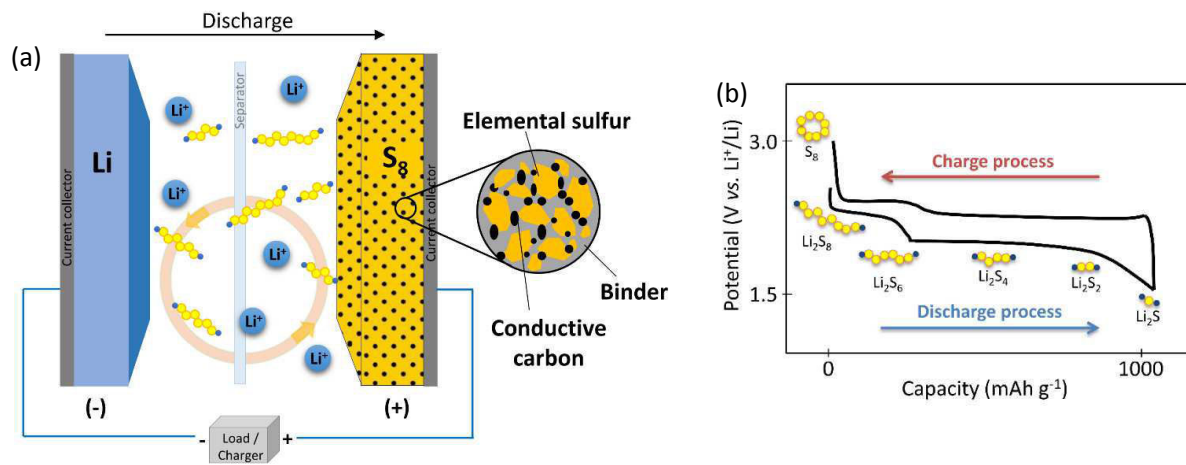
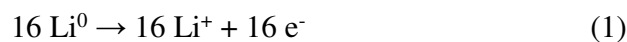
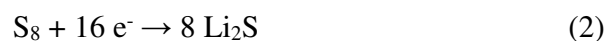


Figure 1. Représentation schématique d'une batterie Li/S (a); Courbe de charge/décharge (b).

Le système Li/S est basé sur la réaction électrochimique du soufre avec le lithium, qui permet la formation du produit de fin de décharge  $\text{Li}_2\text{S}$ . A l'état initial, l'accumulateur Li/S est chargé (pas de source de lithium à l'électrode positive), et le système est tout d'abord déchargé : l'électrode négative de lithium est oxydée, et produit des ions lithium. Ces derniers diffusent au travers de l'électrolyte, tandis que les électrons sont collectés par le circuit extérieur. Ainsi, une réaction d'oxydation a lieu en décharge à l'électrode négative (1):



En parallèle à l'électrode positive, le soufre est réduit, selon l'équation (2):



Au final, la réaction globale de décharge est la suivante (3), et se produit à une tension d'environ 2,15 V:



En raison de la faible masse molaire du soufre, et du fait que deux électrons peuvent être échangés par atome de soufre, la capacité théorique de stockage massique du soufre est très importante, de 1675 mAh g<sub>soufre</sub><sup>-1</sup>.

Une particularité du système Li/S réside dans son mécanisme de charge/décharge atypique et complexe. En effet, la technologie Li/S n'est pas basée sur des réactions d'insertion/désintercalation du lithium dans une structure hôte. De même, la réaction du soufre avec le lithium n'entraîne pas la formation directe du composé Li<sub>2</sub>S. En revanche, la décharge s'accompagne de la formation d'un nombre important d'intermédiaires réactionnels, appelés polysulfures de lithium (Li<sub>2</sub>S<sub>x</sub>, 3 < x ≤ 8), qui sont solubles dans l'électrolyte organique. Les propriétés de ces intermédiaires polysulfures (leurs couleurs en solution, leurs solubilités, etc.) sont très dépendantes de la taille des chaînes soufrées. Ainsi, nous pouvons distinguer plusieurs groupes de polysulfures de lithium :

- (i) les polysulfures à chaînes longues, *i.e.* Li<sub>2</sub>S<sub>8</sub>, Li<sub>2</sub>S<sub>6</sub>;
- (ii) les polysulfures à chaînes intermédiaires, *i.e.* Li<sub>2</sub>S<sub>4</sub>;
- (iii) les polysulfures à chaînes courtes, *i.e.* Li<sub>2</sub>S<sub>3</sub>, Li<sub>2</sub>S<sub>2</sub> and Li<sub>2</sub>S.

Plus la taille de la chaîne soufrée est courte, moins le polysulfure de lithium sera soluble dans l'électrolyte. Ainsi, le produit de fin de décharge Li<sub>2</sub>S est quant à lui parfaitement insoluble dans l'électrolyte.

Lors de la décharge, la molécule de soufre S<sub>8</sub> cyclique est ouverte par réduction du soufre, et les premiers polysulfures Li<sub>2</sub>S<sub>8</sub> sont formés. Au cours de la décharge, la longueur des chaînes de polysulfures est progressivement réduite lorsque la réduction du soufre se poursuit en solution. En fin de décharge, le composé solide Li<sub>2</sub>S est formé. Cette réaction de décharge se caractérise par deux quasi-plateaux de potentiel : à 2,4 V et 2,1 V (Figure 1b). De manière simplifiée, le plateau à haute tension est attribué à la réduction du soufre et à la formation des polysulfures à chaînes longues. La plage de potentiel intermédiaire (2,4 – 2,1 V) correspond à la période pendant laquelle la réaction électrochimique a lieu en solution, et tous les polysulfures de lithium sont dissous dans

l'électrolyte. Enfin, le plateau à plus basse tension (2,1 V) est attribué à la formation des polysulfures à chaînes courtes, et à la formation des produits de fin de décharge solide  $\text{Li}_2\text{S}_2/\text{Li}_2\text{S}$ . Au cours de la recharge, les processus électrochimiques inverses se produisent, au travers de l'observation de quasi-plateaux. Dans un premier temps, l'oxydation des polysulfures à chaînes courts en chaînes plus longues a lieu (formation de  $\text{Li}_2\text{S}_3$ ,  $\text{Li}_2\text{S}_4$ ,  $\text{Li}_2\text{S}_6$ ,  $\text{Li}_2\text{S}_8$ ). Dans un second temps, le soufre élémentaire est de nouveau formé à l'électrode positive et précipite à sa surface. Il convient néanmoins de noter que ce mécanisme, tel que décrit, est une vision simplifiée du système, qui est en réalité plus compliqué.

Comme mentionné préalablement, le système présente un certain nombre de limitations, qui explique pourquoi les performances obtenues en pratique sont toujours bien en deçà des performances potentiellement accessibles. Les problématiques actuelles de l'accumulateur Li/S peuvent être reliées aux différents composants: (1) à l'électrode positive, en raison de la forte isolation électrique du soufre, de sa solubilité partielle dans l'électrolyte entraînant de l'autodécharge, des changements importants de la morphologie de l'électrode lors de la décharge; (2) à l'électrolyte, en raison de la solubilité des produits intermédiaires de décharge, qui entraînent un mécanisme de navette redox et réduisent l'efficacité coulombique du système; et (3) à l'électrode négative de lithium métal, bien connue pour sa possible formation de dendrites et sa réactivité importante.

La littérature traitant de l'accumulateur Li/S est très riche, et le nombre de publication à ce sujet est en constante augmentation. Ainsi, ce résumé ne traite pas de l'état de l'art de la technologie Li/S. Le prochain chapitre est dédié aux résultats obtenus sur l'optimisation de l'électrode positive de soufre.

## **Chapitre 2: Electrode positive de soufre sur collecteur de courant aluminium – étude et détermination des paramètres importants**

Dans ce chapitre, un procédé simple de préparation des électrodes de soufre sur feuillard aluminium a été employé, dans le but de comprendre le système, d'en déterminer les paramètres importants afin d'optimiser les performances des électrodes, tout en conservant des méthodes de préparation simples et facilement transférables à plus grande échelle. En particulier, nous nous



sommes intéressés à la corrélation entre la morphologie des électrodes, leurs propriétés électriques (étudiées par spectroscopie d'impédance électrochimique) ainsi que leurs propriétés électrochimiques. Nous avons pu démontrer comment les additifs d'électrode, à la fois le liant polymère et l'additif carboné, affectaient les performances électrochimiques et les propriétés de l'électrode.

Les électrodes ont été préparées par un procédé simple (illustré sur la Figure 2a), mettant en œuvre des matériaux commerciaux bas coût, avec l'objectif de préparer des électrodes présentant des taux de chargement supérieurs à  $2 \text{ mg}_{\text{soufre}} \text{ cm}^{-2}$  (ou  $\geq 3,35 \text{ mAh cm}^{-2}$ ) et dont la méthode de préparation serait facilement transférable à plus grande échelle. Une composition 'référence' d'électrode positive a été fixée : 80/10/10 en pourcentage massique (m%) de  $\text{S}_8$ /carbone/liant. L'électrolyte liquide sélectionné était composé de LiTFSI 1M +  $\text{LiNO}_3$  0,1M dissous dans un mélange de TEGDME/DIOX 1/1 en volume, et cette composition a été conservée pour tous les tests présentés par la suite. Toutes les performances électrochimiques ont été réalisées en configuration piles boutons (Figure 2b), dans laquelle l'électrode négative de lithium métal était employée. Dans le cas des mesures par spectroscopie d'impédance électrochimique, des piles boutons symétriques ont également été préparées à partir d'électrodes identiques, *i.e.* S-S et Li-Li.

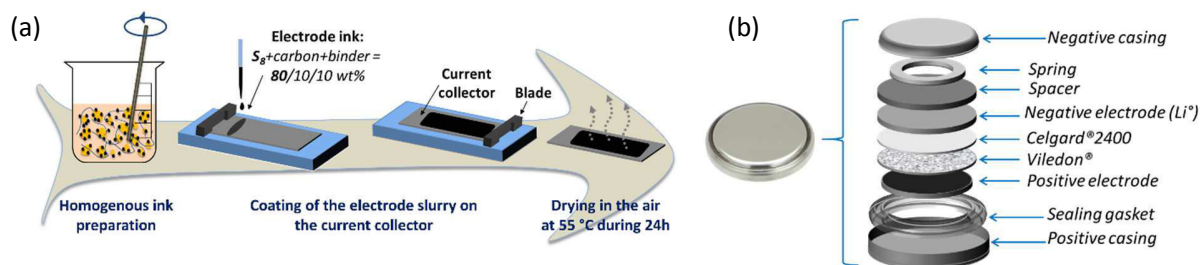


Figure 2. Représentation schématique de la préparation (a) d'une électrode de soufre et (b) d'une pile bouton.

Dans un premier temps, deux additifs conducteurs carbonés ont été évalués dans la composition d'électrode positive, SuperP<sup>®</sup> and Ketjenblack<sup>®</sup>, présentant tous deux une forme sphérique, une taille de particule respective de 40 et 30 nm, mais en revanche une surface spécifique développée très différente (respectivement de 60 et 800  $\text{m}^2 \text{ g}^{-1}$ ). Des performances électrochimiques très similaires ont été obtenues pour les deux formulations d'électrodes. Ces résultats ont permis de démontrer que, malgré la surface développée du carbone Ketjenblack<sup>®</sup>, aucun effet bénéfique n'est

obtenu en pratique vis-à-vis de la capacité de décharge, ce qui peut être expliqué par l'absence d'accessibilité des polysulfures de lithium vis-à-vis de cette surface spécifique.

Dans une seconde étape, l'effet de la morphologie de l'additif carboné a également été étudié. Dans cette optique, des fibres de carbone VGCF<sup>®</sup> (Vapor Growth Carbon Fibers; surface spécifique de 13 m<sup>2</sup> g<sup>-1</sup>) ont été employées, et les formulations d'électrodes suivantes ont été évaluées : 10 m% de SuperP<sup>®</sup>, 10 m% de VGCF<sup>®</sup> ou 5+5 m% de SuperP<sup>®</sup> + VGCF<sup>®</sup>, tandis que les pourcentages de soufre et de liant polymère PVdF étaient maintenus constants respectivement à 80 m% et 10 m%. Les performances en cyclage de ces trois électrodes se sont avérées très similaires, et aucune amélioration n'a été apportée par l'utilisation d'additif de type fibres VGCF<sup>®</sup>. Une explication a été proposée, relativement à la méthode relativement simple de préparation des électrodes de soufre, ainsi qu'aux taux de chargement en soufre relativement importants (~ 3,5 mAh cm<sup>-2</sup>).

Dans un troisième temps, la comparaison de deux liants de nature différente a été réalisée, et les propriétés de cyclabilité, électriques et d'adhésion ont ensuite été évaluées. Pour cela, le PVdF a été comparé au mélange de polymères CMC/NBR (Carboxyméthylcellulose, Nitrile Butadiène Rubber), déjà reporté dans la littérature pour une utilisation en électrode positive de soufre. De plus, le mélange CMC/NBR est également connu pour ses bonnes propriétés de flexibilité, de forces de liaison élevées et de résistance thermique. Enfin, il est également mis en œuvre en solution aqueuse, ce qui est potentiellement très intéressant du point de vue environnemental. Au contraire, le liant PVdF est quant à lui mis en œuvre dans la NMP, un solvant organique toxique. Les électrodes ont été cyclées à C/20 et C/5, tandis que les performances électrochimiques se sont avérées très similaires, à la fois en tenue en cyclage et capacité de décharge, même si légèrement supérieures dans le cas du mélange CMC/NBR. Une étude post-mortem des électrodes cyclées a permis de mettre en évidence une meilleure adhésion des électrodes de CMC sur aluminium, par rapport à l'adhésion des électrodes à base de PVdF qui se décollaient facilement du collecteur.

Un autre paramètre a été étudié, *i.e.* l'effet du taux de chargement en soufre des électrodes, notamment sur la cyclabilité du système Li/S. Pour cela, différentes électrodes ont été préparées avec des taux de chargement en soufre croissants : 2,77 → 3,35 → 4,03 → 4,71 → 5,69 mg<sub>Soufre</sub> cm<sup>-2</sup> (liant CMC/NBR). La Figure 3 présente les résultats de cyclage obtenus à C/20. A régime lent, il a pu être constaté que le profil de potentiel lors de la décharge était peu affecté par le taux

de chargement de l'électrode en soufre (faible augmentation de la surtension des cellules avec l'augmentation du taux de chargement). De manière surprenante, il a pu être mis en évidence le fait que les électrodes fortement chargées en soufre permettaient même de restituer une capacité de décharge plus stable en cyclage. Ce résultat non intuitif peut être expliqué par un rapport soufre/électrolyte qui diffère en fonction du taux de chargement de l'électrode de soufre : lorsque ce taux augmente, le rapport soufre/électrolyte augmente, de même que l'efficacité coulombique du système. Ainsi, le mécanisme de navette redox est diminué, la dissolution des polysulfures de lithium dans l'électrolyte limitée, ce qui peut expliquer l'amélioration de la rétention de capacité en cyclage.

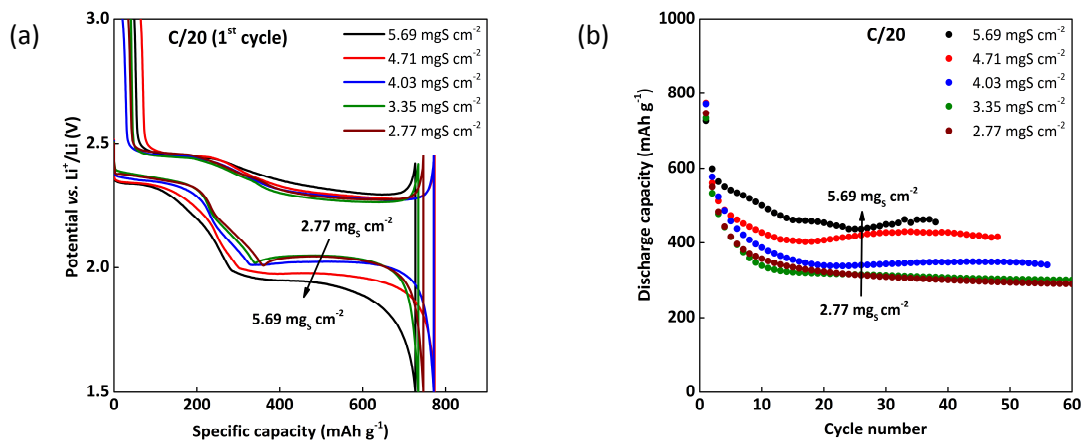


Figure 3. Performances électrochimiques d'électrodes de soufre, composée de S/SuperP<sup>®</sup>/CMC et présentant différents taux de chargement: (a) profils de cyclage initiaux à C/20, (b) et rétention de capacité en cyclage.

A régime plus rapide (C/5), le plateau de décharge à bas potentiel est davantage affecté par le taux de chargement des électrodes en soufre, ce qui se caractérise par une augmentation de la surtension des cellules. Ce phénomène peut s'expliquer par l'augmentation de la viscosité de l'électrolyte, en raison de la quantité d'espèces polysulfures plus importante pour les électrodes à fort taux de chargement, et la cinétique de réaction relativement lente sur le second plateau de décharge liée à la formation d'espèces peu/pas solubles. Les électrodes à base de PVdF ont démontré un comportement similaire, avec de meilleures performances en termes de rétention de capacité pour les électrodes les plus chargées en soufre. En traçant l'évolution de la capacité de décharge restituée, en fonction du taux de chargement en soufre, un point optimum a pu être mis en évidence.

Ainsi, la préparation des électrodes avec des taux de chargement en soufre supérieurs à l'optimum ne semble pas avoir d'intérêt, puisque l'utilisation du soufre au sein de ces électrodes ne sera pas optimale (entre 4 et 6  $\text{mg}_{\text{Soufre}} \text{cm}^{-2}$  selon le liant), et la capacité obtenue en pratique ne sera pas améliorée.

Nous avons également étudié les propriétés électriques des électrodes de soufre par spectroscopie d'impédance électrochimique. Pour ce faire, et dans le but de supprimer la contribution de l'électrode négative de lithium métal, des cellules symétriques ont été préparées, à partir de deux électrodes de soufre identiques. Un exemple de diagramme de Nyquist est présenté sur la Figure 4, sur laquelle quatre régions peuvent être distinguées.

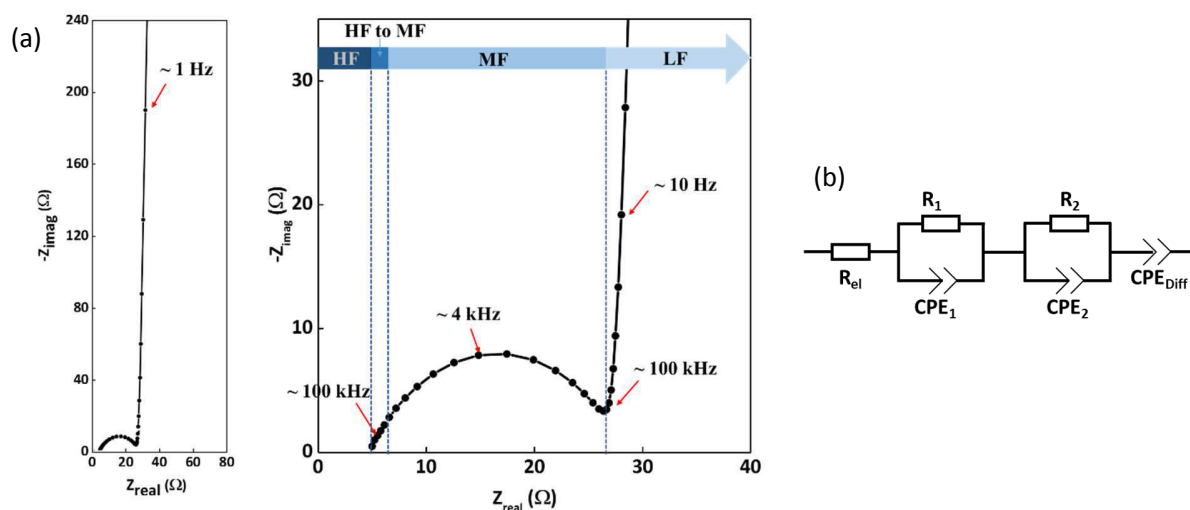


Figure 4. Diagramme de Nyquist d'une cellule S-S symétrique, composée de deux électrodes de soufre (S/SuperP<sup>®</sup>/PVdF), présentant un taux de chargement en soufre  $\sim 7,0 \text{ mg}_{\text{soufre}} \text{cm}^{-2}$  pour une épaisseur d'électrode d'environ  $130 \mu\text{m}$  (a). Schéma du circuit équivalent correspondant (b).

A haute fréquence, les mesures d'impédance permettent de mettre en évidence l'effet de la résistance d'électrolyte, du contenant et du support de la pile bouton, ainsi que des câbles de connexion, et la réponse peut être modélisée par une résistance ohmique (R). La réponse à basse fréquence (LF) d'une électrode poreuse peut être décrite par un module de Warburg restreinte, associé à une diffusion semi-infinie restreinte, et qui peut être expliqué par le caractère bloquant de l'électrode de soufre à l'état initial. L'interprétation de la réponse à moyenne fréquence (MF) et du demi-cercle correspondant est plus controversée. Pour expliquer ce phénomène, des

expériences complémentaires ont été réalisées, et il a été démontré que la résistance du demi-cercle était proportionnellement à l'épaisseur de l'électrode de soufre, comme présenté sur la Figure 5.

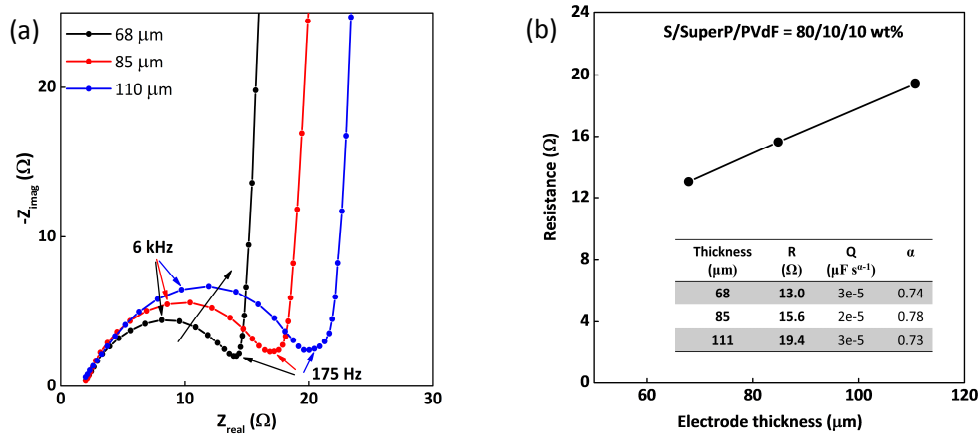


Figure 5. Evolution du diagramme de Nyquist pour trois cellules symétriques S-S, préparées à partir d'électrodes de soufre (S/SuperP<sup>®</sup>/PVdF) d'épaisseurs différentes (a). Paramètres du demi-cercle associé à la réponse à MF, de même que la valeur de résistance tracée en fonction de l'épaisseur de l'électrode (b).

Cette évolution indique clairement que la réponse à moyenne fréquence est associée aux propriétés intrinsèques de l'électrode, et non aux propriétés de l'interface électrode/collecteur de courant. Dans le but de comprendre davantage l'origine de ce demi-cercle à moyenne fréquence, les particules de soufre ont été remplacées par des particules de Al<sub>2</sub>O<sub>3</sub>, également isolantes électroniques (comme le soufre) et présentant la même taille (~ 20 μm) ainsi que la même morphologie, mais ne pouvant pas donner lieu à un transfert de charge (à la différence du soufre). L'impédance des électrodes Al<sub>2</sub>O<sub>3</sub>/SuperP<sup>®</sup>/PVdF a été mesurée, pour trois épaisseurs différentes. Le même type d'évolution que précédemment (Figure 5) a été observé, ce qui a permis d'affirmer que le demi-cercle, visible à MF, n'était pas associé au transfert de charge à l'électrode positive. Il semble que la réponse soit plutôt gouvernée par la morphologie et le réseau conducteur électronique de l'électrode, qui sont dictés par le rapport carbone/liant, le procédé d'élaboration et la nature du conducteur et du liant utilisés.

Il a pu être mis en évidence le fait que la réponse à moyenne fréquence était liée à la non homogénéité de l'encre servant à la préparation de l'électrode. Cette résistance a pu être diminuée de manière notable grâce à l'utilisation d'une méthode de mélange plus énergétique de l'encre avant enduction en utilisant un Dispermat<sup>®</sup>, en comparaison d'un simple mélange manuelle réalisé classiquement à la spatule (Figure 6a). Les électrodes réalisées à base de CMC et via l'utilisation

d'une étape de Dispermat<sup>®</sup>, présentent également une résistance relativement faible à moyenne fréquence. Ces résultats indiquent que la nature du liant a peu d'effet sur la réponse en impédance à moyenne fréquence, tandis que l'effet de la méthode de préparation est davantage prépondérant pour l'homogénéité de l'électrode.

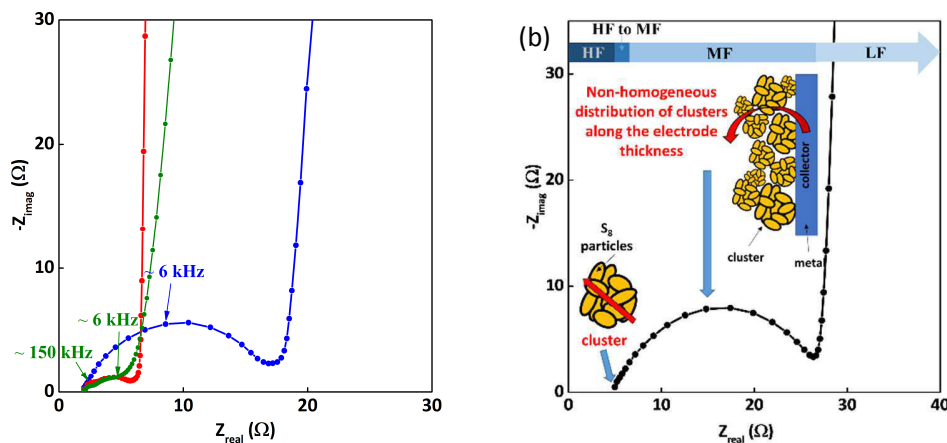


Figure 6. Diagramme de Nyquist d'une cellule symétrique S-S (a), préparée à partir d'électrodes de soufre à base de PVdF, à partir d'une encre mélangée manuellement (bleu) ou avec Dispermat<sup>®</sup> (rouge). Pour comparaison, une électrode à base de CMC, préparée avec Dispermat<sup>®</sup>, est également représentée (vert). Représentation schématique des phénomènes se produisant au sein de l'électrode (b).

Au final, la réponse à moyenne fréquence a été attribuée à la réponse intrinsèque de l'électrode, alors que la résistance élevée a été expliquée par une faible homogénéité de l'électrode et de sa morphologie, et donc à un réseau percolant ionique et électronique moins efficace et responsable d'une polarisation supplémentaire du système. Une représentation schématique des phénomènes et des limitations est visible sur la Figure 6b.

### **Chapitre 3: Collecteur de courant carboné, poreux et 3D: une piste prometteuse pour l'optimisation de l'électrode de soufre**

Une piste potentielle pour l'augmentation du taux de chargement des électrode de soufre, ainsi que pour l'amélioration des propriétés mécaniques de ces dernières, sans pour autant sacrifier les capacités pratiques restituées, consiste à utiliser un collecteur de courant 3D et poreux. Dans ce

chapitre, nous nous sommes intéressés à un feutre de carbone non-tissé, qui a été employé en tant que collecteur de courant pour l'électrode de soufre.

Le non-tissé de fibres de carbone utilisé dans ces travaux est un matériau classiquement employé dans les piles à combustible en tant que 'gas diffusion layer' (GDL). Il s'agit d'un produit commercial de chez Freudenberg (H2315), qui est très bon conducteur électronique, composé de fibres de carbone d'un diamètre d'environ 10  $\mu\text{m}$ . Ce matériau présente une tortuosité importante, comme visible sur les images de microscopie électronique à balayage (MEB, Figure 7a). Le feutre est flexible, d'une épaisseur d'environ 210  $\mu\text{m}$ , avec une porosité d'environ 80 % pour une masse d'environ 9,5  $\text{mg cm}^{-2}$ . Sa surface spécifique (mesurée par BET) s'est avérée délicate à déterminer, puisqu'en limite de détection de l'appareil ( $\sim 0,05 \text{ cm}^2 \text{ g}^{-1}$ ). Lors de la préparation de l'électrode, l'encre a simplement été enduite sur une feuille de feutre de non-tissé, la large porosité du substrat permettant à l'encre de pénétrer à l'intérieur des pores et de l'épaisseur du non-tissé (Figure 7b). Ces électrodes, nommées 'S-on-NwC', ont permis d'atteindre des taux de chargement en soufre de 6  $\text{mg}_{\text{soufre}} \text{ cm}^{-2}$  (voire davantage).

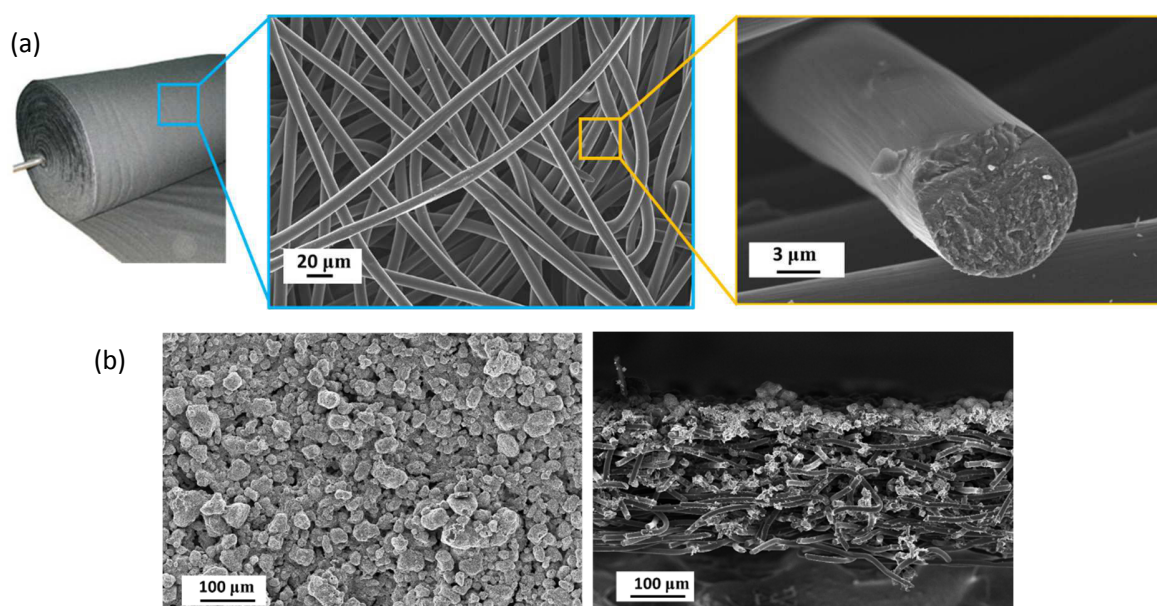


Figure 7. Images MEB du feutre de non-tissé de fibres de carbone (a) et d'une électrode 'S-on-NwC': vue de dessus et vue en coupe (b).

Les performances électrochimiques obtenues de manière typique pour ces électrodes 'S-on-NwC', en combinaison d'une électrode négative de lithium métal, sont présentées sur la Figure 8.

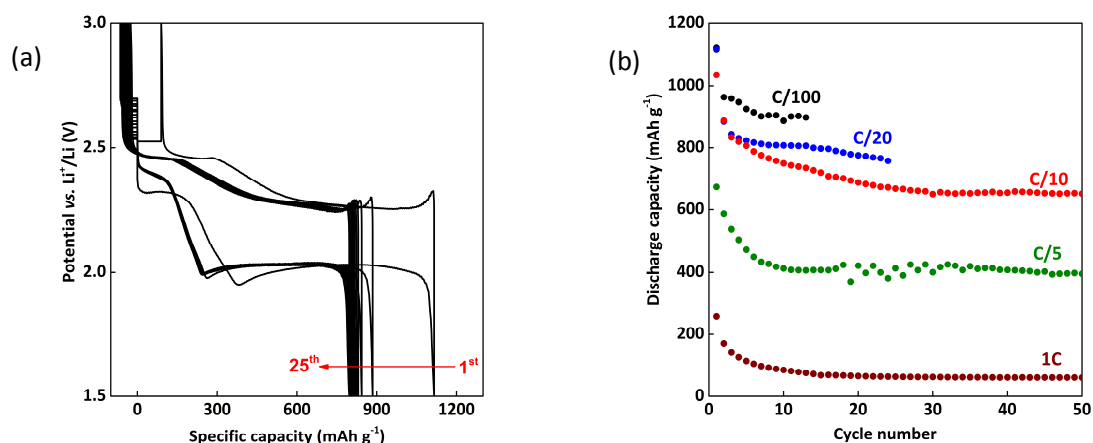


Figure 8. Cyclage galvanostatique d'une électrode 'S-on-NwC' (taux de chargement en soufre de  $4,42 \text{ mg cm}^{-2}$ ) cyclée à C/20 vs. Li : profil de charge/décharge (a), et rétention de capacité à différents régimes (b).

Il a pu être démontré qu'à faible et moyen régime de cyclage (jusqu'à C/10), une capacité de décharge relativement stable, d'environ  $700 - 800 \text{ mAh g}^{-1}$  pouvait être obtenue, ce qui est plus important que les performances rapportées sur les électrodes enduites sur aluminium. En revanche, les performances à plus haut régime sont diminuées, puisque des électrodes d'une telle épaisseur ne sont logiquement pas adaptées pour des applications de puissance.

Dans le but de comparer de manière fidèle, les performances électrochimiques obtenues avec les deux types de collecteurs de courant, aluminium et non-tissé de fibres de carbone ('S-on-Al' vs. 'S-on-NwC'), des électrodes présentant des mêmes taux de chargement en soufre ont été préparées, et les résultats de cyclage sont présentés sur la Figure 9. Ainsi, de manière évidente, l'utilisation de feutre de carbone permet un gain en capacité d'environ  $300 \text{ mAh g}^{-1}$  par rapport à une électrode sur aluminium.



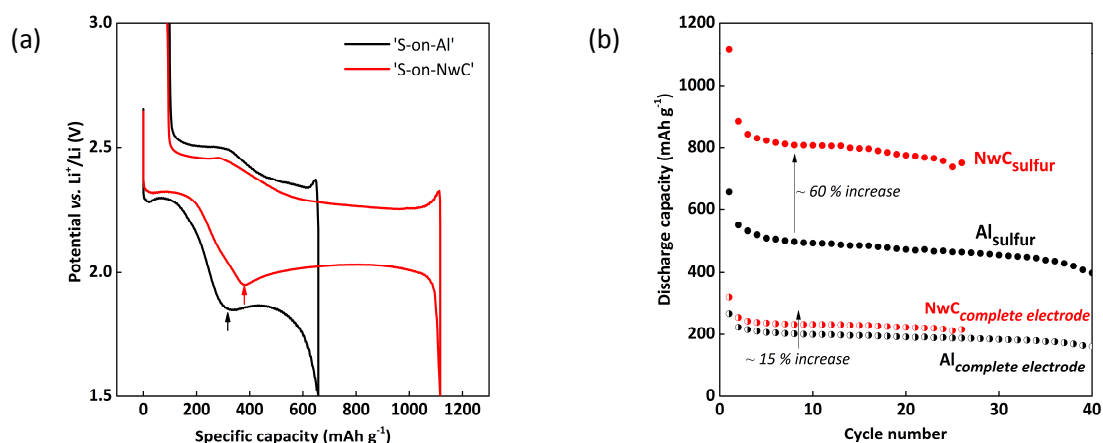


Figure 9. Résultats de cyclage obtenus pour des électrodes de soufre, de compositions identiques, et présentant un taux de chargement en soufre d'environ  $4,4 \text{ mg cm}^{-2}$ , mais enduites sur deux collecteurs de courant différents : sur aluminium (noir) et sur feutre de carbone (rouge). Courbe de charge/décharge du premier cycle à  $C/20$  (a) et rétention de capacité (b).

La Figure 10 présente les images MEB d'une électrode 'S-on-NwC' en fin de décharge, sur laquelle la formation de produits solides est attendue. Il peut être noté que toute la surface offerte par les fibres de carbone est couverte pas un dépôt dense. Ainsi, il peut être conclu que les fibres de carbone participent au processus de décharge, en offrant une surface développée conductrice pour le dépôt de produits solides et isolants. En revanche, la surface développée par les fibres est relativement faible ( $0,05 \text{ cm}^2 \text{ g}^{-1}$ ), et il est peu probable que cette surface permette d'expliquer l'amélioration significative des performances en décharge, en comparaison des électrodes sur aluminium.

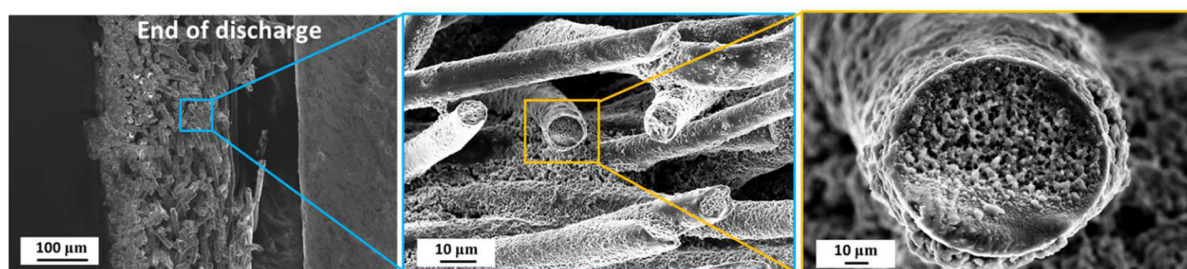


Figure 10. Images MEB d'une électrode 'S-on-NwC' après une première décharge: vue en coupe, et grossissement sur une fibre de carbone unitaire.

Le cyclage des électrodes sans séparateur Viledon<sup>®</sup> (réservoir d'électrolyte poreux et épais) a permis de discriminer davantage les électrodes sur aluminium et sur feutre de non-tissé. Tandis

que les électrodes préparées sur aluminium ne restituent aucune capacité sans Viledon<sup>®</sup>, en raison de la faible porosité de l'électrode et du faible volume d'électrolyte disponible, l'électrode sur collecteur de carbone permet au contraire de contenir une réserve suffisante d'électrolyte liquide, et le cyclage est réalisé de manière quasi-inchangée. Ces résultats démontrent que la structure poreuse du feutre de carbone permet de contenir une réserve d'électrolyte importante au contact des espèces électrochimiques actives, permettant ainsi un bon contact entre le soufre et l'électrolyte, et retardant la précipitation des espèces formées en décharge.

Pour aller plus loin dans la compréhension des phénomènes de polarisation, des mesures d'impédance électrochimique ont été réalisées sur des cellules symétriques (Figure 11). En présence du feutre de carbone, la réponse en impédance du système est largement diminuée par rapport à une électrode sur aluminium, ce qui indique une résistivité plus faible de l'électrode.

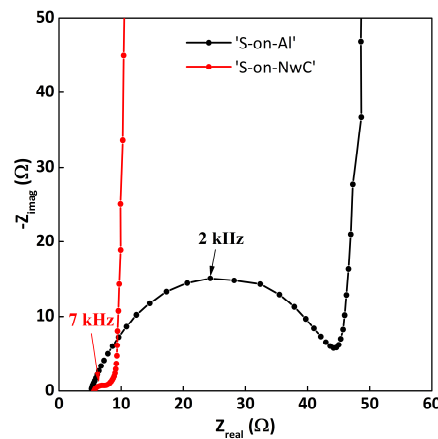


Figure 11. Mesures d'impédance et diagramme de Nyquist correspondant, obtenu pour des cellules symétriques à partir de deux types d'électrodes: 'S-on-Al' (noir) et 'S-on-NwC' (rouge), ces deux électrodes ayant été préparées à partir de la même encre, et avec un taux de chargement en soufre identique.

Les raisons de la diminution conséquente du demi-cercle à moyenne fréquence sont expliquées par la meilleure connectivité électronique apportée par le feutre de carbone. En effet, les agrégats de soufre et de carbone se retrouvent connectés au réseau de fibres de carbone, ce qui permet de réduire considérablement la résistance intrinsèque de l'électrode. Ainsi, l'inhomogénéité de l'électrode n'est plus un facteur prépondérant en ce qui concerne la réponse de l'électrode en impédance, et l'apport du réseau 3D du feutre de carbone permet un chemin de percolation électronique efficace.

En conséquence, l'effet bénéfique du feutre de carbone, déjà démontré en ce qui concerne les électrodes fortement chargées en soufre, permet également de limiter la polarisation des électrodes grâce au réseau conducteur 3D du feutre. Une représentation schématique des bénéfices apportés par le feutre de carbone, en comparaison de l'aluminium, est présentée sur la Figure 12.

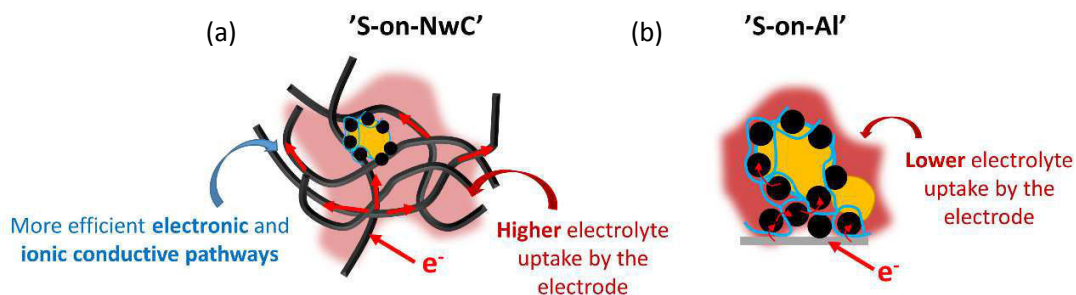


Figure 12. Représentation schématique des bénéfices du feutre de carbone poreux et 3D (a), en comparaison du feuillard d'aluminium 2D (b).

## **Chapter 4: Li-ion/S système - un système sans lithium-métal**

Le problème de croissance dendritique du lithium métal lors du fonctionnement du système (Li/S) est une motivation forte pour s'orienter vers le développement de système Li-ion/S utilisant à l'électrode négative, du graphite ou du silicium. Cependant, afin d'éviter une pré-lithiation de l'électrode négative, une positive lithiée doit être développée, de ce fait  $\text{Li}_2\text{S}$  a été utilisé comme matériau actif en place du soufre. Ce matériau offre une capacité de  $1166 \text{ mAh g}^{-1}$ , et permet de réaliser un accumulateur à l'état déchargé évitant le phénomène d'autodécharge lors du stockage de l'accumulateur à l'état initial. Cependant, ce matériau présente certains inconvénients, comme de très faibles conductivités ionique et électronique, ce qui requière, pour une utilisation optimale, d'assurer un contact intime entre les particules de  $\text{Li}_2\text{S}$  et le carbone conducteur électronique. De plus, il est très peu soluble dans les solvants organiques, ce qui limite sa cinétique d'oxydation et est sensible à l'humidité, d'où une manipulation délicate en boîte à gants. Dans ce chapitre, parallèlement au développement d'un système à positive  $\text{Li}_2\text{S}$ , nous nous sommes intéressés à la compréhension des phénomènes régissant les réactions électrochimiques.

Les électrodes de  $\text{Li}_2\text{S}$  ont été préparées en reprenant le protocole développé pour les électrodes de soufre, avec les différentes étapes de préparation réalisées en boîte à gants. La composition de l'électrode utilisée est la suivante : 70/20/10 wt% ( $\text{Li}_2\text{S}$ /SuperP®/PVdF). La tenue en cyclage du

système Li/Li<sub>2</sub>S est similaire à ce qui a été obtenue pour les cellules Li/S, *i.e.* une diminution importante de la capacité au cours du cyclage, suivie d'une stabilisation. De plus, la valeur de capacité déterminée en se reportant à la quantité de soufre est identique à ce qui est obtenue pour les cellules 'S-on-Al' (capacité stable d'environ 350 – 400 mAh g<sup>-1</sup>). La différence notable entre les deux systèmes réside dans leur première charge (Figure 13).

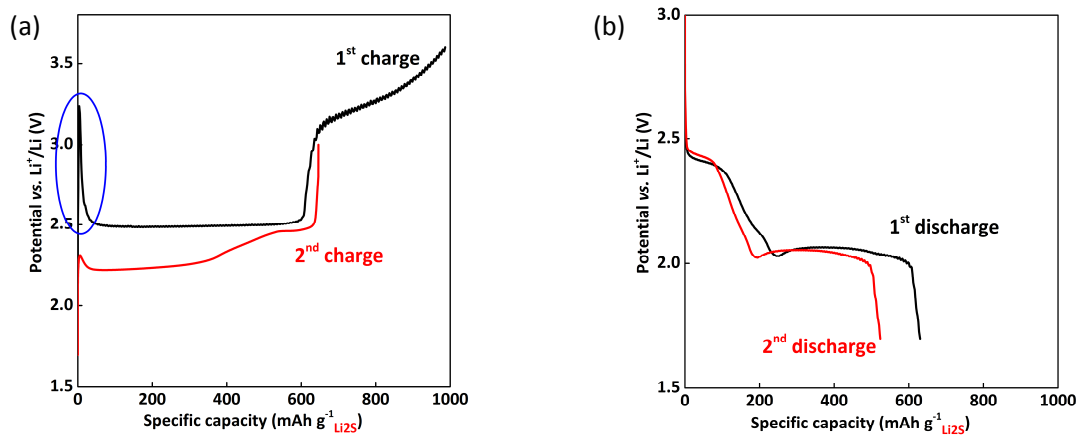


Figure 13. Réponse électrochimique d'une électrode Li<sub>2</sub>S/SuperP<sup>®</sup>/PVdF cyclée vs. Li à C/20. Profil du potentiel des deux premières charges (a) et des deux premières décharges (b). Quantité de matière active 1,23 mg<sub>Li<sub>2</sub>S</sub> cm<sup>-2</sup>. Marque en bleu montrant l'activation initiale du système.

Comme observé sur la Figure 13a, le profil de la première charge diffère de celui de la charge suivante, de plus un phénomène d'activation est observé dès le début de la première charge. Ce phénomène est généralement observé pour les électrodes de Li<sub>2</sub>S, et est associé à la difficulté d'oxyder Li<sub>2</sub>S présent sous forme de particules micrométriques. La fin de la charge s'accompagne d'une augmentation continue du potentiel avec des valeurs augmentant jusqu'à plus de 3,5 V, ce qui n'est plus observé lors des cycles suivants.

Malgré un protocole d'élaboration des électrodes reproductibles, l'allure de la première charge diffère d'une électrode à l'autre (Figure 14a), sans pouvoir relier cette évolution à des paramètres d'électrode, comme la quantité de Li<sub>2</sub>S par cm<sup>2</sup>, par exemple.

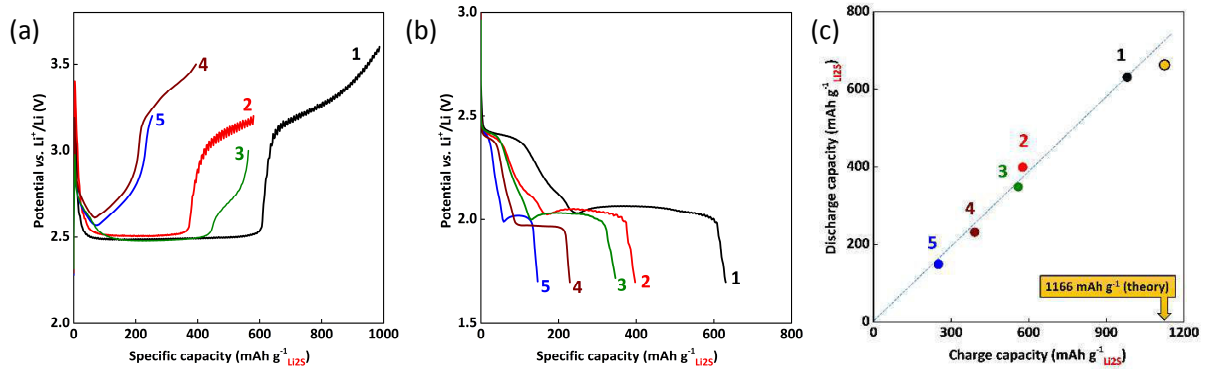


Figure 14. Exemples de profils de charge initiale (a) et décharges correspondantes (b) lors du cyclage d'une électrode  $\text{Li}_2\text{S}/\text{SuperP}^{\text{®}}/\text{PVdF} = 70/20/10 \text{ wt\%}$  vs. Li à C/20 ou C/10, avec différentes valeurs du potentiel de coupure. Relation linéaire entre capacité de charge et de décharge (c).

Malgré des profils de charge différents, les différentes décharges présentent les profils attendus (Figure 14b). Il est ainsi évident que le processus électrochimique obtenu à haut potentiel n'est pas associé à des réactions parasites, mais bien à l'oxydation de  $\text{Li}_2\text{S}$ , puis des longs polysulfures en soufre. De ce fait, une relation linéaire entre capacité de première décharge et capacité de première charge est obtenue (Figure 14c).

Afin de mieux appréhender le mécanisme électrochimique mis en jeu, des mesures GITT ont été réalisées. Cette technique permet de mesurer, pour différents états de charge, le potentiel à l'équilibre du système (Figure 15).

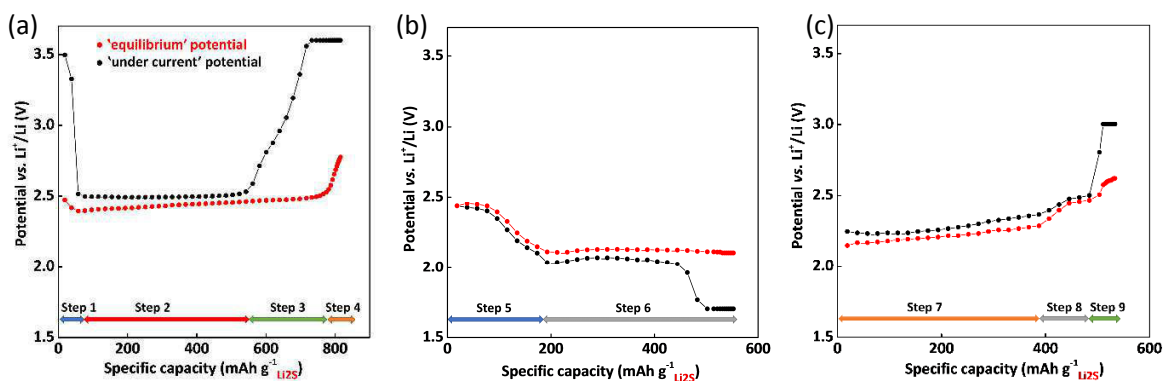


Figure 15. Résultats de la mesure GITT obtenus pour une cellule  $\text{Li}/\text{Li}_2\text{S}$ . La mesure GITT est composée de séquences galvanostatiques à C/20 de 20 minutes, *i.e.* courant de  $98 \mu\text{A cm}^{-2}$ , suivies d'un temps de relaxation de 30 min: 1<sup>st</sup> charge (a), 1<sup>st</sup> décharge (b), 2<sup>nd</sup> charge (c).

Il est clair que les potentiels à l'équilibre, lors de la première et de la deuxième charges sont différents, impliquant des mécanismes électrochimiques différents. De plus, les études DRX *in situ* de cellules Li/Li<sub>2</sub>S au cours du cyclage, ont montré la présence de Li<sub>2</sub>S pendant quasi toute la charge, avec la formation de soufre en fin de charge. La Figure 16 résume le mécanisme proposé pour expliquer le profil de la première charge.

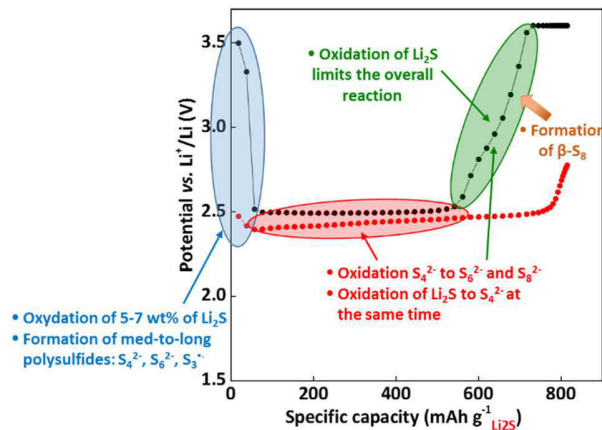


Figure 16. Mécanisme proposé pour la première charge de Li<sub>2</sub>S.

La première charge requière ainsi des conditions particulières, afin d'augmenter la capacité du système. L'activation initiale ('step 1') induisant un saut de potentiel important, le potentiel de coupure du premier cycle doit être relativement élevé, sans entraîner une dégradation prématurée de l'électrolyte. Afin de limiter cette augmentation de potentiel, différentes stratégies peuvent être utilisées, comme une première charge à régime lent ou l'addition d'une faible quantité de polysulfures dans l'électrolyte. Cependant, même pour une première charge présentant une capacité proche de la valeur théorique, (1166 mAh g<sup>-1</sup>), les capacités obtenues en décharge restent voisines de ~ 650 ± 50 mAh g<sup>-1</sup>. Les raisons de cette perte de capacité peuvent être associées à (i) une surface d'électrode insuffisante pour permettre la précipitation des composés de fin de décharge, (ii) une accessibilité faible des polysulfures à l'électrode et (iii) une perte de matière active dans l'électrolyte ou à la surface du lithium métal. L'utilisation d'un collecteur de courant en carbone non tissé (NwC) peut permettre d'améliorer les performances des électrodes de Li<sub>2</sub>S, en effet ce collecteur 3D, a permis d'obtenir des résultats très intéressants pour le système Li/S. La Figure 17 montre le cyclage de deux électrodes de Li<sub>2</sub>S, l'une déposée sur un collecteur en

aluminium, l'autre sur le NwC. Une nette amélioration des capacités est obtenue avec le NwC à faible régime, montrant le caractère bénéfique d'une structure 3D.

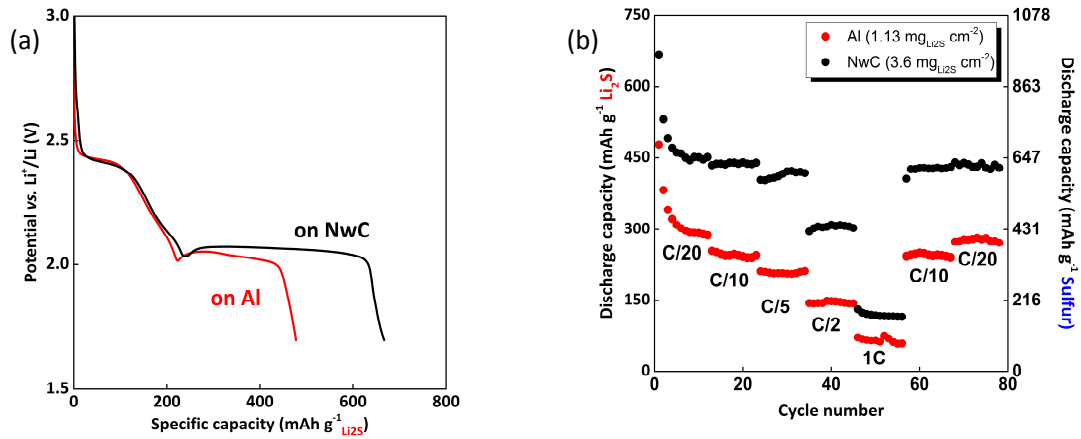


Figure 17. Profils des premières décharges (a) obtenues par cyclage galvanostatique d'une électrode Li<sub>2</sub>S/SuperP®/PVdF déposée sur deux collecteurs de courant Al (en rouge) et NwC (en noir). Les deux électrodes ont cyclé vs. Li à C/20 entre 3,8 V – 1,7 V pour le premier cycle, et entre 2,8 V – 1,7 V pour les suivants. Tenue en cyclage lors du test de puissance (b).

Après avoir évalué, les performances d'une électrode de Li<sub>2</sub>S vis-à-vis d'une électrode de lithium métal, l'étape suivante a été d'étudier le comportement d'une cellule complète Si/Li<sub>2</sub>S. La négative de silicium a été choisie pour, essentiellement, deux raisons: (i) le Si présente une forte capacité et (ii) il peut être cyclé en présence d'un électrolyte à base d'éthers (ce qui n'est pas possible avec le graphite, du fait de phénomène d'exfoliation). La Figure 18 compare la cyclabilité de cellules Li<sub>2</sub>S/Si et Li<sub>2</sub>S/Li. Des performances similaires sont obtenues, avec une bonne cyclabilité du système Li<sub>2</sub>S/Si sur une centaine de cycles.

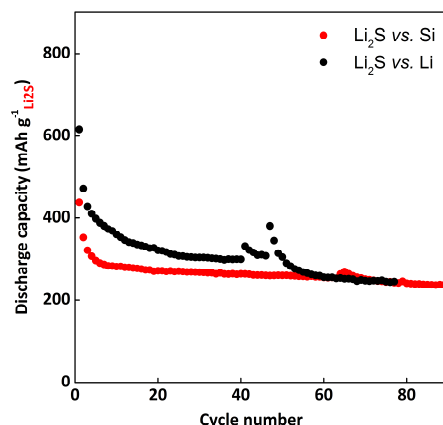


Figure 18. Performance de la cellule Si/Li<sub>2</sub>S (C/20) avec deux électrodes négatives différentes Si (en rouge) et Li (en noir).

## **Chapter 5: Mesure DRX *in situ* et *operando*: Etude des modifications structurales au cœur du matériau actif**

La diffraction des Rayons X a été largement utilisée pour suivre les modifications structurales de l'électrode positive de soufre au cours du cyclage. Quelques études reportent l'utilisation des DRX *in situ* pour suivre l'évolution des changements structuraux du système Li/S au cours du cyclage. Cependant, les opinions restent divisées sur des questions importantes comme l'apparition et la disparition du soufre et de Li<sub>2</sub>S lors du cyclage, et la réversibilité des phénomènes électrochimiques. L'un des objectifs de notre étude a été d'observer les changements structuraux au cours du cyclage, de les relier aux nombres d'électrons échangés et de répondre à certaines questions posées.

Les études DRX *in situ* et *operando* ont été réalisées en utilisant deux appareils synchrotrons: ESRF (Grenoble, France) et SOLEIL (Saclay, France), ce qui nous a permis d'étudier différentes cellules Li/S au cours du cyclage. L'influence du régime (C/20 et C/8) et du nombre de cycles ont également été évalués. L'analyse des résultats a été menée avec une approche originale qui a permis d'obtenir une évolution quantitative de Li<sub>2</sub>S au cours du cyclage et de proposer un mécanisme de formation des composés solides. Une cellule souple comprenant trois trous a été



conçue spécifiquement (Figure 19) afin d'étudier l'évolution de la cellule complète et l'évolution de chacune des électrodes (position [1] et [3]).

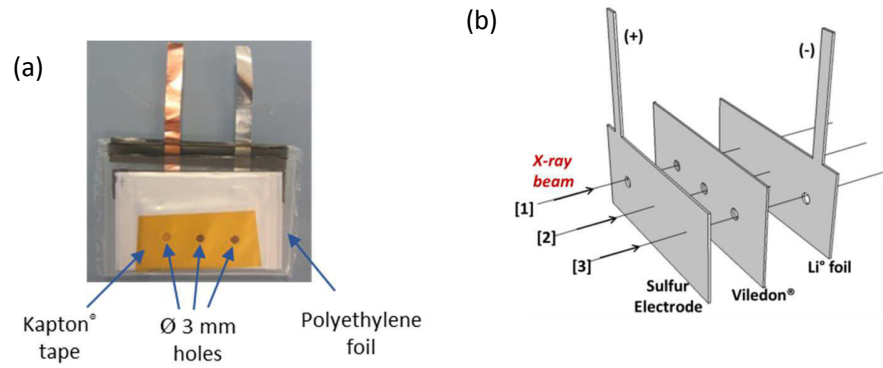
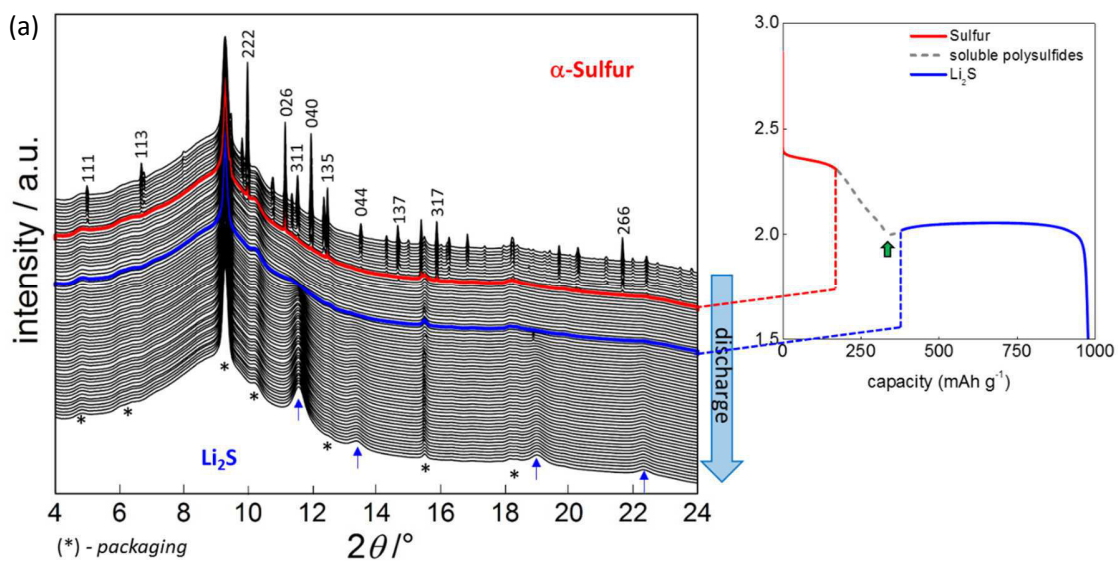


Figure 19. Cellule souple pour étude *In situ* DRX (a) et représentation schématique de celle-ci (b)

La Figure 20 présente les spectres DRX enregistrés durant le premier cycle à C/20, et les données électrochimiques correspondantes. La courbe de cyclage présente le profil classique d'une cellule Li/S avec des capacités de décharge et de charge de  $980 \text{ mAh g}^{-1}$  et  $976 \text{ mAh g}^{-1}$  respectivement.



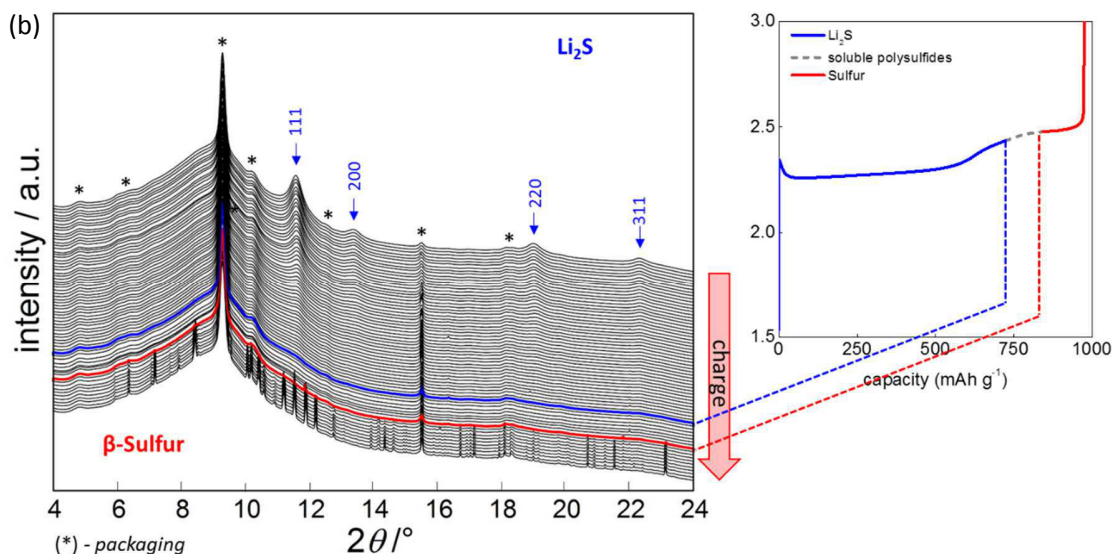


Figure 20. Spectres DRX *in situ* obtenus sur la cellule complète (position [2]) durant la première décharge (a) et charge (b). Les lignes continues indiquent précisément la transition phase solide/composé soluble.

Le diffractogramme de la cellule avant cyclage présente les raies du soufre  $\alpha$  de structure orthorhombique ( $\alpha\text{-S}_8$ ). Durant la décharge, l'intensité des raies décroît, pour disparaître totalement à la fin du premier plateau de la décharge, ce qui prouve que tout le soufre est consommé par réduction avec formation de polysulfures solubles. Entre les deux plateaux de décharge (2,3 V – 2,0 V), le matériau actif est soluble et aucune raie DRX n'est détectée. Au début du second plateau, quatre raies ((111), (200), (220) et (311)) associées aux  $\text{Li}_2\text{S}$  cristallins commencent à croître. Une taille de cristallites de  $\text{Li}_2\text{S}$  de  $\sim 8,8$  nm est obtenue en fin de décharge. Nos résultats *in situ* et *operando* montrent clairement, pour la première fois, la formation de  $\text{Li}_2\text{S}$  cristallin sur l'électrode positive dès le début du plateau à bas potentiel, indiquant des réactions électrochimiques (*i.e.* réduction of  $\text{S}_4^{2-}$ ,  $\text{S}_3^{2-}$ ,  $\text{S}_2^{2-}$ ) simultanées et non consécutives (Figure 21a). Lors de la charge, la disparition de  $\text{Li}_2\text{S}$  est observée mais du fait de son caractère isolant et insoluble,  $\text{Li}_2\text{S}$  est présent jusqu'à un état de charge de 75 %. A la fin de la charge, les polysulfures solubles sont oxydés en  $\text{S}_8$  cristallin. Le soufre ne revient pas à sa structure initiale ( $\alpha\text{-S}_8$ ), mais il apparaît sous sa forme monoclinique, le  $\beta$ -soufre, bien que celui-ci soit instable thermodynamiquement. Ces travaux de thèse sont les premiers à avoir montré ce changement structural du soufre en  $\beta\text{-S}_8$ . La structure  $\beta\text{-S}_8$  se transforme en  $\alpha\text{-S}_8$  lors de la relaxation de la batterie.

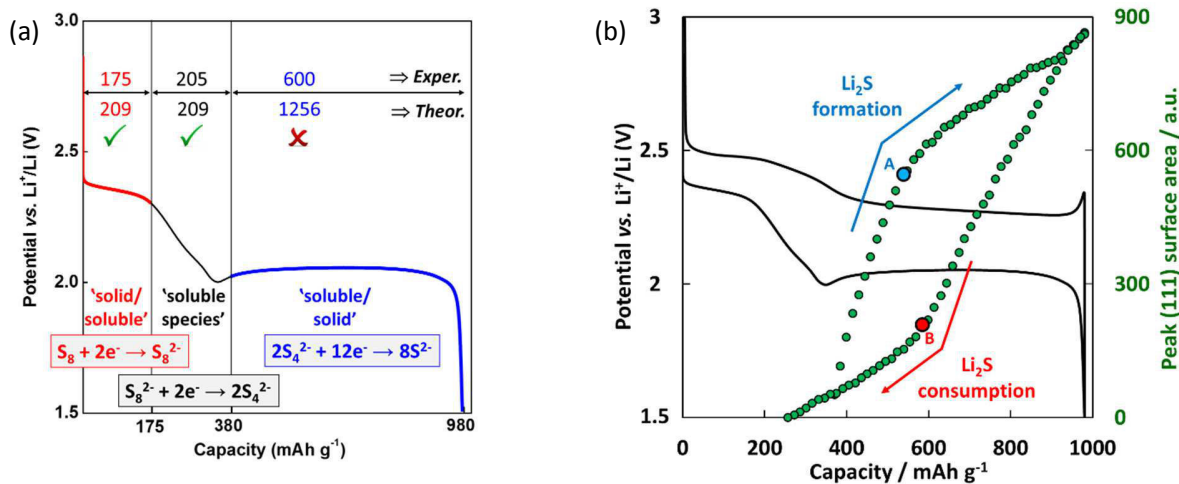


Figure 21. Comparaison des capacités (théorique vs. expérimentale) obtenues pour les différentes zones (a); formation de Li<sub>2</sub>S (bleu) et consommation de Li<sub>2</sub>S (rouge) au cours du cycle initial à C/20. Evolution de l'aire de la raie (111) en fonction de la capacité.

Afin d'obtenir une évolution quantitative du Li<sub>2</sub>S formé/consommé et de proposer un mécanisme électrochimique de réduction/oxydation des polysulfures, une méthodologie spécifique a été mise en place. Une étude par DRX *ex situ* de mélanges Li<sub>2</sub>S/S<sub>8</sub> de compositions définies a permis d'associer l'aire de la raie (111) de Li<sub>2</sub>S à la quantité de Li<sub>2</sub>S formé. Le processus de réduction se produit en deux étapes, tout d'abord, la réduction des S<sub>4</sub><sup>2-</sup> avec formation uniquement de Li<sub>2</sub>S, puis une réaction concurrentielle apparaît, les données, en termes d'électrons échangés, sont cohérentes avec la formation de la phase Li<sub>2</sub>S<sub>2</sub> en addition de Li<sub>2</sub>S. Ce changement de mécanisme électrochimique pourrait être attribué au recouvrement de la surface de l'électrode par un film passif de Li<sub>2</sub>S. Dans nos conditions expérimentales, le produit de fin de décharge est composé d'un mélange Li<sub>2</sub>S<sub>2</sub>/Li<sub>2</sub>S comprenant majoritairement Li<sub>2</sub>S<sub>2</sub> (*i.e.* 60 %). Lors de la charge, Li<sub>2</sub>S et Li<sub>2</sub>S<sub>2</sub> semblent s'oxyder à des vitesses similaires. Durant la deuxième étape de charge, l'oxydation de Li<sub>2</sub>S devient moins sélective, du fait de l'oxydation aisée des polysulfures à longues chaînes présents dans l'électrolyte.

Cette évolution a été suivie sur un grand nombre de cycles, les formation/consommation de Li<sub>2</sub>S (et S<sub>8</sub>) sont obtenues pour des états de charge/décharge similaires au 26<sup>th</sup> cycle qu'au premier. L'effet du régime a également été évalué, l'hystéresis observée à C/20 est également obtenue pour un régime élevé de C/8. La formation de β-S<sub>8</sub> à la fin de la charge a également été confirmée sur un grand nombre de cycles.

## **Chapter 6: Utilisation de la Spectroscopie d'Impédance Electrochimique (SIE) pour la caractérisation des cellules Li/S**

L'étude DRX a permis d'apporter des informations pertinentes sur la formation/consommation des composés cristallins, pour aller plus en avant dans la compréhension des mécanismes électrochimiques du système Li/S, nous avons mené des études par spectroscopie d'impédance électrochimique (SIE). Des études menées par SEI dans la littérature l'ont été avec différents objectifs comme la caractérisation des propriétés de transport (mesure de conductivité), étude des films passifs, évaluation de la réponse électrique des électrodes en fonction de leur composition et l'étude des mécanismes électrochimiques. La technique SIE est facile à mettre en place, par contre l'interprétation des résultats est difficile. Et de nombreuses interprétations divergeantes sont reportées dans la littérature.

Des études à basses températures (cyclage et SIE) ont aussi été menées, afin d'obtenir des informations sur les cinétiques de réaction, les basses températures permettant de séparer plus facilement les phénomènes électrochimiques.

Toutes les mesures SIE ont été réalisées sur des cellules classiques deux-électrodes Li/S, avec comme électrode positive une électrode 'S-on-NwC', et des électrodes de lithium comme électrode de référence et contre-électrode. Nous n'avons pas utilisé de systèmes trois électrodes, pour des problèmes de reproductibilité liés à l'absence d'une électrode de référence stable. Cependant, afin de pouvoir séparer les contributions des deux électrodes, des cellules symétriques (Li-Li et S<sub>8</sub>-S<sub>8</sub>) ont été réalisées et les spectres d'impédance mesurés. Cette méthodologie a permis d'associer la réponse électrochimique du système Li/S à des phénomènes physiques.

La Figure 22 présente les réponses obtenues par SIE d'une cellule complète Li/S et de cellules symétriques Li||Li et S<sub>8</sub>||S<sub>8</sub>.

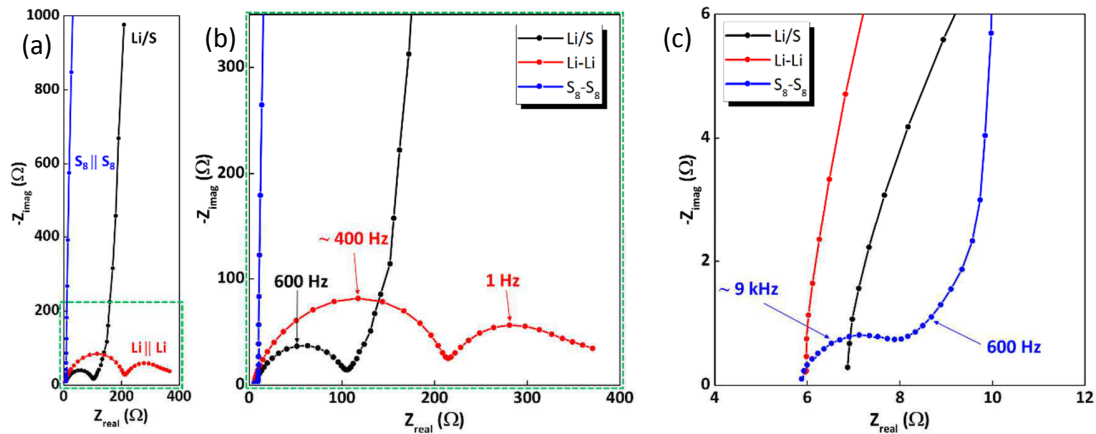


Figure 22. Diagrammes de Nyquist obtenus pour la cellule Li/S avant cyclage (en noir), cellules symétriques Li||Li (en rouge) et S8||S8 (en bleu) (a,b); Réponse HF du système S8||S8 (c).

Il est clair que la réponse MF (Moyenne Fréquence) de la cellule Li/S peut être associée à la réponse de l'électrode négative de lithium, plus précisément au film passif formé à sa surface. De plus, la résistance mesurée dépend de l'état initial du lithium (lithium nettoyé, passivé, etc.). La réponse de l'électrode positive est seulement visible à basse fréquence avec le comportement capacitif de l'électrode de soufre, le soufre ayant un caractère isolant. La réponse MF de l'électrode de soufre est de faible intensité et est associée à la morphologie de l'électrode composite. La réponse HF est attribuée à la résistance de l'électrolyte. Après l'identification des différents composants de la réponse obtenue par SIE, les spectres d'impédance ont été mesurés en fonction de l'état de charge/décharge. La Figure 23 présente l'évolution des graphes d'impédance, dans le plan de Nyquist, au cours du cyclage.

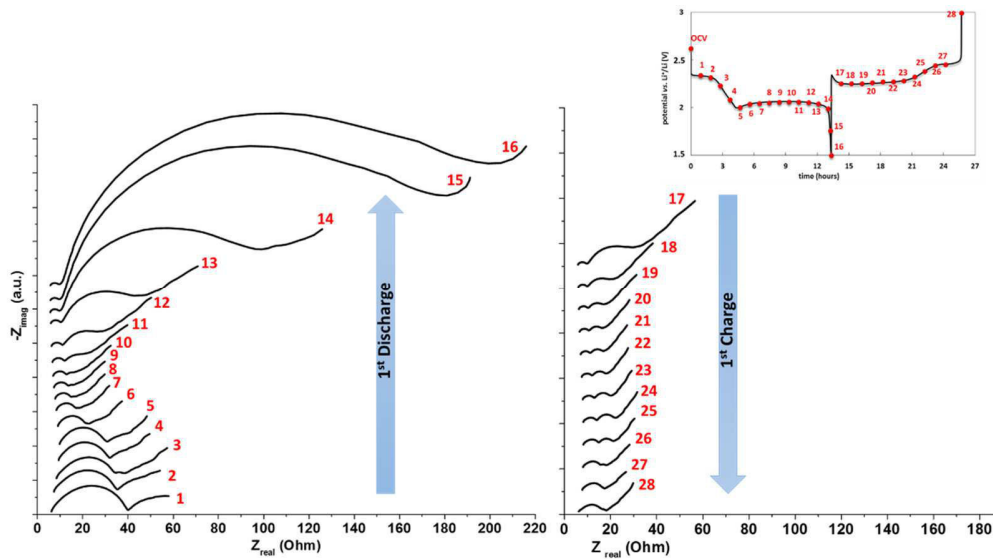


Figure 23. Evolution des spectres d'impédance dans le plan de Nyquist au cours la première décharge et charge. Le numéro du spectre est indiqué en rouge.

Afin de définir un circuit équivalent pertinent, des cellules symétriques ont été réalisées à partir d'électrodes cyclées à 2,1 V et 1,5 V, et leurs réponses électrochimiques ont été mesurées. Suite à cette méthodologie, nous avons proposé un circuit équivalent permettant de lisser les différentes réponses obtenues au cours du cyclage (Figure 24).

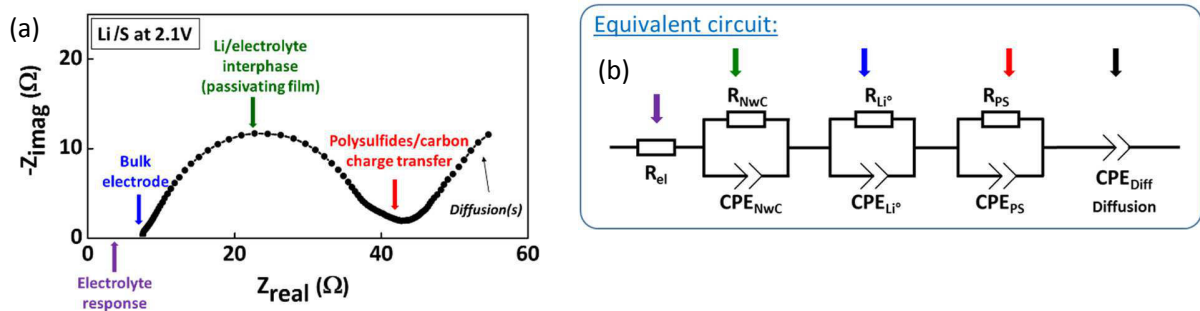


Figure 24. Réponse par SIE d'une cellule Li/S à 2,1 V et sens physique des différentes réponses en fréquence (a); circuit équivalent utilisé pour le lissage des réponses SIE (b).

La discussion suivante va reprendre les différentes interprétations des résultats obtenus en fonction de la fréquence de la réponse: (i) HF, (ii) MF et (iii) LF.

(i) *Région des Hautes Fréquences (> 100 kHz)*

Pour éviter les réponses parasites, les mêmes câbles et boîtier ont été utilisés pour les différentes mesures, l'évolution de la réponse HF est ainsi attribuable qu'à l'évolution de la résistance de l'électrolyte ( $R_{el}$ ). Lors de la décharge, la matière active est réduite sous la forme de polysulfures solubles dans l'électrolyte ( $\text{Li}_2\text{S}_x$ ,  $3 < x \leq 8$ ). Cette dissolution induit une augmentation de la viscosité de l'électrolyte et une augmentation du nombre de porteurs de charge, une évolution de la résistance de l'électrolyte au cours du cyclage est de ce fait attendue (Figure 25).

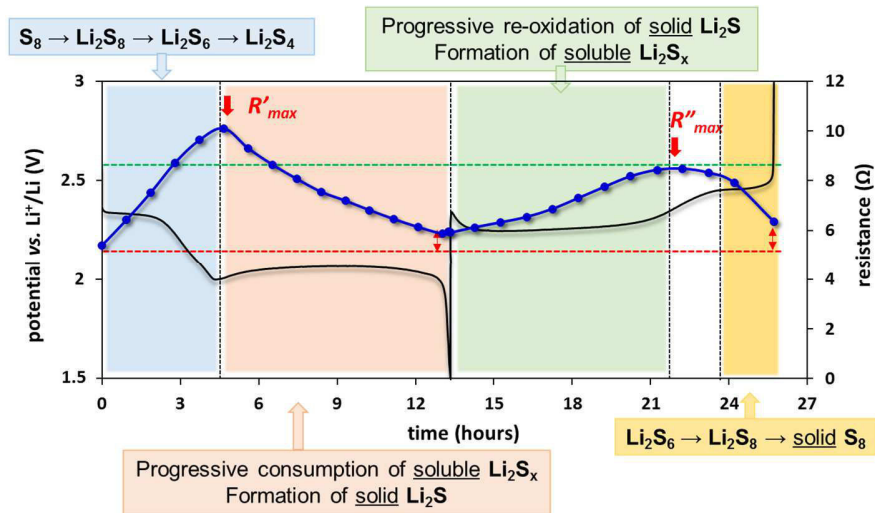


Figure 25. Evolution de la résistance de l'électrolyte au cours du premier cycle, le profil en potentiel est également donné.  $R'_{max}$  et  $R''_{max}$  correspondent aux valeurs maximales de la résistance de l'électrolyte en décharge et en charge respectivement. La ligne en pointillés rouges indique la valeur initiale de la résistance de l'électrolyte, sans polysulfure. La ligne en pointillés verts indique le niveau maximum de la résistance lors de la charge.

On peut, dans un premier temps, noter que l'évolution de la résistance de l'électrolyte est différente lors de la décharge et de la charge, indiquant un mécanisme différent (voir partie sur l'étude DRX). La différence de résistance pour  $R'_{max}$  et  $R''_{max}$  vient du fait que les espèces en présence, pour ces états de décharge/charge particuliers, sont différents. En appui de cette mesure, des études de viscosité de différentes solutions ont été réalisées. Les viscosités de solutions de polysulfures ( $\text{Li}_2\text{S}_4$ ,  $\text{Li}_2\text{S}_6$ ,  $\text{Li}_2\text{S}_8$ ) pour une même concentration (0,1 M) et d'une solution de ( $\text{Li}_2\text{S}_4$ ) à différentes concentrations ont été déterminées. Plus la chaîne de polysulfures est courte, plus la viscosité est élevée, ainsi ( $\text{Li}_2\text{S}_4 \gg \text{Li}_2\text{S}_6 > \text{Li}_2\text{S}_8$ ). L'augmentation de la concentration en  $\text{Li}_2\text{S}_4$  de 0,1M à 1 M fait augmenter de manière très importante la viscosité de la solution, de plus la solution a un

comportement thixotrope i.e. diminution de la viscosité lors du cisaillement, indiquant des interactions fortes au sein de la solution au repos. L'effet viscosité est donc un paramètre important qui permet d'expliquer l'augmentation de la résistance de l'électrolyte malgré une augmentation du nombre de porteurs de charge.

De plus, une corrélation a été obtenue entre l'évolution de la résistance  $R'_{max}$  et la capacité en décharge en fonction du nombre de cycles (Figure 26). Cette évolution semble indiquer qu'au cours du cyclage la concentration en polysulfures devient plus faible dans l'électrolyte, indiquant une perte de matière active sous la forme de composés insolubles, précipités à la surface des électrodes ou au sein de l'électrolyte.

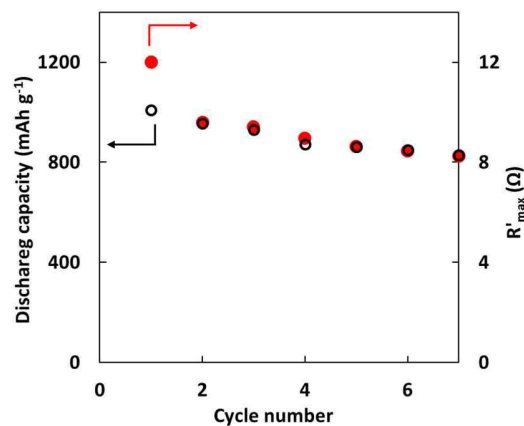


Figure 26. Valeur de la capacité de décharge (en noir) et de la résistance maximale ( $R'_{max}$ ) (en rouge) en fonction du nombre de cycles

(i) ***Région des Moyennes Fréquences (50 kHz – 1 Hz)***

Comme indiqué précédemment, les modifications de la réponse MF sont essentiellement attribuées à l'électrode négative<sup>2</sup> de lithium ( $R_{Li}/ICPE_{Li}$ ), et plus précisément à la réponse du film de passivation initialement présent à sa surface. Nous pouvons noter une diminution significative de la valeur de la résistance dès le début de la décharge (Figure 27), suivie d'une stabilisation de sa valeur au cours de la décharge.



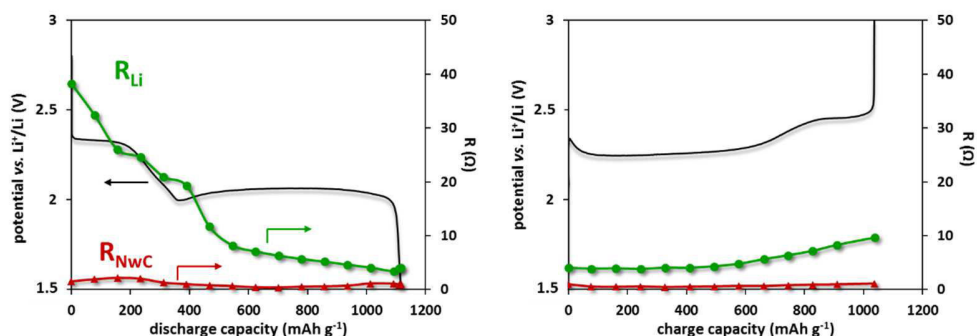


Figure 27. Evolution des valeurs de résistance de l'interphase Li/électrolyte,  $R_{Li}$  (vert) et réponse du volume de l'électrode positive (rouge), surimposition de la courbe de tension.

Dès le début de la décharge, l'oxydation du lithium débute et induit une modification notable du film passif formé à la surface de l'électrode. La contribution de la réponse de l'électrode positive reste constante ( $R_{NWC}/CPE_{NWC}$ ). Cette contribution ( $\sim 1 - 2 \Omega$ , à  $\sim 6 - 9 \text{ kHz}$ ) est masquée par la réponse du lithium à l'état initial, et devient plus visible par la suite, du fait de la diminution de cette dernière.

La Figure 28 montre l'évolution du demi-cercle à LF attribué à la réaction de transfert de charge ( $R_{PS}/CPE_{PS}$ ), associée à la réduction des polysulfures. Cette réponse commence à être visible au début du deuxième plateau de décharge (spectre 6), elle croit en intensité le long du plateau de décharge, jusqu'à la fin de celle-ci. Cette évolution peut être associée à la formation d'un film passif isolant à la surface de l'électrode positive par dépôt de  $\text{Li}_2\text{S}$ , ce qui limite la cinétique de la réaction de transfert et les phénomènes de transport de matière.

Lors de la charge, cette réponse décroît rapidement, du fait de l'oxydation de  $\text{Li}_2\text{S}$ . Lors de la décharge, une augmentation de la capacité est observée à partir du milieu du premier plateau, suivie d'une décroissance rapide, ce qui peut être associée à une modification du mécanisme électrochimique le long du deuxième plateau de décharge en accord avec l'étude DRX.

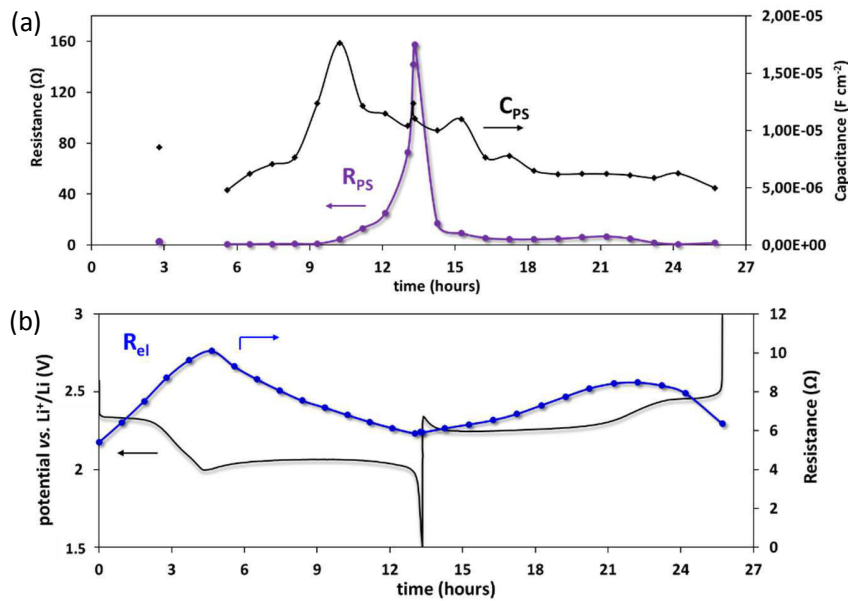


Figure 28. Valeur de résistance et de capacité (a) obtenues par le lissage de la réponse LF (réaction de transfert de charge des polysulfures), profil de cyclage et évolution de la résistance de l'électrolyte (b).

Lors du cyclage à basse température, un troisième plateau en potentiel apparaît clairement entre les deux plateaux généralement observés (Figure 29). Le plateau, à plus bas potentiel, est très dépendant de la température car associé à la formation de  $Li_2S/LiS_2$  composés pas ou peu solubles. La présence d'un seul plateau quel que soit la température est cohérent avec la formation de  $Li_2S$  dès le début du plateau. L'étude par SIE menée à basse température montre une évolution notable de la résistance de l'électrolyte avec un comportement différent de celui obtenu à température ambiante. En particulier, la résistance en fin de décharge reste élevée indiquant la présence de polysulfures en solution, cohérent avec la perte de capacité observée.

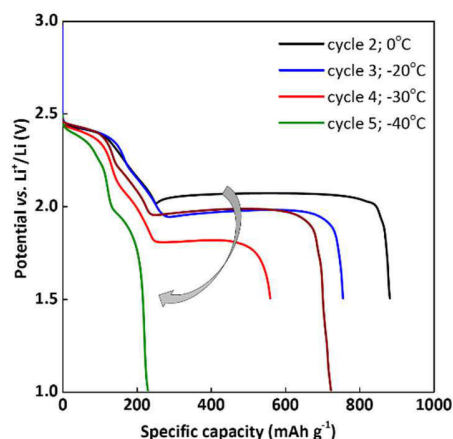


Figure 29. Profils de décharge obtenus à différentes températures 0 °C à -40 °C, cyclage à C/100.

## Conclusions

En conclusions, ces travaux ont permis à la fois de gagner en termes de compréhension du système Li/S et de proposer des solutions innovantes pour l'optimisation des composants et l'amélioration des performances électrochimiques. Le développement d'une méthode simple mais performante pour la préparation des électrodes de soufre sur feutre de fibres de carbone a permis d'améliorer à la fois les performances et les taux de chargement en soufre des électrodes. L'influence des composants d'électrode tels que le liant ou le carbone a été étudié, notamment au travers de mesures de spectroscopie d'impédance électrochimique. Il a été mis en avant l'importance de l'homogénéité de l'électrode vis-à-vis de la polarisation finale de la batterie. L'utilisation du collecteur poreux et 3D en fibres de carbone s'est avérée performante, à la fois pour le soufre élémentaire et le matériau  $\text{Li}_2\text{S}$ . Ce dernier a été étudié du point de vue mécanistique, et un mécanisme de première charge a été proposé. Une preuve de concept d'un accumulateur Li-ion/soufre a également pu être démontrée en pile bouton. Enfin, une étude poussée par diffraction des rayons X et par spectroscopie d'impédance électrochimique a permis d'avancer dans la compréhension des mécanismes et réactions complexes en jeu lors de la charge et de la décharge d'un accumulateur Li/S. Un mécanisme de formation des composés de fin de décharge,  $\text{Li}_2\text{S}$  et  $\text{Li}_2\text{S}_2$  a été proposé, tandis que l'évolution des composants d'une batterie Li/S a été suivie en cyclage par impédance. Ainsi, les paramètres clés du système ont pu être déterminés.

## - Résumé -

### « Accumulateurs Lithium/Soufre: développement et compréhension des mécanismes électrochimiques »

Dans ce travail de thèse, deux objectifs ont été fixés. Le premier a été de mieux comprendre le mécanisme très complexe qui est en jeu dans les accumulateurs Li/S. Pour cela, les modifications structurales du matériau actif ont été observées *in operando* et ont permis de valider un modèle clair concernant les réactions de transformations de phases qui contrôlent le lithium/soufre. La cristallisation d'une forme métastable du soufre (bêta-S<sub>8</sub> monoclinique) en fin de recharge a ainsi été observée pour la première fois lors d'expériences au synchrotron de l'ESRF. La technique d'impédance électrochimique a également donné d'importantes informations sur les cinétiques de ces réactions. Le deuxième objectif visait l'amélioration du système Li/S par l'optimisation des électrodes de soufre afin d'augmenter leurs performances mais également par la fabrication d'électrodes de Li<sub>2</sub>S efficaces permettant la transition vers le Li-ion/S, plus sécuritaire.

Mots clefs: Accumulateurs Lithium/Soufre, Li/S, mécanismes électrochimiques, β-Soufre, *in situ et operando* DRX, spectroscopie d'impédance électrochimique (SIE), non-tissé de fibres de carbone, électrode de Li<sub>2</sub>S

---

## - Abstract -

### « Lithium/Sulfur batteries: development and understanding of the working mechanisms »

In this work two main aspects has been conducted in parallel. The first one was focused on better understanding the very complex working mechanism of Li/S cell. Structural changes evolution of active material upon real time battery operation was explored, giving a clear answer on the solid/liquid reaction evolution, which govern the electrochemistry of Li/S technology. Formation of another allotropic form of sulfur (monoclinic beta-S<sub>8</sub>) during recharging the battery have been reported for the first time ever in Li/S community. Impedance technique applied to such system provided additional information concerning the kinetics of these reactions. Apart from that, another aspect targeted rather on improvements of already existing solutions (making better sulfur electrodes, with significantly improved specific capacities) as well as development the alternative solutions, i.e. fabrication and test of new Li<sub>2</sub>S-based positive electrodes, which could be a promising transition from classical Li/S cells into safer Li-ion/S batteries.

Key words: Lithium/Sulfur batteries, Li/S, working mechanism, β-Sulfur, *in situ* and *operando* XRD, electrochemical impedance spectroscopy (EIS), non-woven carbon, Li<sub>2</sub>S positive electrode